



Tenth Biennial Coherent Laser Radar Technology and Applications Conference

Compiled by

M.J. Kavaya

Marshall Space Flight Center, Marshall Space Flight Center, Alabama

Proceedings of a conference held
in Mount Hood, Oregon,
June 28–July 2, 1999

National Aeronautics and
Space Administration

Marshall Space Flight Center • MSFC, Alabama 35812

Available from:

NASA Center for AeroSpace Information
7121 Standard Drive
Hanover, MD 21076-1320
(301) 621-0390

National Technical Information Service
5285 Port Royal Road
Springfield, VA 22161
(703) 487-4650

Table of Contents

CLRC '99 Sponsors	iv
Conference Digest	
Welcome	v
Conference Chair	v
Conference Organization	v
Exhibits	v
Foreward	v
Scope	v
Past Conferences	vi
Topics to be Presented	vi
Acknowledgements	vi
Conference Program Committee	vii
Conference Advisory Committee	viii
Conference Schedule	ix
Conference Abstracts and Papers	1-316
Index	317-319

CLRC '99 SPONSORS

***National Aeronautics and Space Administration
Headquarters/Office of Earth Science***

***National Aeronautics and Space Administration/
Marshall Space Flight Center/
Global Hydrology and Climate Center***

***National Polar-orbiting Operational Environmental Satellite
System Integrated Program Office***

***National Aeronautics and Space Administration/
New Millennium Program***

***Air Force Research Laboratory/
Directed Energy Directorate***

***National Aeronautics and Space Administration/
Langley Research Center***

CONFERENCE DIGEST

WELCOME, TO THE 10TH BIENNIAL COHERENT LASER RADAR TECHNOLOGY AND APPLICATIONS CONFERENCE (CLRC)

Location:

Timberline Lodge
Mt. Hood, Oregon
June 28 – July 2, 1999

CLRC'99 Conference Chair:

Dr. Michael J. Kavaya
NASA Marshall Space Flight Center
Global Hydrology and Climate Center
Huntsville, AL 35812
256-922-5803
michael.kavaya@msfc.nasa.gov

CLRC'99 Organization:

Debra G. Hallmark and L. Gayle Brown
Universities Space Research Association (USRA)
4950 Corporate Drive, Suite 100
Huntsville, AL 35805
256-895-0582
<http://space.hsv.usra.edu>

Exhibits Presented by:

- Coherent Technologies, Inc.
- DFM Engineering
- Ontar Corporation

Foreward:

The tenth conference on Coherent Laser Radar: Technology and Applications is the latest in a series beginning in 1980 which provides a forum for exchange of information on recent events, current status, and future directions of coherent laser radar (or lidar or ladar) technology and applications.

Scope:

This conference emphasizes the latest advancements in the coherent laser radar field, including theory, modeling, components, systems, instrumentation, measurements, calibration, data processing techniques, operational uses, and comparisons with other remote sensing technologies.

Past Conferences:

Year	Location	Chair	Co-chair
1980	Aspen, CO USA	Huffaker	none
1983	Aspen, CO USA	Huffaker	Vaughan
1985	United Kingdom	Vaughan	Huffaker
1987	Aspen, CO USA	Bilbro	Werner
1989	Munich, Germany	Werner	Bilbro
1991	Snowmass, CO USA	Hardesty	Flamant
1993	Paris, France	Flamant	Menzies
1995	Keystone, CO USA	Menzies	Steinvall
1997	Sweden	Steinvall	Kavaya
1999	<i>Mount Hood, OR USA</i>	<i>Kavaya</i>	<i>Willetts</i>

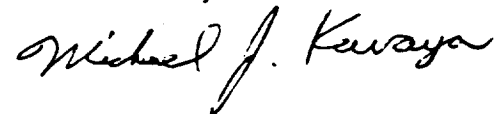
Topics to be presented:

- Aircraft Operations
- Aircraft Missions
- Vibration Measurements
- DIAL
- Theory and Simulation
- Spaceborne Lidars
- New Technology
- Target Characterization
- Detection Advances
- Laser Advances
- System Advances
- CW Lidars
- Wind Measurements

Acknowledgements:

I greatly appreciate the Sponsors and the Program Committee members for their contributions to the CLRC'99. Their dedication and commitment to the Coherent Laser Radar Program is highly commended. I would also like to give a special thank you to Debra and Gayle for the planning and execution of the CLRC'99 and the Conference Digest.

Michael J. Kavaya



Conference Program Committee

Steven B. Alejandro

USAF/AFRL, Albuquerque, NM USA

Kasuhiko Asai

Tohoku Institute of Technology, Japan

Alain Dabas

Meteo-France, Toulouse, France

Rod G. Frehlich

University of Colorado, Boulder, CO USA

Sammy W. Henderson

Coherent Technologies, Inc., Lafayette, CO USA

J. Fred Holmes

Oregon Graduate Institute, Portland, OR USA

Steven C. Johnson

NASA/Marshall Space Flight Center, Huntsville, AL USA

Michael J. Kavaya

NASA/Marshall Space Flight Center/Global Hydrology and Climate Center, Huntsville, AL USA

Dennis K. Killinger

University of South Florida, Tampa, FL USA

Paul F. McManamon

USAF/AFRL, Dayton, OH USA

Stephan Rahm

DLR German Aerospace Center, Wessling, Germany

Richard D. Richmond

USAF/AFRL, Dayton, OH USA

Barry J. Rye

NOAA Environmental Technology Laboratory, Boulder, CO USA

Upendra N. Singh

NASA Langley Research Center, Hampton, VA USA

David M. Tratt

Jet Propulsion Laboratory, Pasadena, CA USA

David V. Willetts

Defence Evaluation and Research Agency (DERA), Great Malvern, UK

Peter Winzer

Technische Universitat Wien, Wien, Austria

Conference Advisory Committee

James W. Bilbro

NASA / Marshall Space Flight Center, Huntsville, AL USA

Pierre H. Flamant

LMD, Ecole Polytechnique, Palaiseau, France

R. Michael Hardesty

NOAA Environmental Technology Laboratory, Boulder, CO USA

R. Milton Huffaker

Coherent Technologies, Inc., Lafayette, CO USA

Robert T. Menzies

Jet Propulsion Laboratory, Pasadena, CA USA

Ove Steinvall

National Defence Research Institute (FOA), Linkoping Sweden

J. Michael Vaughan

Defence Evaluation and Research Agency (DERA), Great Malvern, UK

Christian Werner

German Aerospace Establishment (DLR), Munich, Germany

Conference Schedule

Sunday, June 27

6:00 p.m. - 9:00 p.m. Reception and Registration/Check-in

Monday, June 28

8:00 a.m. - 8:10 a.m.	Opening Remarks/Information	Michael Kavaya
8:00 a.m.	Registration Continued	
8:10 a.m. - 9:50 a.m.	Session 1 - Aircraft Operations	Milton Huffaker, Presider
9:50 a.m. - 10:10 a.m.	Break	
10:10 a.m. - 10:50 a.m.	Session 2 - Aircraft Missions	Fred Holmes, Presider
10:50 a.m. - 11:40 a.m.	Session 3 - Special	Fred Holmes, Presider
11:40 a.m. - 1:10 p.m.	Lunch	
1:10 p.m. - 3:10 p.m.	Session 4 - Vibration Measurements	Paul McManamon, Presider
3:10 p.m. - 3:30 p.m.	Break	
3:30 p.m. - 4:30 p.m.	Session 5 - DIAL	Ove Steinvall, Presider
4:30 p.m. - 5:10 p.m.	Session 6 - Theory and Simulation	Rod Frehlich, Presider
5:10 p.m. - 7:00 p.m.	Free Time	
7:00 p.m. - 8:00 p.m.	Panel Discussion - Markets for CLR	Dennis Killinger, Presider

Tuesday, June 29

8:00 a.m. - 9:30 a.m.	Session 7 - Spaceborne Lidars - 1	Dennis Killinger, Presider
9:30 a.m. - 9:50 a.m.	Break	
9:50 a.m. - 11:10 a.m.	Session 7 - Spaceborne Lidars - 1 (Continued)	Dennis Killinger, Presider
11:10 a.m. - 11:15 a.m.	Announcements	Debra Hallmark, Conference Organizer
11:15 a.m. - 11:20 a.m.	Contest	Gayle Brown, Conference Organizer
11:20 a.m. - 11:50 a.m.	Group Photograph	
11:50 a.m. - 1:00 p.m.	Lunch	
1:00 p.m. - 2:00 p.m.	Free Time	
2:00 p.m. - 3:30 p.m.	Depart for Train Ride	
3:30 p.m. - 7:30 p.m.	Train Ride and Dinner	
7:30 p.m. - 9:00 p.m.	Return to Lodge	

Wednesday, June 30

8:00 a.m. - 9:20 a.m.	Session 8 - New Technology	Richard Richmond, Presider
9:20 a.m. - 9:40 a.m.	Break	
9:40 a.m. - 12:20 p.m.	Session 9- Target Characterization	Robert Menzies, Presider
12:20 p.m. - 7:00 p.m.	Lunch / Free Time / Poster Set-up	
7:00 p.m. - 8:00 p.m.	Reception	
7:00 p.m. - 8:00 p.m.	Session 10 - Posters	

Thursday, July 1

8:00 a.m. - 9:30 a.m.	Session 11 - Detection Advances	Barry Rye, Presider
9:30 a.m. - 9:50 a.m.	Break	
9:50 a.m. - 10:30 a.m.	Session 11 - Detection Advances (Continued)	Barry Rye, Presider
10:30 a.m. - 11:30 a.m.	Session 12 - Laser Advances	Christian Werner, Presider
11:30 a.m. - 1:20 p.m.	Lunch and Advisory Committee Lunch	
1:20 p.m. - 2:30 p.m.	Session 13 - System Advances	Alain Dabas, Presider
2:30 p.m. - 3:30 p.m.	Session 14 - CW Lidars	Michael Vaughan, Presider
3:30 p.m. - 3:50 p.m.	Break	
3:50 p.m. - 5:50 p.m.	Session 15 - Wind Measurements	David Tratt, Presider
5:50 p.m. - 7:00 p.m.	Free Time	
7:00 p.m. - 9:00 p.m.	Theme Dinner	

Friday, July 2

8:30 a.m. - 9:30 a.m.	Session 16 - Spaceborne Lidars - 2	Kasuhiko Asai and David Willetts, Presiders
9:30 a.m. - 9:50 a.m.	Break	
9:50 a.m. - 11:50 a.m.	Session 16 - Spaceborne Lidars - 2 (Continued)	Kasuhiko Asai and David Willetts, Presiders
11:50 a.m. - 11:55 a.m.	Closing Remarks	Michael Kavaya
11:55 a.m. - 12:00 noon	Closing Remarks	Dave Willetts
12:00 noon	END OF CONFERENCE	

Abstracts

Monday, June 28

Aircraft Operations

President: Milton Huffaker

8:10 - 8:40

Coherent Pulsed Lidar Sensing of Wake Vortex Position and Strength, Winds and Turbulence in Airport Terminal Areas

(Invited) Philip Brockman, Ben C. Barker Jr., Grady J. Koch, NASA Langley Research Center and Dung Phu hi Nguyen, Charles L. Britt Jr., Research Triangle Institute

A two micrometer coherent pulsed transceiver and real time data system have been developed as a sensor for the Aircraft Vortex Spacing System (AVOSS) element of the NASA Terminal Area Productivity (TAP) Program for increasing airport throughput under Instrument Meteorological Conditions (IMC). The system has been deployed to Norfolk, JFK and DFW airports. Results of measurements and intercomparisons with other sensors are described.

8:40 - 9:00

Concept of a cw-Laser Doppler Sensor as True-Airspeed Instrument

Juergen Streicher, Ines Leike, Stephan Rahm, Christian Werner, DLR - Lidar Group and Richard Bogenberger, Daimler Chrysler Aerospace, Germany

A virtual instrument was designed based on LabView to optimize a cw-Doppler lidar for airborne applications. The optics parameters and the atmosphere can be selected. Flying in high altitude is a real challenge for the sensor to detect single particles and estimate the Doppler shift.

9:00 - 9:30

Airborne Turbulence Detection and Warning: ACLAIM Flight Test Results

(Invited) Stephen M. Hannon and Hal R. Bagley, Coherent Technologies, Inc., Dave C. Soreide, Boeing Defense and Space Group, David A. Bowdle, University of Alabama in Huntsville, Rodney K. Bogue and L. Jack Ehemberger, NASA Dryden Flight Research Center

The Airborne Coherent Lidar for Advanced Inflight Measurements (ACLAIM), a 2 μm pulsed Doppler lidar, was recently flight tested aboard a research aircraft. This paper presents results from these initial flights, with validated demonstration of Doppler lidar wind turbulence detection several kilometers ahead of the aircraft.

9:30 - 9:50

Juneau Airport Doppler Lidar Deployment: Extraction of Accurate Turbulent Wind Statistics

Stephen M. Hannon, Coherent Technologies, Inc. and Rod Frehlich, Larry Comman, Robert Goodrich, Douglas Norris, John Williams, National Center for Atmospheric Research

A 2 μm pulsed Doppler lidar was deployed to the Juneau Airport in 1998 to measure turbulence and wind shear in and around the departure and arrival corridors. This paper presents a summary of the deployment and results of analysis and simulation which addresses important issues regarding the measurement requirements for accurate turbulent wind statistics extraction.

Aircraft Missions

President: Fred Holmes

10:10 - 10:30

The Multi-center Airborne Coherent Atmospheric Wind Sensor: Recent Measurements and Future Applications

Jeffry Rothermel, NASA/MSFC/Global Hydrology and Climate Center, R. Michael Hardesty, James N. Howell, Lisa S. Darby, NOAA Environmental Technology Laboratory, Dean R. Cutten, University of Alabama in Huntsville/Global Hydrology and Climate Center, David M. Tratt, and Robert t. Menzies, Jet Propulsion Laboratory

The atmospheric lidar remote sensing groups of NOAA Environmental Technology Laboratory, Jet Propulsion Laboratory and NASA Marshall Space Flight Center jointly developed an airborne scanning coherent Doppler lidar. We describe the system, present recent measurements (including the first wind fields measured within a hurricane using Doppler lidar), and describe prospective instrument improvements and research applications.

10:30 - 10:50

WIND Instrument Results of Ground Tests

F. Köpp⁽¹⁾, R. Häring⁽¹⁾, M. Klier⁽¹⁾, E. Nagel⁽¹⁾, O. Reitebuch⁽¹⁾, M. Schrecker⁽¹⁾, J. Streicher⁽¹⁾, Ch. Werner⁽¹⁾, G. Wildgruber⁽²⁾, C. Loth⁽³⁾, Ch. Boiter⁽³⁾, P. Delville⁽³⁾, Ph. Drobinski⁽³⁾, P. H. Flamant⁽³⁾, B. Romand⁽³⁾, L. Sauvage⁽³⁾, D. Bruneau⁽⁴⁾, M. Meissonnier⁽⁵⁾ (1) DLR - Arbeitsgruppe LIDAR, (2) Modulab, 80636 München, Germany, (3) LMD, CNRS, 91128 Palaiseau Cedex, France, (4) Service d'Aeronomie / CNRS / UPMC, 75252 Paris Cedex 05, France, (5) INSU / DT 77 Av Denfert Rochereau, 75014 Paris, France

An airborne coherent Doppler Lidar to retrieve mesoscale wind fields has been developed in the frame of the Franco-German WIND project. The instrument is based on a pulsed CO₂ laser transmitter, heterodyne detection and wedge scanner. The performance of the instrument operating on the ground is reported.

An airborne coherent Doppler Lidar to retrieve mesoscale wind fields has been developed in the frame of the Franco-German WIND project. The instrument is based on a pulsed CO₂ laser transmitter, heterodyne detection and wedge scanner. The performance of the instrument operating on the ground is reported.

SPECIAL

President: Fred Holmes

10:50 - 11:20

Improving Scientific Capabilities in Space in the 21st Century: the NASA New Millennium Program

(Invited) Carol A. Raymond and David Crisp, Jet Propulsion Laboratory

NASA's New Millennium Program (NMP) has been chartered to identify and validate in space emerging, revolutionary technologies that will enable less costly, more capable future science missions. A shuttle-borne demonstration of a coherent Doppler wind lidar is the second NMP mission within the Earth Science Enterprise.

11:20 - 11:40

A Coherent FMCW Lidar Mapping System for Automated Tissue Debridment

Donald P. Hutchinson, Roger K. Richards, Glenn O. Allgood, Oak Ridge National Laboratory

The Oak Ridge National Laboratory (ORNL) is developing a prototype 850-nm FMCW lidar system for mapping tissue damage in burn cases for the U.S. Army Medical Research and Materiel Command. The laser system will provide a 3D-image map of the burn and surrounding area and provide tissue damage assessment.

Vibration Measurements

President: Paul McManamon

13:10 - 13:30

Laser Doppler Vibration Lidar Sensing of Structural Defects in Bridges

Dennis Killinger, Priyavadan Mamidipudi, University of South Florida and J Potter, J. Daly, E. Thomas, Litton Laser Systems, and Shen-en Chen, West Virginia University

Laser Doppler Vibration (LDV) Lidar Sensors have the potential to be used for the remote detection and mapping of the fundamental vibration modes of a distant object such as a bridge. Structural defects in the bridge can be observed as shifts in the node and anti-node location. A laboratory HE-Ne LDV system has provided preliminary data of vibrating targets and a CO₂ LDV lidar is being developed to provide such measurements at ranges up to 1 km.

13:30 - 13:50

Evaluation of Laser-Vibration-Sensing Technology from an Airborne Platform

R.M. Heinrichs, S. Kaushik, D.G. Kocher, S. Marcus, G.A. Reinhardt, T. Stephens, and C.A. Primmerman, Lincoln Laboratory, Massachusetts Institute of Technology

Lincoln Laboratory has begun an effort to evaluate the capability of an airborne laser vibrometer to make high-resolution vibration measurements of ground targets. This paper will present details of each of the major elements of this effort. This will primarily involve the performance prediction of laser vibrometry as expressed by the noise-equivalent vibration amplitude. The contribution to this limiting noise level from atmospheric-piston turbulence and speckle broadening as well as the system-dependent contributions from platform vibrations and pointing jitter will be discussed. Laboratory measurements, which confirm the theoretical noise predictions for speckle, will also be presented.

13:50 - 14:10

2 Micron CW Vibration Sensing Laser Radar

Richard D. Richmond, AFRL/SNJM

This paper describes a 2 micron CW laser radar vibration sensor and presents preliminary results from a field trail conducted at Redstone Arsenal during July '98. Data was collected from a variety of targets, at several ranges and varying atmospheric conditions. Also, similar systems with wavelengths at 1.5 and 10.6 microns also took part in the trials to allow later determination of the wavelength dependence of signals and interfering effects.

14:10 - 14:30

Comparison of Pulsed Waveform and CW Lidar for Remote Vibration Measurement

Sammy W. Henderson, J. Alex L. Thomson, Stephen M. Hannon, and Philip Gatt, Coherent Technologies, Inc.

A pulsed lidar capable of long range measurement of target vibration has been developed. In the paper we describe the pulsed lidar waveform and its measurement capability, the noise sources limiting accurate velocity measurements, and performance comparisons with cw lidar.

14:30 - 14:50

Solid-State Coherent Array Ladar for Vibration Imaging

Philip Gatt, Stephen M. Hannon, Coherent Technologies, Inc., Roger Stettner and Howard Bailey, Advanced Scientific Concepts, and Matt Dierking, AFRL/SNJM

We report on work to develop a novel 2 μ m coherent array technology for vibration imaging applications. The 10x10 focal plane heterodyne array imager utilizes an extended wavelength InGaAs detector array indium bump-bonded to a novel backplane sampling chip. The backplane sampling chip, which has an expected sample rate of 500 MHz/pixel and a buffer depth of 32 samples, is well suited to the doublet pulse ladar waveform for vibration sensing applications. In this paper, we present the top-level system design and theoretical performance predictions.

14:50 - 15:10

Precision Targeting and Identification using LADAR Vibrometry

Chyau N. Shen, Naval Air Warfare Center Aircraft Division and Alexander R. Lovett, Office of the Deputy Under Secretary of Defense for Advanced Systems and Concepts

In FY-98, the Deputy Under Secretary of Defense for Advanced Systems and Concepts initiated the Precision Targeting and Identification (PTI) Advanced Concept Technology Demonstrations (ACTD) to operationally evaluate sensor technologies for target classification and identification. One of the technologies being evaluated is coherent CO₂ laser radar (LADAR) vibrometer. This paper will present description of the ACTD program. Measurements and field data collections made with the Navy ruggedized LADAR system will be discussed. Results of operational evaluation conducted at Ft. Bliss will also be discussed. Finally, future plans will be described.

DIAL

President: Ove Steinvall

15:30 - 15:50

Differential Absorption Measurements of Atmospheric Water Vapor with a Coherent Lidar at 2050.532 nm

Grady J. Koch, Richard E. Davis, NASA Langley Research Center, Amin Dharamsi, Old Dominion University, Mulugeta Petros, Science and Technology Corporation, John C. McCarthy, Sanders—A Lockheed Martin Company

A coherent lidar based on a Ho:Tm:YLF laser was used to probe water vapor by a differential absorption lidar technique. This measurement suggests a dual-use lidar for measuring both atmospheric wind and water vapor at an eyesafe wavelength. While the water vapor measurement was successful, disadvantages of the absorption line coupled with excessive frequency jitter of the injection seed laser limited the accuracy of the measured water vapor concentration. Analysis and designs will be presented on the selection of an optimum absorption line and an enhanced seed laser.

15:50 - 16:10

Realtime Special Analysis of Heterodyne DIAL Signals at Very High Repetition Rate

Holger Linné, Jens Bösenberg, Max-Planck-Institut für Meteorologie, Germany, Dieter Hasselmann, Institut für Meteorologie der Universität Hamburg

An advanced algorithm for realtime spectral analysis of heterodyne lidar data is presented. Examples of measurements performed with a very high repetition rate system demonstrate that an implemented version of this algorithm can retrieve wide-spectrum and backscattered energy at excellent resolution and accuracy. Simultaneous measurements of water vapor and wind are feasible.

16:10 - 16:30

Boundary Layer Wind and Water Vapor Measurements Using the NOAA Mini-MOPA Doppler Lidar

W. Alan Brewer, Volker Wulfmeyer, R. Michael Hardesty, NOAA/ERL/Environmental Technology Laboratory and Barry J. Rye, University of Colorado/NOAA, Environmental Technology Laboratory

The NOAA Environmental Technology Laboratory has developed a multiple-wavelength (line tunable from 9-11 μm), low-pulse-energy (1-3 mJ), high-pulse-rate (up to 500 Hz) CO₂ Doppler lidar for simultaneous investigation of boundary layer wind and water vapor profiles. In this paper we present single-wavelength, Doppler results and preliminary water vapor DIAL measurements.

Theory and Simulation

Presider: Rod Frehlich

16:30 - 16:50

Coherent Lidar Returns in Turbulent Atmosphere from Simulation of Beam Propagation

A. Belmonte, B. J. Rye, W. A. Brewer, R. M. Hardesty, NOAA ERL

This paper describes what we believe to be the first use of simulations of beam propagation in three-dimensional random media to study the effects of atmospheric refractive turbulence on coherent lidar performance. Our method provides the tools to analyze laser radar with general refractive turbulence conditions, beam-angle and beam-offset misalignment, and arbitrary transmitter and receiver geometries.

16:50 - 17:10

Effect of Refractive Turbulence on Doppler Lidar Operation in Atmosphere. Numerical Simulation

V. A. Banakh and I. N. Smalikho, Institute of Atmospheric Optics of the Russian Academy of Sciences, Russia and Christian Werner, DLR Lidar Group, Germany

Study of the refractive turbulence effect on operation of Doppler lidar systems in atmosphere is based on numerical simulation of turbulent distortions of sounding laser beam. For simulation the sounding range is divided into set layers on the front border of each layer a random phase screen is placed. The beam diffraction inside each layer is computed using the fast Fourier transform. Sounding both by ground based lidar systems and by spaceborne ones are considered and obtained results are compared.

Tuesday, June 29

Spaceborne Lidars -1

Presider: Dennis Killinger

8:00 - 8:30

NASA's Earth Science Enterprise Embraces Active Laser Remote Sensing From Space

(Invited) Michael R. Luther, Deputy Associate Administrator for Earth Science, Granville E. Paules III, Office of Earth Science, NASA Headquarters

Several objectives of NASA's Earth Science Enterprise are accomplished, and in some cases, uniquely enabled by the advantages of earth-orbiting active lidar (laser radar) sensors. With lidar, the photons that provide the excitation illumination for the desired measurement are both controlled and well known. The controlled characteristics include when and where the illumination occurs, the wavelength, bandwidth, pulse length, and polarization. These advantages translate into high signal levels, excellent spatial resolution, and independence from time of day and the sun's position. As the lidar technology has rapidly matured, ESE scientific endeavors have begun to use lidar sensors over the last 10 years. Several more lidar sensors are approved for future flight. The applications include both altimetry (ranging) and profiling. Hybrid missions, such as the approved Geoscience Laser Altimeter System (GLAS) sensor to fly on the ICESAT mission, will do both at the same time. Profiling applications encompass aerosol, cloud, wind, and molecular concentration measurements. Recent selection of the PICASSO Earth System Science Pathfinder mission and the complementary CLOUDSAT radar-based mission, both flying in formation with the EOS PM mission, will fully exploit the capabilities of multiple sensor systems to accomplish critical science needs requiring such profiling. To round out the briefing a review of past and planned ESE missions will be presented.

8:30 - 9:00

SPARCLE: A Mission Overview

(Invited) G. D. Emmitt, Simpson Weather Associates, M. Kavaya, T. Miller, Global Hydrology and Climate Center/NASA/MSFC

The SPACe Readiness Coherent Lidar Experiment (SPARCLE) is a NASA mission to demonstrate for the first time the measurement of tropospheric winds from a space platform using coherent Doppler Wind Lidar (DWL). SPARCLE is scheduled to launch in early 2001 on board one of the shuttle orbiters. While primarily a demonstration of the technology's performance at ranges of 300-350 km, the mission will also address sampling issues critical to the design and operation of the follow-on missions. In this paper, we provide a brief overview of the SPARCLE instrument and the experiments being planned.

9:00 - 9:30

Atmospheric Dynamic Mission: Project Status, Concepts Review and Technical Baseline

(Invited) Hans Reiner Schulte, Dornier Satellitensysteme GmbH, Germany

The status of the Atmospheric Dynamic Mission Phase A study will be presented. The study objective is the definition of a Doppler wind Lidar demonstration mission in the frame of the European Earth Explorer programme. In particular, a review of the compared coherent and incoherent LIDAR instrument concepts and the evolving technical baseline will be presented.

9:50 - 10:20

SPARCLE Coherent Lidar Transceiver

(Invited) Mark Phillips, Dane Schnal, Carl Colson, Charley Hale, David D'Epagnier, Matt Gibbens and Sammy Henderson, Coherent Technologies Inc.

This paper discusses the design of the coherent lidar transceiver being developed by Coherent Technologies Inc for the NASA program, SPARCLE (SPAcE Readiness Coherent Lidar Experiment). The paper also discusses risk reduction activities performed during the design phase of the program, addressing injection-seeded operation and frequency offset-locking.

10:20 - 10:40

User Requirements for a Space-borne Doppler Wind Lidar

A.Stoffelen, G.J. Marseille, KNMI, Satellite Data Division

A major deficiency in the current meteorological Global Observing System is that insufficient wind information is being observed. A space-borne Doppler Wind Lidar has the potential to provide the lacking information. Requirements on data quality and simulation results of various lidar concepts, in the context of the ESA Earth Explorer Atmospheric Dynamics Mission, are presented.

10:40 - 11:10

Comparing the Intrinsic, Photon Shot Noise Limited Sensitivity of Coherent and Direct Detection Doppler Wind Lidar

(Invited) Jack A. McKay, Remote Sensor Concepts, LLC

Coherent and direct (noncoherent, optical) detection of Doppler wind speeds are compared, on the basis of Cramer-Rao shot noise limits, to determine the relative laser energy - receiver aperture products needed to achieve any specified measurement precision. The results show that coherent is not fundamentally more sensitive than direct, and that the shorter wavelength of direct detection in fact leads to higher intrinsic sensitivity for direct than for coherent. It will be shown why it is that, despite this result, coherent detection in practice will generally be substantially more sensitive than the direct detection Doppler wind lidar.

Wednesday, June 30

New Technology

President: Richard Richmond

8:00 - 8:20

Rectangular Relief Diffraction Gratings for Coherent Lidar Beam Scanning

H.J. Cole, NASA Marshall Space Flight Center, D.M. Chambers, University of Alabama in Huntsville, S.N. Dixit, Lawrence Livermore National Laboratory, J.A. Britten, Lawrence Livermore National Laboratory, B.W. Shore, Lawrence Livermore National Laboratory, M.J. Kavaya, Global Hydrology and Climate Center/NASA/MSFC

The application of specialized rectangular relief transmission gratings to coherent lidar beam scanning is presented. Two types of surface relief transmission grating approaches are studied with an eye toward potential insertion of a constant thickness, diffractive scanner where refractive wedges now exist. The first diffractive approach uses vertically oriented relief structure in the surface of an optical flat; illumination of the diffractive scanner is off-normal in nature. The second grating design case describes rectangular relief structure slanted at a prescribed angle with respect to the surface. In this case, illumination is normal to the diffractive scanner. In both cases, performance predictions for 2.0 micron,

circularly polarized light at beam deflection angles of 30 or 45 degrees are presented.

Portions of this work were performed under the auspices of the U.S. Department of Energy under contract no. W-7405-Eng-48.

8:20 - 8:40

Tunable Highly-Stable Master/Local Oscillator Lasers for Coherent Lidar Applications

Charley P. Hale, Sammy W. Henderson, and David M. D'Epagnier, Coherent Technologies, Inc.

We report on the development and performance of diode-pumped near-infrared single frequency cw lasers for application in coherent lidar systems. Frequency stability of 1 kHz over millisecond time periods, fast piezoelectric frequency tuning over 10 GHz, and programmable offset frequency locking of two oscillators over ± 4.5 GHz has been demonstrated at cw power levels of over 50 mW.

8:40 - 9:00

Stratified Volume Diffractive Optical Elements as Low-mass Coherent Lidar Scanners

Diana M. Chambers, The University of Alabama in Huntsville, Gregory P. Nordin, The University of Alabama in Huntsville, Michael J. Kavaya, NASA Marshall Space Flight Center

A significant reduction of the mass of transmissive lidar scanners can be achieved by using diffraction gratings rather than prisms. Stratified Volume Diffractive Optical Elements (SVDOE's) are high efficiency gratings well-suited to this application since they can be designed for arbitrary incidence angles (e.g. normal incidence) and are insensitive to incident polarization. We present designs and performance predictions based on a coherent lidar instrument operating at 2 μ m and a 30° deflection angle.

9:00 - 9:20

A Hollow Waveguide Integrated Optic Subsystem for a 10.6 μ m Range-Doppler Imaging Lidar

R. M. Jenkins, R. Foord, R. W. J. Devereux, J. Quarrell, A. F. Blockley, Defence Evaluation and Research Agency and T. Papetti, D. Graham, C. Ingram, Technology Development Corporation

The design, manufacture and trial of a hollow waveguide integrated optic subsystem for an heterodyne Range-Doppler Lidar operating at 10.6 microns are described. The trials were undertaken at the Army Missile Optical Range, Huntsville, Alabama. The results of the work, including images of targets, are presented and described.

Target Characterization

President: Robert Menzies

9:40 - 10:00

Comparison of Continuous Wave CO₂ Doppler Lidar Calibration Using Earth Surface Targets in Laboratory and Airborne Measurements

Maurice A. Jarzembski, NASA/MSFC/Global Hydrology and Climate Center, Vandana Srivastava, Universities Space Research Association/Global Hydrology and Climate Center
Earth's surface signal was measured using a continuous wave 9.1 micron lidar over varying Californian terrain during a 1995 NASA airborne mission. These measurements were compared with laboratory backscatter measurements of various Earth surfaces giving good agreement, suggesting that the lidar efficiency can be estimated fairly well using Earth's surface signal.

10:00 - 10:20

Effect of Aerosol Partical Microstructure on Accuracy of CW Doppler Lidar Estimate of Wind Velocity

V. A. Banakh and I. N. Smalikho, Institute of Atmospheric Optics of the Russian Academy of Sciences, Russia and Ch. Werner, DLR Lidar Group, Germany

The effect of non-Gaussian fluctuations of photocurrent on accuracy of Doppler lidar estimation of wind velocity in atmosphere is studied. Comparative analysis of factors causing the non-Gaussian fluctuations of lidar photocurrent, namely, correlation of particles suspended in a turbulent flow, strong fluctuations of number and size of particles in sounding volume of limited size, variation of backscattering coefficient with height is carried out. Error of Doppler lidar estimate of wind velocity as function of factor listed above is calculated.

10:20 - 10:40

VALID: Experimental Tests to Validate a Multiwavelength Backscatter Database and Intercompare Wind Lidar Concepts

Pierre H. Flamant, Laboratoire de Météorologie Dynamique, France

ESA is funding in 1999 an experimental activity (1) to build a multiwavelength backscatter database to validate a scalling law derived in a previous study, and (2) intercompare the most relevant wind lidar concepts to space applications. VALID will proceed in two steps: Step 1 in May-mid-June for backscatter data, lidars with wavelengths ranging from UV (0.32 μm) to IR (10.6 μm) will be operated on the same site; Step 2 in mid-July will involve coherent and incoherent lidar techniques on the same site.

10:40 - 11:00

A Southern California Perspective of the April, 1998 Trans-Pacific Asian Dust Event

David M. Tratt, Jet Propulsion Laboratory/California Institute of Technology, Robert Frouin, University of California, San Diego, Douglas L. Westphal, Naval Research Laboratory

In late April, 1998 the JPL coherent lidar observed an extreme Asian dust episode. The resultant peak backscatter coefficients exceeded prevailing upper-tropospheric background conditions by at least two orders of magnitude. An analysis of this event will be presented using the lidar profiles, concurrent sunphotometer opacity data, and transport modeling.

11:00 - 11:20

A Global Backscatter Database for Modelling Space-Borne Doppler Wind Lidar

J.M. Vaughan, Defence Evaluation & Research Agency, U.K., A. Culoma, European Space Agency, Netherlands, Pierre H. Flamant, Laboratoire Meteorologie Dynamique, France, C. Flesia, University of Geneva, Switzerland, N. Geddes, Defence Evaluation & Research Agency, U.K.

Available data on atmospheric backscatter over the wavelength range 0.35 to 10.6 μm is reviewed. The most comprehensive data sets derive from measurements over the Atlantic and Pacific in the late '80s and early '90s. A table at 10.6 μm combined with wavelength scaling equations is proposed as a useful measure of global backscatter.

11:20 - 11:40

Lidar Hard Target Calibration: Retroreflection Mechanisms at 2 μm

D. A. Haner and D. M. Tratt, Jet Propulsion Laboratory/California Institute of Technology

The choice of field target materials depends upon the transmitter/receiver polarization characteristics. The depolarization of linear light on and off the retropeak increases generally; whereas the magnitude of the circular polarization reversal is mechanism dependent. This paper

will present results of polarimetric measurements which differentiate the probable reflectance mechanisms operating in materials commonly employed in lidar hard target calibration.

11:40 - 12:00

Backscatter Modeling at 2.1 Micron Wavelength for Space-based and Airborne Lidars Using Aerosol Physico-chemical and Lidar Datasets

V. Srivastava, Global Hydrology and Climate Center/Universities Space Research Association, J. Rothermel and M. Jarzembki, Global Hydrology and Climate Center, NASA, A. D. Clarke, University of Hawaii, H. D. R. Cutten and D. A. Bowdle, Global Hydrology and Climate Center/UAH, J. D. Spinhirne, NASA Goddard Space Flight Center, R. T. Menzies, Jet Propulsion Laboratory

Aerosol backscatter, between 0.35-11 micron wavelength range, was modeled and compared with continuous wave and pulsed lidar measurements. Lidar data converted to 2.1micron backscatter yielded midtropospheric 2.1 micron backscatter background mode of $\sim 8 \times 10^{-10} \text{m}^{-1} \text{sr}^{-1}$ and boundary layer mode of $\sim 2 \times 10^{-7} \text{m}^{-1} \text{sr}^{-1}$, which are ~ 20 and ~ 4 times higher than 9.1 micron backscatter modes, respectively.

12:00 - 12:20

Comparison of Predicted and Measured 2 μm Aerosol Backscatter from the 1998 ACLAIM Flight Tests

David A. Bowdle, University of Alabama in Huntsville/Global Hydrology and Climate Center, Stephen M. Hannon, Coherent Technologies, Inc., Rodney K. Bogue, NASA Dryden Flight Research Center

The 1998 Airborne Coherent Lidar for Advanced Inflight Measurements (ACLAIM) flight tests were conducted aboard a well-instrumented research aircraft. This paper presents comparisons of 2 μm aerosol backscatter coefficient predictions from aerosol sampling data and mie scattering codes with those produced by the ACLAIM instrument.

Poster Session

Wednesday, P.M., June 30

The NASA Coherent Lidar Technology Advisory Team

Michael J. Kavaya, NASA Marshall Space Flight Center/Global Hydrology and Climate Center

The motivation, purpose, history, membership, and current activities of the NASA Coherent Lidar Technology Advisory Team (CLTAT) will be discussed.

Pre-Launch End-To-End Testing Plans for the SPACe Readiness Coherent Lidar Experiment (SPARCLE)

Michael J. Kavaya, NASA Marshall Space Flight Center/Global Hydrology and Climate Center

The motivation, trade-offs, and plans for conducting a thorough pre-launch test of the SPACe Readiness Coherent Lidar Experiment (SPARCLE) Lidar will be discussed.

Comparison of CO₂ Lidar Backscatter With Particle Size Distribution and GOES-7 Data in Hurricane Juliette

Maurice A. Jarzembki, NASA/Marshall Space Flight Center/Global Hydrology and Climate Center, Vandana Srivastava, Universities Space Research Association/Global Hydrology and Climate Center, Eugene W. McCaul, Jr., Universities Space Research Association/Global Hydrology and Climate Center, Gary J. Jedlovec, NASA/Marshall Space Flight Center/Global Hydrology and Climate Center, Robert J. Atkinson, Lockheed Martin Corp./Global Hydrology and Climate Center, Rudy F. Pueschel, NASA/Ames

Research Center, Dean R. Cutten, University of Alabama, Huntsville/Global Hydrology and Climate Center

Backscatter measurements using 9.1 and 10.6 micron continuous wave lidars were obtained along with particle size distributions in 1995 Hurricane Juliette at altitude ~11.7 km. Agreement between lidar backscatter and cloud particle size distribution was excellent. Measurements also correlated well with concurrent GOES-7 infrared images of cloud top height.

Aerosol Backscatter From Airborne Continuous Wave CO₂ Lidars Over Western North America and The Pacific Ocean

Maurice A. Jarzembki, NASA/Marshall Space Flight Center/Global Hydrology and Climate Center, Vandana Srivastava, Universities Space Research Association/Global Hydrology and Climate Center, Jeffrey Rothenmel, NASA/Marshall Space Flight Center/Global Hydrology and Climate Center

Aerosol backscatter measurements using two continuous wave CO₂ Doppler lidars were obtained over western North America and the Pacific Ocean during a 1995 NASA airborne mission. Similarities and differences for aerosol loading over land and ocean were observed. Mid-tropospheric aerosol backscatter background mode was $\sim 6 \times 10^{-11} \text{ m}^{-1} \text{ sr}^{-1}$, consistent with previous lidar datasets.

Performance Analysis for the Space Readiness Coherent Lidar Experiments

Gary D. Spiers, University of Alabama in Huntsville

An overview of the anticipated performance of the Space Readiness Coherent Lidar Experiment will be provided and some of the considerations and issues that went into producing the analysis discussed.

The Effect of Optical Aberrations on the Performance Of A Coherent Doppler Lidar

Gary D. Spiers, University of Alabama in Huntsville

An understanding of the linkage between optical aberrations and the performance of a coherent Doppler lidar is essential to ensuring that a design can be achieved practically. We present results from a back propagated local oscillator heterodyne mixing model that permits parameterization over many of the variables typically of interest to a coherent lidar designer.

Doppler Frequency Estimation and Quality Control by Neural Networks.

ZARADER J.L.⁽¹⁾; GAS B.⁽¹⁾; DOBRINSKI P.⁽²⁾; DABAS A.⁽³⁾

⁽¹⁾ Laboratoire des Instruments et Systèmes, Université Paris VI,

⁽²⁾ Laboratoire de Météorologie Dynamique, Palaiseau

⁽³⁾ Centre National de Recherche Météorologique, Météo-France, Toulouse

We propose in this paper a study of spectrum analysis using neural networks. The signal is simulated by the model proposed by Zmic. Contrary to the classical approach, the resolution is given by the structure of the network (number of output cells). The results are given in function of the spectrum width (), the frequency Doppler (Fd) and the signal to noise ratio (SNR). A parameter (not statistical), estimated at each shoot, give an estimation of the " quality control."

Shipborne Backscattering-Lidar Experiments in Western Pacific Region by Research Ship "Mirai"

Kouroh Tamamushi, Tetuya Sugata, Kazuhiro Asai, Tohoku Institute of Technology, Japan, Ichiro Matsui, Nobuo Sugimoto, National Institute of Environmental Studies, Japan
The 0.53 and 1.06 micron meters backscattering lidars were equipped on the deck of Japanese research ship "Mirai" and the experiments were carried out in the Western Pacific regions in 1999's winter in order to acquire the data set of the height of PBL, clouds (frequency, height, optical depth,

depolarization, etc.), lidar backscattering coefficients in the free troposphere.

Pointing Knowledge for SPARCLE and Space-based Doppler Wind Lidars in General

G. D. Emmitt, Simpson Weather Associates, T. Miller and G. Spiers, NASA/MSFC

The SPACe Readiness Coherent Lidar Experiment (SPARCLE) will fly on a space shuttle to demonstrate the use of a coherent Doppler wind lidar to accurately measure global tropospheric winds. To achieve the LOS accuracy goal of ~ 1 m/s, the lidar system must be able to account for the orbiter's velocity (~ 7750 m/s) and the rotational component of the earth's surface motion (~ 450 m/s). For SPARCLE this requires knowledge of the attitude (roll, pitch and yaw) of the laser beam axis within an accuracy of 80 microradians. (~ 15 arcsec). Since SPARCLE can not use a dedicated star tracker from its earth-viewing orbiter bay location, a dedicated GPS/INS will be attached to the lidar instrument rack. Since even the GPS/INS has unacceptable drifts in attitude information, the SPARCLE team has developed a way to periodically scan the instrument itself to obtain <10 microradian (2 arcsec) attitude knowledge accuracy that can then be used to correct the GPS/INS output on a 30 minute basis.

Heterodyne Efficiency - Theory and Practice

Stephan Rahm, Adelina Ouisse, DLR- Lidar Group, Germany, and Frank Häfner, Daimler Chrysler Aerospace, Germany

Heterodyne efficiency as major quality indicator of a Doppler lidar is discussed in detail to find an optimal receiver configuration for a spaceborne application. A comparison between theory with numerical simulations and experiment is presented for heterodyning two Gaussian beams and also speckles of a rough target.

Enhanced Double-Edge Technique for Doppler Lidar

Peter J. Winzer, Walter R. Leeb, Technische Universität Wien, Europe, and Alexandru F. Popescu, European Space Agency/ESTEC/TOS-MM, The Netherlands, Europe

We present an enhanced version of the double-edge Doppler lidar that - by making use of transmission and reflection of a single edge filter - efficiently uses all input power and does without mutual frequency stabilization of two edges. A comparison with the conventional double-edge technique reveals increased measurement accuracy.

Estimation of Return Signal Spectral Width in Incoherent Backscatter Heterodyne Lidar

Barry J. Rye, NOAA ERL

The sensitivity of estimates of Doppler shift and return power to errors in the assumed signal bandwidth is examined. The precision of estimating the bandwidth itself is considered and compared to its optical limit which is comparable with the estimation precision of the Doppler shift.

1.5- μm Coherent Lidar Using Injection-seeded, LD Pumped Er,Yb:Glass Laser

Kimio Asaka, Takayuki Yanagisawa and Yoshihito Hirano, Mitsubishi Electric Corporation, Japan

A 1.5- μm coherent lidar was developed. It incorporates an injection seeded LD pumped Er,Yb:Glass media as a slave laser and a microchip Er,Yb:Glass module for a seed and as a local source. At a repetition rate of 40-Hz and wavelength of 1.534- μm the laser emits a single frequency, injection seeded pulse of 4.0-mJ. It was used to measure wind velocity to distances longer than 5-km with a good agreement between the experimental data and theory.

Specification of a Coherent Laser Radar for Air Data Measurements for Advanced Aircraft

Christer Karlsson, Per-Otto Amtzen, Göran Hansson and Stan Zyra, Defence Research Establishment (FOA), and Thomas Lampe, SAAB AB

Requirements on components and subsystems of a CLR system for use as an optical air data system for the full flight envelope of an advanced fixed wing aircraft are discussed. A detailed specification of such a test system and its implementation in a pod are presented.

Measurements of Aircraft Wake Vortex Structure By CW Coherent Laser Radar

M Harris, R I Young, Electronics Sector and J M Vaughan, Microwave Management Associates

Measurements have been performed on aircraft during their approach to landing, revealing details of the vortex structure. The data demonstrates the sensitivity of the results to atmospheric conditions with unpredictable trajectories, instabilities and vortex break up being commonly observed.

Polarimetry of Scattered Light Using Coherent Laser Radar

M Harris, Defence Evaluation and Research Agency, U.K.

Dual-channel heterodyne detection has been used to measure both the co- and cross-polarized components of light backscattered from moving solid targets. This process allows the time-varying amplitudes and phases of the two components to be measured and hence the light's polarisation ellipse can be evaluated and followed in real time.

END OF POSTER SESSION

Thursday, July 1

Detection Advances

Presider: Barry Rye

8:00 - 8:20

Stokes Polarimetry for Laser Radar Applications

James K. Boger, Applied Technology Associate, David G. Voelz, AFRL/DEBS, Lenore McMackin, AFRL/VSSS, Ken MacDonald, Boeing North American

We have demonstrated a visible-wavelength imaging technique that uses a referenced polarization measurement to estimate the amplitude and phase of the wavefront emanating from a coherently illuminated target. The image of the target is then recovered by Fourier transformation.

8:20 - 8:40

Vibrating Target and Turbulence Effects on a 1.5 Micron Multi-Element Detector Coherent Doppler Lidar

Pri Mamidipudi and Dennis Killinger, University of South Florida

A 1.5 micron diode laser coherent Doppler lidar with a multi-element 2 x 2 balanced heterodyne detector array has been used to measure the returns from several rotating targets in the laboratory. The multi-detector decorrelation times, cross correlation of speckle patterns, and increased S/N ratios due to coherent integration of the multiple signals have been studied.

8:40 - 9:00

Multiple Wavelength Heterodyne Array Sensing for Space Optics Metrology

Lenore McMackin, David G. Voelz, Air Force Research Laboratory and Harold McIntire, Matthew Fetrow and Kenneth Bishop, Applied Technology Assoc.'s, Inc.

Large space optical systems that are designed to deploy to optical tolerances after reaching their position in orbit require non-contact surface measurement as part of an autonomous deployment control system. We demonstrate the use of variable sensitivity, multi-wavelength heterodyne array interferometry for the automated measurement and control of adaptive optical systems with applications to remote space operation.

9:00 - 9:30

Imaging Coherent Receiver Development for 3-D Lidar

(Invited) Donald P. Hutchinson, Roger K. Richards, Marc L. Simpson, Oak Ridge National Laboratory

Oak Ridge National Laboratory has been developing advanced coherent IR heterodyne receivers for plasma diagnostics in fusion reactors for over 20 years. Recent progress in wide-band IR detectors and high-speed electronics has significantly enhanced the measurement capabilities of imaging coherent receivers. Currently, we are developing a 3-D lidar system based on quantum-well IR photodetector (QWIP) focal plane arrays and a MEMS-based CO₂ laser local oscillator.¹ In this paper we discuss the implications of these new enabling technologies to implement long wavelength IR imaging lidar systems.

9:50 - 10:10

What Can Really Be Gained Using Telescope Arrays in Coherent Lidar Receivers

Peter J. Winzer, Vienna University of Technology, Austria, Europe

We compare the performance of single-telescope receivers to that of phased and non-phased arrays, showing that non-phased arrays perform generally worse than single-telescope receivers, and that the average carrier-to-noise ratio gain of phased arrays with respect to single-telescope receivers increases less than proportionally with the number of array apertures.

10:10 - 10:30

Receiver Arrays in Lidar Wind Measurement From Space

Adeline Ouisse, and Ines Leike, DLR - Lidar Group, Germany

The speckle effect is a problem in wind measurements. Telescope or detector surface multiplication can reduce this effect. This article gives an overview on the work performed at DLR on this topic and focuses on results obtained for a detector array.

Laser Advances

Presider: Christian Werner

10:30 - 10:50

Coherent Laser Radar Using an Injection Seeded Q-Switched Erbium: Glass Laser

Andrew McGrath, Jesper Munch and Peter Veitch, The University of Adelaide, Australia

We have developed and demonstrated the first injection-seeded, long pulse, Q-switched, Er:glass laser for Doppler sensing of clear air turbulence and wind shear. The laser produces transform-limited, eye-safe pulses, achieving a single-shot velocity resolution of 1 m/s. We shall present results and an optimized, next generation design.

10:50 - 11:10

High Efficiency End-Pumped Ho:Tm:YLF Disk Amplifier
Jirong Yu¹, Upendra N. Singh², Mulugeta Petros¹, Theresa J. Axenson¹ and Norman P. Barnes² ¹Science and Technology Corporation, ²NASA Langley Research Center,

We describe a diode-pumped, room temperature Ho:Tm:YLF disk amplifier with optical-to-optical efficiency of 5.6%. An end-pump configuration is used and the amplifier's efficiency is augmented by a higher pump density and a better mode overlap between the pump and probe beam. This highly efficient disk amplifier is a promising candidate for use in an efficient, space coherent lidar system.

11:10 - 11:30

A Proposed 1.55 μm Solid State Laser System for Remote Wind Sensing

Arun Kumar Sridharan, Todd Rutherford, William M. Tulloch, and Robert L. Byer, Stanford University

We will describe a novel design for a laser-diode-pumped Yb:YAG master oscillator power amplifier laser system coupled to an optical parametric amplifier (OPA) based on periodically-poled lithium niobate (PPLN) to achieve a 1 μs pulsed output at 1.55 μm of 2 J at 10 Hz, which is adequate for remote global wind sensing applications.

System Advances

President: Alain Dabas

13:20 - 13:50

Optical Phased Arrays for Electronic Beam Control

(Invited) Terry A Dorschner, Raytheon Systems Company

The state of the art of optical phased arrays (OPA's) will be reviewed and prospective applications discussed, highlighting laser radar and other active sensors. Current OPA performance levels will be summarized and the near-term performance potential forecasted. Comparisons with conventional and emerging new technologies for beam control will be made.

13:50 - 14:10

High-Efficiency Autonomous Coherent Lidar

Philip Gatt and Sammy W. Henderson, Coherent Technologies, Inc.

We report on work to achieve and maintain coherent lidar system efficiency of better than 10% in a field, airborne, or space environment. This is achieved with efficient system design, careful initial alignment and the combination of stable mechanical design and auto-alignment techniques to maintain that alignment during the mission lifetime.

14:10 - 14:30

1.5 and 2 μm Coherent Lidar Study for Wind Velocity and Backscattering Measurement.

Gaspar Guérit⁽¹⁾⁽²⁾, Béatrice Augère⁽²⁾, Jean-Pierre Cariou⁽²⁾, Philippe Drobinski⁽¹⁾, Pierre H. Flamant⁽¹⁾

1) Laboratoire de Meteorologie Dynamique; 2) Office National d'Etudes et de Recherches Aérospatiales

The potential of 1.5 μm and 2 μm solid-state technologies to multipurpose Coherent Doppler Lidar (HDL) application to measure wind velocity and species concentration in the planetary boundary layer, are discussed. Transverse coherence of a backscattered signal and its influence on power estimation accuracy are tested using hard target returns. The instrument design, signal processing technique and experimental results will be presented.

CW Lidars

President: Michael Vaughan

14:30 - 14:50

Analysis of Continuous-Wave Multistatic Coherent Laser Radar for Remote Wind Measurements

Eric P. Magee, Air Force Institute of Technology, AFIT/ENG, Timothy J. Kane, The Pennsylvania State University

The purpose of this research is to investigate the feasibility of utilizing a multistatic configuration for measuring 3-dimensional vector winds with a continuous-wave (CW) lidar. A CW transmitter can be used in the multistatic configuration because the spatial resolution is determined by the system geometry and thus decoupled from the velocity resolution. The narrow spectral width of the CW transmitter improves the lower bound on the mean frequency estimation. Detailed signal-to-noise ratio calculations for the CW transmitter case will be presented.

14:50 - 15:10

Ranging Performance of an FMCW Semiconductor Laser Radar with Linearisation of the Frequency Sweep

Christer Karlsson and Fredrik Olsson, Defence Research Establishment (FOA)

The performance of an FMCW semiconductor laser radar, using only the monochromatic peak of the signal spectrum, has been experimentally studied. The measurements indicate the possibility to achieve a spectral width of the signal peak that is transform limited, which permits the use of a very narrow detection bandwidth. This, in turn, allows for a relatively high signal-to-noise ratio for a low output power.

15:10 - 15:30

Interference of Backscatter From Two Droplets in a Focused Continuous Wave CO₂ Doppler Lidar Beam

Maurice A. Jarzembski, Global Hydrology and Climate Center/NASA/MSFC, Vandana Srivastava, Global Hydrology and Climate Center/Universities Space Research Association

Superposition of backscatter from two silicone oil droplets in a lidar beam was observed as an interference pattern on a single backscatter pulse with a distinct periodicity of 2π , also agreeing extremely well with theory. Slightly differing droplet speeds caused phase differences in backscatter, resulting in the interference pattern.

Wind Measurement

President: David Tratt

15:50 - 16:10

Ground-based Remote Sensing of Wind Vector. Newest Results to Become a Guideline

J. Bösenberg, H. Danzeisen, D. Engelbart, K. Fritzsche, V. Klein, Ch. Münkel, T. Trickl, Ch. Werner, L. Woppowa

Methods which are in discussion to become a guideline in the German organization VDI will be presented. The VDI "Richtlinie VDI 3786 „Umweltmeteorologie", is divided in many parts. VDI 3786, Part 14 shows the possibilities of remote sensing and describes the wind profile measurements. It is necessary for comparison with other instruments to have a guideline which describes also the calibration and performance tests.

16:10 - 16:30

The Accuracy of the True Radial Velocity Measurements in the Turbulent Atmosphere

Alexander P. Shelekhov, Inst. of Atmospheric Optics, Russian Federation

As a rule the accuracy of the Doppler measurements is studied using the assumption that the frequency estimation

is equal to approximately the average Doppler shift or is proportional to the average true radial velocity. But the frequency estimation may be proportional to the true radial velocity. In this paper the accuracy of the true radial velocity measurement is investigated for the different state of the turbulent atmosphere, the different values of the signal-to-noise ratio, the number of the samples and other parameters. The cases of the stable, unstable, and indifferent stratification are considered.

16:30 - 16:50

Doppler Lidar Observations of Wind Features Near Complex Terrain

Lisa S. Darby, Alfred J. Bedard, and Robert M. Banta, National Oceanic and Atmospheric Administration/ETL

In the last decade the NOAA/ETL TEA CO₂ Doppler lidar measurements have contributed significantly to the understanding of wind flow features associated with complex terrain. Positioning this Doppler lidar near mountainous terrain has proven to be an effective setting for measuring terrain-induced flows and the interaction of these flows with the ambient (larger-scale) meteorological conditions. In this paper we briefly review noteworthy results from air quality experiments at two such sites (near Denver, CO and Vancouver, B. C.), and then present more detailed results from the Colorado Springs, CO airport where we investigated wind features that could be hazardous to aviation.

16:50 - 17:10

Bistatic Laser Doppler Wind Sensor at 1.5 μm

M Harris, Defence Evaluation and Research Agency, U.K.

A wind sensor using a bistatic configuration has been successfully demonstrated. This confers improved range resolution at the expense of reduced CNR and increased alignment complexity. System performance has been compared with the results of a theoretical analysis.

17:10 - 17:30

Measuring Turbulence Parameters With Coherent Lidars

A. Dabas, Météo-France CNRM/GMEI, FRANCE, Ph. Drobinski, NRS Laboratoire de Météorologie Dynamique/Ecole Polytechnique, FRANCE, R. M. Hardesty, A. Brewer, NOAA Environmental Technology Laboratory, V. Wulfmeyer, NCAR Atmospheric Technology Division

We present Doppler lidar measurements of the atmospheric dissipative rate of turbulence obtained during a campaign organized by the Environmental Technology Laboratory of the National Oceanic and Atmospheric Administration. Two high resolution Doppler lidars and a Portable Automated Mesonet including a sonic anemometer (from the National Center for Atmospheric Research) were involved. Lidars and sonic-anemometer measurements are compared.

17:30 - 17:50

The Prediction of the Doppler Measurement Accuracy Using a Priori Information about the Turbulent Atmosphere

Alexander P. Shelekhov, Alexei L. Afanas'ev, Inst. of Atmospheric Optics, Russian Federation

The accuracy of the Doppler frequency measurement of the parameters of the turbulent atmosphere is studied for the cases of the stable, unstable, and indifferent stratification. The theoretical prediction of the Doppler measurement accuracy is based on the turbulent atmosphere models of Kaimal and Palmer.

Friday, July 2

Spaceborne Lidars - 2

Presiders: Kasuhiro Asai and David Willetts

8:00 - 8:30

SPARCLE Optical System Design and Operational Characteristics

(Invited) Farzin Amzajerdian, Bruce R. Peters, Ye Li, Timothy S. Blackwell, and Patrick Reardon, The University of Alabama in Huntsville

The SPACe Readiness Coherent Lidar Experiment (SPARCLE) is the first demonstration of a coherent Doppler wind lidar in space. SPARCLE will be flown aboard a space shuttle in the middle part of 2001 as a stepping stone towards the development and deployment of a long-life-time operational instrument in the later part of next decade. SPARCLE is an ambitious project that is intended to evaluate the suitability of coherent lidar for wind measurements, demonstrate the maturity of the technology for space application, and provide a useable data set for model development and validation. This paper describes the SPARCLE's optical system design, fabrication methods, assembly and alignment techniques, and its anticipated operational characteristics.

Coherent detection is highly sensitive to aberrations in the signal phase front, and to relative alignment between the signal and the local oscillator beams. Consequently, the performance of coherent lidars is usually limited by the optical quality of the transmitter/receiver optical system. For SPARCLE having a relatively large aperture (25 cm) and a very long operating range (400 km), compared to the previously developed 2-micron coherent lidars, the optical performance requirements are even more stringent. In addition with stringent performance requirements, the physical and environment constraints associated with this instrument further challenge the limit of optical fabrication technologies.

8:30 - 8:50

Optical Design and Analyses of SPARCLE Telescope

Ye Li, Farzin Amzajerdian, Bruce Peters, Tim Blackwell, Pat Reardon, University of Alabama in Huntsville

SPARCLE demands a high level of performance from its telescope system under stringent physical and environmental constraints. To meet the SPARCLE demanding requirements, the telescope system design utilizes state-of-the-art optical fabrication and coating technologies. This paper describes the telescope design, provides its fabrication and alignment tolerances, and discusses its sensitivity and performance analyses.

8:50 - 9:10

A Program of an ISS/Japanese Experiment Module (JEM) borne Coherent Doppler Lidar

Toshikazu Itabe, Kohei Mizutani, Communications Research Laboratory, Japan, Mitsuo Ishizu, National Space Development Agency of Japan, Japan, Kazuhiro Asai, Tohoku Institutes of Technology, Japan

A feasibility study on key technologies for a ISS/Japanese Experiment Module borne coherent Doppler lidar was started to measure tropospheric winds from space from 1997 FY under the support of one of the Phase II studies of Ground Research Announcement of NASDA and Japan Space Forum. The following key technologies are being studied.

- (1) multi joule 2 mm laser slaved by a frequency stabilized CW laser
- (2) a conical scanning transmitting and receiving telescope
- (3) a coherent detection system, which can compensate Doppler shift due to spacecraft movement.

9:10 - 9:30

Results of the Aladin Impact Study

Christian Werner, Ines Leike and Juergen Streicher, DLR - Lidar Group, Germany, Werner Wergen and Alexander Cress, Deutscher Wetterdienst, Victor Banakh and Igor Smalikho, Institute of Atmospheric Optics/Russian Academy of Sciences, Russia

ESA is planning to perform the Atmospheric Dynamic Mission from the International Space Station. There is no full coverage and there is limited observation time caused by other orientation of the space station. To answer the question of the usefulness of a Doppler lidar on the space station the so called targeted observation was mentioned. Both, sensor specialists and numerical weather prediction scientists worked together. A Doppler lidar simulation program was developed which contains a virtual instrument and the atmosphere with wind, clouds and turbulence parameters. By flying over the targeted area LOS components were calculated which were used for assimilation in a forecast program instead of rawinsonde data and pilot observations.

9:50 - 10:10

Coherent Doppler Lidar Data Products from Space-Based Platforms

Rod Frehlich, University of Colorado

The performance of coherent Doppler lidar estimates of radial velocity are determined for space based platforms using computer simulations with pulse accumulation. The effects of wind shear, wind turbulence, and variations in aerosol backscatter are included.

10:10 - 10:40

Considerations for Designing a Space Based Coherent Doppler Lidar

(Invited) Gary D. Spiers, University of Alabama in Huntsville, Michael J. Kavaya, Global Hydrology and Climate Center/NASA Marshall Space Flight Center

An overview of some of the considerations particular to a space based coherent Doppler lidar for measuring the velocity and position of a target is provided.

10:40 - 11:00

Wind measurements by a 2 μm Space Lidar

J.B Ghibaudo, J.Y. Labandibar ; ALCATEL Space Industries, France, Faucheux ; QUANTEL, Av de l'Atlantique, France, A. Cosentino ; ALENIA, 2 Via dei Romani, Italy, P. Laporta ; Politecnico di Milano, Italy, P. Flamant ; Laboratoire de Météorologie Dynamique, Ecole Polytechnique, France, Armandillo ; European Space Agency, The Netherlands
ALCATEL presents the main results of the feasibility study under ESA contract on a 2 μm coherent lidar instrument capable to measure wind velocity in the planetary boundary layer. ACATEL emphasises the results of the 2 μm coherent detection chain and a 2 μm laser breadboards. The implementation of such an instrument on the International Space Station is also presented with the expected performance.

11:00 - 11:20

Development Of Prototype Micro-Lidar Using Narrow Linewidth Semiconductor Lasers For Mars Boundary Layer Wind and Dust Opacity Profiles

Robert T. Menzies, Greg Cardell, Meng Chiao, Carlos Esproles, Siamak Forouhar, Hamid Hemmati and David Tratt, Jet Propulsion Laboratory, California Institute of Technology

A compact Doppler lidar based on semiconductor diode and fiber laser technology has been developed for boundary layer wind and opacity profiling. This serves as a prototype for a miniature lidar concept suitable for deployment on the surface of Mars. The lidar uses coherent detection at 1.5 μm wavelength.

11:20 - 11:50

Follow-on Missions to SPARCLE

(Invited) G. D. Emmitt, Simpson Weather Associates, T. L. Miller, NASA/MSFC/Global Hydrology and Climate Center

Global tropospheric wind observations are considered the number one unaccommodated atmospheric observation for the new series of NPOESS platforms. The operational meteorology communities have long recognized the potential for improved forecasting skill if accurate wind observations were available around the globe. Recent analyses suggest that wind observations such as those that could be made by a space-based Doppler wind lidars would even result in greater improvements than better temperature soundings. In this paper we present a roadmap that begins with the NASA approved SPACe Readiness Coherent Lidar Experiment (SPARCLE) and ends with an operational DWL on a NPOESS platform.

AIRCRAFT OPERATIONS

Presider: Milton Huffaker

Coherent Pulsed Lidar Sensing of Wake Vortex Position and Strength, Winds and Turbulence in the Terminal Area

Philip Brockman, Ben C. Barker Jr., Grady J. Koch - NASA Langley Research Center Hampton, VA
Dung Phu Chi Nguyen, Charles L. Britt Jr. - Research Triangle Institute Hampton VA
Mulugeta Petros - Science and Technology Corp. Hampton VA

Introduction

NASA Langley Research Center (LaRC) has field-tested a 2.0 μm , 100 Hertz, pulsed coherent lidar to detect and characterize wake vortices and to measure atmospheric winds and turbulence. [Ref. 1] The quantification of aircraft wake-vortex hazards is being addressed by the Wake Vortex Lidar (WVL) Project as part of Aircraft Vortex Spacing System (AVOSS), which is under the Reduced Spacing Operations Element of the Terminal Area Productivity (TAP) Program. [Ref. 2, 3] These hazards currently set the minimum, fixed separation distance between two aircraft and affect the number of takeoff and landing operations on a single runway under Instrument Meteorological Conditions (IMC). The AVOSS concept seeks to safely reduce aircraft separation distances, when weather conditions permit, to increase the operational capacity of major airports.

The current NASA wake-vortex research efforts focus on developing and validating wake vortex encounter models, wake decay and advection models, and wake sensing technologies. These technologies will be incorporated into an automated AVOSS that can properly select safe separation distances for different weather conditions, based on the aircraft pair and predicted/measured vortex behavior. [Ref. 2, 3] The sensor subsystem efforts focus on developing and validating wake sensing technologies.

The lidar system has been field-tested to provide real-time wake vortex trajectory and strength data to AVOSS for wake prediction verification. Wake vortices, atmospheric winds, and turbulence products have been generated from processing the lidar data collected during deployments to Norfolk (ORF), John F. Kennedy (JFK), and Dallas/Fort Worth (DFW) International Airports.

Pulsed Lidar System Description

Coherent Technologies, Incorporated (CTI) developed the Tm: YAG, solid-state, laser transceiver used in the NASA pulsed coherent lidar system. Pulsed lidar has been selected as the baseline technology for an operational wake vortex sensor due to its range resolution and long-range capability. CTI first demonstrated the application of this technology to wake vortex measurement in 1994. [Ref. 4]

The system determines wind velocities along the line-of-sight by measuring the Doppler shift of the laser return due to aerosols entrained in the wind, and calculates range by measuring the elapsed time for the laser pulse return. Laser parameters include a wavelength of 2.0 μm , pulse energy of 7.5 mJ, pulse repetition rate of 100 Hz, and full width half-maximum pulse width of 400 nanoseconds. Airport topography determines the siting position for the lidar, which typically is offset between 350 meters and 1.2 kilometers from the runway centerline. At these ranges, vortices have been tracked even in moderate rain and light fog. Maximum range capability depends on atmospheric conditions; the longest range detection of wake vortices to date is approximately 3 kilometers. The lidar is scanned in a vertical plane, typically perpendicular to the runway centerline, but measurements can be made in other planes. The effective range resolution of the lidar is approximately 30 meters, and the velocity resolution is on the order of 0.5 meters per second, depending on processing parameters. The scan rate, integration time, range of the measurement, and the laser beam diameter determine the vertical resolution, which is typically less than 0.5 meters. The lidar provides a velocity field in the plane being scanned.

Lidar returns are processed in real time. Internal lidar products include various velocity displays, vortex positions, and vortex circulations. Figure 1 shows a plot of the measured velocity versus elevation angle in four adjacent range bins. The displayed velocities are the maximum detected velocities towards and away from the lidar; the plots are centered at the ambient wind velocity. These maximum vortex velocities are determined from Fast Fourier Transforms (FFT) of the heterodyne signal using the highest and lowest frequencies that have magnitudes above a predetermined threshold. After the passage of each aircraft, a file, containing the times each vortex exits the top, bottom, left, or right limits of the corridors, the time that any vortex above a threshold circulation stays within predetermined corridors at the scan plane, and the time the vortex falls below the threshold circulation, is transmitted to AVOSS to confirm predictions of vortex behavior. The file also includes vortex lateral and vertical position and circulation versus time.

The real-time processor, developed at NASA/LaRC, is based on a Signatec 500 Ms/s 8-bit digitizer and Mizar Digital Signal Processor (DSP). A SCRAMNet network transmits data between the scanner, the digitizer, DSP computer, and the real-time display computer, while a computer-controlled, 360-degree hemispherical scanner steers the laser beam.

A 16-meter long trailer serves as a mobile laboratory to house the laser transceiver, operator's console, scanner, signal processing and post-processing computers, as well as video systems, a weather station, and a Global Positioning System (GPS) receiver. The laser beam is expanded before exiting the trailer and is unconditionally eye safe, thus imposes no limits on operation due to concern for personnel safety. The invisible laser beam does not distract pilots or air traffic controllers.

ORF Deployment

The NASA/LaRC WVL Project conducted its initial wake vortex deployment at Norfolk International Airport (ORF) from February 18, 1997, to April 21, 1997. At ORF, the trailer was located in an airport overflow parking lot, and the pulse lidar system was configured to scan landings on Runway 5. The perpendicular range to the extended runway centerline was 375 meters. During this deployment vortices from aircraft as small as a two-engine turboprop were detected and tracked. The majority of the aircraft observed at ORF were MD-80s, DC-9s, and B737s.

JFK2 Deployment

The second deployment was to John F. Kennedy International Airport (JFK) from May 26 through June 6, 1997. During this time, the NASA/LaRC WVL Project conducted wake vortex experiments in coordination with independent vortex measurement sensors from Massachusetts Institute of Technology Lincoln Labs (MIT-LL) and Volpe National Transportation System Center (Volpe Center). MIT-LL deployed a 10.6 μm , continuous wave (CW), CO₂ lidar system that was previously tested at Memphis International Airport and a previous JFK deployment (JFK1). [Ref. 5] The Volpe Center instrument, a Ground Wind Vortex Sensing System (GWVSS), consists of a row of anemometers mounted on 30-foot poles, stretching 500 feet on both sides of the runway centerline. The Volpe Center also tested the same system in the previous tests at JFK and a similar system at Memphis. [Ref. 6]

The three wake vortex sensing systems were configured to simultaneously measure aircraft landings on Runway 31R. The MIT-LL lidar was situated 73 meters to the right of the runway centerline and approximately 700 meters from the end of the runway. The Volpe Center GWVSS was positioned directly underneath the glide slope of Runway 31R. The NASA lidar trailer was 371 meters right of the wind line. All sensors covered the same spatial area in order to collect correlated vortex data.

The wake vortex data observed and recorded by the NASA lidar were analyzed and compared with data from the other wake measurement sensors. The results from the comparison validated the pulsed lidar's ability to detect and measure the trajectory and to estimate the strength of the aircraft generated vortices. The aircraft observed during the deployment were the largest that the pulsed lidar system had the opportunity to measure to date. Many of the wake vortex files recorded were of B757s and B767s with a few B747s and DC10s.

Figure 2 shows the lateral position measurements from all three sensors for wake vortices generated by a B747-400. Figure 3 shows the vertical position of the same vortex pair, as measured by the three wake sensors. Figure 4 shows the circulation estimates for the same data set.

DFW Deployment

From September 15, 1997, through October 10, 1997, the NASA LaRC Wake Vortex Lidar Project participated in the first AVOSS Deployment to DFW International Airport. The wake sensors that participated in the JFK2 deployment, as well as a set of meteorological sensors, were utilized at the AVOSS DFW Deployment. Hinton [Ref. 7] gives a detailed description and results of the AVOSS experiment.

The NASA LaRC Pulsed Lidar System was positioned at the North end of the airport, approximately 1710 meters from the end and 852 meters to the right of Runway 17C. Weather conditions varied from hot humid days to heavy thunderstorms, which developed at the end of the day. This deployment was the longest field test of the pulsed lidar system, and wake vortices from over 500 aircraft were measured. Most the aircraft observed were MD-80 class of airplanes with a few B757s, B767s, and B747s. This was the first time that data from the pulsed lidar system was transferred to AVOSS in real-time.

JFK3 Deployment

From October 19 to 22, 1998, the NASA/LaRC Wake Vortex Lidar Project returned to JFK International Airport to test hardware and software enhancements that were implemented since the DFW deployment. The transceiver had been refurbished by CTI since the DFW deployment and signal processing software modifications were made to improve the real-time data processing program.

The pulsed lidar trailer was positioned at the same location used during the JFK2 deployment. At this location, the pulsed lidar system measured wake vortices generated by aircraft landing on Runway 31R. Over 200 wake vortex data files were recorded during the four-day deployment.

In addition to vortex measurements, the lidar system measured and provided the vertical profiles of line-of-sight (LOS) crosswinds in the plane of the measurement, using range bins that were not influenced by the vortices. Algorithms were developed to compute the vertical profiles of turbulent kinetic energy (TKE)

from the crosswind measurements. (Figure 5) Two sonic anemometer systems were deployed to measure the three components of the atmospheric winds in the vicinity of the runway. A preliminary intercomparison between TKE measurements based on the three dimensional sonic anemometer winds and the one-dimensional lidar winds indicate a general agreement in trend with some bias.

Summary

During four field deployments, a pulsed wake vortex lidar system has demonstrated the ability to provide vortex tracks for a variety of aircraft in weather conditions ranging from clear to heavy rain and light fog. NASA researchers and contractors are in the process of implementing hardware and software modifications to improve the performance of the pulsed coherent lidar system. In addition, investigation of the system's ability to provide turbulence data will continue. The NASA/LaRC Wake Vortex Lidar Project will support AVOSS Demonstrations at DFW in the fall of 1999 and spring of 2000.

References

- ¹Britt, Charles L.; Nguyen, Dung Phu Chi; and Koch, Grady: "Pulsed Lidar Measurements of Aircraft Wake Vortices at DFW and JFK." AIAA 99-0982, 37th AIAA Aerospace Sciences Meeting & Exhibit, January 11-14, 1999, Reno, NV.
- ²FAA Integrated Wake-Vortex Program Plan in Support of the DOT/FAA/NASA Memorandum of Agreement Concerning Wake-Vortex Systems Research." DOT/FAA/RD-94/16, DOT-VNTSC-FA427-94-2, August 1994.
- ³D. A. Hinton, "Aircraft Vortex Spacing System (AVOSS) Conceptual Design," NASA Technical Memorandum 110184, August 1995.
- ⁴S. M. Hannon, J. A. Thomson, "Aircraft Wake Vortex Detection and Measurement With Pulse Solid-state Coherent Laser Radar," Journal of Modern Optics, November 1, 1994.
- ⁵R. M. Heinrichs, R. E. Freehart, T. J. Dasey, and R. S. Mandra, "Development and Performance of a CW Coherent Laser Radar for Detecting Wake Vortices," Coherent Laser Radar Conference, Keystone, Colorado, July 23-27, 1995.
- ⁶Abramson, S. and Burnham, D. C., "Ground-Based Anemometer Measurements of Wake Vortices from Landing Aircraft at Airports," Proceedings of 78th Fluid Dynamics Panel Symposium, Characterization and Modification of Wakes from Lift: Vehicles in Fluids, AGARD CP-584, Trondheim, Norway, May 1996.
- ⁷Hinton, David A.; Chamock, James K.; Bagwell, Donald R.; and Grigsby, Donner: "NASA Aircraft Vortex Spacing System Development Status," AIAA 99-0753, 37th Aerospace Sciences Meeting & Exhibit, January 11-14, 1999, Reno, NV.

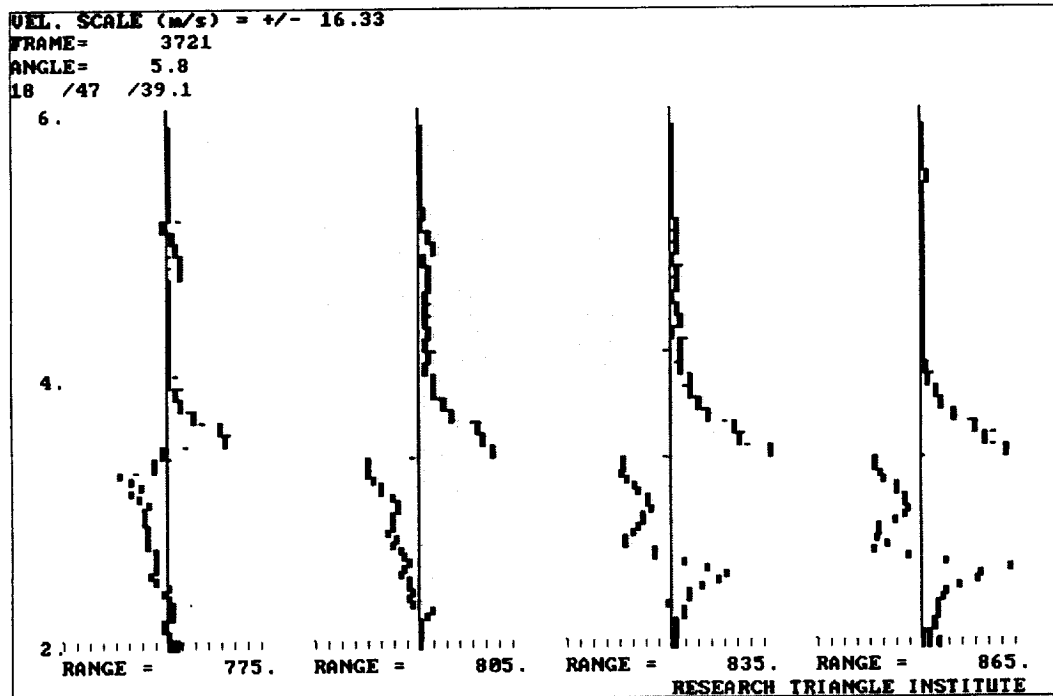


Figure 1- Plot of the measured velocity vs. elevation angles (2 to 6 degrees) for four adjacent range bins. The center of the closest vortex is located in between the range 805 and 835 meters, at an elevation angle of 3.5 degrees. The far vortex can also be seen in the range 835 and 865 meters, at an elevation angle of 2.5 degrees.

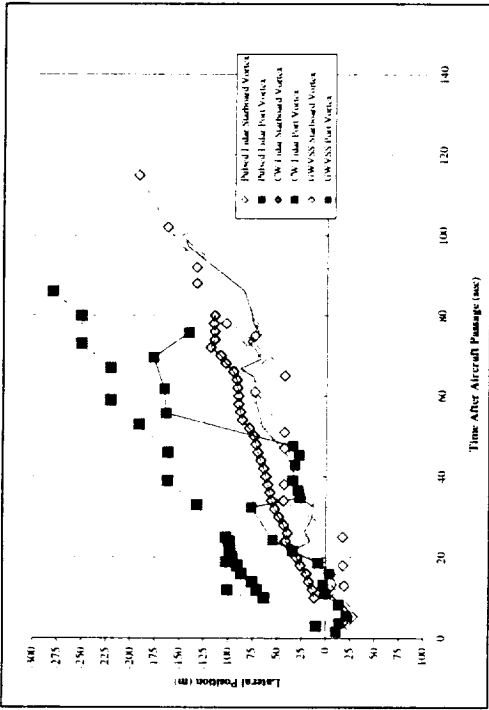


Figure 2-Lateral Position Measured by Wake Sensors of Vortices Generated by B747-400.

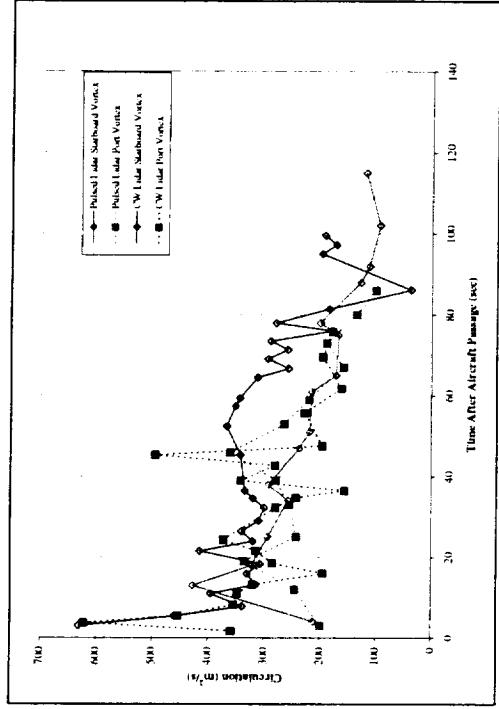


Figure 4-Normalized Circulation Measured by Wake Sensors of Vortices Generated by B747-400.

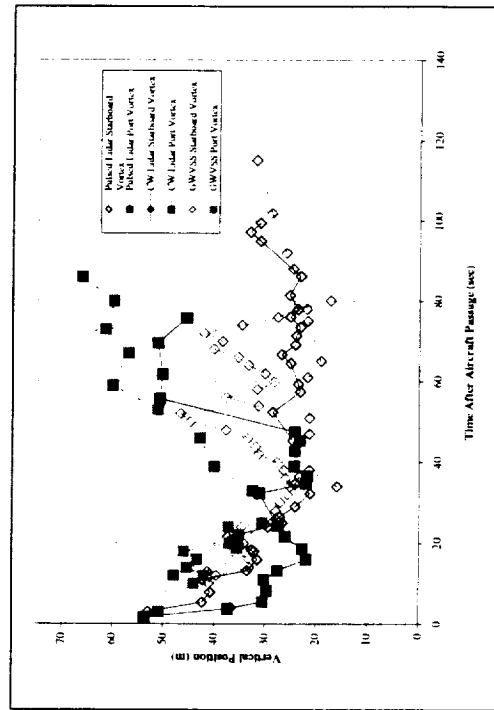


Figure 3-Vertical Position Measured by Wake Sensors of Vortices Generated by B747-400.

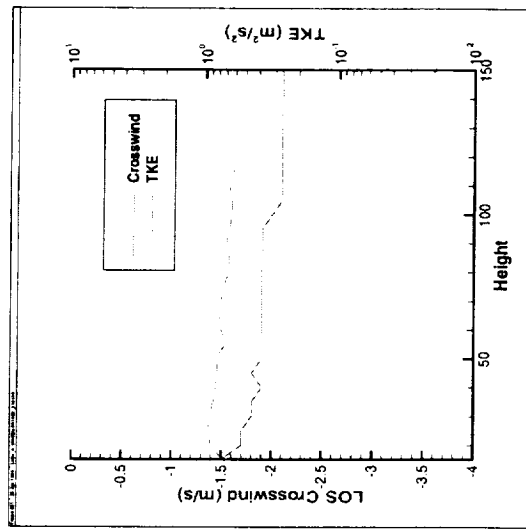


Figure 5 - Vertical Profile of Line of Sight Crosswind and TKE vs. Altitude (meters).

Concept of a cw-laser Doppler sensor as a true airspeed instrument

Juergen Streicher, Ines Leike, Stephan Rahm, Christian Werner, and
Richard Bogenberger⁺

DLR - Lidar Group
P.O.B. 1116
D-82230 Wessling, Germany
Phone: 49 8153 28 1609
Fax: 49 8153 28 1608
e-mail: Juergen.Streicher@DLR.de

⁺DaimlerChrysler Aerospace
P.O.B. 801160
81663 Muenchen, Germany

Introduction

The speed, the angle of attack, and angle of side slip of an aircraft is normally measured by pitot probes and vanes located very close to the aircraft. As modern combat aircraft become more and more independent from aerodynamic flight, formerly unusual flight conditions, like stall or reverse glide, will produce nonsense results on the conventional probes.

The idea behind this concept is to use a remote sensing technique for a close observation of the motion of aircraft relative to its surrounding media without influence from itself. This can be done by detecting the Doppler shift of the aerosols in the vicinity of the aircraft using a laser radar.

Technique

The volume of interest is illuminated by highly monochromatic (i.e. an almost perfect dirac function in the frequency domain) laser light, the back scattered radiation will show a frequency shift relative to the emitted frequency if the scatterers (aerosol particles and molecules) move relatively to the path of the light (LOS: line of sight component). The frequency shift is dependent on the wavelength of the laser and of course on the speed of the particles in the line of sight direction.

The Doppler laser radar principle for itself is divided in either different emitting techniques using pulsed or continuous light sources, or detection techniques using direct or heterodyne/homodyne, i.e. coherent receivers. The specifications of the sensor (see also following table), very high accuracy (0.5 m/s) of the speed at a fixed distance of some meters (3 - 8 meters) but at flight levels up to 40 kft, eliminate clearly pulsed laser sources: the pulse length ought to be in the order of the measurement distance which results in a spectral width of the emitted frequency that is much larger than the aimed accuracy (Fourier transform of the pulse shape). Moreover pulsed systems show optical and electrical disturbances at close measurement ranges resulting from high energy bursts which are necessary to illuminate that few particles sufficiently.

Table 1: requirements for a true airspeed sensor

velocity range:	30 m/s to 650 m/s \pm 0.25 m/s
velocity variation:	$< 25 \text{ m/s}^2$
repetition rate:	40 Hz
measurement distance:	8 m
optical window:	$< 80\text{mm } \varnothing$
altitudes:	S.L. to 40 kft (max. 65 kft)

The remaining laser Doppler systems, whereat cw systems are more often called anemometer because of the lack of ranging, are distinguished by their different detection techniques: incoherent, direct detection or coherent, heterodyne or homodyne detection.

The information, i.e. Doppler shift, can not be measured directly with either techniques: as the laser frequency, which characterises the carrier, is in the order of some Terahertz neither the carrier frequency nor the frequency shift (up to some Megahertz) can be measured directly.

Direct detection

The Doppler shift will be visualised either by interferometry (fringe imaging) or transformed into a intensity information (edge filter). In both cases the laser wavelength has to be stabilised at some kHz. The observation of one and almost only one measurement volume is realised by a slant top view on the laser beam propagation axis (bistatic, offaxis arrangement). The critical items of such a system are so far: adjustment of the transmitter and receiver axis, frequency stabilisation of the laser. Furthermore the different scattering processes (Mie by aerosols and Rayleigh by molecules) have to be separated first.

Coherent detection

The received radiation will be mixed with a small portion of the laser source itself, either at the same carrier frequency (homodyne) or at a slightly shifted frequency (heterodyne). As a result the difference (Doppler shift plus offset in case of heterodyne) can be recorded directly in form of a beating in the order of some Megahertz. The ranging is done by focussing the beam (coaxis arrangement), the volume is well defined by the diffraction limit. Nevertheless one should note, that the scatterers (aerosols only) become more and more extinct with increasing altitude.

Realisation

As a first step a coherent detection continuous wave anemometer has been realised in form of a virtual instrument (computer simulation). This virtual instrument will allow to study the performance of a true airspeed sensor under different environmental conditions depending on instrumental parameters, like focal length, receiver diameter, measurement time, wavelength etc.

The particular problem consists in the statistical nature of this measurement process, especially for large altitudes. Since the measurement volume is very small and only a few scatterers (aerosol particles) are present, the received signal may not be continuous. Instead, we expect single „blips“ and samples with no return signal at all.

The beam radius $W(z)$ of a focused beam at distance z is

$$W(z) = W'_0 \sqrt{1 + \lambda^2(z-f)^2 / \pi^2 W'^4_0} ,$$

where λ is the wavelength, f is the focal length and W'_0 is the beam radius at the focus

$$W'_0 = W_0 / \sqrt{1 + W_0^4 \pi^2 / \lambda^2 f^2} .$$

W_0 is the aperture radius. We define an enlarged measurement volume as a cuboid with length of sides l ,

$W(f-l/2)$ and $v_A t$, where v_A is the aircraft's speed, t is the measurement time and l is the length of measurement volume (input parameter).

For each of the N particles contained in the enlarged measurement volume the coordinates (x,y,z) are chosen equally distributed between $(0,0,0)$ and $(W(f-l/2), v_A t + W(z), l)$. For each particle the backscatter cross section is chosen according to the particle size distribution function.

A particle with coordinates (x,y,z) enters the measurement volume only if $x < W(z)$. It contributes to the signal for times

$$t \in \left(y / v_A, y / v_A + 2\sqrt{W^2(z) - x^2} / v_A \right) .$$

The contribution to the heterodyne signal for this particle is

$$\kappa_k(t) = \begin{cases} \sqrt{\sigma_k} \frac{2\pi}{\lambda z_k^2 W_0^2} \frac{1}{(A^2 + B^2)} \exp(2\pi i \xi) & \text{for } tv_A \in \left(y, y + 2\sqrt{W^2(z) - x^2} \right) \\ 0 & \text{else} \end{cases}$$

where

$$A = \frac{3}{2W_0^2}, \quad B = \frac{\pi}{\lambda z_k} \left(1 - \frac{z_k}{f} \right),$$

x is an equally random distributed random variable between 0 and 1 and σ_k is the backscatter cross section of particle k .

Finally, the heterodyne signal is given by

$$S(t) = 2\text{Re} \sqrt{P_{LO}P_T} \exp \left\{ 2\pi i t (v_{OFF} - 2v_{LOS} / \lambda) \right\} \sum_{n=1}^N \kappa_k(t).$$

where v_{OFF} is the offset frequency (frequency difference between transmitter laser and local oscillator frequencies), P_{LO} and P_T are local oscillator and transmitter laser power, respectively and v_{LOS} is the LOS projection of the aerosol particles speed. It is assumed, that all particles have the same speed during the measurement time. The optical heterodyne signal is transformed into an electrical current using a virtual receiver front end, and finally frequency analysed using Fourier transform (power spectrum peak finder). Figure 2 shows the front panel of the virtual true air speed sensor. The expected blips caused by the lack of scatterers (about 400 particles during the measurement time of 1 ms) can be seen clearly in the optical signal (graph in the right upper corner), whereas the electrical current (center graph) apparently contains noise only. The accumulated power spectrum (500000 samples divided by 512 samples per spectra \approx 1000 spectra) contains nevertheless clearly the relative speed of the aircraft (symmetric peaks at ± 5 MHz in the bottom graph include still the local oscillator offset of here 250 MHz).

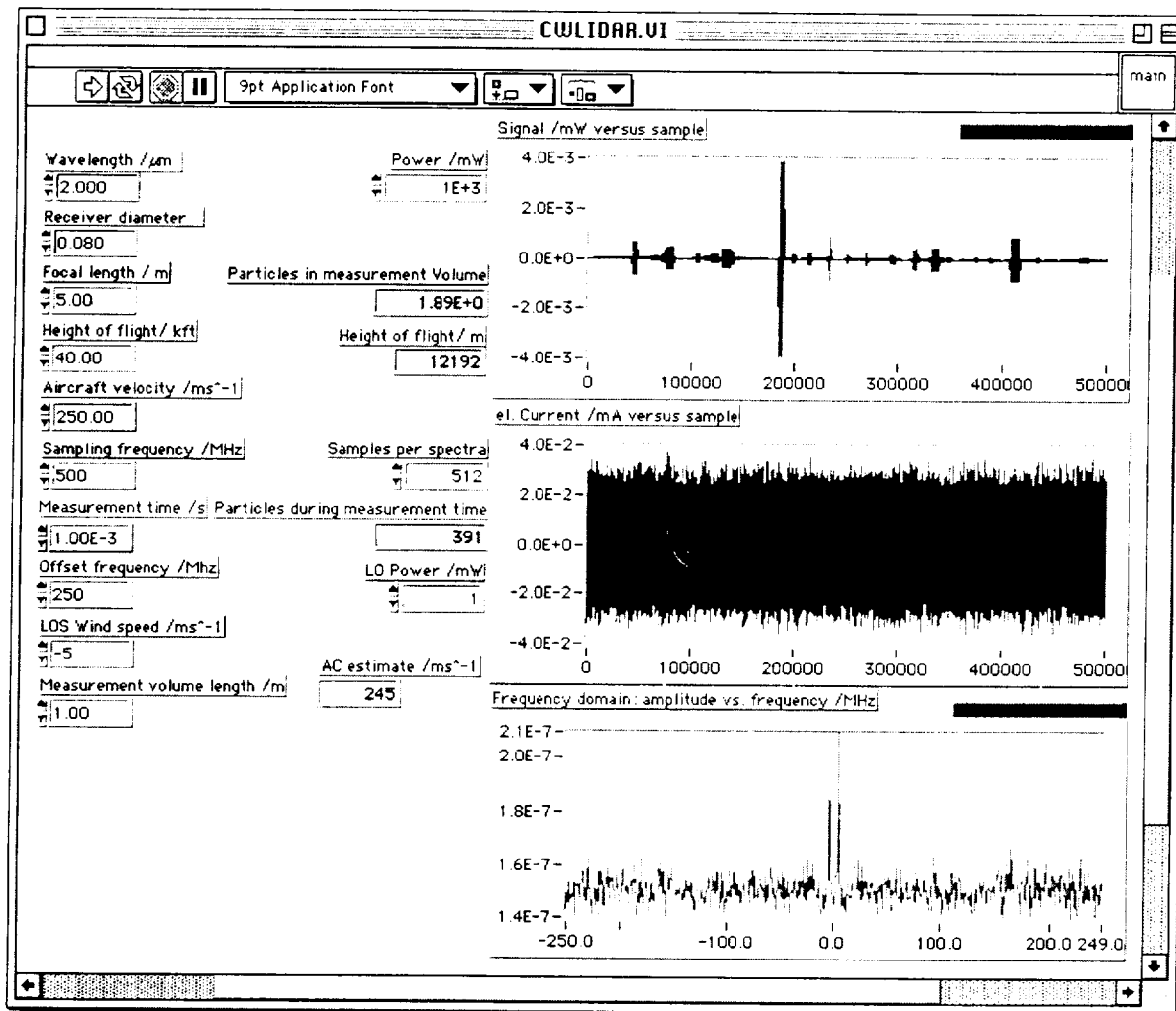


Figure 2: front panel of coherent detection Doppler lidar true airspeed sensor

Conclusion

So far sample calculations using the virtual instrument have shown, that a cw power of 1 W is necessary to ensure the envisaged accuracy of 0.5 m/s in LOS direction at the critical altitude of 40 kft. The simulation will be enhanced including 4 axis measurement geometry (3D plus 1 dimension redundancy) to retrieve full true airspeed information.

Airborne Turbulence Detection and Warning: ACLAIM Flight Test Results

**Stephen M. Hannon and
Hal R. Bagley**

*Coherent Technologies, Inc.
655 Aspen Ridge Drive
Lafayette, Colorado USA 80026
Voice: (303) 604-2000, Fax: (303)-604-2500
e-mail: steveh@ctilidar.com*

Dave C. Soreide

*Boeing Defense and Space Group
Seattle, Washington USA*

David A. Bowdle

*University of Alabama in Huntsville
Global Hydrology and Climate Center
Huntsville, Alabama USA*

**Rodney K. Bogue and L. Jack
Ehernberger**

*NASA Dryden Flight Research Center
Edwards, California USA*

INTRODUCTION

The Airborne Coherent Lidar for Advanced Inflight Measurements (ACLAIM) is a NASA/Dryden-lead program to develop and demonstrate a 2 μm pulsed Doppler lidar for airborne look-ahead turbulence detection and warning. Advanced warning of approaching turbulence can significantly reduce injuries to passengers and crew aboard commercial airliners. The ACLAIM instrument is a key asset to the ongoing Turbulence component of NASA's Aviation Safety Program, aimed at reducing the accident rate aboard commercial airliners by a factor of five over the next ten years and by a factor of ten over the next twenty years. As well, the advanced turbulence warning capability can prevent "unstarts" in the inlet of supersonic aircraft engines by alerting the flight control computer which then adjusts the engine to operate in a less fuel efficient, and more turbulence-tolerant, mode.

Initial flight tests of the ACLAIM were completed in March and April of 1998. This paper and presentation gives results from these initial flights, with validated demonstration of Doppler lidar wind turbulence detection several kilometers ahead of the aircraft.

SENSOR DESCRIPTION AND MEASUREMENT CONFIGURATION

Figure 1 shows a picture of the ACLAIM hardware as installed aboard the National Center for Atmospheric Research (NCAR) Electra research aircraft. The Doppler lidar system, designed and built by Coherent Technologies, Inc., operated at an eyesafe wavelength of 2.0125 μm (Tm:YAG) with a pulse energy of 12 mJ and a pulse repetition frequency of 100 Hz. The pulse duration was 460 nsec (70 m) and the output range resolution was typically 100 m. For these initial flights, the ACLAIM operated with a single line of sight directed 2 deg down and 0.5 deg out from the aircraft axis. With a nominal 2 deg pitch angle, the line of sight was reasonably well matched to the flight track. The aperture diameter was 10 cm (8 cm beam diameter) and the optics were usually focused at a nominal range of 1 km. A variety of real-time data displays were available during the flight, including signal to noise, estimated backscatter, relative airspeed ahead and a short-term-average velocity structure function at 300 m separation. Raw data samples were recorded at the 100 megasample/sec rate out to 9.5 km and are available for post-processing.

The Electra is four-engine turboprop, with a maximum airspeed of 310 knots (160 m/s) and an

operating ceiling of 28,000 feet (8.4 km). The Electra has a sophisticated array of aerosol instrumentation, a gust probe, global positioning equipment, and data acquisition systems to allow comparisons between the lidar and the aircraft systems. These data were recorded and are available for atmospheric characterization analyses and off-line correlation with the lidar observations.

Wavelength: 2.0125 μm
Pulse Energy: 12 mJ
PRF: 100 Hz
Pulse Duration: 460 nsec (70 m)
Aperture Size: 10 cm
Focal Range: Selectable: 1 km and collimated (typ)
Look Direction: Forward-looking: -2 deg down
 and 0.5 deg out from A/C axis
Signal Processor: CTI RASP
Integration Time: 1 sec (typical)
Aircraft Data: Nav, gust probe, aerosol probes (3)

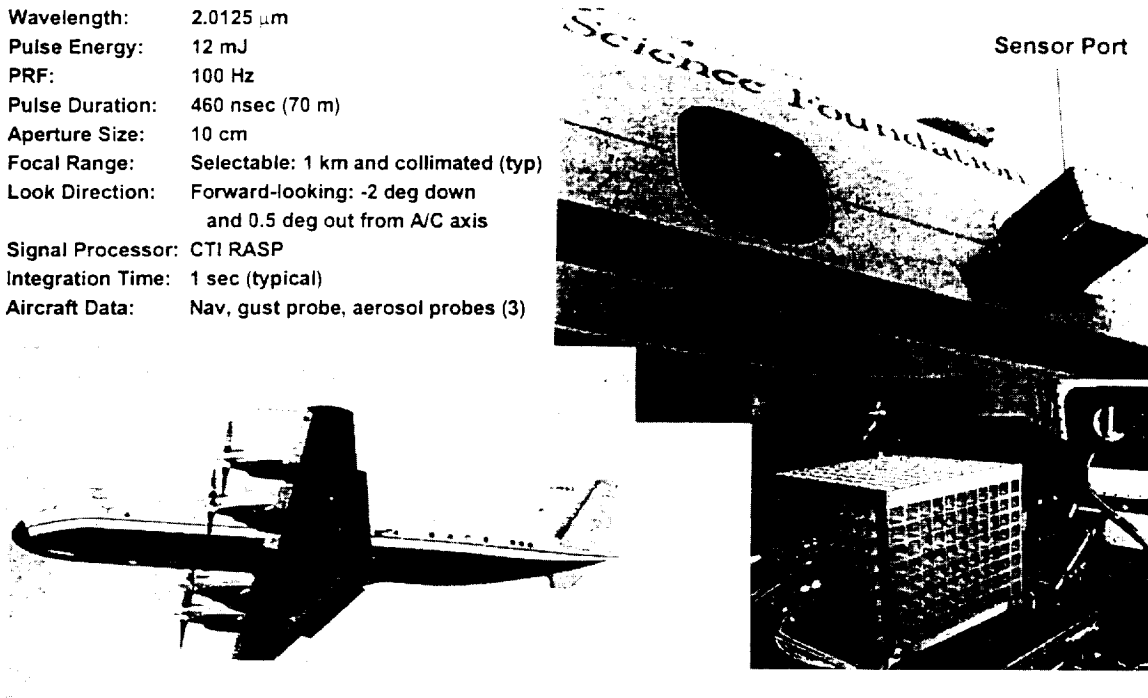


Figure 1 Photograph of NCAR/Electra research aircraft, ACLAIM lidar mounting location and nominal specifications for the Spring, 1998 flight tests.

FLIGHT TESTS

The ACLAIM test flights were conducted over the eastern ridge of the Rocky Mountains and the adjacent High Plains in the west-central U.S.. The five flights comprised roughly 14 hours of flight data. All flights operated out of the Jefferson County Airport in Broomfield, Colorado, between Denver and Boulder. Most flights occurred over eastern Colorado and northern New Mexico. A few short flight legs also penetrated southeastern Wyoming and northwest Nebraska. The maximum flight altitude was 25,000 ft MSL, but a majority of the flight data was collected at altitudes between 10,000 and 15,000 ft MSL where significantly greater wind turbulence regions were encountered.

The primary atmospheric target was patchy lee-wave turbulence near the eastern ridgeline of the Rocky Mountains. Secondary targets included continuous convective turbulence with high aerosol backscatter at lower altitudes over the plains, and quiescent air with low aerosol backscatter at higher altitudes. Throughout the field program, ACLAIM operated quite well. Turbulent features were detected and measured as far as 8 km ahead of the aircraft in high backscatter, and as far as 2-4 km ahead in low backscatter. Turbulence was often accompanied by enhanced aerosol backscatter.

Sample Turbulence Detection

The Doppler lidar's capability to detect turbulent disturbances ahead of the aircraft was clearly demonstrated during the Electra flights. A number of turbulent/gust features were identified on the real time display, tracked as they approached the aircraft, and felt, as the airplane penetrated the

disturbed region. Correlation analyses comparing the time-lagged lidar-measured axial velocity and the eddy dissipation rate with similar measures derived from onboard (in situ) sensors showed good agreement. Figure 2 and Figure 3 plot preliminary lidar-derived turbulence detection metrics for a turbulent feature encountered during the second flight. This encounter was the strongest encounter of the flight program. Figure 2 shows the time history of the lidar-estimated, and time-lagged, eddy dissipation rate (cube root) co-plotted with the RMS vertical velocity and RMS vertical acceleration data, using a five second time window. The correlation appears to be very good, and the scatter plot in Figure 3 bears this out.

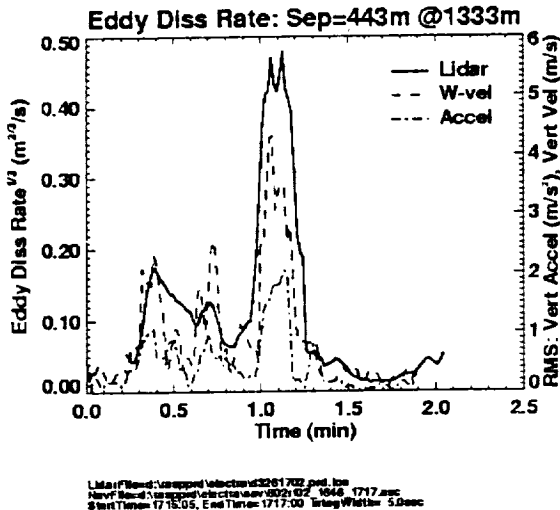


Figure 2 Time history of lidar-measured eddy dissipation rate time lagged and co-plotted with onboard (in situ) RMS vertical velocity and RMS vertical acceleration for a turbulent encounter during the second flight.

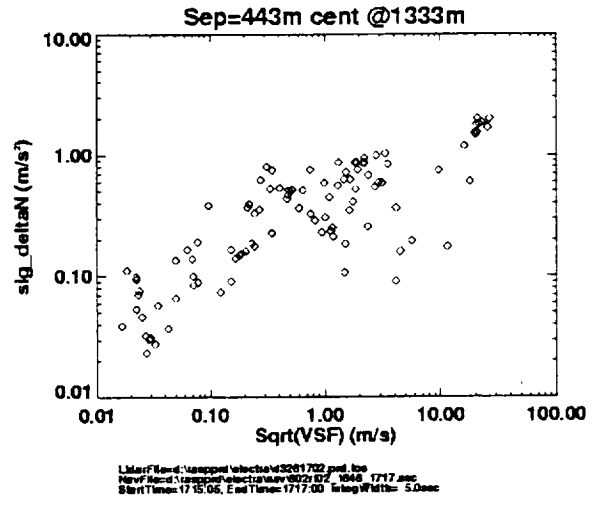


Figure 3 Scatter plot of the RMS vertical acceleration (y-axis) versus the square root of the lidar-measured velocity structure function (x-axis). Data applies to the time sequence plotted in Figure 2.

Sample Lidar-Estimated Aerosol Backscatter

During the flight tests, ground-based calibrations against a diffuse flame-sprayed aluminum (FSA) hard target were conducted before and/or after most flights. These calibrations provided a baseline for detecting and diagnosing drifts or changes in the lidar optical efficiency that may have developed during the flight program, although none were detected. They also provided an absolute radiometric calibration reference for real-time and off-line estimation of the atmospheric aerosol backscatter coefficient, β .

Figure 4 and Figure 5 show the estimated 2 micron backscatter coefficient, β in $\text{m}^{-1}\text{sr}^{-1}$, for selected mid-altitude portions of the second flight. Figure 4 plots the data as a function of the aircraft pressure altitude (MSL) and Figure 5 plots the data as a function of the aircraft ground altitude (AGL). During a majority of the subject flight window, the aircraft was flying upwind and downwind and perpendicular to a ridge line in the Wet Mountains of south-central Colorado. Elevated aerosol backscatter levels showed high correlation with the wind turbulence level. The lower altitude values of the backscatter coefficient are near $10^{-7} \text{m}^{-1}\text{sr}^{-1}$ and are often below $10^{-8} \text{m}^{-1}\text{sr}^{-1}$ above 4000 m MSL. Backscatter estimates for higher altitudes will be presented at the conference.

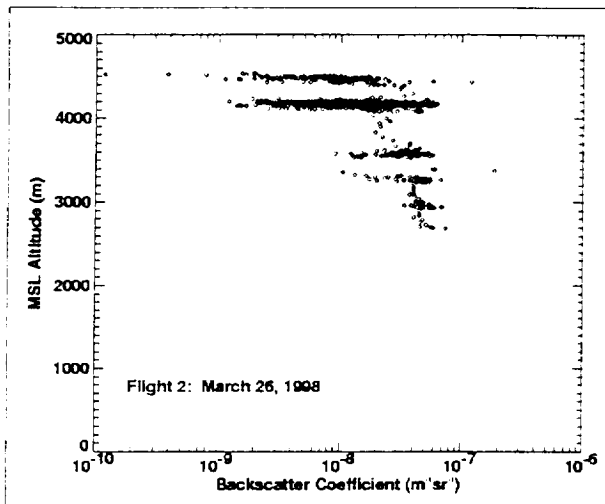


Figure 4 Corrected backscatter estimates versus MSL altitude for Flight 2 on March 26, 1998.

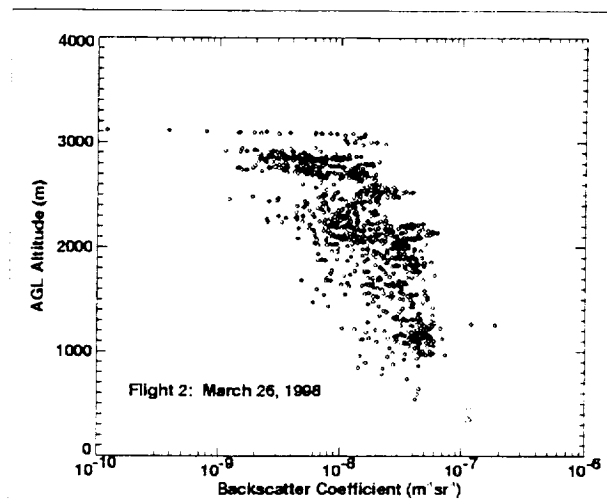


Figure 5 Corrected backscatter estimates versus AGL altitude for Flight 2 on March 26, 1998.

SUMMARY

The initial ACLAIM/Electra flight tests were successfully completed in the Spring of 1998. The lidar hardware and software proved to operate reliably and the maximum measurement range met or exceeded expectations. Real-time advanced detection of turbulent features was routinely demonstrated, with very good correlation with the aircraft's encounter with the same air masses a few to several tens of seconds later. The success of these test flights and the results of the post-flight analyses have important implications for NASA's Space-Readiness Coherent Lidar Experiment (SPARCLE), and the Turbulence component of NASA's Aviation Safety Program (AvSP). The SPARCLE program, with the objective to obtain global-scale wind measurements from low earth orbit on the Space Shuttle, will primarily benefit from the improved understanding of the aerosol backscatter distribution at $2 \mu\text{m}$. The AvSP Turbulence program will primarily benefit from the verifiable lidar database used to support turbulence characterization and turbulence detection algorithm development.

ACKNOWLEDGMENTS

This research is sponsored by the National Aeronautics and Space Administration. The views expressed are those of the authors and do not necessarily represent the official policy or position of the U.S. Government.

Juneau Airport Doppler Lidar Deployment: Extraction of Accurate Turbulent Wind Statistics

Stephen M. Hannon

*Coherent Technologies, Inc.
655 Aspen Ridge Drive
Lafayette, Colorado USA 80026
(303) 604-2000, e-mail: steveh@ctilidar.com*

Rod Frehlich, Larry Cornman, Robert Goodrich, Douglas Norris, John Williams

*Research Application Program
National Center for Atmospheric Research
Boulder, Colorado 80307 USA*

INTRODUCTION

A 2 μm pulsed Doppler lidar was deployed to the Juneau Airport in 1998 to measure turbulence and wind shear in and around the departure and arrival corridors. The primary objective of the measurement program was to demonstrate and evaluate the capability of a pulsed coherent lidar to remotely and unambiguously measure wind turbulence.

Lidar measurements were coordinated with flights of an instrumented research aircraft operated by representatives of the University of North Dakota (UND) under the direction of the National Center for Atmospheric Research (NCAR). The data collected is expected to aid both turbulence characterization as well as airborne turbulence detection algorithm development activities within NASA and the FAA. This paper presents a summary of the deployment and results of analysis and simulation which address important issues regarding the measurement requirements for accurate turbulent wind statistics extraction.

SENSOR DESCRIPTION

The Doppler lidar was an eyesafe coherent Doppler lidar operating at a wavelength of 2.012 μm with a pulse energy of 4.5 mJ (nominal), a pulse duration of 400-500 nsec (FWHM intensity), a pulse repetition frequency (PRF) of 100 Hz, a beam diameter of 5 cm (e^{-2} intensity full width), and a hard aperture of 10 cm. An 8'x7'x8' (WxLxH) wood frame fiberglass shelter housed the lidar, scanner, and control and signal processing electronics. Lidar data was collected and processed at 100 Hz using a CTI-developed RASP (Real-time Advanced Signal Processor). The nominal velocity bandwidth was ± 22 m/sec (± 43 knots). During most of the Juneau data collection, an extended bandwidth mode was utilized with a velocity range of ± 45 m/sec (± 87 knots).

The lidar data was ported in real time to a remote operations center via an RF modem link. A graphical user interface (GUI) in the operations center enabled the operator to manipulate the scanner and signal processing configuration. The radial range resolution of the sensor, which is defined by the pulse duration and the processed range gate size, was 75-100 m. The minimum transverse resolution, which is defined by the beam width, was approximately 15 cm at 3 km. For a scanning configuration, the transverse resolution is defined by the slew rate and integration time.

MEASUREMENT CONFIGURATION

Figure 1 is a map of the Juneau International Airport area. The location of the lidar, operations center and two of the three radar wind profilers are also indicated. Three departure configurations are shown: the Lemon Creek departure, the Fox departure, and the Channel departure. The lidar azimuth scans were designed to track along these departure paths which were flown by the research aircraft. Therefore, the elevation angle was a function of the azimuth angle. The data region used for the analyses presented here is indicated.

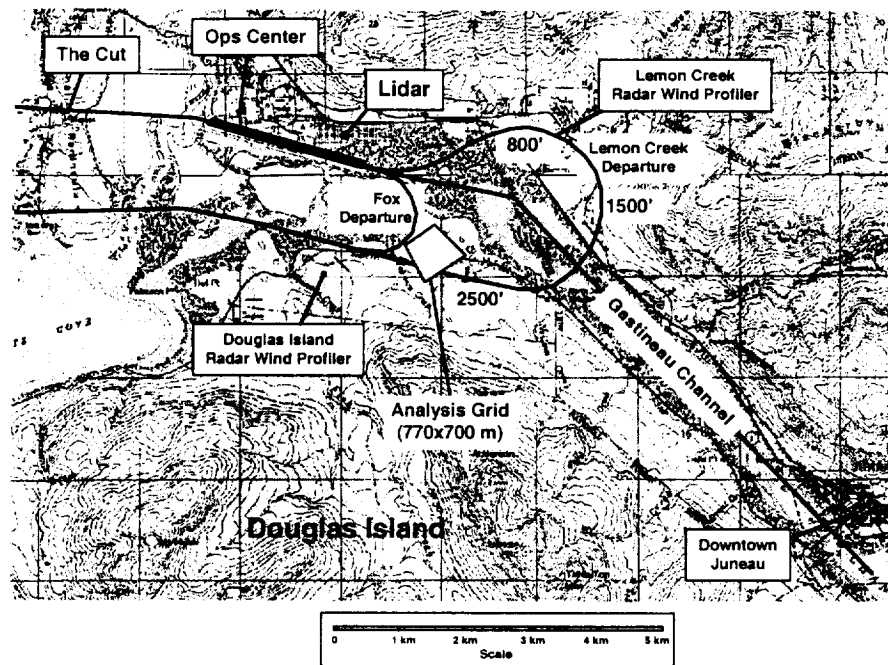


Figure 1 Map of Juneau International Airport and vicinity indicating the operations center location, lidar location, flight patterns and terrain features.

EXTRACTION OF TURBULENCE STATISTICS

Statistical estimates for atmospheric turbulence are useful for understanding boundary-layer processes and linking observations to longer-term predictions of hazardous wind conditions. Until recently, extraction of statistical measures including eddy dissipation rate and turbulent kinetic energy has been limited to in situ point sensors such as anemometers or gust probes aboard research aircraft. The accurate estimation of these statistical measures was successfully demonstrated with a pulsed Doppler lidar operating in a staring mode.¹ Care must be taken to account for the Doppler range resolution, which serves to spatially average the velocity and so underestimate the eddy dissipation rate. The system estimation error must also be taken into account in many cases.

The velocity structure function at range r and for separation distance s is defined as

$$D_v(s, r, t) = \left\langle \left[v'(r - s/2, t) - v'(r + s/2, t) \right]^2 \right\rangle$$

where $v'(r, t) = v(r, t) - \langle v(r) \rangle$, and the mean velocity $\langle v(r) \rangle$ is the total ensemble average over a locally stationary time interval. The eddy dissipation rate ϵ is related to the structure function, and this relationship has a fairly simple form in certain regimes, such as $D_v(s, r) = C_v \epsilon^{2/3} (r) s^{2/3}$, with $C_v = 2$ (see Monin and Yaglom²). In reality, the ensemble average is only approximated. For staring beam data, the ensemble is approximated by a long duration time series of the observed radial velocities. For the Juneau deployment, the lidar was scanning and the ensemble approximation is derived from a combination of temporal and spatial integration.

¹ R. G. Frehlich, S. M. Hannon, and S. W. Henderson, "Coherent Doppler lidar measurements of wind field statistics," *Boundary-Layer Meteorol.* **86**, 233-256 (1998).

² A. S. Monin and A. M. Yaglom, *Statistical Fluid Mechanics: Mechanics of Turbulence*, Vol. 2, MIT Press (1975).

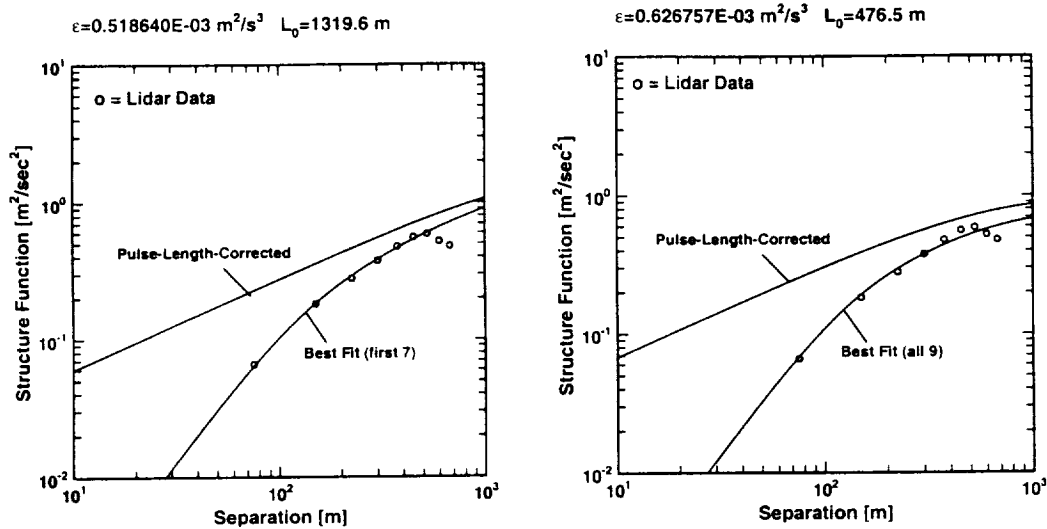


Figure 2 Velocity structure function versus separation distance. Open circles are lidar estimates derived from five consecutive azimuth scans through a region measuring 700 m by 770 m. The left panel shows the best fit structure function using the first seven estimates (separation <550 m). The right panel shows the best fit structure function using all nine estimates. The effects of the pulse duration and processing window are removed as described in Ref. 1, but for a Von Karman structure function model. Best fit ϵ and outer scale (L_0) are given at the top of each plot.

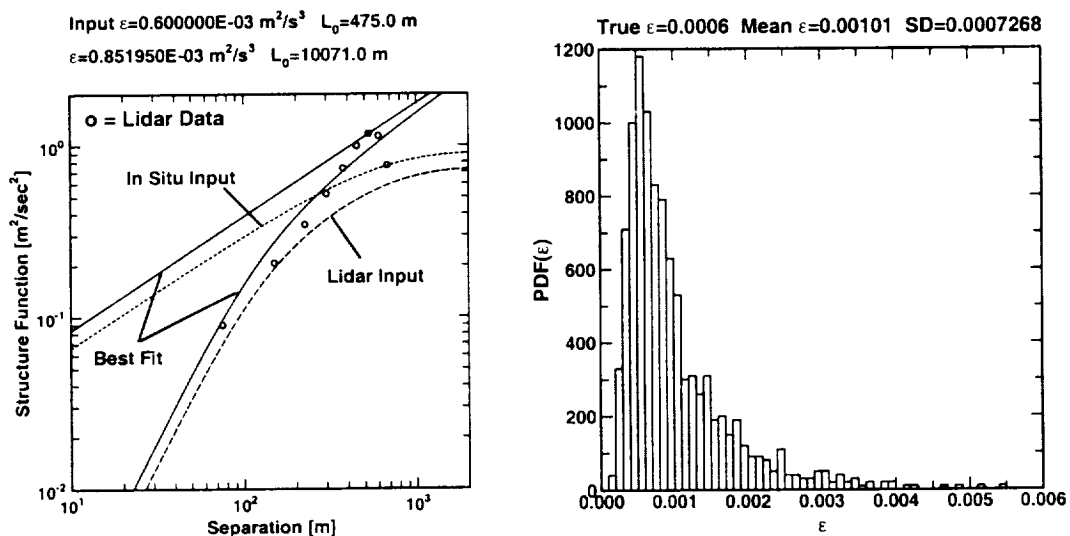


Figure 3 Results of a lidar simulation with a 2D turbulence model.³ The left panel shows a single realization for one scan through a 700 m by 770 m region and the turbulence parameters of Figure 2. The right panel shows a histogram from 1000 simulated scans with an input eddy dissipation rate of $0.006 \text{ m}^2/\text{s}^3$. The estimated mean and standard deviation are $0.001 \text{ m}^2/\text{s}^3$ and $0.0007 \text{ m}^2/\text{s}^3$, respectively.

³ R. G. Frehlich, "Effects of Wind Turbulence of Coherent Doppler Lidar Performance," *J. Atmos. Oceanic Technol.* **11**, 54-75 (1997).

Figure 2 shows structure function estimates derived from five consecutive azimuth scans through a region measuring 700 m by 770 m (some 100 independent measurements per scan). The best fit eddy dissipation rate and outer scale estimates are observed to vary by roughly 15% and more than 50%, respectively, depending on the maximum separation distance used in the fitting algorithm. The mean value for ϵ derived from in situ aircraft data during five penetrations of the analysis grid was $0.00068 \text{ m}^2/\text{s}^3$, in reasonably good agreement with the lidar predictions.

Figure 3 shows the results of a lidar simulation with a 2D turbulence model and system and atmospheric parameters designed to match the experimental conditions. A single realization for a single scan through a 700 m by 770 m region is shown along with a histogram from 1000 simulated scans. The histogram indicates that the estimate statistics are nearly exponential (low order Gamma), with a simulation mean and standard deviation of $0.001 \text{ m}^2/\text{s}^3$ and $0.0007 \text{ m}^2/\text{s}^3$, respectively.

Figure 4 shows the structure function estimates for the 2D windfield-plus-lidar simulation and an ensemble derived from 1000 scans through the 700 m by 770 m region. The nine-point fit to the lidar data yield eddy dissipation rate and outer scale estimates within 3% and 10% of the input values.

SUMMARY

An eyesafe, solid-state two micron Doppler lidar was successfully deployed at the Juneau Airport in March and April of 1998. The lidar velocity data has been processed to extract turbulent statistics estimates with a combination of temporal and spatial averaging to approximate the ensemble average. Substantial fluctuations were observed in both the eddy dissipation rate and the outer scale for averages over a single scan through a 700 m x 770 m region. The fluctuations were reduced by the addition of temporal averaging over five consecutive scans. A detailed simulation was employed to further explore the requirements for generating the ensemble average. The simulation showed that even after averaging 1000 scans, the fluctuations are still noticeable. These fluctuations are not due to lidar estimation error. Rather, they are directly attributable to the real fluctuations that exist in the wind field and the limited number of independent realizations of the largest scales within the averaging period and region. Additional results and analyses will be presented at the conference.

ACKNOWLEDGMENTS

This research is sponsored by the National Aeronautics and Space Administration and by the National Science Foundation through an Interagency Agreement in response to requirements and funding by the Federal Aviation Administration's Aviation Weather Development Program. The 2 μm Doppler lidar transceiver was developed under a NASA Phase II Small Business Innovative Research (SBIR) grant (P. Brockman, technical monitor). The views expressed are those of the authors and do not necessarily represent the official policy or position of the U.S. Government.

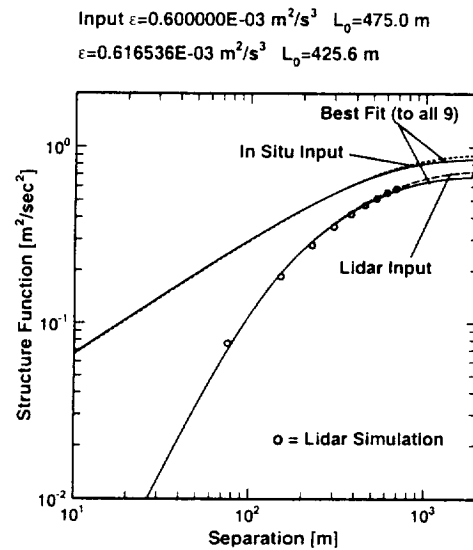


Figure 4 Velocity structure function estimates versus separation distance for the simulation of Figure 3. Open circles are the lidar estimates derived from 1000 consecutive azimuth scans through a region measuring 700 m by 770 m.

AIRCRAFT MISSIONS

Presider: Fred Holmes

The Multi-center Airborne Coherent Atmospheric Wind Sensor: Recent Measurements and Future Applications

Jeffrey Rothermel
Global Hydrology and Climate Center
NASA Marshall Space Flight Center
977 Explorer Boulevard
Huntsville, Alabama 35806

R. Michael Hardesty, James N. Howell, Lisa S. Darby
Atmospheric Lidar Division
NOAA Environmental Technology Laboratory
325 Broadway
Boulder, Colorado 80303

Dean R. Cutten
University of Alabama in Huntsville
Global Hydrology and Climate Center
977 Explorer Boulevard
Huntsville, Alabama 35806

David M. Tratt and Robert T. Menzies
Laser Remote Sensing Group
Jet Propulsion Laboratory
4800 Oak Grove Drive
Pasadena, California 91109

1. Introduction

The coherent Doppler lidar, when operated from an airborne platform, offers a unique measurement capability for study of atmospheric dynamical and physical properties. This is especially true for scientific objectives requiring measurements in optically-clear air, where other remote sensing technologies such as Doppler radar are at a disadvantage in terms of spatial resolution and coverage. Recent experience suggests airborne coherent Doppler lidar can yield unique wind measurements of--and during operation within--extreme weather phenomena. This paper presents the first airborne coherent Doppler lidar measurements of hurricane wind fields.

The lidar atmospheric remote sensing groups of National Aeronautics and Space Administration (NASA) Marshall Space Flight Center, National Oceanic and Atmospheric Administration (NOAA) Environmental Technology Laboratory, and Jet Propulsion Laboratory jointly developed an airborne lidar system, the Multi-center Airborne Coherent Atmospheric Wind Sensor (MACAWS). The centerpiece of MACAWS is the lidar transmitter from the highly successful NOAA Windvan[1]. Other field-tested lidar components have also been used, when feasible, to reduce costs and development time. The methodology for remotely sensing atmospheric wind fields with scanning coherent Doppler lidar was demonstrated in 1981[2]; enhancements were made and the system was reflowed in 1984[3]. MACAWS has potentially greater scientific utility, compared to the original airborne scanning lidar system[2,3], owing to a factor of ~60 greater energy-per-pulse from the NOAA transmitter. MACAWS development was completed and the system was first flown in 1995. Following enhancements to improve performance, the system was re-flown in 1996 and 1998. The scientific motivation for MACAWS is three-fold: obtain fundamental measurements of subgrid scale (i.e., ~2-200 km) processes and features which may be used to improve parameterizations in hydrological, climate, and general/regional circulation models; obtain similar datasets to improve understanding and predictive capabilities for similarly-scaled processes and features; and simulate and validate the performance of prospective satellite Doppler lidars for global tropospheric wind measurement.

2. Instrument Description

Details on the MACAWS instrument and methodology are described in detail elsewhere[4,5]. Briefly, MACAWS consists of: a frequency-stable pulsed transverse-excited atmospheric pressure CO₂ laser emitting 0.5-1.0 J per pulse between 9-11 μm (nominally 10.6 μm) at a nominal pulse repetition frequency of ~20 Hz; a coherent receiver employing a cryogenically-cooled HgCdTe detector; a 0.3 m off-axis paraboloidal telescope shared by the transmitter and receiver in a monostatic configuration; a ruggedized optical table and three-point support structure; a scanner using two counter-rotating germanium wedges to refract the transmitted beam in the desired direction[6]; an inertial navigation system (INS) for frequent measurements of aircraft attitude and speed; data processing, display, and storage devices; and an Operations Control System (OCS) to coordinate all system functions. During flight, laser pulses are transmitted through the scanner, mounted in the left side of the aircraft ahead of the wing. INS measurements of aircraft pitch, roll, and velocity are input to the OCS, which, to maintain precise beam pointing,

rapidly adjusts the scanner to compensate for aircraft attitude and speed changes. Using the INS measurements and scanner settings the OCS estimates and subtracts the frequency contribution to the Doppler-shifted signal due to the component of aircraft motion along the line of sight, yielding LOS wind velocities with respect to earth coordinates. Two-dimensional wind fields are obtained as described below. LOS velocity, backscatter intensity, and wind fields are displayed in real-time to assess lidar performance and data quality, and for in-flight guidance. Data stored for

later analysis include digitized in-phase and quadrature components of the amplified detector output (in limited quantities); laser and signal processor settings and diagnostics; intensity, velocity, and spectral width from multi-lag covariance calculations[7,8]; INS outputs; scanner settings; and aircraft housekeeping.

In addition to the ability to compensate for platform motion in real-time, MACAWS has the unique capability to steer the lidar beam with varying degrees of sophistication, Fig. 1(a-c). In the simplest case (Fig. 1(a)), vertical profiling of LOS velocity and backscatter above or below flight level is achieved by maximally refracting the beam up or down, subject to a refractive limit of ± 32 deg. Profiles at steeper angles over limited regions, with attitude compensation, may be achieved by banking the aircraft. A field of two-dimensional winds (Fig. 1(b)), or scan plane, is measured by alternately directing the beam forward and aft by 20 deg from normal relative to the flight heading. Two-dimensional wind velocity is then calculated at the intersections using trigonometry. The scanner and OCS attempt to compensate for heading changes due, e.g., to cross-winds and turbulence. When profiles are required over an atmospheric volume, the scanner may be programmed to obtain multiple scan planes by changing the elevation of the beam between scans (Fig. 1(c)). Thus, wind fields at multiple vertical levels may be mapped.

Previous comparisons with winds derived from the DC-8 INS indicate horizontal wind velocity errors of $\sim 1 \text{ ms}^{-1}$ and ~ 10 deg or less, and pointing errors of 0.1 deg or less under minimally-turbulent conditions[4].

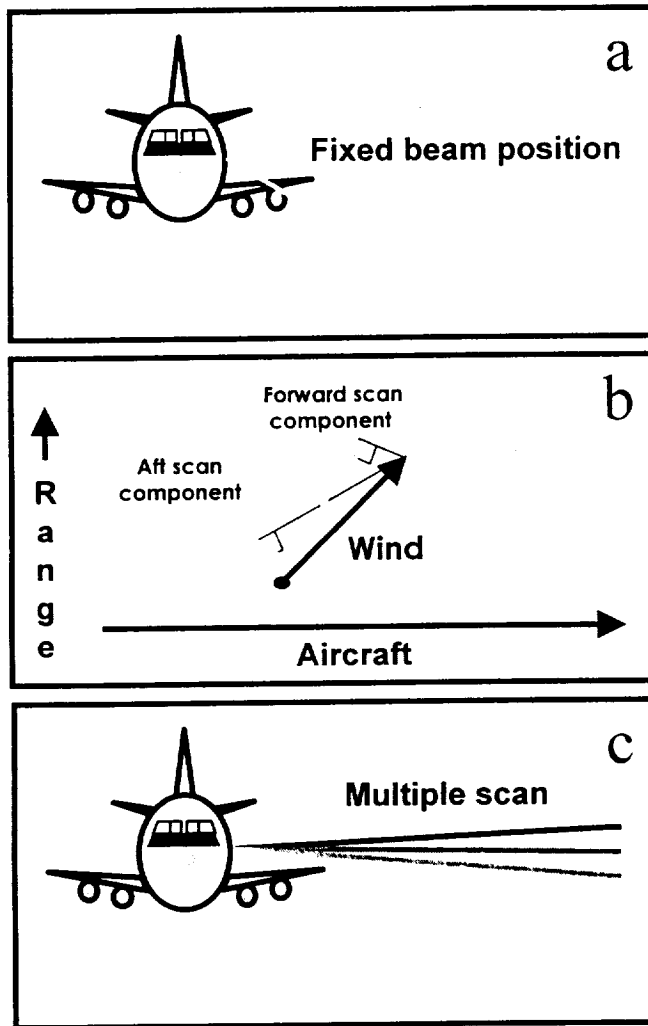


Figure 1. MACAWS beam scanning capabilities: (a) Profiling and angular dependence; (b) wind field in a single scan plane; (c) Three-dimensional coverage (multiple scan planes)

3. Experiment and Results

Measurements were made during 13 August – 22 September, 1998 as part of the Convection and Moisture Experiment (CAMEX-3) and Texas-Florida Underflight (TEFLUN) field programs sponsored by the NASA Office of Earth Science. The purpose of TEFLUN was to validate a space-based radar for measuring tropical rainfall. CAMEX-3 research objectives were to study tropical cyclone intensification and tracking in the western Atlantic Ocean and Gulf of Mexico, using a variety of sensors based on “state-of-the-art” active, passive, optical, and microwave remote sensing technologies[9]. NASA aircraft were based at Patrick Air Force Base in east-central Florida. Aircraft from the NOAA Atlantic Oceanographic and Meteorological Laboratory Hurricane Research Division and the US Air Force 53rd Weather Reconnaissance Squadron, based elsewhere, also participated. Flights were made into hurricanes Bonnie (twice), Danielle (twice), Earl (once), and Georges (twice). Mission profiles

involved flights into the hurricane proper and/or its environment. Eye penetrations typically were made at 35,000 ft pressure altitude (10.7 km) owing to aircraft safety considerations. Sampling of moist, low-level inflow of air into the hurricane (implicated as a possible mechanism for rapid intensification) was conducted in the less-disturbed environment from altitudes of 17,000-25000 ft (5.2 – 7.6 km). During most of the eyewall penetrations, the aircraft experienced light, and occasionally moderate, turbulence. At least one lightning strike to the aircraft occurred, with no adverse affect on the scientific instrumentation.

Figure 2 shows a portion of the eyewall winds in the northwest quadrant at 10.4 km altitude during an eyewall transect of Bonnie as the cyclone made landfall in the Carolinas. The approximate location of the analysis is indicated on a visible satellite image obtained ~20 minutes earlier. The gridded two-dimensional wind velocities were calculated using the National Center for Atmospheric Research (NCAR) software package ‘Custom Editing and Display of Reduced Information in Cartesian space,’ CEDRIC[10]. Owing to the vertical distribution of scan patterns (-20, -10, 0, 10, 20 deg), horizontal wind fields were calculated from 10.1 – 10.5 km in 100 m vertical intervals. Results show an extremely tight velocity gradient along the inner edge of the eyewall. Wind velocities were in good agreement with flight-level winds derived from the aircraft INS.

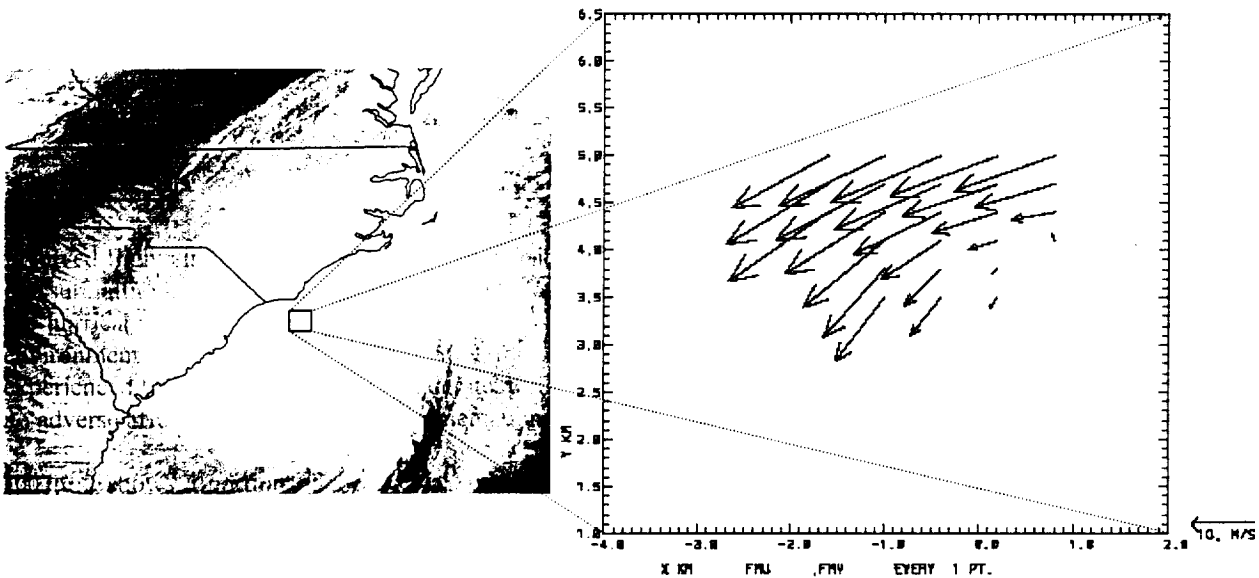


Figure 2. Eyewall wind measurements in Hurricane Bonnie, 26 August 1998, 1625 UTC, with MACAWS airborne coherent CO₂ Doppler lidar. These represent the first hurricane wind measurements with Doppler lidar.

4. Conclusions

Our experience has confirmed that airborne coherent Doppler lidar has the capability to obtain wind measurements within the hurricane, in the absence of hydrometeors where conventional scanning Doppler radars have insufficient scatterers to map the wind field. Thus, it is possible to achieve a more complete picture of hurricane dynamical structure, especially if measurements by airborne Doppler lidar and radar are coordinated in space and time. Our results, though, were dependent on cloud distribution and opacity. Best performance was achieved in the optically-thin cirrus region of the central dense overcast (CDO), a broad shield of cirrus cloud centrally-located in the upper level of the cyclone (see Fig. 2 for an example). Propagation occasionally extended to 20 km or more, owing to minimal beam attenuation. At other times, however, optically-dense cloud precluded wind measurements beyond the lidar minimum range of ~1.5 km.

Future applications include simulation and validation of planned satellite Doppler wind lidars (SDWL). In particular, plans are underway to underfly the SPACe Readiness Coherent Lidar Experiment (SPARCLE) Space Shuttle mission planned for spring 2001[11,12]. SPARCLE is the second mission to be conducted under the NASA New Millennium Program Earth Orbiting component (EO-2) to transition remote sensing technologies to space. Since there is no space heritage for Doppler lidar measurements, a variety of validation measurements are planned

throughout the two-week shuttle mission. MACAWS will provide fine-spatial resolution measurements with which to evaluate the representativeness of SPARCLE winds.

Finally, we note that technological maturity may be defined in a number of ways, such as turnkey system operation, system miniaturization, or measurements from space. Our experience suggests perhaps another criterion for maturity, namely successful operation in a hostile meteorological environment.

5. Acknowledgments

We gratefully acknowledge the assistance of W.A. Brewer, S.P. Sandberg, and R.M. Banta, NOAA Environmental Technology Laboratory; R.D. Marchbanks and A.M. Weickmann, U. Colorado, Cooperative Institute for Research in Environmental Sciences; C. Esproles, Jet Propulsion Laboratory; S.H. Harper and R.W. Lee, Lassen Research; S.C. Johnson, NASA Marshall Space Flight Center; P.A. Kromis, Computer Sciences Corporation; and the DC-8 staff of NASA Dryden Flight Research Center. In particular, we gratefully acknowledge Dr. Ramesh Kakar, NASA Office of Earth Science, without whose support this program would not be possible.

6. References

1. Post, M.J. and R.E. Cupp: Optimizing a pulsed Doppler lidar. *Appl. Opt.* **29** (1990) 4145-4158.
2. Bilbro, J.W., G.H. Fichtl, D.E. Fitzjarrald, and M. Krause: Airborne Doppler lidar wind field measurements. *Bull. Amer. Meteor. Soc.* **65** (1984) 348-359.
3. Bilbro, J.W., C.A. Dimarzio, D.E. Fitzjarrald, S.C. Johnson, and W.D. Jones: Airborne Doppler lidar measurements. *Appl. Opt.* **25** (1986) 3952-3960.
4. Rothermel, J., D.R. Cutten, R.M. Hardesty, R.T. Menzies, J.N. Howell, S.C. Johnson, D.M. Tratt, L.D. Olivier, and R.M. Banta: The Multi-center Airborne Coherent Atmospheric Wind Sensor, MACAWS. *Bull. Amer. Meteor. Soc.*, **79**, 581-599 (1998).
5. Howell, J.N., R.M. Hardesty, J. Rothermel, R.T. Menzies: Overview of the first Multicenter Airborne Coherent Atmospheric Wind Sensor (MACAWS) experiment: conversion of a ground-based lidar for airborne applications. *Proc. Soc. Photo. Instrum. Eng.*, **2833**, 116-127 (1996).
6. Amirault, C. T., C. A. Dimarzio: Precision pointing using a dual-wedge scanner. *Appl. Opt.*, **24**, 1302-1308 (1985).
7. Lee, R.W. and K.A. Lee, 1980: A poly-pulse-pair signal processor for coherent Doppler lidar. *Reprints, Topical Meeting Coherent Laser Radar for the Atmos.*, Aspen CO, Opt. Soc. Amer., paper WA2, 1-4.
8. Rye, B.J. and R.M. Hardesty, 1994: Spectral matched filters in coherent laser radar. *J. Modern Opt.*, **41**, 2131-2144.
9. More information on CAMEX-3 may be found on the World Wide Web at the following uniform resource locator: <http://ghrc.msfc.nasa.gov/camex3/>.
10. Mohr, C.G. and L.J. Miller, 1983: CEDRIC - A software package for Cartesian space editing, synthesis, and display of radar fields under interactive control. *Preprints, 21st Conf. Radar Meteor.*, Edmonton, Alta., Canada, Amer. Meteor. Soc., 569-574.
11. M.J. Kavaya and G. D. Emmitt: The Space Readiness Coherent Lidar Experiment (SPARCLE) Space Shuttle Mission. Invited paper 3380-02, Proc. SPIE Vol. 3380, p. 2-11, Conference on Laser Radar Technology and Applications III, 12th Annual International Symposium on Aerospace/Defense Sensing, Simulation, and Controls, AeroSense, Orlando, FL (14 April 1998).
12. M. J. Kavaya and G. D. Emmitt: Tropospheric Wind Measurements From Space: The SPARCLE Mission And Beyond. Invited paper OS4-1, Digest of the 19th International Laser Radar Conference (ILRC), p 553, NASA/CP-198-207671/PT2, Annapolis, MD USA (July 1998).

WIND Instrument

Results of ground tests

F. Köpp⁽¹⁾, R. Häring⁽¹⁾, M. Klier⁽¹⁾, E. Nagel⁽¹⁾, O. Reitebuch⁽¹⁾, M. Schrecker⁽¹⁾,
J. Streicher⁽¹⁾, Ch. Werner⁽¹⁾, G. Wildgruber⁽²⁾,
C. Loth⁽³⁾, Ch. Boitel⁽³⁾, P. Delville⁽³⁾, Ph. Drobinski⁽³⁾, P. H. Flamant⁽³⁾, B. Romand⁽³⁾, L. Sauvage⁽³⁾,
D. Bruneau⁽⁴⁾, M. Meissonnier⁽⁵⁾

(1) DLR - Arbeitsgruppe LIDAR
D-82230 Wessling, Germany
tel : 49 8153 28 1321
fax : 49 8153 28 1608
e-mail : oliver.reitebuch@dlr.de

(2) Modulab, 80636 München, Germany

(3) LMD, CNRS, 91128 Palaiseau Cedex, France

(4) Service d'Aeronomie / CNRS / UPMC, 75252 Paris Cedex 05, France

(5) INSU / DT 77 Av Denfert Rochereau, 75014 Paris, France

An airborne coherent Doppler Lidar to retrieve mesoscale wind fields has been developed in the frame of the Franco-German WIND project. The instrument is based on a pulsed CO₂ laser transmitter, heterodyne detection and wedge scanner. The performance of the instrument operating on the ground is reported.

1. Introduction

WIND developed within a common project by CNRS-CNES / DLR is an airborne coherent infrared Doppler lidar for wind velocity measurement. The system is based on pulsed CO₂ laser technology, heterodyne detection and a conical scanning system. Tests and validation measurements of the WIND instrument were done on the ground before integration on aircraft. During December 3 to December 8, 1998 several field tests totalling several hours of experiments were made at Palaiseau with several weather conditions like clear air, snow and rain. The objective was to retrieve the wind field and to check the instrument performance. Intercomparison of wind measurements were made using radiosonde soundings from Trappes located approximately 12 km west of Palaiseau.

2. Instrumental set-up

The instrument was installed in the LMD container in a configuration close to the position defined for aircraft installation. The output energy was varying from 120 mJ to 200 mJ depending of the ageing of the gas. The TE laser pulse was sent through the 20 cm telescope to the atmosphere either vertically or horizontally after propagating successively through various optics on the optical bench. Conical scans were done by using the scanner wedge followed by the aircraft optical window. A full scan with a zenith angle of 30° was completed every 20 s. Horizontal shots were done by putting a dedicated two axis mirror system on the roof of the container.

The signal processing is based on the method of early digitizing. The reference and the atmospheric signals are digitised with 200 MHz to achieve a high bandwidth needed for airborne operation. The real-time display capabilities include the received atmospheric signal, a velocity azimuth display (VAD) and some housekeeping data. The raw data of each record are stored on hard disks. A total amount of 36000 shots with about 1 Gbyte will be gathered during 1 hour of operation.

In a first step - a quality analysis - the raw data will be checked. Several automatic checks will be performed to exclude shots for data processing. This comprises checks on housekeeping data, aircraft attitude, time synchronisation and trigger signals or digitised pulse monitor raw data. After excluding bad shots the data analysis of the pulse monitor signal and the atmospheric signal is done. The steps for data analysis are digital mixing, filtering, decimation and frequency estimation. Radial velocity from the received signal is calculated by using the pulse-pair frequency estimator from single shots with a vertical resolution of 250 m. The wind vector is calculated from the line of sight component for the specific altitude levels using a sine-fit-procedure.

3. Results

Several sets of test measurements have been done horizontally in the planetary Boundary Layer (PBL). Atmospheric signals could be obtained during foggy conditions up to 9 km. Hard target measurements were done on several days. The signature of two hard targets spaced by 300 m could clearly be identified in the signals.

Results of a measurement done on December 5, 1998 are presented below. The synoptic condition on this day is characterised by a low pressure region east of Denmark. Cold, northwesterly air flew over North France on the back of this low. Clear air conditions with a cloud layer at about 3 km to 4 km could be observed. Comparisons with data of a radiosonde launched at Trappes (approximately 12 km west of Palaiseau) were made.

Figure 1 shows the received atmospheric signal (0 to 40 dB) versus range (0 to 10 km) versus shot number (0 to 200). Layers of high backscattered intensity can be seen between 0.5 km to 1 km and 3 km to 4 km (cloud layer). The sine-wave fitting (frequency in MHz vs. scan angle) for one conical scan for the height of 3.5 km is shown in Figure 2. The LOS frequency is shown only for pulses which passed the quality check routines. The calculated horizontal wind-magnitude is 22.8 m/s and the direction is 295°. The root-mean-square-error of the sine-fit is 1.95 m/s.

A comparison of the calculated horizontal wind speed from lidar signals at 13 UTC and data of a radiosonde launched at Trappes at 12 UTC is shown in Figure 3. There is a good agreement of radiosonde and lidar measurements between 0 km to 1 km and 3 km to 4 km, where the received signal is high (see Fig. 1).

4. Conclusion

Tests conducted with several weather conditions show that the WIND instrument is able to make accurate wind profile measurement with a VAD technique. The horizontal velocity component can be obtained by using sine-fit with good accuracy when SNR is greater than 1. A first flight will be performed in June 1999, with special emphasis on testing of routines for correcting flight attitude from GPS (Global Positioning System) and IRS (Inertial Reference Systeme) with ground return from lidar.

Acknowledgement

The development was supported by DLR (Deutsches Zentrum für Luft- und Raumfahrt), CNES (Centre National d'Etudes Spatiales) and INSU/CNRS (Centre National Recherche Scientifique).

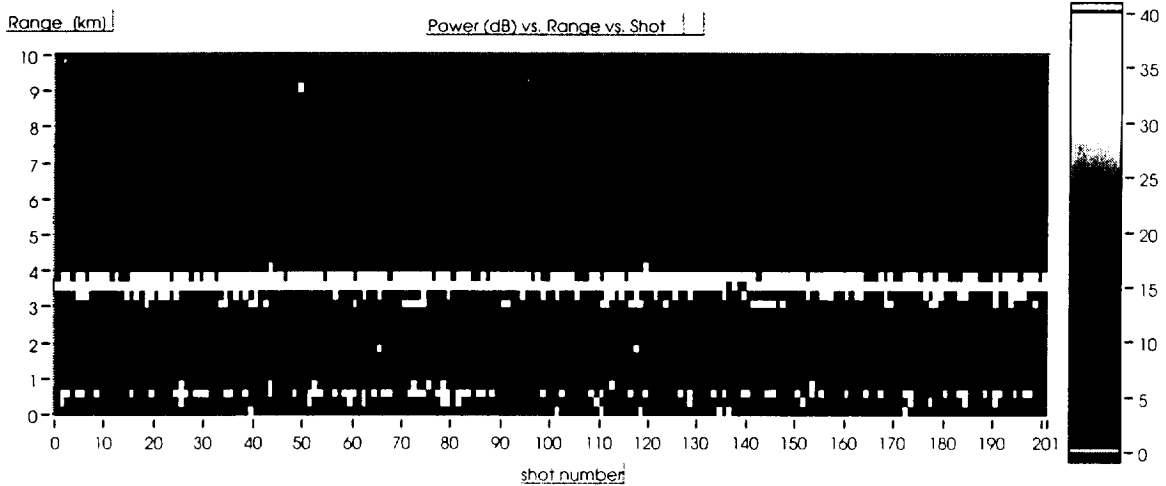


Figure 1: Received atmospheric power (colour coded in dB) vs. shot number vs. range (km) of 200 shots measured with conical scan on December 5, 1998, 13 UTC at Palaiseau; high intensities between 3 km and 4 km within a cloud layer

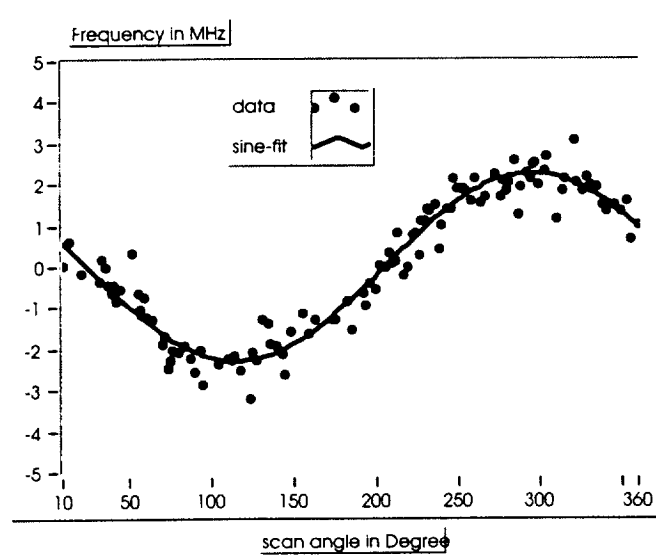


Figure 2 : Frequency (MHz) vs. scan angle at a height of 3.5 km on December 5, 1998, 13 UTC.

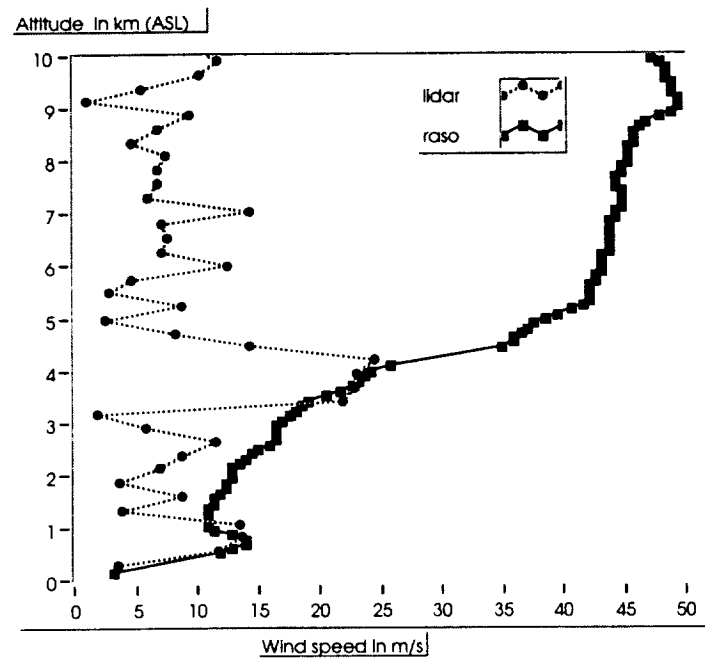


Figure 3 : Comparison of horizontal wind speed (m/s) of radiosonde (Trappes, 12 UTC) and lidar (Palaiseau, 13 UTC) on December, 5

SPECIAL

Presider: Fred Holmes

Improving Scientific Capabilities in Space in the 21st Century: the NASA New Millennium Program

Carol A. Raymond (Jet Propulsion Laboratory, MS 183-501, 4800 Oak Grove Drive, Pasadena, CA 91109; 818-354-8690; craymond@jpl.nasa.gov)

David Crisp (Jet Propulsion Laboratory, MS 180-404, 4800 Oak Grove Drive, Pasadena, CA 91109; 818-354-7969; dcrisp@pop.jpl.nasa.gov)

NASA's New Millennium Program (NMP) has been chartered to identify and validate in space emerging, revolutionary technologies that will enable less costly, more capable future science missions. The program utilizes a unique blend of science guidance and industry partnering to ferret out technology solutions to enable science capabilities in space which are presently technically infeasible, or unaffordable. Those technologies which present an unacceptably high risk to future science missions (whether small PI-led or operational) are bundled into technology validation missions. These missions seek to validate the technologies in a manner consistent with their future uses, thus reducing the associated risk to the first user, and obtaining meaningful science data as well.

The SPace Readiness Coherent Lidar Experiment (SPARCLE) was approved as the second NMP Earth Observing mission (EO2) in October 1997, and assigned to Marshall Space Flight Center for implementation. Leading up to mission confirmation, NMP sponsored a community workshop in March 1996 to draft Level-1 requirements for a doppler wind lidar mission, as well as other space-based lidar missions (such as DIAL). Subsequently, a study group was formed and met twice to make recommendations on how to perform a comparison of coherent and direct detection wind lidars in space. These recommendations have guided the science validation plan for the SPARCLE mission, and will ensure that future users will be able to confidently assess the risk profile of future doppler wind missions utilizing EO2 technologies. The primary risks to be retired are: (1) Maintenance of optical alignments through launch and operations on orbit, and (2) Successful velocity estimation compensation for the Doppler shift due to the platform motion, and due to the earth's rotation. This includes the need to account for all sources of error associated with pointing control and knowledge. The validation objectives are: (1) Demonstrate measurement of tropospheric winds from space using a scanning coherent Doppler lidar technique that scales to meet future research (e.g. ESSP) and operational (e.g. NPOESS) mission requirements. Specifically, produce and validate LOS wind data with single shot accuracy of 1-2 m/s in regions of high signal-to-noise ratio (SNR), and low atmospheric wind turbulence and wind shear, (2) Collect the atmospheric and instrument performance data in various scanning modes necessary to validate and improve instrument performance models that will enable the definition of future missions with greater confidence. Such data include aerosol backscatter data over much of the globe, and high SNR data such as that from surface returns, and (3) Produce a set of raw instrument data with which advanced signal processing techniques can be developed. This objective will permit future missions to better understand how to extract wind information from low backscatter regions of the atmosphere.

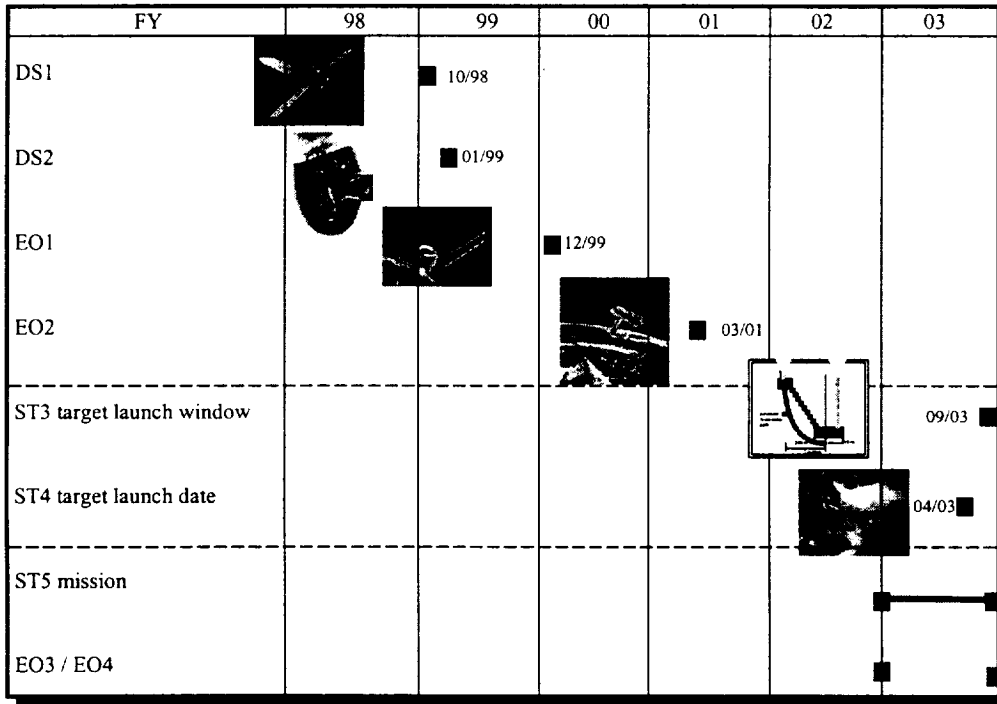
To date, four NMP technology validation missions are in the implementation phase, and three others are seeking final approval for implementation. Deep Space 1 (DS1), launched in July 1998, is slated to visit asteroid 1992 KD in July 1999. DS1 has successfully validated a solar electric (ion) propulsion system. In addition, two innovative compact instruments, the Miniature Integrated Camera Spectrometer (MICAS) and the Plasma Experiment for Planetary Exploration (PEPE) have been validated. The Mars Microprobe Project (DS2) was launched in January 1999 as a piggyback on the Mars 98 lander, carrying two tiny probes that will crash land into the south polar region of Mars in December 1999. The primary validation experiments on DS2 are a non-ablative aeroshell entry vehicle, and several microinstruments within the probe. The first Earth Observing NMP mission (EO1), set to launch in December of 1999, will demonstrate a lightweight, low-cost system to replace the Landsat ETM+ instrument, and will include a validation of a hyperspectral imager. EO2 (SPARCLE) will test a coherent doppler wind lidar from a shuttle platform in 2001. Pending final approval, Space Technology (ST) 3 will validate technologies for a separated spacecraft optical interferometer, and ST4/Champollion will demonstrate technologies for sample return as well as carrying out the objectives of the planned Champollion comet lander.

The third Earth Observing mission (EO3) is currently being defined. The mission definition process began with a NASA Research Announcement (NRA) soliciting concepts for advanced measurement techniques from orbits other than low-Earth, which would facilitate the goals of the Earth Science Enterprise's long-term plans. Four concepts were chosen and teams formed to carry out a detailed mission design study. A solicitation for breakthrough enabling technologies to populate the concepts was issued and technology providers were selected in June. A selection of one concept to be implemented as the EO3 mission will be made in the fall. Future Earth Science Enterprise NMP missions will likely follow this process, with a new solicitation of measurement concepts released every 2-3 years.

Timely and accurate science input is critical to the success of the program. A New Millennium Science Working Group provides top-level input on existing gaps in capabilities to carry out high-priority future science missions. Competitively selected science teams are tasked with scientific validation, data analysis, and archiving. In the case of EO2, a NRA is due to be released in 1999 to solicit a science team.

Finally, as NMP is a technology validation program, a database is being constructed to archive the results of the technology validation experiments. This database will provide potential users with adequate information to estimate the cost and risk associated with using a NMP-validated technology for the first time.

A tentative NMP schedule is shown below.



A COHERENT FMCW LIDAR MAPPING SYSTEM FOR AUTOMATED TISSUE DEBRIDMENT

Donald Hutchinson, Sc.D., Roger Richards, Ph.D., Glenn Allgood, Ph.D.
Instrumentation and Controls Division, Oak Ridge National Laboratory
Oak Ridge, TN 37831

Introduction

The Oak Ridge National Laboratory (ORNL) is developing a prototype 850-nm FMCW lidar system for mapping tissue damage in burn cases for the U.S. Army Medical Research and Material Command. The first phase of this project involved the development a prototype FMCW laser radar system for mapping tissue damage in burn cases for the U.S. Army Medical Research and Material Command. In its final form, the laser system will provide a 3-D image map of the burn and surrounding area and provide tissue damage assessment. The local coordinates of the damaged tissue will be reconciled with real-world coordinates for ultimately positioning and controlling a pulsed laser for automated removal of the dead or necrotic tissue.

Evaluation of Laser Interaction with Tissue

The first task was to chose the optimum laser wavelength for providing a return signal for ranging. The wavelength selection was derived from models available in the literature on IR laser interaction with tissue. The laser wavelength for this lidar system is in the near-infrared at 850 nm. This choice was based on two considerations: (1) Low relative absorption in skin and (2) high scattering from hemoglobin. 850 nm is near the minimum in skin absorption, while the absorption coefficient for whole blood is nearly 10 times higher. The "absorption" coefficient is primarily due to scattering, more so for blood than skin. Our initial model for the debridement measurement assumes a two layer target, the skin surface which reflects a portion of the incident light due to a Fresnel relectivity of ~3.5%(skin index of refraction ~1.31) and a layer containing blood in undamaged tissue below the burn damaged skin. The return laser signal should then contain primarily two components, one from the surface and one from the blood layer below the burn.

Development of FMCW Lidar Breadboard

Once the wavelength was chosen, a solid state laser at the appropriate wavelength was purchased and a prototype lidar system constructed. The lidar is a Michleson interferometer design with a chirped-frequency laser diode. The laser is a distributed-feedback diode, Model SDL- 5722-H1, which produces approximately 150-mW of power at a wavelength of 850-nm. The laser diode is isolated from stray-light feedback from the optics system with a ferrite isolator. In order to calibrate the lidar system, measurements were made of the thickness of a fused silica optical flat. The reference mirror was blocked for these measurements to simulate the return phase produced only by the thickness of the target. The blue curve in Figure 1 represents the captured return from a 0.6463-inch thick fused silica optical flat.

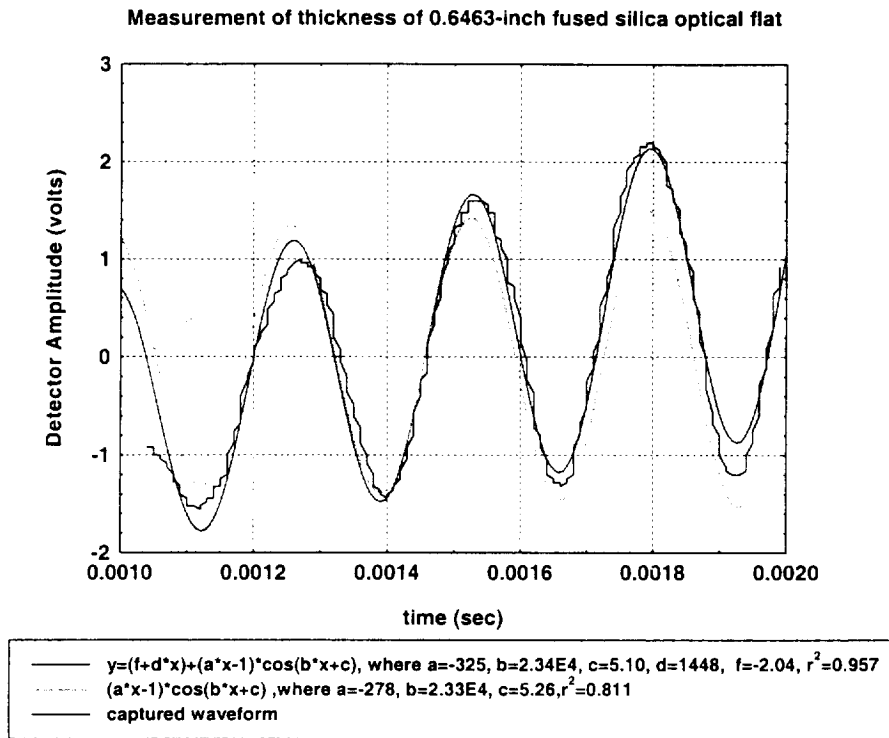


Figure 1 An optical flat is used to calibrate the lidar system.

The red curve is the best fit to a four parameter model that includes a ramp offset represented by the term “ $d*x + f$ ”, a ramping amplitude on the cosine term represented by the term “ $1+a*x$ ”, and the “ b ” term in the argument of the cosine is given by $b = 2\pi f$, where f is the measured beat frequency. For this optical flat the index of refraction, n , is 1.453. After the radian beat frequency “ b ” is determined from fitting the model to the captured waveform, the thickness of the flat may be calculated from the equation

$$t = \frac{bc}{4n\alpha}$$

- where t = thickness
- c = speed of light
- n = index of refraction
- α = bandwidth /sec of the laser chirp.

The calculated value of the thickness $t = 0.1672$ -mm, compared to a mechanically measured value of 0.16715-mm. The error is ~1.8% or approximately 300 microns. There are two factors not yet accounted for in our model. These parameters are (1) the linearity of the laser chirp, which we know from our observations is slightly non-linear, and (2) the exact value of α , the laser chirp bandwidth. The non-linearity of the chirp can be measured in real time with an additional detector we plan to incorporate in our system and the bandwidth can be determined with better accuracy with straight forward improvements in our optical set-up. We expect a measurement accuracy of 30-50 microns in our final system.

VIBRATION MEASUREMENTS

Paul McManamon

Laser Doppler Vibration Lidar Sensing of Structural Defects in Bridges

Dennis Killinger, Priyavadan Mamidipudi

University of South Florida

Tampa, FL 33620

and

J. Potter, J. Daly, E. Thomas

Litton Laser Systems

Apopka, FL 32703

and

Shen-en Chen

West Virginia University

Morgantown, WV 26506-6103

Laser Doppler Vibration (LDV) Lidar systems are being developed for the remote detection of the vibration of targets at both short and long ranges. Recently they have been used for remote detection of the vibration and movement (acceleration) of buildings, structures, and bridges. Along these lines, we are developing a LDV system that can be used for the mapping of the vibrational modes of a bridge through the measurement of the velocity and acceleration of the bridge structure along the length of the bridge. It is the intent of the research to determine the structural integrity of the bridge through these measurements.

Previous work using LDV systems to detect defects in a structure have mostly relied upon the measurement of the change in vibrational or resonance frequencies of the structure as a function of the load or structural failure of a member occurred. However, recent work related to the structural failure modes in a bridge have shown that in many cases the fundamental vibration frequency of the bridge remains almost the same, but that the placement of the nodes and anti-nodes of the resonance vibration of the bridge shifts in location due to a crack or defect in the bridge structure.

Figure 1 shows the Third Bending Mode vibration pattern measured for a 60 ft long Aluminum Bridge that is used as a portable bridge for heavy Army Tanks. The vibration modes and frequencies were measured using the attachment of a large number of commercial accelerometers along one of the three main I-Beams of the bridge. The accelerometers were placed at a separation of about a few inches. As seen in the Figure, the main vibration mode has about 3 nodes and occurred at a frequency of about 9 Hz. Extensive analysis of the vibration frequencies and node location showed that the location of the nodes were very dependent upon the structural integrity of the beam. When a crack or defect occurred in the beam, then the nodes shifted slightly in position.

A complex Strain Energy computer simulation program was developed and used to quantify the link between the node movement and the residual stress in the beam

Previous measurements using a CO₂ LDV Lidar system developed by CLS/Litton Laser showed that the fundamental vibration frequencies of a bridge could be measured at one point along the bridge. Figure 2 shows a measurement of the vibration of a test structure measured using both the CO₂ LDV and a commercial accelerometer. Of interest is the fact that the vibrations of the Golden Gate Bridge were also measured by the LDV system at a range of 2 km. These initial LDV measurements established the sensitivity of the system. However, these preliminary measurements did not provide spatial scanning or mapping of the vibration nodes. As such, an extensive program was developed to provide a vibration map directed toward the use for both civilian bridges and the Portable Tank bridge. Figure 3 shows a schematic of a system being developed which will mount a LDV system upon a Gantry that will be placed over the Tank Bridge. The LDV system will be positioned along the bridge as the bridge is vibrated using commercial shakers.

The LDV system that will be used is being developed in two stages. A commercial LDV system (Ometron VS 100) uses a 1 mW He-Ne laser source and is being used for initial mapping of the surfaces. Preliminary laboratory measurements of the He-Ne LDV have been taken using both vibrating speaker cones and steel I-beams as targets. These results have been compared with results obtained with a commercial accelerometer. For example, Fig. 4 shows velocity and accelerometer results from the speaker target for the two measurement systems. As can be seen, good agreement was observed. One of the difficulties with the He-Ne system is that the laser source is not single longitudinal mode, so that multi-speckle effects are observed resulting in loss of signal at ranges that are multiples of the laser cavity length. This necessitates an automated focusing arrangement with the system

To avoid these speckle effects and to work at longer ranges, a new single-frequency CO₂ Laser Doppler Velocimetry system is being built. This system will use a 5 W CW laser and have a detection range of about 2 km. It is expected that the LDV Lidar system will be used both on the Gantry for the Portable Bridge mapping and at longer ranges for remote bridge measurements.

This work has been supported by Army TACOM (University of West Virginia and Litton Laser Division) and by the Florida I-4 Corridor Industrial Initiative (University of South Florida).

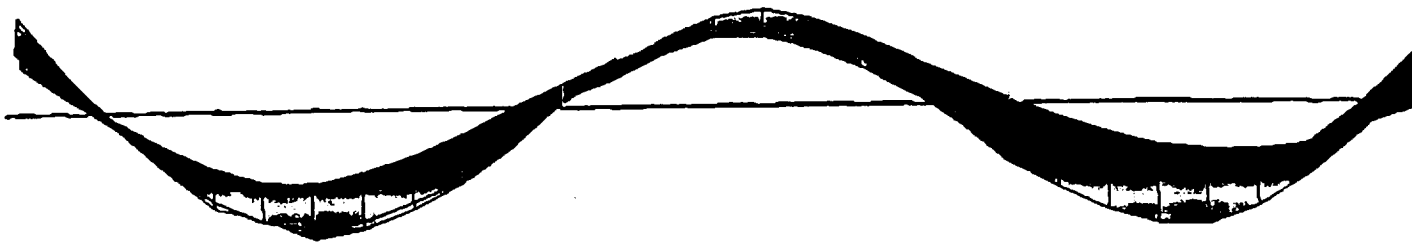


Fig. 1 Map of the main resonance vibration (Third bending mode) of a Portable Army Tank Bridge (60 ft long, Aluminum I-beams). The mode pattern was measured using a set of accelerometers.

BEST-FIT MODE FREQUENCIES AND DAMPING COEFFICIENTS ARE SIMILAR FOR LASER AND ACCELEROMETER DATA

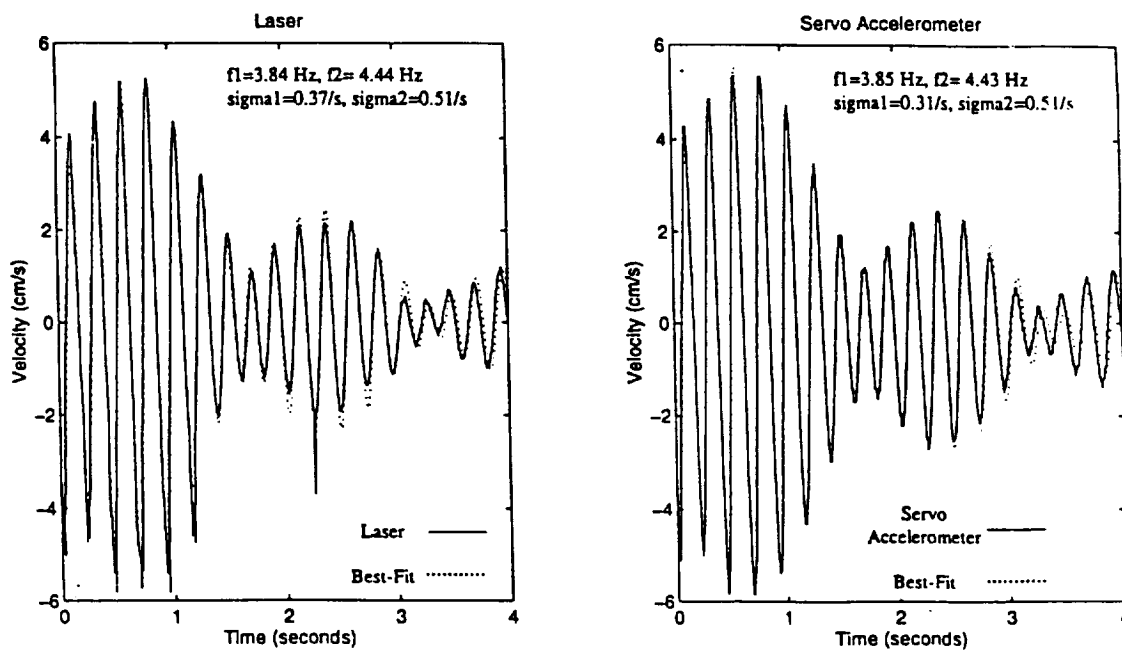


Fig. 2 Measurement of the impulse response vibration of a test structure using simultaneously a CO₂ LDV and a commercial accelerometer.

AVLB Depot Setup

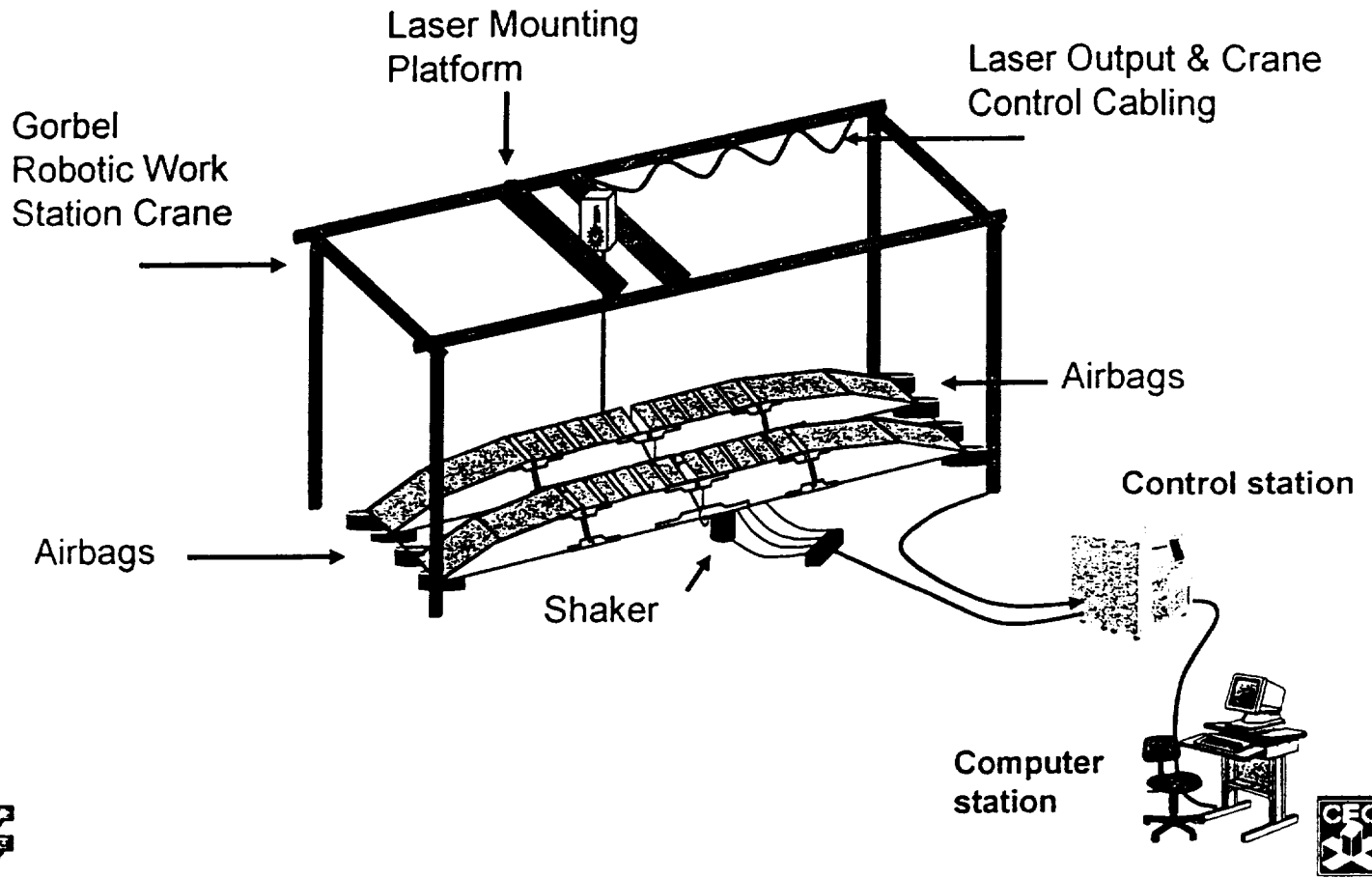


Fig. 3 Schematic of LDV and Gantry to be used to map vibration modes of Portable Bridge.

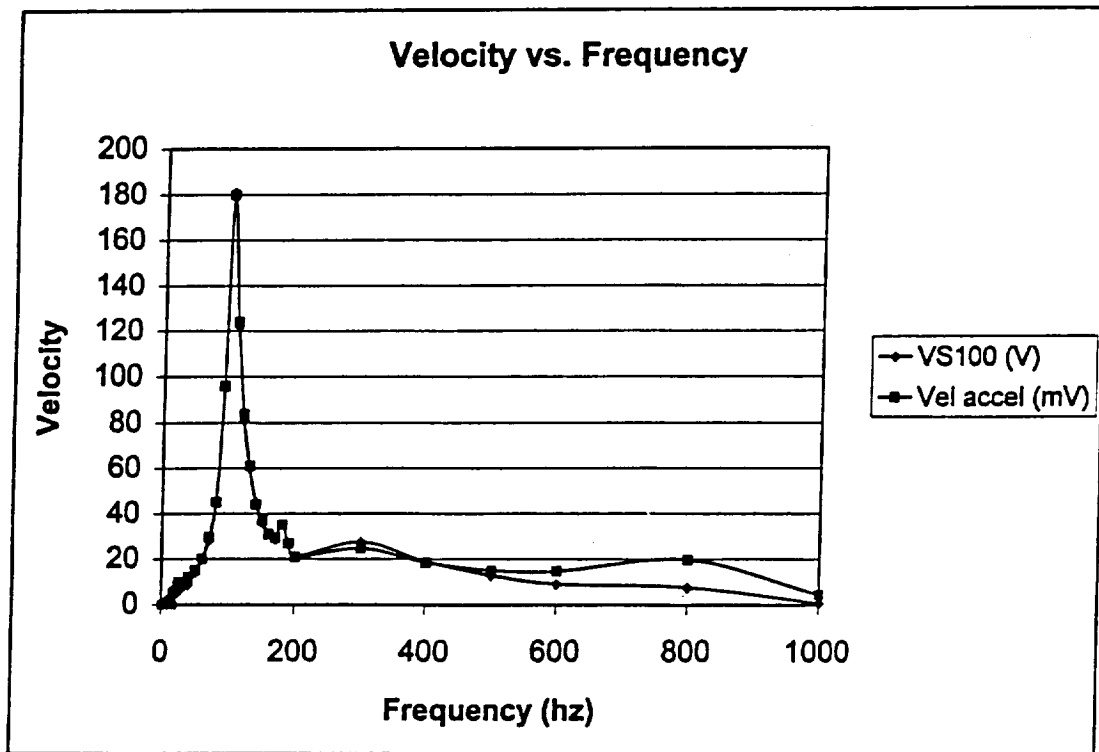
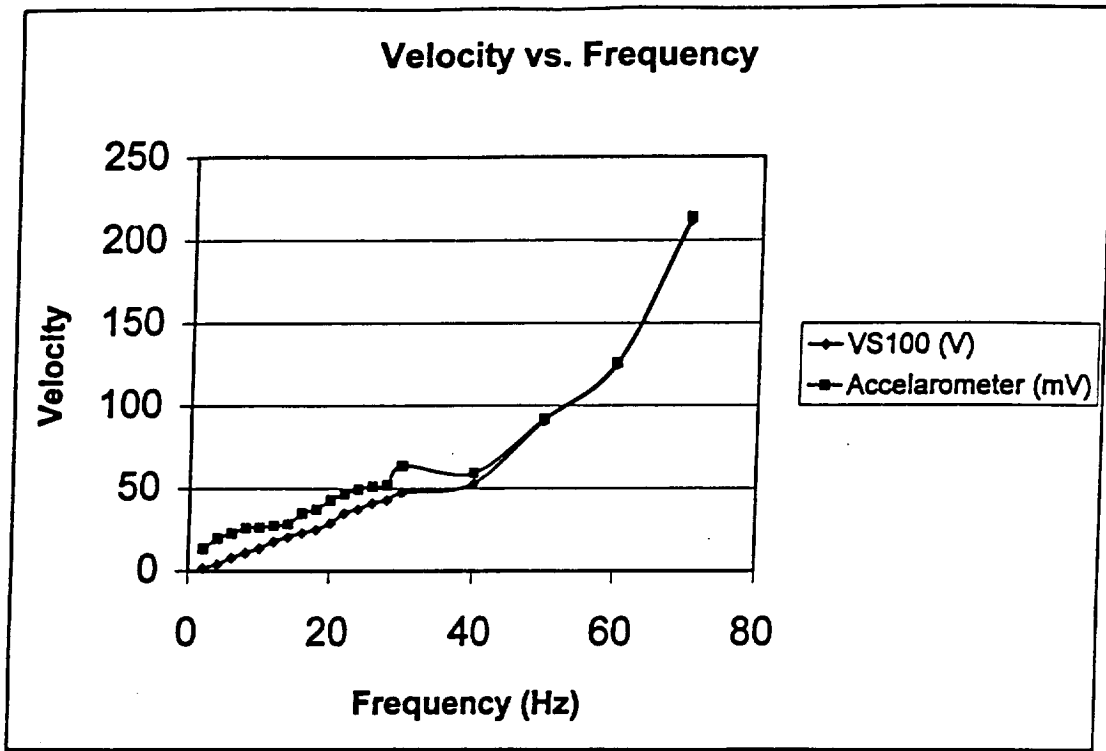


Fig. 4 Measurement of the velocity and acceleration of a laboratory vibrating speaker cone target using both a He-Ne LDV system and commercial accelerometers.

Evaluation of Laser-Vibration-Sensing Technology From An Airborne Platform*§

R.M. Heinrichs, S. Kaushik, D.G. Kocher, S. Marcus, G.A. Reinhardt, T. Stephens, and C.A. Primmerman

Lincoln Laboratory
Massachusetts Institute of Technology
244 Wood Street
Lexington, MA 02420
(781)-981-7945, (781)981-5069 (fax), *heinrichs@ll.mit.edu*

Abstract

Lincoln Laboratory has begun an effort to evaluate the capability of an airborne laser vibrometer to make high-resolution vibration measurements of ground targets. This paper will present details of each of the major elements of this effort. This will primarily involve the performance prediction of laser vibrometry as expressed by the noise-equivalent vibration amplitude. The contribution to this limiting noise level from atmospheric-piston turbulence and speckle broadening as well as the system-dependent contributions from platform vibrations and pointing jitter will be discussed. Laboratory measurements, which confirm the theoretical noise predictions for speckle, will also be presented.

Introduction

The ability to make remote-vibration measurements from an airborne platform has a variety of applications. The goal of the present effort is to generate a feasibility assessment of the laser-vibrometry concept and to estimate the ultimate resolution capability that such a system would potentially have. This has primarily included analysis and laboratory measurements. A point design for a laser-vibrometry system on board a high-altitude airborne platform has been developed and the basic characteristics of the system have been defined, resulting in an overall performance evaluation. This includes the effects of speckle and platform vibration and pointing jitter as well as considerations of atmospheric piston turbulence, laser phase noise, and algorithm performance. Laboratory measurements have also been performed, which verify the predictions for the effects of target speckle, algorithm performance, and atmospheric turbulence. This paper briefly presents the overall results of the analysis, followed by selected results from the laboratory experiments.

System Analysis

The nominal airborne platform chosen for the vibrometer point design is capable of maintaining altitudes in excess of 20 km with a loitering velocity of 200 m/s. The laser is assumed to be a continuous wave (CW) erbium-doped fiber laser. The CW requirement is necessary in order to maximize the number of independent speckle realizations that can be averaged over in a given interval of time. The laser beam is directed from the platform towards the ground, typically within 45° of nadir. The pointing requirements for the beam on the ground are dictated by two different coherence lengths. The first is the signal-phase-coherence length, which is the distance over which the beam spot on the ground can move before the signal phase changes due to the generation of a new speckle realization. This distance is on the order of the spot diameter, meaning that the laser-spot position on the ground must be maintained to within about 25% of the spot diameter over some period of time in order to maintain signal coherence. As discussed below, other speckle-broadening effects cause this time to be quite short, typically • 1 ms. The second coherence length is referred to as the vibration-coherence-length. This is the distance on the ground over which the vibration phase of the ground target remains essentially constant. This distance can be significantly larger than the laser-spot diameter depending on the nature of the target.

For the airborne platform, the signal bandwidth is dominated by the so-called speckle bandwidth. This is the spectral broadening of the signal due to the rate at which the signal phase changes as the target speckle realization changes. One way to view speckle broadening is to consider the velocity spread of the return signal due to the fact that different points of the illuminated spot are moving at different velocities relative to the platform. In

* This research is sponsored by the Defense Advanced Research Projects Agency, under Air Force Contract F19628-95-C-0002.

§ "The views expressed are those of the authors and do not reflect the official policy or position of the U.S. government."

effect, the illuminated spot is rotating relative to the laser radar, with the front part of the spot moving towards and the rear part of the spot moving away from the airborne platform (Figure 1). The speckle-broadened bandwidth for a nadir-pointing coherent laser radar is independent of wavelength and given approximately by: $2^{1/2}V_p/D$, where V_p is the airborne platform velocity and D is the aperture diameter. For a nominal 20-cm aperture diameter and 200-m/s velocity, the speckle bandwidth is about 1.4 kHz.

The carrier-to-noise ratio (CNR) of the nominal system has been calculated and is shown in Figure 2. In calculating this quantity, a typical diffuse ground reflectivity of 20% at the 1.5- μ m wavelength is assumed, as well as a 20-cm aperture diameter, a 20-km range, 70% detector quantum efficiency, 30% heterodyne mixing efficiency, 50% round-trip optical efficiency, and a signal bandwidth of 10 x the speckle bandwidth (~ 10 kHz). The CNR is proportional to the transmitted power, the laser wavelength, and to the cube of the transmit/receive aperture diameter (D_A^3 is from the solid angle subtended by the receiver and another factor of D_A is from the inverse dependence of the speckle bandwidth on the aperture diameter). A functional block diagram of the vibrometer is shown in Figure 3. The system is a bistatic coherent laser radar in which the return light is frequency shifted in an acousto-optic modulator (AOM). This is done in order to remove the positive/negative velocity ambiguity and to reduce system sensitivity to any unshifted component that may come out of the AOM on axis. The platform motion-compensation system consists of a Kalman filter, which utilizes accelerometer, pointing, and platform-navigation information to provide control signals for the variable downmixing synthesizer and error-correction signals for the digital-output stream. The estimated computational power required for a single-channel system with real-time data processing is approximately 10 MFLOPS.

System Performance Evaluation

This section presents the results of system-performance calculations, which account for limitations due to speckle broadening, platform compensation, atmospheric turbulence and laser phase noise. The total phase-noise variance of the system is assumed to be a sum of the uncorrelated variances from each of these effects:

$$\sigma_{\phi}^2 = \sigma_S^2 + \sigma_P^2 + \sigma_A^2 + \sigma_L^2$$

where the different contributions are from speckle, platform pointing-jitter and vibration, atmospheric piston turbulence, and laser phase noise, respectively. The impact of each of these noise sources is quantified according to the noise-equivalent vibration amplitude (NEVA = $(\lambda/2\pi)\sigma$). Calculations of the NEVA for each of these terms has been performed and is summarized below.

The speckle-limited NEVA includes the CNR performance calculation, which includes the effect of detector noise. The signal detected by a coherent laser radar from a vibrating target is frequency modulated (FM) by the vibration frequency. The speckle-limited NEVA is determined by assuming a spectrogram-processing technique¹ in which the raw data are broken into sequences of length approximately equal to the inverse speckle bandwidth. The Cramer-Rao-limited performance is then assumed for the first-moment estimation of the FFT's of each sequence.² A final FFT of the first-moment frequency estimates versus sequence time produces the vibrational spectrum, with σ_S being given by the single-sequence first-moment standard deviation divided by the square root of the number of sequences. For the airborne scenario assumed here, the speckle bandwidth is about 1.4 kHz and a typical sequence length would be about 1.4 ms.

The next noise term to consider is due to platform vibration and pointing jitter. Pointing jitter affects system performance by generating a varying contribution from the line-of-sight (LOS) platform velocity to the Doppler-shifted signal. Platform vibrations impact more directly towards the high-precision LOS velocity measurements that the system makes. Both of these effects must ultimately be compensated for by measuring the pointing jitter with angle-rate sensors and the platform vibrations with accelerometers and removing these contributions in post processing (or by varying the frequency of an IF downmixing oscillator). The Allied Signal Ring Laser Gyro Model RL-34 angle-rate sensor was identified as a candidate for providing the required measurement resolution for pointing-jitter compensation. Correspondingly, the BEI / Sundstrand QA-700 Servo Accelerometer was also identified as providing high-resolution platform-vibration measurements. The residual error sources from each of these devices was taken into consideration in the system-performance analysis.

Atmospheric turbulence can affect the performance of the laser vibrometer in two ways: mixing efficiency loss due to wavefront distortion and signal clutter due to atmospheric-piston variations. The greatest contribution is due to piston variations. Kolmogorov turbulence theory dictates that, within the inertial subrange, the atmospheric-piston contribution should contribute as an $f^{-4/3}$ power law to the NEVA. These have been modeled for typical atmospheric-turbulence cases and included in the overall performance analysis.

The final noise term considered is due to laser-phase fluctuations. The nominal CW, 1.5- μm , fiber laser would require active frequency stabilization to a level that has already been demonstrated in laboratory environments.³ A model has been developed for the frequency dependence of the uncompensated laser-phase fluctuations and it too has been included in the performance analysis.

Putting all the laser-vibrometry noise sources together, the combined sensitivity prediction for the airborne vibrometer is shown in Figure 4. This figure shows the NEVA predicted for each of the major contributors: platform pointing jitter, speckle broadening, laser phase noise, and atmospheric-piston variations. Also shown is the total noise prediction for the system. As can be seen, atmospheric-piston variation dominates the performance for this system. This limits the sensitivity of the system to vibration amplitudes of several microns at 1-Hz frequencies with the noise level decreasing (sensitivity improving) as $f_v^{-4/3}$, where f_v is the ground-vibration frequency. The power-law dependence is representative of the dominant noise source of atmospheric-piston fluctuations.

Laboratory Measurements

Laboratory measurements have been conducted that verify the expected performance of a laser vibrometer in the presence of speckle broadening and simulated atmospheric turbulence. The basic laboratory setup involves measurements from a rotating target, for speckle simulation, or from a fixed target with atmospheric-turbulence-simulating phase screens translated across the beam. Only the results of the speckle-broadening measurements are presented here. The laser used for these measurements was a 1.06- μm CW micro-laser developed by Micracor. The beam from the laser was collimated and directed onto the rotating target whose rotation rate was precisely controlled with a direct-drive motor to produce a spectral broadening of 4 kHz. The results of measurements where the target was not vibrating are shown in Figure 5. In this case, the average noise level for the measurement was within 2 dB of the predicted measurement sensitivity from the Cramer-Rao analysis of the spectrogram algorithm. This result adds confidence to our predictions for the speckle-limited sensitivity and spectrogram-algorithm performance for the flight system.

Conclusions

In conclusion, Lincoln Laboratory has undertaken an effort to evaluate the ultimate resolution capability of remote laser vibrometry from an airborne platform. This effort has involved a combination of systems analysis, theoretical modeling, and laboratory measurements. The results to date have indicated the general efficacy of the approach. Nevertheless, laser vibrometry from an airborne platform remains technically challenging and investigations are continuing.

References

1. A.L. Kachelmyer and K.I. Schultz, "Spectrogram Processing of Laser Vibration Data," *SPIE* **1936**, 78 (1993).
2. B.J. Rye and R.M. Hardesty, "Discrete Spectral Peak Estimation in Incoherent Backscatter Heterodyne Lidar I: Spectral Accumulation and the Cramer-Rao Lower Bound," *IEEE Trans. Geosci. Remote Sensing*, **31**, 16 (1993).
3. M. Kouroggi, C. Shin, and M. Ohtsu, "A 250 Hz spectral linewidth 1.5- μm MQW-DFB laser diode with negative-electrical-feedback," *IEEE Photonics Tech. Lett.*, **6**, 496 (1991).

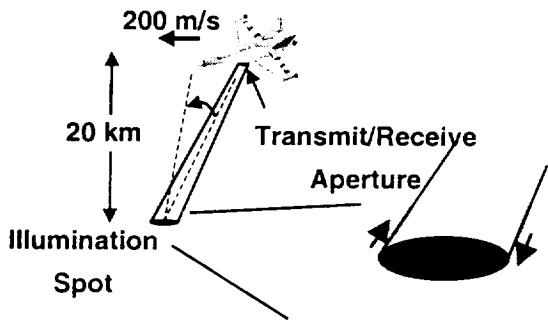


Figure 1. Diagram showing source of spectral spread due to speckle broadening.

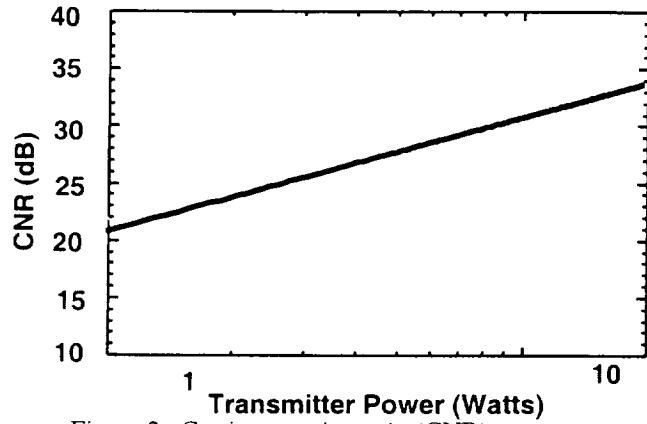


Figure 2. Carrier-to-noise ratio (CNR) versus transmit power for a 20-cm aperture, 20-km altitude, system.

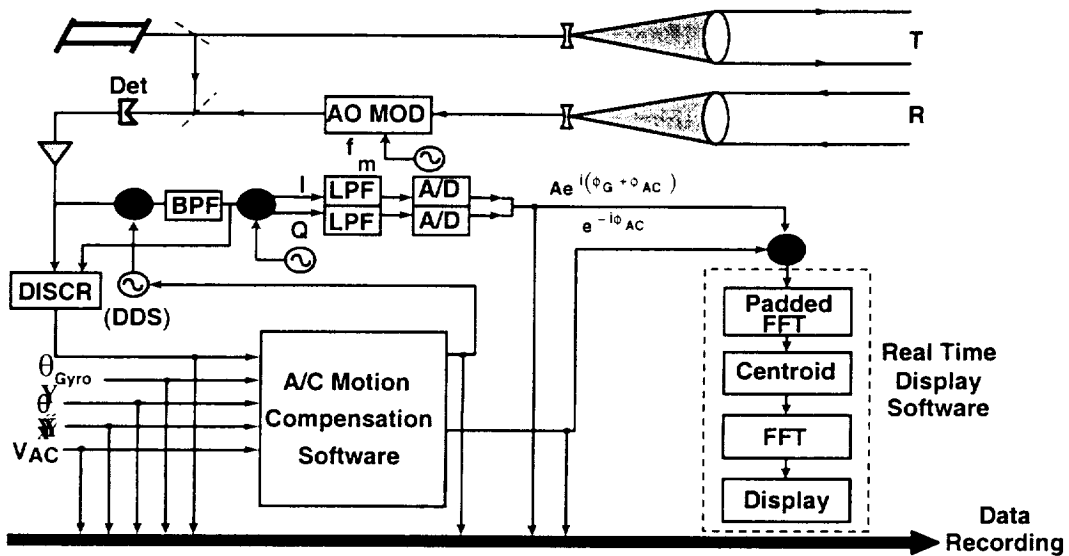


Figure 3. Functional block diagram of laser-vibrometer system on an airborne platform.

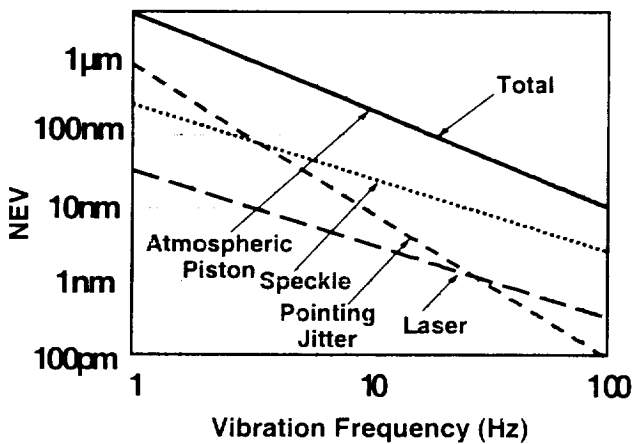


Figure 4. Noise-equivalent vibration amplitude versus vibration frequency for all major noise sources.

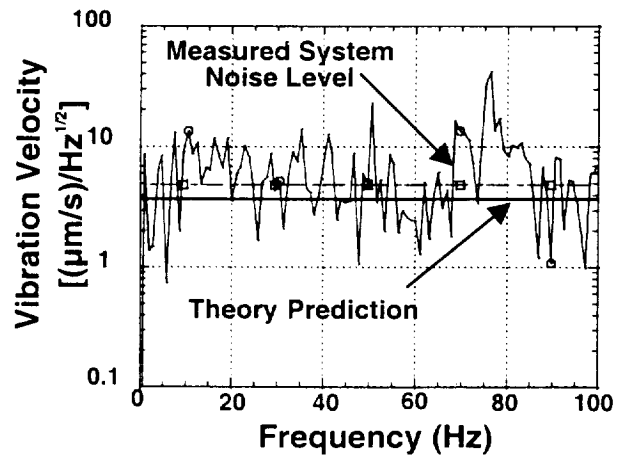


Figure 5. Speckle-limited noise versus vibration frequency from laboratory measurements. Solid line is Cramer-Rao lower-bound theoretical prediction.

2 MICRON CW VIBRATION SENSING LASER RADAR

July 1999

Richard D. Richmond
AFRL/SNJM
Air Force Research Laboratory
Wright-Patterson AFB Ohio, 45433

1.0 INTRODUCTION: Coherent laser radar (ladar) has been shown to be a highly sensitive sensor for measuring surface vibrations. For long range vibration measurements, CO₂ based lasers operating around 10.6 microns have been used extensively. Advances in solid state laser technology have extended the range of useful wavelengths for laser vibration sensors (LVS) down to 1.5 – 2 microns. With the advent of shorter wavelength solid state laser radar systems, multiple wavelength choices for such sensors have generated questions concerning the optimal laser wavelength for such sensors. An LVS is sensitive to vibration amplitudes that are comparable to the laser wavelength. Therefore, these new shorter wavelength systems are able to measure small vibration induced displacements than their earlier counterparts. Shorter wavelengths also can take advantage of increased atmospheric transmission possible by tuning the laser away from water vapor and molecular absorption. This paper will describe a 2-micron LVS transceiver, signal processor and the preliminary results of a field test conducted at Redstone Arsenal in Alabama during July 1998.

2.0 SYSTEM DESCRIPTION: The heart of the LVS is the laser. In this system, a Tm:YALO CW laser operating at 2.02 microns and producing 150 milliwatts provided the laser energy that was used for both the transmitted beam and the reference local oscillator. The output of the laser was fiber coupled to the transmit/receive head, which measured approximately 8" (w) x 12" (l) x 4" (h). In the head, the beam first went through a beam splitter where approximately 10% of the beam was split out for the local oscillator and shifted by 27 MHz through an electro-optic modulator. The remainder was expanded and transmitted through the 50 mm transmit telescope. The returning beam backscattered from the target was collected in a similar and co-aligned receive telescope. Both the returning beam and the local oscillator beam are combined onto a photo-diode detector. The layout of the transmit/receive head is illustrated in Figure 1.

The technique used to develop the vibration spectra for targets is the spectrogram approach (1). Figure 2 illustrates the spectrogram processor. The returning signal is mixed with the local oscillator and the difference frequency (27 MHz for this system) is then mixed with the IF frequency to generate a low frequency IF (500 kHz). This output is lowpass filtered and then sampled with the 2 MHz digitizer. Samples from the digitizer are then input into a Fast Fourier Transform (FFT). Centroiding then determines a frequency estimate for that sample. This correlates to a velocity and a time history of such velocities is built up to input into a second FFT. The output of this second FFT processor is the vibrational frequency spectrum. This system develops velocity estimates at a 2 kHz rate yielding a Nyquist frequency capability of up to 1 kHz.

1. Kachelmyer, A.L., Shultz, K.I., "Laser Vibration Sensing", *The Lincoln Laboratory Journal*, Vol 8, Number 1, 1995

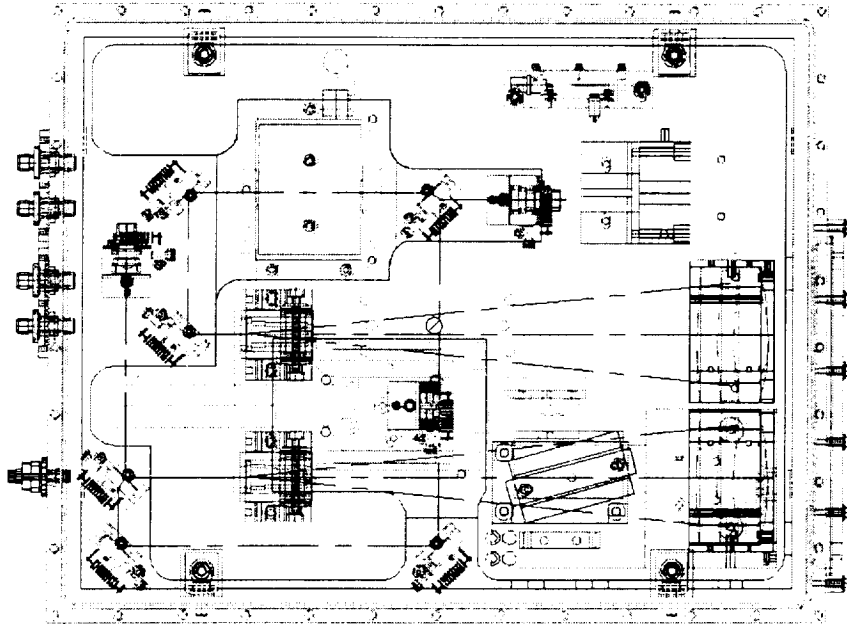


FIGURE 1: Schematic of laser vibrometer transmit/receive head

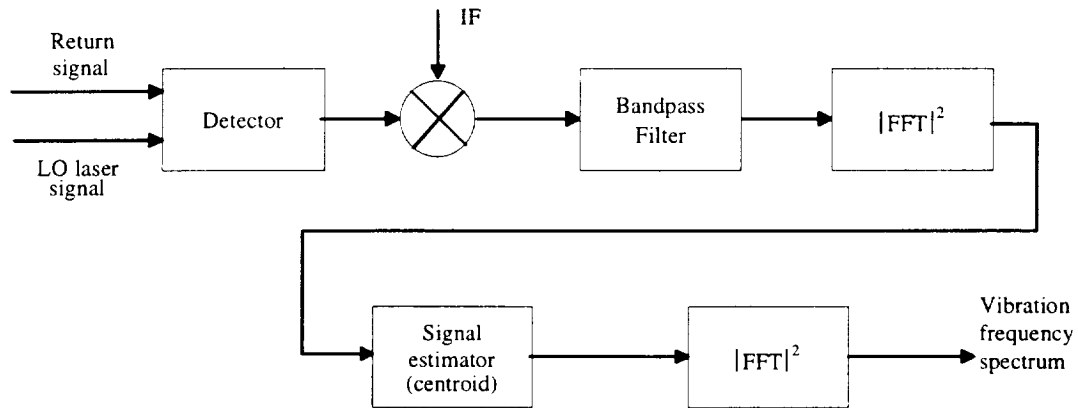


FIGURE 2: Block diagram of CW spectrogram processor.

3.0 TESTING: Performance Predictions: The system, target and atmospheric parameters were used to predict the range performance of this system. Using the standard laser radar equation, CNR curves were generated for 2 atmospheric conditions. These results are shown in Figure 3. Velocity, and ultimately frequency, accuracy is affected by the CNR. Earlier experiments have shown excellent accuracies with CNR's of 10 dB or more. Looking at Figure 3, the useable range for the system could be in excess of 2.5 km even for relatively poor atmospheric conditions.

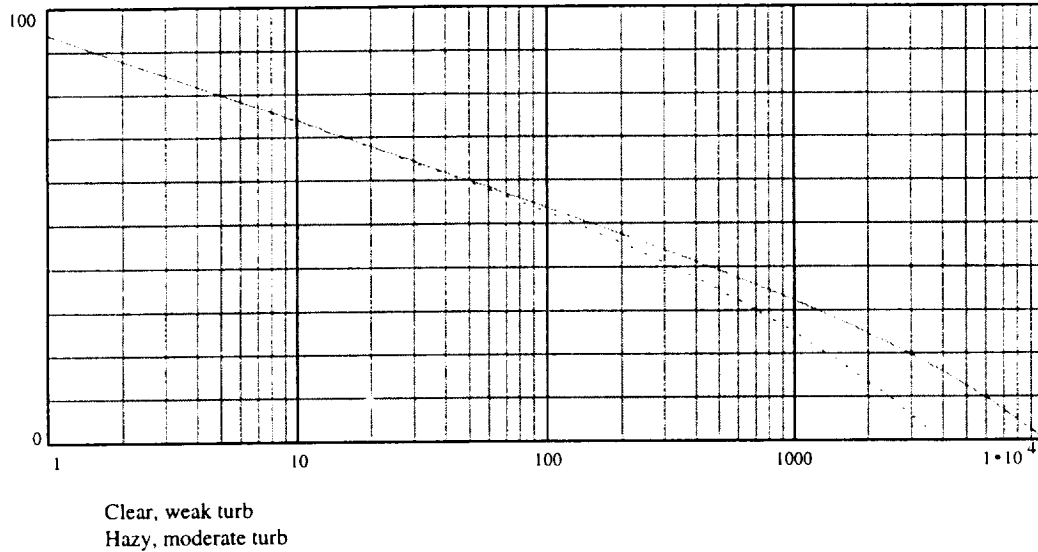


Figure 3. CNR (dB) vs. Range (m) for different atmospheric conditions

Huntsville Field Trials: In order to address some of the questions concerning wavelength dependence on LVS performance, this 2-micron system was one of the LVS systems operated during a NATO sponsored field trial hosted by the US Army at Redstone Arsenal in Huntsville Alabama. The tests took place during July 1998 when normal levels of heat, humidity and solar heating induced refractive turbulence are high. The objective of this effort was to improve our understanding of how phenomenologies such as atmospheric turbulence and attenuation affect the performance of laser radar vibration sensors. Scaling these effects with laser wavelength was also an important part of the purpose of this effort.

Site Description: At the test range, the LVS systems were housed in shelters located on top of a mound at the southern end of the range. The mound was approximately 5 meters high and offered an unobstructed view of the range. The terrain of the range was slightly rolling and grass covered. Targets could be placed within the range at distances of up to 5 km. Sensors for measuring visibility and turbulence were also operating during the tests. Typical battlefield obscurants such as white phosphorus (WP) and fog-oil could also be generated during the tests.

Test Targets: Targets available during these tests included: a M2 Bradley, M60 Tank, T-72 soviet tank, and US and soviet armored personnel carriers.

Test Results: Figure 4 is a 55-second time history of the spectrum obtained from a tank located at 1000 meters. The tank was viewed from the side and the measurement point was at the front end of the tank body. As can be seen from this figure, there is a strong line in the spectrum around 59 Hz. There was an obvious concern that this line was actually a noise signal from the 60 Hz power. In order to test this, the aim point of the LVS was moved from the tank to the ground nearby. At that point, the signal went away, confirming that the signal was actually coming from the tank. The next figure (Figure 5) shows the spectrum obtained over 47 seconds from an aim point located near the center of the target body. Here again, the 59 Hz signal is apparent, although the magnitude is lower and much more noise is visible in the spectrum.

The next set of spectra (Figures 6 & 7) is from an armored personnel carrier (APC) viewed from the side. In Figure 6, the target is at 1000 meters and viewed through clear air. Total time is approximately 70 seconds. In Figure 7, the target is at 560 meters and the total time is similar to the previous figure. At the beginning of this data collection, a fog oil smoke generator located upwind from the target by about 50 meters was started. Approximately half way through the measurement, the fog completely obscured the target. Although the smoke was totally opaque in the visible, there was no discernable change in the return signal carrier-to-noise or in the spectrum magnitudes. Preliminary measurements of the fog particulate indicated that the mean particle size was around 3 microns.

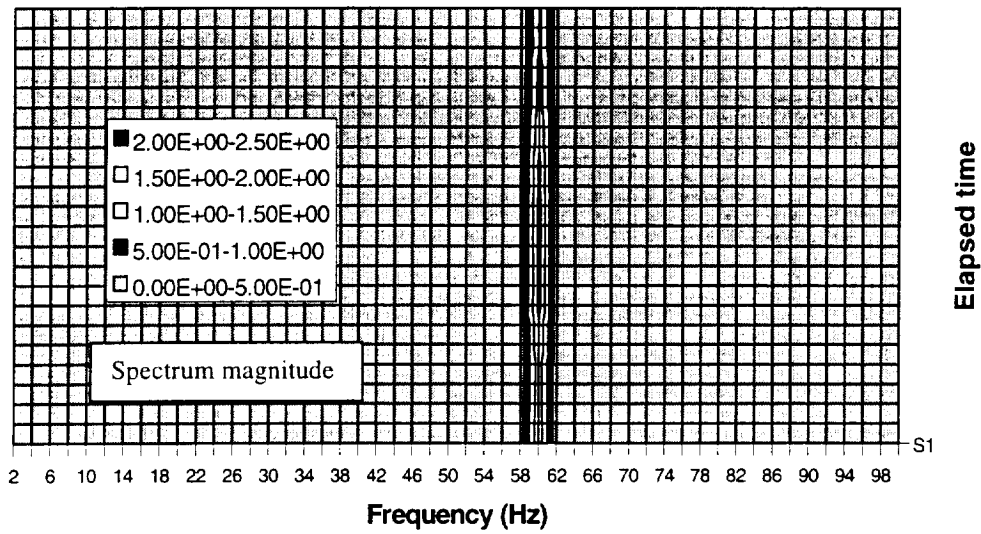


Figure 4. Spectrum from tank at 1000 meters. Sampled near front of body.

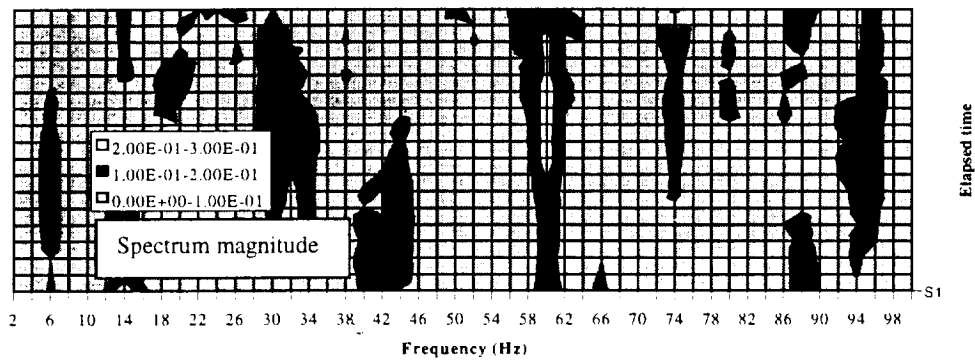


Figure 5. Spectrum from tank at 1000 meters. Sampled at center of body.

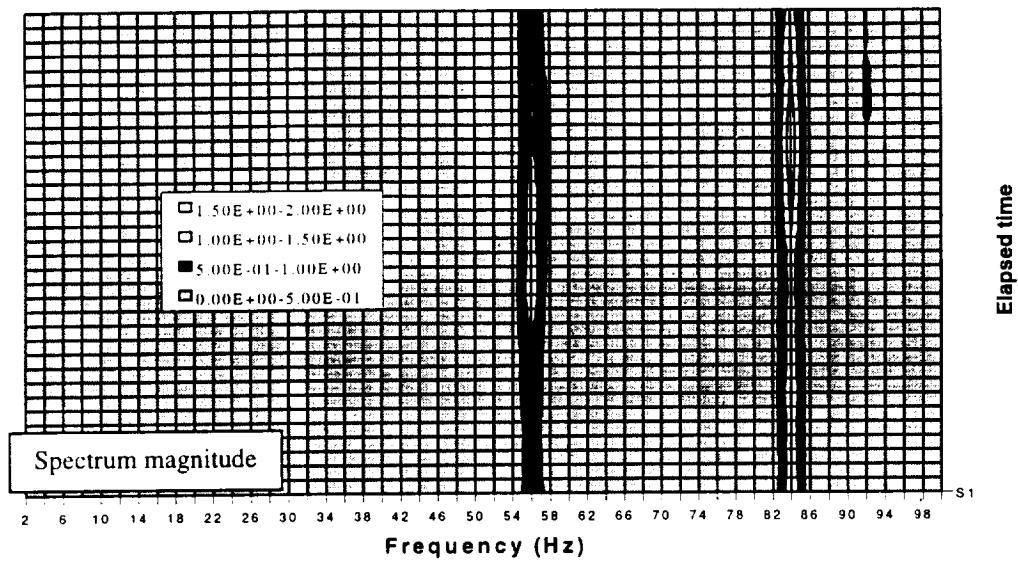


Figure 6. Spectrum from APC at 1000 meters with no obscurants

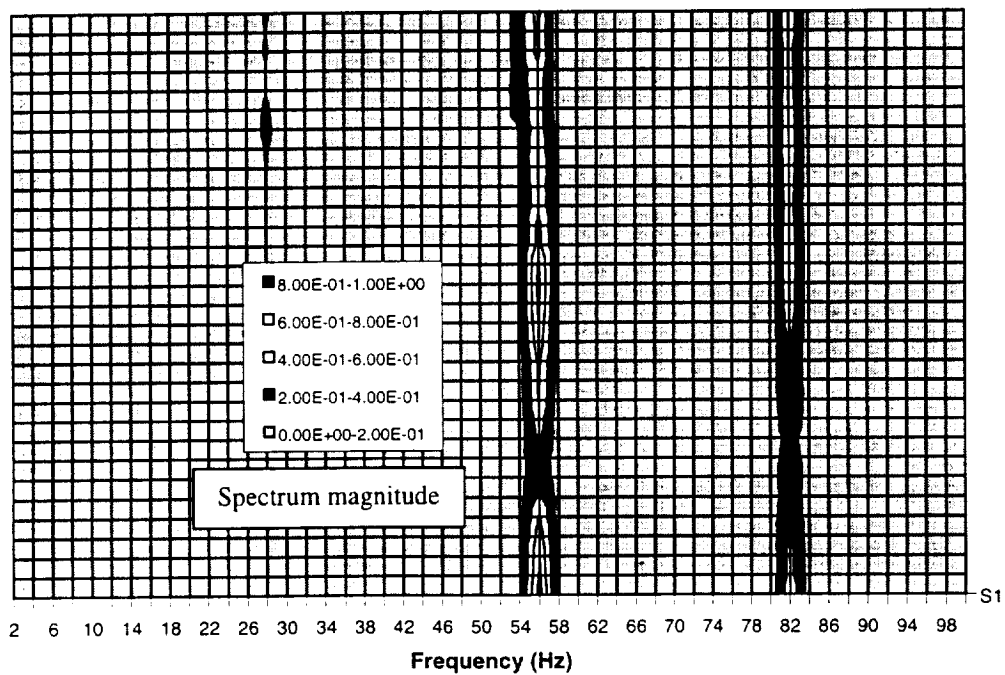


Figure 7. Spectrum from APC at 560 meters during fog-oil release

Atmospheric Effects: At the shorter wavelength used by this system (compared to the CO₂ laser based systems used previously), atmospheric turbulence (C_n^2) could have a significant impact on the range capability of the lidar. Figure 8 illustrates the predicted effect of turbulence on this sensor. The range is set at 560 meters and the other system parameters are the same as in Figure 3. The solid line graphs the change in CNR(dB) with changes in C_n^2 over the normal range of expected values. The time and location of the tests (July in Huntsville) were chosen because normal summer heat and humidity levels could be expected to produce large values and changes in C_n^2 . Unfortunately, the weather during the tests was unusually mild and stable with very low levels of turbulence even

near the ground and along the sight path of the laser sensor. The highest level of measured C_n^2 was only 8.9×10^{-14} . The boxed point in Figure 8 points to the drop in SNR for that level of turbulence. The reduction is less than 3 dB. The other problem with trying to correlate turbulence measurements with the lidar signal is the long interval between turbulence measurements. These measurements were recorded at 1 minute intervals and represent an average during the period. The lidar was making measurements at kHz rates and generating spectral estimates every second. Each measurement could be taken through a significantly different turbulence level never seen on the longer scale.

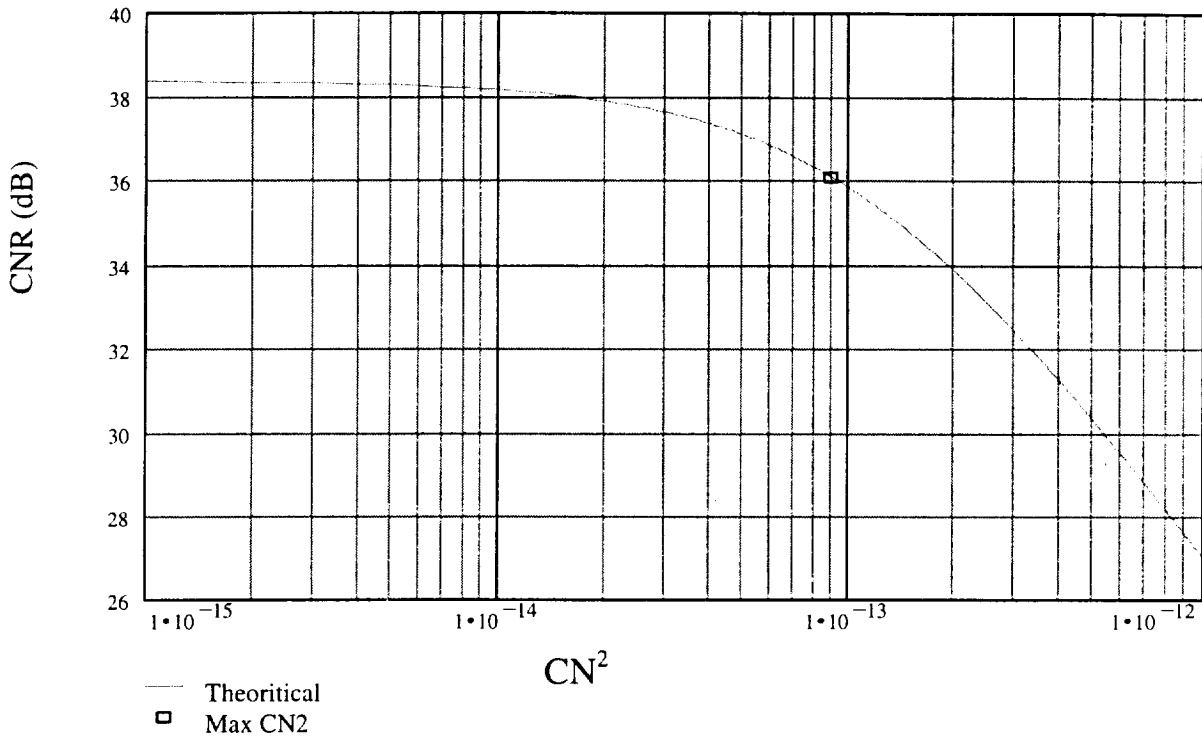


Figure 8. CNR (dB) vs. C_n^2 with target at 560 meters

4.0 CONCLUSIONS

A significant amount of data has been collected under a variety of atmospheric and seeing conditions. The data presented here have illustrated the viability and robustness of shorter wavelength laser vibrometry systems. Of particular interest was the result from the fog-oil tests. There would have been little or no absorption of the signal by the fog-oil, but the particle sizes should result in relatively large scattering of the laser energy. The results would be a rather large effective attenuation (sum of but the absorption and backscatter). Although the sample set is too small to draw any firm conclusions, the fact that no apparent increased attenuation was observed could significantly impact perceptions about laser based sensor performance in the presence of battlefield obscurants. Only a small sample of the data collected during this trial has been processed and analyzed. Much work remains to be done on correlating measured signal strengths and atmospheric conditions and the effect of these phenomena on the ability of the sensor to monitor spectra. Also, in the coming months the various researchers involved in this test will be comparing results in an attempt to quantify wavelength dependencies. However, we are pleased with the results obtained so far and consider the test to be a real success.

Comparison of Pulsed Waveform and CW Lidar for Remote Vibration Measurement

*Sammy W. Henderson, J. Alex L. Thomson, Stephen M. Hannon, and Philip Gatt
Coherent Technologies, Inc.
655 Aspen Ridge Drive
Lafayette, Colorado USA 80026
(303)-604-2000*

INTRODUCTION

Continuous wave (cw) lidar systems have been utilized for several years to measure the vibrations of remotely located structures and vehicles. The measured vibration spectra allows identification of the vehicle and/or the detection of irregular vibrations indicating structural or engine failure. As an example, a cw lidar operating at 2-microns was successfully utilized to measure the vibration spectra of various targets at ranges up to 2 km as part of the Redstone Arsenal Combined Experiments in Laser Radar Program¹ in July, 1998. We have recently developed an agile pulsed waveform coherent lidar^{2,3} which is similar to pulse pair and poly-pulse-pair waveforms which are routinely used in microwave Doppler radar for both hard target and aerosol target applications. We have extended these waveforms to eyesafe, near infrared optical wavelengths (2-micron initially demonstrated). The base waveform format comprises a pair of pulselets (doublet pulse), each of duration τ , separated by T_s seconds. The range resolution is governed by the pulselet duration τ , while the velocity precision is inversely proportional to the pulselet separation, T_s . Figure 1 and 2 illustrate the base pulse format and the basic measurement principle.

The agile waveform has the following advantages over cw lidar.

- The range resolution provided by the waveform eliminates spurious signals due to scatter of haze, clouds, netting, etc. between the lidar and the target. Also, range resolved vibration spectra of the target offers significant additional discrimination ability in many cases.
- The pulsed waveform increases detection probability by optimizing CNR, providing greater range at fixed average power or decreased average power at fixed range.
- The short widely-spaced pulses of the waveform allow efficient data collection and processing.
- The doublet waveform is well suited to allow possible implementation of the DPCA (Displaced Phase Center Antenna) technique⁴ of virtually stopping the platform motion to significantly reduce velocity measurement noise due to speckle and turbulence. This will provide a significant sensitivity advantage when measurements are made from a high-speed platform, e.g., an airplane or satellite.

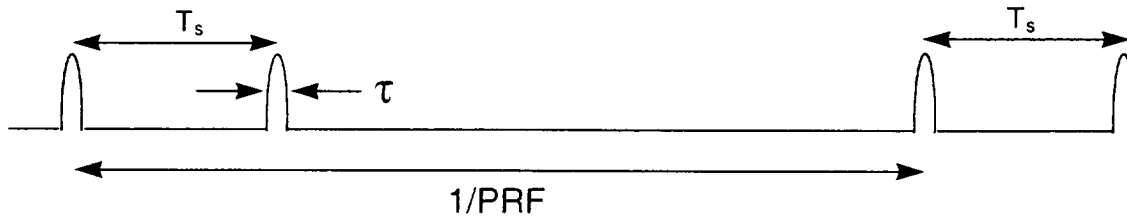


Figure 1 General doublet pulse format showing pulselet duration τ , pulselet separation T_s and doublet repetition frequency PRF.

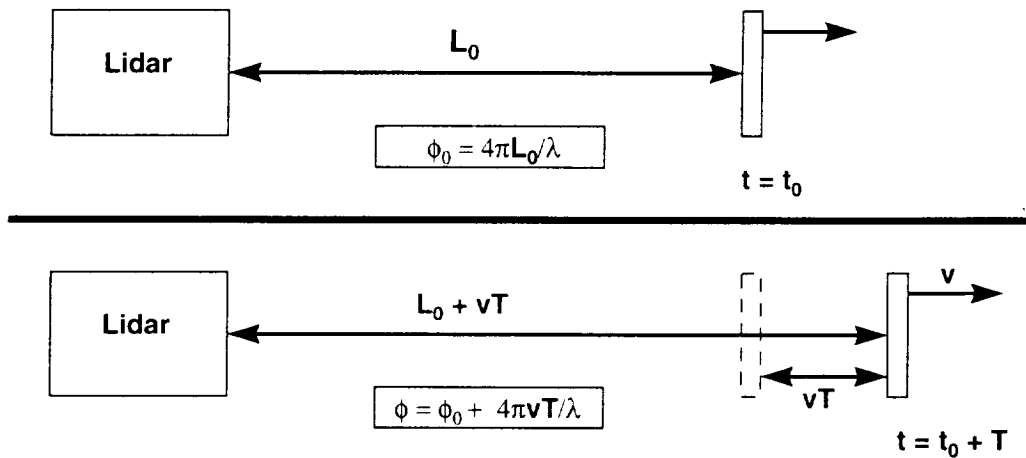


Figure 2 The doublet pulse measures the target velocity by essentially measuring the phase change between the first pulselet and the second pulselet caused as the range to target is increased or decreased by an amount vT , where v is the velocity and T is the pulselet separation.

CTI has developed a breadboard agile waveform lidar based on these principles and has utilized it to perform demonstration measurements at short range. Due to space limitations, only one example is presented here – additional examples and description can be found in Reference 5. Figure 3 shows a sample velocity time series (left panel) and vibration spectra (right panel) measured with the doublet pulse lidar from a speaker at short range. The system easily detects the two frequencies driving the speaker. Note that the noise floor level of the spectrum is <10 microns/second/ $\sqrt{\text{Hz}}$ ($<10^{-4}$ $\text{mm}^2/\text{s}^2/\text{Hz}$). This noise floor was obtained using only 500 discrete velocity measurements evenly spread over 4 seconds – a larger number of measurements would result in an additional decrease in the noise floor.

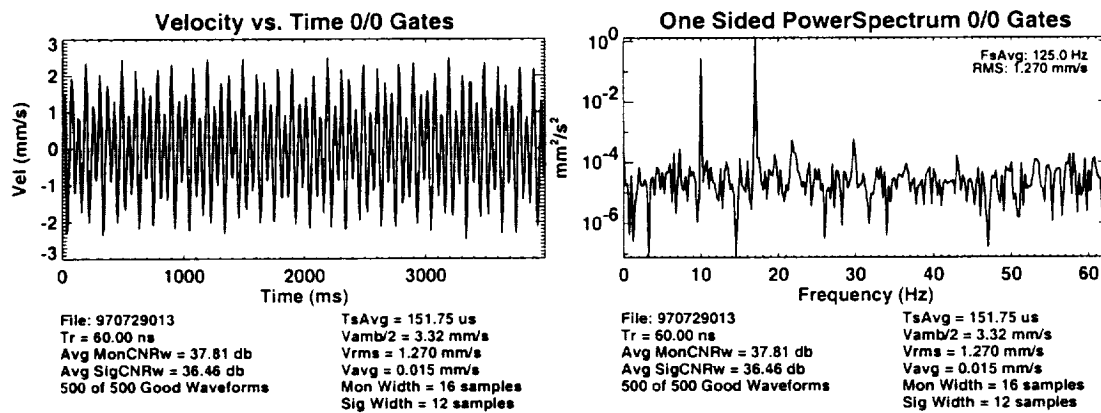


Figure 3. Sample complex vibration time series (left panel) and spectrum (right panel) for a simple target. The two frequencies, 10 and 17 Hz, used to drive the speaker at low amplitude are clearly evident in the spectrum. Note that the noise floor is <10 microns/second/ $\sqrt{\text{Hz}}$.

LONG-RANGE MEASUREMENT POTENTIAL

Detailed analysis and numerical simulations that include the effects of the lidar, the atmosphere and the target have been performed at CTI for a number of scenarios. Our analysis indicates that $10 \text{ micron/second}/\sqrt{\text{Hz}}$ velocity sensitivity can in principle be obtained at ranges in excess of 100 km from a airborne or satellite-based platform using moderate transmit laser powers and state-of-the-art coherent lidar and pointing technology. We have also used the breadboard doublet pulse system to demonstrate significant waveform agility. The PRF, number of pulses in the transmitted waveform, and pulse spacing can be varied allowing the waveform to be optimized for a particular application. The initial detection of a target at long range is enhanced significantly by reducing the PRF and increasing the pulse energy, as illustrated in Figure 4. At shorter ranges where sufficient signal is available, the PRF is increased (resulting in lower pulse energy) and the pulse spacing and number of simultaneous pixels is varied to optimally interrogate the target. The short widely-spaced pulses in the agile waveform enable practical coherent arrays and multiple pixel processing whereas, in a cw system, multiple pixel measurements would be prohibitive. CTI has recently started programs to demonstrate a 5-10 W agile waveform transmitter and a coherent detector array that will allow simultaneous multiple-pixel measurements of target vibration.

In order to make sensitive measurements at long range, velocity measurement noise from the following sources must be properly mitigated.

- Frequency jitter noise, due to fluctuations of the local oscillator laser frequency during the round-trip time to the target and back.
- Platform motion noise, due to imprecise knowledge of the platform motion along the line of sight and imprecise knowledge of the beam pointing direction.
- Turbulence advection noise, due to the beam translating through turbulent refractive index eddies in the atmosphere resulting in the optical path length being modulated.
- Speckle noise, due to decorrelation of the phase of the scattered field at the receiver resulting from relative motion of the lidar aperture and the speckle field.

- Shot noise, due to the ability to accurately measure the signal frequency (phase) given the coherent measurement time (limited by speckle) and the signal to noise level (shot noise).

In the presentation, we will describe the effects of these noise sources and mitigation techniques. Modeling and experimental data will be used to show measurement capability and compare cw and pulsed lidar systems.

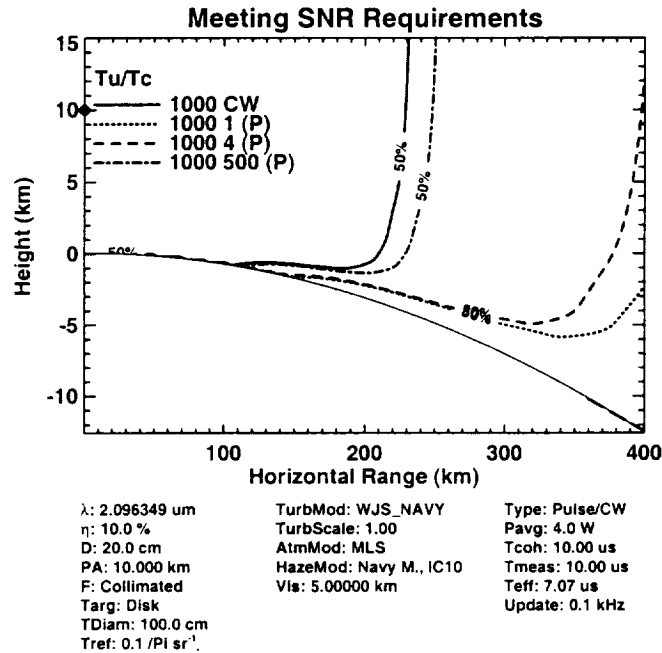


Figure 4. Contours of maximum measurement range (50% probability of detection) of a 1 m diameter 0.03/sr reflectivity target using a 2-micron wavelength, 10% efficiency lidar with a 20 cm transmit/receive aperture located at a 10 km height (see diamond on left axis). Other lidar, target, and atmospheric parameters listed below plot. The signal coherence time, T_c , is assumed to be 10 microseconds and the required measurement update time, T_u , is assumed to be 10 milliseconds ($T_u/T_c = 1000$). This results in different number of incoherent signal averages for cw vs pulsed systems. The contours compare cw (cw, solid curve) 100 Hz PRF pulsed (1P, dotted curve), 400 Hz PRF pulsed (4P, dashed line), and 50 kHz pulsed (500P, dash-dot line) lidar performance.

REFERENCES

1. Richard Richmond, "2 Micron CW Vibration Sensing Laser Radar," see paper this conference
2. Sammy W. Henderson, J. Alex L. Thomson, Stephen M. Hannon, Timothy J. Carrig, Philip Gatt, and Dale Bruns, "Wide-Bandwidth Eyesafe Coherent Laser Radar for High Resolution Hard Target and Wind Measurements," paper W8, 9th Conference on Coherent Laser Radar, Linkoping, Sweden, 1997
3. J. Alex Thomson, Stephen M. Hannon, and Sammy W. Henderson, "Doublet Pulse Coherent Laser Radar for Precision Range and Velocity Measurements," US Patent 5,815,250, 1998
4. M. Skolnik "Radar Handbook". 2nd ed. McGraw Hill, New York, New York, 1990, Sec. 16
5. Stephen M. Hannon, J. Alex Thomson, Sammy W. Henderson, Phillip Gatt, Robert Stoneman, and Dale Bruns, "Agile Multiple Pulse Coherent Lidar for Range and Micro-Doppler Measurements," SPIE Vol. 3380, pg 259

Solid-State Coherent Array Ladar for Vibration Imaging

Philip Gatt and Stephen M. Hannon
Coherent Technologies, Inc.
655 Aspen Ridge Dr.
Lafayette, CO 80026

Roger Stettner and Howard Bailey
Advanced Scientific Concepts
2020 Alameda Padre Serra., # 123
Santa Barbara, CA 93103

Matt Dierking
AFRL/SNJM, Building 622
3109 P Street
Wright-Patterson AFB, OH 45433

INTRODUCTION

We report on work to develop a 2 μm coherent array technology for vibration imaging applications. The novel 10x10 focal plane heterodyne array imager utilizes an extended wavelength InGaAs detector array indium bump-bonded to a novel silicon array digitizer chip. The backplane sampling chip, which has an expected sample rate of 500 MHz/Pixel and a buffer depth of 32 samples, is well suited to the doublet pulse ladar waveform and therefore for vibration sensing applications.¹ Frame rates of 1 kHz are expected for the first demonstrations expected within the next year. In this paper, we describe the general system design and present system performance predictions.

GENERAL DESIGN CONSIDERATIONS FOR DOUBLET PULSE IMAGER

The doublet pulse transmit waveform comprises two short-duration 'pulselets' separated by a time sufficient to achieve good Doppler resolution. The short pulselet duration controls the range resolution and the long pulselet separation enables excellent velocity precision. The doublet pulse provides coherent Doppler ladar systems a substantial time bandwidth product (TB) of 10,000 or more with a very modest processing requirement. The details of this waveform and sample experimental range and vibration sensing results can be found elsewhere.^{1,2}

The design approach is to exploit the fundamental low duty cycle that characterizes the doublet pulse waveform. For example, a doublet pulse with a 5-10 nsec pulselet duration and a 50-100 μsec pulselet separation has a 0.01% duty cycle. A backplane sampling chip, which is bump-bonded to an InGaAs detector array, will sample/hold a set of some 32-64 samples per pixel (array element) per pulselet. The backplane sampling pixels can be individually addressed and the samples are read out serially. In this way, requirements for the downstream databus are significantly reduced and a single front-end digitizer can be utilized.

For a pulse repetition frequency (PRF) of 1 kHz and a pulselet separation of 100 μsec , we have 900 μsec (1000 μsec minus the 100 μsec pulselet separation) to ship the samples out to the signal processor. For a 10x10 array and 8 bits of vertical resolution, this amounts to 2.8 kbytes of data every waveform (pair of pulses). For a 1 kHz PRF, this corresponds to 3 Mbytes/sec, and is readily achieved with existing signal processor hardware. The figure below illustrates the timing for a single pulselet return for a single pixel.

¹ S. M. Hannon, J. A. Thomson, S. W. Henderson, P. Gatt, R. Stoneman, D. Bruns, "Agile Multiple Pulse Coherent Lidar for Range and Micro-Doppler Measurement," *Proc. SPIE* **3380**, 259 (1998).

² S. W. Henderson, J. A. L. Thomson, S. M. Hannon, T. J. Carrig, P. Gatt, and D. L. Bruns, "Wide-Bandwidth Eyesafe Coherent Laser Radar for High Resolution Hard Target and Wind Measurements," *Proc. 9th Conf. On Coherent Laser Radar*, Linkoping, Sweden, 160 (1997).

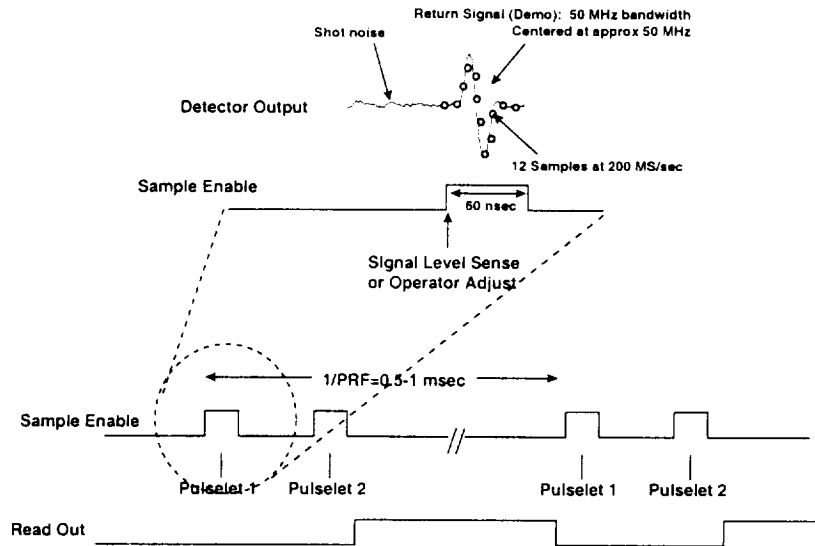


Figure 1 Top-level timing diagram for doublet pulse backplane sampling

SYSTEM OVERVIEW

Figure 2 is a functional block diagram for the solid-state coherent array imager. The system will nominally operate in a floodlight illumination mode with up to a $300 \mu\text{rad}$ divergence out of the telescope (defocused mode). The more darkly shaded subsystems represent existing hardware requiring little, if any modification for the proposed demonstration and characterization measurements. The other subsystems, the hybrid array, and the associated drive electronics comprise the core portion of the ongoing development activities.

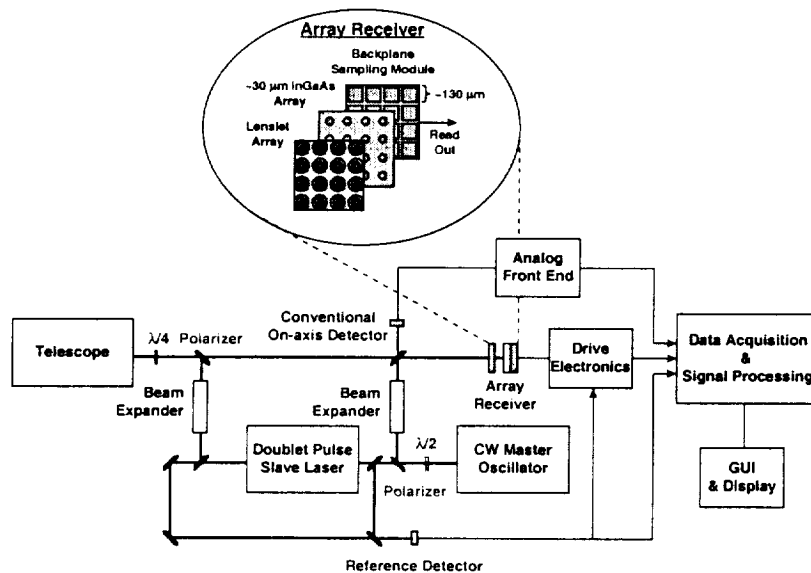


Figure 2 Functional block diagram for coherent array ladar for doublet pulse vibration imaging

Detector Array and Backplane Technology

For wavelengths up to $2.2 \mu\text{m}$, InGaAs-based detectors can be used. With lattice-matched InGaAs to InP, the cut off wavelength of the material is $1.6 \mu\text{m}$. For longer wavelength operation, lattice mismatched InGaAs on an InP substrate is often selected. However, the dark current will be significantly higher than

the lattice-matched InGaAs. Fortunately, for coherent detection operation, the increase in dark current is generally not a problem. The detectors will be back-illuminated, which is expected to reduce their quantum efficiency from values as high as 90% for single-element, front-illuminated detectors. In order to improve detector bandwidth, the detector size will be smaller than the focal plane pitch size (roughly $30\ \mu\text{m}$ as compared with a nominal pitch of $130\ \mu\text{m}$). The fill factor will be improved through the use of a diffractive lenselet array.

The backplane sampling module is being developed at Advanced Scientific Concepts. This chip, named the Staring Underwater Laser Radar (SULAR) chip, utilizes capacitor banks integrated with shift registers to achieve a sample-and-hold capability. The SULAR chip is bump-bonded to the InGaAs focal plane. The detector array converts light to electrical current and the SULAR chip integrates and stores the detector current. An on-chip amplifier is used to boost the signal levels during the read-out process.

The SULAR write cycle timing is shown below for a DC-coupled configuration. An AC-coupled configuration will also be developed. First, the sample capacitor $C1$ is reset with voltage V_{rst} . Next ϕ_{RST} is opened to allow signal integration. Lastly, ϕ_{CK} is opened to hold the sample value. On the next clock rising edge, the cycle is repeated for capacitor $C2$. $C1$ is left open circuited to hold the value for the read cycle. This cycle is repeated for all capacitors in the bank and for all the pixels in the array.

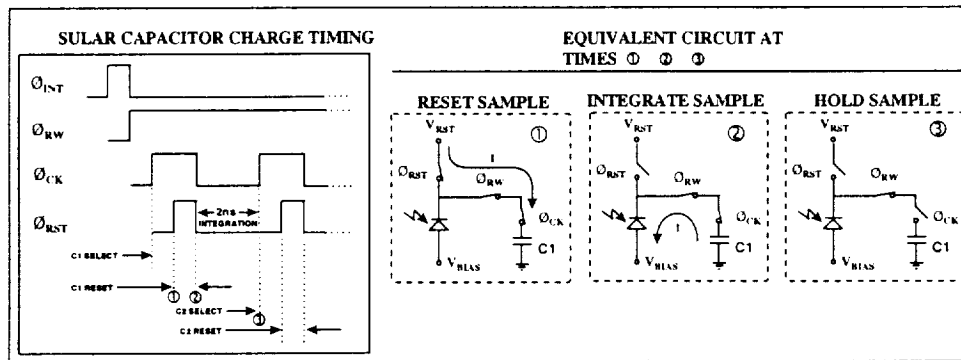


Figure 3 Generalized timing description for a DC-coupled backplane sampling module configuration. Each pixel data bank in the array is addressed for serial output.

With all capacitor sample and holds filled for all 100 pixels in parallel, the next step is to read out the samples. A shift register is used to address each pixel data bank in the array for serial output. For each pixel data bank selected, the drive electronics board is reactivated at a much reduced rate (3 MHz), and data is output to the A/D converter for digitizing. In this manner, all sample values for all pixels are read serially with a single A/D board.

Performance Predictions

In this section, we present narrowband SNR, or CNR, performance predictions for a ground-based 10×10 coherent array imager. Both DC-coupled and AC-coupled focal plane configurations have been modeled. For the DC-coupled design, sample timing jitter becomes important because the local oscillator (LO) light always illuminates the detector and depletes the charge on the sample capacitor. Timing jitter will cause sample-to-sample fluctuations in the discharge due to the LO, which act as noise. An AC-coupled configuration significantly reduces this noise.

The SNR for each of the 100 array elements is plotted below as a function of horizontal-path range for a 1 mJ, $2.012\ \mu\text{m}$ transmitter. The SNR is approximate and does not account for nonuniform Gaussian illumination pattern (outer pixels will have lower SNR than the central pixels). A Boulder winter day refractive turbulence profile has been assumed with a platform altitude of 1 m. An effective transmit beam diameter of 0.8 cm is assumed and the range at which the SNR loss due to refractive turbulence is 3 dB is indicated by a vertical line ($2\rho_0 = D_b$). The refractive turbulence effects are reduced for higher above-ground-level optical paths. The left-hand panel assumes a 15 psec RMS timing jitter with a $10\ \mu\text{A}$

detector dark current (worst case hybrid configuration) and the right-hand panel assumes a 5 psec RMS timing jitter with a 1 μA detector dark current (best case hybrid configuration). Other system parameters are given in the parameter list beneath each plot. The three curves in each plot correspond to the quantum-limited SNR (solid), AC coupled finite LO current SNR (dash) assuming $I_{LO} = 100 \mu\text{A}$, and the DC coupled SNR (dotted line) assuming the optimum DC-coupled LO current ($I_{LO} \sim 10 \mu\text{A}$). The plots show that the AC-coupled configuration will achieve significantly better SNR, which will enable vibration measurements out to a range of 4-5 km, depending on the target reflectivity (0.032 sr^{-1} assumed).

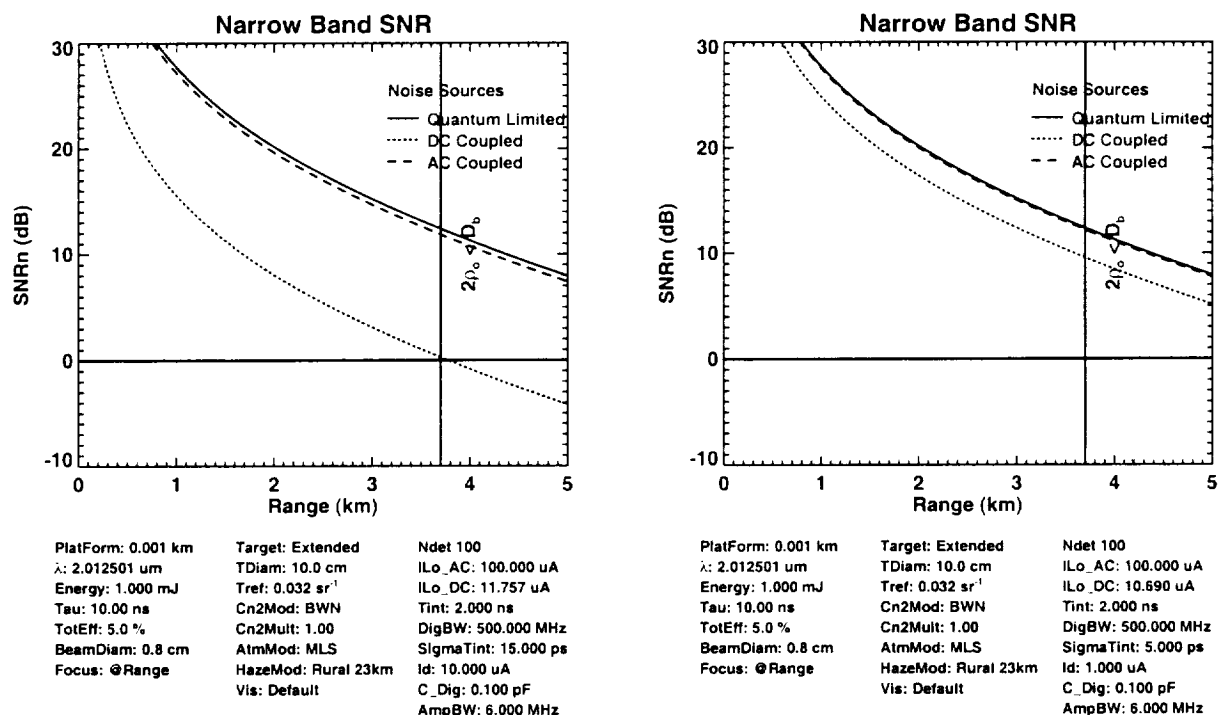


Figure 4 10x10 2 μm array imager single pixel SNR performance analysis for 1 mJ pulselet energy and shot-noise limited performance (sold curve), DC-coupled w/ optimum ($\sim 10 \mu\text{A}$) LO current (dotted curve), and AC-coupled with $\sim 10 \mu\text{A}$ LO current (dash). The left panel shows performance for the worst case ($I_d=10 \mu\text{A}$ and $\sigma_T=15 \text{ ps}$) and the right panel shows performance for the best case ($I_d=1 \mu\text{A}$ and $\sigma_T=5 \text{ ps}$) sensor scenarios. Other parameters are given in the tables beneath each plot.

SUMMARY

A novel 2 μm coherent lidar array imager is being developed which enables a cost-effective solution to the vibration imaging problem. The design exploits the unique aspects of the doublet pulse coherent lidar waveform and a recently-developed hybrid focal plane technology. Noise models have been developed for the detector and backplane sampling module and indicate that 4-5 km stand-off range will be possible for near term 10x10 element array measurements with 1 mJ of pulse energy. The detector array and backplane sampling modules are under development and initial demonstration measurements are expected to be completed within the year.

ACKNOWLEDGEMENTS

This work is being funded by the Air Force SBIR program (M. Dierking, AFRL/SNJM, technical monitor).

**Precision Targeting and Identification
using
LADAR Vibrometry**

Chyau N. Shen
Naval Air Warfare Center Aircraft Division
Patuxent River, MD 20670

Alexander R. Lovett
Office of the Deputy Under Secretary of Defense
for Advanced Systems and Concepts
Washington, D.C.

ABSTRACT

In FY-98, the Deputy Under Secretary of Defense for Advanced Systems and Concepts initiated the Precision Targeting and Identification (PTI) Advanced Concept Technology Demonstrations (ACTD) to operationally evaluate sensor technologies for target classification and identification. One of the technologies being evaluated is coherent CO₂ laser radar (LADAR) vibrometer. This paper will present description of the ACTD program. Measurements and field data collections made with the Navy ruggedized LADAR system will be discussed. Results of operational evaluation conducted at Ft. Bliss will also be discussed. Finally, future plans will be described.

DIAL

Presider: Ove Steinvall

Differential Absorption Measurements of Atmospheric Water Vapor with a Coherent Lidar at 2050.532 nm

Grady J. Koch
NASA Langley Research Center
MS 468
Hampton, VA 23681

Richard E. Davis
NASA Langley Research Center
MS 474
Hampton, VA 23681

Amin Dharamsi
Department of Electrical and Computer Engineering
Old Dominion University
Norfolk, VA 23529

Mulugeta Petros
Science and Technology Corporation
101 Research Dr.
Hampton, VA 23666

John C. McCarthy
Sanders—A Lockheed Martin Company
PO Box 368
Nashua, NH 03060

Introduction

Wind and water vapor are two major factors driving the Earth's atmospheric circulation, and direct measurement of these factors is needed for better understanding of basic atmospheric science, weather forecasting, and climate studies. Coherent lidar has proved to be a valuable tool for Doppler profiling of wind fields, and differential absorption lidar (DIAL) has shown its effectiveness in profiling water vapor. These two lidar techniques are generally considered distinctly different, but this paper explores an experimental combination of the Doppler and DIAL techniques for measuring both wind and water vapor with an eye-safe wavelength based on a solid-state laser material. Researchers have analyzed and demonstrated coherent DIAL water vapor measurements at 10 μm wavelength based on CO_2 lasers.^{1,2} The hope of the research presented here is that the 2 μm wavelength in a holmium or thulium-based laser may offer smaller packaging and more rugged operation than the CO_2 -based approach. Researchers have extensively modeled 2 μm coherent lasers for water vapor profiling, but no published demonstration is known.^{3,4} Studies have also been made, and results published on the Doppler portion, of a Nd:YAG-based coherent DIAL operating at 1.12 μm .⁵ Eye-safety of the 1.12 μm wavelength may be a concern, whereas the longer 2 μm and 10 μm systems allow a high level of eyesafety.

System Design

The lidar used for these experiments was originally built for profiling boundary layer winds and detection of aircraft wake vortices.⁶ The laser material used, Ho:Tm:YLF, was experimentally found to be tunable over approximately 2 nm centered at either 2051.5 nm or 2062.5 nm. HITRAN simulations showed an absorption line at 2050.532 nm, which was used as the on-line wavelength for the DIAL measurement. The absorption cross-section, as calculated by HITRAN, of this line is $9.1 \times 10^{-24} \text{ cm}^2$ at ground level and 1 atm pressure. Linewidth at standard temperature and pressure is 65 pm at full-width-half-maximum. This particular line is not ideal, as a stronger absorption cross section is desired and the wing of the line is overlapped by a CO_2 absorption feature. One reason for proceeding with DIAL experiment using this absorption line was that our laser could be conveniently tuned onto it. Another motivation for using this line is that the laser material used is similar to the design underway for the Space Readiness Coherent Lidar Experiment (SPARCLE), in which wind will be profiled from the orbiting space

shuttle.⁷ The DIAL studies undertaken here are then relevant in investigating whether a SPARCLE-type design could also be used for water vapor measurement.

Studies are currently underway using HITRAN-PC simulations to identify H₂O absorption lines in the 1.9 to 2.2 μm region that would be better suited for the type of application discussed here. This range corresponds to the wavelengths obtainable by the activators holmium or thulium in various host materials.

A block diagram of the lidar system is shown in Figure 1. The pulsed laser, drawn within a dashed box, is a bow-tie configuration pumped by two sets of diode laser arrays. A continuous wave laser, also shown in a dashed box, serves as both the local oscillator and injection seed source. Both the pulsed oscillator and master oscillator lasers were built under ARPA funding and are currently on loan to NASA from the Air Force. The injection seeding scheme includes a piezo-electric translator (PZT) to sweep the pulsed laser cavity during the pulse build-up time; the acousto-optic Q-switch is fired when a resonance is detected between the injection seed and pulsed laser cavity. An acousto-optic modulator is used to create a 105 MHz intermediate frequency between the local oscillator and pulsed laser. The pulsed laser is capable of producing 4.5 mJ at 20 Hz in a 180 ns pulsewidth. However, during these experiments the diode pump arrays were near the end of their lifetime and the resulting pulse energy was only 0.75 mJ at 20 Hz. Laser output is transmitted to the atmosphere via a 4-inch diameter off-axis paraboloid telescope. The outgoing pulse and the atmospheric return signal are separated by a polarization relationship imposed by the combination of a quarter-wave plate and polarizing beam splitter. Photodiodes in a dual-balanced circuit provide the RF heterodyne signal.

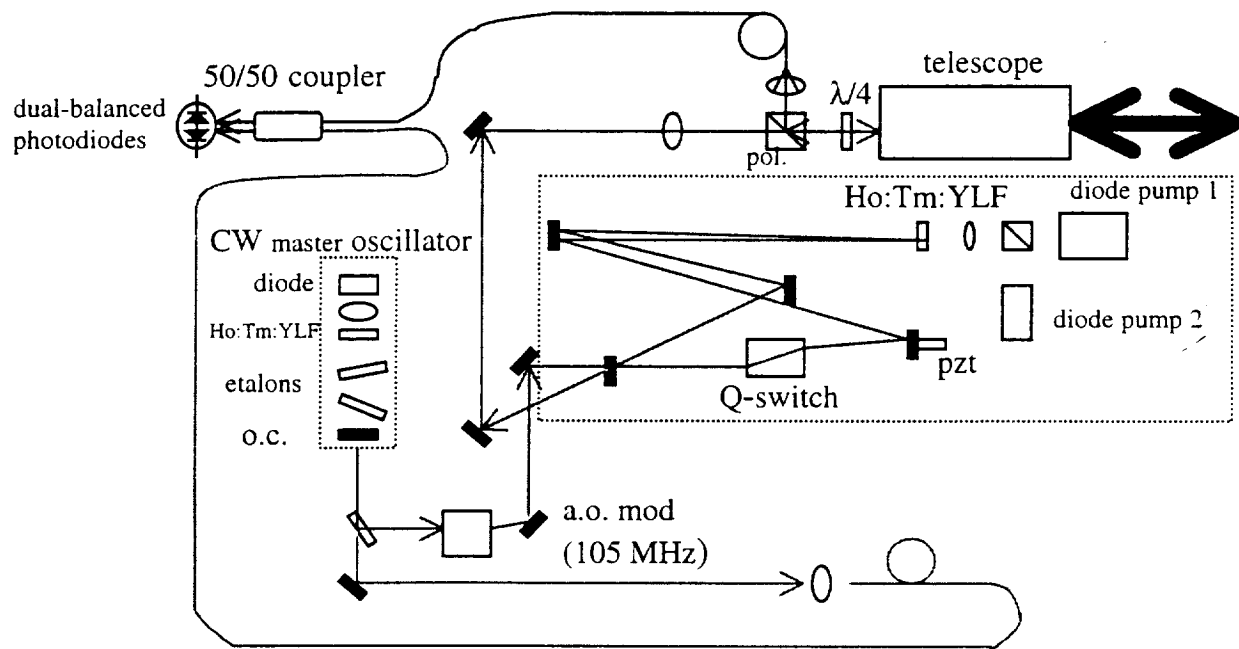


Figure 1: Block diagram of optical system.

Signal processing was adapted from an RF spectrum analyzer, which was tuned to the intermediate frequency with a 3 MHz passband. The spectrum analyzer then displayed the power in the atmospheric return (at the intermediate frequency) as a function of time. Data was averaged and stored with a digital oscilloscope. Further processing, including the DIAL calculation, was performed with MATLAB algorithms on a personal computer.

Tuning on and off the absorption line was done by manually tilting an etalon inside the master oscillator laser. Tuning was first done on-line by adjusting the etalon while monitoring wavelength on a wavemeter. The wavelength could typically be tuned within 3.5 pm of line center. 100 shots were then

averaged of the atmospheric return. Such a large number of averages is required to reduce speckle noise. During the 100 shot averaging period the laser wavelength might drift as much as 3 pm from its starting wavelength. These errors in drift and on-center tuning degrade the accuracy of the DIAL measurement, and a stabilized laser design is currently under development. After the on-line shots were recorded the master oscillator laser was then manually tuned off line, typically to 2051.934 nm. The tuning to off-line would require as much as 2.5 minutes to accomplish, as the wavelength could require this long to stabilize after the etalon adjustment. 100 shots of off-line data were then acquired. Such a long time between on and off line measurements is too long because the atmosphere can change characteristics in this interval. Designs are also underway to use two different master oscillator lasers—one tuned on-line and the other off-line. Switching between the two could take place in a matter of seconds.

Sample DIAL Measurement

The only available correlative measurement to compare with the DIAL measurement were reports of ground-level temperature and relative humidity from a weather station at Norfolk International Airport, some 25 miles distant from our laboratory. To compare with this ground-level measurement the laser was directed near horizontal. A straight horizontal path was not possible from the window of our laboratory due to obstruction by trees, so the beam was directed at 15° elevation. The laser beam was directed in azimuth to be perpendicular to the ambient wind direction to keep the Doppler shift from pushing the heterodyned atmospheric return out of the signal processing passband. In a zenith-looking mode (which would provide the most useful scientific data) this passband issue would not exist. Figure 2 shows smoothed atmospheric returns tuned both on and off the water vapor line. 100 shots were averaged of the on and off wavelengths. The differential absorption is readily apparent as seen by the difference in slope between the two lines. Data before 200 m range is not displayed since during the period of time corresponding to this range the photodetectors are saturated by internal reflections of the outgoing laser pulse.

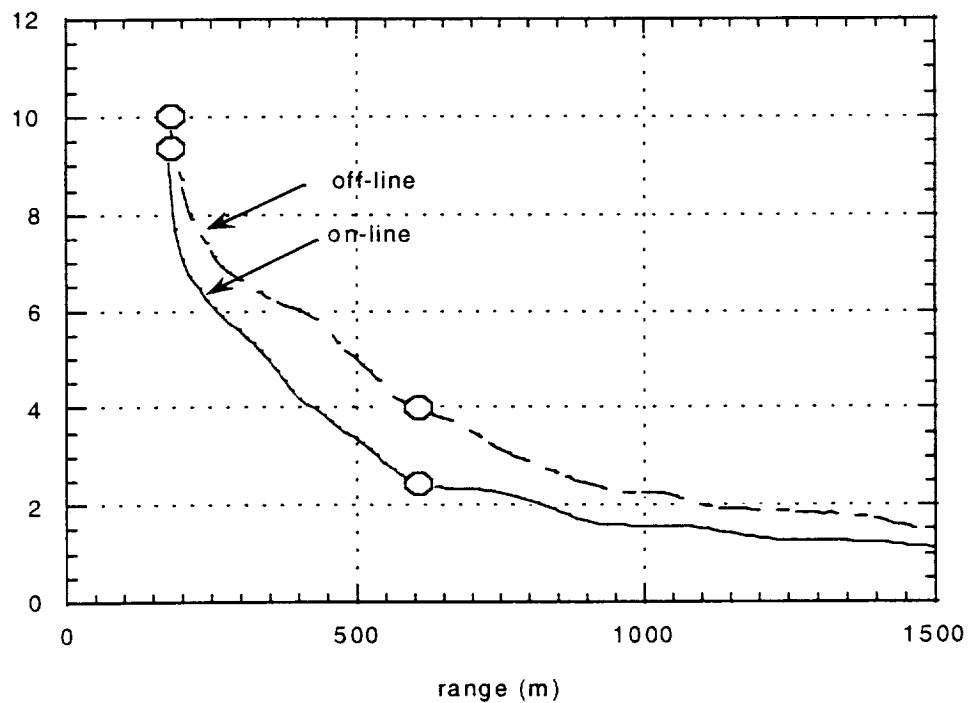


Figure 2: Water vapor DIAL measurements. Six such measurements were made on different days.

A DIAL calculation was made based on the points indicated in Figure 2. Data beyond 600 m range was not considered as the signal-to-noise ratio has dropped so low beyond this point that a DIAL calculation at a further range would be unreliable. The water vapor concentration calculated from these data points is 5.2×10^{17} molecules/cm³; the concentration based on the weather station measurements of 21.1°C and 45% relative humidity is 2.8×10^{17} molecules/cm³. If the weather station data is accepted as truth then the DIAL measurement has an 86% error. A desired accuracy for meteorological and scientific purposes is less than 20%. Sources of error in the DIAL measurement are wavelength jitter, speckle, low signal-to-noise ratio (due to limited pulse energy), and a long time between on-line and off-line measurements. A stronger, non-overlapped absorption line would also enhance accuracy by making the difference between on and off line absorption more pronounced.

Conclusions

Though the coherent DIAL measurements were successful with this 2 μm wavelength system, the accuracy of the measurement must be improved to be useful for scientific applications. Toward this goal a master oscillator is being built which includes an output coupler mounted on a PZT. This laser will be locked to the absorption line using a wavelength modulation technique. Replacement of the pulsed oscillator pump diodes would allow a higher pulse energy for enhanced signal to noise ratio and DIAL accuracy. Alternate pulsed laser designs are being considered with regard to pulse repetition frequency (to allow more averaging for speckle noise reduction) and selection of a line with a stronger absorption cross section.

References

1. R.M. Hardesty, "Coherent DIAL measurement of range-resolved water vapor concentration," *Appl. Opt.*, Vol. 23, pp. 2545-2553, 1984.
2. W.A. Brewer, V. Wulfmeyer, R.M. Hardesty, and B.J. Rye, "Combined wind and water-vapor measurements using the NOAA mini-MOPA Doppler lidar," Nineteenth International Laser Radar Conference, NASA publication NASA/CP-1998-207671/PT2, pp.565-568, 1998
3. M.J. Kavaya, S.W. Henderson, E.C. Russell, R.M. Huffaker, and R.G. Frehlich, "Monte Carlo computer simulations of ground-based and space-based coherent DIAL water vapor profiling," *Appl. Opt.*, Vol. 28, No. 5, pp.840-851, 1989.
4. C.J. Grund, R.M. Hardesty, and B.J. Rye, "Feasibility of Tropospheric Water Vapor Profiling Using Infrared Heterodyne Differential Absorption Lidar," DOE report DE-A103-94ER61761, 1995.
5. S. Lehmann, J. Bosenberg, F. Jansen, and H. Linne, "All Solid State Heterodyne DIAL System for Simultaneous Water Vapor and Wind Measurements," Nineteenth International Laser Radar Conference, NASA publication NASA/CP-1998-207671/PT2, pp.763-765, 1998.
6. G.J. Koch, B.C. Barker, and C.L. Britt, "Development of an Operation Wake Vortex Sensor Based on Pulsed Coherent Lidar," 9th conference on Coherent Laser Radar, 1997.
7. U.N. Singh, J. Yu, M. Petros, N.P. Barnes, and M.W. Phillips, "2-Micron Diode-Pumped Pulsed Laser Transmitter for SPARCLE: A Coherent Wind Lidar Shuttle Mission," Nineteenth International Laser Radar Conference, NASA publication NASA/CP-1998-207671/PT2, pp.603-607, 1998.

Realtime spectral analysis of heterodyne DIAL signals at very high repetition rate.

Holger Linné, Jens Bösenberg
Max-Planck-Institut für Meteorologie, Hamburg
Bundesstr. 55, D-20146 Hamburg, Germany

Dieter Hasselmann
Meteorologisches Institut der Universität Hamburg
Bundesstr. 55, D-20146 Hamburg, Germany

Introduction The use of all solid state lasers has considerably improved the reliability of lidar systems in the last few years and broadened the range of potential applications. This is particularly true for lidars using heterodyne detection for wind sensing and possibly differential absorption lidar (DIAL) for water vapor or other trace gas measurements. These lasers show best performance at high repetition rate in the kHz rather than 10 Hz range at the expense of relatively low energy per pulse. The enormous amount of data generated by these systems calls for efficient data acquisition and reduction schemes. This is particularly demanding because one advantage of wind lidars compared to radars is the better spatial resolution and potentially better accuracy. So there is a definite need for computationally efficient evaluation schemes to retrieve the Doppler frequency and the backscattered signal power from high repetition rate systems, especially in the low signal regime.

Recently a data acquisition system based on direct digitization of heterodyne lidar signals has been introduced which is capable of accepting data at a shot rate of up to 1 kHz, and providing sufficient (and scalable) processing power for flexible on-line data reduction [Linné and Bösenberg, 1998]. In this paper we discuss the details of data reduction schemes for optimizing the resolution and accuracy of retrievals of wind and backscattered power.

Theoretical background The output of a heterodyne receiver in an atmospheric lidar system is the result of superposition of many randomly phased scattered fields from individual aerosol particles. It is well represented as a Gaussian random process. The goal of the data analysis is to estimate the return power, Doppler shift, and possibly spectral width of the return signal, corresponding to the zeroth, first, and second spectral moments. The random nature of

the signal caused by the speckle field requires some sort of averaging in order to achieve any useful accuracy in the parameter estimation. Because even for high repetition rate systems the correlation time is shorter than the time between successive laser shots only incoherent averaging schemes can be applied. In the frequency domain a suitable function retaining all relevant information is the periodogram, i.e. the square modulus of the Fourier transformed signal. In the time domain the choice would be the complete autocovariance function.

A straightforward approach to signal processing of heterodyne lidar returns is to digitize directly the output of the detector at intervals Δt , which is chosen sufficiently small to resolve the expected Doppler shift. The achievable range resolution is determined by the laser pulse width τ , the observation time T for one range gate should be selected as $T \gtrsim 4\tau$ to obtain sufficiently independent information from successive range bins. In case of a Gaussian pulse shape the monitor signal of the transmitted pulse is

$$A_e(t) = A \cdot \exp\left\{-\frac{t^2}{2\tau^2}\right\} \cos(2\pi f_e t + \theta) \quad (1)$$

where A is the amplitude and θ is an (arbitrary) phase.

In the spectral domain the key parameters are the Nyquist frequency $f_N = 1/2\Delta t$, the spectral width of the transmitted pulse $w = 1/\sqrt{8}\pi\tau$, and the elementary bandwidth $\Delta f = 1/T$. The condition for independent range gates then reads $\Omega = w/\Delta f \gtrsim 0.4$. For best range resolution rather small values for Ω should be chosen, implying that only very few points in the discrete spectrum, on the order of 4, will contain the signal energy.

We obtain spectral density estimates at frequencies $f_j = j\Delta f, j = 0 \dots M/2$, where $M = T/\Delta t$ is the

number of samples per range gate. The spectral density at these frequencies is given by

$$(\Delta f)^{-1} F(f_j) = \frac{N}{f_N} + \frac{S}{w} \frac{1}{\sqrt{2\pi}} \exp\left\{-\frac{(f_p - f_j)^2}{2w^2}\right\} \quad (2)$$

Summing $F(f_j)$ for $j \geq 0$ the signal and noise variances are S and N . The relevant nondimensional parameters are the wideband signal to noise ratio $SNR = S/N$, the normalized Doppler shift $f_D T = (f_p - f_e)T$, and the nondimensional spectral width $\Omega = w/\Delta f$. Any unbiased estimators for these parameters have a variance at best equal to the Cramer Rao lower bound (CRB). For methods to calculate the CRB we refer to the literature [Frehlich, 1993], [Rye and Hardesty, 1993]. Best performance is achieved with maximum likelihood estimators, where the CRB is actually attained.

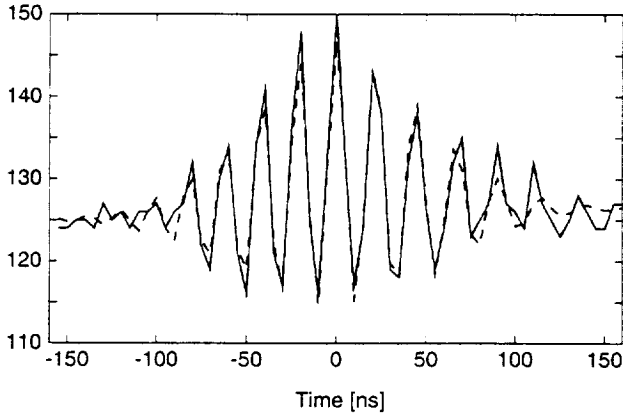


Figure 1: Monitor pulse (solid line) and best-fit model (dotted line). The Parameters of the model fit according to Eq. (3) are $A = 17$, $B = 2.3$, $t_0 = 152ns$, $\tau = 51ns$, $f_e = 46.9MHz$, $\phi = -53.1MHz/\mu s$, $\theta = -1.68$, $\xi = 5.1\mu s^{-1}$ and $\rho = 126$

In real lidar systems some adverse effects of actual laser and detector performance must be accounted for. Some of the common problems are: the frequency of the transmitted laser pulse jitters with respect to the local oscillator, it may also change during the pulse (chirp), and the temporal shape of the pulse can deviate considerably from Gaussian. The local oscillator can exhibit intensity fluctuations, e.g. caused by relaxation oscillations of the laser or “spiking”, and the detector circuit can pick up unwanted electromagnetic interference signals (EMI). Therefore the data processing scheme should not only be optimized for operation under ideal conditions, but also provide possibilities for at least largely reducing the problems caused by non-ideal system performance. For our system, the most important system imperfections were

frequency jitter, EMI (pickup of radio signals from a nearby TV-tower), and local oscillator amplitude instabilities. One reason for our choice of processing in the spectral domain is the fact that the problems just mentioned have rather well defined spectral properties, so corrections are best made in the frequency domain.

Algorithms Because the center frequency f_e of the transmitted pulse can vary considerably from shot to shot with respect to the local oscillator frequency, a good estimate of f_e for each shot is most important. This is obtained from a separately recorded monitor pulse produced by an internal reflection in the lidar system. This signal is virtually free from speckle effects, so a single realization is sufficient to provide good spectral estimates. The monitor pulse for our system is well described by the model of [Frehlich et al., 1994], but with the addition of a ‘direct detection’ term and a linearly increasing pedestal:

$$A_e(t) = A \cdot \gamma \cdot \cos(2\pi f_e t + \pi\phi(t - t_0)^2 + \theta) + B^2 \cdot \gamma^2 + \xi t + \rho \quad (3)$$

$$\gamma = \exp\left(-\frac{(t - t_0)^2}{2\tau^2}\right)$$

This corresponds to a harmonic oscillation with frequency f_e , modulated by a linear chirp ϕ , having a Gaussian envelope of width τ , sitting on a pedestal with offset ρ linearly increasing in time at a rate of ξ , a direct detection component of amplitude B^2 , and all that slightly corrupted by white noise. Fig. 1 demonstrates that real laser pulses are in excellent agreement with this model. Realistic values of the model parameters are provided in the figure caption.

For our system a rather large shot to shot jitter of f_e is observed. An estimate of f_e is obtained for each individual shot. This value is subtracted from the frequencies of the periodograms of both the monitor pulse and the atmospheric returns. Since this operation has to be performed for each individual shot only rather simple algorithms for determining f_e are feasible. We have assessed the performance of two simple and, for reference, one more sophisticated but time consuming estimator for the center frequency using simulated data:

M1: first spectral moment in a narrow band around the maximum of the periodogram (in a given spectral region)

M1i: an iteration of 1 around the so determined center frequency, using interpolated values for the

periodogram at frequencies not contained in the discrete spectrum of the transformed signal

MF: estimation of the center frequency by fitting the monitor pulse model in the time domain.

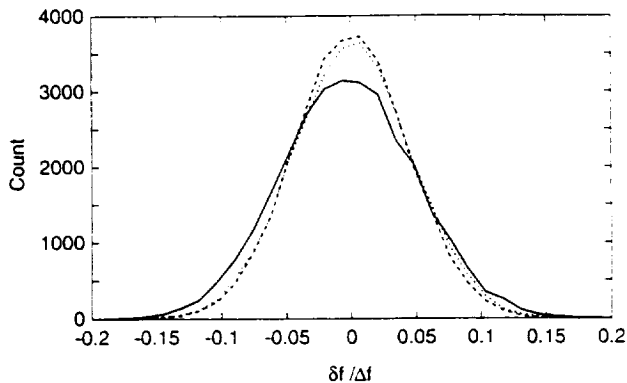


Figure 2: PDF of the error in frequency estimation δf from the monitor pulse when scanning the frequency f_e over a range of $3\Delta f$. The lines shown are for the *M1* - estimator (solid line), *M1i* - estimator (dotted line) and the *MF* - estimator (dashed line).

The results are shown in Fig. 2. For noise-free data *M1* shows a small bias depending on the relative position of the center frequency with respect to the center of the resolved bands, but at realistic noise levels the scatter due to noise is at least as large as the systematic bias. In *M1i* the bias is largely suppressed, scatter is smaller than for *M1*. *MF* shows slightly better performance than *M1i*, but cannot be implemented because it is too time consuming for real-time processing. For most cases *M1* is an efficient and sufficiently accurate estimator, *M1i* would be slightly better but has not yet been implemented for online processing.

Variants of the spectral methods, some utilizing the high resolution available in the f_e -correction shift have also been applied to the return signal. With the coarse shift f_e is determined only to the precision Δf . For reasonable range resolution the signal is then concentrated in about 4 spectral bands, making it difficult to use parametric fits to determine the signal parameters in Eq. (2). We have tested whether the situation improves, when at fixed Δf the f_e -shift is made with r_e -fold higher resolution, creating a denser frequency spacing, at the expense of the number of shots accumulated in each band. For $\Omega = 0.7$, $M = 64$ and a realistic jitter we have simulated 500×10^4 realizations ('shots') for each $\Phi = M \cdot SNR/2$, with Φ ranging from 0.1 to 200. The spectra were accumulated over $n = 10^4$ shots, yielding $K_s = 500$ samples for each estimator.

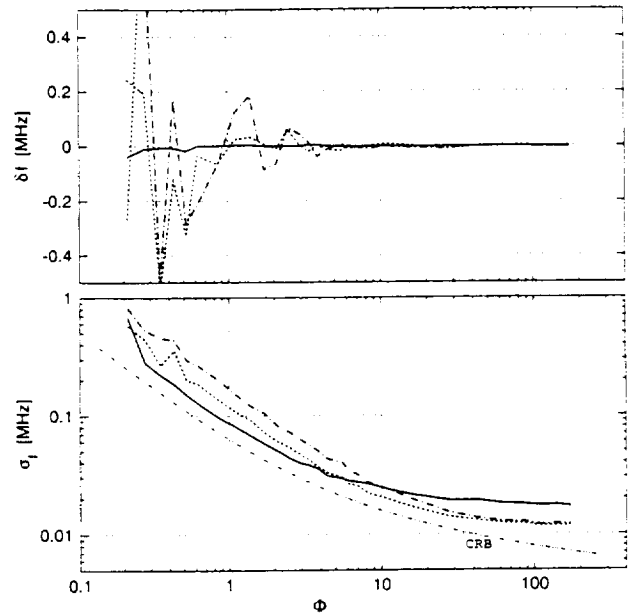


Figure 3: Bias (top panel) δf and standard deviation σ_f of simulated Doppler estimators accumulated over 10^4 shots. The estimators are *M1* (dotted line), *M1i* (dash-dotted line) and *G5* (solid line). The CRB on σ_f (converted to *MHz* with $T = 320ns$) is shown for comparison. See text for details.

Estimators for the Doppler-shift were *M1*, *M1i* explained above and a parametric fit G_5 (with $r_e = 5$) to the Gaussian spectrum in Eq. (2). For total backscattered energy the zeroth spectral moment in a narrow band around the peak *M0* and the Gauss-fit G_5 were used. Both Φ -estimators (Fig. 4) behave very similarly, have a negative bias of about 5% and the expected relative standard deviation σ_Φ/Φ of roughly $1/\sqrt{(2\pi\Omega)}$ at high *SNR*. The Doppler estimators (Fig. 3) show little bias for all estimators except for the *M*-estimators at $\Phi \lesssim 4$, which is also the crossover value, above which *M1* shows less variance than the Gauss-fit.

Application to atmospheric measurements.

In a field measurement campaign on the island of Gotland in the Baltic Sea the heterodyne lidar system described in [Lehmann et al., 1998] has been operated in conjunction with the data acquisition of [Linné and Bösenberg, 1998]. The beam was pointed vertically to measure the vertical wind speed with high temporal and spatial resolution. As an example Fig. 5 shows the variance spectrum of the vertical wind speed at a height of 480 m above sea level for one hour of measurement time during October 28, 1998. The wind was obtained from accumulated periodograms using *M1* for the determination of f_e on a

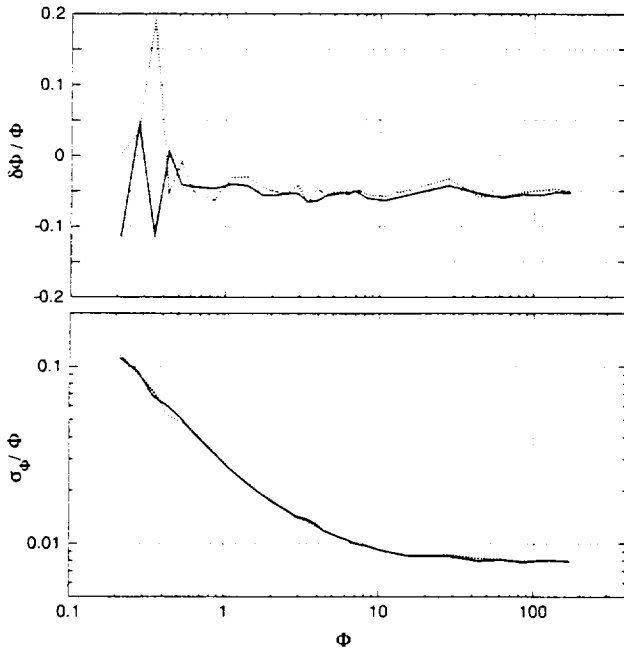


Figure 4: Relative bias (top panel) $\delta\Phi/\Phi$ and relative standard deviation σ_Φ/Φ of simulated Φ -estimators. These are $M0$ (dotted line) and G_5 (solid line). See text for details.

shot-by-shot basis, coarse shift of the resulting periodogram with a resolution of Δf was used in the accumulation of periodograms. These operations were performed in real-time. 2000 laser shots were averaged every 10 s. The wind speed was retrieved from these accumulated periodograms with the $M1i$ algorithm.

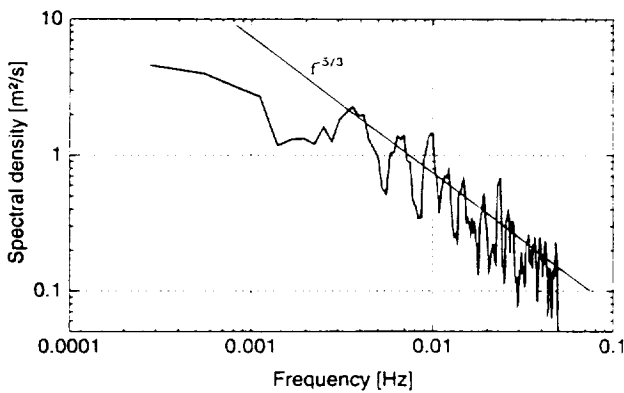


Figure 5: Power spectrum of vertical wind in a height of 480 m. (98-10-28 14:40-15:40 UT). Resolution 48 m vertically, 10 s temporally.

The wind spectrum shows the well known $f^{-5/3}$ dependence for frequencies larger than about 0.01 Hz. This behaviour is found up to the Nyquist frequency

of 0.05 Hz, indicating that the variance is mainly due to atmospheric variability rather than system noise. It is concluded that under these conditions the system noise has a standard deviation of significantly less than 7 cm/s . This is in good agreement with the estimated performance of the retrieval algorithms for a signal level of about 4 coherently detected photons per range gate.

Conclusion The detailed analysis of algorithms for wind and backscatter retrievals from heterodyne lidar signals shows, that very high precision can be reached for both parameters. Using a high repetition rate laser a precision of $\lesssim 5\text{ cm/s}$ for the vertical wind and a relative accuracy of 1% for aerosol backscatter can be achieved within the boundary layer, for 10s temporal and 50m vertical resolution, even for a rather small pulse energy of $\lesssim 0.5\text{ mJ}$. From this it is concluded that such a system is very well suited for studies of turbulent transport in the boundary layer. It has been demonstrated that the necessary data reduction can be performed in real-time, when advanced signal acquisition and processing techniques are used.

References

- [Frehlich, 1993] Frehlich, R. (1993). Cramer-Rao Bound for Gaussian random processes and applications to radar processing of atmospheric signals. *IEEE Trans. Geosci. Remote Sensing*, 31:1123-1131.
- [Frehlich et al., 1994] Frehlich, R., Hannon, S. M., and Henderson, S. W. (1994). Performance of a 2- μm coherent Doppler lidar for wind measurements. *J. Atmos. Oceanic Technol.*, 11:1517-1528.
- [Lehmann et al., 1998] Lehmann, S., Bösenberg, J., Jansen, F., and Linné, H. (1998). All solid state heterodyne DIAL system for simultaneous water vapor and wind measurements. In *Nineteenth International Laser Radar Conference July 6 - 10, 1998*, volume NASA/CP-1998-207671/PT2, pages 763 - 765.
- [Linné and Bösenberg, 1998] Linné, H. and Bösenberg, J. (1998). Heterodyne DIAL at high repetition rate: a solution for the data acquisition problem. In *Nineteenth International Laser Radar Conference July 6 - 10, 1998*, volume NASA/CP-1998-207671/PT2, pages 759 - 762.
- [Rye and Hardesty, 1993] Rye, B. J. and Hardesty, R. M. (1993). Discrete Spectral Peak Estimation in Incoherent Backscatter Heterodyne Lidar. I: Spectral Accumulation and the Cramer-Rao Lower Bound. *IEEE Trans. Geosci. Remote Sensing*, 31:16-27.

Boundary Layer Wind and Water Vapor Measurements using the NOAA mini-MOPA Doppler lidar

W. Alan Brewer, Volker Wulfmeyer, and R. Michael Hardesty
NOAA/ERL/Environmental Technology Laboratory
325 Broadway, Boulder, CO 80303
abrewer@etl.noaa.gov (303) 497-7859 / (FAX: -5318)

Barry J. Rye
Cooperative Institute for Research in Environmental Sciences
University of Colorado/NOAA, Environmental Technology Laboratory
325 Broadway, Boulder, CO 80303

Abstract

The NOAA Environmental Technology Laboratory has developed a multiple-wavelength (line tunable from 9-11 μm), low-pulse-energy (1-3 mJ), high-pulse-rate (up to 500 Hz) CO₂ Doppler lidar for simultaneous investigation of boundary layer wind and water vapor profiles. In this paper we present single-wavelength, Doppler results and preliminary water vapor DIAL measurements.

THEORY AND SIMULATION

Presider: Rod Fehlich

COHERENT LIDAR RETURNS IN TURBULENT ATMOSPHERE FROM SIMULATION OF BEAM PROPAGATION

*A. Belmonte, B.J. Rye, W. A. Brewer, R. M. Hardesty
Environmental Technology Laboratory
R/E/ET2,
NOAA ERL
325 Broadway
Boulder, CO 80303-3328*

Introduction

This paper describes what we believe to be the first use of simulations of beam propagation in three-dimensional random media to study the effects of atmospheric refractive turbulence on coherent lidar performance. The results presented here are based on propagation through an atmosphere characterized by uniform refractive turbulence; transmitted and virtual (back-propagated) local oscillator beams are assumed to be matched, perfectly aligned, Gaussian, and truncated at the antenna aperture by an amount that would maximize system antenna efficiency in the absence of turbulence. However, our method provides the tools to analyze laser radar with general refractive turbulence conditions, beam-angle and beam-offset misalignment, and arbitrary transmitter and receiver geometries.

Refractive turbulence in atmospheric backscatter coherent lidar

Any reader who has worked with coherent lidars knows how difficult is to predict the performance of the instrument. It is not unusual to find out that the effective lidar range has been drastically reduced in relation to previous measurements. Explanations such as low aerosol concentration, increased atmospheric absorption, and technical problems such as misalignment or laser performance are the most frequently cited when the lidar system whatever the laser wavelength. At shorter wavelengths, the effects of refractive turbulence on ground-based systems have certainly to be included among these factors (see figure 1). It is so closely related and strongly dependent on near field and misalignment problems, that it is often hard to establish the exact cause of lidar dysfunction. So, we are required to study the features of coherent laser radar behavior under realistic conditions if we want to assess properly the feasibility of proposed measurements, define new applications or maximize the system performance.

Early analytical work on the problem^{1,2} explained only the reduction of lidar efficiency caused by beam spreading in bistatic systems. The discussion of more realistic lidars with common transmit/receive antennas (monostatic geometry)^{3,4} predicted that the average signal-to-noise ratio (SNR) of perfectly aligned systems should be generally rather higher than was given by the bistatic model - indeed, that under some conditions it could be higher than expected when no turbulence was present. This result could be explained physically by noting that, on application of the reciprocity theorem, a lidar return can be expressed as the overlap integral of the transmitter and back-propagated local oscillator^{5,6} beams in the target plane. This reduces the problem of calculating lidar returns to one of computing irradiance along the two beam propagation paths, a method used in the simulations reported here. The signal enhancement that occurs in the monostatic geometry arises because both small-scale scintillation and large-scale beam wander are common to the two beams. For the lidar application, other authors⁷ have used expansions based on the path-integral formulation to describe the problem in the limits of weak and strong turbulence, with some approximations. While the analytical approach leads to understanding of the basic physical problems, it is usual to consider only the higher moments of the field. These moments are usually difficult to estimate and no simple analytical solutions are known outside those obtained for simplified beam geometries (defined through untruncated Gaussian functions) and unrealistic atmospheric characterization (usually by random wedges where only beam wander and no scintillation is considered).

The simulations used here are based on the well-established method of modeling the atmosphere by a set of two-dimensional Gaussian random phase screens with an appropriate phase power spectral density.⁸ Though the accuracy of the moments from simulation of plane and spherical waves in random media is well established,⁹ we have extended this approach to the more complex problem of Gaussian and truncated Gaussian beams propagation. Before applying the

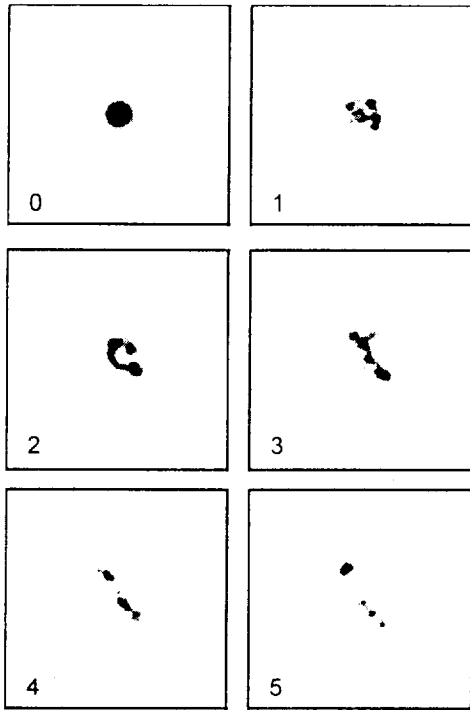


Figure 1. A beam propagated through a turbulent atmosphere look quite different to free-space propagated Gaussian Beams. It results obvious that the behavior of the coherent lidar is going to be affected by the intensity distortions of any scale we see at the pictures: beam wander, beam spreading and scintillation modify the system performance. The pictures show instantaneous images of a collimated Gaussian beam at ranges from 0 to 5-km at 1 km intervals along an atmospheric path. The wavelength is $2 \mu\text{m}$ and a 14-cm diameter transmitter telescope 1.76 time the beam diameter truncates the beam. The level of refractive turbulence C_n^2 has the typical daytime value of $10^{-14} \text{ m}^{-2/3}$.

results to general lidar geometries, we have studied the effects of the refractive turbulence on the propagated beams in order to verify our simulations (this is not reported here). In addition to the very general applicability of this approach noted at the end of the last section, use of the technique is extremely useful for developing an intuitive knowledge of the problem involved

Simulation results based on the parameters of a real system

The presented simulations of the effects of refractive turbulence consider the National Oceanic and Atmospheric Administration (NOAA) Environmental Technology Laboratory collimated Gaussian monostatic laser radar system. The parameters of the lidar are a wavelength close to $2 \mu\text{m}$, transmitter and receiver aperture of 14 cm, and a optimal beam truncation by the telescope aperture of 1.76, which maximizes the far-field system-antenna efficiency of a lidar using a

suboptimal local oscillator geometry in the absence of refractive turbulence.¹⁰ We assume that the photodetector, whose noise is dominated by shot noise, has uniform quantum efficiency and collects all the energy of the local oscillator and back-scattered field. All simulations use the von Karman turbulence spectrum with an inner scale $l_0 = 1 \text{ cm}$ and assume homogeneous turbulence along a horizontal path.¹¹ The calculated measures of performance are the system-antenna efficiency (the fraction of the available optical power recorded by the heterodyne receiver) and the SNR of the laser radar as a function of range and level of refractive turbulence C_n^2 .^{1,7}

The effects of refractive turbulence as a function of range (figures 1 and 2) are pronounced for ranges as short as a few hundreds of meters under typical diurnal condition of strong and moderate turbulence (C_n^2 values between 10^{-12} and $10^{-14} \text{ m}^{-2/3}$). Figure 2 shows the average SNR normalized by that for free-space propagation: SNR enhancement, when this ratio is greater than 1, is evident at ranges shorter than 1 Km.. While the small-scale scintillation structure (see figure 1) explains this effect, the spreading of the transmitted beam at larger ranges reduces system performance below the result for no refractive turbulence. For a typical nighttime C_n^2 lesser than $10^{-14} \text{ m}^{-2/3}$ (figure 3), the effects of refractive turbulence are present for ranges greater than 1 Km . We again observe enhancement and subsequent performance reduction with respect to the free-space propagation, but these effects have different magnitudes and occur at much longer ranges.

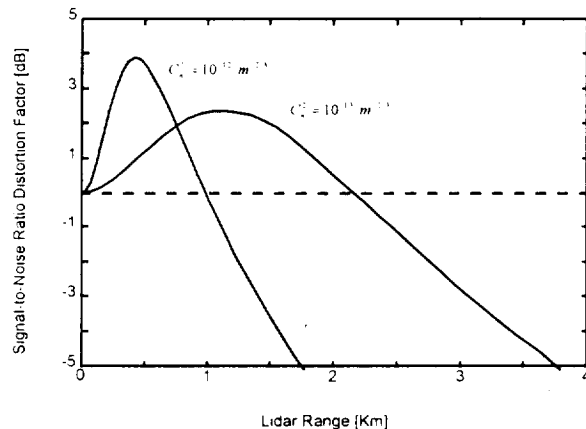


Figure 2. The importance of the refractive turbulence on the coherent lidar performance in daytime (strong and moderate turbulence) is pronounced for ranges as short as a few hundreds meters. By using the simulation of truncated Gaussian beam propagation in three-dimensional random media, the figure shows the average SNR (in dB) normalized by the case of no refractive turbulence as a function of range R and level of refractive turbulence C_n^2 . The lidar system parameters are wavelength of $2 \mu\text{m}$, 14-cm transmitter and receiver aperture, and optimal beam truncation by the telescope of 1.76.

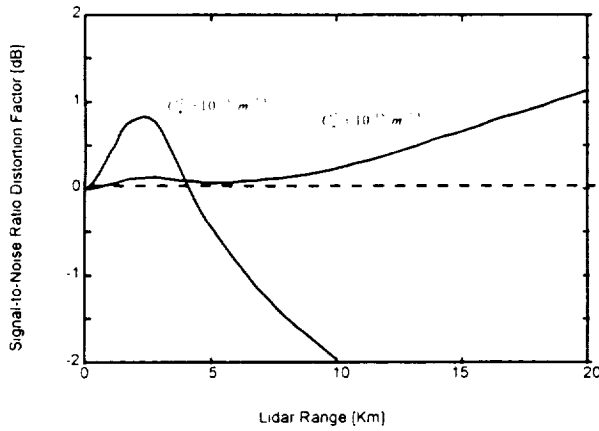


Figure 3. The importance of the refractive turbulence at night (moderate and weak turbulence) is clearly manifest for ranges larger than 1 Km. The lidar system parameters are similar to those of figure 2.

Figure 4 shows the effects of the refractive turbulence on coherent lidar performance using the system-antenna efficiency. For free-space propagation, the truncation chosen maximized the coherent detection power for returns from the far field of our telescope by minimizing the beam size on the target plane. However, it seems very clear from the simulated results that the atmospheric turbulence distorts this result even when we propagate the beam in weak turbulence: the beam spreading due to atmospheric turbulence is relevant in most of the considered propagation conditions. Even more, simulations have shown that for moderate and strong turbulence, where the effective beam size after turbulence spreading is nearly the same for any truncation, the use of truncation cannot minimize the beam size and only contributes unnecessary power loss. So, though further analysis should be considered, these results seem to indicate that in the presence of strong enough turbulence, optimal truncation should be smaller than those used when no refractive turbulence is assumed.

Parameterization

Lidars intended for profiling over long ranges are generally operated with a collimated transmit beam. For this case, the wave fronts of the transmitter and BPLO beams are planar at the lidar antenna, and the physics of the SNR and heterodyne efficiency are described by the transmitter field at the exit of the aperture, the receiver telescope, and the local oscillator field for a given wavelength and level of refractive turbulence C_n^2 . For free space propagation, it is easy to establish how the lidar performance depends on aperture diameters D , wavelength λ , and distance R through the dimensionless Fresnel number $N_F = kD^2/4R$.¹

For turbulence propagation the field is scattered on turbulence inhomogeneities when propagating from transmitter to the scattering plane which causes beam spread and intensity fluctuations. A larger incoherent image at the target caused by the beam spread produces the loss of coherence of the back-scattered field and lidar performance to degrade. Otherwise, the fluctuations in irradiance at the target cause enhancement of the coherent lidar SNR compared with free-space propagation. The study of turbulence effects due to both spreading and intensity fluctuation shows clearly the dependency on just the dimensionless parameter $N_T = kr_0^2/4R$, where r_0 is the transverse-field coherence diameter on the receiver plane of a point source located at the target.¹² Although previous work¹ has used N_T similar parameters for describing beam expander effects, we have showed that the combination of both N_F and N_T allow characterizing intensity fluctuations in a similar way.

It is easy to appreciate the similarity between this parameter N_T , describing the refractive turbulence effects on the propagated beam, and the Fresnel number N_F , describing the free-space propagation: now the coherence diameter assumes the role of the telescope aperture diameter. As a consequence, we might expect that any atmospheric propagation problem defined by the same parameters N_F and N_T have the same solution, i.e., any lidar problem characterized by identical N_T and N_F should work with similar performances.

Figures 5 and 6 show some of the consequences derived of the previous hypothesis when we check them by

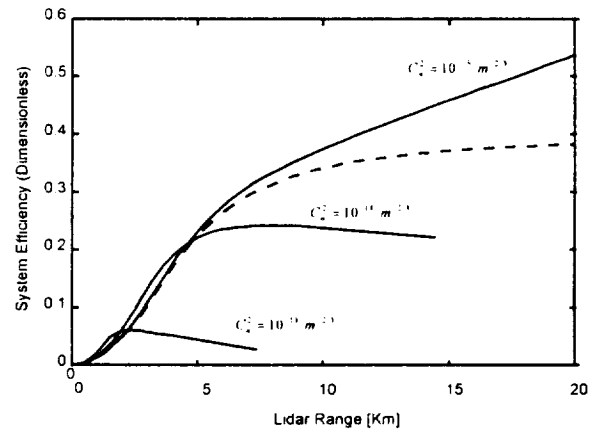


Figure 4. The system-antenna efficiency, as a function of range R and level of refractive turbulence C_n^2 is a useful measurement of the coherent lidar performance. The lidar system parameters are the same than in previous figures. It shows different levels of refractive turbulence C_n^2 along with the case of free-space propagation (dashed curve), for which the proposed 1.76 optimal truncation maximizes the heterodyne efficiency at 0.4 for returns from the far field of the telescope (ranges greater than 15 km).

Conclusions

Current desktop computers that allow users to visualize and analyze numerical simulations and interact with the results rapidly could boost research productivity in the study of coherent laser radar systems. Furthermore, simulating tools turn out to be extremely useful for insight into problems as complex as the propagation of coherent lidar signal through atmospheric turbulence.

We have here described some results of our simulations and the relations appearing from dimensionless N_T and N_F parameter dependencies. For different beam geometries and turbulence paths we have used the simulation of Gaussian beam propagation in three-dimensional random media to analyze the effects of the refractive turbulence on the behavior of coherent lidar. Beam truncation of both transmitted and local oscillator, and the use of a non-approximated turbulence spectrum allow study of the problems in a very realistic way.

In particular, simulations provide a way to study the relatively intractable problems arising from misalignment and aberrations of the optical system in the presence of refractive turbulence. We have used extensions of this work to overcome the lack of analytical results in the study of both the relative variance and the probability-density function of the coherent power or SNR that result from turbulent fluctuations.

The work described in this paper was carried out at Environmental Technology Laboratory, National Oceanic and Atmospheric Administration. Aniceto Belmonte is on leave from Department of Signal Theory and Communications, Universitat Politècnica de Catalunya, 08034 Barcelona, Spain. His work was partially supported by a NATO Fellowship.

References

1. H. T. Yura. *Opt. Acta* 26, 627 (1979)
2. J. H. Shapiro, B. A. Capron, and R. C. Hamey. *Appl. Opt.* 20, 3292 (1981)
3. S. F. Clifford and S. Wandzura. *Appl. Opt.* 20, 1502 (1981)
4. B. J. Rye. *J. Opt. Soc. Am.* 71, 687 (1981)
5. A. E. Siegman. *Appl. Opt.* 5, 1588 (1966)
6. D. L. Fried and H. T. Yura. *J. Opt. Soc. Am.* 62, 600 (1972)
7. R. G. Frehlich and M. J. Kavaya. *Appl. Opt.* 30, 5325 (1991)
8. J. A. Fleck, J. R. Morris, and M. D. Feit. *Appl. Phys.* 10, 129 (1976)
9. J. M. Martin and S. M. Flatté. *J. Opt. Soc. Am.* A7, 838 (1990)
10. B. J. Rye and R. G. Frehlich. *Appl. Opt.* 31, 2891 (1992)
11. A. M. Prokhorov, F. V. Bunkin, K. S. Gochelashvily and V. I. Shishov. *Proc. of the IEEE* 63, 790 (1975)
12. R. L. Fante. *Proc. of the IEEE* 63, 1669 (1975)

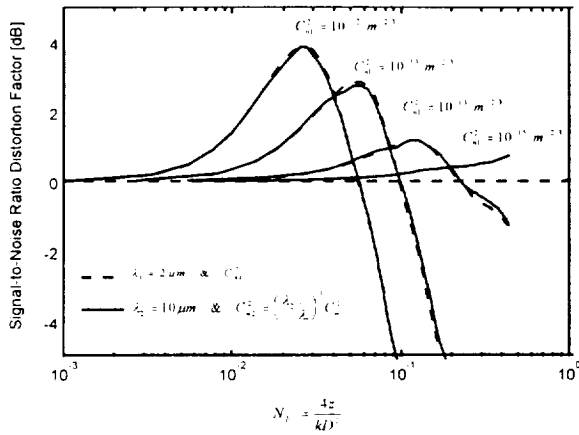


Figure 5. The wavelength dependence of coherent lidar behavior on atmospheric turbulence appears when we assume the same dimensionless N_T and N_F parameters. The simulation of the same system at different wavelengths λ_1 and λ_2 (in the figure 2 and $10 \mu\text{m}$, respectively; the rest of parameters as figures 2) show similar results by scaling the range R a factor $R_1/R_2 = \lambda_2/\lambda_1$ and changing the level of refractive turbulence C_n^2 by $C_{n1}^2/C_{n2}^2 = (\lambda_1/\lambda_2)^2$. The SNR normalized by the case of no refractive turbulence for a $2 \mu\text{m}$ system can be deduced from the $10 \mu\text{m}$ case by stretching the range R a factor 5 and tightening C_n^2 by 125.

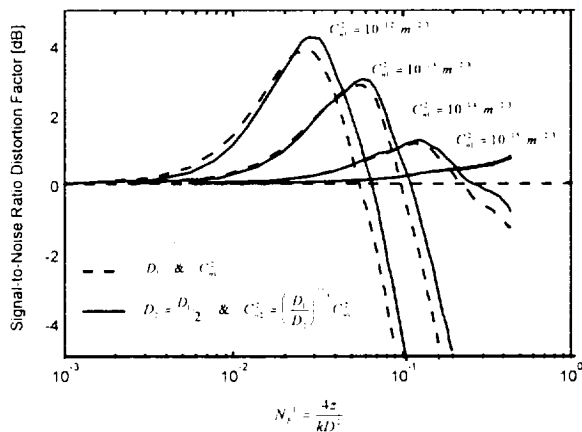


Figure 6. The aperture dependence of coherent lidar behavior tested by the simulations proves our hypothesis. When in two simulations we consider different apertures D_1 and D_2 and the rest of system parameters remain identical, we obtain similar results by scaling the range R a factor $R_1/R_2 = (D_1/D_2)^2$ and the turbulence C_n^2 by $C_{n1}^2/C_{n2}^2 = (D_2/D_1)^{11/3}$. In the figure, where the parameters are the same as described for figure 2, when the aperture reduces a factor 2, $D_2 = D_1/2$, the turbulence level must increase one order of magnitude in order to obtain equivalent SNR behavior.

means of our simulations. Similar dependencies between the different parameters defining the coherent system configuration and the atmosphere condition appear easily from the study of the similarity between the parameters N_F and N_T . They allow us to analyze several realistic problems by using the results of the same simulation.

**EFFECT OF REFRACTIVE TURBULENCE ON DOPPLER LIDAR
OPERATION IN ATMOSPHERE.
NUMERICAL SIMULATION**

V.A. Banakh and I.N. Smalikho

Institute of Atmospheric Optics of the Russian Academy of Sciences,
Akademicheskii prospekt, 1. Tomsk, 634055, Russia
e-mail: banakh@ldw.tomsk.su
smalikho@iao.tsc.ru

Ch. Werner

DLR Lidar Group, PO 1116, D-82230 Wessling, Germany
e-mail: Christian.Werner@dlr.de

1. Introduction

The effect of refractive turbulence on coherent laser radar is studied in a number of works, for example [1-3], where the mean power of coherent signal and signal to noise ratio (SNR) are calculated using analytical methods. To account for the correlation of the direct and return waves propagating along the sounding path the different approximate methods, such as phase screen approximation [1-3] or asymptotical methods for calculations in the regimes of weak or strong turbulence [4] are used. Along with the mean signal power the variance of turbulent fluctuations of coherent signal power plays important role in coherent laser radar characterization also. At the same time the analytical approach for calculation of the power fluctuations is not necessarily successful. In this paper to study the effect of refractive turbulence on coherent lidar the numerical simulation is used.

2. Algorithm for calculation of complex amplitude of laser beam field in a turbulent atmosphere

To calculate random distributions of the amplitude and the phase (complex amplitude) of field of the beam propagating along the path of x length in a turbulent atmosphere, we used the algorithm based on random phase screens simulation. In the details this algorithm is justified and described, for example, in review [5]. The idea of the method is that the all path of x length is divided into N layers each of Δx thickness. On the front border of each layer a random phase screen is placed, on passing which the beam undergoes phase distortions, i.e. the complex amplitude of the beam $E(x_i, \rho)$ is multiplied by $\exp\{j\psi(x_i, \rho)\}$, where ψ is the simulated random phase, $x_i = i\Delta x$, $i = 0, \dots, N - 1$, and $\rho = \{z, y\}$ is the transverse coordinate. Then the beam diffraction is computed inside each layer using the fast Fourier transform

$$E(x_{i+1}, \rho) = \mathbb{F}^{-1} \left\{ \exp \left[-j \frac{(2\pi)^2 \Delta x}{2k} \kappa^2 \right] \mathbb{F} \left[E(x_i, \rho) e^{j\psi} \right] \right\} \quad (1)$$

where \mathbb{F} and \mathbb{F}^{-1} are the direct and inverse Fourier transforms, correspondingly, $k = 2\pi/\lambda$ is the wave number, κ is spectral coordinate.

The phase screen simulation is the most efficient in spectral domain. We use the Karman model for the power spectrum of phase fluctuation of the wave passed through the turbulent layer of Δx thickness [6]

$$\Phi_\psi(\kappa) = 0.265 \sigma_\psi^2 \frac{(8.42L_n)^2}{[1 + (8.42L_n)^2 \kappa^2]^{11/6}} \cdot \quad (2)$$

where

$$\sigma_\psi^2 = 1.27 C_n^2 L_n^{5/3} k^2 \Delta x \quad (3)$$

is the variance of wave phase fluctuations, C_n^2 is the structure parameter of refractive index fluctuations, L_n is the outer scale of turbulence. Hence, setting initial distribution of a laser beam field $E(0, \rho)$, the medium parameters C_n^2 , and L_n one can simulate random distributions of field of laser beam propagating along ground path of $x = N\Delta x$ length. Ensemble averaging of obtained random realizations allows us to calculate various statistical characteristics of the beam field.

We assume that distance between lidar and probing volume far exceeds the longitudinal size of the probing volume determined by the duration of sounding pulse and that scattering of light by aerosol particles is equivalent to the scattering on the diffuse target. At the end of path the obtained distribution of a beam field $E(x, \rho_{mn})$ is multiplied by the uncorrelated complex backscattering coefficients K_{mn} ($\langle K_{mn}K_{m'n'}^* \rangle = \langle |K|^2 \rangle \delta_{mm'} \delta_{nn'}$, δ is the Kronekker delta) which obey the Gaussian law of distribution. Here the location of transverse coordinates $\rho_{mn} = \{\Delta lm, \Delta ln\}$ is determined by the nodes of the uniform mesh with resolution Δl , where $m, n = 1, 2, \dots, N_y, N_y^2$ is the number of mesh nodes.

For simulation of complex amplitude of a scattered beam on return way the same scheme with the same set of phase screens is used. To avoid «the diffraction» on the edges of calculation mesh we used the special procedure of spatial filtration. At the plane of receiving telescope $x = 0$ the calculated values of scattered wave $E_s(0, \rho)$ are multiplied by the telescope transmittance function $P_t(\rho)$ ($P_t(\rho) = 1, |\rho| \leq d/2, P_t(\rho) = 0, |\rho| > d/2$, where d is the telescope diameter) and for calculation of the beam field distribution at the telescope focal plane the procedure of fast Fourier transform is used. Multiplying obtained result by complex amplitude of local oscillator field $E_L^*(\rho)$ and performing integration over variable ρ (detector surface) we obtain valid component of the coherently detected signal.

By means of variation of the parameters $N_y, \Delta l, N, \Delta x$ we can simulate the sounding beam propagation along paths with different geometry (horizontal, vertical, slant, and so on). Below we show the results of simulation of laser beam propagation along horizontal paths with constant C_n^2 . In calculations we put $\lambda = 2 \mu\text{m}$, initial beam radius $a_0 = 7.5 \text{ cm}$, telescope diameter $d = 30 \text{ cm}$ and telescope focus length $f_t = 1 \text{ m}$.

3. Results of simulation

The intensity distribution of laser beam at the distance $x = 3 \text{ km}$ from the lidar for the structure parameter $C_n^2 = 10^{-14} \text{ m}^{-2/3}$ is shown in Fig. 1. Fig 2 demonstrates the instantaneous intensity distribution of the backscattered laser beam at the plane of the receiving telescope aperture, and in Fig. 3 we show the intensity distribution at the focal plane of the telescope. It is seen, that the speckle pattern at the focal plane is similar to the pattern at the telescope receiving plane.

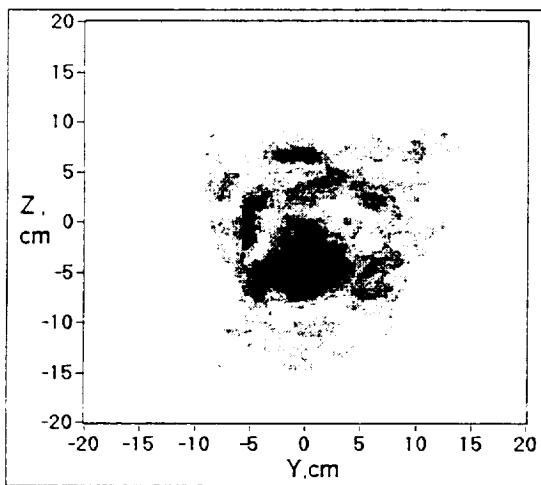


Fig. 1.

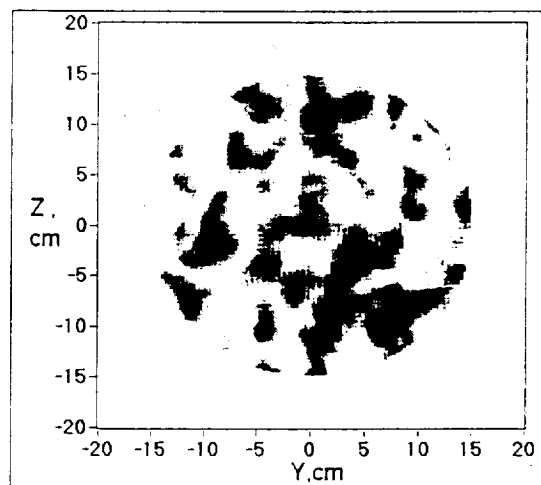


Fig. 2.

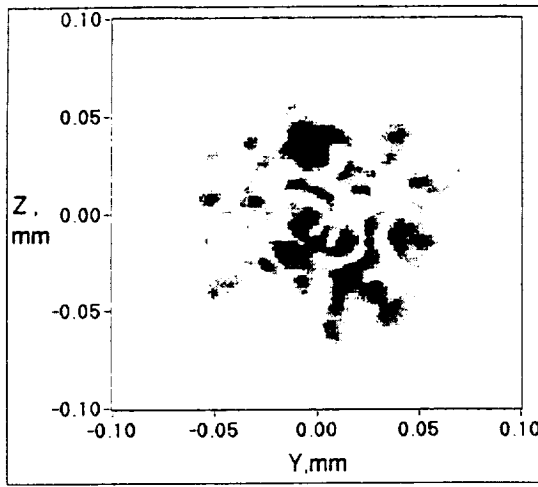


Fig. 3.

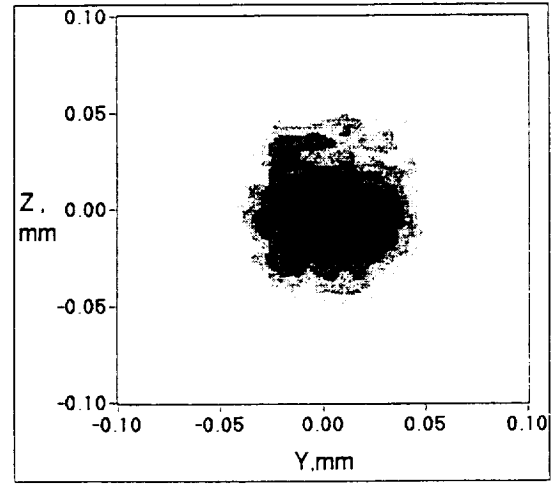


Fig. 4.

Temporal scales of the signal power fluctuations caused by variations of backscattering coefficient τ , and by refractive turbulence τ_r , diverge considerably [4]. The scale τ_r , determined by the sounding pulse duration is in the range of part of microsecond, and the scale τ , determined by the time of transferring of turbulent inhomogeneities is in the range of part of second.

Response time of the receiver T satisfies the condition: $\tau_r \ll T \ll \tau$. As a consequence random distortions of the intensity distribution at the photodetector are determined completely by refractive turbulence. Fig. 4 shows the focal intensity distribution averaged over 100 realizations of scatterers random distribution in case of «frozen» refractive turbulence.

The instantaneous intensity distributions at the focal plane of the telescope for $C_n^2 = 0$ and $C_n^2 = 10^{-13} \text{m}^{-2/3}$ on 3 km path are shown in Fig.5 and Fig. 6 respectively. From comparison of the simulation results in Figs. 3, 5, 6 it follows that considerable increase of the spot size on 3-km path is observed for strong turbulence $C_n^2 = 10^{-13} \text{m}^{-2/3}$ only.

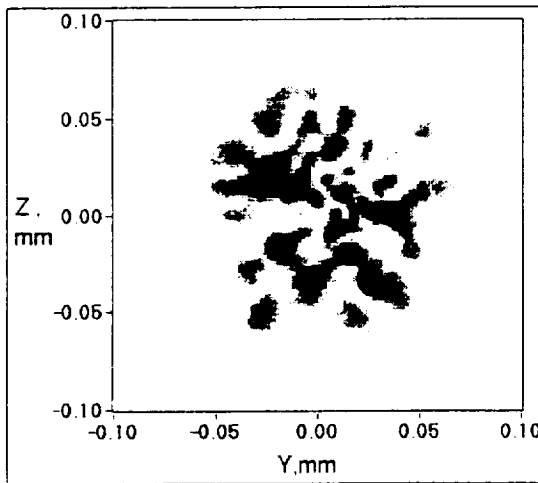


Fig.6.

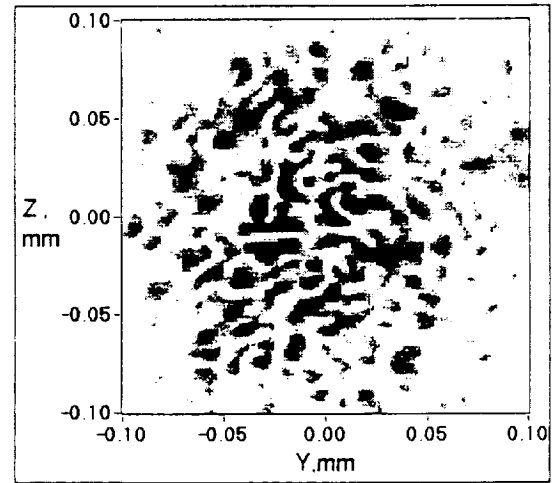


Fig.5.

Figs. 7, 8 give the focal plane instantaneous intensity distributions for path length $x = 10 \text{ km}$ and $C_n^2 = 0$, $C_n^2 = 10^{-14} \text{m}^{-2/3}$, respectively. Comparison of the data in Fig. 3 ($x = 3 \text{ km}$, $C_n^2 = 0$) and Fig. 7 ($x = 10 \text{ km}$, $C_n^2 = 0$) shows that increasing of path length leads to considerable decrease of the spot size at the focal plane and the number of speckles due to improvement of spatial coherence of backscattered wave incident on the telescope

with accordance van Zittert Zernicke theorem. In contrast to 3 km path for path length $x = 10$ km considerable increase of the focal plane spot size due to turbulence is observed (compare Figs. 7 and 8).

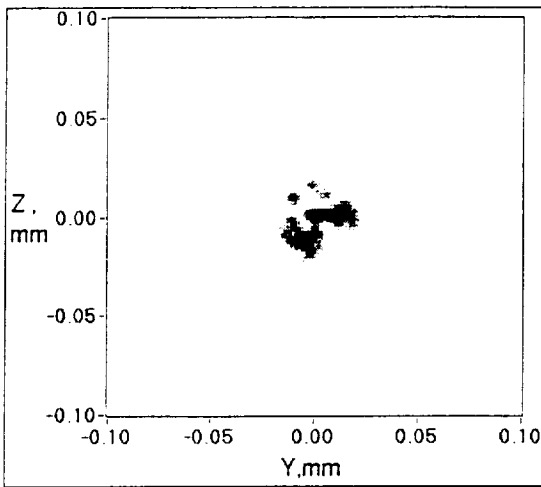


Fig.7.

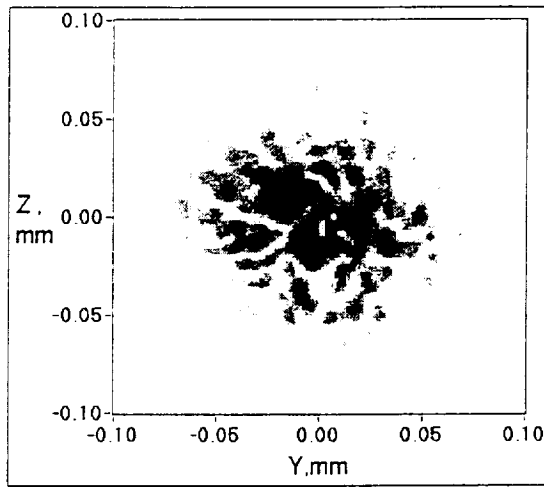


Fig.8.

Developed algorithm allows us to simulate the effect of refractive turbulence on Doppler lidar run with different geometry of sounding and location: on the ground, aircraft and space. Simulation of temporal variation of Doppler signal accounting for the wind turbulence can be made by simulation of temporal variation of backscattering coefficients K_{mn} using the procedure [7, 8].

References

1. S.F. Clifford and S. Wandzura, «Monostatic heterodyne lidar performance: the effect of the turbulent atmosphere», Appl. Opt. **20**, №3, 514-516 (1981).
2. R. Frehlich and M.J. Kavaya, «Coherent laser radar performance for general atmospheric refractive turbulence», Appl. Opt. **30**, №36, 5325-5352 (1991).
3. R. Frehlich, «Effect of refractive turbulence on coherent laser radar», Appl. Opt. **32**, №12, 2122-2139 (1993).
4. V.A. Banakh and V.L. Mironov, Lidar in a Turbulent Atmosphere (Artech House, Boston, Mass., 1987).
5. V.P. Kandidov, «Monte-Carlo method in nonlinear statistical optics», Uspekhi fizicheskikh nauk **166**, №12, 1309-1338 (1996) [in Russian].
6. V.I. Tatarskii, The Effect of the Turbulent Atmosphere on Wave Propagation (Keter, Jerusalem, 1971).
7. R. Frehlich, «Effect of wind turbulence on coherent Doppler lidar performance», J. Atmos. Oceanic Technol. **14**, 54-75 (1997).
8. V.A. Banakh, I.N. Smalikho, «Estimation of the turbulence energy dissipation rate from the pulsed Doppler lidar data», Atmospheric and Oceanic Optics, **10**, №12, 957-965 (1997).

SPACEBORNE LIDARS - 1

Presider: Dennis Killinger

NASA's Earth Science Enterprise Embraces Active Laser Remote Sensing From Space

Michael R. Luther
Deputy Associate Administrator for Earth Science

Granville E. Paules III
Lead Technologist
Office of Earth Science

NASA Headquarters
Office of Earth Science
Mail Code YF
300 E. Street, SW
Washington, DC 20546

granville.paules@hq.nasa.gov

and

mluther@mail.hq.nasa.gov

Several objectives of NASA's Earth Science Enterprise are accomplished, and in some cases, uniquely enabled by the advantages of earth-orbiting active lidar (laser radar) sensors. With lidar, the photons that provide the excitation illumination for the desired measurement are both controlled and well known. The controlled characteristics include when and where the illumination occurs, the wavelength, bandwidth, pulse length, and polarization. These advantages translate into high signal levels, excellent spatial resolution, and independence from time of day and the sun's position. As the lidar technology has rapidly matured, ESE scientific endeavors have begun to use lidar sensors over the last 10 years. Several more lidar sensors are approved for future flight. The applications include both altimetry (ranging) and profiling. Hybrid missions, such as the approved Geoscience Laser Altimeter System (GLAS) sensor to fly on the ICESat mission, will do both at the same time. Profiling applications encompass aerosol, cloud, wind, and molecular concentration measurements. Recent selection of the PICASSO Earth System Science Pathfinder mission and the complementary CLOUDSAT radar-based mission, both flying in formation with the EOS PM mission, will fully exploit the capabilities of multiple sensor systems to accomplish critical science needs requiring such profiling. To round out the briefing a review of past and planned ESE missions will be presented.

SPARCLE: A MISSION OVERVIEW

G.D. Emmitt
Simpson Weather Associates
Charlottesville, Va 22902
804-979-3571

M. Kavaya
T. Miller
Global Hydrology and Climate Center
NASA/MSFC
Huntsville, AL
256-922-5858

Abstract

The SPACe Readiness Coherent Lidar Experiment (SPARCLE) is a NASA mission to demonstrate for the first time the measurement of tropospheric winds from a space platform using coherent Doppler Wind Lidar (DWL). SPARCLE is scheduled for launch in early 2001 on board one of the shuttle orbiters. While primarily a demonstration of the technology's performance at ranges of 300-350 km, the mission will also address sampling issues critical to the design and operation of follow-on missions. In this paper we provide a brief overview of the SPARCLE instrument and the experiments being planned.

Introduction

Over the last few decades, lidars have been used to measure the line-of-sight component of the winds. The lidars have been operated from buildings, vans and aircraft. Several countries (and agencies within) currently operate wind lidars from the ground. Only a few have installed Doppler lidars in aircraft. Within the USA, the lead agencies for airborne Doppler lidar are the DoD, NASA and NOAA. While the ground-based lidars employ both direct and coherent detection technology, most of the airborne systems are coherent lidars. Building upon the heritage of airborne flight, NASA has chosen a coherent detection lidar concept for its New Millennium Program's Earth Observing - 02 Mission. In keeping with the NMP's charter to demonstrate the readiness of new technologies for scientific research and applications, the mission is known as the SPACe Readiness Coherent Lidar Experiment or SPARCLE.

SPARCLE has several objectives, some of which are clearly related to demonstrating the technology and others that are more oriented towards demonstrating the accuracy and

representativeness of the data products. Below are the mission objectives as currently stated in its Mission and Science Requirements Document:

- Confirm that the coherent Doppler lidar technique can measure line-of-sight winds to within 1-2 m/s accuracy
- Collect data to permit validation and improvement of instrument performance models
- Collect wind and backscatter data for future mission optimization and for atmospheric studies

In the remainder of this paper, we will briefly describe the instrument (see other papers at this conference for more detail on the hardware), some of the major technology challenges, and the general scope of the on-orbit operations plan.

The Instrument

SPARCLE is built around the coherent detection technique for sensing the line-of-sight (LOS) component of the motion of aerosols being carried by the wind. Although much of the airborne heritage for coherent Doppler wind lidars (DWL) has been with CO₂ lasers, a 2 micron, solid-state laser has been chosen for the space-based system. Compared with operations at CO₂ wavelengths, 2 microns offers shorter pulse lengths, a more Gaussian shaped pulse, and improved sensitivity (per Joule) in the lower backscatter regions of the atmosphere. Table 1 summarizes the primary characteristics of the SPARCLE instrument which is shown attached to a shuttle cross-bay truss in Figure 1.

Table 1
SPARCLE Instrument Characteristics

Aperture (nominal)	25 cm
Laser energy/pulse	100 mJ
Pulse repetition frequency	6 Hz
Scan angle (nadir)	30°
Scan azimuth range	0 – 360°
Scan scheme	Step-stare
Detection technique	Heterodyne (coherent)
Tuning scheme	Master oscillator sets transmitting laser
Tuning range	± 4.5 GHz
Single-shot sensitivity (β_{50})	$5 \times 10^{-6} \text{ m}^{-1} \text{ sr}^{-1}$ minimum $5 \times 10^{-7} \text{ m}^{-1} \text{ sr}^{-1}$ goal

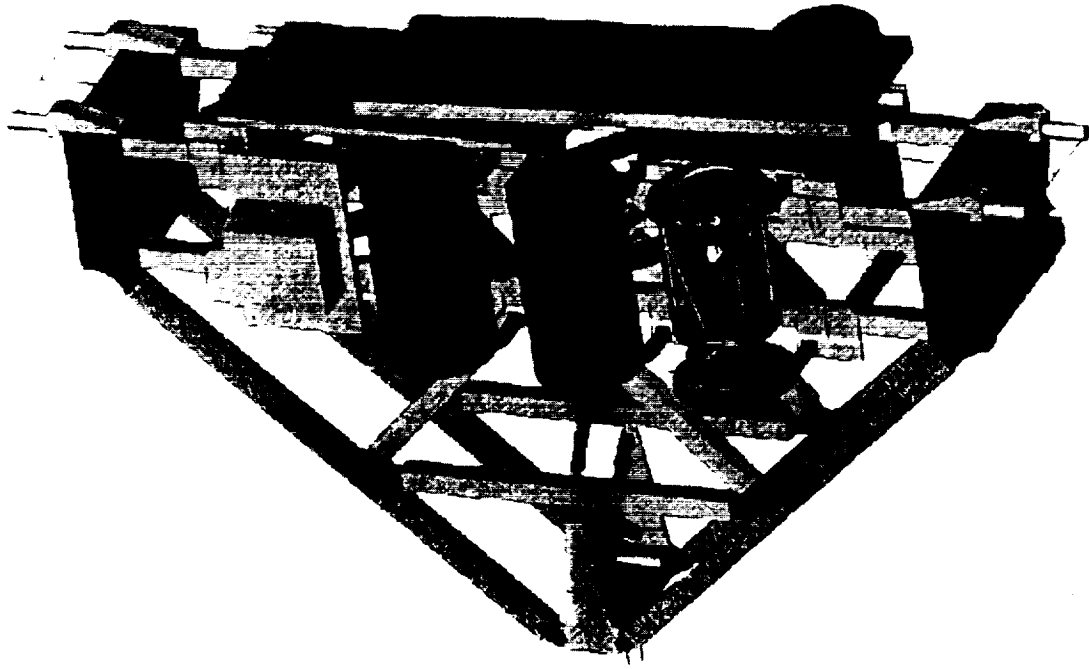


Figure 1: SPARCLE on a Cross Bay Truss

As with most maiden missions for a technology, there are several key engineering challenges. Table 1 mentions most of the top level goals of the SPARCLE. However, there are other technological issues that have, over the course of early mission design activities, become highlighted. Pointing knowledge, thermal effects on optics, and end-to-end far-field pre-flight alignment are three such areas of engineering focus.

In the absence of a ground return, the accuracy of any individual LOS wind measurement is directly dependent upon the accuracy of the pointing knowledge and the subsequent accounting for platform motion and the relative motion of the earth's surface. The measurement error budget, 80 microradians is allocated to roll, pitch and yaw. Given that the instrument's alignment with the orbiter's navigation references is subject to on-orbit mechanical and thermal misalignments, a dedicated GPS/INS will be attached to the instrument's housing. Even so, additional measures are required to meet the LOS accuracy goal of 1 m/s. The SPARCLE team has developed a strategy that uses the lidar ground returns obtained during a conical scan to compute the optical axis attitude to within a few microradians and instrument height to within a few meters. Combining the special scans with the GPS/INS capability, the required pointing knowledge will be obtained. Another paper that goes into more detail on the subject of pointing knowledge is being presented at this conference by Emmitt, Miller and Spiers.

For budgetary reasons, no special efforts have been made to optimize the thermal efficiency of the SPARCLE instrument components for this demonstration mission. Thus heat rejection and thermal control have presented several challenges to the engineers, one of which has been the need to maintain isothermal conditions across the optical

components. The heterodyne detection technique requires optical surfaces and media (e.g. silicon wedge) to have aberrations less than .1 of a wavelength to get maximum SNR for the total system. For the SPARCLE instrument this means that care must be taken to limit gradients across the wedge scanner to less than a few tenth's degree centigrade. Special coatings and low conductivity materials have reduced the thermal gradients to acceptable levels.

One of the reasons for a space-flight to demonstrate the DWL is the need to show that the optical alignments required for 300-350km ranges can be achieved and maintained. With the turbulence and attenuation along a long (> 50km) horizontal path through the atmospheric boundary layer, it is not easy to check the pre-flight optical alignment of ± 7 microradians. The SPARCLE team has prepared a plan for the far field alignment check that involves using a beam expander and a nitrogen filled, 500m tunnel. At this time, the tunnel approach has not been demonstrated. Another paper on this subject is being presented at this conference by Kavaya.

The Experiments

The SPARCLE will, as its first priority, demonstrate that an accurate (< 1.0m/s) LOS observation of the tropospheric wind can be made with coherent detection from space. The first set of observations will involve staring at a fixed azimuth angle and collecting an extended series of ground and aerosol returns (Mode 1 in Table 2). The stability of the measured ground speed (0.0 m/s relative to the air motion) will be evidence of the end-to-end system design and performance. The expected RMSE of the ground speed measurement is ($\ll 1.0$ m/s) on a single shot.

With the exception of a lag angle compensation experiment, the remainder of the SPARCLE operations will be exploring various scanning (a.k.a. sampling) and shot accumulation strategies (Table 2). The issue of the optimum way to scan a lidar beam from space remains unresolved. The options range from one fixed azimuth (no scanning and only one perspective) to continuous conical scanning. In between lie various combinations of forward and aft shots, retroscanning and step-staring. Since SPARCLE will not employ active lag angle compensation, the continuous conical scan will be approximated with a 16 point in 16 seconds step-stare scan (Mode 4b in Table 2)

The comments column in Table 2 explains the general purpose of the individual scans and thus no further discussion is offered here. However, experiment Mode 5 is quite different than the others. The slew rate of the scanner between dwell angles for all the wind sampling modes will be ~ 40 -50 degrees per second. The returns from any shots taken during the angle transitions will not be detectable. The return signal falls off very rapidly for angular rates of change $> .05$ degrees/sec during the round trip time of the laser pulse. While the step-stare scan was chosen for SPARCLE to simplify the instrument and to allow various scanning modes to be explored, there is still a possibility that continuous conical scanning may be desired for a follow-on mission. This may be the

case if the telescope is quite large (> 50 cm) and heavy making the step-stare scan technically

Table 2: Operational Science Modes

SCAN MODE	LIDAR POINTING	ORBITER ATTITUDE	MINIMUM MODAL TIME	COMMENTS
1A	Azimuth: Fixed, selectable for all angles between 0 and 359°. Dwell: variable up to 90 min. Slew: slow (~ 10 deg/sec)	-ZLV ± 1 degree deadband	3 hours 30 minute segments	Used for LOS data collection to support signal searching, shot accumulation, etc.
1B	Azimuth: Fixed at 90 or 270 Dwell: variable up to 90 min. Slew: N/A	30 degree roll ± .1 degree deadband	1.5 hours	Used to check pointing knowledge, vertical velocity, cloud porosity, long shot accumulation...
2A	Azimuth: 45 and 135 Dwell: 25 to 35 seconds (TBD) Slew: medium (~ 30 deg/sec)	-ZLV ± 1 deg deadband	3 hours 3 consecutive 30 minute segments	Used to obtain vector wind obs with highest number of accumulated shots.
2B	Azimuth: + 45 and -45 Dwell: up to 30 seconds Slew: medium (~30 deg/sec)	-ZLV ± 1 deg deadband	3 hours 3 consecutive 30 minute segments	Used to evaluate a scan mode proposed by ESA
3A	Azimuth: 45,-45,135,-135 in sequence. Dwell: 12-16 seconds (TBD) Slew: fast (~60 deg/sec)	-ZLV ± 1 deg deadband	1.5 hours	Used to demonstrate two profiles per scan sequence
3B	Azimuth: 30,-30,-60,+60,-120,+120,+150,-150 Dwell: 5-8 seconds (TBD) Slew: fast	-ZLV ± 1 deg deadband	3 hours 3 consecutive 30 minute segments	Most likely step-stare pattern to be used on first operational mission
3C	Azimuth: 12 points TBD Dwell: 2-4 seconds (TBD) Slew: fast	-ZLV ± 1 deg deadband	1.5 hours	Fastest matched fore and aft samples
4A	Azimuth: 0 to 359 by 10 deg Dwell: 2.5 seconds Slew: slow	-ZLV ± 1 deg deadband	optional	Used to generate optimal cycloid pattern for VAD processed vector wind
4B	Azimuth: 0 to 359 by 22.5 deg Dwell: .5 seconds Slew: fast	-ZLV ± 1 deg deadband	3 hours 3 consecutive 30 minute segments	16 points in 16 seconds to simulate a continuous conical scan
4C	Azimuth: 0 to 180 by 10 deg, 181-359 by 180 deg Dwell: 2.5 seconds Slew: Slow between 0-180 Fast between 180-359	-ZLV ± 1 deg deadband	1.5 hours	Same as 4A except more efficient use of time
5	Azimuth: 0-360 Dwell: N/A Slew: variable between .05 and .20 deg/sec	-ZLV ± 1 deg deadband	optional	Used to validate lag angle compensation modeling
6	Azimuth: 0,45,90,...315 Dwell: 1 second Slew: fast	-ZLV ± 1 deg deadband or ± .1 deg	3-5 hours 2-5 minute segments	Used to provide time calibration for SPARCLE GPS/INS

indefensible. The SPARCLE scanner will be able to slew at rates < .01 degrees/second. Thus by slowly accelerating the scanner from rest up to a slew rate of .1 degrees/second while the laser is transmitting at 6 Hz, the falloff of signal strength as a function of lag angle should be determined.

A goal of the SPARCLE is to record 50 hours of raw level 0 data out of the receiver A/D channels. This will amount to ~ 100 Gbytes of data, uncompressed. While there is expected opportunities for downlinking some of the raw data during the flight, the plan is too have ~100 Gbytes of mass storage on-board. Some on-board processing of the raw data will be done as part of the pointing knowledge algorithms and to facilitate finding the ground return in the case of extremely poor (> 3 degrees error) pointing knowledge at turn on. Downlinking of this processed data and ground-based processing of downlinked streams of raw data will provide the SPARCLE team with real-time evidence of the performance of the SPARCLE instrument. Experiment scheduling will be effected by the real-time analysis of the processed data and the global weather conditions.

Since SPARCLE is a first step on the road to a fully operational wind lidar, there will be a significant effort to validate instrument's performance as well as the data products. A validation plan has been prepared for the NMP. In addition to the global network of wind observing systems (Rawindsondes, scatterometers, cloudtracked winds, surface meteorological towers/bouys,etc.), groundbased and airborne Doppler lidars will provide many opportunities for comparison. Global weather model analyses will also be used to identify where the SPARCLE observations and the inferred winds differ and agree.

Although the SPARCLE instrument will have a very modest sensitivity which will limit most of its observations to the boundary layer and clouds, it is still possible that the SPARCLE mission will return, on occasion, sufficient global data coverage to demonstrate a positive impact on weather forecasts and phenomenological diagnostics (e.g. hurricanes, orographic cyclogenesis, etc).

Acknowledgements

The authors recognize the support from NASA Headquarters and the contributions of the following organizations to the SPARCLE mission: University of Alabama at Huntsville, Marshall Space Flight Center, Jet Propulsion Laboratory, Langley Research Center, National Oceanographic and Atmospheric Administration, Goddard Space Flight Center, Coherent Technologies Inc. and Simpson Weather Associates, Inc.

Atmospheric Dynamic Mission: Project Status, Concepts Review and Technical Baseline

Hans Reiner Schulte, Dornier Satellitensysteme GmbH, 88039 Friedrichshafen, Germany
Didier Morangais, Matra Marconi Space, 31077 Toulouse, France

1) Introduction

The Atmospheric Dynamics Mission (ADM) study is one of four Earth Explorer Core Missions phase A studies in the frame of the ESA EOPP/Envelope Programme. This programme is directed towards research/demonstration missions addressing understanding of different Earth system processes. The particular aim of the ADM is the measurement of vertically resolved wind fields for assimilation in numerical weather prediction models to alleviate a deficiency in the current observational network and to support climate research. The actual measured quantity is a single horizontal wind vector component measured in vertical of 1km extension from ground up to 20km altitude. The measurement is performed by a Doppler wind lidar in clear air and above optically thick clouds. In the ADM study a trade off between various coherent and incoherent instrument concepts covering the wavelengths range from 0.355 μ m to 10.6 μ m has been performed to identify the most promising solution in view of measurement requirements, mission constraints and technical feasibility. This process has led to the selection of a baseline for the ADM mission featuring a direct detection lidar instrument on board of a dedicated small satellite in a 400km sun synchronous (dawn-dusk) orbit.

2) Trade-off Process

The instrument trade-off was based on fixed boundary conditions derived from mission constraints (Table 2). Although originally an accommodation on the international space station (ISS) was foreseen the mission constraints where from the beginning selected in view of representativeness for a later operational mission on a small satellite in a polar orbit. Main criteria in the trade-off where compliance to the observational requirements for the ADM mission (Table 1) and technical maturity/feasibility.

Table 1: Measurement Requirements

	Troposphere	Stratosphere
Altitude Range	0-16 km	16-20 km
Vertical Integration Length	<1.0 km	<2.0 km
Horizontal Integration Length	50 km	
Number of Profiles	100 per hour	
Profile Separation	> 200 km	
Wind Observation Accuracy	< 2 m/s	no requirement
Reliability	>80 %	
Correlated Error	<0.1 m/s	

Table 2: Technical Constraints

	Precursor Mission
Orbit altitude	400 km
Payload Mass	226.5 kg
Payload Volume	86x117x 24 cm ³
Power	< 1 kW

3) Candidate Instrument Concepts

Considering availability of laser technology, CO₂ gas laser, 2 μ m solid state laser (Tm:YLuAG) and frequency tripled Nd:YAG were identified as most promising for the transmitter while Nd:YAG on its base frequency and on the doubled frequency where rejected for eye safety reasons. For the CO₂ laser a wavelength of 9.11 μ m and for the Tm:YLuAG laser a wavelength of 2.0218 μ m have been selected to benefit from low atmospheric attenuation at these frequencies. Three instrument designs where performed to sufficient level of detail to judge feasibility and maturity of needed technologies and to allow assessment of measurement performance. Key characteristics of the three designs are given in Table 3.

The CO₂ gas laser based instrument and the 2 μ m solid state laser based instrument designs are both coherent lidar instruments exploiting aerosol backscattering. Different strategies for the processing of the heterodyne signal where adopted. In the gas laser concept a fixed frequency LO is used and electrical processing is employed to compensate for earth rotation and satellite pointing induced Doppler variations which, for an accommodation on the space-station, are much larger than the bandwidth resulting from the wind velocity measurement interval. In the 2 μ m instrument design a tuneable LO-laser is employed to account for the predictable Doppler shift, thus generating a heterodyne signal at fixed center frequency to be processed in a bandwidth determined by the wind search range. For selecting a more convenient located LO frequency (or frequency range) in both cases a deliberate squint looking of the LOS was introduced to generate a mean Doppler shift due to the spacecraft motion. The coherent instruments employ both the same processing

strategy: Doppler estimation using filtered power density spectra accumulated over the shots obtained in the along track integration interval.

To reduce the data volume on the down link an on-board DSP is employed to calculate the power density spectra of the different altitude cells and to accumulate the spectra over several shots.

Table 3: Candidate Concepts

	Coherent 1	Coherent 2	Direct Detection	
Wavelength	9.11 μm	2.0218 μm	0.355 μm	
Pulse Energy	1.8 J	0.5 J	0.1 J	
PRF	10 Hz	10 Hz	100 Hz	
Pulse B/W (FWHM)	0.72 MHz	1.26 MHz	30 MHz	
Power Demand	200 W	200 W	230 W	
Instrument Mass	130 kg	100 kg	170 kg	
Telescope Aperture	0.7 m	0.7 m	0.7 m	
LOS	el: 35° az: 57.39°	el: 35° az: 78.58°	el: 35° az: 90°	
Scatter Mechanism	Mie	Mie	Mie	Rayleigh
Receiver	heterodyne	heterodyne	direct detection	direct detection
Processing Principle	DSP, filtered PDS	DSP, filtered PDS	Fizeau Spectrometer, Accumulation CCD	dual filter, Accumulation CCD

For both coherent candidates the transmitters are the design drivers. The CO₂ gas laser is critical in volume and mass resources. A 1.8 J / 10 Hz laser was identified to be the best compromise for the ADM design. Significant scaling of the transmitter design inherited from earlier technology and feasibility studies is required since the ADM instrument is designed for much lower resource demand.

For the 2 μm design a seeded high power oscillator on the base of a TuYLuAG crystal, generating 0.5J pulses at 10Hz pulse repetition frequency, was selected under consideration of resource demand and availability of technology in the ADM development time frame. A design driver is the need to cool the crystal to 200K operation temperature.

The direct detection candidate employs a 0.1J / 100Hz transmitter using a frequency tripled Neodymium-YAG laser (seeded medium power oscillator plus amplifier stage). The echo signal is processed using two different receiver channels, one for Mie signals and one for Rayleigh backscattered signals. Both are operated simultaneously using a spectral separator. The Mie channel employs fringe detection (Fizeau interferometer) the Rayleigh channel a derivative of the double edge detection technique. The decision to employ a double edge detection principle on the Rayleigh channel results from a trade-off involving component criticality and performance. The double edge and fringe imaging techniques offer similar performances for the Rayleigh receiver but the latter requires tighter alignment and detector requirements. Seizing for this instrument type is the receiver technology including filters, interferometer and accumulation CCD detector.

4) Comparison

The instrument designs were compared with respect to compliance to the measurement requirements (Table 1) and technological maturity. As no design is capable to meet the measurement requirements in all points it was necessary to develop a measure to compare the relative merits of the designs and to assess the growths potential. The coherent designs are characterised by a bandwidth of the transmitted pulse comparable to the required resolution in the frequency domain. Under this conditions the rms error of the estimation results (without attempt to filter “bad shots”) reaches the performance limit due to occasional failure to detect the signal. Hence the detection problem at weak SNR is the performance limiting factor for the coherent designs rather than the rms performance of the frequency estimator at good SNR which is the driver for Rayleigh signal evaluation. Generally the analysed coherent designs show a pronounced threshold behaviour with compliant measurement accuracy above a characteristic backscattering coefficient rapidly degrading for lower backscattering values due to failure to detect the signal (bad shots). In figure 1 the performance of the 2 μm design is shown in the context of the applied atmospheric model (effective β stands for backscattering coefficient corrected for the nominal 2-way absorption in the respective altitude). The line “Accuracy Threshold” gives the minimum required backscattering coefficient for a compliant measurement in a rms sense when no attempt is made to separate bad shots. The line “Reliability Threshold” gives the minimum required backscattering coefficient for a 80% probability to detect the signal. The lowest percentile curve of the atmospheric model [1] above the “Reliability Threshold” at a given altitude is indicative for the percentage of measurements that can not be identified from the SNR as being compliant to the measurement requirement. Similarly the lowest percentile line above the “Reliability Threshold” indicates the percentage of atmospheric conditions under which the reliability requirement from Table 1 is not met. Only in about 25% of all cases

compliant measurements can be expected above 10km altitude and only occasionally above 15km altitude while even at altitudes as low as 4km up to 25 % of all measurements under clear air conditions are likely not to yield compliant results. Similar results are obtained for the $9.11\mu\text{m}$ design where the threshold values are about 2dB more favourable when calculated for a Gaussian pulse-shape but this advantage is largely voided when accounting for the actual spectral properties of the gas laser. Accounting also for the technical risks in both designs finally the $2\mu\text{m}$ was identified as the most promising coherent concept. Due to the direct measurement principle very low correlated errors among the measurements may be expected especially if a pulse monitor is integrated to directly measure the transmitted signal spectrum. Remaining correlated errors are mainly driven by pointing uncertainties during measurements where no ground echo can be evaluated as reference.

The competing direct detection system relies mostly on its Rayleigh channel for acquiring the wind measurements. As the received signal has a bandwidth about 200 times larger than the required frequency resolution the measurement performance is characterised by the rms error of the applied detection principle under the given SNR. Signal detection is no problem under clear atmosphere conditions over the entire altitude range. Moreover the Rayleigh SNR shows comparatively small variations over the measurement altitude range except for the lowest 3 km where aerosols dependent attenuation may be significant. This leads to a measurement performance in terms of LOS rms wind measurement error as depicted in Figure 2. Under the constraints of the space station chosen for the comparison of the candidate designs the Rayleigh channel performance is nevertheless not compliant to the measurement requirements although the capability to reliably measure at high altitudes appears to be very attractive.

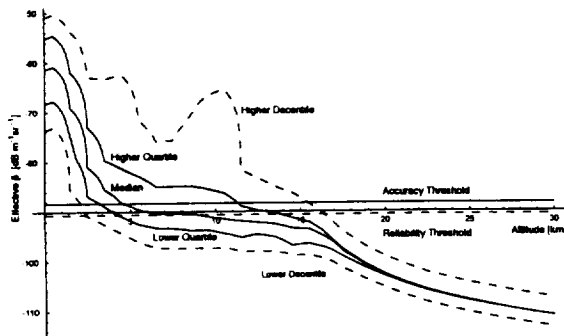


Figure 1: Coherent 2 ($2\mu\text{m}$) Performance

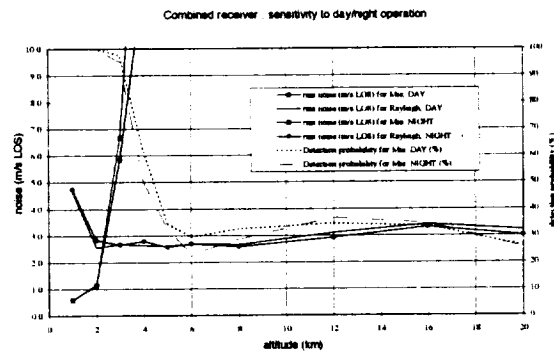


Figure 2: Direct Detection ($0.355\mu\text{m}$) Performance

A Mie channel has been incorporated into the incoherent design for several reasons. It has complementary performance to the Rayleigh channel because it allows measurements in the planetary boundary layer where abundant aerosols may lead to high attenuation impairing Rayleigh channel performance. A strong aerosol signal furthermore affects Rayleigh channel estimation accuracy such that knowledge of the interfering signal allows for correction. In a third function the Mie channel allows reliable calibration measurements on the transmitted signal as zero Doppler reference and whenever ground is not obscured by optically dense cloud it allows ground echo measurements to be used as absolute velocity reference. The additional channel therefore plays a major role in the calibration strategy of the instrument. The direct detection Mie channel features intrinsic lower performance than the coherent Mie channel because of its larger frequency resolution. Nevertheless, both performance feature the same basic characteristics: strong dependency on the atmosphere and threshold effect (non-detection above a given altitude). The reduced Mie channel performance is however due to the ancillary nature of this channel of no concern to the overall performance of the instrument.

The issues of correlated measurement errors are due to the indirect frequency measurement principle more involved for a direct detection system than for a heterodyne lidar as the problem of response calibration is added to the calibration issues applicable to both concepts. However analysis of the calibration concept indicates that results comparable to heterodyne instruments can be achieved since the dominating error is in both cases the LOS estimation error in periods without ground echo reference.

As all candidate designs under the space station constraints are not compliant to the measurement requirements it was necessary to assess the growths potential. The strongest constraint of the space station accommodation is the volume limitation and poor pointing stability finally limiting the telescope aperture. A telescope with 1.1m aperture can be easily accommodated on a small satellite. Going to a dedicated satellite has furthermore the advantage to optimise the pointing performance to the instruments needs thus simplifying instrument operation conditions. Cooling and power constraints are also relaxed. For the heterodyne and the direct detection designs the growth potential mainly comes from the increased telescope aperture and to a lesser degree from the possibility to improve the transmitter. For the heterodyne preferred candidate this leads to lowering the threshold values in Figure 2 for about 5 dB (larger telescope diameter plus increased pulse repetition

frequency) which is still insufficient for reliably measuring at high altitudes. The direct detection design however has the potential to achieve the measurement requirements over the entire altitude range with the enlarged telescope feasible on a free flyer,

Assessment of technological criticality showed higher criticality for transmitter and telescope/relay optics for the coherent candidate design, particularly due to the cooling requirements and the need for diffraction limited optics and associated alignment issues. The direct detection receiver subsystem was judged slightly more critical than the heterodyne one, due a somewhat higher complexity and to the components requirements. However in view of the availability of tested breadboards of many critical items of the direct detection receiver in summary the direct detection instrument concept was considered to be of slightly lower risk than the coherent competitor. Nevertheless both concepts were considered to be feasible such that decision on the baseline concept was to be made based on judgement of the measurement performance.

The majority of the mission advisory group (MAG) for the ADM mission gave a clear vote in favour of the direct detection candidate based on the predicted performance characteristics. Furthermore already for the demonstration mission implementation on a free flyer with the advantages in measurement performance and coverage was considered essential .

5) Selected Baseline

Consequently the direct detection instrument on board of a dedicated small satellite in a sun synchronous orbit (dawn-dusk) has been selected as baseline for the ADM. A telescope aperture of 1.1m and a transmitter with 0.13J pulses at 100Hz has been adopted. The satellite will be operated in yaw steering mode to compensate for most of the earth rotation Doppler shift thus allowing to optimise spectral ranges to the wind search range.

The instrument architecture is shown in Figure 3. Specific details not already mentioned above in the general description are:

- Blocking filter chain for the suppression of background radiation which allows daylight operation at insignificant performance degradation
- Rayleigh/Mie frequency multiplexer as integral part of the Mie channel blocking filter chain
- Backside illuminated accumulating CCD detectors with programmable shift /accumulation sequence are used for Mie and Rayleigh channel (Quantum efficiency >75%, Read-out noise after accumulation below 0.3e-/pixel/shot (quasi photoncounting))
- A fraction of the transmitted signal is injected in the receiver path for zero Doppler calibration evaluated in every shot and for periodically invoked response calibration (about once per orbit)
- An programmable optical PLL is employed to slave the transmitter seeder to a stabilised low power laser to allow controlled frequency shifts of the transmitter as needed for periodical response calibration of the receiver chain

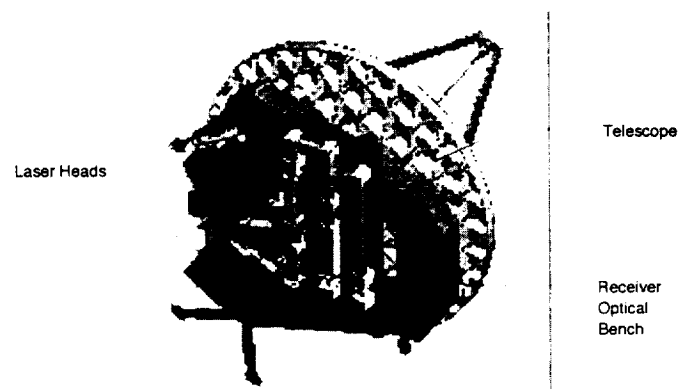


Figure 3: Selected Baseline Core Instrument

6) Reference

[1] J.M.Vaughan et al., "A global database for modelling Space-Borne Doppler Wind Lidar", this conference.

Acknowledgement: This work was performed under contract of the European Space Agency in the frame of the Industrial part of the Phase-A of the Atmospheric Dynamics Mission.

SPARCLE Coherent Lidar Transceiver

Mark Phillips, Dane Schnal, Carl Colson, Charley Hale,
David D'Epagnier, Matt Gibbens and Sammy Henderson
Coherent Technologies Inc.
Lafayette CO 80026
E-mail: markp@ctilidar.com

1. INTRODUCTION

NASA is planning to demonstrate the technical readiness of two micron laser and lidar technology for space-based global wind measurements by operating a Ho,Tm:YLF laser-based lidar transceiver from the Space Shuttle. This demonstration experiment is entitled "SPAcE ReAdiness Coherent Lidar Experiment", or "SPARCLE". Coherent Technologies Inc (CTI) is responsible for developing the flight-hardened coherent lidar transceiver for SPARCLE. The transceiver is based on a 100mJ, 6Hz injection-seeded single frequency Q-switched Ho,Tm:YLF laser operating at the eyesafe wavelength of 2051nm.

In the final flight hardware configuration, the hardware provided by CTI will be contained in two Hitchhiker canisters, referred to as the Optics Canister and the Transceiver Support Canister. Partial layout of these two canisters showing the CTI supplied hardware is shown in Figure 1. The Optics Canister contains several assemblies including the lidar transceiver, a 25x expanding telescope, and a wedge scanner. These are mounted on a common support structure to maintain accurate alignment of the optical system. The support structure is directly mounted to the canister top-plate assembly which contains the canister optical window.

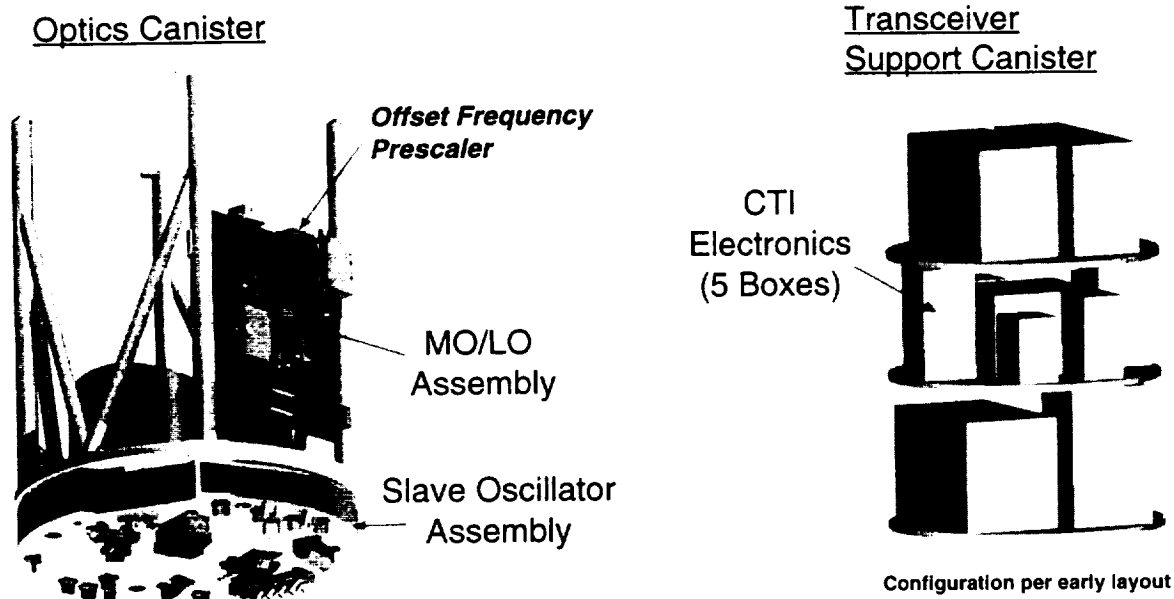


Figure 1. Hitchhiker canisters containing the lidar transceiver optics and support electronics

The lidar transceiver optics supplied by CTI are combined into two separate assemblies. These are referred to as the Slave Oscillator (SO) Assembly and the Master Oscillator/Local Oscillator (MO/LO) Assembly. The SO Assembly contains the Ho,Tm:YLF slave oscillator, mode-matching optics, and the transceiver transmit/receive optics. The support plate for the SO Assembly and the relative alignment of the transmit and receive optical paths on the plate are accurately located with respect to the telescope and scanner to minimize optical aberration in the integrated

optical system and to provide accurate pointing knowledge. The MO/LO Assembly contains two cw single frequency lasers, a master oscillator (MO) and a local oscillator (LO). The primary reason for using two cw lasers is to facilitate removal of the Orbiter velocity component from the wind speed measurements. The MO/LO Assembly also contains the lidar transceiver heterodyne optics network and photo-receivers. Optical connection between the two assemblies is achieved using space-qualified single mode fiber patch leads.

The Transceiver Support Canister contains all the CTI-supplied support electronics. These are split up into five modular boxes to facilitate heat removal from the electronics boards to the main support structure of the canister. The five electronics sub-assemblies are referred to as the Slave Pump Driver (SPD), the MO/LO Driver (MOD), the Q-switch Driver (QSD), the Ramp-and Fire Control (RFC), and the MO Frequency Control (MOFC).

2. TRANSCEIVER DESIGN

The transceiver is based on a 100mJ, 6Hz injection-seeded Q-switched Ho,Tm:YLF slave oscillator. The slave oscillator design was developed by CTI based on a breadboard laser demonstrated by NASA-LaRC¹. The slave oscillator is injection-seeded with a frequency agile master oscillator (MO) that is frequency offset-locked to a local oscillator (LO). The frequency offset-locking technique was developed by CTI, based on initial work performed by NASA-JPL². Both the MO and the LO are based on CTI's CW single frequency laser, the METEOR. Light from the two CW lasers is routed by a single mode polarization-maintaining fiber network. This network also combines the return lidar signal with the local oscillator. The MO is tunable over a frequency range of +/-4.5GHz, with respect to the fixed LO frequency, allowing correction for the Shuttle orbital velocity during conical scanning of the lidar.

2.1. Top-Level Configuration

Figure 2. shows the top-level configuration of the transceiver, indicating how the key components are functionally combined. The slave oscillator is the initial generator of the pulsed lidar waveform. It is Q-switched by an acousto-optic modulator to produce 200ns duration pulses. The slave oscillator is injection-seeded with a single frequency CW master oscillator (MO) to produce transform-limited single frequency output pulses. The slave oscillator cavity is ramped in length to match the frequency of an axial mode of the resonator to the master oscillator frequency. When resonance is detected, the Q-switch modulator is de-activated and the Q-switch pulse is generated under a frequency-matched condition, thereby achieving stable single frequency Q-switched operation of the slave oscillator.

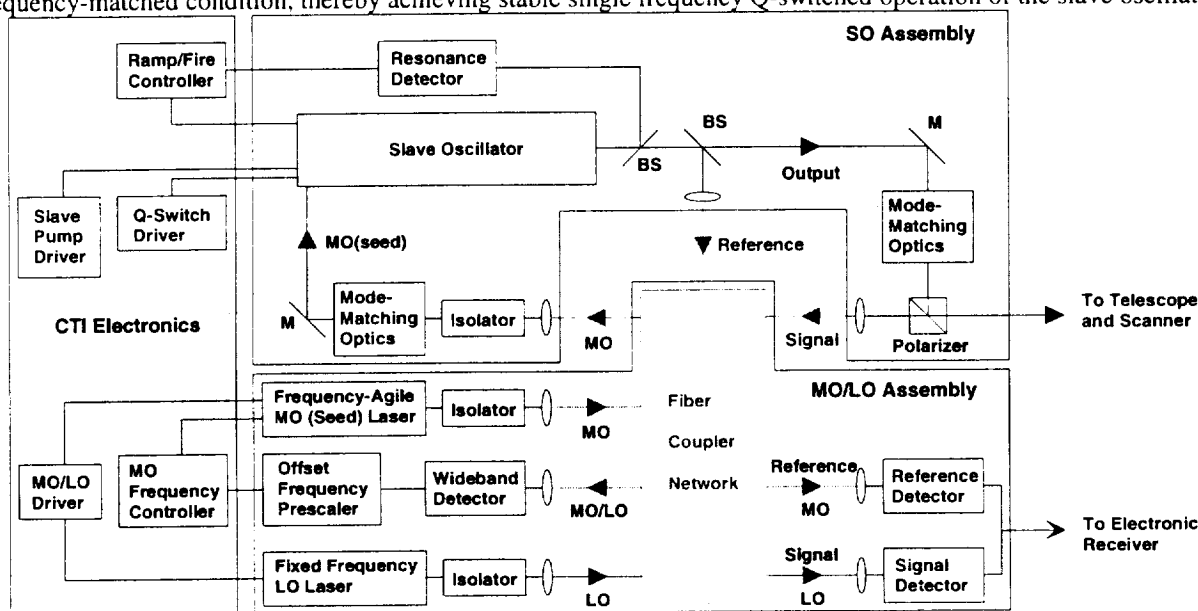


Figure 2. Block diagram of lidar transceiver layout

The transceiver has two single frequency cw lasers, the master oscillator (MO) and the local oscillator (LO). The MO is used to seed the slave oscillator and is mixed with a fraction of the optical pulse emitted from the slave oscillator to determine the frequency spectrum of the emitted lidar waveform (reference signal) via heterodyne detection. The LO is similarly used to determine the lidar return signal spectrum via heterodyne detection. Light from the MO and LO is routed about the transceiver via a single mode polarization-maintaining fiber network, containing several fiber couplers and in-line optical isolators. The fiber network is also used to optically mix the MO light with the reference pulse and the LO with the return signal. The heterodyne signals are generated by the reference and signal detector/preamplifier packages, which are optically coupled to the single mode fiber network. A wideband detector and preamplifier is required to frequency offset-lock the MO and LO. Part of the light from the MO and LO is combined in the fiber network and transmitted to the wideband detector. The resulting beat signal is used by the MO Frequency Controller (part of the CTI electronics) to accurately set the MO center frequency with respect to that of the fixed frequency LO. Three frequency measurements are made to determine accurately the Doppler shift imposed on the lidar return signal by aerosols and dust particles entrained in the target atmosphere. The emitted waveform spectrum is measured with respect to the MO frequency, the return signal spectrum is measured with respect to the LO frequency, and the MO/LO frequency offset is measured at the time of injection-seeding the slave oscillator.

The mode profile of the output beam from the slave oscillator is adjusted by mode-matching optics to best match the telescope beam propagation parameters for efficient lidar operation. A set of mode-matching optics is similarly used to match the seed beam profile emitted from the optical fiber network to that of the slave oscillator intracavity field for efficient injection-seeded operation.

2.2. Key Design Characteristics

The lidar transceiver is being developed to a large number of design requirements in order to meet both performance and safety issues associated with operation of the hardware from the Space Shuttle platform. Some of the key performance characteristics derived from these requirements are listed in Table 1.

Table 1. Key lidar transceiver characteristics

Parameter	Characteristic	Unit
Laser material	Ho,Tm:YLF	
Operating wavelength	2051	nm
Emitted pulse energy	100	mJ
Pulse repetition frequency	6	Hz
Pulse duration	200	ns
Spectral bandwidth	<1.2 times transform limit	
Beam quality (M^2)	1.4	
Output beam diameter	7.4	mm
Beam pointing angle stability	<25 (shot-to-shot)	μ rad
(relative co-alignment of 7.4mm diameter BPLO and transmit beams)	<50 (thermal excursion)	μ rad
LO center frequency stability	200 (over 4ms)	kHz
MO center frequency stability	100 (over 100 μ s)	kHz
MO frequency agility w.r.t. LO	+/- 4.5	GHz
Transceiver system efficiency (without telescope)	25	%
Heterodyne bandwidth	50 to 500	MHz
Noise floor flatness	<+/- 1	dB
Operating temperature range	0 to 25 (Optics Can hardware)	$^{\circ}$ C
	-20 to 40 (Electronics Can hardware)	$^{\circ}$ C
Survival temperature range	-20 to 40 (Optics Can hardware)	$^{\circ}$ C
	-40 to 60 (Electronics Can hardware)	$^{\circ}$ C
Vibration	Shuttle launch loads	

2.3. Frequency Offset-Locking

As part of the risk reduction activities planned for SPARCLE, CTI recently demonstrated locking of cw single frequency master and local oscillator frequencies to a center frequency accuracy of 10kHz over a frequency offset tuning range of +/-4.4GHz. This accuracy is maintained over tens of seconds. The intrinsic short term frequency stability of each laser is less than 100kHz over a 100 microsecond period. This frequency variation is super-imposed on the offset frequency selected by the locking electronics. The offset-locking circuitry includes a wideband detector and preamplifier and a closed loop circuit that is part of the master oscillator frequency controller (MOFC). The output of the controller drives the master oscillator piezo-electric stretcher element so as to achieve the correct MO frequency with respect to the LO frequency. The beat frequency between the two lasers is detected by the wideband detector and compared with a preset frequency in the electronic circuit. The piezo-electric stretcher is then adjusted in length until the beat frequency matches the preset frequency value.

As part of the recent offset-locking demonstration, CTI showed that the two lasers could be frequency offset-locked over discrete frequency steps of 1GHz, selected arbitrarily between -4.4GHz and +4.4GHz. A 30ms period was required after initial instruction to change frequency for the master oscillator to re-establish its characteristic stability of less than 100kHz frequency jitter over 100 microseconds.

2.4. Injection-Seeded Operation

CTI has also demonstrated injection-seeded Q-switched operation of a slave oscillator breadboard laser, reconfigured to match the flight hardware layout. A 15mW single frequency Ho,Tm:YLF laser with 50dB optical isolation was used to seed the slave oscillator through the first diffraction order of the Q-switch³. Seeding was found to be extremely stable with an efficiency (percentage of pulses seeded) exceeding 99%. Typical data indicated a pulse duration (intensity FWHM) of about 200ns, single frequency operation of the seeded laser at a frequency offset from the seed laser frequency by 25.5MHz (due to seeding through the Q-switch), and a pulse spectral bandwidth of about 1.4 MHz. The FFT spectrum indicated that axial mode beating in the laser was suppressed by more than 40dB from the seeded frequency component, verifying stable injection-seeded operation of the laser. The time-bandwidth product for the injection-seeded pulses was 0.277, verifying the ability of the ramp-and-fire seeding technique to produce near-transform limited single frequency injection-seeded Q-switched operation.

3. DEVELOPMENT STATUS

The lidar transceiver is currently in the detailed design phase. In addition to completing the detailed design of the instrument, we are performing risk reduction measurements to demonstrate the MO/LO frequency stability and the pointing stability of the slave oscillator and transmit/receive optical mounts over the operational and storage environmental and vibration levels. All performance requirements have been demonstrated under laboratory conditions using the breadboard SO laser and prototype MO and LO lasers. Initial testing indicates that mirror mounts for the slave oscillator meet the alignment tolerance requirements over the operational temperature range, but additional testing is required to verify this. It also remains to test the full slave oscillator with flight hardware over the same operational temperature range. Prototype master and local oscillators have been shown to maintain frequency and amplitude settings subsequent to experiencing the expected launch vibration spectrum. CTI is currently assessing the frequency stability of the master and local oscillators as a function of thermal cycling over the survival and operational temperature ranges. Details of these results and other ongoing test activities prior to CDR will be discussed in the meeting.

REFERENCES

1. Yu et al., "125-mJ diode-pumped injection-seeded Ho,Tm:YLF laser", *Opt. Lett.*, 23, 780-782 (May 15, 1998).
2. Menzies et al., "Frequency-agile Tm,Ho:YLF local oscillator for a scanning Doppler Wind Lidar in Earth Orbit", Paper Tu4, 9th Conference on Coherent Laser Radar, Linkoping, Sweden (1997).
3. Henderson et al., "Fast resonance-detection technique for single-frequency operation of injection-seeded Nd:YAG lasers", *Opt. Lett.*, 11, 715-717 (November 1986).

User Requirements and Performance of Space-borne Doppler Wind Lidars

A. Stoffelen, G.J. Marseille
KNMI, Observations and Modeling Department, Satellite Data Division
P.O. Box 201, NL-3730 AE De Bilt, The Netherlands
e-mail: marseill@knmi.nl

1. Introduction

The skill of current NWP models relies much on the availability of meteorological observations. Because NWP models have improved much over the last decades and advanced 4-dimensional variational techniques are now being used for the analysis, a need for information on the sub-synoptic scales becomes apparent for a further improvement of NWP. On these scales the atmospheric dynamics are determined by the wind field, rather than the atmospheric temperature field. The relevance of wind profile data for NWP has been verified by Observational System Experiments (OSE's) carried out by ECMWF 3D-variational assimilation system, the German weather service [1] and at NCEP [2] with the conventional TEMP/PILOT wind profiler network. Over these varied data assimilation systems and periods it was found that i) though the wind profile network is relatively sparse and inhomogeneous, it provides the backbone for NWP, ii) wind profile information in the PBL alone does not show much impact, the winds in the free troposphere and lower stratosphere are most relevant and iii) TEMP temperature profile information has relatively little impact as compared to wind profile data. Furthermore, the prime factor determining meteorological instability is vertical wind-shear. In the tropics, for an accurate definition of the Hadley circulation, 3-dimensional wind information has been lacking. Conventional wind profile data lack coverage and uniform distribution over the globe. Thus, we need wind profilers in order to improve the meteorological Global Observing System. For this purpose, there are efforts worldwide to provide independent observations of the atmospheric wind field at all levels in the lower atmosphere, primarily troposphere and stratosphere. Only a Doppler wind lidar (DWL) has the potential to provide the requisite data by means of direct observations in clear air globally (i.e. above cloud in case of overcast conditions).

In the context of the Earth Explorer missions, the European Space Agency (ESA) is preparing a mission aiming at the observation of the atmospheric wind field, namely the Atmospheric Dynamics Mission (ADM) [3]. Its main component will be a DWL called ALADIN (atmospheric laser Doppler instrument). The primary long-term objective of ADM is to provide observations of profiles of the radial (LOS) wind component. The usefulness of such observations has been shown in a series of assessment studies (e.g. [4,5,12,13]). In addition, this mission would also provide much needed ancillary information as e.g. cloud top heights or aerosol distribution.

On the requirement side, the World Meteorological Organization (WMO) has defined requirements on data quality for wind profile measurements and these have been further refined in the context of the ADM. Several technological options exist for the realization of a DWL, but each with different performances and costs. This document will present a review on the overall needs as well as the different levels of requirements identified and the implementation possibilities.

2. Doppler wind lidar data quality requirements

2.1 Generic Requirements for Global Wind Observations

Driven by the recent evolution of NWP requirements a set of generic user requirements for global wind observations can be derived stemming from WMO [6]. For short to medium range weather forecasting the requirements are defined in Table 1. For the study of large-scale processes of the climate system similar requirements apply.

	PBL	Troposphere	Stratosphere
Vertical domain	0-2 km	2-16 km	16 - 20 km
Vertical resolution	< 0.1 km	< 0.5 km	< 2.0 km
Horizontal domain	global		
Horizontal resolution	< 100 km		
Accuracy (RMS component error)	< 1.5 m/s	< 1.5 m/s	< 2 m/s
Temporal sampling	< 3 hrs		

Table 1: Generic Requirements for Operational Meteorology and NWP. The wind requirement applies for a horizontal wind component.

2.2 The Observational Requirements for the Atmospheric Dynamics Mission

The observational requirements of the ADM (Table 2) correspond to a mission fully exploiting the technique. These would e.g. require global coverage, near-real-time data delivery and frequent revisits. Implementation would most probably require more than one DWL embarked on a free flying satellite designed in such a way that the observations can be exploited operationally.

	PBL	Troposphere	Stratosphere
Vertical Domain	0 - 2 km	2 - 16 km	16 - 20 km
Vertical integration length	< 0.5 km	< 1.0 km	< 2.0 km
Horizontal Domain	global		
Horizontal integration length	< 50 km		
Temporal sampling	6 hrs		
LOS profiles/6 hours	2000		
Profile separation	> 200 km		
Accuracy (HLOS wind component)	2 m/s	2 - 3 m/s	3 m/s (if available)
reliability	95%		
Timeliness	near real-time		

Table 2: Target ADM Observational requirements for operational meteorology, NWP and climatological use

Comparing tables 1 and 2, resolution has been changed to integration length in order to provide a more instrumental definition. To maintain the requirements on accuracy the vertical integration length has been relaxed in the PBL and troposphere. The horizontal integration length has been decreased to reduce wind variability within a sample. The number of LOS profiles per 6 hours indicates the useful DWL observations with the specified accuracy and reliability. Reliability should be understood as the number of DWL measurements provided to the end user that contain useful information about the (mesoscale) wind, divided by the total number of profiles provided to the user. Assuming a coarse sampling, the profiles are required to be independent and as such separated by at least 200 km. The accuracy requirement has been relaxed to fit the accuracy that is estimated for the current operational conventional sonde network. It is expected that this accuracy remains useful in the coming decade. Currently, the conventional wind profile network is a key component of the Global Observing System [13].

In order to test the feasibility of an operational DWL mission for NWP and climate studies, a minimum set of requirements has been defined for the ADM to demonstrate the potential impact on NWP and climate, see Table 3. With respect to Table 2, the temporal and horizontal domain are reduced and a single platform flying in a dawn-dusk polar orbit will be used. The number of component profiles per 6 hours is decreased for a demonstration-only mission. It is expected that even the decreased number of measurements will make it possible to usefully assess the impact of DWL for meteorological analysis.

	PBL	Troposphere	Stratosphere
Vertical Domain	0 - 2 km	2 - 16 km	16 - 20 km
Vertical integration length	< 0.5 km	< 1.0 km	< 2.0 km
Horizontal Domain	80 S - 85 N		
Horizontal integration length	< 50 km		
Temporal sampling	12 hrs		
LOS profiles/6 hours	300		
Profile separation	> 200 km		
Accuracy (HLOS wind component)	2 m/s	2 - 3 m/s	3 m/s (if available)
reliability	95%		
Timeliness	near real-time		

Table 3: Minimum observational requirements for impact demonstration mission

3. Simulated DWL concept performances

Here we focus on the accommodation of a DWL on the International Space station (ISS) which was first considered. The overall mission performance is then determined by ISS characteristics such as attitude variations and limited resources and instrument characteristics as emitted laser wavelength and detection technique of the atmospheric return signal, *i.e.* coherent detection in the NIR versus incoherent (direct detection) in the UV. The last couple of years various concepts have been studied extensively. A lidar performance analysis simulation, LIPAS, tool [7] has been developed for trade-off purposes of various concepts as attached on the ISS. For the coherent concepts, a 10 micron system based on carbon dioxide (CO₂) laser technology and a 2 micron solid state laser system seem most promising. For the incoherent concept, a 0.355 micron laser with combined MIE (for aerosol returns below 2 km) and Rayleigh (for molecular returns above 2 km) receiving channels seems most promising. The typical numerical values for these concepts are summarised in Table 4. These values are mainly determined by platform limitations. Simulated performances are displayed in Figure 1

wavelength	10 micron	2 micron	0.355 micron
laser energy (J)	1.8	0.5	0.1
telescope diameter (m)	0.7	0.7	0.7
vertical resolution (m)	1000	1000	1000
shot accumulation (w.u.)	70	140	720
orbit height (km)	400	400	400
scan angle (degrees)	35	35	35
signal processing	Capon	Capon	centroiding/double edge

Table 4: Typical parameter values of candidate DWL concepts. Shot accumulation is performed on a 50 km long sample. The Capon estimator [8] has been adopted for signal processing of coherently detected signals.

Relating the performances of Figure 1 to the user requirements of section 2, none of the concepts fulfils them completely. For the coherent concepts, reliability is the crucial performance parameter which drops below the requirements already above 4 km for 10 micron and above 2.5 km for 2 micron. For the incoherent concept, the crucial parameter for the MIE (aerosol) channel is detection probability, *i.e.* percentage of signals with sufficiently high SNR for wind component estimation. For the Rayleigh (molecule) channel, the SNR is always sufficiently high because of negligible low background noise. Then, the observation error is the crucial parameter. Thus the incoherent 0.355 micron concept provides good quality data below 2 km from the MIE channel and fairly good quality data up to 20 km from the Rayleigh (molecule) channel. Performance optimisation is ongoing in the ADM phase A study for an implementation of a DWL on a free-flyer platform.

4. Conclusions

In the light of the Atmospheric Dynamics mission several Doppler wind lidar concepts, when embarked on the ISS, have been studied. Their performances in clear air, *i.e.* above cloud in case of overcast conditions, have been simulated. Relating them to the user requirements, the coherent concepts (10 micron CO₂ and 2 micron solid state laser) have poor performances above 4 km and their impact on NWP and climate are expected to be small. The 0.355 micron incoherent concept with combined MIE and Rayleigh receiver comes much closer to the user requirements. However, for impact demonstration, the performance of an ISS mission is insufficient.

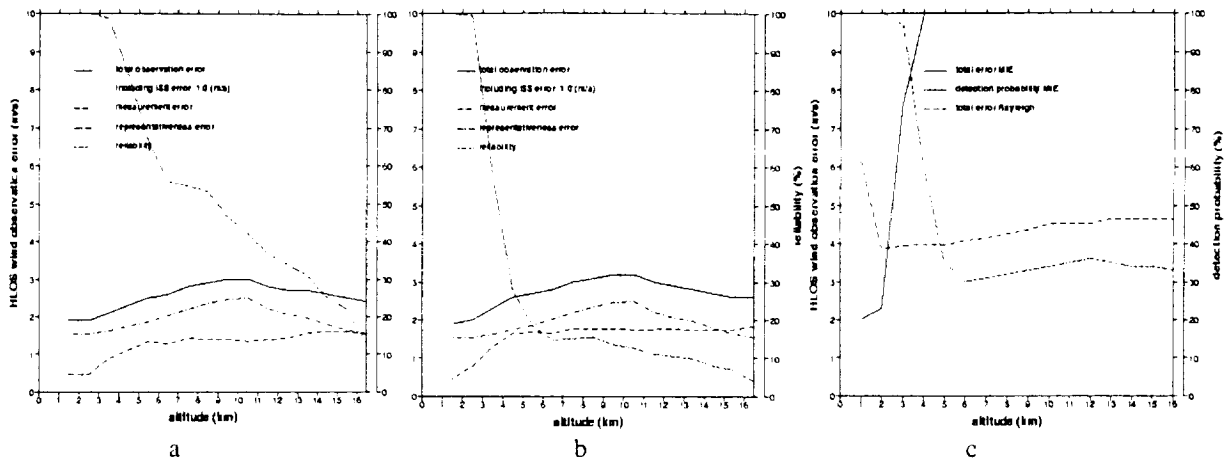


Figure 1. Clear air (no clouds) performances of horizontal line-of-sight (HLOS) wind components of proposed DWL concepts embarked on the ISS, a) 10 micron, b) 2 micron, c) 0.355 micron. The total error in c) includes instrument error, representativeness error and ISS error. The ISS error includes all errors due to ISS attitude variations. Detection probability is the percentage of return signals with sufficient SNR.

The target set of requirements (Table 2) is expected to be met by a constellation of free flyers. To study the impact of DWL data on NWP and climate studies, Observational System Simulator Experiments (OSSE's), using the ECMWF OSSE data base [8,9], have been performed. They confirmed the importance of wind profile data (e.g. [2,11]). Since these experiments were low resolution and, sometimes, carried out with rather degraded systems, further OSSE work will be carried out with state-of-the-art data assimilations systems. In addition, the effects of cloud and visibility of moisture fluxes and vertical wind-shear [10] will be investigated in order to further assess the potential of a DWL to improve analyses of the atmosphere's dynamics.

5. References

- [1] Wergen, W. (1998), personal communication
- [2] Atlas, R. (1998), personal communication.
- [3] European Space Agency (1996): *Report for Assessment: Atmospheric Dynamics Mission*; ESA SP-1196(4) <http://www.estec.esa.nl/explorer>
- [4] Lorenc, A.C., Graham, R.J. (1992): *Preparation for the use of Doppler wind lidar information in meteorological assimilation systems*; ESA-CR(P)-3454
- [5] Courtier, P., P. Gauthier, F. Rabier (1992): *Study of preparation for the use of Doppler wind lidar information in meteorological assimilation systems*; ESA-CR(P)-3453
- [6] World Meteorological Organisation (WMO) (1996): *Guide to Meteorological Instruments and Methods of Observation*, 6th Edition, WMO-No. 8
- [7] Veldman, S.M., Knobbout, H.A., Stoffelen, A., Marseille, G.J., Fuchs, J. (1999), *Lidar Performance Analysis Simulator LIPAS*, accepted paper for DASIA 99 conference proceedings
- [8] Frehlich, R.G., Yadlowsky, M.J. (1994), *Performance of Mean-Frequency Estimators for Doppler Radar and Lidar*, Journal of Atmospheric and Oceanic Technology, Vol 11, no5
- [9] Stoffelen, A., B. Becker, J. Eyre, H. Roquet, (1994), *Theoretical Studies of the Impact of Doppler Wind Lidar Data - Preparation of a Data Base*, ESA-CR(P)-3861
- [10] Stoffelen, A., Marseille, G.J. (1998): *Study on the Utility of a Doppler Wind Lidar for Numerical Weather Prediction and Climate*, ESA Contract No. 11982
- [11] Pailleux, J., A. Baverez, C. Cardinali and J.-N. Thépaut (1998): *4D Variational Assimilation of Ozone and Doppler Wind Lidar Data*, Proceedings of the 9th Conference on Satellite Meteorology and Oceanography, EUM P 22, 598-599
- [12] Wergen, W. et al., *ALADIN impact study*, Seminar on Atmospheric Dynamics, ESTEC, 1998
- [13] Isaksen, L., *TEMP/PILOT observation impact studies*, Seminar on Atmospheric Dynamics, ESTEC, 1998

Comparing the Intrinsic, Photon Shot Noise Limited Sensitivity of Coherent and Direct Detection Doppler Wind Lidar

Jack A. McKay
Remote Sensor Concepts, LLC
3200 19th St NW
Washington, DC 20010
j.a.mckay@worldnet.att.net

Introduction

Remote measurement of atmospheric wind speeds with "direct" detection Doppler lidar, i.e., optical interferometry for Doppler shift measurement, has long been considered as an alternative to coherent, heterodyne techniques. Direct detection offers some practical advantages, including elimination of the local oscillator, elimination of wavefront phase preservation concerns, availability of very mature and efficient laser technology, and the possibility of using Rayleigh (molecular) backscatter to overcome dependence on atmospheric aerosols. These advantages are particularly significant for the measurement of global wind profiles from low Earth orbit, and concepts for satellite based direct detection systems are currently under development in the United States and in Europe.

The principal liability of direct detection appears to be its relatively low sensitivity. In 1986 a study by R.T. Menzies¹ concluded that direct detection, aerosol backscatter systems would require roughly an order of magnitude higher laser power-receiver aperture product than coherent systems to achieve the same measurement accuracy. The high cost of spaceflight systems with high laser output power and large receiver aperture has deterred development of the direct detection alternative.

The work by Menzies did not yield explicit reasons for this large difference in sensitivity between coherent and direct detection. The Menzies study included optical and detection efficiency estimates, and aerosol backscatter wavelength dependences, so it is not clear whether the difference found was a fundamental property of direct versus coherent detection, or was a consequence of assumptions of system parameters.

Here the physics of direct and coherent detection, in the framework of the Cramer-Rao Lower Bound (CRLB) estimate to measurement precision, is explored, in order to determine whether direct detection is in fact intrinsically less sensitive than coherent detection, in theory and in practice. The analysis is extended from the aerosol-only systems considered by Menzies to a

comparison of a Rayleigh backscatter direct detection Doppler wind lidar (DWL) to an aerosol backscatter, coherent alternative.

Approach

The CRLB yields an estimate of the minimum statistical uncertainty of the knowledge of the centroid of a frequency distribution, based on the concept of each photon being a random sampling of that distribution. Here all questions of optics and detector quantum efficiencies are set aside, so that the result will not depend on any assumption of hardware performance parameters. Let us suppose that the receiver system would, absent the Doppler analysis optics (the Fabry-Perot interferometer of the direct detection systems), measure N photocounts, and that the source signal spectrum can reasonably be described by a Gaussian with $1/e$ width Δv_e . Then the CRLB to the standard deviation of the measurement, δv , is given by²

$$\delta v = \kappa \Delta v_e / (2N)^{1/2} \quad (1)$$

where the factor κ is unity for a perfect, lossless Doppler analyzer, which could simply measure the frequency of each photon without loss and without degradation of the source spectrum. In reality, κ will be greater than 1, due not to imperfections of hardware but to the physics of the Doppler analyzer.

For the coherent system, the intrinsic loss mechanisms include speckle noise at high levels, and small signal suppression at low³. The minimum theoretically achievable value of κ is about 2.3 (Figure 1).

The intrinsic losses of direct detection Doppler analysis are due to the Fabry-Perot etalon that is used for frequency shift determination, via either the "fringe imaging" technique generally associated with P.B. Hays⁴ and D. Rees⁵, or the "edge technique", developed by CNRS⁶ and advocated by Gentry and Korb⁷. N in Eq. (1) for direct detection is the number of *potential* photocounts, i.e., the number *incident* on the etalon. The factor κ describes photon losses due to etalon

reflectance, and broadening of the backscatter spectrum by the nonzero etalon passband width. These techniques have been modeled to determine the factor κ as a function of the etalon parameters^{8, 9}.

In Figure 2, for fringe imaging direct detection, each trace corresponds to a certain ratio of the source spectral width $\Delta\nu_s$ to the etalon free spectral range (FSR), while the abscissa describes the etalon passband width in units of $\Delta\nu_e$.

An optimized direct detection Doppler analyzer can have, at best, $\kappa \approx 2.5$. (Values of etalon finesse much less than 10 are not useful, because the fringe begins to overflow the FSR.) A practically identical result is obtained for double-edge technique direct detection. Thus, entirely by coincidence, the minimum value of κ for direct detection is close to the minimum of 2.3 found for coherent detection. Hence, *there is no fundamental difference in sensitivity, as described by CRLB uncertainty vs. the number of photocounts, between coherent and direct detection.*

This pertains, of course, to a common wavelength of operation. In practice, direct detection wavelengths are generally shorter than coherent wavelengths. Providing for the wavelength dependence of backscatter coefficients β , the number of photons per unit laser energy, and the λ factor for conversion of Doppler frequency to Doppler velocity, the ratio of CRLB velocity uncertainties can be written

$$\frac{\delta u_{dir}}{\delta u_{coh}} = \left(\frac{\kappa_{dir} \Delta\nu_{dir}}{\kappa_{coh} \Delta\nu_{coh}} \right) \left(\frac{\lambda_{dir}/\beta_{dir}}{\lambda_{coh}/\beta_{coh}} \right)^{1/2} \quad (2)$$

The $\kappa\Delta\nu$ products describe the instrument conditions, while the λ/β ratios are defined by the wavelength of operation and the corresponding atmospheric backscatter.

Now β in general increases with decreasing wavelength, especially for the submicron aerosols of the free troposphere. Then, since there is no significant difference in the minimum values of κ for direct and coherent detection, and assuming that lasers can be made with arbitrarily small values of $\Delta\nu$, *the shorter wavelength of operation gives direct detection a fundamental advantage in sensitivity over coherent detection.* That is, if $(\kappa\Delta\nu)_{dir} \approx (\kappa\Delta\nu)_{coh}$, then $\delta u_{dir} < \delta u_{coh}$.

Aerosol system comparison

It will be assumed here, perhaps optimistically, that the optimal operating point of coherent detection, with $\kappa \approx 2.3$, is achievable. The calculation referred to in Figure 1 indicates that, for an enhanced-density, free-troposphere aerosol, a large scale coherent system will be able to reach this optimal regime, though a system as modest as SPARCLE will not, nor will the larger system in the case of a low density, "background" aerosol. (This comparison is complicated by the fact that the operating point of the coherent DWL is signal

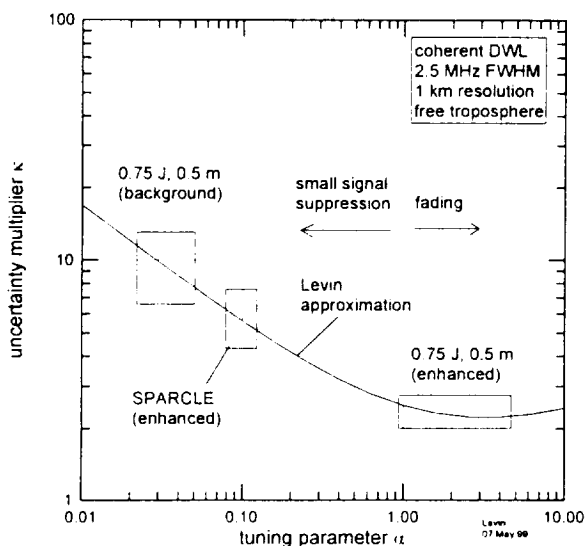


Fig. 1. CRLB factor κ for coherent detection. The optimal operating point has $\kappa \approx 2.3$, and happens to coincide with the regime of tuning parameter α (roughly, photocounts per fade).

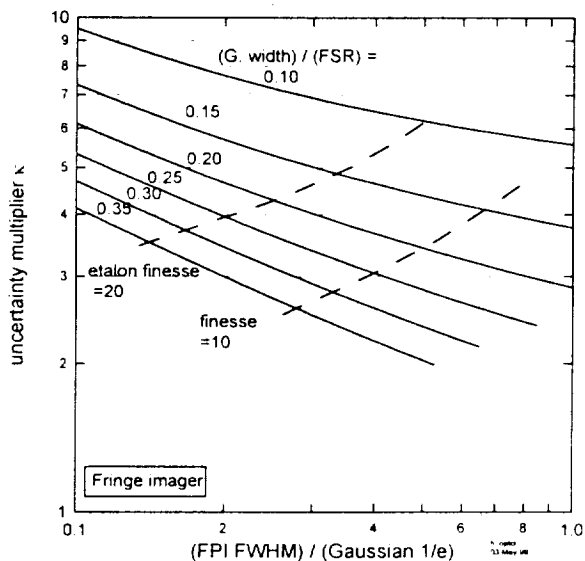


Fig. 2. Uncertainty multiplier κ for fringe imaging direct detection. Each trace corresponds to a certain etalon optical gap, while the abscissa describes the passband width. For reasonable values of etalon finesse, the lowest possible value of κ is about 2.5.

level dependent, while for direct detection it is not.) For a SPARCLE-like system with a laser FWHM of 2.5 MHz, wavelength 2.05 μm , operating at the κ minimum indicated by Figure 1, the product $\kappa\Delta\nu=5.75$ MHz.

For comparison, direct detection, aerosol backscatter DWLs operating at 1.064 μm will be evaluated. If we take $\beta\propto\lambda^{-2.5}$, as is plausible for free-troposphere aerosols, then the ratio of λ/β factors of Eq. (2) amounts to 0.32. Then, if a direct detection DWL has a $\kappa\Delta\nu$ factor of 18 MHz or smaller, it will have smaller measurement uncertainty than coherent. (The results to follow will not depend on this selection for aerosol backscatter wavelength scaling.)

Figure 2 can be used to select an optimized etalon for a direct detection, aerosol backscatter system, with $\lambda=1.064$ μm , also with $\kappa=2.5$. The optimal etalon passband width is $0.40\Delta\nu_e$ (using the Gaussian model for the laser line). Figure 3 shows the etalon optical gap versus the laser spectral width for these optimal conditions.

Achieving equal $\kappa\Delta\nu$ products for coherent and direct detection calls for an Nd:YAG laser with spectral linewidth 10 MHz FWHM, which is feasible. But inspection of Figure 3 shows that the corresponding etalons will be enormous, with optical gaps measured in meters. Practical etalons are limited to optical gaps of perhaps 150 mm, and the largest-gap etalon that has flown in space has a gap of only 12.6 mm.

In addition to the practicality of the optimal etalon there

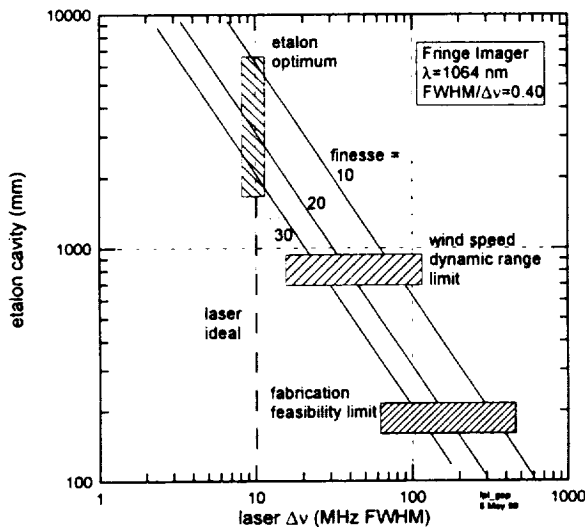


Fig. 3. Etalon cavity length, vs. laser spectral width, for an optimized fringe imaging, aerosol backscatter DWL. Very narrow laser spectral linewidths corresponds to etalon gaps larger than are permitted by dynamic range requirements, and larger than are practically feasible.

is a problem of wind speed dynamic range. For the fringe imager, the backscatter must remain within the etalon free spectral range, which sets a limit of perhaps 800 mm to the usable etalon gap (for ± 50 m/s dynamic range). For the edge technique, the backscatter must remain within the etalon passband, leading to a much more stringent maximum gap, about 100 mm. Hence, even if it were possible to build an etalon large enough to reach the optimal operating point, that etalon could not be used in a system with useful wind speed dynamic range.

When these limitations are incorporated into the etalon Doppler analyzer analysis, one finds that the result is very distant from the minimum- κ optimum (Figure 4). The largest usable etalons will have passband widths on the order of 80 MHz, and there is little benefit in employing lasers with spectral linewidths much less than this. Evaluating practical direct detection Doppler analyzers, assuming a 60 MHz laser linewidth, and etalons selected for either the maximum practical optical gap (fringe imaging) or for adequate dynamic range (edge technique), it is found that the product $\kappa\Delta\nu$ is several hundred MHz, vs. the 18 MHz that would yield a match to the coherent reference. Since the square of the ratio of $\kappa\Delta\nu$ to this reference value describes the power-aperture product needed to overcome the deficit, this suggests that the direct detection, aerosol backscatter DWL will have to be very much larger than the coherent system, by factors on the order of several hundred, to equal the measurement precision of the coherent DWL.

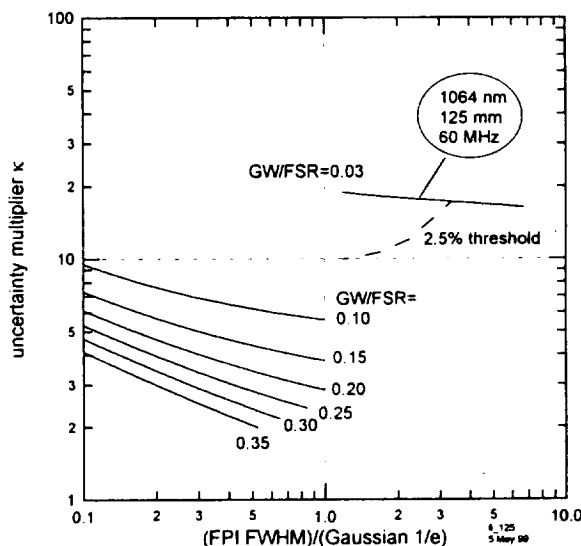


Fig. 4. CRLB factor κ for the fringe imager, with scales expanded to show the locus of a practical etalon, with 125 mm optical cavity length. The factor κ is 12 or higher, referenced to a laser spectral width of 60 MHz.

The Rayleigh backscatter is so wide that it is, in effect, a noise background, which in the free troposphere at 1.06 μm can be much larger than the aerosol signal. The solar background will similarly be much larger than the aerosol backscatter signal for a sunlit-cloud background. Allowing for these unavoidable noise sources, one concludes that *the direct detection DWL must have roughly three orders of magnitude greater power-aperture product to match the coherent DWL.*

This result follows from the impossibility, due to dynamic range requirements as well as etalon technology limitations, of building an aerosol backscatter direct detection DWL with a very narrow line laser and a CRLB-optimized Doppler analysis etalon.

Rayleigh backscatter direct detection comparison

A UV direct detection DWL could use Rayleigh backscatter, and a procedure similar to the above can be applied to compare this to the same coherent/aerosol reference system above. The difficulty with Rayleigh backscatter is, of course, the great spectral width of this signal, ≈ 3.3 GHz at $\lambda=355$ nm, or 500-600 m/s in Doppler velocity units. It turns out then that it is possible to operate in the optimal etalon regimes defined by Figures 2 and 3, with practical etalons and without wind speed dynamic range difficulties. Then $\kappa \approx 2.5$, but of course Δv is now a very large number, regardless of the laser linewidth. The CRLB comparison then yields a δu ratio on the order of 40 for an enhanced aerosol density in the free troposphere, and δu on the order of 2 for a background aerosol density in the free troposphere.

The relatively strong Rayleigh signal ameliorates the problem of the solar background, and, for the background-aerosol case, the power-aperture product required for a direct detection DWL to match coherent must be larger by a factor on the order of 8. This may be quite easily achieved in practice; the Zephyr UV system, for example, was to have 130 times the power-aperture product of SPARCLE.

Thus it is found again that the direct detection DWL is substantially less sensitive than the coherent DWL. In this case the origin of the lower sensitivity is, of course, the spectral linewidth of Rayleigh backscatter.

Conclusion

The general notion that direct detection is less sensitive, in terms of the power-aperture product needed to achieve a specified measurement precision, is confirmed. Ideally direct detection is equal to or even

superior to coherent in terms of sensitivity. For an aerosol backscatter system, however, the very narrow laser linewidth and etalon passband width that would yield highest sensitivity are incompatible with wind speed dynamic range requirements, and with etalon fabrication feasibility limits. A practical aerosol-backscatter direct detection system would require three orders of magnitude higher power-aperture product than coherent to yield the same sensitivity.

In the case of the Rayleigh backscatter system, the optimal etalon for highest sensitivity is feasible, and does not conflict with wind speed dynamic range requirements, but the instrument sensitivity is severely compromised by the spectral width of Rayleigh backscatter. In an atmosphere of high aerosol density, the coherent DWL has greatly superior sensitivity. Only in an atmosphere of very low aerosol density does direct detection come close to coherent, requiring as little as a factor 8 advantage in power-aperture product for equal measurement precision.

References

1. Menzies, R.T., "Doppler lidar atmospheric wind sensors: a comparative performance evaluation for global measurement applications from earth orbit". *Appl. Opt.* **25**, 2546-2553 (1986).
2. Rye, B.J., "Comparative precision of distributed-backscatter Doppler lidars". *Appl. Opt.* **34**, 8341-8344 (1995).
3. Rye, B.J., and R.M. Hardesty, "Estimate optimization parameters for incoherent backscatter heterodyne lidar". *Appl. Opt.* **36**, 9425-9436 (1997); errata: *Appl. Opt.* **37**, 4016 (1998).
4. Skinner, W.R., and P.B. Hays, "Incoherent Doppler lidar for measurement of atmospheric winds". *Proc. SPIE* **2266**, 383-394 (1994).
5. Rees, D., and I.S. McDermid, "Doppler lidar atmospheric wind sensor: reevaluation of a 355-nm incoherent lidar". *Appl. Opt.* **29**, 4133-4144 (1990).
6. Chanin, M.L., A. Garnier, A. Hauchecorne, and J. Porteneuve, "A Doppler lidar for measuring winds in the middle atmosphere". *Geophys. Res. Lett.* **16**, 1273-1276 (1989).
7. Korb, C.L., B.M. Gentry, and C.Y. Weng, "Edge technique: theory and application to the lidar measurement of atmospheric wind". *Appl. Opt.* **31**, 4202-4213 (1992).
8. McKay, J.A., "Modeling of direct detection Doppler wind lidar: I. the edge technique". *Appl. Opt.* **37**, 6480-6486 (1998).
9. McKay, J.A. "Modeling of direct detection Doppler wind lidar: II. the fringe imaging technique". *Appl. Opt.* **37**, 6487-6493 (1998).

New Technology

Presider: Richard Richmond

Rectangular Relief Diffraction Gratings for Coherent Lidar Beam Deflection

H.J. Cole
NASA Marshall Space Flight Center
EB52
Huntsville, AL 35812
Tel. 256-544-6790
Fax. 256-544-2659
helen.cole@msfc.nasa.gov

D.M. Chambers
Center for Applied Optics
University of Alabama in Huntsville
Huntsville, AL 35899
Tel. 256-544-4706
Fax. 256-544-2659
chambers@email.uah.edu

S.N. Dixit
Lawrence Livermore National Laboratory
Livermore, CA 94550
Tel. 925-423-7321
Fax. 925-422-5537
dixit1@llnl.gov

J.A. Britten
Lawrence Livermore National Laboratory
Livermore, CA 94550
Tel. 925-423-7653
Fax. 925-422-5537
britten1@llnl.gov

B.W. Shore
Lawrence Livermore National Laboratory
Livermore, CA 94550
Tel. 925-422-6204
Fax. 925-422-5537
shore2@llnl.gov

M.J. Kavaya
Mail Code HR20
Global Hydrology and Climate Center
NASA Marshall Space Flight Center
Huntsville, AL 35812 USA
Tel. 256-922-5803
Fax. 256-922-5772
michael.kavaya@msfc.nasa.gov

Introduction

LIDAR systems require a light transmitting system for sending a laser light pulse into space and a receiving system for collecting the retro-scattered light, separating it from the outgoing beam and analyzing the received signal for calculating wind velocities. Currently, a shuttle manifested coherent LIDAR experiment called SPARCLE includes a silicon wedge (or prism) in its design in order to deflect the outgoing beam 30 degrees relative to the incident direction. The intent of this paper is to present two optical design approaches that may enable the replacement of the optical wedge component (in future, larger aperture, post-SPARCLE missions) with a surface relief transmission diffraction grating. Such a grating could be etched into a lightweight, flat, fused quartz substrate. The potential advantages of a diffractive beam deflector include reduced weight, reduced power requirements for the driving scanning motor, reduced optical sensitivity to thermal gradients, and increased dynamic stability.

Although it has been known for quite some time that rectangular surface relief transmission gratings can have very high efficiency in the first diffraction order, most reported work [1-3] has not addressed efficiency with regard to polarization, or has concerned itself with linearly polarized incident light in the TE state. The authors from Lawrence Livermore National Laboratory have reported on high-efficiency fused silica lamellar transmission gratings for use in the UV [4]. Although the grating design in that paper was optimized for TE polarization efficiency, the following TM polarization response was modelled and reported to be above 80 percent. Because the coherent LIDAR application at hand dictates that circularly polarized must be transmitted by the diffraction grating under development, not only does the the grating efficiency need to be as high possible, but it should be nearly the same for TE and TM polarizations. Very recent work has been reported by Gerritsen and Jepsen [5] predicting that, by proper choice of grating parameters including fill factor (which is defined as the ratio of the dielectric ridge width over the grating period), simultaneously high diffraction efficiencies in both TE and TM states are possible by design.

This paper presents two separate rectangular relief transmission grating design approaches that yield 30 degree total beam deflection for 2.06 micron wavelength light. The goal is to place as much light as possible into a single transmitted order (which is taken to be -1) while maintaining circular polarization. The first design approach discussed below models diffraction from a grating in fused silica having slanted grooves. In this case the diffraction grating is designed for normally incident illumination. The second concept design shown below considers a vertical, rectangular relief, or lamellar, grating geometry where the grating is appropriately designed for off-normal illumination at an angle of 15 degrees.

The Slanted Groove Grating Approach with Normal Illumination

Gratings whose profiles are symmetric about a vertical plane will, when illuminated at normal incidence, place the diffracted radiation symmetrically about the grating normal. The present goal, however, is to force the diffraction into order -1 while excluding order $+1$. To accomplish this, with normal illumination, it is necessary to have a grating whose profile is asymmetric. The design concept presented here models diffraction from an asymmetric grating profile in fused silica where grooves are slanted with respect to the substrate normal. Slanted groove grating designs for equal for TE and TM efficiency have been modeled here using design codes based on the modal method [6-7]. It appears that for highest efficiency, in either polarization, it is desirable to have ridges whose sides are vary nearly parallel. It is very likely, however, that actual grooves will have some taper upon fabrication, and therefore profile designs for the slanted grating approach include a small taper.

There are two possibilities for orientation of the diffraction grating with respect to the LIDAR optical system. As the grating surface is etched on one side of its flat substrate, the diffractive surface may either face outward toward space or inward toward the optical system. More specifically, the light is either incident from the fused silica (at normal incidence to the flat back face of the substrate) and exits through the grating into air, or else the light enters from air, through the grating, and is transmitted through the silica (and thence into air). The modeling predicts differences between these two cases, and so the design is specific for a particular use. For the slanted groove task at hand, the highest mutual efficiencies for TE and TM polarizations appear to best satisfied by the former case where the grating faces away from the optical system.

The following is an example of a design, assuming that either the entry to the grating is normal to the grating surface and from above, or, that the reciprocal is true and that entry is from below at 30 degrees to the normal. Figure 1 illustrates the grating design; dark portions are fused silica, light portions are air. The grating period is 4.0 microns and the ridges here are at a mean angle of 20 degrees. A normally incident beam from above is bent 30 degrees clockwise into the -1 order. The grooves are 4.2 μm deep, and the ridges taper from 0.7 microns (at air interface) to 0.9 microns width (at silica interface). This design gives a TE efficiency of 80.7 percent and TM efficiency of 80.5 percent in the -1 diffraction order.

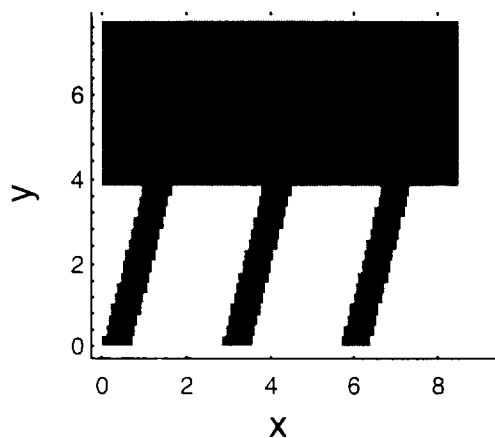


Figure 1. A grating design for 30 degree beam deflection. Dimensions are in microns.

Lamellar Grating Design with Off-normal Illumination

A lamellar grating can be described as a binary, rectangular surface relief structure where the sidewalls of the structure are parallel to the surface normal. When appropriately designed and geometrically illuminated in a Littrow configuration[8], the lamellar grating exhibits high diffraction efficiency in a single diffraction order. The Littrow relationship, which follows from the basic grating equation, is given as $2\sin\theta = -n\lambda/d$ where θ is the angle of incidence with respect to the surface normal, n is the diffraction order, λ is the wavelength and d is the grating period. The Littrow relationship is satisfied when the n th order diffracted wave, in reflection, and the incident beam are propagating in opposite directions. Figure 2 illustrates the Littrow mounting geometry used for the current application. It can be seen for a total deflection angle of 30 degrees, as is needed for the LIDAR application at hand, the incident angle, θ , is 15 degrees. With knowledge of the angle of incidence, wavelength of light, and the diffraction order, the period of the grating must be 3.86 microns.

Additional grating parameters including groove depth and grating fill factor have been modeled using codes based on rigorous coupled wave theory [9-10]. The modeling was performed with the goal of maximizing the grating efficiency in both TE and TM polarizations, while keeping them as nearly equal as possible. The following is an example of a lamellar grating design in Littrow where the angle of incidence is 15 degrees. The rectangular groove depth is 3.8 microns, the ridge width is 1.00 microns, and the period is 3.86 microns. The diffraction efficiencies for the TE and TM polarization states are equal at 81 percent. Figure 3 is an illustration of a simulated plane wavefront entering the designed grating from the left at the 15 degree incidence angle. In this case, the orientation of the grating surface faces inward toward the optical system; the wavefront shown enters from air and diffracts into the fused silica substrate at right.

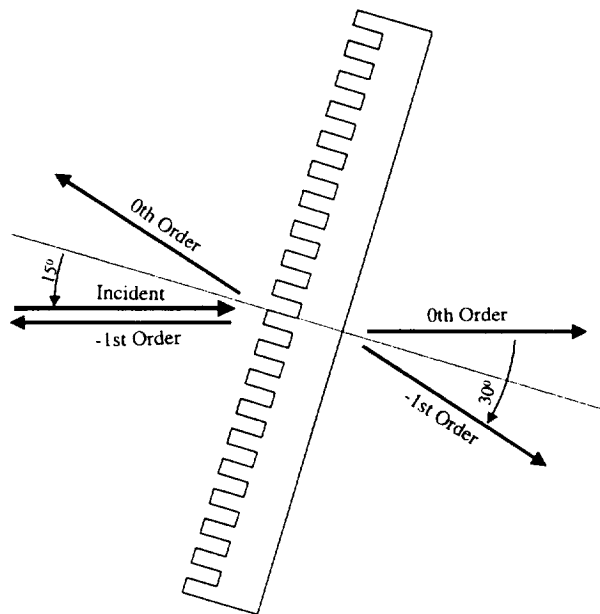


Figure 2. Diffraction Geometry for Lamellar Grating

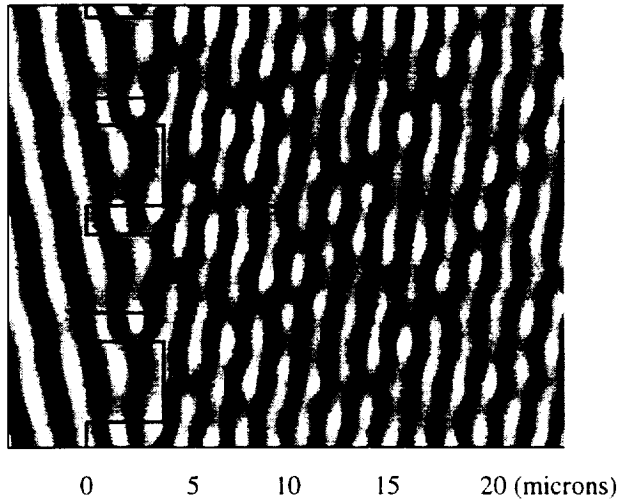


Figure 3. Simulation of plane wavefront as it diffracts through lamellar grating.

Summary

This paper has discussed two separate surface relief transmission grating design approaches that yield 30 degree total beam deflection of 2.06 micron wavelength light into the -1 transmitted diffraction order. An example design for each approach is presented. The slanted groove design described yields diffraction efficiencies of 81 percent for TM and TE polarization states. Coincidentally, the lamellar grating design, which is illuminated in Littrow, predicts 81 percent efficiency in each of the polarization states as well. Optical system requirements associated with SPARCLE were imposed, thereby fixing the operating wavelength, the grating period, and the angle of incidence. Modal and rigorous coupled wave analyses codes were used to specify the groove depth, grating ridge width, and sidewall taper based on the need for high and equal TE and TM response. If equality of efficiency for the two polarizations were not a concern, then it would be possible to select these parameters so as to achieve efficiency exceeding 81%, perhaps in both states. Future work should consider this possibility as it relates to system level performance. Finally, the authors would like to recognize the importance of preserving the relative phase relationship of TE and TM and plan to include this parameter in the next phase of design refinement.

References

- [1] M.G. Moharam, T.K. Gaylord, *J. Opt. Soc. Am.* 72, 1385-1392 (1982).
- [2] R.C. Enger, S.K. Case, *J. Opt. Soc. Am.* 73, 1113-1118 (1983).
- [3] M.G. Moharam, T.K. Gaylord, et. al., *Appl. Opt.* 23, 3214-3220 (1984).
- [4] H.T. Nguyen, B.W. Shore, S.J. Bryan, J.A. Britten, et. al., *Optics Letters* 22, 142-144 (1997).
- [5] H.J. Gerritsen, M.L. Jepsen, *Appl. Opt.* 37(24), 5823-5829 (1998).
- [6] L. Li, *J. Mod. Optics* 40, 553-73 (1993).
- [7] L. Li, *J. Opt. Soc. Am. A* 10, 2581-91 (1993).
- [8] R. Petit, *Electromagnetic Theory of Gratings*, Springer-Verlag, New York, p. 14 (1980).
- [9] M.G. Moharam, E.B. Grann, D.A. Pomett and T.K. Gaylord, *J. Opt. Soc. Am. A*, 12, 1068-76 (1995).
- [10] M.G. Moharam, D.A. Pomett, E.B. Grann and T.K. Gaylord, *J. Opt. Soc. Am. A*, 12, 1077-86 (1995).

Portions of this work were performed under the auspices of the U.S. Department of Energy under contract no. W-7405-Eng-48.

Tunable Highly-Stable Master/Local Oscillator Lasers for Coherent Lidar Applications

Charley P. Hale, Sammy W. Henderson, and David M. D'Epagnier
Coherent Technologies, Inc.
655 Aspen Ridge Drive
Lafayette, CO 80026
(303) 604-2000

1. Introduction

Advances in coherent lidar using eyesafe solid state lasers in recent years have driven the development of increasingly compact, high performance single frequency cw lasers for use as master oscillator (MO) and local oscillator (LO) sources in these remote sensing instruments. As the "master clock" frequency reference in the lidar, the MO laser's frequency stability over the time of flight of the measurement is directly linked to the lidar velocity measurement accuracy and resolution. As solid state transmitter laser technology and output powers advance, longer measurements become feasible and MO stability requirements increase accordingly; emerging coherent lidar technologies such as micro-Doppler¹ (remote vibration sensing) place even greater burdens on MO performance to prove practical. Enhancement of single frequency tunability is also a pressing concern in the performance of these reference sources, to accommodate applications such as the upcoming NASA SPARCLE mission² and other applications requiring fast frequency tuning and active offset locking to other sources.

In this paper we review the status of MO work at CTI, including the development and performance of the latest generation of eyesafe two micron MO sources, the METEOR. We also review the results of fast-programmable, highly stable multi-GHz offset locking between two METEOR sources, and discuss such a system's application toward large platform motion-induced Doppler shift compensation from low earth orbit.

2. METEOR Sources

The METEOR laser has its design origins in mid-1990's USAF/CTI programs intended to promote the maturing of critical lidar technologies, including transmitter lasers, master oscillators, and transceiver design. A number of different two micron laser materials have been exploited at CTI for various application-driven purposes. As a result much emphasis has been placed in our MO designs on developing lasers that use optically isotropic crystals such as YAG and LuAG, as well as naturally birefringent crystals such as YLF, and on designs which provide broad tunability in the same format regardless of the crystal type. Such flexibility and interchangeability is difficult in otherwise attractive cw SLM formats such as the NPRO.³

Figure 1 is a photograph of the METEOR with the hermetic cover removed, to better illustrate some of the key components of the laser. The output from a broad area emitting cw diode laser is collected and refocused into the end of the laser rod; the diode is thermoelectrically tuned and stabilized at the optimum wavelength for absorption in the laser crystal (typically ~ 781 nm). A simple two element lens system produces a nominally round focus in the rod. The two micron laser resonator is mounted on a second thermoelectric cooler, which stabilizes the cavity length around room temperature and permits continuous fine tuning of the laser wavelength across one free spectral range (FSR) of the resonator, typically ~ 0.2 nm. Chassis and resonator materials are carefully chosen to provide a very high level of dimensional stability and environmental immunity, and in the case of the resonator, a good balance between adequate thermal tuning sensitivity and environmental temperature insensitivity.

The resonator is comprised of the laser rod (incident surface coated for high reflectivity at the laser wavelength and high transmission at the pump wavelength; second surface AR coated), a thin, dielectric coated intracavity etalon, and a concave, slightly transmissive output coupler. In the case of isotropic crystals, a very thin Brewster plate is added to control linear polarization; in the case of birefringent crystals, the laser is inherently highly linearly polarized without a Brewster plate. The thickness and reflectivity of the coated intracavity etalon is designed to simultaneously provide both the necessary modal

selectivity to induce SLM operation in the laser, and a wide FSR for broadly tuning the laser frequency. Using thin fused silica etalons, tuning of up to ~ 11 nm in these eyesafe lasers is achieved; using resonator thermal tuning, any frequency within this tuning range is accessible.

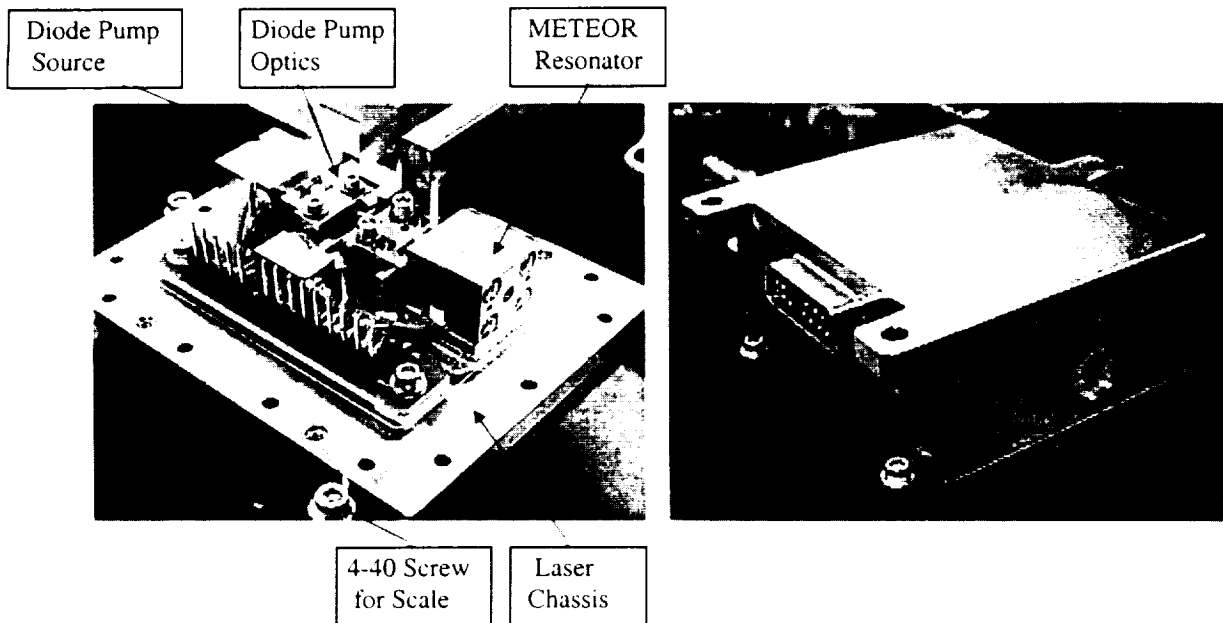


Figure 1. METEOR single frequency cw laser head. Left: hermetic cover removed to show key components. Right: hermetic cover in place.

Table 1 summarizes the characteristics and performance of the different METEORs developed to date, including a comparatively non-eyesafe Yb:YAG device operating near 1.03 μm .

	Yb:YAG	Tm:YAG	Tm:LuAG	Tm,Ho:YLF
cw MLM Power (mW)	> 150	> 150	> 150	> 150
cw SLM Power (mW)	> 50	> 50	> 50	> 50
SLM Wavelength Setting Range (nm)	1030.9-1031.4	2008-2018	2020-2030	2047-2059 2060-2069
SLM User Tuning Range (GHz)	± 2	± 5	± 5	± 5
Spatial Beam Quality	TEM ₀₀	TEM ₀₀	TEM ₀₀	TEM ₀₀

Table 1. METEOR SLM solid state laser parameters developed at CTI to date.

Single longitudinal mode powers obtained are often well in excess of 50 mW cw; for example, a Tm,Ho:YLF METEOR was constructed for a cw remote vibrometry system that produced in excess of 200 mW cw SLM near 2052 nm. Amplitude stability has been measured to be stable to better than 3%. Figure 2 shows the results of optically beating two identical Tm,Ho:YLF METEORs together on the surface of a strained layer InGaAs photodiode. The lasers were independently free-running and not actively locked to each other. Multiple, randomly selected samples of the beat note were recorded on a digital oscilloscope for record lengths of interest for most terrestrial and space-based lidar applications, and FFTs were performed on each sample to obtain a measure of the linewidth (frequency jitter/drift) of the lasers for different sample periods. The data plotted represents the linewidth of a single laser, by dividing the measured linewidth values by $\sqrt{2}$. Linewidths for the METEOR are plotted for values 3 dB and 6 dB down from the peak of the FFT spectra. As can be seen in Figure 2, linewidths of ~ 1 kHz over 1 ms time periods have been achieved; this corresponds in a two micron lidar measurement to ~ 1 mm/sec velocity measurement accuracy over 150 km ranges. MO stability of this quality is approaching that required for

micro-Doppler vibrometry applications at long ranges. Since the two lasers are not locked the linewidth at longer times is dominated by the linear drift of the two laser frequencies over the 1 ms- 1 s time spans.

The optomechanical design of the METEOR is extremely robust, to accommodate increasingly demanding application environments. Recent random vibration test measurements of two fiber coupled units showed no degradation in performance or substantial frequency shift after repeated vibration to levels in excess of 9.2 g rms.

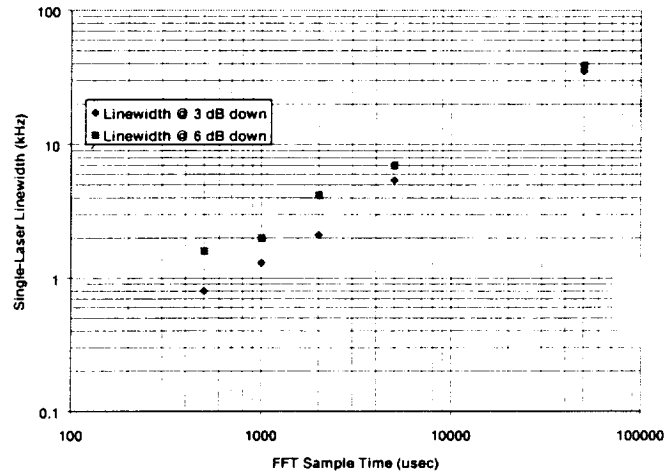


Figure 2. Measured linewidths (jitter and drift) of a Tm:Ho:YLF METEOR, obtained by heterodyning two identical lasers together and performing FFTs of the resulting beat frequency at various time intervals.

3. Frequency Offset Locking

Our involvement in the NASA SPARCLE coherent lidar in-space experiment (scheduled for shuttle launch in 2001) has prompted the next level of development of METEOR sources, capable of surviving the launch environment and having the necessary long term frequency stability and programmable frequency agility to comply with this demanding application. The very high shuttle motion-induced Doppler shift coupled with the constantly changing line-of-sight angle associated with the planned conical scan pattern, results in a frequency shift of the return signal over a ± 4.5 GHz range. Specifically, it is desirable to correct for this platform motion by actively, programmably frequency offset-locking separate master and local oscillators by a predetermined amount. This frequency offset allows the heterodyne signal between MO light and the reference pulse, and the heterodyne signal between the LO light and the return lidar pulse, to both have frequency content restricted to an RF bandwidth of ~ 500 MHz. This in turn enables highly efficient heterodyne detection by detector/preamplifier devices with large dynamic range, high quantum efficiency, and low noise characteristics; characteristics that are beyond the state of the art in $2 \mu\text{m}$ sensitive photodiode circuits having the necessary multi-GHz bandwidths that would be required without MO/LO offset locking.

We recently demonstrated a programmable frequency offset locking MO/LO system that exceeds the performance necessary for the SPARCLE application. A fast piezo tunable version of the METEOR was developed that demonstrates up to 9 GHz of frequency agility at up to 20 kHz small-signal frequency response. Other key components of the offset locking circuit include a wide band InGaAs photodiode⁴/preamplifier, phase sensitive detector/integrator, and drive electronics to control the PZT that forms part of the resonator structure of the MO source. A PC was used to command the control circuit to step to specific offset frequencies over the ± 4 GHz range.

We performed a series of experiments to quantify the ability of the wide band offset locking system to programmably step from one offset frequency to another, using the LO laser as a fixed reference and the PZT tunable MO to produce the actively locked offset. A high resolution optical spectrum analysis technique was devised that allowed us to measure step magnitude, settling time, and MO frequency stability during and after the frequency step. Using this technique, we were able to determine that the MO frequency stability settled to better than 80 kHz peak-to-peak within 30 msec of completing a 1 GHz step command.

A wide band electronic spectrum analyzer was also used to monitor the long term frequency stability of the actual multi-GHz offset frequency (as measured by sampling the output of the wide band optical detector real-time) being maintained between the two lasers; Figure 3 shows the power spectra of the beat signal when set at a representative 2 GHz offset, using a 1000 second sweep. The offset is held stable to better than 100 kHz over this time, and was found to hold the offset frequency accuracy to 5 kHz over 60 sec (the limit of the measurement time). These levels of performance are well beyond those required for the SPARCLE application, and enhancements in the circuit are in progress that will even further extend the performance.

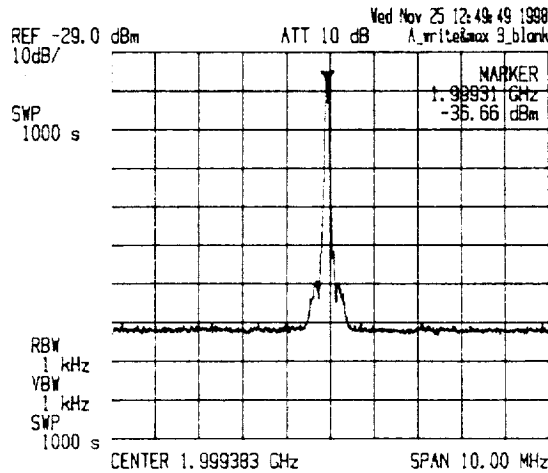


Figure 3. Maximum laser offset frequency excursions for a 1000 sec sweep over a 10 MHz span

4. Summary

A number of different solid state laser crystals have been used in the METEOR laser format to produce extremely frequency-stable, high cw power, broadly tunable sources in the 1-2 μm wavelength region. In conjunction with NASA's SPARCLE in-space lidar experiment, we have recently demonstrated fast, programmable frequency offset locking between a fixed LO and frequency agile MO to ± 4.5 GHz, to 5 kHz accuracy. Future work in our efforts to develop ultra stable frequency cw sources includes further development of Yb:YAG and Yb:YLF lasers, Tm,Ho:YAG operation at 2.09 μm , higher environmental (vibration and temperature) immunity, and higher frequency stability to comply with requirements of long range coherent vibrometry applications.

The authors wish to acknowledge the support of the US Air Force (Richard Richmond) and the Manufacturing Technology Directorate of the Air Force Research Laboratory, WPAFB; and the support and technical assistance of Michael Kavaya of NASA Marshall (SPARCLE program) and Robert Menzies of Jet Propulsion Laboratory.

5. References

1. S.M. Hannon, J.A. Thomson, S.W. Henderson, P. Gatt, R. Stoneman, and D. L. Bruns, "Agile Multiple Pulse Coherent Lidar for Range and Micro-Doppler Measurement," SPIE Laser Radar Technology and Applications III, Volume 3380, 259-269, 1998.
2. F. Amzajerjian and M.J. Kavaya, "Development of Solid State Coherent Lidars for Global Wind Measurements," paper M7 at 9th Conference on Coherent Laser Radar, Linköping, Sweden (June 23-27, 1997).
3. T.J. Kane, A.C. Nilsson, and R.L. Byer, "Frequency stability and offset locking of a laser-diode-pumped Nd:YAG monolithic nonplanar ring oscillator," Opt. Lett. **12**, 175 (1987).
4. Custom 5 GHz bandwidth InGaAs detector provided by F. Amzajerjian, NASA MSFC.

Stratified Volume Diffractive Optical Elements as Low-mass Coherent Lidar Scanners

Diana M. Chambers

Center for Applied Optics

The University of Alabama in Huntsville, Huntsville, AL 35899

Phone: (256) 890-6030 x420, Fax: (256) 890-6618, e-mail: chambers@email.uah.edu

Gregory P. Nordin

Dept. of Electrical and Computer Engineering

The University of Alabama in Huntsville, Huntsville, AL 35899

Phone: (256) 890-6215 x410, Fax: (256) 890-6618, e-mail: nordin@ece.uah.edu

Michael J. Kavaya

Mail Code HR20, Global Hydrology and Climate Center

NASA Marshall Space Flight Center, Huntsville, AL 35812

Phone: (256) 922-5803, Fax: (256) 922-5772, e-mail: michael.kavaya@msfc.nasa.gov

I. Introduction

Transmissive scanning elements for coherent laser radar systems are typically optical wedges, or prisms, which deflect the lidar beam at a specified angle and are then rotated about the instrument optical axis to produce a scan pattern.^{1,2} The wedge is placed in the lidar optical system subsequent to a beam-expanding telescope, implying that it has the largest diameter of any element in the system. The combination of the wedge diameter and asymmetric profile result in the element having very large mass and, consequently, relatively large power consumption required for scanning. These two parameters, mass and power consumption, are among the instrument requirements which need to be minimized when designing a lidar for a space-borne platform. Reducing the scanner contributions in these areas will have a significant effect on the overall instrument specifications.

Replacing the optical wedge with a diffraction grating on the surface of a thin substrate is a straight forward approach with potential to reduce the mass of the scanning element significantly. For example, the optical wedge that will be used for the SPACe Readiness Coherent Lidar Experiment (SPARCLE) is approximately 25 cm in diameter and is made from silicon with a wedge angle designed for 30 degree deflection of a beam operating at $\sim 2 \mu\text{m}$ wavelength.¹ The mass of this element could be reduced by a factor of four by instead using a fused silica substrate, 1 cm thick, with a grating fabricated on one of the surfaces.

For a grating to deflect a beam with a $2 \mu\text{m}$ wavelength by 30 degrees, a period of approximately $4 \mu\text{m}$ is required. This is small enough that fabrication of appropriate high efficiency blazed or multi-phase level diffractive optical gratings is prohibitively difficult. Moreover, bulk or stratified volume holographic approaches appear impractical due to materials limitations at $2 \mu\text{m}$ and the need to maintain adequate wavefront quality. In order to avoid the difficulties encountered in these approaches, we have developed a new type of high-efficiency grating which we call a Stratified Volume Diffractive Optical Element (SVDOE).³ The features of the gratings in this approach can be easily fabricated using standard photolithography and etching techniques and the materials used in the grating can be chosen specifically for a given application. In this paper we will briefly discuss the SVDOE technique and will present an example design of a lidar scanner using this approach. We will also discuss performance predictions for the example design.

II. SVDOE approach

The SVDOE structure consists of binary grating layers interleaved with homogeneous layers as illustrated in Figure 1. Ridges in the grating layers are composed of a high refractive index material whereas the grooves and homogeneous layers utilize a material with a low refractive index. The binary grating layers modulate a wavefront as it passes through the structure and the homogeneous layers allow diffraction to occur. While the individual binary grating layers are relatively thin, incorporation of diffraction via the homogeneous layers permits an SVDOE to attain diffraction efficiencies comparable to a volume holographic element in which modulation and diffraction are spatially coincident throughout the medium.

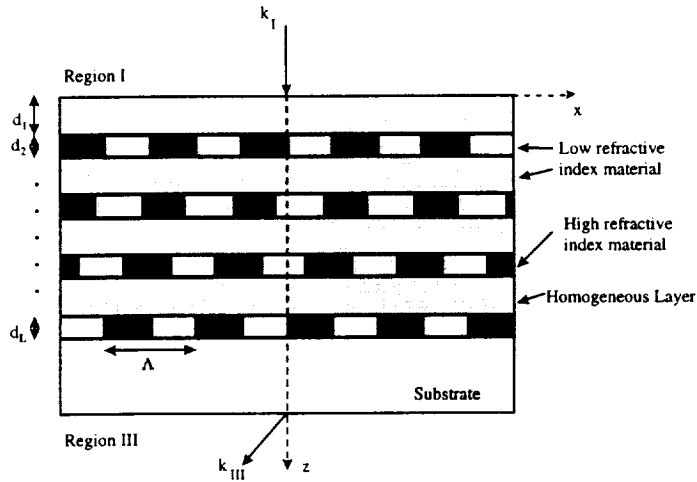


Figure 1: Schematic illustration of a stratified volume diffractive optic element (SVDOE).

Since the layers in this type of structure must be fabricated sequentially, the binary grating layers can be laterally shifted relative to one another (as illustrated in Figure 1) to create a stratified diffractive optic structure analogous to a volume grating with slanted fringes. This allows an element to be designed with high diffraction efficiency into the first order for any arbitrary angle of incidence (including normal incidence for the lidar beam scanner application).

III. Modeling and design

Depending on the choice of materials, the grating structure discussed above can include a relatively large refractive index difference between the materials in the grating layer. For the specific example application considered here, there is also a small period to wavelength ratio (e.g. < 10). Accurate prediction of diffraction efficiency under these conditions requires a rigorous electromagnetic diffraction theory. Rigorous coupled-wave analysis (RCWA) as formulated by Moharam, *et. al.*^{4,5} was chosen to model the behavior of these stratified structures. We have also included in our algorithm the re-formulation of the coupled-wave equations as published by Li⁶ to improve convergence for TM polarization and conical diffraction.

We developed a systematic design process for SVDOE's and applied it to the design of a lidar scanner element. The specific wavelength of $2.06 \mu\text{m}$ was chosen since that wavelength was under consideration during initial instrument planning.⁷ The grating period was set to be $4 \mu\text{m}$ in order to achieve a deflection angle of ~ 30 degrees at that wavelength. Candidate homogeneous layer and grating groove materials are expected to have a refractive index of approximately 1.5. Since there are a number of material choices for the grating ridges that have suitable transmission properties at $2.06 \mu\text{m}$, we evaluated designs with grating ridge refractive indices of 1.6, 1.75, and 2.0, yielding Δn (refractive index difference) values of 0.1, 0.25, and 0.5, respectively. We also considered designs consisting of 2, 3, 4, and 5 grating layers.

Our studies revealed that scanner designs with three grating layers, regardless of Δn value, yielded a diffraction efficiency of 89%. The diffraction efficiency increased with the number of grating layers, but to only 96% for a five-layer device. Since an element with three layers requires fewer fabrication steps than one with five layers and difference in efficiency was relatively small, we chose to concentrate on a three grating layer design. Likewise, fabrication issues dictate selection of the grating ridge material such that $\Delta n = 0.5$ since this leads to physically thinner grating layers. This in turn implies a reduced grating ridge aspect ratio (i.e., grating thickness divided by the ridge width), which is more easily fabricated than larger aspect ratio features.

Geometric specifications for the three grating layer structure with $\Delta n = 0.5$, designed for normal incidence, are illustrated in Figure 2. The SVDOE is implemented on a substrate that also has a refractive index of 1.5. Each grating layer is $1.046 \mu\text{m}$ thick, the homogeneous layers are each $4.300 \mu\text{m}$ thick, and the offset increment between adjacent grating layers is $0.931 \mu\text{m}$. A cover layer is shown on top of the SVDOE to protect the features on the uppermost grating. The RCWA prediction of diffraction efficiency in the first diffracted order for a beam normally incident is 89.1%.

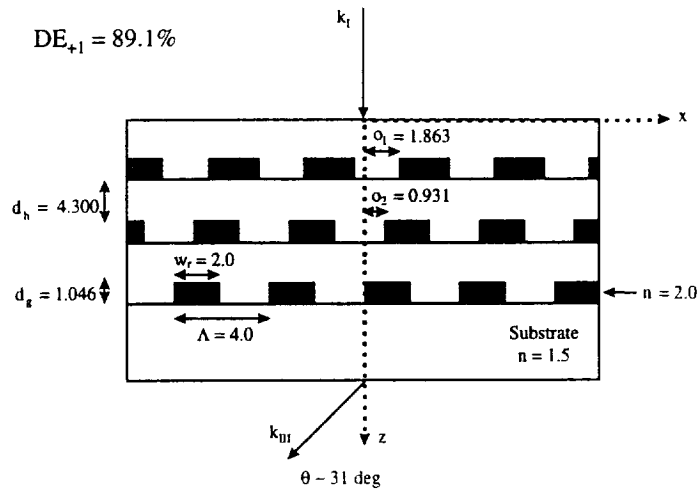


Figure 2: Specifications for prototype design of a lidar scanner element.

The lidar beam incident on the scanner will be circularly polarized. For optimum performance of the lidar heterodyne detection scheme, that polarization must be maintained as the beam traverses the scanner element. This implies that diffraction efficiency must be insensitive to polarization of the incident beam. Figure 3 shows the diffraction efficiency for the three grating layer structure as a function of the input beam incidence angle for both TE and TM polarizations. Note that the efficiency remains greater than 85% in a region of +/- 1 degree about normal incidence for both polarizations. The broad peak about normal incidence provides misalignment tolerance when the element is placed in the lidar system.

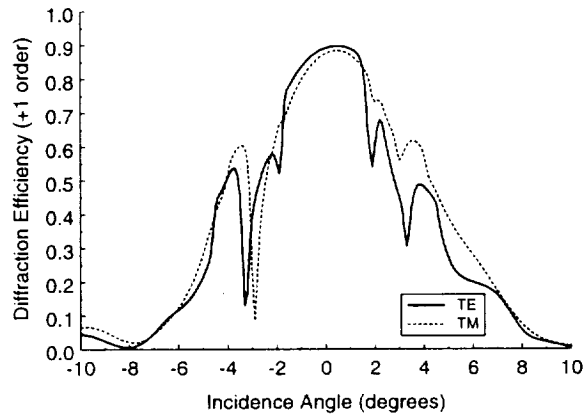


Figure 3: Diffraction efficiency as a function of incidence angle for both TE and TM polarizations. Three grating layers, $\lambda_0 = 2.06\mu\text{m}$, $n_I = 1.5$, $n_{III} = 1.5$, $n_{\text{ridge}} = 2.0$, $n_{\text{groove}} = 1.5$, $d_{\text{grating}} = 1.046\mu\text{m}$, $d_{\text{homogeneous}} = 4.300\mu\text{m}$.

Our implementation of the RCWA simulation yields an expression for the electric and magnetic fields as they traverse the SVDOE structure. Figure 4 is a representation of the electric field in the three layer prototype lidar scanner element design considered here. A plane wave is shown entering the SVDOE at normal incidence from the left of the figure. Small interference effects between the incident and reflected waves can be seen in the incident region. As the wavefronts pass through the first grating layer they are slightly disrupted while passing through the second grating layer causes them to become completely fractured. The third grating layer connects a lagging wavefront with a leading wavefront to effect the redirection of the beam to the desired deflection angle. The exiting medium in this figure is the substrate, with refractive index of 1.5.

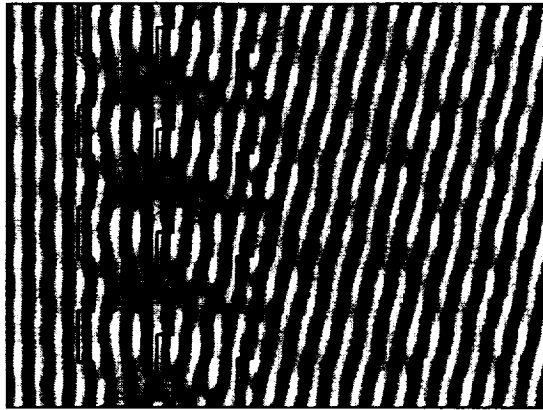


Figure 4: RCWA representation of electric field as it traverses the SVDOE prototype lidar scanner. Three grating layers, $\lambda_0 = 2.06\mu\text{m}$, $\theta = 0^\circ$, $n_1 = 1.5$, $n_{\text{III}} = 1.5$, $n_{\text{ridge}} = 2.0$, $n_{\text{groove}} = 1.5$, $d_{\text{grating}} = 1.046\mu\text{m}$, $d_{\text{homogeneous}} = 4.300\mu\text{m}$.

Anticipated challenges in fabricating an SVDOE include accurate alignment of the grating layers to achieve the desired layer-to-layer offset and deposition of the homogeneous layers with the desired thickness. To assess the tolerances required for these parameters during fabrication, we performed a statistical study of the effects of zero-mean gaussian random deviations of each parameter from the design values. The results of this study showed that the grating layer offsets must be aligned within approximately 30 nm of their design position to maintain a diffraction efficiency above 85%. Also, the tolerance on homogeneous layer thickness is not as critical as the grating offset accuracy to maintain a high diffraction efficiency and need only be maintained to within 50 nm.

IV. Summary

We have presented an approach to creating a high-efficiency grating that could be applied to the design of low-mass scanning elements for coherent laser radar systems. We have used instrument parameters representing those of the SPARCLE mission to design a scanning element with a predicted diffraction efficiency of 89.1%. Replacing the SPARCLE wedge with a diffractive scanning element as discussed here would reduce the mass of that component by a factor of four.

Our future efforts in SVDOE's will initially be directed toward fabricating gratings and experimentally validating our models and design techniques. As mentioned above, challenges in fabricating these elements will include developing processes that allow the design to be produced within the tolerances necessary to achieve high diffraction efficiency. The first generation of demonstration elements will have an aperture diameter of two inches. Future elements will explore scale-up issues in expanding the aperture to the full diameter required by operational lidar systems.

References

1. R.M. Hardesty, J. Rothermel, R.T. Menzies, J.N. Howell and L.D. Olivier, "The MACAWS airborne doppler lidar: instrument description and measurement results," , Proc. of the Ninth Conf. on Coherent Laser Radar, pp. 240-243, June 23-27, 1997, Swedish Defense Research Establishment (FOA), Linkoping, Sweden.
2. M.J. Kavaya and G.D. Emmitt, "The SPace Readiness Coherent Lidar Experiment," SPIE Aerospace/Defense Sensing and Controls Conf., April 13-17, 1998, Orlando, FL, USA
3. D.M. Chambers and G.P. Nordin, "Stratified volume diffractive optical elements as high efficiency gratings," J. Opt. Soc. Am. A, to be published May 1999.
4. M.G. Moharam, E.B. Grann, D.A. Pommet and T.K. Gaylord, "Formulation for stable and efficient implementation of the rigorous coupled-wave analysis of binary gratings," J. Opt. Soc. Am. A, **12**, 1068-76 (1995).
5. M.G. Moharam, D.A. Pommet, E.B. Grann and T.K. Gaylord, "Stable implementation of the rigorous coupled-wave analysis for surface-relief gratings: enhanced transmittance matrix approach," J. Opt. Soc. Am. A, **12**, 1077-86 (1995).
6. L. Li, "Use of Fourier series in the analysis of discontinuous periodic structures," J. Opt. Soc. Am. A, **13**, 1870-1876 (1996).
7. F. Amzajerdian, Center for Applied Optics, The University of Alabama in Huntsville, Huntsville, AL 35899, (personal communication, 1996).

The “s” polarised beams from the MO and LO lasers are injected into waveguide ports “A” and “B” respectively. A 2% sample of the MO laser is mixed with the LO laser to provide a heterodyne reference signal via output port “D”. The half wave plate in the main transmit path converts the incident “s” polarised light into “p” polarised light. This is highly transmitted through the Brewster plate and leaves the subsystem at waveguide exit port “F”. A small amount of light is reflected from the outer and inner surfaces of the Brewster plate. This is dumped from the subsystem via exit port “E”.

A quarter wave plate external to the subsystem converts the “p” polarised output beam into circularly polarised light. Subsequently this is directed at the target. Scattered light returned from the target undergoes a second pass through the quarter wave plate. This results in the generation of “s” polarised light which is coupled back into port “F”. This is highly reflected from the Brewster plate onto a 90% reflecting 45° beam splitter where it is mixed with the local oscillator field prior to being focused onto the “heterodyne signal” detector at exit port “G”.

The half wave plate and the 45° thin film polariser in the local oscillator path allow the magnitude of the “s” polarised beam reaching the “heterodyne signal” detector to be adjusted. The orientation of the half wave plate defines the relative magnitudes of “s” and “p” polarised light in the transmitted beam while the thin film polariser highly reflects “s” polarised light whilst it highly transmits “p” polarised light.



Figure 2. Photograph of hollow waveguide integrated optic subsystem based on schematic design illustrated in figure 1. Photograph taken with lid of subsystem removed allowing clear view of integrated components and connecting waveguides.

3. Manufacture and Assessment of the HOW-IO Subsystem

A photograph showing a plan view of the 200×200×20mm HOW-IO subsystem with nine of its integrated components in position is shown in figure 2. In relation to identifying the waveguides and integrated components figure 1 provides a useful cross-reference. The subsystem was formed in a polycrystalline alumina substrate utilizing computer controlled machining techniques. The machining process started with the creation of the alignment slots for the optical components. These were designed for components which were 20.0 mm square and 4.0 mm thick. The 2.0 mm square interconnecting waveguides were formed between the alignment slots in a secondary milling operation. Machining tolerances were dictated by the design criteria described in earlier work [1]. For the 2.0 mm wide waveguides that the subsystem is based on, this equated to needing lateral alignment accuracy's between waveguides and components of ± 0.1

mm, and angular alignment accuracy's, between waveguides and reflective components, of ± 0.5 mrad. The required angular alignment tolerances also imposed limits on the parallelism of transmitting components.

With the machined polycrystalline substrate in hand, the optical alignment of the subsystem merely involved the location of the components in the appropriate alignment slots. The optical characteristics of the completed subsystem were assessed by means of beam profile and power transmission measurements. The profile measurements all yielded beams of good TEM₀₀ form confirming that very accurate alignment of the waveguides and integrated components had been achieved. The measured values of power transmission were also in good agreement with the data provided by the optical component manufacturer (II-VI, Saxonburg, Pennsylvania) in conjunction with predicted waveguide coupling and attenuation losses.

4. Optical Interfacing of the HOW-IO Subsystem at AMOR

As illustrated in figure 3 for the trials at AMOR the HOW-IO subsystem had to be integrated with a range of existing components. These included, a TDC multi-fold CO₂ master oscillator (MO) laser, a Honeywell local oscillator (LO) laser, the AMOR transmit/receive telescope and three wide-band HgCdTe detectors. The multi-fold laser is based on a 3.0 m long 2.0 mm square hollow waveguide cavity. The cavity incorporates 26 folds. The use of the folds allows the total 3.0 m path to be accommodated in a ceramic substrate having an area of only 130 x 150 mm. The multi-fold laser was actively mode locked using an acousto-optic modulator to produced a 50 MHz mode-locked pulse train with a mean power of 20.0 watt. The output beam from the multi-fold MO laser was coupled into the HOW-IO subsystem with an

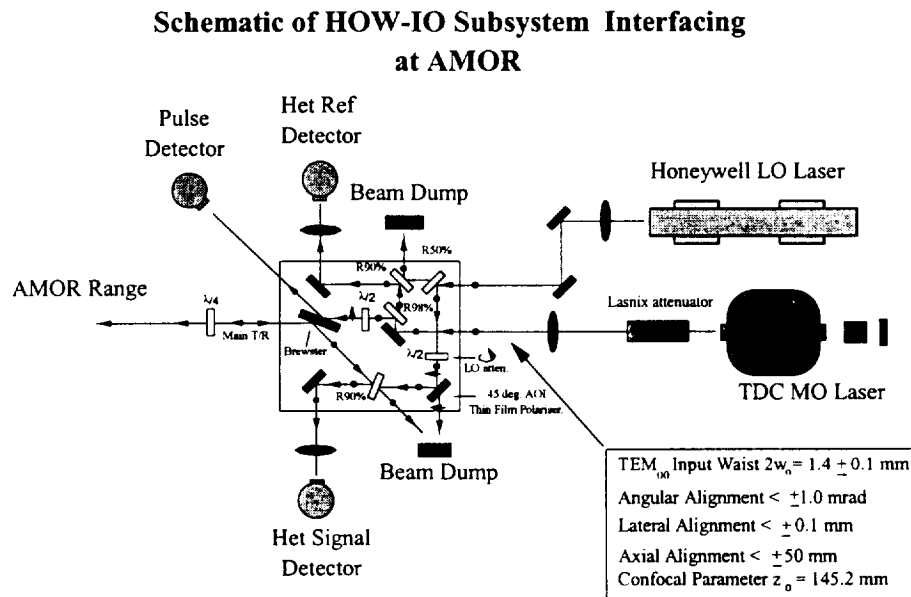


Figure 3. Schematic of interfacing of HOW-IO subsystem with TDC multifold master oscillator source and Honeywell local oscillator sources at the AMOR optical range.

appropriate combination of mirrors and lenses. Efficient fundamental mode coupling was achieved by producing a well aligned beam with a $1/e^2$ diameter of 1.4mm at waveguide input port "A". A similar input beam was produced from local oscillator laser at input port "B". The output beam from the subsystem was expanded and collimated to a $1/e^2$ diameter of 12.5 mm prior to being coupled into the 80:1 AMOR transmit telescope. The result was a 1.0 m diameter beam at the target. The target illumination profile was verified using a scanned detector beam profiling system.

The wide-bandwidth output from HgCdTe “heterodyne signal” detector at exit port “G” was analyzed using a electronic signal processor developed by TDC for target signature measurements. This produced a 14 channel output. Each channel represented a range resolution cell and contained the Doppler information corresponding to the portion of the target falling in that cell. The range gates were synchronized with respect to the mode-locked pulsed output from the MO by means of a pulse detector placed at a exit port “E” of the HOW-IO subsystem.

5. Measurements of Range-Doppler Images

With the HOW-IO subsystem properly interfaced with the additional components, the complete configuration could be operated as an imaging Lidar. Following signal-to-noise measurements on test objects the system was used to generate Range-Doppler images of a series of targets. These could be translated, tilted, spun and precessed with respect to the illuminating beam. Figure 4 illustrates a set of Range-Doppler images of a rotating cone at four different aspect angles. All the results obtained were analogous to those produced with a well aligned free-space system. This confirmed that the hollow waveguide integrated optic approach to 10.6 μ m coherent Lidar can lead to systems with equivalent performance but in a much more rugged, stable and compact form. Such systems are ideal for fielding on military platforms.

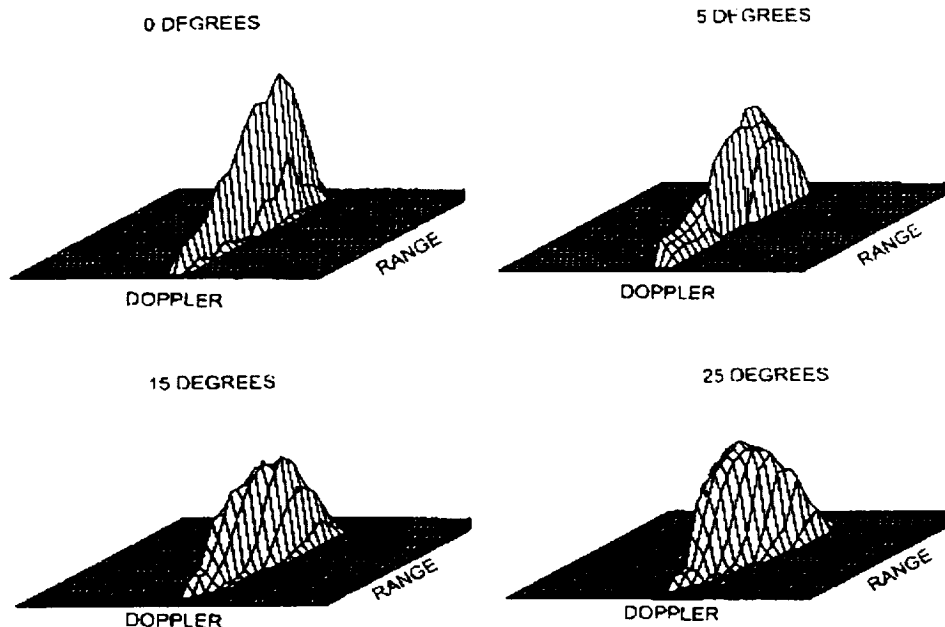


Figure 4. Measured Range-Doppler images of a rotating cone at aspect angles of: 0, 5, 15 and 25 degrees. Note increasing signal magnitude from front to rear of cone and broadening of Doppler spread produced by rear of cone with increasing aspect angle

5. References

[1] R M Jenkins, R W J Devereux and A F Blockley, “Hollow waveguide integrated optics: A novel approach to 10.6 μ m LIDAR,” Jn Mod. Opt., vol. 45, No. 8, pp 1613-1627, 1998.

TARGET CHARACTERIZATION

Presider: Robert Menzies

Comparison of continuous wave CO₂ Doppler lidar calibration using earth surface targets in laboratory and airborne measurements

Maurice A. Jarzembski
NASA/MSFC/Global Hydrology and Climate Center
977 Explorer Blvd., Huntsville, AL 35806

Vandana Srivastava
Universities Space Research Association
Global Hydrology and Climate Center
977 Explorer Blvd., Huntsville, AL 35806

1. Introduction

Routine backscatter, β , measurements by an airborne or space-based lidar from designated earth surfaces with known and fairly uniform β properties can potentially offer lidar calibration opportunities. This can in turn be used to obtain accurate atmospheric aerosol and cloud β measurements on large spatial scales. This is important because achieving a precise calibration factor for large pulsed lidars then need not rest solely on using a standard hard target procedure. Furthermore, calibration from designated earth surfaces would provide an in-flight performance evaluation of the lidar. Hence, with active remote sensing using lasers with high resolution data, calibration of a space-based lidar using earth's surfaces will be extremely useful.

The calibration methodology using the earth's surface initially requires measuring β of various earth surfaces simulated in the laboratory using a focused continuous wave (CW) CO₂ Doppler lidar and then use these β measurements as standards for the earth surface signal from airborne or space-based lidars. Since β from the earth's surface may be retrieved at different angles of incidence, β would also need to be measured at various angles of incidences of the different surfaces. In general, Earth-surface reflectance measurements have been made in the infrared,¹ but the use of lidars to characterize them and in turn use of the Earth's surface to calibrate lidars has not been made. The feasibility of this calibration methodology is demonstrated through a comparison of these laboratory measurements with actual earth surface β retrieved from the same lidar during the NASA/Multi-center Airborne Coherent Atmospheric Wind Sensor (MACAWS) mission² on NASA's DC8 aircraft from 13 - 26 September, 1995. For the

selected earth surface from the airborne lidar data, an average β for the surface was established and the statistics of lidar efficiency was determined. This was compared with the actual lidar efficiency determined with the standard calibrating hard target.

2. Lidar Theory

The measured SNR from a hard target (HT) with ρ_{HT} [sr⁻¹] using a CW lidar is given by,³

$$SNR_{HT} = \frac{\eta_{HT} P \pi R^2 T \rho_{HT} f(L)}{B h \nu}, \quad (1)$$

where range dependence, $f(L)$, is given by

$$f(L) = \frac{1}{L^2 \left[1 + \left(\frac{\pi R^2}{\lambda L} \right)^2 \left(1 - \frac{L}{F} \right)^2 \right]}, \quad (2)$$

where $h\nu$ is laser photon energy, P is laser power, R is lidar beam $(1/e)^2$ intensity radius at telescope primary mirror, F is distance to focal volume center, and B is data system bandwidth, and η is overall lidar system efficiency. The transmission efficiency T is given by $T = \exp(-2\alpha L)$. HT can stand for a standard calibrating hard target (CHT) or earth hard target (EHT), since both present a surface of scattering. At the lidar beam focal volume, $L = F$, Eqs. (1)-(2) reduce to

$$SNR_{HT} = \frac{\eta_{HT} P \pi R^2 T \rho_{HT}}{B h \nu F^2}. \quad (3)$$

Using a CHT with known⁴ ρ_{CHT} , η_{CHT} can be determined.⁵ Once η_{CHT} is known then measured SNR_{HT} from any other HT surfaces can lead to ρ_{HT} . Thus, ρ_{EHT} for a variety of earth surface compositions can be characterized in the laboratory. Subsequently, the characterized earth surfaces can be used as calibration targets in flight to get η_{EHT} for airborne or space-based lidars. Lastly, once η_{EHT} has been determined, then it could be further corrected to

η_{AEROSOL} , the lidar efficiency determined using laboratory-generated aerosols which is more realistic assessment of the actual lidar efficiency to be used for atmospheric measurements.⁵

3. Laboratory Experiment and Airborne Mission

The NASA/Marshall Space Flight Center's (MSFC's) focused CW CO₂ Doppler lidar operating at 9.1 μm wavelength was used for measuring β . Further details of this research can be found elsewhere⁶ as well as details of the lidar operation and its calibration procedure.^{5,7}

A. Backscatter from Simulated Earth Surfaces

Laboratory simulation was conducted with a variety of homogeneous HT's made from earth's surface materials. The material was glued onto 8-inch-diameter plexiglass disks. For vegetation targets, vegetation was cut into small pieces with sizes of roughly several millimeters. The HT's were attached to a rotating motor shaft. For the earth surface simulations, SNR_{EHT} was measured as a function of angle of incidence ϕ at $L = F$.

Using Eqs. (1)-(2), η_{CHT} was determined from the measured $\text{SNR}_{\text{CHT}}(L)$ of two CHT's, sandpaper (SND) and flame-sprayed aluminum (FSA), giving $\eta_{\text{CHT}} \sim 0.165 \pm 13\%$. This was then the lidar system efficiency for determining ρ_{EHT} for various simulated EHT surfaces. Figure 1 shows ρ_{EHT} as a function of ϕ for the targets. In general, dependence of ρ_{EHT} on ϕ is small, showing that there are several naturally occurring targets that behave like the standard FSA and SND CHT's. For the simulated EHT surfaces, sand and soil targets give the highest ρ_{EHT} , while vegetation targets give the lowest. Additionally, the vegetation targets dried out had negligible change on ρ_{EHT} . However, wetting all targets with water lowered the ρ_{EHT} dramatically for all ϕ .

Since β measurements from actual earth surfaces using an airborne-focused CW lidar are done at random range values, depending on the aircraft altitude and roll; therefore, measurements of the range response of β from the simulated earth surfaces were performed in the laboratory. Figure 2 shows range response of HT made from beach sand, pine, and the SND CHT. The beach sand and pine HT's show very good agreement with lidar theory similar to the SND CHT.⁵ Range response of β for the other HT's (not shown in Fig.2) also were in very good agreement with the lidar theory. These results suggest that signal from these types of earth surfaces at ranges other than $L = F$ can be used in conjunction with Eqs. (1)-(3) to estimate η_{EHT} .

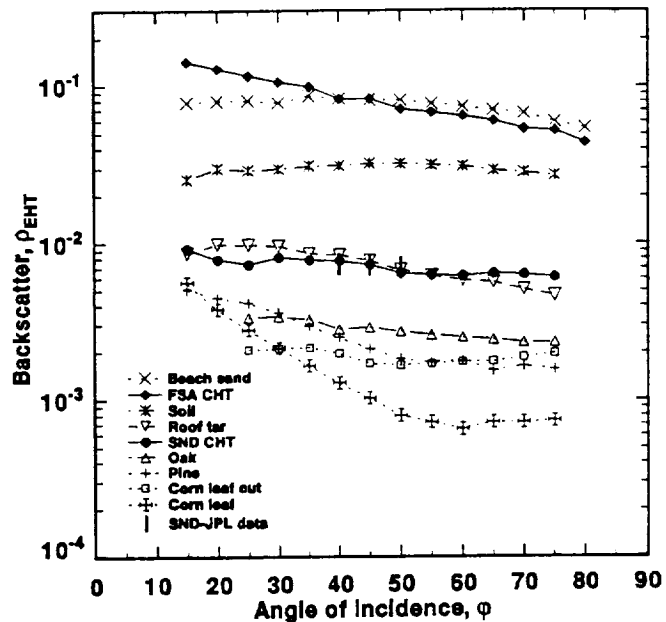


Figure 1. Laboratory backscatter measurements as a function of angle of incidence ϕ using the NASA/MSFC 9.1 μm focused CW Doppler lidar from simulated earth surfaces for land-type targets.

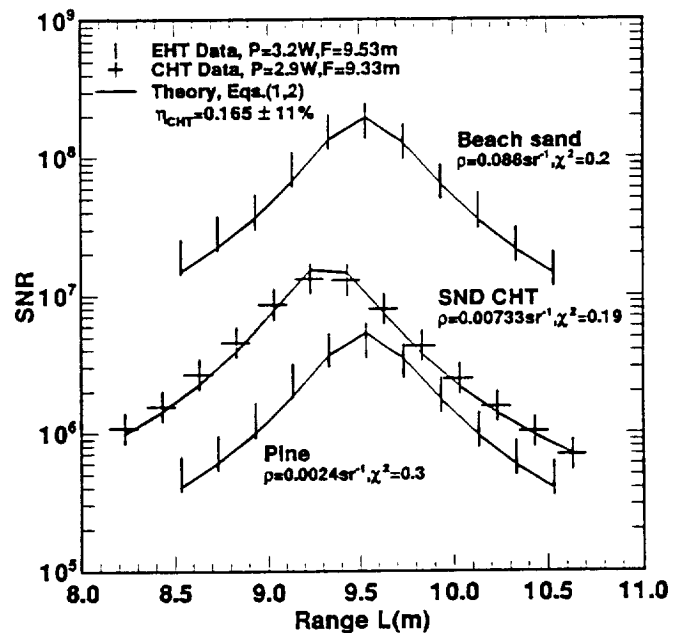


Figure 2. Measured backscattered SNR as a function of range L for beach sand and pine HT's and the (SND) calibrating HT.

The investigated targets give a range of possible variation in the ρ_{EHT} that may be encountered from real earth surfaces composed of

different materials. For mixed surfaces, if the fractions of different materials can be estimated, then an average ρ_{EHT} can be estimated by weighted mixing of their individual ρ_{EHT} 's. With the use of passive satellite imagery, like LANDSAT, it may be possible to fractionate different types of surfaces encountered in the lidar sampled surface area. For calibration purposes, homogeneous surfaces would be best; but if these were not available, than an average ρ_{EHT} of a composite surface could be used.

B. Earth Surface Return

The same NASA/MSFC airborne CW focused lidar retrieved an earth surface β at the unfocused part of the beam along with atmospheric aerosol β at the beam focus during aircraft rolls over the complex California terrain during the 1995 MACAWS mission. The lidar beam was focused at ~ 54 m through a modified aircraft right side viewing germanium window in front of the aircraft wing. Since the outgoing lidar beam to the earth's surface and the β from the surface can undergo appreciable atmospheric attenuation due mostly to presence of aerosol, CO_2 , and H_2O ; therefore, the atmospheric attenuation coefficients were determined and the retrieved SNR from the earth's surface was compensated for this attenuation.

Figure 3 shows $\text{SNR}_{\text{EHT}} = \text{SNR}/T$ at various ranges from the Coastal Range Mountains in California northeast of Santa Cruz. The variability of SNR_{EHT} , is caused by significant heterogeneity encountered due to low β vegetation interspersed with high β nonvegetation areas. Forested areas interspersed with open land in the Coastal Range Mountains gave an SNR_{EHT} between soil and vegetation values, showing that the targets were very heterogeneous, mixed with vegetation-type and nonvegetation-type. Figure 3 also shows curves of predicted SNR_{EHT} as a function of L using Eqs. (1)-(2) for three earth surface types simulated in the laboratory having $\rho_{\text{EHT}} = 0.08, 0.03, \text{ and } 0.002 \text{ sr}^{-1}$ (Fig. 2) corresponding, respectively, to sand, soil, and vegetation. These curves were derived with the various lidar parameter values during the mission as: $h\nu = 2.1818 \times 10^{-20} \text{ J}$, $P = 4.4 \text{ W} \pm 3\%$, $R = 0.0265 \text{ m} \pm 3\%$, $F = 54.0 \text{ m} \pm 2\%$, $B_{\text{DSP}} = 141 \text{ kHz} \pm 1\%$ and $\eta_{\text{CHT}} \sim 0.126 \pm 18\%$. The curves provide a good envelope of possible SNR_{EHT} from surfaces that may contain similar materials.

4. Lidar Calibration from Earth's Surface

Homogeneous or even uniform heterogeneous targets would be preferred for in-flight calibration as they would give well defined

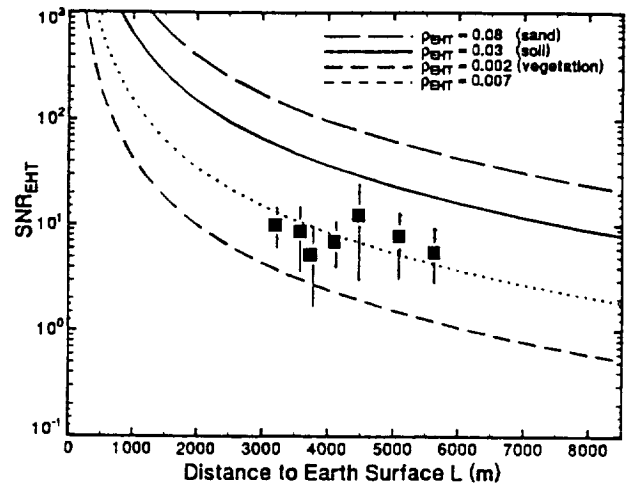


Figure 3. Measured backscattered SNR normalized by transmission efficiency T for earth surface northeast of Santa Cruz, California using the $9.1 \mu\text{m}$ focused CW lidar along with comparison with lidar theory [Eqs. (1)-(2)] using lidar parameters cited in the text for three representative backscatter values of various earth surface types. Variability of earth surface backscatter is depicted by the vertical line through each data point which gives range of SNR_{EHT} at a given distance. Variability in L , due to variability in both radar altitude and roll angle, is within the data symbol width.

SNR_{EHT} , leading to well defined η_{EHT} . However, since the earth's surface targets sampled during the mission were mostly heterogeneous with varying SNR_{EHT} , any estimation of η_{EHT} [using Eqs. (1)-(2)] from these data sets would also be associated with some variability. Figure 4(a) is a histogram of the data in Fig. 3, showing the frequency of occurrence of measured SNR normalized by T and $f(L)$. This histogram gives the distribution of range-independent SNR_{EHT} showing the variation encountered due to surface inhomogeneity only. From these statistics of range-independent SNR_{EHT} , the statistics of η_{EHT} were determined with an average ρ_{EHT} of 0.007 sr^{-1} estimated for the curve that best fit the selected data samples shown in Fig. 3. The distribution of η_{EHT} is shown in Fig. 4(b). This earth surface target, being quite non-uniform, gives a mean $\eta_{\text{EHT}} \sim 0.15$ with variation of about 80%. The uncertainty in the η_{EHT} estimation here is dominated by the variability in the SNR_{EHT} from the complex heterogeneous surfaces. If an appropriately varying ρ_{EHT} were known for such a target, then the

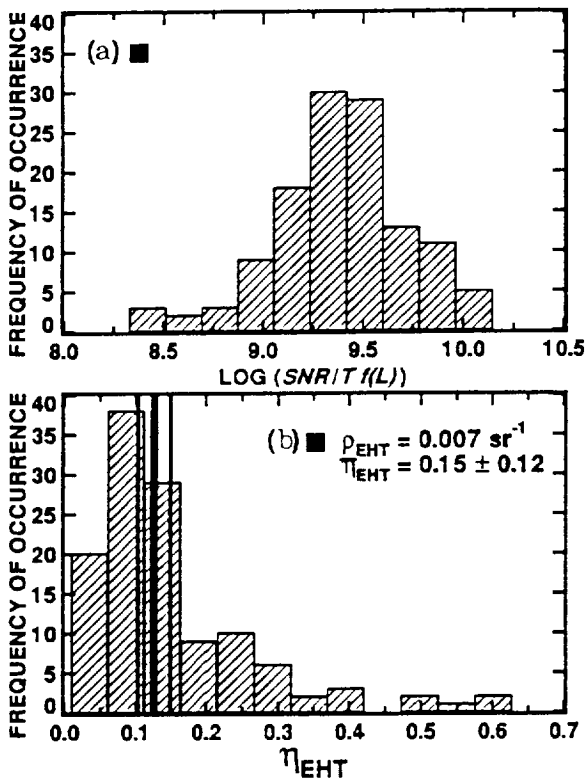


Figure 4. Histograms of (a) measured SNR normalized by the transmission efficiency T and $f(L)$ and (b) calculated lidar efficiency η_{EHT} for an average ρ_{EHT} of 0.07 sr^{-1} as assessed from Fig. 3 from the Coastal Range Mountains northeast of Santa Cruz, California. The SND $\eta_{\text{CHT}} = 0.12 \pm 18\%$ for this mission is shown within the bold vertical lines for comparison with η_{EHT} .

estimation of η_{EHT} would be much less uncertain. Nevertheless, this distribution shows that if the earth's surface β is known then the lidar efficiency can be estimated with a fair degree of accuracy, preferably using uniform earth surface targets during flight for airborne or space-based lidar.

5. Conclusion

Characterization of lidar β of simulated earth surfaces, such as vegetation and non-vegetation, in the laboratory for their possible application as calibration targets for airborne and space-based lidars during flights were investigated. These targets provide a fair envelope of land-type earth surface β for several materials. β of most dry earth surfaces at various angles of incidence showed only weak to negligible angular dependence. The SNR data measured in the airborne MACAWS mission over the complex heterogeneous surfaces lie within the bounds of the values obtained in the

laboratory. Thus, data from different regions could be used for in-flight calibration to estimate the lidar efficiency and the associated uncertainty. The earth's surface-derived lidar efficiency obtained with the average ρ_{EHT} of complex heterogeneous surfaces encountered during the mission gave good agreement with the CHT-derived lidar efficiency. Therefore, by measuring SNR_{EHT} from earth surfaces with known ρ_{EHT} , using an airborne or space-based lidar, the lidar system efficiency can be estimated for atmospheric measurements. Obtaining absolute calibrated β measurements using this method instead of signals in relative units has very important advantages leading to crucial information and immense research opportunities for various aspects of global aerosol modeling in terms of its impact on climate, pollution, and hydrological processes.

REFERENCES

1. W. L. Wolfe and G. J. Zissis, *The Infrared Handbook* (1978), Chap. 3.
2. J. Rothermel, D. R. Cutten, R. M. Hardesty, R. T. Menzies, J. N. Howell, S. C. Johnson, D. M. Tratt, L. D. Olivier, and R. M. Banta, "The Multi-center Airborne Coherent Atmospheric Wind Sensor, MACAWS," *Bull. Amer. Meteor. Soc.* **79**, 581-599 (1998).
3. C. M. Sonnenschein and F. A. Horrigan, "Signal-to-noise relationships for coaxial systems that heterodyne backscatter from the atmosphere," *Appl. Opt.* **10**, 1600-1604 (1971).
4. M. J. Kavaya, R. T. Menzies, D. A. Haner, U. P. Oppenheim, and P. H. Flamant, "Target reflectance measurements for calibration of lidar atmospheric backscatter data," *Appl. Opt.* **20**, 2619-2628 (1983).
5. M. A. Jarzembski, V. Srivastava, and D. M. Chambers, "Lidar calibration technique using laboratory-generated aerosols," *Appl. Opt.* **35**, 2096-2108 (1996).
6. M. A. Jarzembski and V. Srivastava, "Comparison of continuous-wave CO_2 lidar calibration by use of Earth-surface targets in laboratory and airborne measurements," *Appl. Opt.* **37**, 7120-7127 (1998).
7. J. Rothermel, D. M. Chambers, M. A. Jarzembski, V. Srivastava, D. A. Bowdle, and W. D. Jones, "Signal processing and calibration of continuous-wave focused CO_2 Doppler lidars for atmospheric backscatter measurement," *Appl. Opt.* **35**, 2083-2095 (1996).

EFFECT OF AEROSOL PARTICLE MICROSTRUCTURE ON ACCURACY OF CW DOPPLER LIDAR ESTIMATE OF WIND VELOCITY

V.A. Banakh and I.N. Smalikho

Institute of Atmospheric Optics of the Russian Academy of Sciences,
Akademicheskii prospekt, 1. Tomsk, 634055, Russia
e-mail: banakh@ldw.tomsk.su
smalikho@iao.tsc.ru

Ch. Werner

DLR Lidar Group, PO 1116, D-82230 Wessling, Germany
e-mail: Christian.Werner@dlr.de

1. Introduction

An estimate of radial wind velocity V_D obtained from data of cw Doppler lidar is the sum of the radial velocity \bar{V}_r , averaged over probing volume and the error V_e [1]. Statistical independence of \bar{V}_r and V_e as well as statistical independence of velocity errors measured at different moments allow us to estimate the error variance $\sigma_e^2 = \langle V_e^2 \rangle$ from the temporal spectrum or structure function of wind velocity measured by Doppler lidar [1]. Comparison of the experimental values σ_e^2 obtained at very high signal-to noise ratio (SNR) [1] with the estimates by formula [2]

$$\sigma_e^2 = \frac{1}{8\sqrt{\pi}} \frac{\lambda}{t_0} \sigma_s, \quad (1)$$

where λ is the wavelength, t_0 is the integration period and σ_s is the Doppler spectrum width (in m/s), shows that for small probing volumes the experimental values σ_e far exceed (approximately in order of magnitude) the theoretical estimates σ_e based on Eq.(1). In order to explain this discrepancy between theory and experiment in this paper we analyze the effect of aerosol particle microstructure on accuracy of wind velocity estimates from data of cw Doppler lidar obtained at small probing volumes.

2. Algorithms of simulation

On short paths (range $R \sim 50 + 100$ m or less) probing volume of cw Doppler lidars can measure only a few cubic centimeters in volumes. In this case according to rough estimates based on known data for the microstructure of atmospheric aerosol [3] it is necessary to take into account the concentration and size distribution of particles in analysis of Doppler lidar run.

In contrast to previously used approaches of numerical simulation (see, for example Ref. 4,5) to study the effect of aerosol microstructure we have developed the following algorithm. The entire path of sounding is divided into N very thin layers (slices). We assume that within separate slice the aerosol particles move with the same velocity. Using the lognormal probability density function of particle size distribution with the mean $\langle a \rangle$ and standard deviation σ_a the random realization of sizes a are simulated. Assuming that all particles have the same complex refractive index $m = n + jk$ the backscattering amplitudes A_i are calculated using Mie theory [6]. For each wave scattered by separate particle the initial phase Ψ_i is simulated as uniformly distributed random value.

Random distribution of radial wind velocity $V_r(\Delta r l)$, where Δr is the slice width, $l = 1, 2, \dots, N$, is simulated in the spectral domain using von Karman model for wind velocity spectrum [7] with two input parameters: velocity variance σ_v^2 and outer scale of turbulence L_v . Besides, we take into account the movement of particles across the laser beam with the velocity V_{\perp} . Based on the results of simulation of the listed above parameters the received signal $j_s(t)$ at a moment t is calculated as

$$j_s(t) = \sum_{l=1}^N E_l(t) \exp \{j2kV_r(\Delta r l)t\}, \quad (2)$$

where

$$E_l(t) = \sum_{i=1}^{N'} A_{li} q(\Delta r l, x_i + V_{\perp} t) \exp \{j\Psi_{li}\},$$

q is the function describing distribution of probing beam in l -th slice [1], $k = 2\pi/\lambda$, N' is the number of aerosol particles in l -th slice, x_i is the x -coordinate of i -th particle in transverse plane. One can add in Eq.(2) simulated noise component $j_n(t)$ as additive Gaussian white noise ($j_s(t) + j_n(t)$).

3. Results of simulation

The results were obtained for the case of very high SNR, when the term $j_n(t)$ can be neglected. We put the following parameters: $\sigma_v = 1.5$ m/s, $L_v = 50$ m, $\langle V_r \rangle = 13$ m/s, $V_{\perp} = 2$ m/s, $n = 1.6$, $\kappa = 0.05$ and $\rho_c = 100$ cm⁻³, where ρ_c is the concentration of particles.

Fig. 1 shows the example of simulation of the signal power $P(t) = |j_s(t)|^2$ as function of time for parameters $\langle a \rangle = 0.1$ μ m, $\sigma_a = 0.075$ μ m, $R = 50$ m, $\lambda = 10.6$ μ m, and initial laser beam radius $a_0 = 7.5$ cm when the effective probing volume $V_{\text{eff}} \approx 4$ cm³. Large peak in simulated data with the width equals approximately 2 ms is caused by dominant effect of separate large particle on the power of backscattered wave. Similar behavior of signal power is observed in atmospheric experiments at small sizes of the probing volume [8]. The Doppler spectrum with frequency resolution 20 KHz (velocity resolution 0.1 m/s) and the integration period 5 ms (average over 100 spectra) is shown in Fig. 2 as solid curve. The spectrum simulated using the approach [9] for the case of full averaging of the signal power fluctuation is shown as dashed curve. The difference between these spectra is caused by the effect of separate large particles on signal fluctuations.

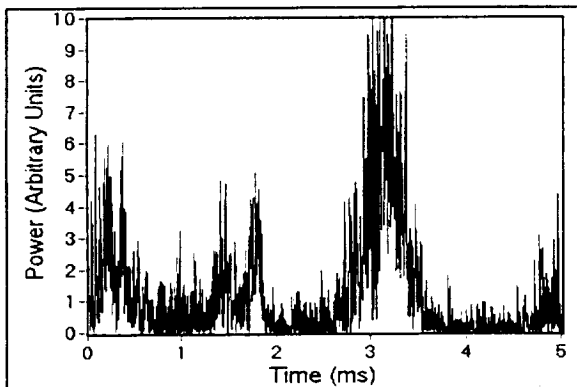


Fig. 1.

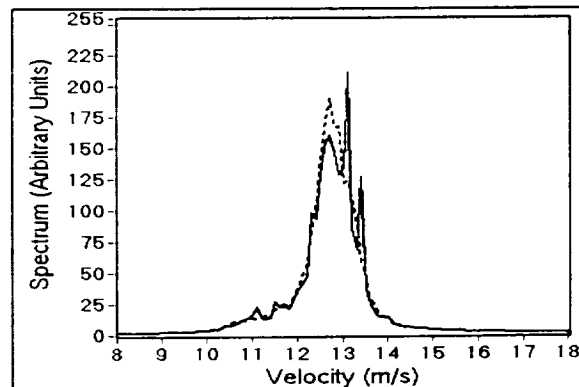


Fig. 2

In Fig. 3 the probability density function (PDF) of the simulated signal power $F(P)$ for specified above parameters is shown as solid curve. For calculation of $F(P)$ 10000 independent realizations were used. The dashed line depicts the exponential PDF corresponding to the case of Gaussian statistics of the signal. One can see that at the large ratios $P/\langle P \rangle$, where $\langle P \rangle$ is the mean signal power, the PDF deviates strongly from the exponential distribution. That is the signal statistics is non-Gaussian one in the case of small probing volume.

Random error V_e we determined as the difference between mean velocities estimated respectively from the spectrum marked in Fig. 2 by solid curve and from the spectrum corresponding to full averaging of the power fluctuations (dashed curve in Fig. 2). To calculate the error standard deviation σ_e we used 1000 independent realizations of V_e . Figure 4 illustrates calculated by such a way values σ_e as function of $\langle a \rangle$ at the fixed ratio $\sigma_a/\langle a \rangle = 0.75$. Figure 5 shows the error σ_e versus σ_a at $\langle a \rangle = 0.1 \mu\text{m}$.

Analysis of the data in Figs. 4, 5 shows that the maximal velocity estimate error σ_e takes place when the number of particles contributing to the signal power is smallest. Actually, at small values σ_a the probability of entering of large particles in probing volume is small, a lot of particles contribute to the lidar signal, and the error σ_e is minimal. With increasing σ_a the probability of appearing of large particles in probing volume increases. Although their number is comparatively small, the main part of the signal power is produced as a

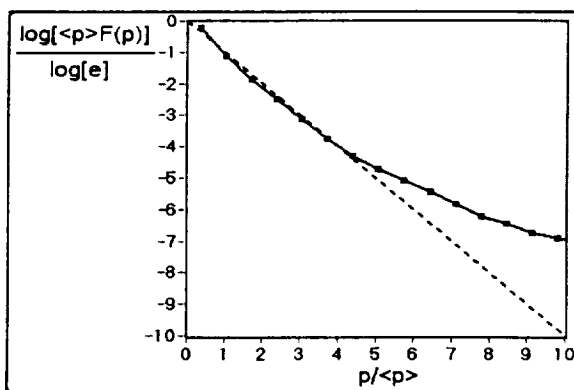


Fig 3.

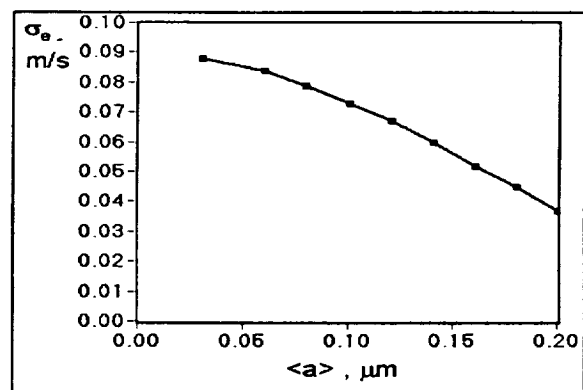


Fig. 4.

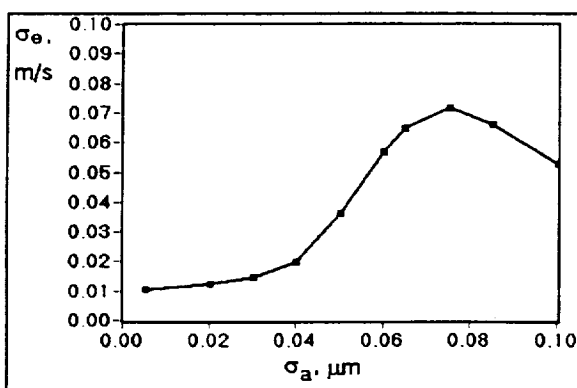


Fig. 5.

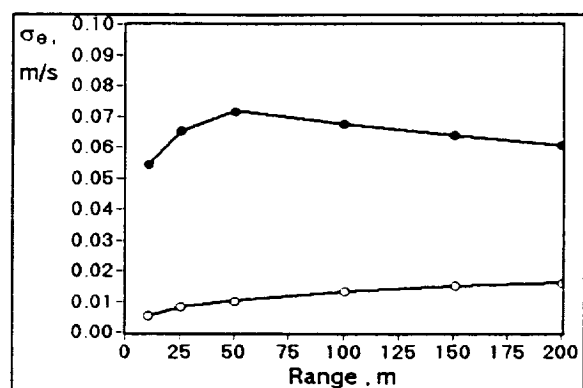


Fig. 6.

result of light scattering precisely by these large particles because of increasing the backscattering section $\sigma_{\pi}(a/\lambda, m)$ with a . As a consequence the error standard deviation σ_e increases and at $\sigma_a = 0.075 \mu\text{m}$ it becomes maximal. But with further increasing σ_a the contribution of large particle scattering to the signal decreases due to decreasing of the backscattering section σ_{π} for large particles with size $a \geq 2.2 \mu\text{m}$. As a result the number of

aerosol particle contributing mainly to the lidar signal increases and σ_e decreases for $\sigma_a > 0.075$. The same reason explains the decrease of σ_e with increasing $\langle a \rangle$ for specified in calculations ratio $\sigma_a / \langle a \rangle = 0.75$.

Figure 6 shows σ_e versus range R at $\langle a \rangle = 0.1 \mu\text{m}$ and $t_0 = 5 \text{ ms}$. Dark circles correspond to the case $\sigma_a = 0.075 \mu\text{m}$ and white circles are the result of calculation at $\sigma_a \rightarrow 0$. It is seen that when all particles have the same size ($\sigma_a \rightarrow 0$) the velocity estimate error σ_e increases monotonously with range R . This is in agreement with the result of calculation σ_e by Eq. (1) (in inertial subrange of turbulence, when longitudinal size of probing volume $\Delta z = (\lambda/2) (R/a_0)^2 < L_v$, the Doppler spectrum width σ , increases with the range R [1]). But in practical situations the standard deviation $\sigma_a \neq 0$ [3] and R – dependence of σ_e is not monotonous, as it follows from the data in Fig. 6 (dark circles). With range increasing the error σ_e first increases and then decreases due to significant increase of the probing volume $V_{\text{eff}} \sim R^3$ and, consequently, the number of scattering particles. From comparison of two curves in Fig. 6 it follows that under certain conditions the aerosol microstructure may be the determining factor in accuracy of wind velocity statistics measurement by Doppler lidar.

References

1. V.A. Banakh, I.N. Smalikho, F. Köpp, and Ch. Werner, «Measurements of turbulent energy dissipation rate with a cw Doppler lidar in the atmospheric boundary layer», J. Atmos. Oceanic Technol. (1999, accepted for publication).
2. R.J. Keeler, R.J. Serafin, R.L. Schwiesow, D.H. Lenschow, J.M. Vaughan, and A.A. Woodfield, «An airborne laser air motion sensing system. Part I: Concept and preliminary experiment», J. Atmos. Oceanic Technol. **4**. 113-127 (1987).
3. V.E. Zuev and G.M. Krekov, Optical Models of the Atmosphere, (Gidrometeoizdat, Leningrad, 1986), 256 p. [in Russian].
4. R. Frehlich, «Effect of wind turbulence on coherent Doppler lidar performance», J. Atmos. Oceanic Technol. **14**. 54-75 (1997).
5. V.A. Banakh, I.N. Smalikho, «Estimation of the turbulence energy dissipation rate from the pulsed Doppler lidar data», Atmospheric and Oceanic Optics, **10**. №12. 957-965 (1997).
6. A. Ishimaru, Wave Propagation and Scattering in Random Media (Academic Press, New York, 1978). Vol. **2**. 278 p.
7. I.L. Lumley and H.A. Panofsky, The Structure of Atmospheric Turbulence (Interscience, New York, 1964) 264 p.
8. R.M. Hardesty, R.J. Keeler, M.J. Post, and R.A. Richter, «Characteristics of coherent lidar returns from calibration targets and aerosols», Appl. Opt. **20**. 3763-3769 (1981).
9. V.A. Banakh, N.P. Krivolutsky, I.N. Smalikho, and Ch. Werner, «Simulation of scanning cw Doppler lidar», Proc. 19-th International Laser Radar Conference, Annapolis, July 1998 / PT2. 731-734.

**VALID : Experimental tests to validate a multiwavelength backscatter database and
intercompare wind lidar concepts**

Pierre H. Flamant

(1) Laboratoire de Météorologie Dynamique,
Centre National de la Recherche Scientifique
Ecole Polytechnique, 91 128 Palaiseau cedex, FRANCE
tel : 33 1 69 33 45 50
fax : 33 1 69 33 30 05
E-mail : flamant@lmd.polytechnique.fr

Abstract :

ESA is funding in 1999 an experimental activity (1) to built a multiwavelength backscatter database to validate a scalling law derived in a previous study, and (2) intercompare the most relevant wind lidar concepts to space applications. VALID will proceed in two steps : Step1 in May-mid-June for backscatter data, lidars with wavelengths ranging from UV (0.32 μm) to IR (10.6 μm) will be operated on the same site ; Step2 in mid-July will involve various coherent and incoherent lidar techniques on the same site.

A SOUTHERN CALIFORNIA PERSPECTIVE OF THE APRIL, 1998 TRANS-PACIFIC ASIAN DUST EVENT

David M. Tratt
Jet Propulsion Laboratory
California Institute of Technology
4800 Oak Grove Drive
Pasadena, CA 91109-8099

Robert J. Frouin
Scripps Institution of Oceanography
University of California, San Diego
9500 Gilman Drive
La Jolla, CA 92093-0221

Douglas L. Westphal
Marine Meteorology Division
Naval Research Laboratory
7 Grace Hopper Avenue
Monterey, CA 93943-5502

The Jet Propulsion Laboratory (JPL) coherent CO₂ backscatter lidar has been in almost continuous operation since 1984 and has now accumulated a significant time-series database tracking the long-term and seasonal variability of backscatter from the atmospheric column above the Pasadena, Calif. locale (Tratt and Menzies, 1994). A particularly noteworthy episode observed by the lidar in 1998 was a particularly extreme instance of incursion by Asian-sourced dust during the closing days of April. Such events are not uncommon during the northern spring, when strong cold fronts and convection over the Asian interior deserts loft crustal material into the mid-troposphere whence it can be transported across the Pacific Ocean, occasionally reaching the continental US. However, the abnormal strength of the initiating storm in this case generated an atypically dense cloud of material which resulted in dramatically reduced visibility along the length of the Western Seaboard. These dust events are now recognized as a potentially significant, non-negligible radiative forcing influence (Parungo *et al.*, 1994).

The progress of the April 1998 dust cloud eastward across the Pacific Ocean was initially observed in satellite imagery and transmitted to the broader atmospheric research community *via* electronic communications. The use of Internet technology in this way was effective in facilitating a rapid response correlative measurement exercise by numerous atmospheric observation stations throughout the western US and its success has resulted in the subsequent establishment of an *ad hoc* communications environment, data exchange medium, and mechanism for providing early-warning alert of other significant atmospheric phenomena in the future (Husar *et al.*, 1998).

The first lidar observations of the extreme Asian dust event made from the JPL site (34° 12' N; 118° 10' W; 390 m MSL) were acquired on April 27, 1998. Its evolution was tracked by the lidar throughout that entire week, and was well advanced into the dissipation phase when the onset of stormy conditions on May 2, which persisted into the following week, obscured the final decay stages. Near-concurrent measurements of atmospheric optical depth were also recorded during this same interval by an autonomous sun-sky scanning spectral radiometer stationed on San Nicolas Island off the California coast at geographical coordinates: 33°15' N, 119°29' W, 133 m MSL. This dataset recorded a significant increase in atmospheric optical depth on April 25 over San Nicolas which slowly diminished over the following 5 days (Fig. 1). These data also yield retrievals of aerosol size distribution which may be used to cross-validate grosser features of the lidar soundings (see Fig. 2).

Ex post facto analysis of the event using the US Navy Aerosol Analysis and Prediction System (NAAPS, Westphal *et al.*, 1998) accurately hindcasted arrival of the dust cloud in the Los Angeles region on April 25-27, although the simulation matrix has insufficient resolution to maintain the vertical structure of the dust as revealed by the lidar profiles. Figure 3 shows the development of the dust cloud above the JPL lidar site through the height of the event, as modeled using NAAPS.

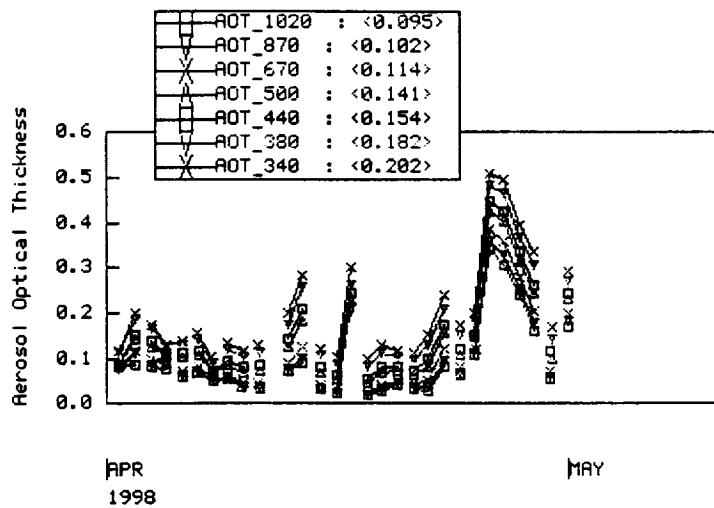


Figure 1. Aerosol optical thickness (AOT) time-series above San Nicolas Is., Calif. recorded with a spectrally scanning sunphotometer for the time period containing the dust event. The sharp increase in AOT toward the end of April marks the first arrival of the dust cloud in the region on April 25.

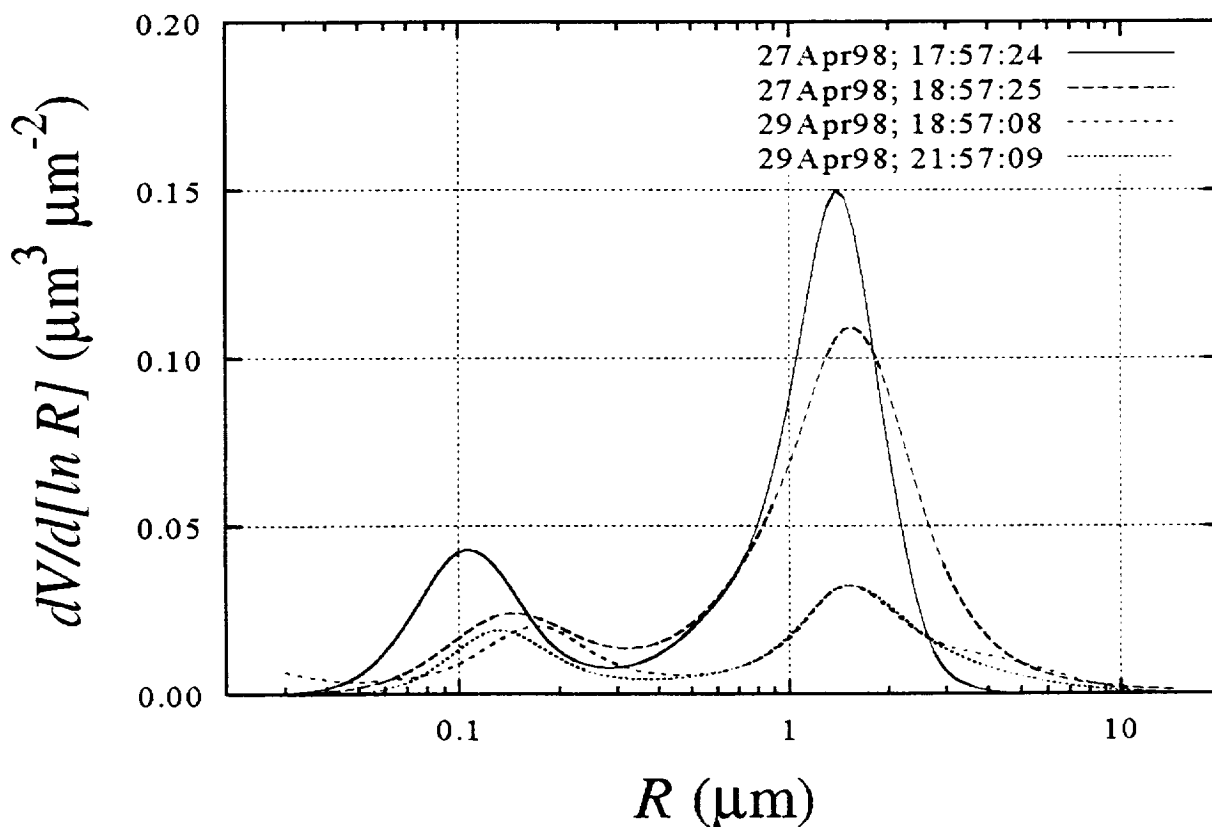


Figure 2. Retrieved column-integrated aerosol volume size distributions (particle radius R) above San Nicolas Is., Calif. corresponding to four different time intervals within the dust event.

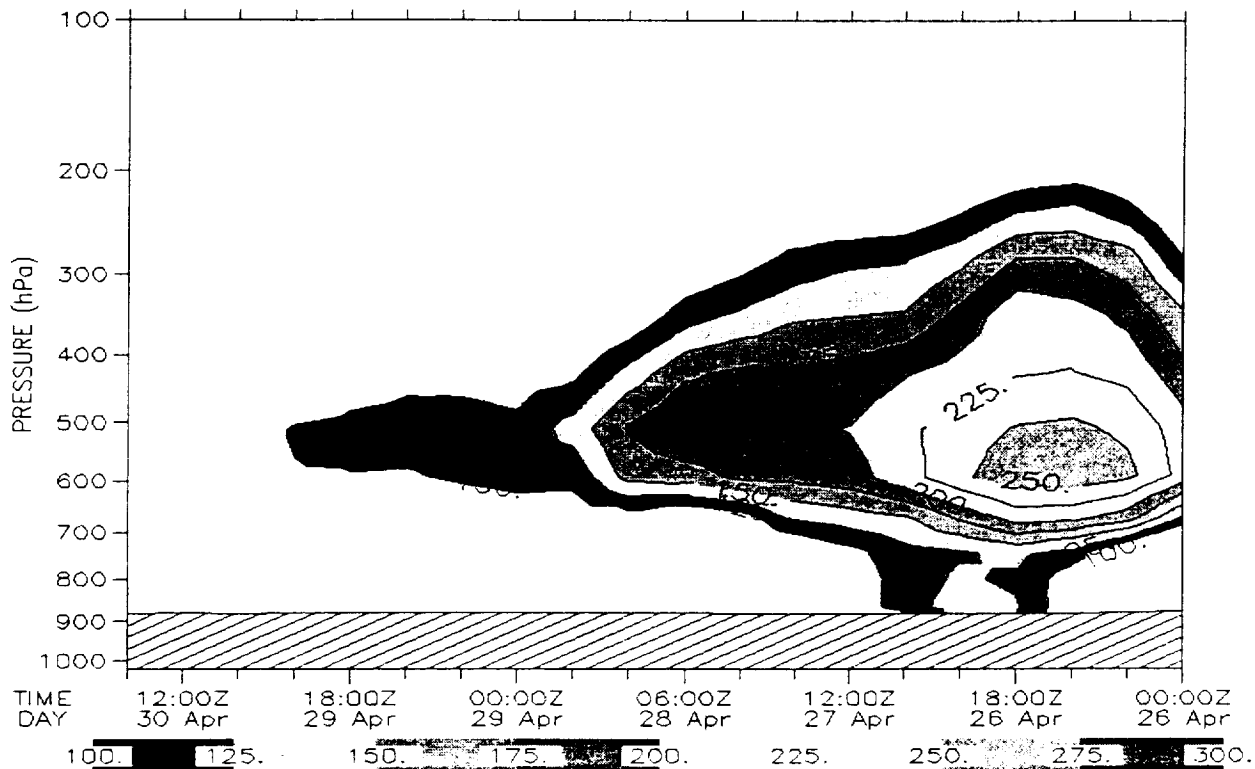


Figure 3. Modeled time-series dust concentration above Pasadena, Calif. for the period 26-30 April, 1998. Gray-scale contours represent mass density expressed in $\mu\text{g m}^{-3}$.

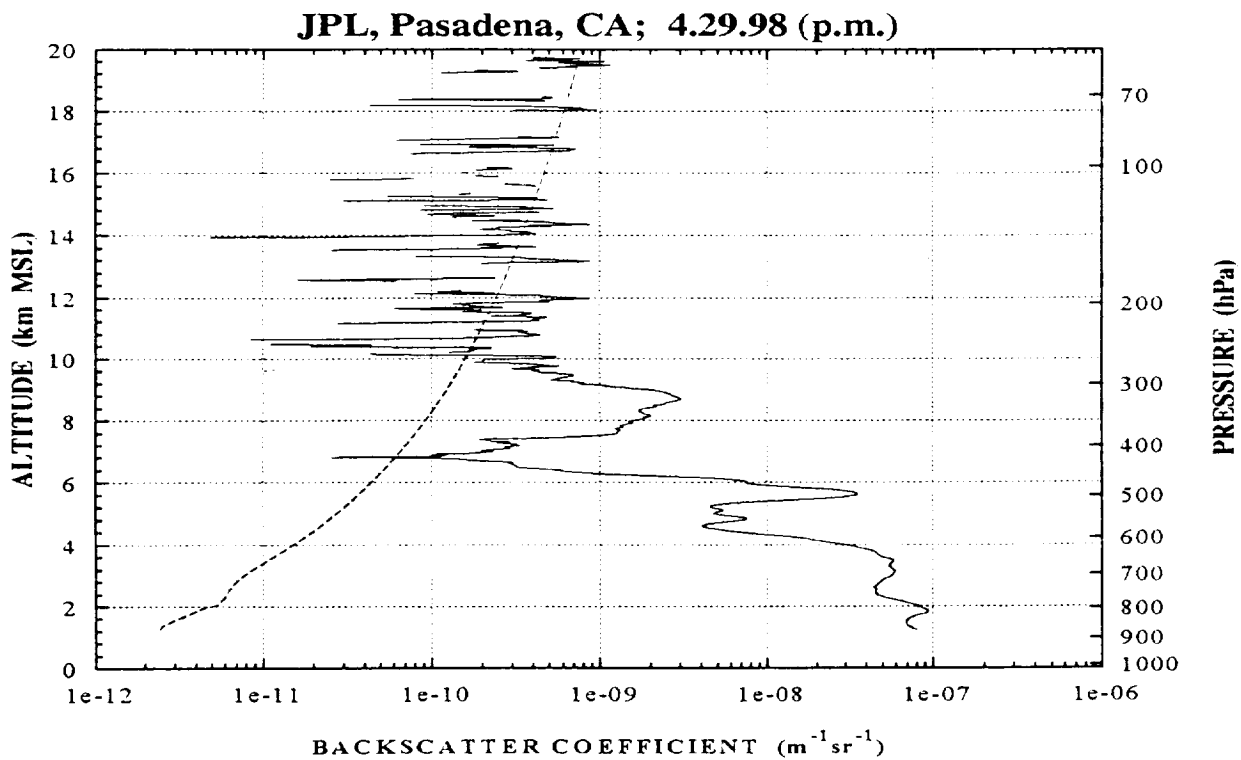


Figure 4. Vertically-resolved backscatter at the 10.6- μm JPL lidar operating wavelength acquired on May 29, 1998, at around 22:00 UTC. (The broken curve denotes the system sensitivity.)

For comparison, Figure 4 shows the JPL lidar profile obtained on the afternoon of April 29, 1998 at approximately 22:00 UTC. The thin strongly-scattering layer encountered at ~5.5 km MSL corresponds to the modeled centroid of the dust cloud, which appears at the 550 mbar level in the NAAPS simulation (Fig. 3). Although the elevated feature centered near 8.5 km MSL in Fig. 4 does not appear in the NAAPS simulation, air parcel back-trajectory analyses from this altitude zone flowed back to the dust generating region of China in 9-10 days (Fig. 5), coinciding with the passage through that region on April 19 of a rapidly moving shallow trough which, through analysis of surface observations and satellite imagery, has been identified as the chief progenitor of the eastward-transported dust (Westphal *et al.*, 1998).

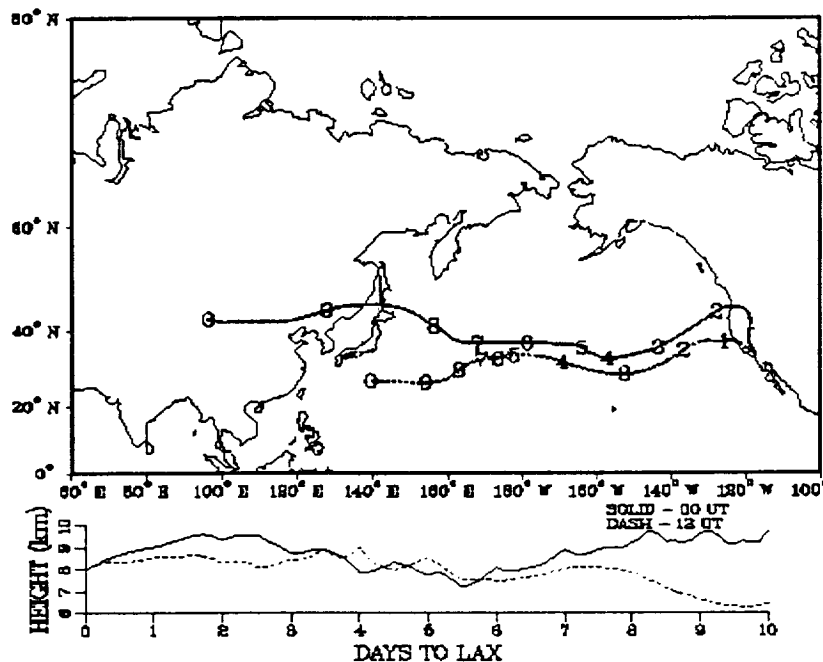


Figure 5. Air-parcel backtrajectory analysis from the 8-km MSL altitude level above the Los Angeles area on April 29, 1998.

Acknowledgments

Portions of this work were carried out by the Jet Propulsion Laboratory, California Institute of Technology, under contract with the National Aeronautics and Space Administration (NASA). Additional support was provided by NASA under contract NAS-97135. The support of the Office of Naval Research and the Naval Research Laboratory through programs PE-0602435N and PE-06-1153 is gratefully acknowledged. O. Dubovik and A. Smirnov of the NASA Goddard Space Flight Center AERONET team are gratefully acknowledged for provision and validation of aerosol size distribution retrievals. Air-parcel backtrajectory analyses were provided by R. Schnell and J. Harris at the NOAA Climate Monitoring and Diagnostics Laboratory.

References

- Husar, R. B., *et al.*, 1998: <http://capita.wustl.edu/Asia-FarEast/>
- Parungo, F., Z. Li, X. Li, D. Yang, and J. Harris, 1994: Gobi dust storms and The Great Green Wall. *Geophys. Res. Lett.*, **21**(11), 999-1002.
- Tratt, D. M., and R. T. Menzies, 1994: Recent climatological trends in atmospheric aerosol backscatter derived from the Jet Propulsion Laboratory multiyear backscatter profile database. *Appl. Opt.*, **33**(3), 424-430.
- Westphal, D. L., T. F. Hogan, and M. Liu, 1998: Dynamical Forcing of the Chinese Dust Storms of April 1998. Presented at the Fall Meeting of the American Geophysical Union, San Francisco, December 9-13, 1998.

A Global Backscatter Database for Modelling Space-Borne Doppler Wind Lidar

J.M. Vaughan, Defence Evaluation & Research Agency, Malvern, U.K.

A. Culoma, European Space Agency, Noordwijk, Netherlands

Pierre H. Flamant, Laboratoire Meteorologie Dynamique, Palaiseau, France

C. Flesia, University of Geneva, Geneva, Switzerland

N. Geddes, Defence Evaluation & Research Agency, Malvern, U.K.

The aim of this study is to provide a source reference compendium and database of atmospheric properties relevant to the design considerations of a space-borne Doppler Wind Lidar (DWL). The broad wavelength range under consideration is 0.35 μm to 10.6 μm . Within this range atmospheric aerosol backscatter coefficients at seven specific wavelengths: 0.35 μm , 0.53 μm , 1.06 μm , 1.5 μm , 2.1 μm , 9.1 μm and 10.6 μm are discussed on the basis of information derived from existing literature and the latest available material that has been documented and may be considered validated. The assessment also includes consideration of material presented and made available at meetings of the NOAA Working Group on Space-Based Lidar Winds held up until January 1998.

For the Atlantic region the most comprehensive database currently available at 10.6 μm is that of the SABLE and GABLE trials. These measurements were conducted in the historically clean period, 1988-1990, well after the El Chichon eruption but before the Mt Pinatubo event. They are thus likely to provide a background level of backscatter coefficients. The measurements of backscatter were made during 80 flights over the Atlantic in 6 different regions and/or seasons over a 3 year period. The material has been extensively analysed and presented in figures, histogram and tabular form. For the present work the data has been further evaluated and values of median, quartiles and deciles are shown in Table 1.

For the Pacific region measurements of backscatter were made in the GLOBE programme at a range of wavelengths, together with optical particle counter analysis of aerosols. In particular, data at 1.06 μm from the Globe II trial in Spring 1990 has been presented in medians, quartiles and deciles. Modelling has also been carried out on the particle counter measurements to provide backscatter values over the range 10.6 to 0.53 μm .

This and other material, together with general considerations of the impact of optical properties on a space-borne lidar, and analysis of backscatter scaling laws with wavelength are discussed. The overall conclusion is that the best currently available representation of the global atmospheric backscatter at different wavelengths is given by Table 1 scaled with the following equations.

The backscatter $\beta(\lambda, z)$ at wavelength λ and height z may be determined from:

$$\beta(\lambda, z) = \beta_o(10.6\mu\text{m}, z) \left[\frac{10.6\mu\text{m}}{\lambda(\mu\text{m})} \right]^\alpha \quad \text{.....1}$$

where $\beta_o(10.6\mu\text{m}, z)$ is the scattering (in Table 1) at $10.6\mu\text{m}$. The scaling exponent α that provides the best consensus for the wavelength range $0.35\mu\text{m} - 2.1\mu\text{m}$ is given by:

$$\alpha(\lambda(0.35-2.1\mu\text{m}), z) = 0.24 \left| \log_{10}(\beta_o(10.6\mu\text{m}, z)) \right| - 0.62 \quad \text{.....2}$$

For the wavelength $9.1\mu\text{m}$ account must be taken of the sharp resonances in refractive index for certain materials (notably sulphates) found in the atmosphere. For this wavelength a scaling exponent given by:

$$\alpha(9.1\mu\text{m}, z) = 1.25 \left| \log_{10}(\beta_o(10.6\mu\text{m}, z)) \right| - 8.25 \quad \text{.....3}$$

provides the best consensus fit.

Examination of data and isolated measurements in the literature shows reasonable agreement, generally within a factor of 2 and often better, of the backscatter values derived from Table 1 and Equations 1-3. They are thus presented as a useful measure of the global backscatter to be expected on currently available information over the range of wavelengths.

It should be noted that new material on atmospheric properties is of course continually being published and made available to the scientific and lidar community. The present work attempts to provide the best possible view of relevant atmospheric properties at the present time. Over the coming years it may be anticipated that further refinement of the data will be possible. In particular it may be hoped that experimental backscatter measurements for at least one shorter wavelength, made directly over many regions and seasons, will provide a truly authoritative global data

base for this waveband. Nevertheless on the basis of the available existing knowledge it is difficult to envisage any gross changes outside the spectrum of variability presently discussed and documented. As such it may be hoped that the present work will provide a source reference for some years to come.

Table 1: β (π , 10.6 μm) $\text{m}^{-1} \text{sr}^{-1}$, for the Atlantic region derived during the 'clean' atmospheric period 1988-90 and presented as a good measure of global backscatter at this wavelength

Height (Km)	Lower Decile	Lower Quartile	Median	Higher Quartile	Higher Decile
15-16	$< 4.0 * 10^{-12}$	$7.6 * 10^{-12}$	$1.7 * 10^{-11}$	$2.5 * 10^{-11}$	$6.8 * 10^{-11}$
14-15	$< 4.0 * 10^{-12}$	$6.8 * 10^{-12}$	$1.8 * 10^{-11}$	$3.2 * 10^{-11}$	$1.3 * 10^{-10}$
13-14	$\sim 5.0 * 10^{-12}$	$1.1 * 10^{-11}$	$2.3 * 10^{-11}$	$4.2 * 10^{-11}$	$1.8 * 10^{-10}$
12-13	$\sim 5.0 * 10^{-12}$	$1.3 * 10^{-11}$	$2.5 * 10^{-11}$	$4.9 * 10^{-11}$	$2.9 * 10^{-10}$
11-12	$\sim 5.0 * 10^{-12}$	$1.1 * 10^{-11}$	$2.7 * 10^{-11}$	$6.2 * 10^{-11}$	$4.5 * 10^{-10}$
10-11	$6.2 * 10^{-12}$	$1.4 * 10^{-11}$	$3.2 * 10^{-11}$	$1.3 * 10^{-10}$	$4.3 * 10^{-8}$
9-10	$6.2 * 10^{-12}$	$1.7 * 10^{-11}$	$3.5 * 10^{-11}$	$1.7 * 10^{-10}$	$3.0 * 10^{-8}$
8-9	$6.2 * 10^{-12}$	$1.7 * 10^{-11}$	$4.3 * 10^{-11}$	$2.0 * 10^{-10}$	$8.0 * 10^{-9}$
7-8	$6.3 * 10^{-12}$	$1.9 * 10^{-11}$	$4.4 * 10^{-11}$	$2.0 * 10^{-10}$	$2.6 * 10^{-9}$
6-7	$6.5 * 10^{-12}$	$2.0 * 10^{-11}$	$4.4 * 10^{-11}$	$2.0 * 10^{-10}$	$2.5 * 10^{-9}$
5-6	$9.0 * 10^{-12}$	$2.5 * 10^{-11}$	$5.7 * 10^{-11}$	$3.6 * 10^{-10}$	$8.1 * 10^{-9}$
4-5	$1.5 * 10^{-11}$	$3.8 * 10^{-11}$	$8.5 * 10^{-11}$	$5.6 * 10^{-10}$	$1.1 * 10^{-7}$
3-4	$2.6 * 10^{-11}$	$7.1 * 10^{-11}$	$1.9 * 10^{-10}$	$9.7 * 10^{-10}$	$9.5 * 10^{-8}$
2-3	$4.6 * 10^{-11}$	$1.4 * 10^{-10}$	$7.2 * 10^{-10}$	$6.6 * 10^{-9}$	$1.1 * 10^{-7}$
1-2	$1.9 * 10^{-10}$	$1.8 * 10^{-9}$	$2.2 * 10^{-8}$	$1.6 * 10^{-7}$	$1.6 * 10^{-6}$
0-1	$9.3 * 10^{-9}$	$4.1 * 10^{-8}$	$2.8 * 10^{-7}$	$1.6 * 10^{-6}$	$5.1 * 10^{-6}$

TARGET CALIBRATION: RETRO-REFLECTION MECHANISMS AT 2 μm

David A. Haner and David M. Tratt
Jet Propulsion Laboratory
California Institute of Technology
4800 Oak Grove Drive
Pasadena, CA 91109

INTRODUCTION

With the growing use of 2- μm eye-safe solid-state laser transmitters in coherent Doppler lidar applications, there is increased interest in the reflectance properties of hard target calibration materials at this wavelength. One of the factors to be considered is the polarization characteristic of the transmitter/receiver. The two fundamental lidar systems are either based upon the backscattering of linearly polarized or circularly polarized light (Kavaya, 1987). Consequently, the response of calibration materials to the particular state of polarization of the incident radiation is an important consideration. Ideally the calibration materials should have a similar reflectance response to that of the remote scattering medium that is being observed. Also the material should be most efficiently adapted to the polarization characteristics of the lidar system.

There are two measurement parameters that are useful in presenting the characteristics of polarization of reflecting materials (see References). The first is the linear polarization ratio: $\mu_l = I_{ol}/I_{sl}$, where ol denotes opposite linear and sl denotes same linear. The second is circular polarization ratio: $\mu_c = I_{sc}/I_{oc}$, where ol denotes opposite circular and sc denotes same circular. Notice that the ratios are inverted with respect to same polarization. It is the relative values of these polarization ratios that are used to characterize the retro-reflectance mechanism.

Measurement of these parameters is conveniently obtained by using the Stokes vectors corresponding to the polarized backscatter at and near the retro-angle.

RETRO-REFLECTION MECHANISMS

Two distinct processes are recognized as contributing to the retro-reflection mechanism: shadow hiding and coherent backscattering.

Shadow hiding

This type of backscattering is thought to be caused by single scattering from a particle or surface into the backward direction and tends to preserve the plane of linear polarization. However, it would reverse the handedness of circularly polarized light. Generally the forward scattered light preserves the plane of linear polarization and retains the handedness of circularly polarized light. It is clear that both μ_l and μ_c should tend to increase with scattering angles less than 180°.

Coherent backscattering

This type of backscattering is thought to be caused by multiple scattering of light. The result of multiple scattering of linearly polarized light will tend not to change the plane of polarization; thus the scattering angle dependence will appear similar for either process. However, the handedness of circularly polarized light will reverse on each impact; thus μ_c will decrease for smaller scattering angle. To distinguish between which of these mechanisms is most effective when light is incident on a particular backscattering material; the magnitudes of μ_c at the retro-angle and a few degrees off-retro need to be measured for various materials with differing surface and bulk properties.

There is another property of the retro-peak that characterizes these two mechanisms in the backscatter process, this being the angular width of the retro-peak. The shadow hiding mechanism is generally characterized by a broad peak, whereas the coherent backscattering mechanism gives rise to a very narrow peak (Gu *et al.*, 1993).

EXPERIMENT

The 2.06- μm solid state laser radiation is incident on a quarter-wave plate oriented with its optical axis at 45° with respect to the horizontal plane of polarization. This right circularly polarized beam is incident onto a 50% beamsplitter at 45° to the beam. The reflected radiation from the beamsplitter is incident onto the reflecting material set at 45° to the beam. The retro-reflected radiation is incident onto a polarimeter composed of a rotatable quarter wave plate and a linear polarizer placed before a PbS detector. The detector signal was phase detected with reference to the chopped beam. The final data were the four components of the Stokes vector for the reflected radiation.

RESULTS

Data from a selected set of calibration materials currently undergoing characterization are presented in Table 1.

MATERIAL	μ_i (retro)	μ_i (off-retro)	μ_c (retro)	μ_c (off-retro)	MECHANISM
Sulfur/acetone	0.45	0.92	1.34*	1.01	shadow/coherent
Styrofoam, HD	0.47	0.85	0.935	0.952	shadow/?
Flame-sprayed Al	0.23	0.24	0.738	0.428	?/coherent

(Not completely reversed)

Table 1. Polarization ratios for selected target materials.

These results show that for the sulfur target both mechanisms appear to be active. By contrast, the Styrofoam measurements indicate no contribution from the coherent mechanism, whereas the converse situation applies for the case of flame-sprayed aluminum. These findings suggest that there are other physical properties, such as the scattering mean free path (Peters, 1992), which need to be defined in order to clarify the importance of the backscatter mechanism.

ACKNOWLEDGMENT

This work was performed at the Jet Propulsion Laboratory, California Institute of Technology, under contract with the National Aeronautics and Space Administration.

REFERENCES

- Gu, Z. -H., J. Q. Lu, A. A. Maradudin, A. Martinez, and E. R. Mendez (1993): Coherence in the single and multiple scattering of light from randomly rough surfaces. *Appl. Opt.* **32**, 2852-2859.
- Hapke, B. W., R. M. Nelson, and W. D. Smythe (1993): The opposition effect of the Moon: The contribution of coherent backscatter. *Science* **260**, 509-511.
- Kavaya, M. J. (1987): Polarization effects on hard target calibration of lidar systems. *Appl. Opt.* **26**, 796-804.
- MacKintosh, F. C., and S. John (1988): Coherent backscattering of light in the presence of time-reversal-noninvariant and parity-nonconserving media. *Phys. Rev. B.* **37**, 1884-1897.

Ostro, S. J., and E. M. Shoemaker (1990): The extraordinary radar echoes from Europa, Ganymede, and Callisto: A geological perspective. *Icarus* **85**, 335-345.

Peters, K. J., (1992): Coherent-backscatter effect: A vector formulation accounting for polarization and absorption effects and small or large scatterers. *Phys. Rev. B.* **46**, 801-812.

Pitter, M., E. Jakeman, and M. Harris (1997): Heterodyne detection of coherent backscatter. *Opt. Lett.* **22**, 393-395.

Backscatter modeling at 2.1micron wavelength for space-based and airborne lidars using aerosol physico-chemical and lidar datasets

V. Srivastava¹, J. Rothermel², M.A. Jarzembki², A.D. Clarke³, D.R. Cutten⁴, D.A. Bowdle⁴, J.D. Spinhirne⁵, and R.T. Menzies⁶

1 Global Hydrology and Climate Center, University Space Research Association, Huntsville, AL 35806; 2 Global Hydrology and Climate Center, NASA, Huntsville, AL; 3 University of Hawaii, Honolulu, HI; 4 Global Hydrology and Climate Center, UAH, Huntsville, AL; 5 NASA Goddard Space Flight Center, Greenbelt, MD; 6 Jet Propulsion Laboratory, NASA, Pasadena, CA

1. Introduction

Space-based and airborne coherent Doppler lidars designed for measuring global tropospheric wind profiles in cloud-free air rely on backscatter, β , from aerosols acting as passive wind tracers. Aerosol β distribution in the vertical can vary over as much as 5-6 orders of magnitude (Rothermel et al., 1989; 1996a, Srivastava et al., 1997; Tratt et al., 1994; Spinhirne et al., 1997; Jarzembki et al., 1999). Thus, the design of a wavelength-specific, space-borne or airborne lidar must account for the magnitude of β in the region or features of interest.

The SPACE Readiness Coherent Lidar Experiment (Kavaya et al. 1998), under development by the National Aeronautics and Space Administration (NASA) and scheduled for launch on the Space Shuttle in 2001, will demonstrate wind measurements from space using a solid-state 2 μm coherent Doppler lidar. Consequently, there is a critical need to understand variability of aerosol β at 2.1 μm to evaluate signal detection under varying aerosol loading conditions. Although few direct measurements of β at 2.1 μm exist, extensive datasets, including climatologies in widely-separated locations, do exist for other wavelengths based on CO₂ and Nd:YAG lidars ((Rothermel et al. 1989; 1996a, Tratt et al., 1994; Menzies et al., 1997; Spinhirne et al., 1997). Datasets also exist for the associated microphysical and chemical properties. An example of a multi-parametric dataset is that of the NASA GLOBAL Backscatter Experiment (GLOBE) in 1990 (Bowdle and Fitzjarrald; 1987), in which aerosol chemistry and size distributions (Clarke et al. 1993) were measured concurrently with multi-wavelength lidar backscatter observations. More recently, continuous-wave (CW) lidar backscatter measurements at mid-infrared wavelengths have been made during the Multicenter Airborne Coherent Atmospheric Wind Sensor (MACAWS) experiment in 1995 (Jarzembki et al. 1999). Using Lorenz-Mie theory, these datasets have been used to develop a method to convert lidar backscatter to the 2.1 μm wavelength. This paper presents comparison of modeled backscatter at wavelengths for which backscatter measurements exist including converted $\beta_{2.1}$.

2. Measurements

The GLOBE datasets consist of 15 flights over the Pacific Ocean on NASA's DC-8 aircraft. For β modeling and intercomparison, datasets primarily from flight#12 (F12) were used. This 7.5hr flight from Darwin, Australia, to Tokyo, Japan, occurred on May 31, 1990. Several datasets from the following instruments were used. (i) University of Hawaii's Laser Optical Particle Counter (LOPC) provided thermally-differentiated aerosol size distributions during GLOBE from which different aerosol compositions were inferred (Clarke, 1993) and used to model aerosol β at various wavelengths (Srivastava et al., 1997). (ii) Two NASA/MSFC Continuous Wave (CW) focused 9.1 and 10.6 μm CO₂ lidars obtained high-resolution, high sensitivity β data (Rothermel et al., 1996b) concurrent with the LOPC microphysics data during GLOBE, enabling excellent intercomparison with aerosol β modeling (Srivastava et al., 1997). These lidars also obtained β in 1995 during 9 flights in MACAWS, over the western coastal regions of North America and California, comprising ~ 52 flight hours of data. (iii) NASA/GSFC pulsed Nd:YAG 0.53 and 1.06 μm lidar and NASA/JPL Pulsed CO₂ 9.25 μm lidar measured high-resolution, vertical aerosol β profiles (Spinhirne et al., 1997; Menzies et al., 1997) during GLOBE. β near the aircraft from pulsed lidars provided comparison with modeled β using LOPC aerosol microphysics and with the CW lidars.

3. Modeling

Aerosol β_λ at a given wavelength (λ) is a function of particle composition (complex refractive index, m), size (r), and number concentration (N_0). In general, if m , r , N_0 , were well-determined, then β_λ can be obtained for any λ (Srivastava et al., 1992, 1997). Assuming spherical particle shape allows the use of Lorenz-Mie scattering theory. Furthermore, aerosols can have very different composition with differing m which in turn depends on λ . These compositions can be pure, partially mixed, or completely mixed. Different aerosol loading conditions require

different mixing assumptions. In this paper two models are used, which are described in detail in Srivastava et al. (1997). For clean to moderate loading conditions, a simple internal mixed phase sulfate model was used where the sulfuric acid and ammonium sulfate components are mixed together, while the dust component remains unmixed. For high aerosol loading conditions, (e.g. PBL) with aged coarse aerosols, an internally mixed composite was used where all the components are mixed together.

4. Intercomparison with lidar data

Since no β measurements at 2.1 μm exist with concurrent aerosol size distribution data, modeled β_λ must be compared with simultaneous lidar β_λ measurements to validate the modeling. This step is essential to establish the validity of the technique for conversion to $\beta_{2.1}$. Comparison at shorter λ 's, where nonsphericity may play a stronger role, provides a rudimentary check for the sphericity assumption, while comparison at longer infrared λ 's, where heterogeneous composition effect is better observed, validates the mixing models (Srivastava et al., 1997).

Time series plots of both modeled and measured β_λ at selected λ for F12 are shown in Fig. 1. Figure 1(a)

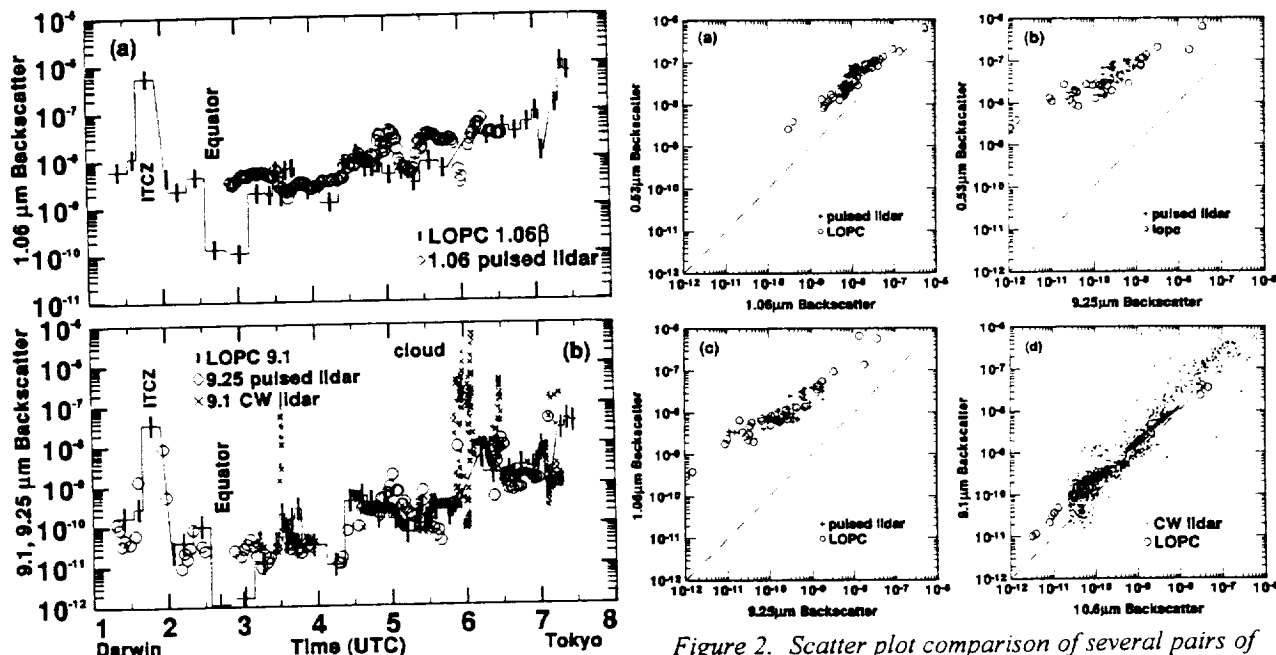


Figure 1. Comparison of measured lidar β with modeled β using measured LOPC size distribution from GLOBE F12 going from Darwin, Australia, to Tokyo, Japan, on May 31, 1990

Figure 2. Scatter plot comparison of several pairs of wavelengths for F12 between lidar β and modeled β : (a) 0.53 - 1.06 μm β , (b) 0.53 - 9.25 μm β , (c) 1.06 - 9.25 μm β , and (d) 9.1 - 10.6 μm β .

shows good comparison of $\beta_{1.06}$ at the Nd:YAG wavelength. The equatorial region showed low β_λ , (with short spike in the ITCZ region), slowly increasing to moderate loading in the subtropics, and high β_λ loading in an Asian dust plume advected over the Pacific Ocean. Figure 1(b) shows modeled β_λ at longer infrared wavelength using LOPC compared to the measurements with JPL's 9.25 μm CO_2 pulsed lidar $\beta_{9.25}$ data and the MSFC's CW lidar $\beta_{9.1}$. Except where some scattered clouds were encountered, there is excellent agreement. These results show that the effect of aerosol composition, most noticeable in the infrared, is properly modeled using the LOPC data. Scatter plots of β_λ between two wavelengths, obtained from either a single instrument or a pair of instruments with similar sampling characteristics, are shown in Fig.2. The wavelength pair measured by the pulsed lidars is then compared with the same pair modeled by the LOPC, giving excellent agreement over several orders of magnitude of β_λ .

5. Wavelength dependence of backscatter

Figure 3 shows the λ -dependence of β_λ as a 3-D grey-shaded surface from 0.3 to 12 μm during F12. Each shade spans a difference of 0.5 on the log (β_λ) scale with 12 shades covering the range of $-12 < \log(\beta) < -6$. Though this data is taken mostly at ~ 8 km altitude, this figure shows both widely varying aerosol loading and widely varying λ -dependence. The changes in the inclination of the surface plot show the $\beta_\lambda - \lambda$ variation for different aerosol

loading conditions encountered at different locations. In the clean conditions (e.g. Equator and subtropics), $\beta_\lambda - \lambda$ surface is the steepest indicating maximum λ -dependence. In contrast, in higher aerosol loading (e.g. ITCZ and near Tokyo) this surface is not so steep indicating weaker λ -dependence. The complex λ -dependence is due to material resonances in the refractive indices at certain infrared wavelengths which enhance the β_λ , like at 9.1 μm . Hence, the λ -dependence cannot be simply averaged. Only specific comparisons between β_λ at different wavelengths can quantify the effect of λ on β_λ . Thus, for weak loading, $\beta_{2.1}$ is about 10 to 20 times higher than $\beta_{9.1}$ giving $\beta \sim \lambda^{-1.5}$ to $\beta \sim \lambda^{-2.2}$, respectively. For strong loading, $\beta_{2.1}$ is a factor of 3 to 5 times higher than $\beta_{9.1}$ giving $\beta \sim \lambda^{-1}$. These experimental relationships agree well with the theoretical λ -dependence predicted (Srivastava et al., 1992).

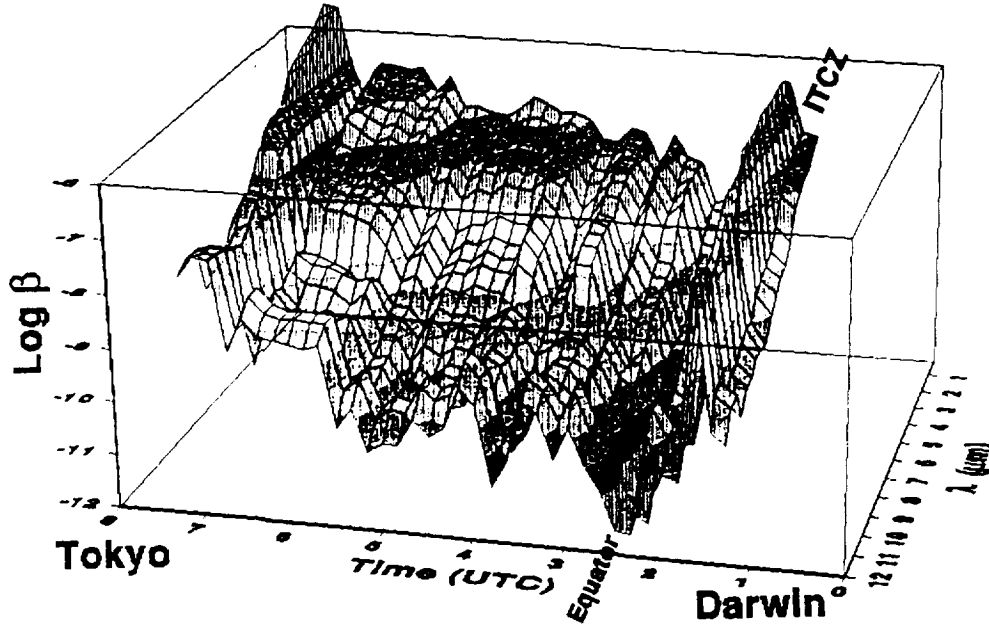


Figure 3. A 3-D grey-shaded surface representation of calculated λ -dependence of β using measured LOPC, size distribution data obtained during GLOBE flight F12 from Darwin, Australia, to Tokyo, Japan, on May 31, 1990.

6. Conversion to 2.1 μm backscatter

Figure 3 shows the λ -dependence of β_λ can be quite complex; conversion from one wavelength to another cannot be obtained by a simple linear extrapolation. Hence, an empirical conversion function for each wavelength-pair has been developed that takes into account the change in λ -dependence as a function of the magnitude of β_λ . Scatter plots, using LOPC size distribution data, are shown in Fig. 4 between β_λ at a specific lidar λ and $\beta_{2.1}$, in order to get a proper conversion functions. Each function is represented by a best-fitted, second-order polynomial curve drawn through data points associated with each wavelength combination ($\beta_\lambda - \beta_{2.1}$) nonlinear regression analysis. Functional relationship between β_λ and $\beta_{2.1}$ for each curve is given by:

$$\log \beta_{2.1} = a_\lambda (\log \beta_\lambda)^2 + b_\lambda (\log \beta_\lambda) + c_\lambda, \quad (1)$$

where coefficients a_λ , b_λ , and c_λ for selected λ 's are given in Table 1. Figure 5 shows histograms of converted $\beta_{2.1}$.

Table 1: Coefficients for β_λ conversion to $\beta_{2.1}$.

λ (μm)	a_λ	b_λ	c_λ
0.53	0.02305	1.709	2.793
1.06	0.02175	1.557	2.346
9.1	0.01385	1.142	1.115

The data were normalized to remove any vertical biasing due to sampling. Fig. 5a shows converted $\beta_{2.1}$ data from 9.1 μm CW lidar data for all GLOBE flights. This showed a midtropospheric aerosol background mode of $\beta_{2.1} \sim 8 \times 10^{-10}$ and a marine boundary layer (MBL) mode of $\beta_{2.1} \sim 2 \times 10^{-7} \text{ m}^{-1} \text{ sr}^{-1}$. Fig. 5a also shows the converted $\beta_{2.1}$ from the 1.06 μm pulsed lidar data giving a background mode of $\beta_{2.1} \sim 3 \times 10^{-10} \text{ m}^{-1} \text{ sr}^{-1}$ and MBL mode of $\beta_{2.1} \sim 10^{-7} \text{ m}^{-1} \text{ sr}^{-1}$. Fig. 5b shows MACAWS 9.1 μm CW lidar data converted to $\beta_{2.1}$. This data is representative of a coastal area showing midtropospheric background mode of $\beta_{2.1} \sim 1.3 \times 10^{-9} \text{ m}^{-1} \text{ sr}^{-1}$ and a boundary layer mode of $\beta_{2.1} \sim 10^{-7}$ to $10^{-6} \text{ m}^{-1} \text{ sr}^{-1}$, which are slightly higher than GLOBE modal values.

7. Conclusion

Wavelength-dependent backscatter conversion functions have been obtained and validated using direct β measurements over an order of magnitude wavelength range. It is now possible to convert measured backscatter at an arbitrary wavelength to $2.1\mu\text{m}$, the design wavelength for SPARCLE, as part of the pre-flight simulation studies and on-orbit performance assessments. These results indicate an average mid-tropospheric backscatter background mode of $\beta_{2.1} \sim 8 \times 10^{-10}$ and a boundary layer mode between $\beta_{2.1} \sim 10^{-7}$ to $10^{-6} \text{ m}^{-1}\text{sr}^{-1}$. Our technique may be extended to other prospective lidar design wavelengths where direct backscatter measurements are lacking.

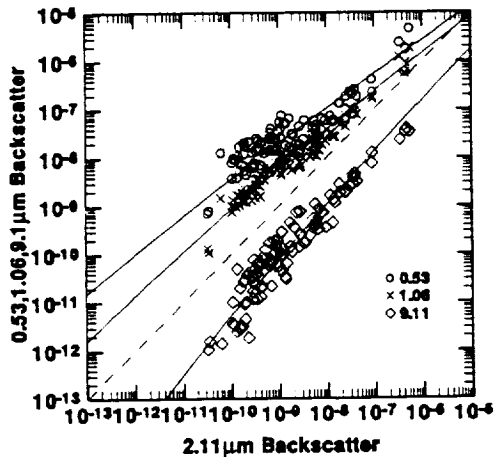


Figure 4. Several $\beta(\lambda)$ comparisons with $\beta_{2.1}$. Curves give second-order polynomials of Eq. 1.

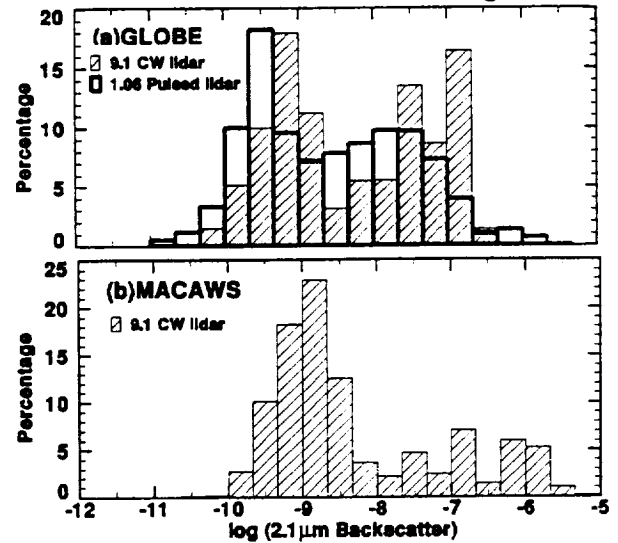


Figure 5. Histograms of converted $\beta_{2.1}$

Acknowledgments: We gratefully acknowledge the support of Dr. Ramesh Kakar, NASA Office of Earth Science.

References

- Bowdle, D. A., and D. E. Fitzjarrald, "The GLOBal Backscatter Experiment (GLOBE) program," *Technical Digest, Topical Meeting on Coherent Laser Radar*, Aspen, CO, Opt. Soc. Amer., **16**, 103-111 (1987).
- Clarke, A. D., "Atmospheric nuclei in the Pacific midtroposphere: their nature, concentration, and evolution", *J. Geophys. Res.*, **98**, 20,633-20,647, (1993).
- Jarzembski, M. A., V. Srivastava, and J. Rothermel, "Vertical aerosol variability from an airborne focused continuous wave CO_2 lidar", *Applied Optics: Lasers Photonics and Environment Optics*, (1999).
- Kavaya, M.J. and G.D. Emmitt, "The Space Readiness Coherent Lidar Experiment (SPARCLE) Space Shuttle Mission," invited paper 3380-02, Conf. Laser Radar Technol. Applic. III, 12th Ann. Intl. Symp. Aerospace / Defense Sensing, Simulation, and Controls, AeroSense, 14 Apr, Orlando, FL, *Proc. SPIE*, **3380**, 2-11 (1998).
- Menzies, R.T., and D.M. Tratt, "Airborne lidar observations of tropospheric aerosols during Global Backscatter Experiment (GLOBE) Pacific circumnavigation missions of 1989 & 1990," *J. Geophys. Res.* **102**, 3701-3714 (1997).
- Rothermel, J., D. A. Bowdle, J. M. Vaughan, and M. J. Post, "Evidence of a tropospheric aerosol backscatter background mode," *Appl. Opt.* **28**, 1040-1042 (1989).
- Rothermel, J., D.A. Bowdle, and V. Srivastava, "Mid-tropospheric aerosol backscatter background mode over the Pacific Ocean at $9.1 \mu\text{m}$ wavelength," *Geophys. Res. Lett.*, **23**, 281-284 (1996a)
- Rothermel, J., D. M. Chambers, M. A. Jarzembski, V. Srivastava, D. A. Bowdle, and W. D. Jones, "Signal processing and calibration of continuous-wave CO_2 Doppler lidars for atmospheric backscatter measurement," *Appl. Opt.* **35**, 2083-2095 (1996b).
- Spinhirne, J.D., S. Chudamani, J.F. Cavanaugh, and J.L. Bufton, "Aerosol and cloud backscatter at 1.06, 1.54, and $0.53 \mu\text{m}$ by airborne hard-target-calibrated Nd:YAG/methane Raman lidar," *Appl. Opt.* **36**, 3475-3490 (1997).
- Srivastava, V., M. A. Jarzembski, and D. A. Bowdle, "Comparison of calculated aerosol backscatter at 9.1 and $2.1 \mu\text{m}$ wavelengths", *Appl. Opt.: Lasers, Photonics and Environ. Opt., Rapid Comm.*, **31**(12), 1904 (1992).
- Srivastava, V., A.D. Clarke, M.A. Jarzembski, and J. Rothermel, "Comparison of modeled backscatter using measured aerosol microphysics with focused CW lidar data over Pacific," *J. Geophys. Res.* **102**, 16,605-16,617 (1997).
- Tratt, D. M., and R. T. Menzies, "Recent climatological trends in atmospheric aerosol backscatter derived from the Jet Propulsion Laboratory multiyear backscatter profile database," *Appl. Opt.* **33**, 424-430 (1994).

Comparison of Predicted and Measured 2 μm Aerosol Backscatter from the 1998 ACLAIM Flight Tests

David A. Bowdle

*University of Alabama in Huntsville
Global Hydrology and Climate Center
977 Explorer Boulevard
Huntsville, Alabama USA 35806*

Voice: 205-922-5955, Fax: 205-922-5723, e-mail: David.Bowdle@msfc.nasa.gov

Stephen M. Hannon

*Coherent Technologies, Inc.
Lafayette, Colorado USA*

Rodney K. Bogue

*NASA Dryden Flight Research Center
Edwards, California USA*

ABSTRACT

The 1998 Airborne Coherent Lidar for Advanced Inflight Measurements (ACLAIM) flight tests were conducted aboard a well-instrumented research aircraft. This paper presents comparisons of 2 μm aerosol backscatter coefficient predictions from aerosol sampling data and mie scattering codes with those produced by the ACLAIM instrument.

POSTER SESSION

The NASA/MSFC Coherent Lidar Technology Advisory Team

Michael J. Kavaya

NASA Marshall Space Flight Center

Global Hydrology and Climate Center, Mail Code HR20

Huntsville, Alabama 35812 USA

michael.kavaya@msfc.nasa.gov

256-922-5803

Introduction

The SPACe Readiness Coherent Lidar Experiment (SPARCLE) mission was proposed as a low-cost technology demonstration mission, using a 2-micron, 100-mJ, 6-Hz, 25-cm, coherent lidar system based on demonstrated technology.^{1,2} SPARCLE was selected in late October 1997 to be NASA's New Millennium Program (NMP) second earth-observing (EO-2) mission. To maximize the success probability of SPARCLE, NASA/MSFC desired expert guidance in the areas of coherent laser radar (CLR) theory, CLR wind measurement, fielding of CLR systems, CLR alignment validation, and space lidar experience.

This led to the formation of the NASA/MSFC Coherent Lidar Technology Advisory Team (CLTAT) in December 1997. A threefold purpose for the advisory team was identified as: 1) guidance to the SPARCLE mission, 2) advice regarding the roadmap of post-SPARCLE coherent Doppler wind lidar (CDWL) space missions and the desired matching technology development plan³, and 3) general coherent lidar theory, simulation, hardware, and experiment information exchange.

The current membership of the CLTAT is shown in Table 1. Membership does not result in any NASA or other funding at this time.

We envision the business of the CLTAT to be conducted mostly by email, teleconference, and occasional meetings. The three meetings of the CLTAT to date, in Jan. 1998, July 1998, and Jan. 1999, have all been collocated with previously scheduled meetings of the Working Group on Space-Based Lidar Winds, chaired by Dr. Wayman E. Baker⁴.

The meetings have been very productive. Topics discussed include the SPARCLE technology validation plan including pre-launch end-to-end testing, the space-based wind mission roadmap beyond SPARCLE and its implications on the resultant technology development, the current values and proposed future advancement in lidar system efficiency, and the difference between using single-mode fiber optical mixing vs. the traditional free space optical mixing.

Position Paper

An additional undertaking of the CLTAT is the writing of a position paper on various CLR topics.⁵ The initial motivation for the position paper was to obtain consensus and agreement from the CLTAT members, and provide documentation thereof, of various CDWL measurement issues important to the SPARCLE mission. The position paper has since been expanded to include topics of importance to both the future space wind missions, and to coherent lidar remote sensing in general. It also lists references that discuss each subject. Some of the topics in the current draft of the position paper are listed in Table 2.

The CLTAT members are contributing to the discussion, the topic selection, the writing, and the editing of the position paper. The various subjects are in widely different stages of completion. A draft will be available to the conference attendees for comments.

References

1. M.J. Kavaya and G. D. Emmitt, "The Space Readiness Coherent Lidar Experiment (SPARCLE) Space Shuttle Mission," Proc. SPIE Vol. 3380, p. 2-11, Conference on Laser Radar Technology and Applications III, 12th Annual International Symposium on Aerospace/Defense Sensing, Simulation, and Controls, AeroSense, Orlando, FL (14 April 1998).
2. The SPARCLE WWW page is at: <http://www.ghcc.msfc.nasa.gov/sparcle/>
3. M. J. Kavaya and G. D. Emmitt, "Tropospheric Wind Measurements From Space: The SPARCLE Mission And Beyond," Digest of the 19th International Laser Radar Conference (ILRC), p 553. NASA/CP-198-207671/PT2. Annapolis, MD USA (July 1998).
4. For information, contact Dr. Wayman E. Baker, NOAA/NWS/NCEP, at 301-763-8019 or at wayman.baker@noaa.gov
5. "Position Paper Of NASA's Coherent Lidar Technology Advisory Team," edited by M. Kavaya, unpublished (1999).

TABLE 1. CLTAT MEMBERS			
1.	Steven B. Alejandro	USAF/AFRL	alejands@smtpgw1.plk.af.mil
2.	Farzin Amzajerjian	UAH/CAO	Farzin.Amzajerjian@msfc.nasa.gov
3.	Jack L. Bufton	NASA/GSFC	jack.bufton@gsfc.nasa.gov
4.	Charles A. DiMarzio	Northeastern University	cdimarzio@lynx.neu.edu
5.	G. David Emmitt	Simpson Weather Associates, U. VA	gde@thunder.swa.com
6.	Pierre H. Flamant	LMD, Ecole Polytechnique	flamant@lmdx04.polytechnique.fr
7.	Rod G. Frehlich	U. CO/CIRES	rgf@cires.colorado.edu
8.	R. Michael Hardesty	NOAA/ETL	mhardesty@etl.noaa.gov
9.	Sammy W. Henderson	Coherent Technologies, Inc.	sammy@ctilidar.com
10.	Steve C. Johnson	NASA/MSFC	Steve.Johnson@msfc.nasa.gov
11.	Gary W. Kamerman	FastMetrix, Inc.	gary.kamerman@ibm.net
12.	Michael J. Kavaya	NASA/MSFC	michael.kavaya@msfc.nasa.gov
13.	Robert T. Menzies	NASA/JPL	rtn@lrs.jpl.nasa.gov
14.	Madison J. Post	NOAA/ETL	mpost@etl.noaa.gov
15.	Barry J. Rye	U. CO/CIRES	brye@etl.noaa.gov
16.	Upendra N. Singh	NASA/LARC	u.n.singh@larc.nasa.gov
17.	Gary D. Spiers	UAH/CAO	Gary.D.Spiers@msfc.nasa.gov
18.	Christian Werner	DLR (German Aerospace Establishment)	christian.werner@dlr.de
19.	David V. Willetts	DERA	dwillets@dera.gov.uk
20.	David M. Winker	NASA/LARC	d.m.winker@larc.nasa.gov

TABLE 2. CLTAT POSITION PAPER SUBJECTS
Signal-to-Noise Ratio (SNR) Equation
Shot Accumulation For Wind Measurement
Effect Of Single Shot Observation Time (Range Gate Length) On Wind Measurement
Effect On Wind Measurement Performance As Aerosol Backscatter Decreases
Effect Of Using A Fiber Receiver vs. Free Space Mixing
Difference Between Theoretical And Experimental SNR
Effect Of Refractive Turbulence On Space-Based CDWL
Correct Receiver Direction Given Translation Of Space-Based CDWL
Benefits Of Using A Balanced Detector
Optimum Beam Sizes
Improved SNR From Using Customized LO Field
Definitions Of CDWL System Efficiency
Optical Preamplifier
Combining Multiple Transmitter Laser Beams
Combining Multiple Receiver Apertures
Effect Of Interaction Of Polarized Light Coherent Lidars With Aerosol Backscatter Mueller Matrix Elements
Linkage Of Optical Subsystem Aberrations And Position Errors To Lidar System Efficiency/SNR
Explanation Of Terms

Pre-Launch End-To-End Testing Plans for the SPace Readiness Coherent Lidar Experiment (SPARCLE)

Michael J. Kavaya

NASA Marshall Space Flight Center

Global Hydrology and Climate Center, Mail Code HR20

Huntsville, Alabama 35812 USA

michael.kavaya@msfc.nasa.gov

256-922-5803

Introduction

The SPace Readiness Coherent Lidar Experiment (SPARCLE) mission was selected in late October 1997 to be NASA's New Millennium Program (NMP) second earth-observing (EO-2) mission.^{1, 2} The SPARCLE mission is managed by NASA Marshall Space Flight Center (MSFC), which is providing project management, mission and science requirements, instrument engineering, instrument integration, and space qualification. Key SPARCLE partners include the NASA Langley Research Center (LaRC) for the pulsed solid-state laser technology, the NASA Jet Propulsion Laboratory (JPL) for the tunable continuous-wave solid-state laser technology, the University of Alabama in Huntsville Center for Applied Optics (UAH/CAO) for optomechanical design, Coherent Technologies, Inc. (CTI) for the flight laser subsystem, and Simpson Weather Associates (SWA) for science guidance. SPARCLE will utilize the NASA Hitchhiker (HH) program, managed by the NASA Goddard Space Flight Center (GSFC) for riding on the space shuttle. The SPARCLE lidar is nominally a 2-micron, 100-mJ, 6-Hz, 25-cm, conically step-stare scanning (30-deg. nadir angle) coherent lidar system based on demonstrated technology.

SPARCLE is intended to be the first step in providing global tropospheric wind vector profiles to NASA, NOAA, and other agencies. The goals of SPARCLE are: 1) to demonstrate that the coherent Doppler wind lidar (CDWL) technology and technique can provide the desired future wind measurements, 2) to validate wind measurement performance prediction models for use in assessing proposed future follow-on missions, and 3) to measure characteristics of the atmosphere, clouds, and earth surface for optimum design of future missions³.

In order to achieve these goals, the SPARCLE lidar must be successful in two distinct areas. First, the quality of each optical component, and the integration and alignment of all the components, must be sufficient to achieve or exceed a lidar sensitivity that allows adequate signal-to-noise ratio (SNR). Second, with adequate SNR, the requirement to demonstrate high accuracy wind measurement must be met. (Adequate SNR is a necessary, but not sufficient, requirement for accurate wind measurement.) A combination of specifications on the lidar instrument, its attachment to the shuttle, use of position and

attitude information from lidar and non-lidar sensors, and pointing knowledge algorithms will meet this second requirement.

The topic of this paper is the pre-launch demonstration of the first requirement, adequate sensitivity of the SPARCLE lidar.

Sensitivity Requirement

The SPARCLE lidar sensitivity requirement reflects a compromise between the need to keep cost and risk low by utilizing demonstrated technology and the limited accommodation resources of a shuttle/HH mission, and the need to measure the wind frequently and accurately enough throughout the troposphere to achieve the mission goals. The requirement on the SPARCLE lidar is sensitivity to aerosol backscatter of $5 \times 10^{-6} \text{ m}^{-1} \text{ sr}^{-1}$ or better (lower). This corresponds to lidar system efficiency (LSE) of approximately 1%. (Note that the coherent lidar community has not converged on a single definition of LSE. We define it here as the dimensionless quantity obtained by starting with SNR and backing out the “noise” term $h\nu B$, and the terms for laser pulse energy, aerosol backscatter coefficient, receiver area, 2-way atmospheric transmission, range to the target, and the speed of light factor $c/2$. This is an “absolute” and not a “relative” or “normalized” definition. The LSE can theoretically approach values near 0.4^{4,5}.) The assumptions that accompany the aerosol backscatter requirement are: 300-km orbit height, target aerosol 1 km above ground level, 30-deg. laser beam nadir angle at the shuttle (leading to 31.6-deg. nadir angle at the target and 348-km range to the target for a spherical earth), 0.84 1-way atmospheric intensity transmission, 250-m processed data vertical resolution, 20-m/s or ± 10 -m/s horizontal wind velocity search space (a priori knowledge), single shot wind velocity estimate, and 50% probability of obtaining a “good” estimate⁶.

The aerosol backscatter coefficient requirement is simply a performance benchmark. It does not indicate that wind can not be measured in atmospheric regions with lower values. For example, accumulating 50 lidar shots for each wind measurement, and employing a processed data vertical resolution of 2000 m yields good wind velocity estimates 90% of the time in air with an order of magnitude less aerosol backscatter. These operating parameters allow 8 line-of-sight (LOS) wind measurements to be combined into 4 vector wind measurements for each 100 km of shuttle forward motion. Greater shot accumulation would allow measurement in even “cleaner” air.

Test Options

The options available for testing SPARCLE LSE prior to launch were examined and contrasted. Figure 1 shows the decision tree. The choices recommended to the SPARCLE project manager are capitalized and underlined. A final decision of the approach that SPARCLE will utilize is pending as of this writing.

A complete end-to-end test is recommended for SPARCLE due to the sensitivity of the LSE to misalignment (and other lidar parameters), and the difficulty of bounding this misalignment with subsystem tests and analyses. Since SPARCLE must operate at nominal target ranges near 348 km, a near-field test is not sufficiently sensitive for determining misalignments. For example, Figure 2 shows the decrease in SNR for the SPARCLE lidar vs. misalignment angle between the transmitted beam direction and the back-propagated local oscillator (BPLO) direction for five different ranges of a hard target⁷. (The misalignment angle shown applies to the large beam side of the SPARCLE beam-expanding telescope. Sensitivity on the small beam side of the telescope, which is true inside of the lidar system, is smaller by the telescope magnification factor of 25, e.g., 10 μrad corresponds to 250 μrad .) In Figure 2 the focal lengths of both the transmitted and BPLO beams are set to 345 km. Examination of other values of matched and unmatched focal lengths yields similar results. Target ranges as large as 2 km are inadequate to confirm alignment. The adequacy of a 10-km target range will depend on the allocation for $\Delta\theta$ in the overall SPARCLE sensitivity budget, coupled to the achievable accuracy in measuring SNR during the sensitivity test. Figure 2 is consistent with the calculated SPARCLE Rayleigh range, $\pi D^2/4\lambda$, of 18 km.

- Sub-system tests plus analyses
- END-TO-END TEST
 - Near-field, short-range
 - FAR FIELD
 - Mountain to mountain
 - Diffuse hard target
 - Aerosol target
 - Mountain side target
 - Ground to Space
 - SIMULATED FAR FIELD AT SHORTER RANGE WITH ADDITIONAL OPTICS
 - Single refractive focusing element
 - Single reflective focusing mirror
 - TWO-MIRROR REFLECTIVE AFOCAL BEAM REDUCER
 - Small sphere target
 - CALIBRATED DIFFUSE HARD TARGET
 - Outdoors
 - ENCLOSED TUBE
 - Atmospheric pressure
 - EVACUATED TUBE
 - SPARCLE outside evacuated tube
 - SPARCLE IN VACUUM

Figure 1. SPARCLE pre-launch sensitivity test decision tree

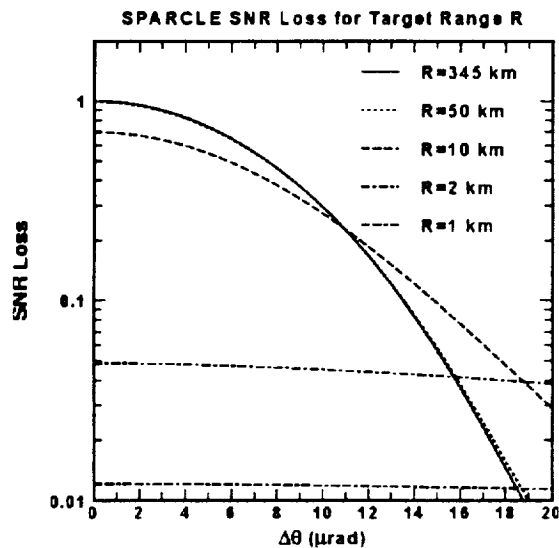


Figure 2. SNR vs. misalignment angle for various target ranges

An even greater challenge than misalignment occurs with the values of the transmitter and BPLO focal lengths. Figure 3 shows SNR vs. focal length for four target ranges. The transmitter and BPLO focal ranges are assumed equal to each other. The target range and the two focal ranges must all be greater than approximately 20 km.

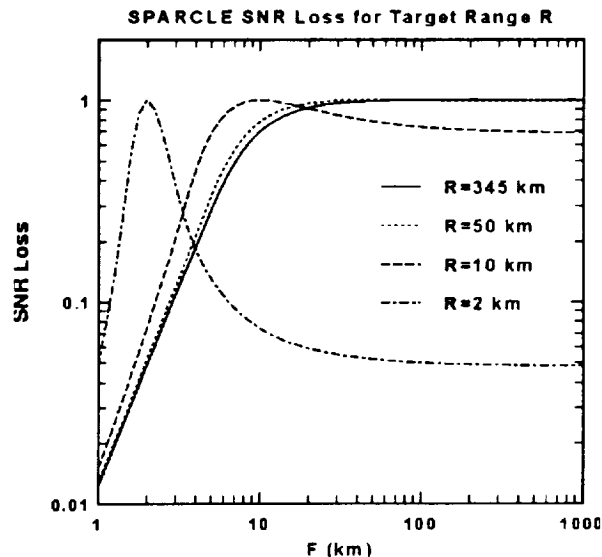


Figure 3. SNR vs. focal range for various target ranges

Two objections to an actual, long-range, far field test are LSE measurement uncertainty and cost. Refractive turbulence and atmospheric extinction effects will be large and difficult to quantify over large ranges. High costs are predicted when traveling to a mountain site, ensuring the cleanliness of the SPARCLE hardware, and providing pointing control to hit a small target. Using the mountainside or natural aerosols for the target would require the contemporaneous measurement of target reflectance by a second calibrated lidar. Since a 500-m long enclosed tube is available at MSFC, we recommend its use for a simulated far field test. Compared to an outdoor test, the enclosed tube test does not require the fabrication of an outdoor clean room, and does facilitate other SPARCLE space qualification tests such as thermal and vacuum. Since the Rayleigh range is proportional to D^2 , the use of an auxiliary beam-reducing telescope allows simulation of the far field within the tube. A single refractive or reflective focusing optic would add the need to exactly position the target in range. Using a small sphere as the target would require the conversion of its reflectance to the equivalent diffuse target reflectance, and the elimination of backscattered light from surrounding objects. Existing coherent lidar calibration targets are available from the Air Force Research Laboratory at Wright-Patterson AFB, OH. We recommend using one of the AF targets after updating its reflectance calibration at the coherent lidar target calibration facility at JPL.

References

1. M. J. Kavaya and G. D. Emmitt, "The Space Readiness Coherent Lidar Experiment (SPARCLE) Space Shuttle Mission," Proc. SPIE Vol. 3380, p. 2-11, Conference on Laser Radar Technology and Applications III, 12th Annual International Symposium on Aerospace/Defense Sensing, Simulation, and Controls, AeroSense, Orlando, FL (14 April 1998).
2. The SPARCLE WWW page is at: <http://wwwghcc.msfc.nasa.gov/sparcle/>
3. M. J. Kavaya and G. D. Emmitt, "Tropospheric Wind Measurements From Space: The SPARCLE Mission And Beyond," Digest of the 19th International Laser Radar Conference (ILRC), p 553, NASA/CP-198-207671/PT2, Annapolis, MD USA (July 1998).
4. Y. Zhao, M. J. Post, and R. M. Hardesty, "Receiving efficiency of monostatic pulsed coherent lidars. 1: Theory," Appl. Opt. 29(28), 4111-4119 (1990).
5. B. J. Rye and R. G. Frehlich, "Optimal truncation and optical efficiency of an apertured coherent lidar focused on an incoherent backscatter target," Appl. Opt. 31(15), 2891-2899 (1992).
6. R. G. Frehlich and M. J. Yadlowsky, "Performance of Mean-Frequency Estimators for Doppler Radar and Lidar," J. Atmos. and Oceanic Tech. 11(5), 1217-1230 (1994).
7. Sensitivity plots provided by Dr. Rod G. Frehlich, University of Colorado, rgf@terra.colorado.edu

Comparison of CO₂ lidar backscatter with particle size distribution and GOES-7 data in Hurricane Juliette

Maurice A. Jarzembski¹
NASA/Marshall Space Flight Center

Vandana Srivastava¹
Universities Space Research Association

Eugene W. McCaul, Jr.¹
Universities Space Research Association

Gary J. Jedlovec¹
NASA/Marshall Space Flight Center

Robert J. Atkinson¹
Lockheed Martin Corp.

Rudy F. Pueschel
NASA/Ames Research Center, Moffett Field, CA 94035

Dean R. Cutten¹
University of Alabama, Huntsville

¹ Global Hydrology and Climate Center, 977 Explorer Blvd., Huntsville, AL 35806

Two NASA/MSFC continuous wave (CW) focused Doppler lidars obtained in-situ high-resolution calibrated backscatter measurements in the upper levels of Hurricane Juliette as part of the 1995 NASA/Multicenter Airborne Coherent Atmospheric Wind Sensor (MACAWS) mission on board NASA's DC8 aircraft. These were also intercompared with in-situ cloud particle size distributions obtained from NASA/Ames Research Center's forward scattering spectrometer probe (FSSP), the DC8 aircraft infrared (IR) surface temperature radiometer data, and the Geostationary Operational Environmental Satellites (GOES-7) 11 μ m IR emission images with their corresponding estimates of cloud top temperature and height. Two traverses of Hurricane Juliette's eye were made off the west coast of Mexico at altitude ~11.7 km on 21 September 1995. During this DC8 flight, late stages of eyewall decay-replacement cycles were observed, giving the appearance of an annular eye with clouds in the central region.

A Geostationary Operational Environmental Satellites (GOES-7) 11 μ m IR emission image of Juliette at 2100 UTC is shown in Fig.1. The flight track is shown overlaid on the image with

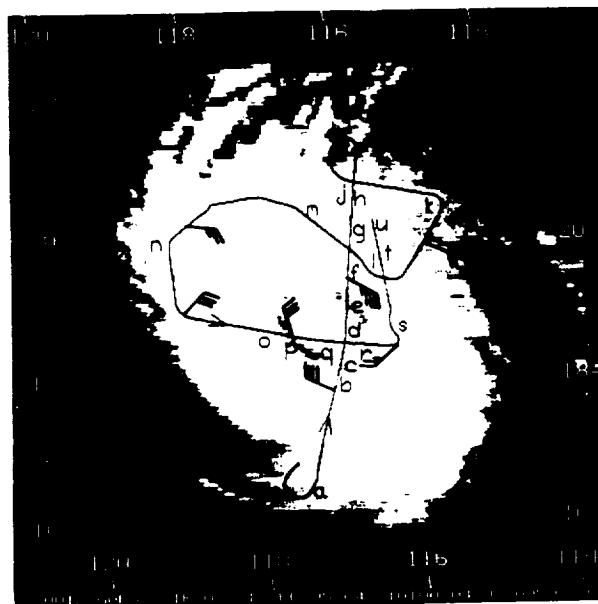


Figure 1. GOES-7 IR image of Hurricane Juliette on 21 September 1995 at 2100 UTC. The co-located position of the NASA DC8 flight track is shown from 2010 to 2250 UTC.

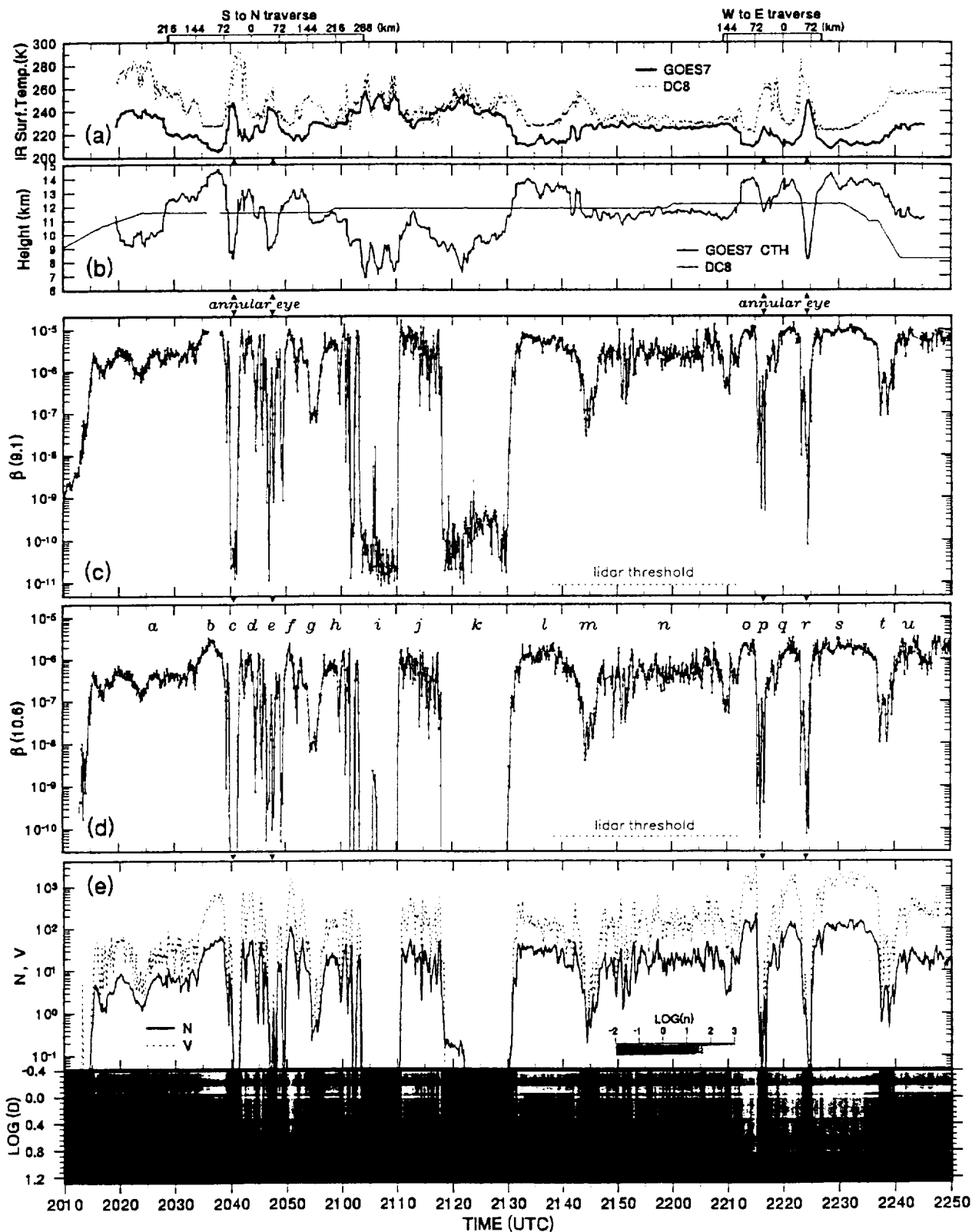


Fig.2. (a) Measured IR surface cloud-top temperature (CTT) from GOES-7 and DC8 radiometer and (b) calculated cloud-top height (CTH) from GOES-7 along the DC8 flight track. CW lidar backscatter β ($\text{m}^{-1} \text{sr}^{-1}$) measurements at (c) $9.1\mu\text{m}$ and (d) $10.6\mu\text{m}$ wavelengths; and (e) FSSP measurements of total particle number concentration N (cm^{-3}), inferred total particle volume V ($\mu\text{m}^3 \text{cm}^{-3}$), and shaded cross section of $\log(dn/d\log(D))$. Broad-scale features labeled alphabetically on the $10.6\mu\text{m}$ β time series plot are identified in Fig. 1.

encountered storm features labeled alphabetically. From five GOES-7 IR images, the digital IR cloud-top temperature, corresponding to the closest pixel to the co-located position of the DC8 flight track, was converted to cloud-top height (CTH), shown in Fig.2(a). The resolution of the data is ~ 8 km. The DC8 flight altitude is also shown in Fig.2(a). There are seven distinct, broad-scale regions where the CTH is greater than the DC8 cruising altitude.

The focused CW Doppler lidars, operating at 9.1 and 10.6 μm CO_2 wavelengths, are coherent homodyne instruments measuring the backscattered signal from particles in the lidar sample volume, ~ 54 m from the aircraft beyond the DC8 right wing. Details of this work, the lidars, data acquisition, and calibration can be found elsewhere [Jarzembski *et al.*, 1997]. Both lidar β measurements were obtained with 3-s integration times, giving horizontal along-track resolution of ~ 0.72 km. β at 9.1 and 10.6 μm are shown in Fig.2(b) and (c), respectively. Dramatic β variations, some spanning over five orders of magnitude, are evident, showing a variety of features (labeled alphabetically on the 10.6 μm β time series plot in order to facilitate comparison with the GOES-7 data) at 20-150 km scales. Very fine-scale (~ 2 km scale) β variations were also detected. Despite the dramatic variability in β magnitude, both independent β measurements exhibit similar features that agree spatially, temporally, and in relative magnitude. These features agree well with the more coarse CTH data.

The total particle number density, N , and the particle size distributions, $dn/d\log(D)$ (where n is the number of particles in the size bin around size D) at 10-s integration time from the FSSP (sample volume $\sim 10^{-3}$ m^3) are shown in Fig.2(e). Total particle volume V obtained from a spherical particle approximation is also shown in Fig.2(e) to give a rough estimate of cloud ice content. Although caution needs to be exercised in interpreting FSSP size distribution data taken inside clouds in the presence of ice particles, the agreement between the two independent data sets, β and N , (along with $dn/d\log(D)$ and V) is excellent with logarithmic correlation of ~ 0.86 , depicting the direct proportionality between β and N .

β at 9.1 and 10.6 μm differ by the wavelength dependence factor and is measured to be around 6 ± 2 . A lower ratio of ~ 2 would indicate presence of sulfuric acid aerosols; however, this was not encountered even under the lowest β conditions within Juliette, suggesting less likelihood of

stratospheric air intrusion, which would contain mostly sulfuric acid aerosols.

Within a cloud, β variations give direct indications of cloud density variations. High β is associated with high number density which indicates strong convective activity, leading to high CTH. Low β due to low number density indicates lesser convective activity which would not support a high CTH. Hence, whenever the DC8 is in clouds, variations of lidar-measured β along the flight track correspond to the crossing of contours of the field of cloud particle density, the latter of which is in turn associated with cloud activity as indicated by the CTH (Fig.2a). In regions where the CTH is above the DC8, comparison of CTH with the two separate in-situ data sets shows the correlation between $\log N$ and CTH, and between $\log \beta$ and CTH (remapped to a common grid of CTH data) to be ~ 0.69 and ~ 0.5 , respectively. Because these correlations cannot fully account for differences associated with the dissimilar spatial resolutions of the in situ versus satellite data sources, we suspect that the real correlation is even higher. Therefore, in vigorous convective systems CTH itself may be a possible indirect indicator of changes in the particle density field and β variations at a given height within the upper levels of the cloud. In vigorous convective systems, CTH may give a possible indirect indicator of changes in particle density field and β variations within deep cirrus clouds.

This is the first time a comparison has been made among satellite imagery parameters and in-situ calibrated β from airborne CW lidars and cloud particle size distributions in a hurricane, showing good agreement between β at 9.1, 10.6 μm , cloud particle size distributions, and CTH. Further field work should be pursued to determine the height dependence of the β -CTH correlations and their possible utility for parameterization of global backscatter fields within clouds.

Acknowledgement. Authors are grateful to R. Kakar, NASA HQ's, for funding the NASA/MSFC CW lidars and NASA/ARC FSSP on the MACAWS mission.

REFERENCE

- Jarzembski, M. A., V. Srivastava, Eugene W. McCaul, Jr., Gary J. Jedlovec, Robert J. Atkinson, Rudolf F. Pueschel, and Dean R. Cutten, "Comparison of lidar backscatter with particle distribution and GOES-7 data in Hurricane Juliette," *Geophys. Res. Lett.*, 24, 1063-1066 (1997).

Aerosol backscatter from airborne continuous wave CO₂ lidars over western North America and the Pacific Ocean

Maurice A. Jarzembski
NASA/Marshall Space Flight Center

Vandana Srivastava
Universities Space Research Association

Jeffrey Rothermel
NASA/Marshall Space Flight Center

Authors are located at the Global Hydrology and Climate Center, 977 Explorer Blvd., Huntsville, AL 35806

1. Introduction

Atmospheric aerosol backscatter, β , variability gives a direct indication of aerosol loading. Since aerosol variability is governed by regional sources and sinks as well as affected by its transport due to meteorological conditions, it is important to characterize this loading at different locations and times. Lidars are sensitive instruments that can effectively provide high-resolution, large-scale sampling of the atmosphere remotely by measuring aerosol β , thereby capturing detailed temporal and spatial variability of aerosol loading. Although vertical β profiles are usually obtained by pulsed lidars, airborne-focused CW lidars, with high sensitivity and short time integration, can provide higher resolution sampling in the vertical, thereby revealing detailed structure of aerosol layers.¹⁻⁵

During the 1995 NASA Multicenter Airborne Coherent Atmospheric Wind Sensor (MACAWS) mission,⁶ NASA MSFC airborne-focused CW CO₂ Doppler lidars, operating at 9.1 and 10.6- μm wavelength, obtained high resolution in situ aerosol β measurements to characterize aerosol variability. The observed variability in β at 9.1- μm wavelength with altitude is presented as well as comparison with some pulsed lidar profiles.

2. Flight Mission and CW Lidar Description

The MACAWS mission consisted of nine flights (denoted as F1, . . . , F9) on the NASA DC8 aircraft during 13 - 26 September 1995. Regions of overflights included along the North American west coast from southern California to northern Oregon, the San Joaquin and Sacramento Valleys in California, the Sierra Nevada and Coastal Range Mountains, and the Pacific Ocean off the coast of Oregon, California, and the Baja peninsula of Mexico. Approximately 52 flight hours of aerosol β data at 9.1- μm wavelength were obtained at various

altitudes over a combined horizontal distance of over 30,000 km. Sampling was also performed during numerous ascents and descents between ~0.1- and 12-km altitude. The data over land and ocean comprised 44.8% and 55.2%, respectively, of the total data.

The NASA MSFC CW 9.1- μm Doppler lidar beam was focused at ~54 m from the aircraft ahead and beyond the DC8 right wing tip, into the atmosphere. Measurements were obtained with a 3-s integration time with resolution ranging from ~0.36 to 0.72 km. Details of this paper, the calibration, instrument design, signal processing, and performance are provided elsewhere.⁷⁻⁹

3. Backscatter Profile Measurements

Quasi-vertical β profiles were obtained during various aircraft ascents and descents. The altitude for the profiles was derived by pressure and not radar. Typically, a 1-km change in altitude corresponded to roughly 10-km horizontal distance. Absolute uncertainty in the β measurements was ~20% for high to moderate signal conditions and ~34% for low signal conditions, while relative uncertainty between adjacent β values was less than 1%, due mostly to subtle laser power fluctuations. The lidar β sensitivity was $\sim 8 \times 10^{-12} \text{ m}^{-1} \text{ sr}^{-1}$. A description of the main features in β variability as well as intercomparison with each other and some comparison with other pulsed lidar datasets taken over similar terrain is also presented.

A. Profiles over western U.S. coastal marine region

Fig. 1 shows β profiles off the coast of Oregon, a region affected by marine as well as land air masses due to their close proximity to the coast. The height of the coastal marine boundary layer (MBL) aerosol was not very deep, going only up to ~1.5-km altitude, after which β decreased by ~2 orders of

magnitude. There also appeared to be a slight elevated layer near 3-km altitude. Throughout this profile, the wind direction ($\sim 10 \text{ m s}^{-1}$) was northerly to easterly, from the upper to the lower troposphere, respectively (wind speed and direction were obtained from the DC8 wind data). The two profiles obtained were $\sim 3.3 \text{ hr}$ and $\sim 150 \text{ km}$ apart, and showed quite good agreement for the altitude regime covered. This indicates horizontal and temporal uniformity of the relatively clean large-scale airmass encountered in this region.

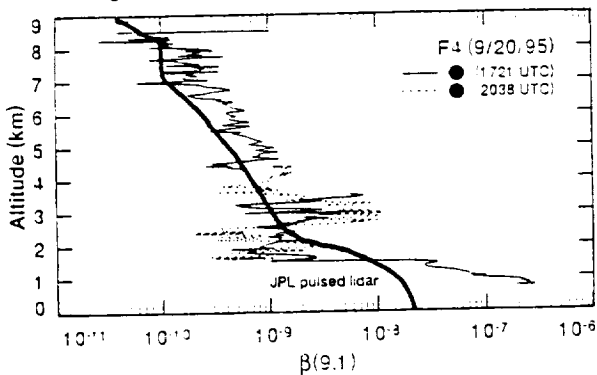


Fig. 1 β profiles over the ocean off the coast of Oregon.

For comparison, Fig. 1 includes a geometric mean aerosol β profile retrieved by the airborne JPL pulse lidar⁷ at a $9.25\text{-}\mu\text{m}$ wavelength over the northern Pacific Ocean between latitudes 20°N and 60°N for the fall 1989 and spring 1990 GLOBE mission. This mean profile averaged over spatial extent of several hundred kilometers in the mid-Pacific shows good overall agreement with the coastal profile. The major difference is that the mean profile is generally lower than that observed during MACAWS where possible continental land mass effect off the coast may contribute to the increase. This agreement shows that profiles obtained over clean remote marine regions may not be that dissimilar from those observed near coastal regions except when there is land-derived aerosols loading the MBL. These comparisons are needed for it is hard to obtain data over remote marine regions as compared to the coastal regions; hence, understanding the similarities and dissimilarities between the remote and coastal marine regions for different times and locations can facilitate understanding of global aerosol distribution.

B. Profiles over San Francisco coastal urban region

β profiles taken over the coastal urban region of the south San Francisco Bay area which could reflect

airmasses from both the ocean and land, including urban pollution are shown in Fig. 2. These profiles were made during the DC8 takeoff and landing at Moffett Field. They show several layers and changing features with considerable variability, especially in the lower troposphere. The height of the PBL aerosols also varied from as low as 1.3 km in Fig. 2(a) to nearly 3 km in Fig. 2(b). These distinct differences in aerosol loading could be due, in part, to the wind direction transporting different airmasses. For Fig. 2(a), cleaner marine air may be transported into the south Bay area with a lesser influence of land aerosols, while for Fig. 2(b), more land-derived aerosols may be transported and thus showing higher aerosol β in the lower troposphere. In fact, Fig. 2(a) shows a remarkably similar structure to that found in Fig. 1 off the coast of Oregon with similar shallow MBL. Despite the

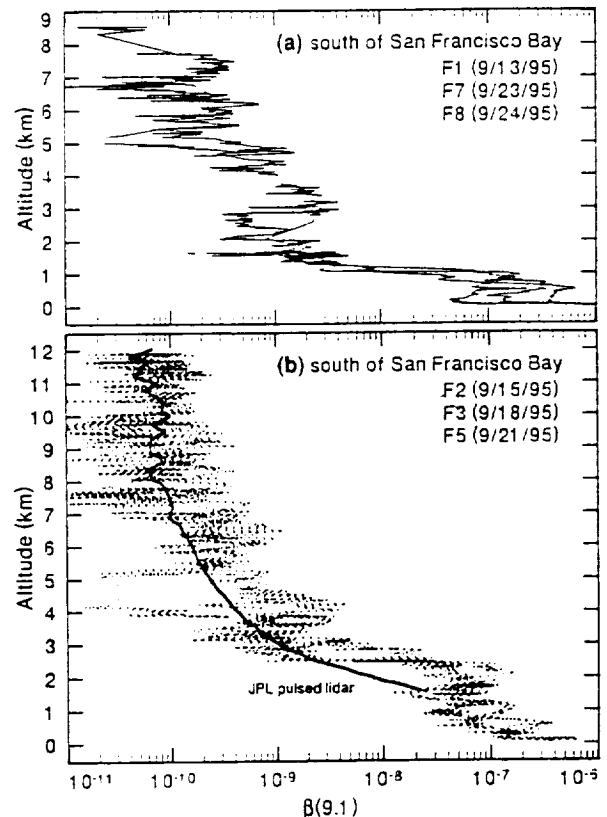


Fig. 2 β profiles obtained during takeoff and landing near the south San Francisco Bay area for: (a) composite of profiles during F1, F7, and F8 with winds in the upper troposphere from the northwest and in the lower troposphere mainly from the west, and (b) composite of profiles during F2, F3, and F5 with winds in the upper troposphere from the west or north and in the lower troposphere mainly from the south or northeast.

dramatic differences in β values in the lower troposphere, β levels in the middle and upper troposphere do not show significant differences.

For comparison, the β climatology obtained by the JPL ground-based 9.25- μm pulsed lidar is shown as their geometric mean β profile over Pasadena, California (1984-1992) in the Fig. 2(b) profile.¹¹ Agreement is quite good (within a factor of 2) between climatological observations over this ~8.5-yr period in the Los Angeles coastal urban area and the observations over the coastal urban area of the south San Francisco Bay region.

C. Mid-tropospheric aerosol layers in marine, urban, and rural regions

A deep aerosol layer above the PBL was encountered between altitudes of 3 to 7 km in all of the profiles obtained during F9 [Fig. 3(a)-(d)]. This flight spanned a spatial distance of ~1,500 km off the North American coast to the Sacramento Valley, CA and south of the San Francisco Bay. The β levels in the middle troposphere were over an order of magnitude higher than those observed for other profiles shown in Figs. 1 and 2, over both the ocean and land. Winds were westerly at 10 to 20 m s^{-1} , confirmed by 500 mb weather map data. This suggests that the aerosol loading in the middle troposphere could be due to an Asian continental dust plume event being advected by the jet stream over the Pacific Ocean. Since several profiles were obtained at widely different regions over both the ocean and land with an enhanced β aerosol layer encountered at all of the locations, it shows the widespread nature of this deep mid-tropospheric plume. For over the Pacific Ocean (P2-P6) just below the layer near 2 and 3 km, β dropped to very low values, approaching the detection threshold of the lidar. However, it did not drop as sharply over the land (P7-P9) just below the layer. The β in the MBL was highly variable as compared to any other sampling in the boundary layer. Profiles over the ocean, P2-P6, show shallow MBL aerosol height of ~1 to 1.5 km; whereas, profiles further inland (P7-P8) exhibit higher MBL, reaching up to 3 km [Fig. 3(c)], similar to Fig. 2(b). The boundary layer aerosol height over the coastal San Francisco Bay area [Fig. 3(d)] was also found to be quite shallow, similar to Figs. 1, 2(a), 3(a) and (b), possibly due to the influence of the sea breeze, as the winds were from the northwest.

Aerosol layers can get lofted to mid-tropospheric heights and they can extend over large distances. Evidence of such large-scale elevated aerosol layers, displaying similar characteristics to those shown in Fig. 3, have also been observed at other times by

pulsed lidars. A layer extending over altitudes of 4.5 to 7 km was observed off the east coast of China on May 31, 1990, using the JPL airborne pulsed lidar at 9.25- μm wavelength and is shown in Fig. 3(b) for comparison.¹² This layer consisted of an aged, well-mixed Asian continental aerosol that was transported over the Pacific and diluted with clean marine tropospheric air. Clean β conditions were found below this elevated layer, similar to that of Fig. 3.

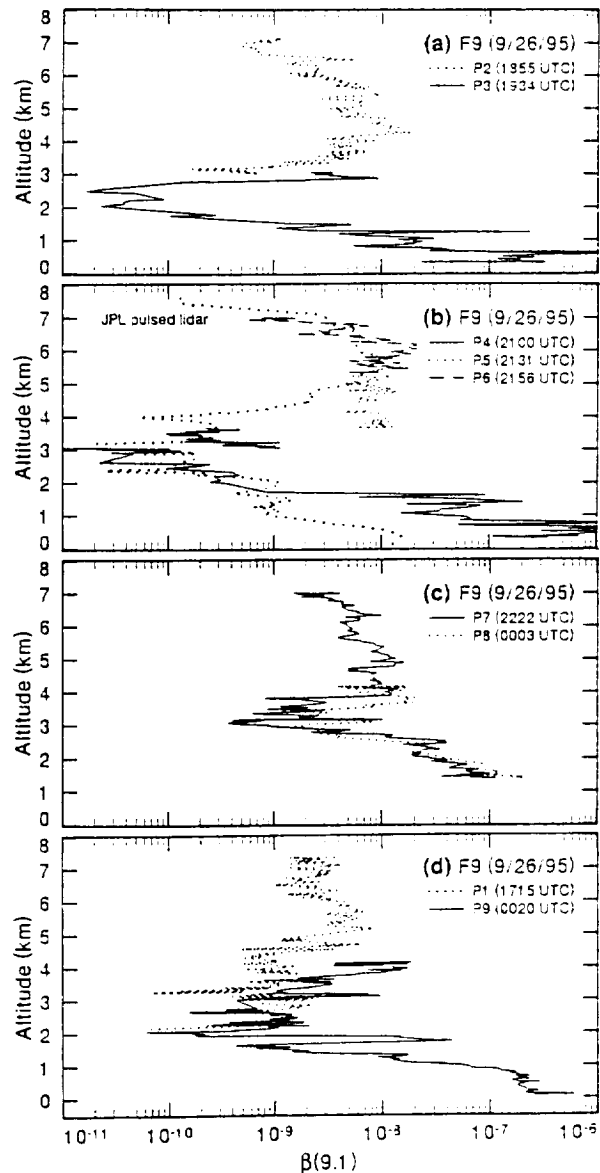


Fig. 3 β profiles obtained during F9 showing elevated aerosol layer above the planetary boundary layer (a) and (b) off the coast of California (P2-P6), (c) over the Sacramento Valley (P7, P8), and (d) over the San Francisco Bay region (P1, P9).

4. Vertical backscatter variation statistics

Figure 4 summarizes the percentage of occurrence of β for the entire 9.1 μm CW lidar data obtained during the MACAWS mission, including both quasi-vertical β profiles and horizontal transits. A total of 52,982 measurement opportunities have been included to arrive at the bar-type histogram. The quasi-stable aerosol background mode peaks at value of $\sim 10^{-10} \text{m}^{-1} \text{sr}^{-1}$ for the middle and upper troposphere.

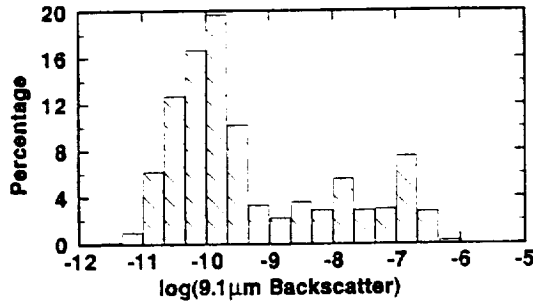


Fig. 4. Histogram of percentage of occurrence.

5. Conclusion

The NASA/MSFC airborne-focused CW CO_2 Doppler lidar, due to its high-resolution and sensitivity, could provide detailed structure of aerosol layers, depicting various loading conditions over the western North American coast. Comparison between the quasi-vertical CW lidar profiles with mean profiles obtained from pulsed lidars is remarkably good for generally the same type of regions. As expected, aerosol loading is dependent on wind direction and location of aerosol sources. The upper level aerosol layers that seemed to have been advected long distances over the ocean, significantly altered the mid troposphere structure of aerosols above the PBL. Since aerosol loading and removal of aerosols are regional phenomena, routine monitoring of them is required on large scales to understand their global variation and impact.

Acknowledgments: The authors gratefully thank R. Kakar, NASA Headquarters, for funding the NASA MSFC CW lidars on the MACAWS mission.

REFERENCES

1. S. B. Alejandro, G. G. Koenig, D. Bedo, T. Swirbalus, R. Frelin, and J. Woffinden, J. M. Vaughan, D. W. Brown, R. Callan, P. H. Davies, R. Foord, C. Nash, and D. J. Wilson, "Atlantic atmospheric aerosol studies 1. Program overview and airborne lidar," *J. Geophys. Res.* **100**, 1035-1041 (1995).
2. J. M. Vaughan, D. W. Brown, C. Nash, S. B. Alejandro, and G. G. Koenig, "Atlantic atmospheric aerosol studies 2. Compendium of airborne backscatter measurements at 10.6 μm ," *J. Geophys. Res.* **100**, 1043-1065 (1995).
3. D. A. Bowdle, J. Rothermel, J. M. Vaughan, D. W. Brown, and M. J. Post, "Aerosol backscatter measurements at 10.6 micrometers with airborne and ground-based CO_2 Doppler lidars over the Colorado high plains: 1. Lidar intercomparison," *J. Geophys. Res.* **96**, 5327-5335 (1991).
4. J. L. Gras and W. D. Jones, "Australian aerosol backscatter survey," *Appl. Opt.* **28**, 852-856 (1989).
5. R. L. Schwiesow, R. E. Cupp, V. E. Derr, E. W. Barrett, R. F. Pueschel, and P. C. Sinclair, "Aerosol backscatter coefficient profiles measured at 10.6 μm ," *J. Appl. Met.* **20**, 184-194 (1981).
6. J. Rothermel, D. R. Cutten, R. M. Hardesty, R. T. Menzies, J. N. Howell, S. C. Johnson, D. M. Tratt, L. D. Olivier, and R. M. Banta, "The Multi-center Airborne Coherent Atmospheric Wind Sensor, MACAWS," *Bull. Amer. Meteor. Soc.* **79**, 581-599 (1998).
7. M. A. Jarzembski, V. Srivastava, and J. Rothermel, "Vertical variability of aerosol backscatter from an airborne-focused continuous-wave CO_2 lidar at 9.1- μm wavelength," *Appl. Opt.* **38**, 908-915 (1999).
8. M. A. Jarzembski, V. Srivastava, and D. M. Chambers, "Lidar calibration technique using laboratory-generated aerosols," *Appl. Opt.* **35**, 2096-2108 (1996).
9. J. Rothermel, D. M. Chambers, M. A. Jarzembski, V. Srivastava, D. A. Bowdle, and W. D. Jones, "Signal processing and calibration of continuous-wave focused CO_2 Doppler lidars for atmospheric backscatter measurement," *Appl. Opt.* **35**, 2083-2095 (1996).
10. R. T. Menzies and D. M. Tratt, "Airborne lidar observations of tropospheric aerosols during the Global Backscatter Experiment (GLOBE) Pacific circumnavigation missions of 1989 and 1990," *J. Geophys. Res.* **102**, 3701-3714 (1997).
11. D. M. Tratt and R. T. Menzies, "Recent climatological trends in atmospheric aerosol backscatter derived from the Jet Propulsion Laboratory multiyear backscatter profile database," *Appl. Opt.* **33**, 424-430 (1994).
12. R. T. Menzies and D. M. Tratt, "Airborne CO_2 coherent lidar for measurements of atmospheric aerosol and cloud backscatter," *Appl. Opt.* **33**, 5698-5711 (1994).

Performance Analysis for the Space Readiness Coherent Lidar Experiment

Gary D. Spiers
 Center for Applied Optics
 University of Alabama in Huntsville
 Huntsville
 AL 35899
 Gary.Spiers@msfc.nasa.gov
 (256) 544 5787

Introduction

The primary function of SPARCLE is to validate the ability of coherent Doppler lidar to accurately measure atmospheric winds. The requirements for SPARCLE are listed in table (1).

Line of sight velocity accuracy	Wind Measurement Accuracy $\sigma_{LOS} < 2$ m/s, 1 m/s of which is attributable to instrument error or uncertainty and the rest to platform pointing and alignment. Assumes single shot LOS, in regions of high SNR and low wind turbulence and shear.
Vertical position accuracy	The accuracy of the height assignment of the wind data above the GPS reference ellipsoid shall have an RMS error < 50 meters.
Horizontal position accuracy	The accuracy of the horizontal location of the wind data shall have a RMS error < 500 meters.
Aerosol backscatter sensitivity (β_{50} , single shot)	$5 \times 10^{-7} \text{ m}^{-1} \text{ sr}^{-1}$ (goal) $5 \times 10^{-6} \text{ m}^{-1} \text{ sr}^{-1}$ (acceptable)

Table 1) Key SPARCLE performance requirements [1]

There are a number of issues that must be considered when assessing the anticipated performance of a space based coherent lidar. These are shown schematically in figure (1).

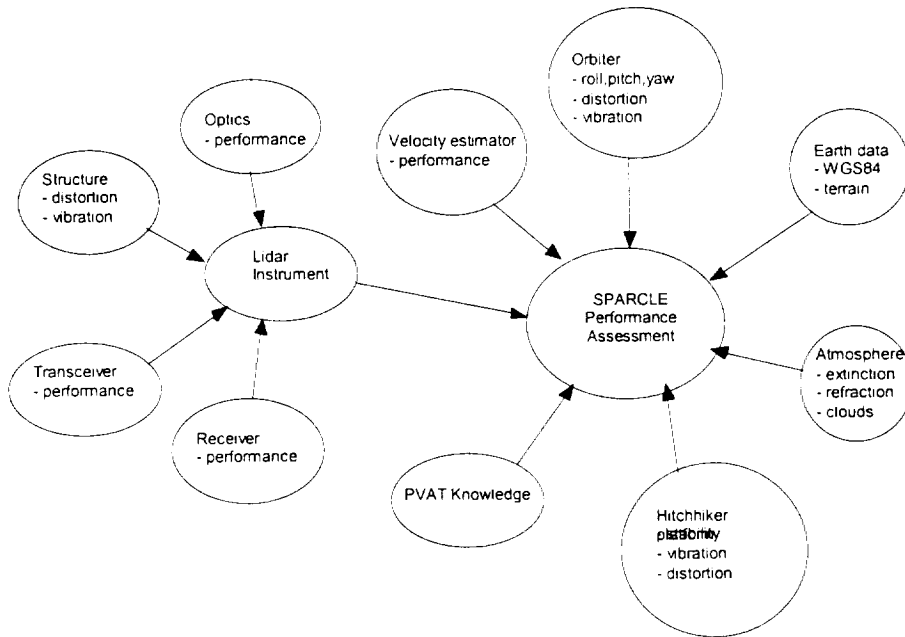


Figure 1) Contributors to the performance of SPARCLE.

Methodology

Performance of the instrument is evaluated through a combination of tools. These include error budgets for each of the major requirements, a Monte Carlo simulation that includes the statistics of the processes involved and individual tools for evaluating specific contributors (see for example [4]).

Line of Sight Velocity Accuracy

The line of sight velocity accuracy consists of two requirements, one attributable to the lidar instrument and one attributable to the combination of the lidar instrument and platform. Knowledge of the instrument's attitude (nadir and azimuth angle) is crucial to obtaining the required line of sight velocity accuracy [2].

There are a number of key problems associated with obtaining the attitude of an instrument on a Hitchhiker [5] platform. Timely attitude data is not available through the Hitchhiker interface and the Hitchhiker platform is not a precision pointing platform. Therefore SPARCLE can not rely on pre-launch alignment of the SPARCLE instrument with respect to a known attitude determination system in order to meet the 2 m/s line of sight velocity error requirement. To meet the requirement SPARCLE provides its own attitude knowledge system which uses the ground return signal of the lidar to initialise the INS portion of an integrated INS/GPS [3]. This also removes the need for absolute calibration of the lidar instrument nadir and azimuth angles prior to launch, placing repeatable rather than absolute nadir and azimuth requirements on the lidar hardware.

The lidar instrument portion of the line of sight velocity accuracy requirement has contributions from the measurement of the master oscillator/local oscillator offset, slave oscillator/master oscillator offset and return signal frequencies. Additional contributions come from local oscillator errors associated with frequency drift during the round trip time and assumptions used in the tuning algorithm. In combination these errors associated with frequency measurement contribute ~ 0.75 m/s to the line of sight velocity accuracy. The nadir and azimuth portion of the line of sight velocity accuracy budgeted to the instrument contribute a further ~ 0.33 m/s to the line of sight error to give a total line of sight velocity error of ~ 0.82 m/s.

Instrument position and orbit inclination knowledge errors (if not corrected in post processing) contribute to an incorrect determination of both the ground velocity and the nadir angle at the ground. These errors contribute ~ 0.37 m/s to the line of sight velocity accuracy whilst the accuracy of determining the instrument velocity contributes an additional ~ 0.1 m/s to the line of sight velocity accuracy error. The final contribution to the line of sight velocity accuracy comes from a combination of the ability to correctly initialise the INS using the lidar, the subsequent drift and resolution of the INS gyroscopes and change, due to thermal or vibration environments, of the INS position with respect to the lidar. These contribute a further ~ 0.89 m/s to give an RSS total for the combined instrument and platform of ~ 1.3 m/s.

Position

The GPS portion of the INS/GPS provides the location of the instrument with respect to WGS84 [6,7] to better than 20 m. The time of flight to the ground in combination with knowledge of the azimuth and nadir angles provides the location of the target with respect to the instrument to within 50 m in the horizontal and ~ 30 m in the vertical.

Backscatter Sensitivity

Table (2) shows the budgeted allowances for the backscatter sensitivity.

Wavelength	2.0512 μm	Pulse energy	100 mJ
Pulse length	0.17 μm	Receiver efficiency	0.25
Clear aperture diameter	0.226 m	Transmit beam 1/e2 diameter	0.185 m
One way optics transmission	0.64	Wavefront aberration	0.69
Polarisation efficiency	0.9	Truncated/untruncated correction	0.59
Misalignment efficiency	0.64	Range to target	384 km
Target altitude	1 km	Nadir angle at target (spherical earth)	31.56 deg.
Vertical resolution of processed data	250 m	One way atmospheric transmission	0.84
Horizontal wind velocity search space	± 10 m/s		
Single shot velocity estimator	Capon, $b_0=75.36$, $\alpha=1.08$, $\gamma=17.45$, $\chi=0.568$, $g_0=18.25$, $\epsilon=1.8$, $\delta=0.765$, $\mu=0.301$		

Table 2) Parameters used in determining the SPARCLE backscatter sensitivity.

It should be noted that the details of the science requirement for SPARCLE specified the backscatter in terms of certain approximations (e.g. spherical earth) rather than 'real world' values and this is reflected in Table (2). At this time it is too early in the program to have data available that validates the parameter allocation indicated in Table (2) however to date none of the relevant subsystems that these requirements flow down to has indicated a problem in meeting their requirements. For the conditions listed in table (2) SPARCLE has a sensitivity (β_{50} , single shot) of $2.7 \times 10^{-6} \text{ m}^{-1} \text{ sr}^{-1}$ or $5.3 \times 10^{-6} \text{ m}^{-1} \text{ sr}^{-1}$ if 3 dB of margin for unexplained loss is included. Note that the margin is not required within the specification for backscatter sensitivity in the SPARCLE science requirements.

One of the important issues related to performance is the misalignment efficiency. Table (3) identifies key contributors to the misalignment efficiency. In addition to the usual lidar contributors such as laser beam pointing jitter, optical subsystem jitter due to vibration and scanner stability there will be misalignment contributions due to nadir angle tipping and due to changes in the attitude of the shuttle during the round trip time. Shuttle attitude drift rates can be controlled through requirements placed on the orbiter in the SPARCLE payload integration plan.

Laser jitter (pulse to pulse at telescope output)	1 μ radian
STS attitude drift (<0.04 deg/sec)	1.6 μ radians
Nadir tipping during the round trip time	2.7 μ radians
Optical subsystem jitter	3 μ radians
Scanner stability	4 μ radians
RSS Total	6 μ radians

Table 3) Round trip pointing jitter budget

One of the important issues in validating this budget is related to on-orbit vibration affecting the optical subsystem jitter. The Hitchhiker platform is not a precision pointing platform and lacks information about its local vibration environment. A lot of accelerometer data has been collected during microgravity experiments on the orbiters but there is insufficient data to reliably translate this experiment specific acceleration data into rates of attitude change which is what we require. Fortunately the magnitude of the accelerometer data implies (with considerable assumptions) that the on orbit vibration environment will contribute negligibly to this misalignment but it is unlikely that this can be absolutely verify prior to launch.

Summary

At this stage in the development of the SPARCLE instrument it is expected to have a backscatter sensitivity of $2.7 \times 10^{-6} \text{ m}^{-1} \text{ sr}^{-1}$, a final line of sight velocity accuracy of $\sim 1.3 \text{ m/s}$ and be capable of locating the measurement with respect to WGS84 to within 50 m in the horizontal and 30 m in the vertical.

Acknowledgements

This work was conducted in support of the NASA NMP EO-2 SPARCLE mission.

References

- [1] "Space Readiness Coherent Lidar Experiment (SPARCLE) Mission and Science Requirements Document", MSFC-RQMT-2828, NASA Marshall Space Flight Center, 1998.
- [2] G.D. Spiers and M.J. Kavaya, "Considerations for Designing a Space Based Coherent Doppler Lidar", Tenth Biennial Coherent Laser Radar Technology and Applications Conference, Mount Hood, 28th June – 2nd July 1999.
- [3] G.D. Emmitt, T. Miller and G.D. Spiers, "Pointing Knowledge for SPARCLE and Space-based Doppler Wind Lidars in General", Tenth Biennial Coherent Laser Radar Technology and Applications Conference, Mount Hood, 28th June – 2nd July 1999.
- [4] G.D. Spiers, "The Effect of Optical Aberrations On The Performance Of A Coherent Doppler Lidar", Tenth Biennial Coherent Laser Radar Technology and Applications Conference, Mount Hood, 28th June – 2nd July 1999.
- [5] "Hitchhiker Customer Accommodations & Requirements Specifications", HHG-730-1503-07, NASA Goddard Space Flight Center, 1994.
- [6] MIL-STD-240, "Department of Defence World Geodetic System (WGS)", 11 January 1994.
- [7] DMATR 8350.2. "Department of Defence World Geodetic System 1984, Its Definition and Relationships with Local Geodetic Systems", Second Edition 1 September 1991.

The Effect Of Optical Aberrations On The Performance Of A Coherent Doppler Lidar.

Gary D. Spiers
 Center for Applied Optics
 University of Alabama in Huntsville
 Huntsville
 AL 35899
 Gary.Spiers@msfc.nasa.gov
 (256) 544 5787

Introduction

The degradation of the performance of a coherent lidar due to phase front distortion introduced by the lidar optics is of considerable interest. The issue was first addressed by Rye [1] using the back-propagated local oscillator (BPLO) approach proposed by Siegman [2]. Rye's work specifically looked at the impact of spherical, coma and astigmatic primary aberrations on performance. This paper extends Rye's work by including additional primary aberrations and also looking at the effect of combinations of aberrations.

Methodology

Using the notation adopted by Rye and Frehlich [3] the heterodyne and system-antenna efficiencies are given by:

$$\eta_h = \frac{(\lambda \cdot r)^2 \cdot T_L}{A_R} \cdot \frac{\int I_T(s) \cdot I_L(s) d^2s}{T_T \cdot T_L \cdot P_T \cdot P_R} \quad \text{and} \quad \eta_s = T_T \cdot \frac{A_R}{A_T} \cdot \eta_h \quad \text{respectively.}$$

Calculations were performed with optimally truncated [3] Gaussian transmit and BPLO beams. Aberrations were then added to both beams and the beams propagated into the far-field where the heterodyne efficiency was determined. The following aberrations were considered:

Aberration	Form	Aberration	Form
Coma	$W_{31} \cdot \left(\frac{\rho}{\rho_{norm}} \right)^3 \cdot \cos(\theta - \theta_0)$	Focus	$W_{20} \cdot \left(\frac{\rho}{\rho_{norm}} \right)^2$
Spherical	$W_{40} \cdot \left(\frac{\rho}{\rho_{norm}} \right)^4$	Cone	$W_{10} \cdot \left \frac{\rho}{\rho_{norm}} \right $
Astigmatism	$W_{22} \cdot \left(\frac{\rho}{\rho_{norm}} \right)^2 \cdot \cos^2(\theta - \theta_0)$	Tilt	$W_{11} \cdot \left(\frac{\rho}{\rho_{norm}} \right) \cdot \cos(\theta - \theta_0)$

Table 1) Aberrations considered

Initial calculations were completed for each individual aberration and then subsequent calculations were conducted for pairs of aberrations. A maximum value of two waves was used for the aberration coefficient W_{nm} in each case. For the calculations conducted $A_R = A_T$ and so only results for η_h will be shown as η_s simply scales by T_T .

Results

Figure (1) shows the effect on heterodyne efficiency of each of the individual aberrations listed in table (1). A plot for tilt is not shown as it causes a beam pointing error but does not introduce a loss in heterodyne efficiency when both transmit and BPLO paths experience the same aberrations, the situation considered here. Although the results for cone aberration are plotted, cone aberration is unlikely in most lidar systems. It should also be noted that a lidar system can be designed to permit removal of focus aberration during alignment of the system.

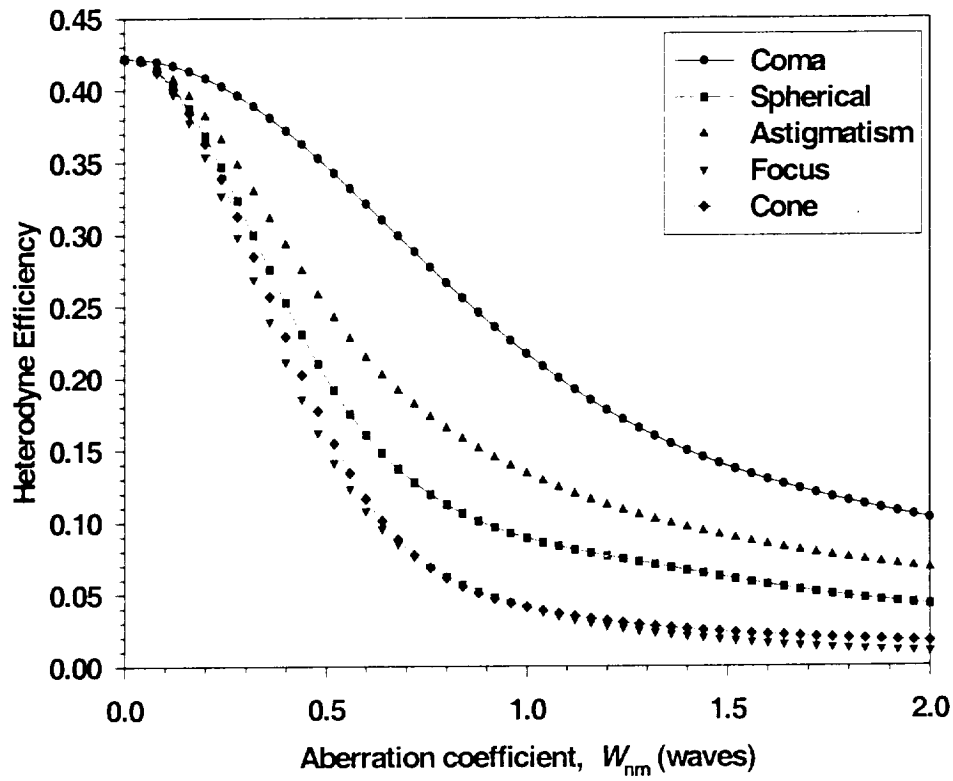


Figure 1) The effect of individual aberrations on heterodyne efficiency.

This figure essentially reproduces the work of Rye [1]. Of more interest is how combinations of aberrations affect the heterodyne efficiency. Some sample contour plots are shown in figures (2-4).

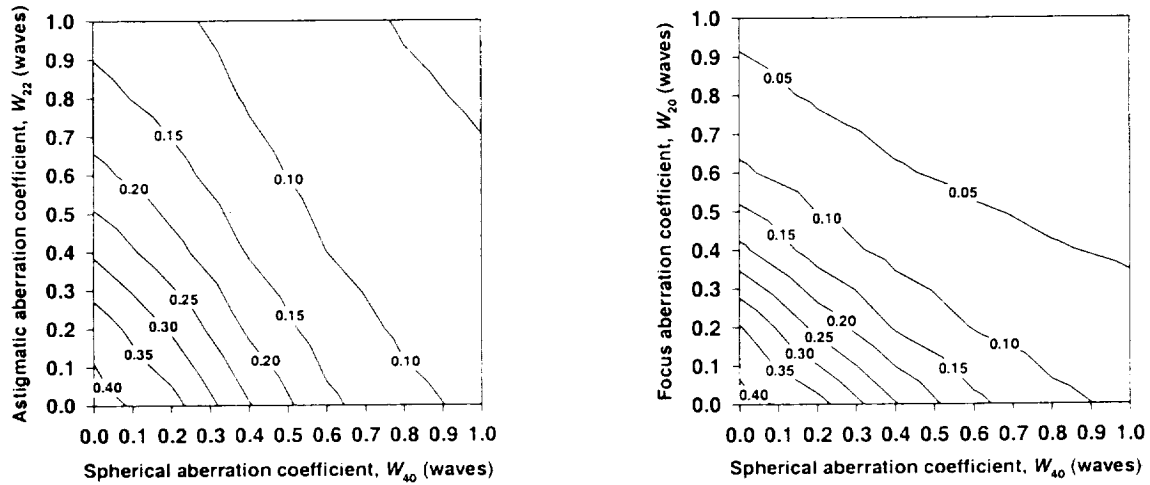


Figure 2) Contour plots of heterodyne efficiency for a) spherical and astigmatic aberrations and b) spherical and focus aberration.

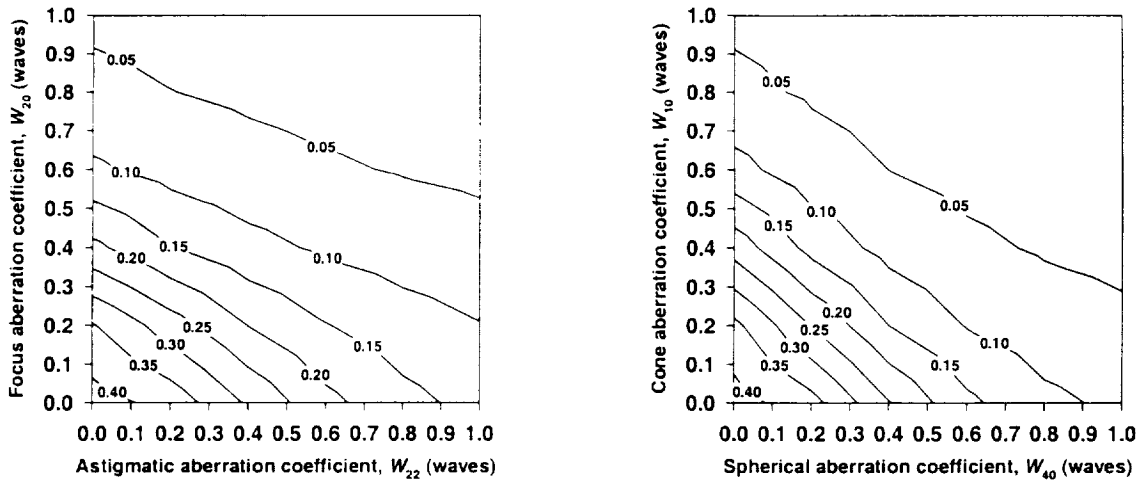


Figure 3) Contour plots of heterodyne efficiency for a) astigmatic and focus aberrations and b) spherical and cone aberrations.

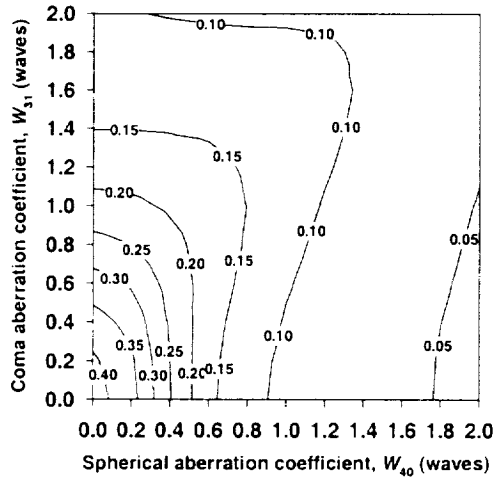


Figure 4) Contour plot of heterodyne efficiency for spherical and coma aberrations

Once the effect of these combinations of aberrations have been determined it becomes possible to use these to more precisely define requirements for optical components. The RMS wavefront error is typically used to define a surface quality. Taking the results from figures (1-4) and calculating the RMS wavefront error for each data point we can produce a scatter plot that depicts heterodyne efficiency as a function of RMS wavefront error (figure (5)).

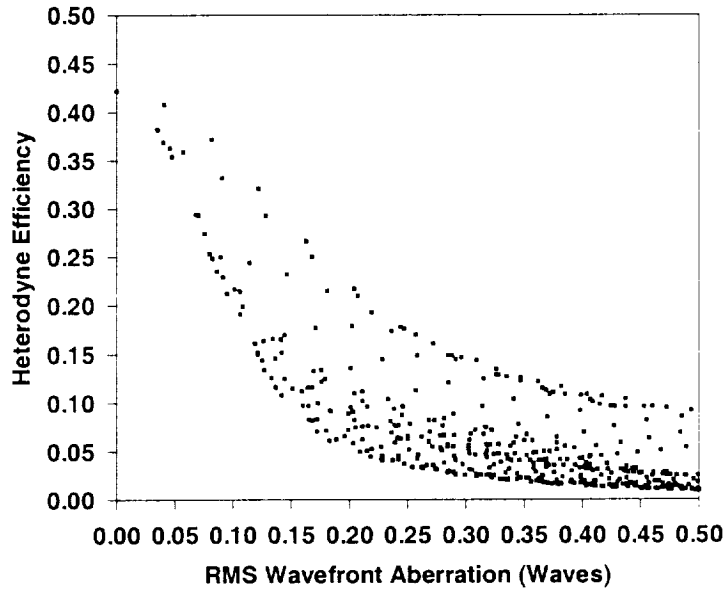


Figure 5) The effect of RMS wavefront aberration on heterodyne efficiency.

If we consider a 3dB reduction in heterodyne efficiency then we can see from figure (5) that in the worst case this requires an RMS wavefront error of ~0.1 waves while in the best case it requires an RMS wavefront error of ~0.2 waves.

Summary

An analysis of the effects of combinations of wavefront aberration errors on the heterodyne mixing efficiency of a coherent lidar has been conducted and results obtained that permit a more quantitative approach to specifying RMS wavefront quality required for a system to meet a given performance developed.

Acknowledgements

This work was conducted in support of the NASA NMP EO-2 SPARCLE mission.

References

- [1] B.J. Rye, Appl. Opt. 21, 839 (1982).
- [2] A.E. Siegman, Appl. Opt. 5, 1588 (1966).
- [3] B.J. Rye and R.G. Frehlich, Appl. Opt. 31, 2891 (1992).

Doppler Frequency Estimation and Quality Control by Neural Networks

Jean-Luc ZARADER⁽¹⁾, Bruno GAS⁽¹⁾, Philippe DROBINSKI⁽²⁾, and Alain DABAS⁽³⁾

(1) Laboratoire des Instruments et Systèmes, Paris, France

(2) Laboratoire de Météorologie Dynamique du CNRS, Palaiseau, France

(3) Centre National de Recherches Météorologiques, Météo-France, Toulouse, France

1. Frequency estimation using neural networks

The analysis of sampled signals gives some difficulties for the power spectral density estimation. The classical estimators using Discrete Fourier Transform, like periodogram and correlogram are the most widely used as their implementation is easy (fast algorithms), but their low spectral resolution limits their range of applications. Moreover, they are sensitive to the noise present in signals. To increase the spectral resolution, we use parametric estimators, like AutoRegressive (AR), Moving Average (MA) and AutoRegressive Moving Average (ARMA) models. An important yet tricky step when using such filters is the search for the optimal structure for the signal modeling. A poor choice will lead to disturbances on the spectral representation. The selection of this order is critical for the noised signals analysis.

In response to these problems we propose a new power spectral density estimator using neural networks. Originally, the neural networks have been mainly used as classifiers. In this study, multilayer neural networks are trained to discern periodic signals according to their frequency.

In §2 we present the neuron and the different neural networks architectures. The estimator and results are presented in §3.

2. The neural networks

a) The neuronal cell

The definition of artificial neural networks is derived from knowledges in neurophysiology and neuro-anatomy. Like human brain, an artificial neural network is built with single cells, named neurons, linked between them by synaptic connections or weights, symbolizing the effect of biological synaptic length. They are, in fact, a simple representation of biological networks but its using in two different phases (training and testing) reminds the behavior of human knowlegde acquisition.

A neuronal cell calculates its state periodocally from the sum of its weighted inputs. Let us note y_i , the output of cell i , v_i its potential or activity, and w_{ij} the synaptic coefficient or weight transmitting, to cell i , the information ψ_j coming from its input j (Fig. 1).

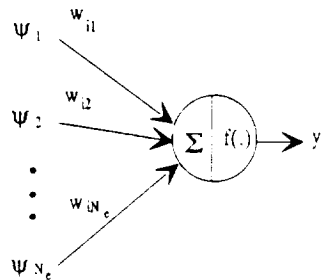


Figure 1 : Representation of cell i

Thus, the state v_i of the cell i is calculated from neuron's states or input units noted

$$\Psi = (\psi_1, \psi_2, \dots, \psi_{N_c})^T \quad (1)$$

The output is :

$$y_i = f\left(\sum_{j=1}^{N_c} w_{ij} \psi_j\right) = f(v_i) \quad (2)$$

With the matricial notation, we have :

$$Y = f(W^T \Psi) \quad (3)$$

where W is the matrix of network's weight, Ψ the input vector and Y the output vector.

The filter transfert function f , also called activation function, is taken continuous and derivable. The sigmoid function has been commonly used, especially because it approaches binary decision functions.

b) The structure

In neural networks, the cells are organized in layers. A network is built with an input layer, an output layer and one or several hidden layers. The multilayer networks are grouped in two classes, following the direction of connections :

- the networks without back links or feedforward networks;
- the networks with back links or feedback networks.

The weights that link the different neurons of network are all directed in the same direction "input layer → output layer". Figure 2 presents a fully connected feedforward network. In this type of network, a neuron receives the information from all cells of the preceding layer.

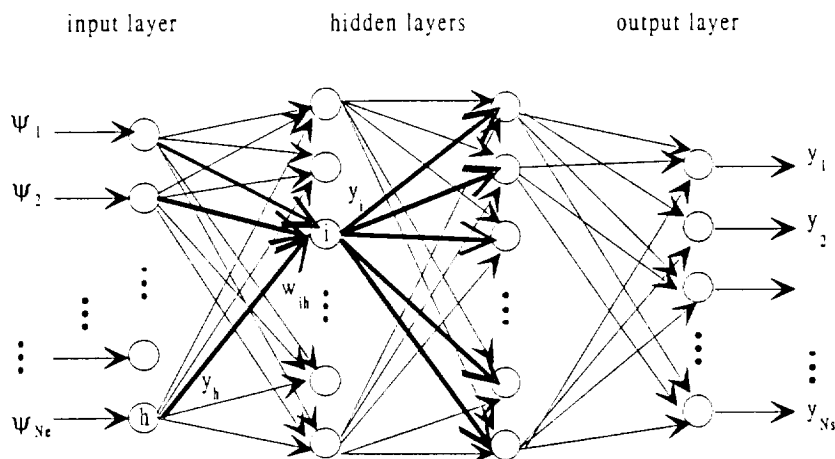


Figure 2 : feedforward networks

However, in some cases, different structures with local weights are used to increase performances. Cells are linked partially to the neurons of the preceding layer.

c) The backpropagation algorithm

The training algorithm of neural networks is used to insure the evolving of all weights of the network during the learning phase. It is based on the gradient criterion, developed for algorithms of adaptative signal processing. The cost function to minimize is calculated from the power of the error between the output vector obtained by propagation of the input vector in the network and the desired output vector. During this supervised training phase, all weights are modified following the value of the error gradient. This method is called method of gradient descent.

But this algorithm have disadvantages. The convergence can be disturbed by the presence of local minima. Some variations of this algorithm are used to try to avoid this difficulty, for example by introducing perturbations in the weight. Intuitively, the presence of additive noise allows to extract the network from an attractor pole. Others approaches are used to optimize the convergence of this algorithm. For example, we can note the presence of an adaptation factor for the weight evolving. Several methods have been developed for the calculation of this factor [Jacobs 1988, Minai and Williams 1990].

Finally, we will note that this algorithm can be used to analyse windowed signals. Often used like classifiers, networks have their weights calculated after complete presentation of training set. For windowed signal analysis, the calculation of the error criterion is global on the complete window of analysis.

Thus, the signal is analyzed block by block called analyzing window. The length of this window depends on the signal properties (temporal stationarity). The cost function is, with these windows of length N_T :

$$J[k] = \sum_{t=1}^{N_T} \sum_{i=1}^S (y_i'[k] - \hat{y}_{pr}^i[k])^2 \quad (4)$$

We have the classical cost function with N_T equal to the total number of the examples of the training set.

3. Frequency estimation

The network input layer receives the input spectral densities of simulated signals obtained using Zrnic's model [Zrnic 1975]. The output layer describes the spectral representation. The input and output cells represent the frequencies between $-F_S/2$ and $F_S/2$, where F_S is the sampling frequency. The network is activated for frequency recognition. From the presentation of a finite spectral density, the network attributes a +1 value to the output if the associated frequency is in the spectrum, -1, if it is not.

To evaluate performances, we have used a training set and testing set. In the training set, we have spectral densities at various carrier-to-noise ratio (CNR) performed by Fourier Transform of simulated signals. The CNR values are -5 dB, 0 dB, 10 dB and infinity (in fact, very large CNR). In the testing set, the CNR varies between -10 dB and 20 dB.

The input layer has 8 neurons, used to hold 8 spectral samples. Low CNR decreases performances of the network. A compromise has to be made to optimize the frequency recognition, between the time of learning phase and the number of patterns by spectral sample. Table 1 summarizes the performance of the network for 27 patterns by frequency.

Training set CNR	27 patterns by frequency
$+\infty$	100.0 %
10 dB	100.0 %
0 dB	98.6 %
-5 dB	95.1 %

Table 1 : Percentage of test patterns correctly classified.

Increasing the size of the training set would improve the performance at -5 and 0 dB [Dabas et al. 1996].

Let us see now how the 3 networks corresponding to training tests at -5 dB, 0 dB, 10 dB and infinity CNR behave with testing sets ranging from -10 dB to 20 dB. Figure 3 shows that neural networks trained at CNR = 10 dB and CNR = $+\infty$ give the same performance, while the performances at low CNR are improved when using a training test at -5 dB and 0 dB ($\approx +6\%$ at -10 dB). The performance of the networks trained at low CNR are even underestimated according to their training performance given in Table 1. One may conclude that it is not necessary to train the frequency estimating network at various CNR : Fig. 3 shows that one may rather chose a low training CNR and increase the number of patterns by frequency, in order to increase the training performance. This is true while CNR is not too low and sensitivity study on the CNR limit has to be conducted.

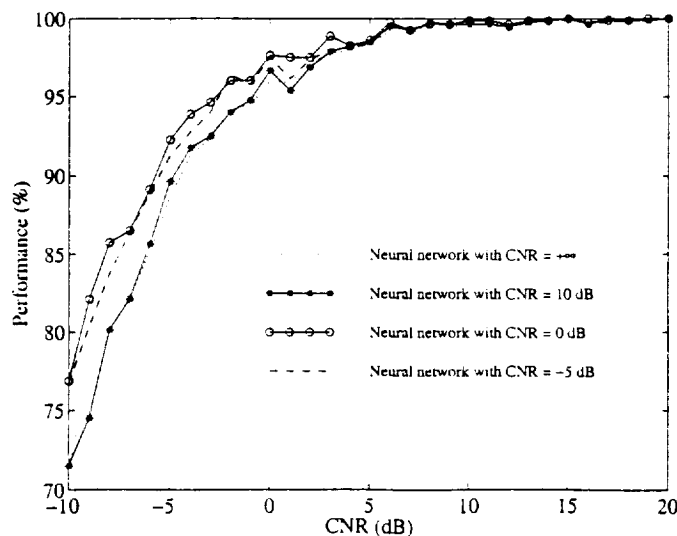


Figure 3 : Percentage of test patterns correctly classified versus CNR. The three curves correspond to 3 different training test : dashed line for -5 dB, circles for 0 dB, stars for 10 dB and dots for infinite CNR.

4. Conclusion

Neural networks have been widely used since 1985 when the backpropagation algorithm has been developed. From that time, the main application has been pattern recognition. In this study, we have tried to use it to classify signals according to their frequency. For that purpose, we have developed a new frequency estimator using a neural network. The performance we have obtained are interesting in terms of resistance to noise.

Compared to others methods, they are successful also because they allow information extraction contained in examples of training set to undertake an optimal segmentation of the representation space. They obtain interesting performances in generalization for examples which are not in the training set.

Future work will be dedicated to increase the spectral resolution and develop a quality control procedure [Dabas et al. 1999] taking advantage of neural network potential.

References

Dabas, A., J.L. Zarader, and P.H. Flamant, 1996 : Decision algorithm for the ALADIN signal processor. *ESA final report, n° 143649*, 100 pp.

Dabas, A., P. Drobinski, and P.H. Flamant, 1999 : Adaptive filters for frequency estimate of heterodyne Doppler lidar returns : Recursive implementation and quality control. *J. Atmos. Oceanic Technol.*, **16**, 361-372.

Jacobs R.A., 1988 : Increased rates of convergence through learning rate adaptation *Neural Networks*, **1**, 295-307.

Minai A.A. and R.D. Williams, 1990

Acceleration of back-propagation through learning rate and momentum adaptation, *International Joint Conference on Neural Networks*, Washington, D.C, IEEE and INNS, Lawrence Erlbaum Associates, McCaull editor, 1676-1679.

Zrnica, D.S., 1975 : Simulation of weatherlike Doppler spectra and signals. *J. Appl. meteorol.*, **14**, 619-620.

Shipborne backscatter lidar experiments in western Pacific region by research ship "Mirai"

Kouro Tamamushi, Tetuya Sugata, Kazuhiro Asai
Graduate School of Engineering, Tohoku Institutes of Technology
Yagiyama Kasumi 35-1, Taihaku-Ku, Sendai 982-, JAPAN
E-mail : asai@titan.tohtech.ac.jp

and

Ichiro Matsui, Nobuo Sugimoto
National Institute for Environmental Studies (NIES)
16-2 Onogawa, Tsukuba, Ibaraki304, Japan
E-mail: nsugimot@nies.go.jp, matsui@nies.go.jp

1. Introduction

The height distributions of Planetary Boundary Layer (PBL), aerosols, clouds are highly required in order to understand the radiative budget of the earth. The height of PBL top is observed between at a few hundred meters and at around 2 km, and is the region of the atmosphere in direct contact with the earth surface. Moisture and heat associated with human activities are trapped within the PBL¹⁾. On the other hand, cirrus clouds in the high troposphere is thought as a blanket effect for the global warming²⁾.

The atmospheric lidar sounding in the Western Pacific Ocean region is very important not only scientifically as above mentioned but also from the view point of the developments of spaceborne lidars. The reason is that only few data set of lidar backscatter experiments in this region have been taken. As part of Global Backscatter Experiment (GLOBE) missions in 1989 and 1990³⁾, the lidar backscatter cross section measurements were carried out in Pacific Ocean region to support the spaceborne Laser Atmospheric Wind Sounder project (LAWS), and recently PEM-West B (Pacific Exploratory Mission) were done to probe the air mass transported from the Asian continent into the Pacific troposphere in 1994⁴⁾. These two campaigns have been made by using the lidars and in situ instruments, i.e. the optical particle counter, particle impactors, equipped in NASA DC-8 research aircraft.

In Japan, a research ship "Mirai (8,800 tons displacement)", which is operated by Japan Marine Science and Technology Center (JAMSTEC) under contract of Science and Technology Agency (STA), was available to use for studies of oceanography and atmosphere from October 1998. Three two-months campaigns per year in the western Pacific Ocean region are scheduled for three years from 1999. We developed the shipborne backscatter lidars in order to participate these campaigns. The primary objectives are not only to take height distribution data of PBL, aerosols, cirrus cloud with dependencies of the longitude and the latitude for improving our knowledge of atmospheric circulation and climate dynamics, but also to support NASDA's spaceborne lidar projects, Mission Demonstration Satellite (MDS) -II "ELISE" mission, the ISS Japanese Experiment Module (JEM)/CDL mission⁵⁾. Especially in JEM/CDL using 2 μ m laser transmitter, the backscatter coefficients at 2 μ m in the free troposphere are strongly desired to design the system and to estimate the sensitivity in the oceans. The extrapolation technique will effectively work to estimate the 2 μ m backscatter coefficients using data set of those at 532 nm and 1064 nm³⁾.

In this paper, we would present our shipborne lidar system and will also give preliminary

backscatter experimental results in February-March 1999 mission.

2.Shipborne lidar system

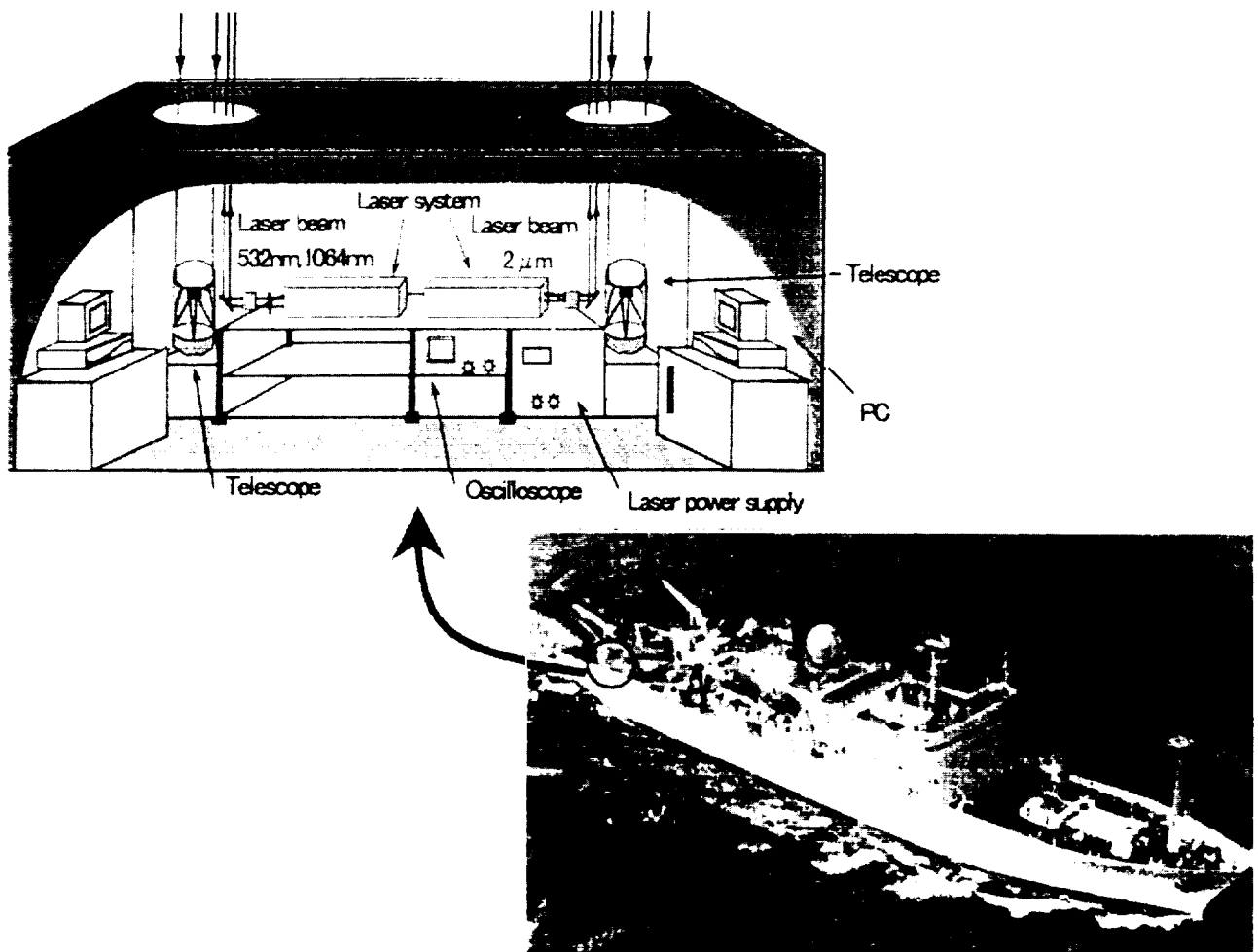
The 532 and 1064 nm backscatter lidars were developed to be equipped on the deck of the research ship. There are some primary concerns for the shipborne backscatter lidar, i.e. contamination problems for a window and optics due to high salted moisture, sprays from breakers. The lidar system was installed in an air-conditioned marine container with a dimension of 4m(L) x 2m(W) x 2.5m(H) in order to prevent them. Table 1 provides basic system specifications. As shown in the table, the lidar transmitter is based on the conventional Nd:YAG laser operating at 532 and 1064 nm. Backscattered signals are divided into four channels using filters after a collection with the receiving telescope with 28 cm dia. Each two channels detect the parallel component and vertical one for measuring the depolarization phenomena of aerosols and cloud at 0.532 μ m and 1.064 μ m, respectively. The 2 μ m coherent doppler lidar, of which the laser transmitter is Tm,Ho:YLF laser, will be equipped with the visible and near infrared lidars Tm,Ho:YLF in the lidar container in future.

Parameter	1064 nm channel	532 nm channel
Laser transmitter energy	100 mJ	50 mJ
Repetition rate	10 Hz	10 Hz
Receiving telescope	28 cm dia.	28 cm dia.
Detector	Si-APD	Photomultiplier
Detection	Analog(2 channel)	Analog (2 channel)
Digitizer	8 bits	8 bits
Another instruments		
GPS Navigation system, Clinometer, Sun photometer, Optical particle counter, Particle impactor, Doppler Radar		

Table.1 Basic system specifications

Another concern is roll and pitch motions associated with the swell. The pitch and roll informations are taken by the clinometer put on the optical bench in order to enable appropriate altitude corrections. An optical detector put close to the transmitting optics provides the trigger signal with TTL level to control the whole system. The trigger signal starts the digitizer and is simultaneously used for picking up the data of roll and pitch angles from the clinometer. Also, the navigation data are used when the lidar data are analyzed. The lidar was designed to have a capability of the backscatter coefficient measurements starting at 300 m from the ship, which corresponds to at he optical overlap distance of the lidar receiver, and extend up to an altitude of 15 km.

Fig.1 Schematic view of container for shipborne backscatter lidar



3. Experiment

The first lidar experiment is being carried out in February-March 1999 in the Western Pacific Ocean region, Mutu-Sekinehama (41N, Aomori Pref., Japan) – Guam(13N) – Solomon Islands(10S) – Bikini atolls(10N) – Shimonoseki (34N, Yamaguchi Pref., Japan). Other campaigns are scheduled in June-July 1999, October-November 1999 in the almost same ocean region.

References

1. Stephen P.Palm, Denise Hagan, Geary Schwemmer and S.H.Melfi; pp39-42, Advances in Atmospheric Remote Sensing with Lidar edited by A.Ansmann, R.Neuber, P.Rairoux and U.Wandinger (Springer,1996)
2. Salem Elouragini, Jacques Pelon and Pierre Flamant; pp87-90, Advances in Atmospheric Remote Sensing with Lidar edited by A.Ansmann, R.Neuber, P.Rairoux and U.Wandinger (Springer,1996)
3. Sury Chudamani, James D.Spinhirne, and Antony D.Clarke; Appl. Optics, 35, 4812(1996)
4. Jens Redemann, Richard P.Turco, Rudolf F.Pueschel, Edward V.Browell, William B.Grant; pp55-58, Advances in Atmospheric Remote Sensing with Lidar edited by A.Ansmann, R.Neuber, P.Rairoux and U.Wandinger (Springer,1996)
5. Toshikazu Itabe, Kohei Mizutani, Mitsuo Ishizu and Kazuhiro Asai; Technical Digest of The 10th Coherent Laser Radar Conference (Mount Hood, Oregon, 1999)

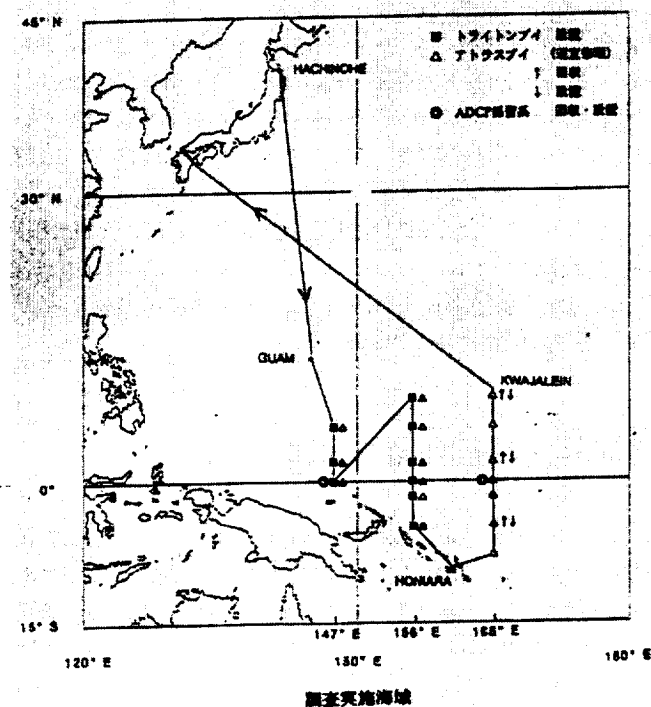


Fig.2 Research ship “Mirai” route in MR99-K01 mission

Pointing Knowledge for SPARCLE and Space-based Doppler Wind Lidars in General

G. D. Emmitt
Simpson Weather Associates
Charlottesville, VA 22902
804-979-3571

T. Miller
G. Spiers
NASA/MSFC
Huntsville, AL 35812
256-922-5882

Abstract

The SPACe Readiness Coherent Lidar Experiment (SPARCLE) will fly on a space shuttle to demonstrate the use of a coherent Doppler wind lidar to accurately measure global tropospheric winds. To achieve the LOS accuracy goal of ~ 1 m/s, the lidar system must be able to account for the orbiter's velocity (~ 7750 m/s) and the rotational component of the earth's surface motion (~ 450 m/s). For SPARCLE this requires knowledge of the attitude (roll, pitch and yaw) of the laser beam axis within an accuracy of 80 microradians (~ 15 arcsec). Since SPARCLE can not use a dedicated star tracker from its earth-viewing orbiter bay location, a dedicated GPS/INS will be attached to the lidar instrument rack. Since even the GPS/INS has unacceptable drifts in attitude information, the SPARCLE team has developed a way to periodically scan the instrument itself to obtain < 10 microradian (2 arcsec) attitude knowledge accuracy that can then be used to correct the GPS/INS output on a 30 minute basis.

Pointing Requirements for DWLs in Space

In some regards, measuring tropospheric winds from space is as much a matter of pointing as it is a matter of detection. In general, the focus of the community of DWL technologists and potential data users tends to be on the laser/telescope/scanner/detector. However, pointing control and knowledge is also critical for space-based (and airborne) DWLs, with knowledge being more demanding than control.

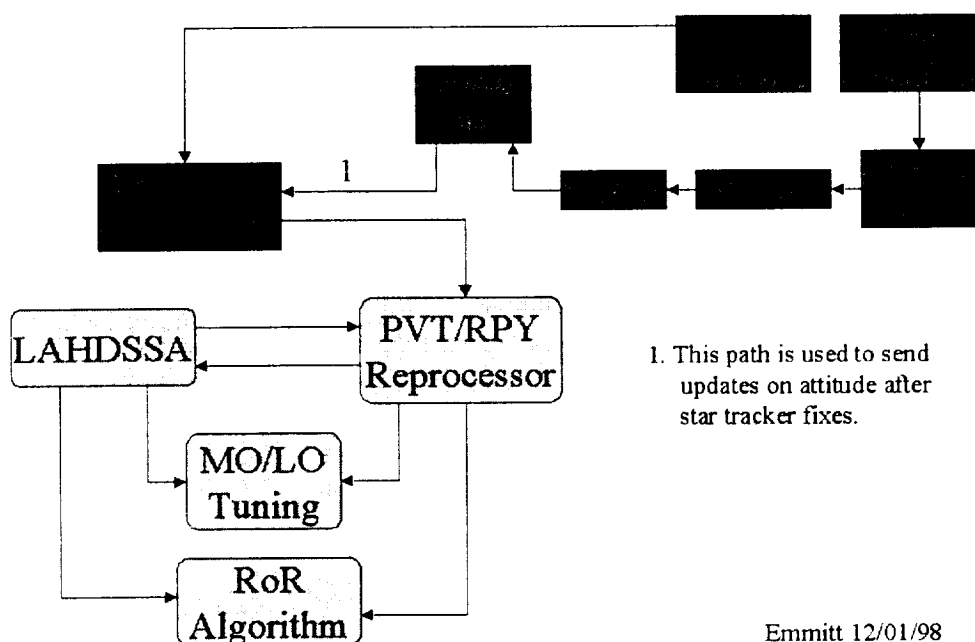
The DWL transmits a beam of photons towards the earth and the reflected photons return with a frequency shift that is a linear combination of the platform's motion relative to the earth's surface, the earth's surface motion due to its rotation and the motion of the beam's target (aerosol or clouds) relative to the ground. The task is to remove the platform and earth rotation components, leaving just the wind (or zero ground speed).

For heterodyne detection in a space-based DWL such as SPARCLE, the output of a local oscillator (LO) is mixed on the detector with the atmospheric returns from the primary transmitter. The goal is to tune the LO to a frequency that will perfectly correct for the earth's rotation and the shuttle's orbit velocity, resulting in a measure of 0.0m/s for the motion of the earth's surface in an earth centered coordinate system. In this case, the measure of the aerosol motion along the same LOS would be equally accurate (without regard to representativeness).

Within the total measurement budget for a <1m/s LOS observation error, the pointing knowledge (roll, pitch and yaw) is allotted ~ 80 μrads. As illustrated in Figure 1, the SPARCLE instrument has access to attitude knowledge from the orbiter through a time delayed route and from its own dedicated GPS/INS mounted very near the laser transmitter/optics canister. The orbiter uses a startracker to update its own attitude system which tends to drift at about .2 degrees per hour. The SPARCLE dedicated GPS/INS is periodically calibrated by the orbiter's system but it (GPS/INS) tends to drift on the order of 100 μrads per hour. Since the shuttle only maneuvers for a startracker update once every 12 or so hours, it is clear that an alternative means to correct the GPS/INS 100 μrads drift will be necessary. The remainder of this paper describes how the SPARCLE instrument will be used to apply corrections to the GPS/INS output to assure better than 50 μrad pointing knowledge.

Figure 1

SPARCLE POINTING KNOWLEDGE SYSTEM PLAN A



Emmitt 12/01/98

The Algorithm

In principal, for any shot containing a signal from the earth's surface, the detected aerosol LOS velocity can be corrected absolutely. However, with nearly 75-80% global coverage of cloud (including sub-visual cirrus), a significant fraction of the time there will be no ground return. Also, even if a return is sensed to be within an acceptable distance of the expected range to surface, salt spray over the ocean, blowing desert sands, and dense plumes of polluted boundary layer air may act to confound the assignment of zero velocity to the ground. Therefore the SPARCLE team decided to develop alternative attitude knowledge by using the DWL in a dedicated scan mode.

The pointing knowledge algorithm is called LAHDSSA (Lidar Attitude/Height Determination and Signal Search Algorithm) and a general outline of its functionality is presented in Figure 2. As the name implies, the algorithm does more than just determine the roll, pitch and yaw of the laser/optics canister. It also serves to search for signal capture in the event that attitude knowledge is off by $> 2-3$ degrees. Such a gross error in attitude knowledge is most likely to occur during initial startup when all the attitude knowledge is based upon the orbiter's systems. Since the SPARCLE instrument will be located a few 10's of meters away from the orbiter's attitude instruments, there is a real potential for significant physical offsets of a few degrees. While every reasonable effort will be made to align the laser beam axis with the orbiter's $-ZLV$ axis prior to launch, there is no economical way to assure a better than ± 1 degree alignment on the ground. After launch, the orbiter's bay may flex due to gravity unloading and/or differential thermal loading. In any case, there is a chance that upon startup, no signal will be detected by the SPARCLE instrument since the receiver bandwidth is limited to the range of velocities associated with ± 2 degrees.

To find the signal, the LAHDSSA methodically searches a prescribed range of the two degrees of freedom; the LO Tuning (LOT) and the Range of Regard (RoR). Figure 2 describes the sequence of actions involved in searching for the signal. Once the signal is found, the LAHDSSA performs an attitude calibration scan to determine the correction values that need to be applied to the roll, pitch and yaw being reported by the SPARCLE GPS/INS. The calibration scan involves taking data at 12 azimuths in 30 degree steps with 1 second dwells at each azimuth. The data from the surface returns are processed on board with a nonlinear function minimization algorithm. Multiple passes through the data result in estimates of the roll, pitch, yaw, altitude, and radial orbiter velocity. Table 1 presents the results of simulating the performance of LAHDSSA for a wide range of error conditions. In general, we expect LAHDSSA to provide attitude knowledge to within 10-20 μ rads each time the calibration scan is executed. At this time, we plan to run LAHDSSA approximately every 30 minutes. The scan will be scheduled in real-time to occur over generally cloud free areas. Since there are only three unknown attitude angles to be solved, only three of the 12 perspectives need to have surface returns. However, the 10-20 μ rads accuracy can only be expected when the number of perspectives with a surface return is greater than 6.

LAHDSSA

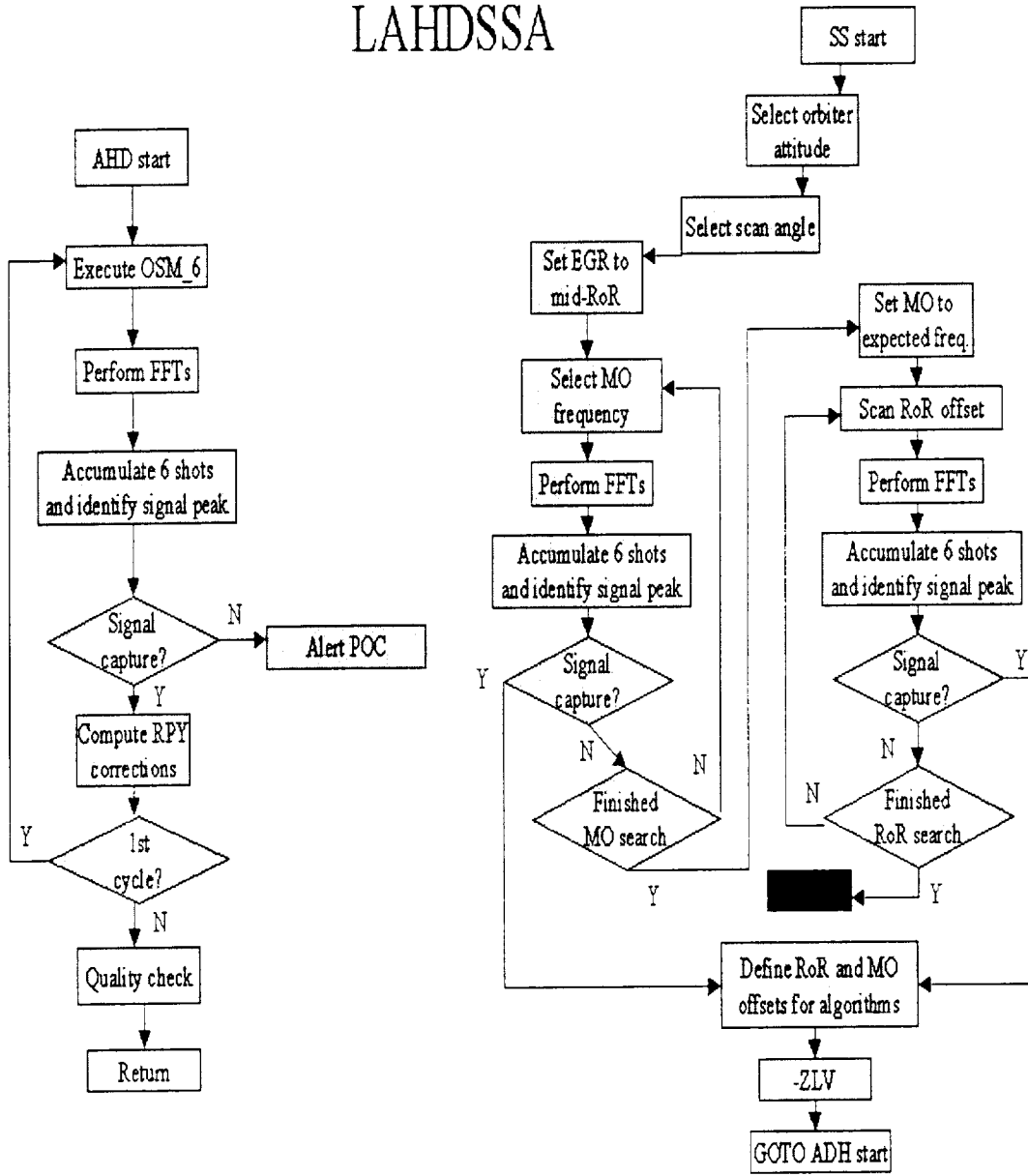


Figure 2

Table 1

RMSE for LAHDSSA estimates of true roll, pitch and yaw of SPARCLE instrument optical axis

Parameter	RMSE	Roll (microrads)	Pitch (microrads)	Yaw (microrads)	Height (meters)
Baseline	0	.09	.01	.01	14
Baseline + 1 μ rad read error	10	5	.04	.7	14
Orbiter tangential speed (m/s)	1.0	6	.06	11	14
	10.0	8	.01	110	14
Orbiter radial speed (m/s)	1.0	18(7)*	124 (2) *	.4	14
	10.0	41(6)*	1266 (1)*	.6	14
dr/dt (deg/sec)	.04	11	.3	.7	8
dp/dt (deg/sec)	.04	2	.08	.6	7
dy/dt (deg/sec)	.04	8	.3	1	7
SIGI roll error (deg)	1.0	3	.2	.3	7
SIGI pitch error (deg)	1.0	2	3	1	8
SIGI yaw error (deg)	1.0	5	.5	3	14

* () after second pass processing.

The combination of star tracker updates from the shuttle orbiter, a dedicated GPS/INS mounted physically close to the SPARCLE lidar and periodic attitude knowledge corrections using LAHDSSA will assure pointing knowledge in excess of that allowed in the total SPARCLE observation error budget.

Acknowledgments

The authors recognize the support from NASA Headquarters and the contributions of the following organizations to the SPARCLE mission: University of Alabama at Huntsville, Marshall Space Flight Center, Jet Propulsion Laboratory, Langley Research Center, National Oceanographic and Atmospheric Administration, Goddard Space Flight Center, Coherent Technologies Inc., and Simpson Weather Associates, Inc.

Heterodyne Efficiency - Theory and Practice

Stephan Rahm, Adelina Ouisse, Frank Häfner*

DLR- Lidar group
P.O. Box 11 16
D-82230 Wessling, Germany
Fax: (+49) 8153 28 1608
e-mail: Stephan.Rahm@dlr.de

*DaimlerChrysler Aerospace
P.O. Box 80 11 69
D-81663 München, Germany

Heterodyne receivers for use in coherent Doppler lidar have been often discussed in books and publications¹⁻⁴. Here an extensive comparison in between practical setup, the theoretic formalism, and numerical simulation is presented both in a qualitative and quantitative way. The often-appearing questions: "Is the lidar receiver aligned perfect?" or „What are the critical parameter in heterodyning“ can then be answered. Also a proposal for an alignment procedure for the receiver of a Doppler lidar will be given.

The formalism of heterodyning two electromagnetic waves is already well known. Here only a short review of the formalism is given for the purpose of quantitative simulation. In general, the electrical field vector of a wave is described by

$$\vec{E}(\vec{x}, t) = \text{Re} \left\{ \vec{E}(\vec{x}, t) \right\} = \text{Re} \left\{ \vec{E}(\vec{x}) \exp \left(j \left(\omega t - \vec{k} \cdot \vec{x} + \varphi \right) \right) \right\} \quad (1)$$

with: \vec{x} geometric vector; \vec{k} : wave vector; t: time; ω : angular frequency.

The approach of a complex field was chosen because then the calculation of the Pointing vector and the heterodyning is straightforward. Combining two optical beams at the beam splitter, the local oscillator (Lo) and the signal (S), the total electrical field $E_{\text{tot}} = E_{\text{Lo}} + E_{\text{S}}$. Now the total optical power passing through an area A is given by:

$$P_{\text{opt}} = \frac{c \epsilon}{2} \iint_A \left(\vec{E}_{\text{Lo}} \cdot \vec{E}_{\text{Lo}} + \vec{E}_{\text{S}} \cdot \vec{E}_{\text{S}} + 2 \text{Re} \left\{ \vec{E}_{\text{Lo}} \cdot \vec{E}_{\text{S}} \right\} \right) dA \quad (2)$$

At sensitive receivers the detector normally is a reverse biased photodiode. The optical power gets there converted to a photo current according to

$$I_{\text{tot}} = \frac{e \eta}{h \nu} P_{\text{opt}} = I_{\text{Lo}} + I_{\text{S}} + I_{\text{h}} \quad (3)$$

with e: elementary charge; η : quantum efficiency; h: Plank constant; ν : frequency. Three currents are contributing: The DC currents caused by Lo and signal beam and the heterodyne term

$$I_{\text{Lo}} = \frac{c \epsilon e \eta}{2 h \nu} \iint_A \vec{E}_{\text{Lo}} \cdot \vec{E}_{\text{Lo}} dA \quad (4a)$$

$$I_{\text{S}} = \frac{c \epsilon e \eta}{2 h \nu} \iint_A \vec{E}_{\text{S}} \cdot \vec{E}_{\text{S}} dA \quad (4b)$$

$$I_{\text{h}}^2 = \frac{1}{2} I_{\text{h}}^2 = \frac{1}{2} \left(\frac{c \epsilon e \eta}{h \nu} \right)^2 \left(\iint_A \text{Re} \left\{ \vec{E}_{\text{Lo}} \cdot \vec{E}_{\text{S}} \right\} dA \right)^2 \quad (4c)$$

In most but not all cases there is the DC current due to the optical signal power negligible compared to the Lo current. In equation 4c the heterodyne current i_h is the peak value according to the definition of the electrical field given in equation 1. From Equation 4c it can be deduced, that the heterodyne current depends from a good matching of the Lo and signal beam in amplitude and phase. A factor that is often used to describe the quality of the matching is the mixing efficiency

$$m = \frac{\left(\iint \operatorname{Re} \left\{ \vec{E}_{Lo} \vec{E}_S^* \right\} dA \right)^2}{\iint \vec{E}_{Lo} \vec{E}_{Lo}^* dA \iint \vec{E}_S \vec{E}_S^* dA} = \frac{i_h^2}{2 I_{Lo} I_S} \quad (5)$$

However the mixing efficiency alone may lead to wrong results. For example consider the case of a poor match of a very small Lo with a large spot of an Airy pattern. At this case you will get a low m with a big detector and an $m \cdot 1$ with a very small detector area. But you will have a pretty bad lidar with this small detector, for most of the received power is lost for the detection process.

To simulate the heterodyning, the detector surface (quantum efficiency) and the incident beams are modelated as two-dimensional arrays.

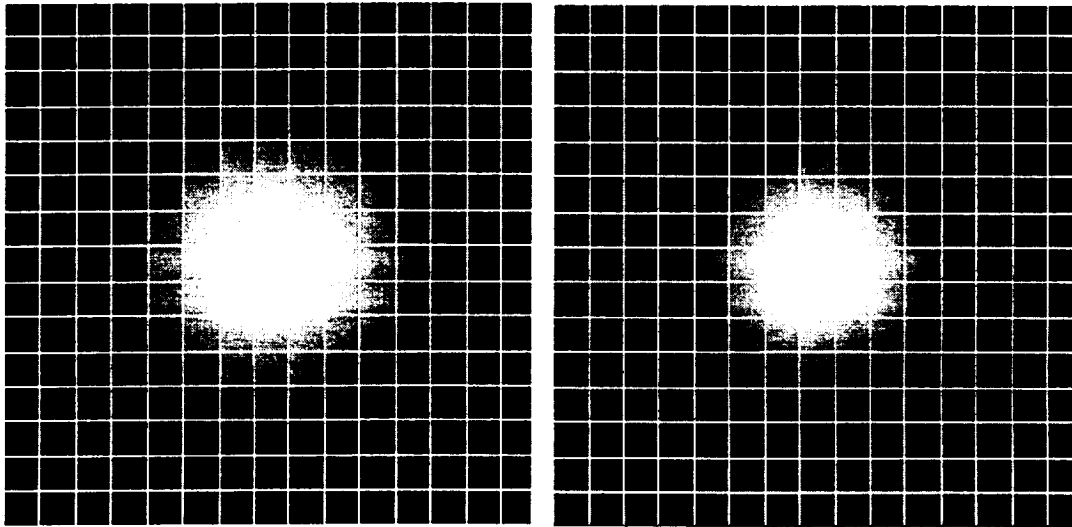


Fig. 1: Sampling of the Gaussian Lo (left) and the Airy pattern of the signal (right) here with a 15X15 array overlaid.

The assumption is that the field does not change too much within one pixel. This calls for a sufficient small pixel size. Empirically an array size of 200 x 200 pixel shows a good agreement between analytical formalism and simulation results. For the calculation of the currents I_{Lo} , I_S , and i_h , equation 4 is applied for each pixel and the results are integrated over the detector surface. The array for the Lo and signal field can either be imported from the optics design program ASAP or some idealised fields (Gaussian, Top Hat, or a Airy pattern) can be calculated within the simulation. All parameters like tilt, shear, spot size, defocus, and power can be choosen.

With this simulation the amplitude matching of Airy and Gaussian Lo for a given detector can easily be done. For example with a 200 μm rectangular detector and a radius of the Airy pattern of 130 μm the optimum radius of the Gaussian Lo can be optimised to $69 \pm 1 \mu\text{m}$. However much more critical than the matching of the size of Lo and signal is the adjustment of the lidar.

The first thing to take care is the fact that tilt and shear are Fourier transform pairs. This means a tilt before the lens (figure 2) is transformed to a shear at the focus (detector) and vice versa. The optical arrangement shown in figure 2 was simulated in LabView[®] to obtain the heterodyne efficiency in dependence of a tilt of the beam splitter and the mirror. With this program, it is possible to simulate the alignment process in a very realistic way. However the simulation deals with ideal lenses and field distributions which is only close to reality at 10.6 μm wavelength. But it is also possible to import the data calculated by an optic design program like ASAP for a higher accuracy with the lack of the “real time feeling”.

In theory it is clear how to align a Doppler lidar. Simply make the signal beam collinear with the Lo beam and focus it on the detector. In practice this makes much more problems, for especially the signal beam is very hard to catch due to an extreme low power level.

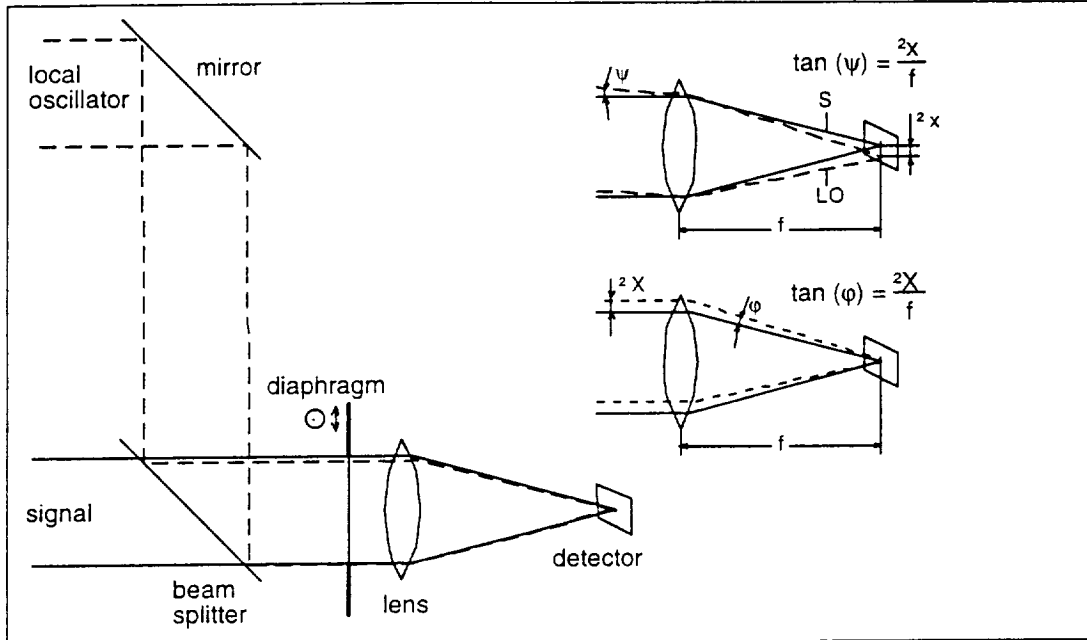


Fig.: 2 Optical setup used to simulate heterodyning.

The arrangement shown in figure 2 was used to simulate the heterodyning and a rather simple alignment procedure with only one auxiliary diaphragm was developed.

1. Shut down the Lo and align the signal beam onto the detector for maximum I_s , this can be done by aiming at a hard target with a pulsed system or by introducing a chopper in a cw system.
2. Place a diaphragm with adapted diameter before the lens so that I_s again gets maximum.
3. Turn on the Lo
4. Adjust the Lo with the mirror to maximum I_{Lo}
5. Adjust the beam splitter to maximum i_h
6. Repeat step three and four until no further improvement is possible. Remove the diaphragm (optional, only necessary for the last tenth of a dB)

Once a good alignment is established simply playing with all possible degrees of freedom can check the critical parameters. The results for a $10.6 \mu\text{m}$ receiver with 5 mm diameter of the Lo and signal beam and 50 mm focal length of the lens are the following.

A tilt is the most critical parameter at the given arrangement. A tilt of only 0.1° causes a drop in the heterodyne current of roughly 8 dB. And 0.2° tilt makes 36 dB (!) loss due to the fact that the spot is beside the detector.

Shear (at the beam splitter) is rather uncritical. For example with a Gaussian beam diameter of 5 mm diameter a shear of 1 mm between the Lo and the signal causes only a drop of only 0.7 dB. To loose 6 dB a shear of 3 mm (!) is necessary!

The comparison between measurements and the simulation has to be discussed very carefully. Especially with high values for the tilt the drop in the heterodyne current may exceed some 60 dB so that even minor diffraction effects may dominate in the heterodyne current. At a shear the comparison between simulation and experiment is more convenient and will be presented here. Figure 3 shows the results of the experiment together with the theory

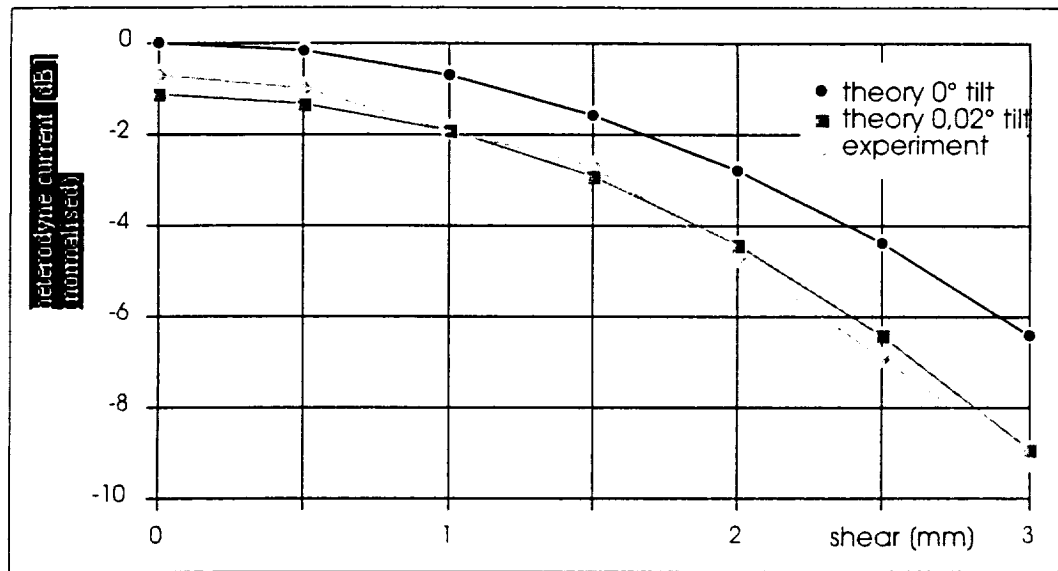


Fig. 3: Simulated values for the heterodyne current over a shear together with measured results.

The theoretic values for the heterodyne current are 0,7 dB higher than the measured ones without any shear. It is expected that this is due to some inaccuracies in alignment and amplitude matching. The difference is increasing with increasing shear. But if an error of 0.02° in tilt is allowed both for the Lo and the signal beam both curves show a quite good coincidence.

Conclusion

We presented a simulation tool written under LabView[®], which calculates the detector current and the heterodyne efficiency for a given optical receiver breadboard in quantitative way. The results of the expected values correspond with the simulation and the experiment. Like expected a tilt between Lo and signal beam is the most critical parameter in aligning a heterodyne receiver. A proposal for a procedure to align a heterodyne receiver with only one auxiliary diaphragm was made. This work was performed under ESA Contract No. 12852/NL/SB.

References

1. R.H. Kingston, "Detection of Optical and Infrared Radiation" Springer Verlag 1978
2. J. J. Degnan and B. J. Klein, "Optical Antenna Gain. 2: Receiving Antennas", Appl. Opt. Vol. 13, No. 10, 2397-2401, (1974)
3. S.C. Cohen, "Heterodyne detection: phase front alignment, beam spot size, and detector uniformity", Appl. Opt., Vol. 14, No 8, 1953-1959, (1975)
4. Receiving efficiency of monostatic pulsed coherent lidars. 1: Theory", Appl. Opt. Vol. 29, No. 8, 4111-4132, (1990)

Enhanced double-edge technique for Doppler lidar

Peter J. Winzer, Walter R. Leeb, Alexandru F. Popescu*

Institut für Nachrichtentechnik und Hochfrequenztechnik, Technische Universität Wien,
Gußhausstraße 25/389, A-1040 Wien, Austria

* European Space Agency, ESTEC/TOS-MM
P.O. Box 299, NL-2200 AG Noordwijk ZH, The Netherlands

1. INTRODUCTION

To make the Doppler shift imposed on backscattered transmit laser radiation accessible to electronic measurement, incoherent Doppler lidar instruments employ a frequency selective device in the optical regime that transforms optical frequency shifts to optical intensity variations. These are processed by direct detection methods (e.g. APDs or CCD arrays).

The edge technique¹ as well as its variation, the double-edge technique,² employ the steep filter slopes (edges) of Fabry-Perot etalons (FPEs) as frequency selective devices. A major shortcoming of the conventional edge technique is the need for using part of the weak received signal for normalization purposes. Furthermore, the double-edge technique requires two FPEs whose transmission functions must be actively stabilized so that their mutual frequency drift is much smaller than their half-width at half maximum (HWHM). In this paper we propose an enhanced, patent-pending version of the double-edge technique that both

- eliminates the need for mutual edge filter stabilization, and
- uses *all* received power for retrieving the Doppler shift information.

We also compare the performance of our system with that of a more conventional double-edge setup that employs two edge filters. (Note that this system is *not* exactly the same as that of Ref. 2 in that the *difference* rather than the *ratio* of the two edge filter outputs is taken. An adequate analysis of the system according to Ref. 2 is more complicated and will be presented in a follow-up paper.)

2. CONVENTIONAL DOUBLE-EDGE SETUP

The basic setup of a possible conventional double-edge (DE) receiver is shown in Figure 1 (a): After splitting off (beamsplitter BS1) a fraction α of the return signal power P_R for normalization purposes ('energy monitor' signal c), beamsplitter BS2 equally distributes the remaining power $(1 - \alpha)P_R$ to two edge filters (A and B). Their outputs produce signals a and b , after conversion to the electrical regime with conversion factor G . As shown schematically in Figure 1 (b), starting from a transmit laser frequency f_0 (at which the filters have transmission values $T_{A,0}$ and $T_{B,0}$), a Doppler shift Δf of the return signal causes the transmission $T_A(f)$ of edge filter A to drop by an amount ΔT_A , whereas that of filter B rises by ΔT_B . To take into account filter loss, the edge filter transmission maximum is assumed to be $1 - L$. Provided that the filters have the same slope and that the frequencies to be measured fall within the linear range of both filters, the relation $\Delta T_A = \Delta T_B = \Delta T$ holds, causing the difference signal $a - b$ for the return radiation to equal

$$a - b = \frac{1}{2}(1 - \alpha)P_R G(T_{A,0} - T_{B,0} - 2\Delta T). \quad (1)$$

As the energy monitor channel produces the signal $c = \alpha G P_R$, the receiver output reads

$$s = \frac{a - b}{c} = \frac{1 - \alpha}{2\alpha}(T_{A,0} - T_{B,0} - 2\Delta T) \quad (2)$$

For further author information:
Tel.: +43-1-58801/38901
Fax: +43-1-5870583
e-mail: pwinzer@nt.tuwien.ac.at

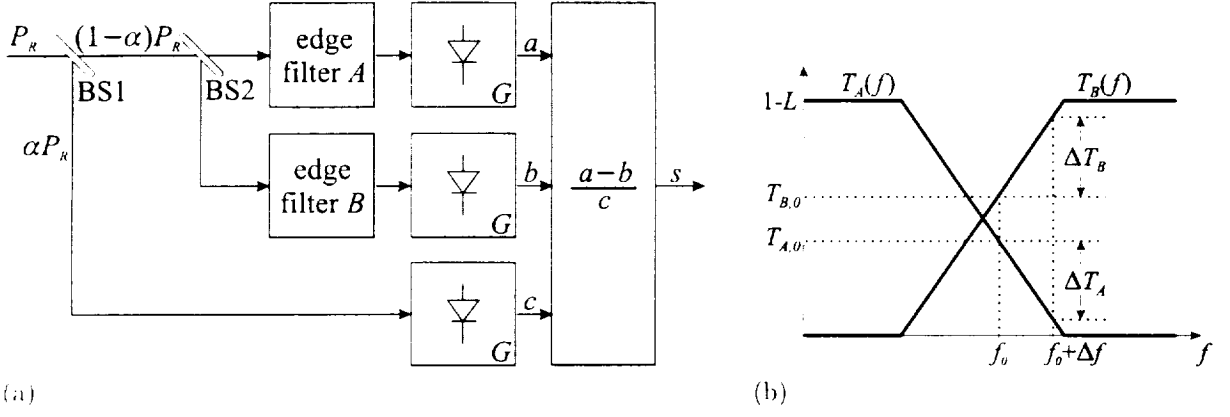


Figure 1. Basic setup of a double-edge (DE) Doppler lidar receiver (a), and principle of functionality (b).

for the return radiation. Subtracting this signal from a reference measurement $s_{ref} = s|_{\Delta T=0}$ of the transmit laser frequency finally yields

$$\Delta s = s_{ref} - s = \frac{1-\alpha}{\alpha} \Delta T, \quad (3)$$

from which the Doppler shift can be extracted.

3. ENHANCED DOUBLE-EDGE TECHNIQUE USING EDGE FILTER TRANSMISSION AND REFLECTION

Figure 2 (a) shows the basic setup of our enhanced version of the DE technique: The return signal power P_R is first passed through a circulator (CIR), a non-reciprocal device that passes power from port 1 to 2, from 2 to 3 and from 3 to 1 only (see e.g. Ref. 3). The circulator's insertion loss is taken account of by a factor $\beta < 1$. While the light *transmitted* through the edge filter is converted to the electrical regime with conversion factor G_X , the filter *reflections* are diverted by the circulator to a detector with conversion factor G_Y . As transmission $T(f)$ and reflection $R(f)$ of any filter are always tied together by

$$T(f) + R(f) = 1 - L, \quad (4)$$

(the filter losses L are assumed to be frequency-independent over the range of possible Doppler shifts) the resulting system is basically a DE receiver with *one edge filter only*, thus eliminating the need for accurately frequency locking two extremely narrow-band filters. Figure 2 (b) illustrates schematically this system's principle of operation: The Doppler-shifted return signal causes the edge transmission to drop by an amount ΔT from its value T_0 obtained at the transmit frequency f_0 , whereas the edge reflection rises to $R_0 + \Delta R$. The difference signal $x - y$ thus reads for the return radiation

$$x - y = P_R \beta G_X (T_0 - \Delta T) - P_R \beta^2 G_Y (R_0 + \Delta R), \quad (5)$$

if we assume the circulator's insertion loss from port 1 to 2 to equal that from port 2 to 3. In order to arrive at an output signal proportional to ΔT , we set $G_X = \beta G_Y$. Having in mind a fair comparison

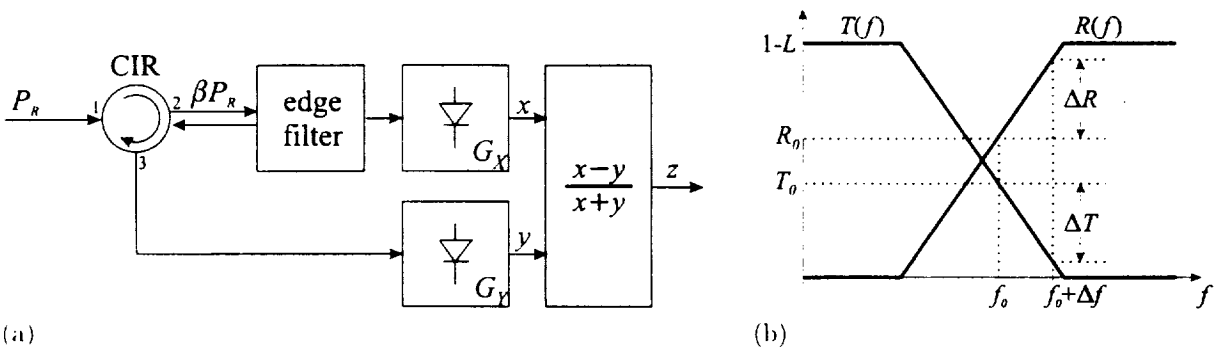


Figure 2. Basic setup of the enhanced DE receiver (a), and principle of functionality (b).

with the conventional DE technique, we assume that the conversion gain has an upper bound G owing to technological constraints. We therefore have $G_X = \beta G_Y = \beta G$, and arrive at

$$x - y = P_R \beta^2 G (2T_0 - 2\Delta T + L - 1), \quad (6)$$

where use has been made of (4): Independent of any edge linearity conditions, the relations $R_0 \equiv 1 - L - T_0$ and $\Delta R \equiv \Delta T$ always hold. For the sum of x and y we similarly find

$$x + y = P_R \beta^2 G (1 - L), \quad (7)$$

which indicates that the sum of the two channels can be used for energy monitoring: there is *no need* for splitting off a fraction of the return signal for normalization purposes within our approach! The receiver output z can be written for the return radiation as

$$z = \frac{x - y}{x + y} = \frac{2T_0 - 2\Delta T + L - 1}{1 - L}. \quad (8)$$

Subtracting this signal from a reference measurement $z_{ref} = z|_{\Delta T=0}$ of the transmit laser frequency, as is done in the conventional DE technique, finally yields

$$\Delta z = z_{ref} - z = \frac{2\Delta T}{1 - L}, \quad (9)$$

from which the Doppler shift can be extracted.

4. PERFORMANCE COMPARISON

In this section we compare the performance of the two DE systems described above on the basis of the expected velocity-measurement error. For simplicity we assume that the slope of the edge is linear over the range of possible Doppler shifts, leading to the relation $\Delta T = \kappa v$ between the change in edge transmission and the velocity v to be measured (κ being a system-independent constant of proportionality). Combining this relation with (3) and (9) and taking note of the randomness of Δs and Δz brought by detection noise yields

$$\hat{\mathbf{v}} = \begin{cases} \frac{\Delta \mathbf{s} \alpha}{\kappa(1 - \alpha)} & \text{for the conventional DE receiver, and} \\ \frac{\Delta \mathbf{z}(1 - L)}{2\kappa} & \text{for the enhanced DE receiver} \end{cases} \quad (10)$$

for the measured velocity $\hat{\mathbf{v}}$, whose ensemble average $\langle \hat{\mathbf{v}} \rangle$ equals the true velocity v . (Note that bold print indicates random quantities.) Computing the standard deviation $\sigma_{\hat{\mathbf{v}}}$ of $\hat{\mathbf{v}}$, the velocity measurement error, we obtain, with the help of (2), (8), and (10),

$$\sigma_{\hat{\mathbf{v}}} = \begin{cases} \frac{2T_{A,0} - 1 + L - 2\Delta T}{2\kappa} \frac{\sigma_{\mathbf{s}}}{\langle \mathbf{s} \rangle} & \text{for the conventional DE receiver, and} \\ \frac{2T_0 - 1 + L - 2\Delta T}{2\kappa} \frac{\sigma_{\mathbf{z}}}{\langle \mathbf{z} \rangle} & \text{for the enhanced DE receiver,} \end{cases} \quad (11)$$

where we assumed that there is enough reference signal to neglect the noise associated with the reference measurements s_{ref} and z_{ref} , and where we set $T_{B,0} = 1 - L - T_{A,0}$, which is valid for a perfectly adjusted conventional DE receiver with linear edge slopes (cf. Figure 1). We next have to evaluate the (inverse) signal-to-noise ratios (SNRs) $\sigma_{\mathbf{s}}/\langle \mathbf{s} \rangle$ and $\sigma_{\mathbf{z}}/\langle \mathbf{z} \rangle$, which requires some precaution: The standard deviation of a fraction of random variables (such as \mathbf{s} and \mathbf{z} are) *cannot* be obtained by simple means in general. For 'moderately high SNRs' for both numerator and denominator, as e.g. Ref. 1 puts it, the formulae

$$\frac{\sigma_{\mathbf{s}}^2}{\langle \mathbf{s} \rangle^2} \approx \frac{\sigma_{\mathbf{a}-\mathbf{b}}^2}{\langle \mathbf{a}-\mathbf{b} \rangle^2} + \frac{\sigma_{\mathbf{c}}^2}{\langle \mathbf{c} \rangle^2} \quad \text{and} \quad \frac{\sigma_{\mathbf{z}}^2}{\langle \mathbf{z} \rangle^2} \approx \frac{\sigma_{\mathbf{x}-\mathbf{y}}^2}{\langle \mathbf{x}-\mathbf{y} \rangle^2} + \frac{\sigma_{\mathbf{x}+\mathbf{y}}^2}{\langle \mathbf{x}+\mathbf{y} \rangle^2} \quad (12)$$

can be used. Checking the validity of these relations, we found that they are only valid if the SNRs of the denominators, i.e. of \mathbf{c} and $\mathbf{x} + \mathbf{y}$, defined as $\langle \mathbf{c} \rangle/\sigma_{\mathbf{c}}$ and $\langle \mathbf{x} + \mathbf{y} \rangle/\sigma_{\mathbf{x}+\mathbf{y}}$ respectively, are larger

than about 5 (i.e. 14dB!), which may be considered more than just 'moderate', especially when working in a typical, photon-starved lidar scenario. (A detailed derivation of this and related results will be the topic of a publication to come.) With the help of (12) and the results of the previous sections, an evaluation of $\sigma_{\mathbf{b}}$ is straightforward once expressions for the encountered noise variances have been found: Assuming realistically that signal-independent *electrical noise* limits system performance, i.e. that all optoelectronic devices add noise with variance σ_0^2 , we have $\sigma_{\mathbf{a}-\mathbf{b}}^2 = \sigma_{\mathbf{x}-\mathbf{y}}^2 = \sigma_{\mathbf{x}+\mathbf{y}}^2 = 2\sigma_0^2$, and $\sigma_{\mathbf{c}}^2 = \sigma_0^2$. Using these relations, we can evaluate the fraction of the velocity measurement standard deviations of the two systems, the measurement enhancement factor E_σ , as

$$E_\sigma = \frac{\sigma_{\mathbf{b},\text{conventional}}}{\sigma_{\mathbf{b},\text{enhanced}}} = \frac{\sigma_{\mathbf{s}}/\langle\mathbf{s}\rangle}{\sigma_{\mathbf{z}}/\langle\mathbf{z}\rangle} \approx \frac{\beta^2(1-L)}{\sqrt{2}\alpha} \left[\frac{(2T_0 - 1 + L - 2\Delta T)^2 + 8\alpha^2/(1-\alpha)^2}{(2T_0 - 1 + L - 2\Delta T)^2 + (1-L)^2} \right]^{1/2}, \quad (13)$$

where we fairly assumed that the transmit laser is equally offset in both systems, i.e. that $T_0 = T_{A,0}$. (We also analyzed the case where signal-dependent noise (e.g. shot noise) dominates: the resulting enhancement is then slightly less, but typically still larger than unity.)

5. DISCUSSION AND CONCLUSION

Figure 3 visualizes equation (13): In (a), the dependence of E_σ on the effective edge filter transmission change $\Delta T/(1-L)$, which proportional to the Doppler shift Δf within our linear model, is shown with the beam splitter reflection α as a parameter. The peak transmission of the extremely high resolution FPEs is assumed to be 10% for this plot (i.e. $L = 0.9$), and the circulator's insertion loss is assumed to be 0.5dB (i.e. $\beta = 0.9$). One clearly sees that the enhanced DE system leads to improvement factors in terms of velocity measurement error of about 50% to 170%. Figure 3 (b) shows E_σ as a function of the filter loss L for $\alpha = 0.3$, revealing that the achievable performance gain is largely independent of L , which proves generally true for $\alpha \gtrsim 0.1$.

These remarkable results go in parallel with the fact that only a *single* FPE (and thus no mutual frequency stabilization!) is necessary in our concept, laying open the great potential of the proposed technique.

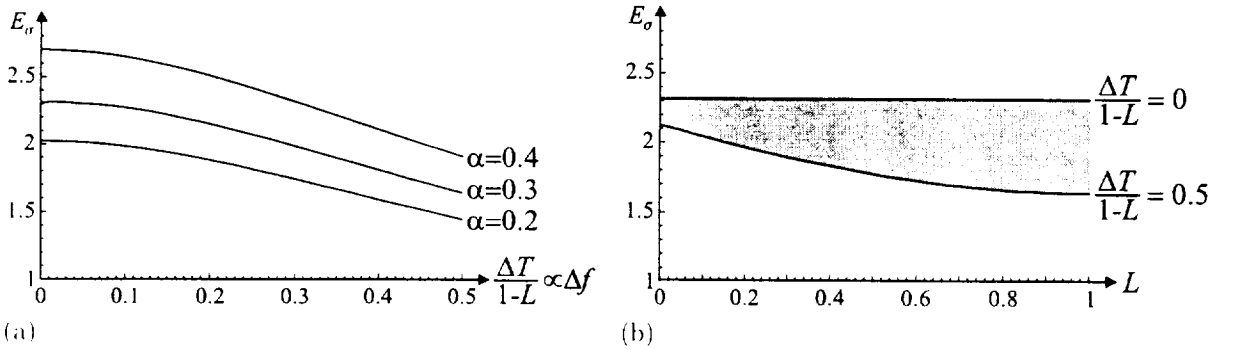


Figure 3. Dependence of the measurement enhancement factor (13), E_σ , that is achieved by using the enhanced double edge technique instead of the conventional one: (a) shows E_σ as a function of the effective edge filter transmission change $\Delta T/(1-L)$, proportional to the Doppler shift Δf , with the beam splitter reflection α as a parameter; (b) shows E_σ as a function of the filter loss L for $\alpha = 0.3$.

ACKNOWLEDGEMENT

Major parts of the work reported here were done under ESA Contract No. 9673/91/NL/PB(SC).

REFERENCES

1. C.L.Korb, B.M.Gentry, C.Y.Weng, *Edge technique: theory and application to the lidar measurement of atmospheric wind*, Appl. Opt. **31**, 4202-4213 (1992).
2. C.L.Korb et al., *Theory of the double edge technique for Doppler lidar wind measurements*, Appl. Opt. **37**, 3097-3104 (1998).
3. N.Kashima, *Passive optical components for optical fiber transmission*, Artech House (1995).

Estimation of return signal spectral width in incoherent backscatter heterodyne lidar

Barry J. Rye

*CIRES (University of Colorado/NOAA)
Environmental Technology Laboratory
R/E/ET2, NOAA ERL, 325 Broadway, Boulder, CO 80303-3328
Phone: (303) 497-6509 FAX: (303) 497-5318 email: brve@etl.noaa.gov*

It can often be reasonably assumed that the spectral profile of the return from an atmospheric backscatter heterodyne lidar is known. But this is not valid when the Doppler shift varies within the period over which return pulses are accumulated, for example if the return is obtained from regions that are spatially well-separated as may happen in the spaceborne experiment SPARCLE, or if there is significant velocity turbulence within the scattering volume observed by a static system. Our interest in estimating the signal spectrum was initiated by an experiment carried out at ETL to simulate a SPARCLE return by sparse sampling of data obtained from a ground-based lidar over a period of several hours.¹ Then the overall spectrum must be estimated along with the Doppler shift and return power. Here we consider only the simplest case when it can be correctly assumed that the spectrum has a Gaussian profile and the only unknown is its bandwidth. Specifically, the expected autocorrelation of the discretely-sampled photodetector output at the k th lag is assumed to be

$$\mu_k = P_N \left\{ \delta \exp\left[-(2\pi f_2 k)^2 / 2\right] \exp(j2\pi f_1 k) + 1 \right\} \quad (1)$$

where P_N is the noise power and the unknowns are the wideband signal-to-noise ratio (SNR) δ , the Doppler shift f_1 , and the signal bandwidth f_2 ; these two frequencies are assumed normalized by being divided by the receiver search bandwidth and are therefore dimensionless. Thus, if a return signal of bandwidth that corresponds to a 1 m/s frequency shift is observed within a receiver of bandwidth corresponding to 50 m/s, then $f_1 = 1/50 = 0.02$.

The precision of optical instruments is usefully compared with the limiting case when the only noise in the system arises from photocount fluctuations which are further assumed to have Poisson statistics. The standard deviations σ , of the three unknowns are then given by^{2,3,4}

$$\frac{\sigma_\delta^2(\delta)}{\delta^2} = \frac{\sigma_{f_1}^2(f_1)}{f_1^2} = \frac{2\sigma_{f_2}^2(f_2)}{f_2^2} = \frac{1}{N} \quad (2)$$

where N is the mean photocount. It is somewhat surprising to observe that the limiting standard deviation of the bandwidth estimate is a factor of $\sqrt{2}$ better than that of the Doppler estimate because it often supposed that the former is the more difficult measurement.

For the heterodyne receiver, the Cramer-Rao lower bounds on the three standard deviations are most simply expressed using formulas that apply to series with Gaussian statistics for which a derivation was provided by Porat and Freidlander.⁵ For a data time series with the Gaussian autocorrelation of Eq. (1),⁶ the results can be expressed in

terms of a signal covariance matrix G containing the elements $g_{ik} = \exp\left[-(2\pi f_2 |k - i|)^2 / 2\right]$ [$0 \leq i < M, 0 \leq k < M$,

where M is the number of complex data points in the demodulated discrete data time series obtained for the return over a range gate]. Defining the matrices $Q = G\delta + I$ and $\Gamma = Q^{-1}$ with elements q_{ik} and γ_{ik} , where I is the identity matrix, the estimate variances are

$$\sigma^2(\delta) = \frac{1}{\sum_{i=0}^{M-1} \sum_{k=0}^{M-1} a_{ik} a_{ki}} \quad (3)$$

where $a_{ik} = \sum_{m=0}^{M-1} \gamma_{im} g_{mk}$,

$$\sigma^2(f_1) = \frac{1}{-4\pi^2 \sum_{i=0}^{M-1} \sum_{k=0}^{M-1} \gamma_{ik} (i-k)^2 q_{ki}}, \quad (4)$$

and

$$\sigma^2(f_2) = \frac{1}{\sum_{i=0}^{M-1} \sum_{k=0}^{M-1} b_{ik} b_{ki}} \quad (5)$$

where $b_{ik} = -4\pi^2 f_2 \delta \sum_{m=0}^{M-1} \gamma_{im} (m-k)^2 g_{mk}$.

Fig. 1 shows the normalized standard deviations $\sigma(\delta)/\delta$, $\sigma(f_1)/f_2$, and $\sqrt{2}\sigma(f_2)/f_2$ calculated using Eqs. (3-5). These ratios are chosen to be similar to those that appear in Eq. (2). Together with the limiting value, $1/\sqrt{N_{\text{eff}}}$, they are plotted as a function of the effective photocount $N_{\text{eff}} = M\delta$ in a heterodyne receiver for the particular values of f_2 and M that are quoted in the caption. The shapes of the three curves for the heterodyne precision are similar. They lie above, sometimes well above, the limiting value. They become asymptotically independent of N_{eff} when N_{eff} is large and the uncertainty in the estimate is dominated by fading rather than signal strength, and asymptotically proportional to $1/\sqrt{N_{\text{eff}}}$ (rather than to $1/N_{\text{eff}}$) when N_{eff} is small and small signal suppression degrades the spectral estimate.⁷

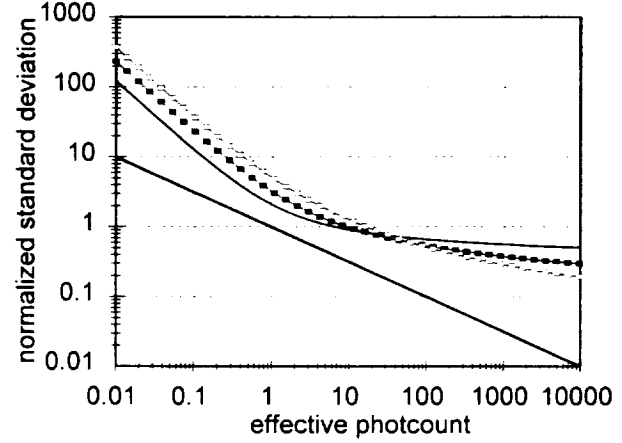


Figure 1: Plot of the normalized standard deviations (see text), $\sigma(\delta)/\delta$ (curved line), $\sigma(f_1)/f_2$ (filled squares), and $\sqrt{2}\sigma(f_2)/f_2$ (open squares) against effective photocount N_{eff} for $f_2 = 0.028$, $M = 10$. The straight line is $1/\sqrt{N_{\text{eff}}}$ (c.f. Eq. 2)

A rather more general representation of these

results can be obtained by plotting, as a function of the time-signal bandwidth product $f_2 M$, the coordinates of the

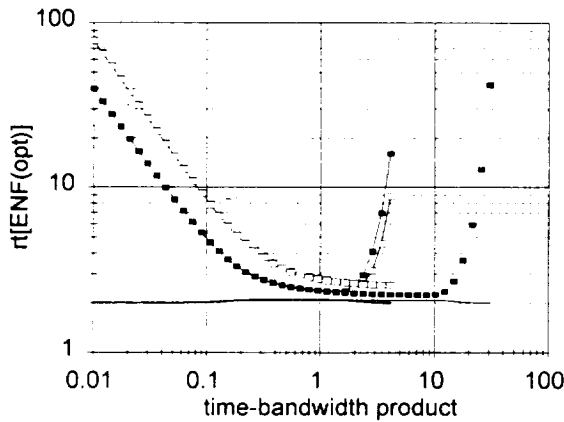


Figure 2: The ratio of the normalized standard deviations of Fig. 1 to $1/\sqrt{N}$ at the optimal operating point for estimates of SNR (no line markers), f_1 (filled squares), and f_2 (open squares); evaluated for $M=10$ (markers joined by lines) and $M=64$ (no lines, except faint line for SNR curve).

points where curves such as those in Fig. 1 approach most closely the $1/\sqrt{N_{\text{eff}}}$ line.⁸ The slope of each curve is then $1/\sqrt{N_{\text{eff}}}$. These operating points are optimal in the sense that they define the conditions under which a given standard deviation can be achieved using minimal signal energy.⁹ The two coordinates plotted in Figs. 2 and 3 are the fraction by which each variance exceeds $1/\sqrt{N_{\text{eff}}}$ and the value of $\alpha = \delta/[\sqrt{2\pi}f_2]$, both calculated at the optimal operating point. The fraction is the optimal estimate noise figure, ENF(opt), which determines how close to the limiting value the measurement precision can be. The tuning parameter, α , is the peak SNR in the combined signal + noise spectrum and describes the lidar parameters at which optimal operation is achieved; in physical terms, it is a measure of the effective photocount per fade interval.⁷ $f_2 M$ is allowed to vary widely. At low values ($f_2 M \ll 1$), the signal data are strongly correlated and only a single fade is sampled within the range gate. At high values ($f_2 M \gg 1$) the signal fluctuates rapidly compared with the discrete sampling frequency but the number of independent fades that are sampled is limited to the

number of data points collected, M .

Fig. 2 indicates that for intermediate values of the time-bandwidth product ($f_2 M \approx 1$) the heterodyne systems can be expected to achieve a standard deviation of about 2 to 3 times the optimal value (noise figures lie between about 4 and 9) whether estimating return power, Doppler shift, or signal bandwidth. Fig. 3 indicates that in order to obtain these results, the parameter α should be about 1.5 for power measurements, about 3 for Doppler shift, and about 10 for signal bandwidth. Recalling that $N_{\text{eff}} = M\delta = \sqrt{(2\pi)\alpha f_2 M}$, it follows that somewhat higher SNR and effective photocount are needed for bandwidth than for the power and Doppler shift estimation. It is in this sense, perhaps, that bandwidth estimation can be regarded as fundamentally more difficult.

Numerical experiments have been carried out using simulated data to check whether the theoretical conclusions given here apply at least to the idealized conditions for which they are designed. Of particular interest are the questions whether bandwidth estimates are biased and their utility if the return signal does not have a Gaussian spectrum.

I am grateful to Alain Dabas for helpful comments on this paper and, of course, to R.M. Hardesty and W.A. Brewer for the collaboration that led to the experiment described in the first reference.

References

1. R.M. Hardesty, W.A. Brewer, and B. J. Rye, "Estimating SPARCLE shuttle lidar performance with ground-based Doppler lidar," Proc. 19th International Laser Radar Conference, Annapolis, MD, 1998, NASA/CP-1998-207652/PT2, pp. 557 - 560.
2. L. Lading and A.S. Jensen, "Estimating the spectral width of a narrowband optical signal," Appl. Opt. 19, 2750-2756, 1980.
3. R.G. Seasholtz, "2D velocity and temperature measurements in high speed flows based on spectrally resolved Rayleigh scattering," in *New Trends in Instrumentation for Hypersonic Research* (ed. A. Boutier), Kluwer Academic Publishers, Boston, 1993, pp. 399-408.
4. B.J. Rye and R.M. Hardesty, "Discrete spectral peak estimation in Doppler lidar. I: incoherent spectral accumulation and the Cramer-Rao bound," IEEE Trans. Geosci. Remote Sensing, GE-31, 16-27, 1993.
5. B. Porat and B. Friedlander, "Computation of the exact information matrix of Gaussian time series with stationary random components," IEEE Trans. on Acoustics, Speech, and Signal Processing, ASSP-34, 118-130 (1986).
6. R.G. Frehlich, "Cramer-Rao bound for Gaussian random processes and applications to radar processing of atmospheric signals," IEEE Trans. Geosci. Remote Sensing, 31, 1123-1131, 1993.
7. B.J. Rye, "Differential absorption lidar system sensitivity with heterodyne reception," Appl. Opt. 17, 3862-4, 1978
8. B.J. Rye and R. M. Hardesty, "Estimate optimization parameters for incoherent backscatter lidar," Appl. Opt. 36, 9425-9436, 1997; Errata, Appl. Opt. 37, 4016 1998.
9. B.J. Rye, "Molecular backscatter heterodyne lidar: a computational evaluation," Appl. Opt. 37, 6321-6328, 1998; see Appendix.

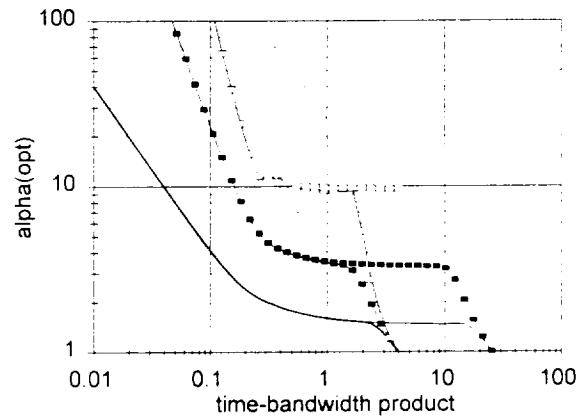


Figure 3: Values of the parameter α needed to achieve optimal operation of heterodyne lidar (incoherent backscatter from target extended in range) for estimating SNR δ , f_1 , and f_2 . Lines and markers as in Fig. 2. The dashed lines indicate constant values of the effective photocount $N_{\text{eff}} = \sqrt{(2\pi)\alpha f_2 M}$ for, from left to right, $N_{\text{eff}} = 1$, $N_{\text{eff}} = 10$, and $N_{\text{eff}} = 64$.

1.5- μm Coherent Lidar Using Injection-seeded, LD pumped Er,Yb:Glass Laser

Kimio Asaka, Takayuki Yanagisawa and Yoshihito Hirano

Mitsubishi Electric Corporation
Ofuna 5-1-1, Kamakura-city, Kanagawa, 247 JAPAN
Phone +81-467-41-2547

1. Introduction

A coherent lidar is an attractive sensor for atmospheric observation because it can measure wind velocity even in clear air conditions. It is needed eye-safety same as other laser equipment used in the field. As the coherent lidar in eye safe wavelength ($>1.4\text{-}\mu\text{m}$ wavelength), one using $2\text{-}\mu\text{m}$ pulsed laser such as Ho,Tm:YAG and Tm:YAG laser is reported.^{1,2}

Compared to $2\text{-}\mu\text{m}$, the wavelength of $1.5\text{-}\mu\text{m}$ has a ten times higher maximum permissible exposure for human eyes. In addition, optical fiber components and devices for use in optical fiber communication are easily available at this wavelength. Therefore, a coherent lidar, which use $1.5\text{-}\mu\text{m}$ pulsed laser, is more attractive than a $2\text{-}\mu\text{m}$ coherent lidar. To our knowledge, a $1.5\text{-}\mu\text{m}$ coherent lidar operation to measure wind velocity hasn't been reported yet. That because a single frequency $1.5\text{-}\mu\text{m}$ laser that had both high repetition rate and enough power for coherent lidar wasn't provided. Nd:YAG + OPO³ and injection-seeded, flash lamp pumped Er:Glass laser⁴ for $1.5\text{-}\mu\text{m}$ coherent lidars were recently reported and are now under development.

We are developing a $1.5\text{-}\mu\text{m}$ coherent lidar using an injection-seeded, LD pumped Er,Yb:Glass laser. In our system, a microchip laser made of Er,Yb:Glass is used for a seed and a local source.

In this paper we describe our system and primary data of measured echo of aerosols.

2. System description

A block diagram of the developed $1.5\text{-}\mu\text{m}$ coherent lidar is shown in Fig. 1. Optical couplers divide the output of a local oscillator in three beams. Two of the beams are used in heterodyne detection. The another one is used as a seed beam in injection seeding of the pulsed laser, after its frequency is shifted by an intermediate frequency ($f_{if} = 85\text{MHz}$) using an acousto-optics (AO) frequency shifter.

The transceiver optics is co-axial. Output beam from the pulsed laser is expanded by a telescope (TEL) and radiated into the atmosphere using a scanner (SCN). The effective diameter of the telescope is 60-mm. In a T/R switch, the received signal is separated from the transmitted beam and is put into a polarized maintained optical fiber. It is mixed with the local beam at the photo receiver to generate the heterodyne beat signal. The beat signal is sent to an AD converter.

The polarized maintained optical fiber is used in order to make the optical arrangement easily in the receiver and to utilize a small, high reliability optical component for the optical fiber communication.

2.1 The local oscillator (LO)

A microchip laser is used as a local oscillator. It was built in a small module by utilizing the

technology of LD modules for optical communication. The size of the microchip laser module is $38.6 \times 31.8 \times 18.5 \text{ mm}^3$. It consists of a pumping LD with a fiber lens, the coupling optics between the LD and an Er,Yb:Glass chip, a sapphire plate and an optical isolator. The output beam from Er,Yb:Glass chip is put into the optical fiber by a coupling lens. A TE cooler controls those temperatures. A 1-W class high brightness Al free InGaAs LD is used for pumping.

The thickness and the reflection of output surface of the Er,Yb:Glass chip were designed as 0.28-mm and 98.3%, respectively. The Er^{3+} ion concentration is $1 \times 10^{20} \text{ cm}^{-3}$ and the Yb^{3+} ion concentration is $1.5 \times 10^{21} \text{ cm}^{-3}$. The Er,Yb:Glass chip was optically and thermally contacted to the sapphire plate with a transparent optics cement. As the sapphire plate is used for thermal spreader, heat removal from the Er,Yb:Glass chip is done along the optical axis of the microchip laser. The changes of output divergence with thermal lens effect are kept small by this method. Then, high coupling efficiency of the output into the optical fiber is maintained.

A microchip laser that uses an isotropic material for laser medium such as Er,Yb:Glass has dual polarized modes that are orthogonal.⁵ The polarization dependent isolator not only reduces a back reflection but also extracts only one of the polarized modes for local beam.

Our microchip laser module has side mode suppression ratio more than 20-dB and a fiber coupled, single frequency output of 23.2-mW is obtained. The wavelength of output beam is 1.534- μm . By the self-delayed heterodyne method using a 91-km length optical fiber, the linewidth of 20.5-kHz was measured.

2.2. The pulsed laser

The laser cavity consists of two high reflective mirrors (HR). Each radius of curvature of those mirrors is 1-m. The cavity length is about 2-m. A LiNbO_3 Pockels cell was used for E/O Q switching. The seed beam from the microchip laser is injected into the cavity through the polarizer PO. The pumping module, which was placed near the center of the cavity, consists of two Er,Yb:Glass rods, four five-stacked LD arrays and water-cooled heat sinks. Pump energy of these LDs is 740-mJ/pulse (0.975- μm wavelength) at 40-Hz repetition rate. The polarizer PO radiates the output pulse from the cavity.

A block diagram of the pumping module is presented in Fig. 2. A pair of parallel lateral surface of each Er,Yb:Glass rod is in contact with heat sinks and the rod is pumped from the other pair of parallel lateral surface by two LD arrays. In this geometry a bifocusing of thermal lens occurs as the heat sink removes the heat generated by pumping in the Er,Yb:Glass rod. Then, in order to compensate the bifocusing effect, the two Er,Yb:Glass rods are arranged in series along the optical axis of the pulsed laser; the lateral surfaces in contact with the heat sinks are intersected perpendicularly each other.

Er,Yb:Glass is a quasi-three-level laser. For this reason, half or more of the Er^{3+} ions must be excited for getting a gain. Accordingly, it is desirable to reduce the volume of Er,Yb:Glass rod in order to obtain a high-density excitation with the same pumping energy. To match this condition the Er,Yb:Glass rod was chosen as $1.2 \times 1.2 \times 10 \text{ mm}^3$ and the Yb^{3+} ion concentration and Er^{3+} ion concentration are $1.5 \times 10^{21} \text{ cm}^{-3}$ and $6 \times 10^{19} \text{ cm}^{-3}$, respectively.

To adjust the cavity length a cavity tuner CT was developed. It has two roof prisms whose spacing is changed by a piezoelectric translator and controlled by a cavity controller CC. A bit of output pulse power is taken out from the HR45 mirror, then used as a reference signal in order to get the control signal of the cavity tuner. The cavity controller changes the cavity length that the beat signal of the reference and local beams is to become constant frequency.

The output pulse energy with and without seeding at 40-Hz repetition rate is 4.0-mJ and 4.6-mJ, respectively. The pulse width of the seeded pulse is 244-ns. Power spectrums of the beat signal, which was measured during 10-minutes, and overwritten on one screen are presented in Fig.3. The seeded-pulse frequency is stabilized within ± 5.7 -MHz (standard deviation).

3. Experimental results

The developed 1.5- μ m coherent lidar was used for wind velocity measuring. The lidar was positioned at about 5-m above the ground and it radiated laser pulses into the atmosphere with an elevation angle of 10°. The pulse energy was 2-mJ in this measurement.

The signal processing is as follows:

Range bin width: 30-m (200-ns)

Window: Hanning

Sampling frequency: 500-MSa/s

Frequency bin width: 488-kHz (0.37-m/s)

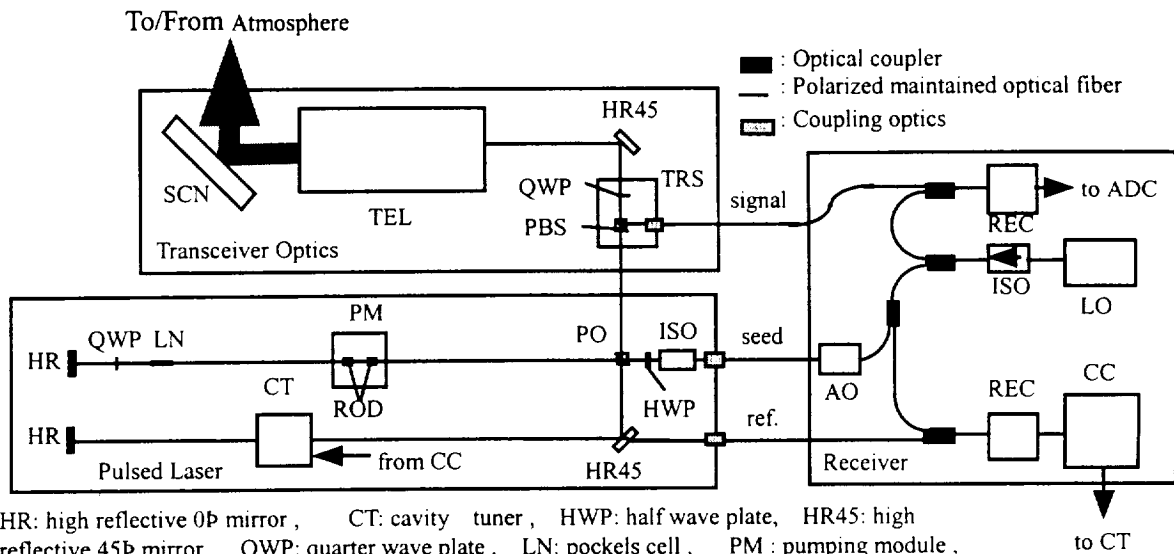
An example of the measurement is presented in Fig. 4. The result has an averaged frequency spectrum of received signals of 100 pulses. The calculated SNR using theoretical coherent lidar equation ⁶ is also shown in Fig. 4. Calculation parameters of Table 1 were used. It is considered that the differences between the measured and the calculated SNR at mid-range were caused by an insufficient adjustment of the transceiver optics. The diameters and phase front radii of the transmitted and the assumed backpropagated local beam were not sufficiently matched at the transceiver optics in this primary measurement. Readjusting them will improve the measured SNR.

4. Summary

We developed a 1.5- μ m coherent lidar that incorporates an injection seeded, LD pumped Er,Yb:Glass laser for a slave laser and a microchip Er,Yb:Glass laser module for a seed and a local source. The laser radiates a single frequency, injection seeded pulse of 4.0-mJ at 1.534- μ m wavelength with a repetition rate of 40-Hz. Experimentally we obtained the echo of aerosols to distances several kilometers by this 1.5- μ m coherent lidar.

References

1. R. Targ et. al. : Appl. Opt., **35** (1996) 7117.
2. S. Hannon and J. Thomson : J. Mod. Opt., **41** (1994) 2175.
3. T. P. Gryson et. al. : *Coherent Laser Radar* , Vol.19, 1995 OSA Technical Digest Series (Optical Society of America, Washington-DC, 1995), p.74.
4. A. J. McGrath et. al. : Appl. Opt., **37** (1998) 5706.
5. S. Taccheo et. al. : Opt. Lett. **20** (1995) 889.
6. R. Targ, M. J. Kavaya, R. M. Huffaker and R. L. Bowles: Appl. Opt., **30** (1991) 2013.



HR: high reflective 0P mirror, CT: cavity tuner, HWP: half wave plate, HR45: high reflective 45P mirror, QWP: quarter wave plate, LN: pockels cell, PM: pumping module, ROD: laser rod, PO: polarizer, ISO: isolator, PBS: polarizing beam splitter, TEL: telescope, SCN: scanner, REC: photo receiver, AO: AO shifter, LO: local oscillator, CC: cavity controller, ADC: AD converter, TRS: T/R switch

Fig.1 Block diagram of the 1.5μm coherent lidar.

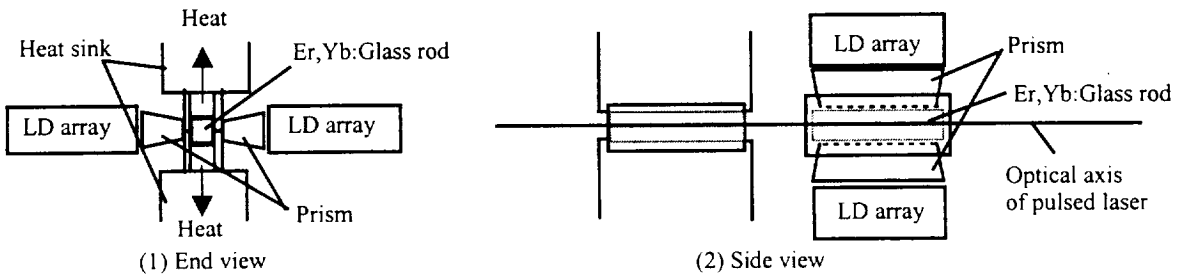


Fig.2 Cross section of the pumping module.

Table 1. Calculated parameters.

Laser Wavelength	: 1.543μm
Atmos. transmission	: 0.9/km
Aerosol Backscatter Coeff.	: $1 \times 10^{-6} \text{ m}^{-1} \text{ sr}^{-1}$
Refractive index structure constant	: $3.3 \times 10^{-15} \text{ m}^{-2}$
Detection efficiency	: 0.06
Beam Diameter	: 60mm
Focal Range	: 2000m
Pulse Energy	: 2mJ
Range Resolution	: 30m

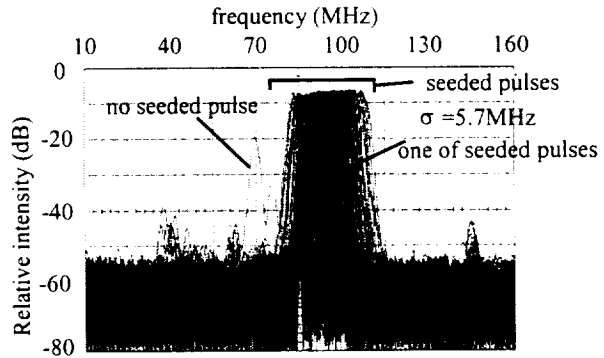


Fig.3 Power spectrums of the beat signal.

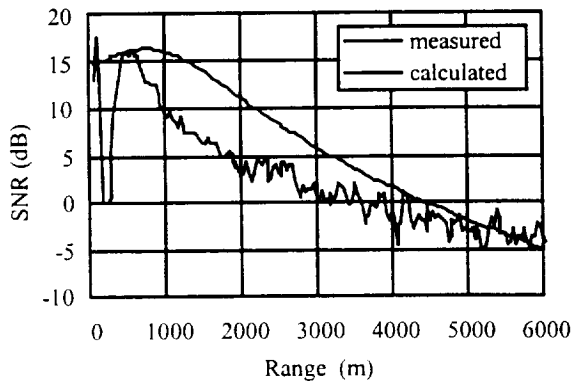


Fig.4 Measured intensity of the beat signal.

Specification of a coherent laser radar for air data measurements for advanced aircraft

Christer Karlsson, Per-Otto Arntzen, Göran Hansson and Stan Zyra

Defence Research Establishment (FOA)

Department of Laser Systems

P. O. Box 1165, S-581 11 Linköping, Sweden

Tel: +46 13 378243, e-mail: chrkar@lin.foa.se

Thomas Lampe

SAAB AB

Flight test methods Department

S-581 88 Linköping, Sweden

Requirements on components and subsystems of a CLR system for use as an optical air data system for the full flight envelope of an advanced fixed wing aircraft are discussed. A detailed specification of such a test system and its implementation in a pod are presented.

Note to the program committee:

The work above is part of a preliminary study of OADS-systems by FOA and SAAB aircraft. The discussions, results and conclusions are hardly entirely "new". However, the work should still be of interest to several other CLR-groups. A poster presentation would be suitable.

MEASUREMENTS OF AIRCRAFT WAKE VORTEX STRUCTURE BY CW COHERENT LASER RADAR

M Harris, R I Young

Electronics Sector, Defence Evaluation and Research Agency

Malvern, Worcestershire, WR14 3PS, UK.

J M Vaughan

Microwave Management Associates

(contact address: DERA Malvern)

The laser sensors group at DERA Malvern has a long history of detailed measurements of aircraft wake vortices. The equipment used has recently been upgraded to achieve improved accuracy in determining the core separation. The use of direction-sensing lidar giving the ability to distinguish the sign (direction) of wind velocity allows the acquisition of superior data compared to earlier DERA trials [1]. The increased ability to define the position of the core vortex gives greater accuracy in measurements of the circulation. The gathering of a large database allows the potential to build a comprehensive picture of vortex evolution and decay. The upgraded equipment was deployed on a trial for Airbus Industrie at Toulouse Blagnac during March 1998, with the aim of making measurements of wake turbulence from aircraft on the final approach to the runway.

Coherent laser radar measures wind velocities by scattering laser light off atmospheric particles and detecting the shift in frequency of the scattered light. This Doppler shift is proportional to the line of sight component of velocity for the particles illuminated by the probe beam. The DERA wake vortex lidar transmits ~5 W of CW output at a wavelength of 10.6 μm , and is housed in a box body vehicle complete with computers to collect the data and perform real-time analysis. A description of this equipment is given in reference [1]. An acousto-optic modulator is used to create an offset of 43.6 MHz allowing velocity direction sensing. An extremely narrow, high attenuation notch filter eliminates the parasitic component (due to internal light scattering) at 43.6 MHz in the detector output prior to spectral analysis by a SAW spectrum analyser. Vortex profiles were obtained by displaying a time sequence of spectra (fig.1) from which the well-defined outline is used to extract information on vortex parameters.

For the trial the laser radar was sited close to the centre line, directly under the aircraft flight path. This geometry (see fig 2) optimises the probability of vortex detection under the commonly prevailing conditions of variable crosswind. The probe beam repeatedly scans the region of space through which the vortex descends, with the beam focus set to the estimated vortex altitude. It is usually possible to probe the vortex pair several times after the aircraft has passed overhead. A conically-scanned laser

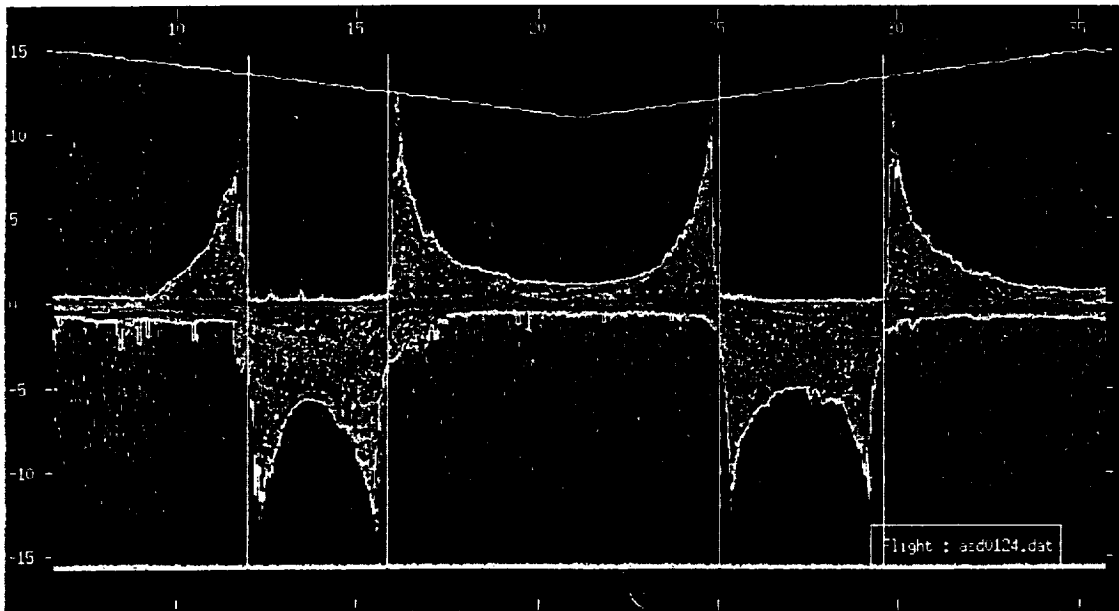


Figure 1: Typical profile resulting from two traverses of the beam through the vortex pair. The vertical axis is velocity in m/s, with positive values indicating motion away from the lidar. The horizontal axis represents time in s, which is converted to a distance using the scan information. The scan angle is shown by the zig-zag line; here, this ranges 20 degrees either side of vertical.

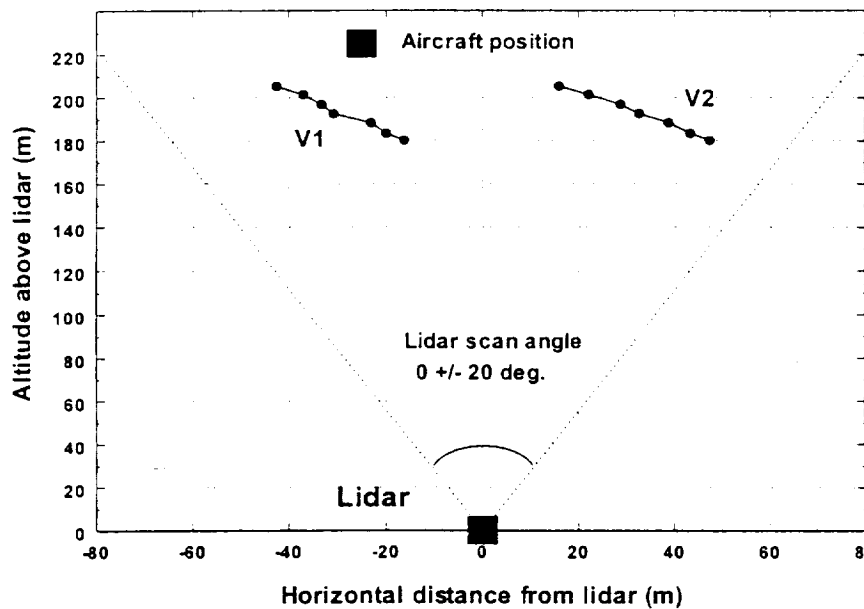


Figure 2: Typical lidar geometry for vortex detection at Toulouse Blagnac. The view is towards the approaching aircraft. The lidar is sited on the centre line and the positions of the two vortex cores (V1 and V2) are plotted at their various intersections with the lidar beam. In this example, the crosswind of 1.34 m/s from the East has caused the vortices to drift to the right. The aircraft was inferred to have passed ~25m E of the centre line.

Doppler velocimeter was mounted in a second vehicle to measure the ambient airflow. This permitted determination of cross wind and up/down drafts required in subsequent analysis, and also for optimisation of scan angle. A suite of software tools has been developed to aid in the analysis of the data records collected during the trial. These tools greatly reduce the amount of time required to process each record.

The trial has resulted in the gathering of a large database of wake vortex measurements and these have all been analysed using the software tools. Additional expert analysis of some records of particular interest was also conducted. While many of the analyses led to results of the desired quality there were, however, some large variations in the value of circulation and vortex separation observed for comparable aircraft. These variations differed from the predicted value, using the elliptical loading approximation, by up to factor of two in either direction. Many of the anomalous examples were further examined by hand and there appears to be no error in the data analysis.

It is likely that some of these anomalies could be explained by:

- 1) Assessment of possible errors in the vortex core position
- 2) The effect of errors in the assessment of aircraft approach position and altitude
- 3) The influence of excessive up and down drafts leading to gross errors in vortex altitude
- 4) local variation in the up/down draft leading to unequal sink rate between the two vortices.

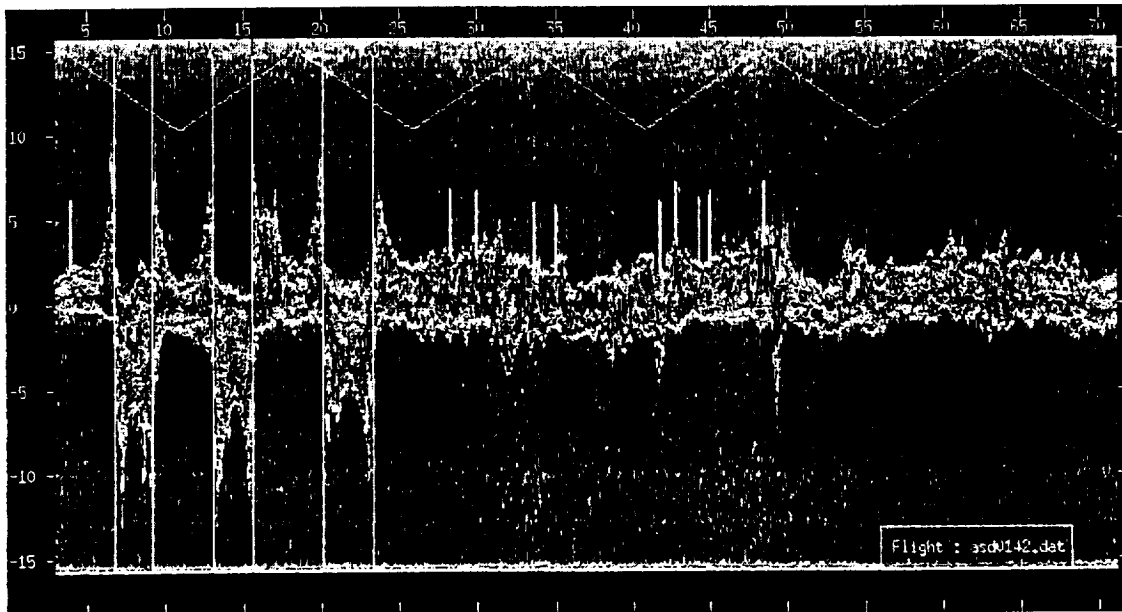


Figure 3: Evidence of vortex break up in turbulence. The vortex pair appears clearly in three scans through the aircraft wake. On subsequent scans, there is no classical vortex visible. The chaotic, turbulent updraft observed is consistent with break-up due to vortex bursting or the Crow instability.

In other anomalous cases, a gross perturbation of the idealised vortex pair could be induced by decay mechanisms including the Crow instability [2] or possibly result from a breakdown of the steady-state

assumption in vortex formation. These explanations are consistent with the behaviour of the intercore down draft in these cases (fig. 3) and there is also additional experimental evidence to support this conclusion. Finally it should be noted that the anomalous results had a tendency to cluster in the early to mid afternoon when atmospheric turbulence was at its highest due to ground heating and convection. Hence we believe that the variability of the results was due to unfavourable conditions rather than to any shortcomings in the lidar technique.

Summary

Laser radar has proved a useful tool for examining vortices and hence determining the necessary separation distances between landing aircraft. Laser radar has a further role to play in the negation of vortices. Detailed measurement of the vortex core may allow for the optimisation of aircraft wing design to ameliorate vorticity and enhance decay. The possibility of making high-quality measurements has been demonstrated on full-scale aircraft in the real atmosphere. Such measurements are thus complementary to the information provided by wind tunnel studies. However, to achieve optimum and reproducible results, the lidar measurements must be made under stringent atmospheric conditions.

Acknowledgements

The work reported here has been funded by Airbus Industrie. The authors wish to acknowledge the essential contributions of the other team members (within DERA and the Airbus consortium) to the preparation and undertaking of the trial. We are also extremely grateful to B Foord and G Constant for technical advice and guidance.

References

- [1] Coherent laser radar and the problem of aircraft wake vortices, G Constant et al. *J Modern Optics* 41 2153 1994

- [2] A method for accelerating the destruction of aircraft wake vortices, SC Rennich & SK Lele, *AIAA* 98-0667, Jan 1998

POLARIMETRY OF SCATTERED LIGHT USING COHERENT LASER RADAR

M Harris

Electronics Sector

Defence Evaluation and Research Agency

Malvern, Worcestershire WR14 3PS, U.K.

Measurement of the polarisation properties of light (*polarimetry*) is a powerful diagnostic tool with uses in many applications including ellipsometry [1]. Evaluation of the ellipse for a pure polarisation state conventionally involves passing the light through wave-plate and polariser elements (which can be rotated either by mechanical or electro-optic means). Here, we will describe use of heterodyne techniques for evaluation of the polarisation ellipse [2-5] for scattered light. The horizontally and vertically polarised components of light scattered from depolarising surfaces were independently measured by a two-channel coherent laser radar. Because of the phase-sensitive nature of heterodyne detection, the relative phase of these components can be measured, and this gives all the information required to construct the polarisation ellipse at any instant. The phenomenon of laser speckle ensures that the intensity and polarisation state fluctuate as the beam scans across the surface of the target. The method described here allows the time-development of the polarisation state to be followed in real time.

The experimental arrangement is depicted in Figure 1. It consists of a bistatic CW coherent laser radar [6] with a CO₂ laser source giving an output of approximately 1 Watt at a wavelength of 10.6 μm . The transmitted beam is linearly polarised with its E-vector horizontal. Scattered light from the target is combined with the local oscillator (LO) at a beamsplitter (BS), and the two output beams from BS are then independently sampled by a pair of detectors (D1 and D2) thus forming a dual-channel detection system. The two channels are arranged to detect the co-polarised component (i.e. horizontal, **h**) in channel 1 and the cross-polarised (vertical, **v**) in channel 2 by means of wire-grid linear polarisers. A half-wave plate is used to rotate the polarisation axis of the local oscillator beam prior to mixing. This allows approximate equalisation of the LO levels at the two detectors, and under these conditions we achieve shot-noise-dominated detection in each channel giving optimised sensitivity. The transmitted beam is

collimated with a diameter (to $1/e^2$ in intensity) of 4.0 cm, giving a detection sensitivity (i.e. time-averaged carrier-to-noise ratio) roughly independent of target range within the Rayleigh length of ~ 100 m. The target consists of a rotating disc (diameter 20cm) on which different surfaces can be attached. Measurements were obtained on various painted surfaces (which demonstrate a high level of depolarisation) at ranges up to ~ 200 m.

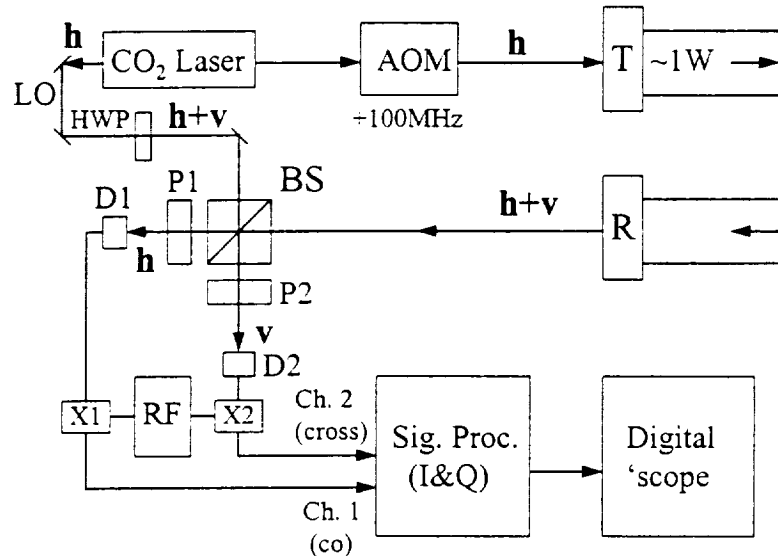


Figure 1: The experimental arrangement. D1 and D2 detect the two orthogonally-polarised channels, as defined by polarisers P1 and P2. The co- and cross-polarised electrical signals in channels 1 and 2 are down-mixed at X1 and X2 respectively before being further processed and stored on a digital oscilloscope.

The outputs from D1 and D2, centred around the carrier at 100.07 MHz, are first downmixed to a more convenient frequency around 50kHz. This permits more straightforward bandpass filtering for the elimination of noise contributions (principally LO shot noise). The outputs from the two mixers faithfully represent the amplitude and phase variations of the two orthogonally polarised components, and they therefore contain all possible information about the classical light field. The polarisation state is easily displayed in real time by connecting the two downmixed channels to the X and Y inputs of an oscilloscope. The Lissajous figure thus displayed represents the polarisation ellipse and its evolution can

be observed as the target is slowly moved to cause development of the speckle pattern. For more accurate measurements, the in-phase and quadrature components (I and Q) of the waveforms in the two channels were measured. It was first necessary to downmix the raw detector output close to the operating frequency of the I and Q demodulators at around 10 MHz. The outputs from the demodulators are then arranged around zero frequency (baseband) and the resulting four channels (I_1 , Q_1 , I_2 and Q_2) are stored on a digital oscilloscope for subsequent computer analysis. I and Q detection at baseband has the advantage of reduced demands on sample rate and bandwidth, as it is no longer necessary for the sample rate to be sufficient to follow the high-frequency carrier. Relative phase corrections are also easily carried out in software during the analysis. The direction of rotation of the ellipse is also obtained by this analysis; this information is not immediately apparent in the simple Lissajous figure.

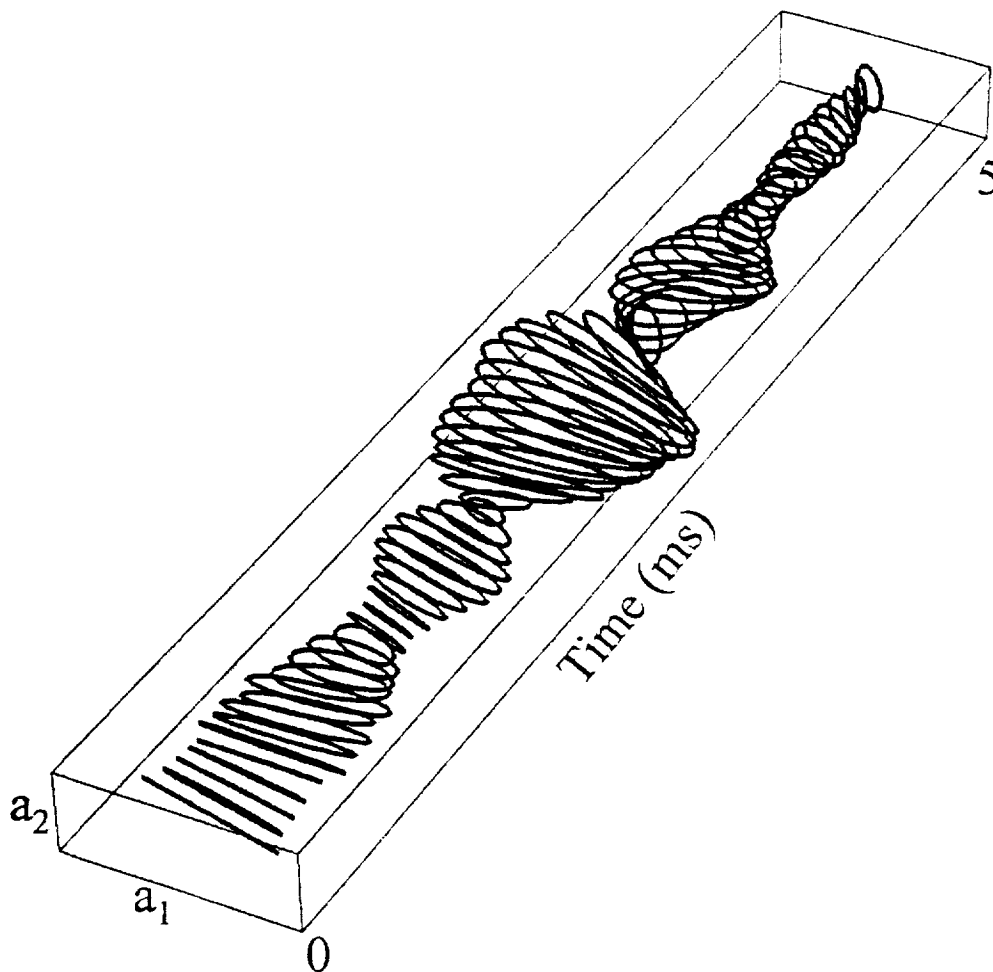


Figure 2: Experimental data on evolution of the polarisation ellipse for dynamic laser speckle. Although the data sample time is $5 \mu\text{s}$, the ellipse is only displayed every $75 \mu\text{s}$ for clarity. The direction of rotation of each ellipse is not indicated here, though this information can be easily calculated from the data.

Typical data are presented in Figure 2, where the polarisation ellipse is plotted as a function of time. Note that the polarisation state changes rapidly when the intensity is low (a “dark” speckle), but is comparatively stable over a bright speckle. There is little correlation between the polarisation state from one bright speckle to the next. Alternative methods of presentation are possible, including projection onto the Poincaré sphere. Such data could be used in a number of possible remote-sensing applications, as well as for surface and sample analysis in the laboratory.

Acknowledgements: The author acknowledges the contributions of D J Wilson of DERA, J Mallott of Heriot-Watt University, Edinburgh and M Handley of Loughborough University.

References

- [1] E Collett, *Polarized light: fundamentals and applications*, (Dekker, New York, 1993)
- [2] J H Rommers & J Howard, *Plasma Phys. and Controlled Fusion*, **38** 1805 (1996)
- [3] R Calvani, R Caponi & F Cisternino, *CSELT Tech. Rep.*, **19** 67 (1991)
- [4] K Oka, T Takeda & Y Ohtsuka, *J. Mod. Opt.* **38** 1567 (1991)
- [5] C-M Feng, Y-C Huang, J-G Chang, M Chang & C Chou, *Opt. Comm.*, **141** 314 (1997)
- [6] J M Vaughan, K O Steinvall, C Werner & P H Flamant, *Proc. of the IEEE* **84** 205 (1996)

DETECTION ADVANCES

Presider: Barry Rye

Stokes Polarimetry for Laser Radar Applications

James K. Boger¹, David G. Voelz², Lenore McMackin³, Ken MacDonald⁴

¹Applied Technology Associates, 1900 Randolph Road SE, Albuquerque, NM 87106

²AFRL/DEBS, 3550 Aberdeen Ave. SE, Kirtland AFB, NM 87117

³AFRL/VSSS, 3550 Aberdeen Ave. SE, Kirtland AFB, NM 87117

⁴Boeing North American, P.O. Box 5670, Kirtland AFB, NM 87185

Abstract

We have demonstrated a visible-wavelength imaging technique that uses a referenced polarization measurement to estimate the amplitude and phase of the wavefront emanating from a coherently illuminated target. The image of the target is then recovered by Fourier transformation.

Keywords: Polarization, Stokes, Pupil Plane, Speckle Imaging, Optical Wavefront

Introduction

We describe a new concept [1], which we refer to as Referenced Polarization Imaging (RPI), for measuring the optical amplitude and phase of a wave. This measurement scheme has several properties that make it attractive for laser radar applications. First, RPI produces a speckled image of the target. Second, the information needed to estimate the amplitude and phase can be obtained essentially instantaneously using pulsed illumination. Third, in a fashion analogous to heterodyne techniques, signals can be recovered even in low-light situations.

In recent years, there has been a great deal of research done on techniques for recovering images from the speckle patterns formed in the far field of coherently illuminated object. One of the motivations for making these measurement in the pupil plane rather than the image plane is the possibility of correcting aberrations caused by the atmosphere. Some of the methods that have been developed are optical heterodyne speckle image, sheared-beam imaging, and aberration-compensated heterodyne imaging. [2-7]

Referenced Polarization Imaging

A target is illuminated by a coherent laser beam and the backscattered signal is collected by a pupil-plane receiver array. If the amplitude and, more importantly, the phase of the speckle field can be measured, then an image of the target can be recovered by numerical Fourier transformation.

The RPI technique consists of mixing this linearly polarized speckle pattern with an orthogonally polarized reference wave. As a result, the phase information in the signal wave appears in the detection plane as a spatial variation in the polarization, from which the amplitude and phase of the signal wave can be extracted using an imaging Stokes polarimeter. Figure 1 is an illustration of the RPI concept.

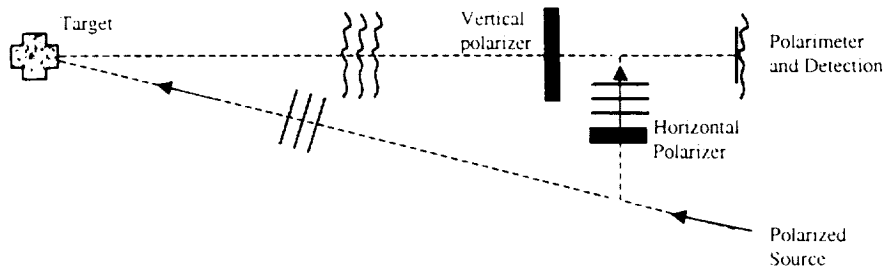


Figure 1. RPI conceptual diagram.

Jones vectors representing the signal and reference waves are given by:

$$E_{sig}(\mathcal{P}) = \begin{bmatrix} 0 \\ A_{sig}(\mathcal{P})e^{i\varphi_{sig}(\mathcal{P})+\delta(t)} \end{bmatrix}$$

$$E_{ref}(\mathcal{P}) = \begin{bmatrix} A_{ref}(\mathcal{P})e^{i\varphi_{ref}(\mathcal{P})} \\ 0 \end{bmatrix}$$

respectively. The extra phase $\delta(t)$, in the signal wave is a time-varying perturbation to the signal caused by atmospheric turbulence or target motion, for example. When the signal and reference waves are added, we can see that the field in the detection plane has a spatially varying polarization:

$$E_{det}(\mathcal{P}) = E_{sig}(\mathcal{P}) + E_{ref}(\mathcal{P}) = \begin{bmatrix} A_{ref}(\mathcal{P})e^{i\varphi_{ref}(\mathcal{P})} \\ A_{sig}(\mathcal{P})e^{i\varphi_{sig}(\mathcal{P})+\delta(t)} \end{bmatrix} \equiv \begin{bmatrix} E_x \\ E_y \end{bmatrix}$$

The output of a Stokes polarimeter is related simply to the four Stokes parameters, which are defined as:

$$S = \begin{bmatrix} S_0 \\ S_1 \\ S_2 \\ S_3 \end{bmatrix} = \begin{bmatrix} E_x^2 + E_y^2 \\ E_x^2 - E_y^2 \\ E_x E_y^* + E_x^* E_y \\ i(E_x E_y^* - E_x^* E_y) \end{bmatrix}$$

The amplitude and phase of the incident speckle pattern are obtained from the Stokes parameters as:

$$A_{sig}(\mathcal{P}) = \sqrt{\frac{1}{2}[S_0(\mathcal{P}) - S_1(\mathcal{P})]}$$

$$\varphi_{sig}(\mathcal{P}) - \varphi_{ref}(\mathcal{P}) + \delta(t) = \arctan\left[\frac{S_2(\mathcal{P})}{S_3(\mathcal{P})}\right] \approx \varphi_{sig}(\mathcal{P})$$

As can be seen in equation 6, the recovered phase is the difference between the phases of the signal and reference waves, plus the time varying perturbation. Since the reference is assumed to be spatially flat and constant, it carries no information and can be ignored. The time varying perturbation, $\delta(t)$, on the other hand, could cause a significant deterioration in the fidelity of the phase measurement. In the laboratory, of course, we avoid this problem by making the experimental setup sturdy. In general, the solution would be to make the polarization measurement in as short a time as possible. Four-channel polarimeters are ideally suited for this, and using a pulsed laser as an illumination source can easily control the measurement time. So, in short, with the proper precautions, we can estimate the phase of the speckle directly from the Stokes data.

The image is obtained by Fourier inversion.

Laboratory Demonstration

We have performed laboratory experiments to demonstrate RPI's capabilities. A depiction of the laboratory setup is shown in Figure 2.

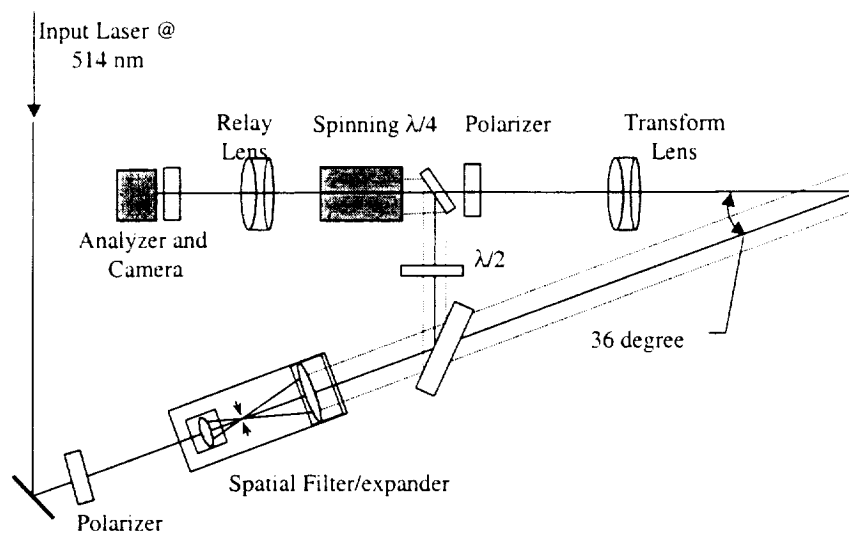


Figure 2. Laboratory Experiment.

The target was flood-illuminated with laser light at a wavelength of 514 nm. The far-field speckle pattern from the target was placed on the entrance face of the polarimeter with a Fourier-transform lens. Since speckle patterns often have mixed polarization, a linear polarizer was used to select only the speckles having vertical polarization, that is, perpendicular to the polarization of the reference wave. The speckled wave from the target and the plane reference wave are mixed on a beamsplitter in front of the polarimeter. For this demonstration, we used a polarimeter comprised of a rotatable quarter-wave plate followed by a fixed analyzer. [8, 9] A lens imaged the entrance face of the polarimeter onto a 640 x 480-pixel CCD array. Relaying the wavefront in this fashion minimizes any potential shift in the speckle pattern as the waveplate rotates.

Note that the use of this type of polarimeter is incidental to the RPI technique, and that any imaging polarimeter that measures four Stokes parameters would do. In particular, in many applications of RPI, the use of a four-channel imaging polarimeter [10] would be advantageous.

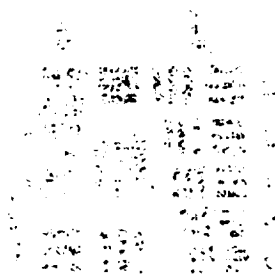


Figure 3. A single-shot recovery has high resolution, but is corrupted by speckle.

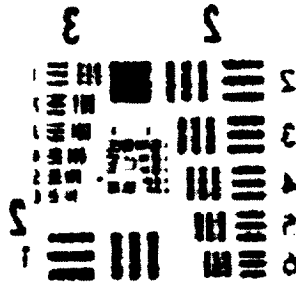


Figure 4. Averaging 10 single-shot images effectively eliminates the speckle.

Conclusion

Some of the advantages of AC measurements like the heterodyne method, such as the ability to increase the signal level over the detector's shot noise limit, are also present in the RPI technique. The principle limitation of heterodyne techniques with respect to RPI is that heterodyne measurements are inherently sequential. In addition, the frequency shifting necessary for making heterodyne measurements often uses light inefficiently.

We have developed and experimentally verified a referenced-polarization technique for recovering the amplitude and phase of the wavefronts from coherently illuminated targets, both reflective and transmissive. The RPI technique is simple and does not require elaborate equipment. Its speed, resolution, and low-light capabilities could make it useful for a variety of laser radar applications.

Acknowledgements

This work was performed under USAF contract F29601-98-C-0012 to the Air Force Research Laboratory at Kirtland AFB, NM. The authors appreciate useful technical discussions with M. P. Fetrow of Applied Technology Associates and L. J. Ulibarri of Boeing.

References

1. J. K. Boger, *Opt. Lett.*, to be published May 1, 1999.
2. J. K. Boger, D. G. Voelz, J. D. Gonglewski, R. Anderson, and R. E. Pierson, *Proc. SOQUE*, Lasers 91, 381 (1992).
3. D. G. Voelz, J. D. Gonglewski, and P. S. Idell, *Appl. Opt.* **30**, 3333 (1991).
4. J. D. Gonglewski, D. G. Voelz, P. S. Idell, and J. Knopp, *Opt. Lett.* **14**, 154 (1989).
5. J. N. Cederquist, J. R. Fienup, J. C. Marron, T. J. Schultz, and J. H. Sheldin, *Proc. SPIE* **1416**, 266 (1991).
6. D. G. Voelz, *Proc. SPIE* **2566**, 74 (1995).
7. L. J. Ulibarri, J. K. Boger, and M. P. Fetrow, *Proc. SPIE* **2827**, 100 (1996).
8. Z. Sekera, *Adv. Geophys.* **3**, 43 (1956).
9. E. Collett, *Polarized Light, Fundamentals and Applications* (Marcel-Decker, New York, 1993).
10. S. A. Hanes, *Proc. SPIE* **2774**, 684 (1996).

Vibrating Target and Turbulence Effects on a 1.5 micron Multi-Element Detector Coherent Doppler Lidar

By

Pri Mamidipudi and Dennis Killinger
Department of Physics
University of South Florida
Tampa, FL 33620

A 1.5 micron Coherent Doppler Lidar system has been developed to study the enhancement in expected lidar S/N through use of a multi-element heterodyne detector array. Preliminary experiments have been conducted and indicate that the coherent summation of two separate balanced heterodyne detector signals seems to provide enhanced detection of the Doppler shifted signal. Initial studies regarding the expected Doppler shift, geometrical vibration effects, and other system noise sources are being studied.

Figure 1 shows a schematic of the 1.5 micron Doppler lidar (laboratory) system. A 30 mW 1.5 micron, single-frequency diode laser is used as the main excitation source. The beam is split into a L.O. channel and a main projected beam followed by a 27MHz shifted Acousto-Optic frequency shifter. The main portion is sent to a rotating target, and the reflected backscatter collected by 2 spatially separated (V groove blocks) fiber-optic, single frequency, polarization preserving fibers. At present, the two collection fibers are separated by 250 microns; as such, this is the effective separation of the two coherent detectors. The two collected signals are branched again into two channels for balanced heterodyne detection. The four channels are detected and the electrical signals analyzed by spectrum analyzers, 4 channel oscilloscopes, and computer interfaced.

Figure 2 shows the four separate signals, with the upper and lower pairs being phase quadrature signals. The coherent summation of the signals was studied, and initial results showed improvement of the S/N under selected target conditions.

We are currently studying the change in the Doppler center frequency, spread of the Doppler shifted signal, and influence on the geometrical and velocity aspects of the target (or lidar). For example, Fig. 3 shows the decorrelation time measured in the Heterodyne signal for a target rotating at 35 Hz. Initial measurements of the effect of vibration wobble in the target and external atmospheric turbulence are being studied and will be reported on.

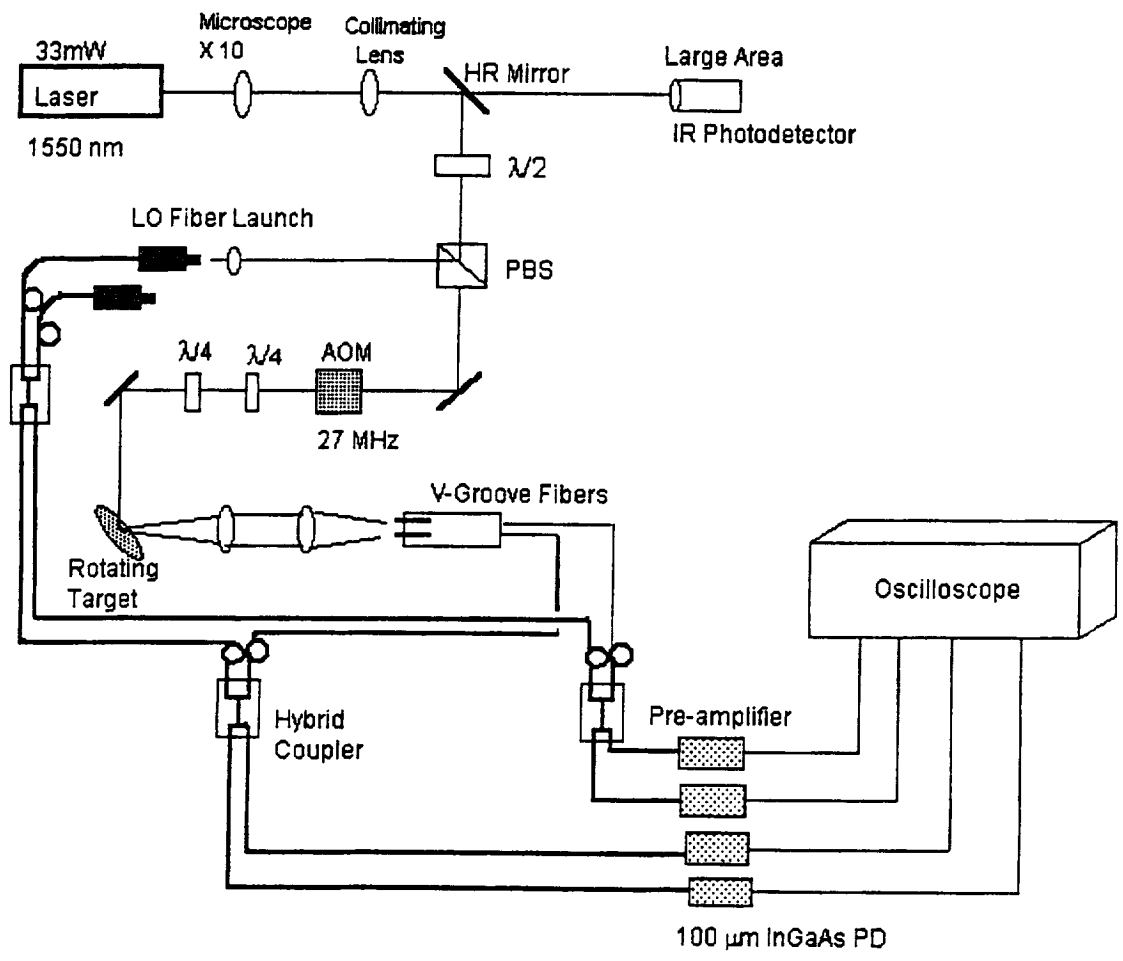


Fig. 1 Schematic of 4 channel Balanced Heterodyne Detection Experiment

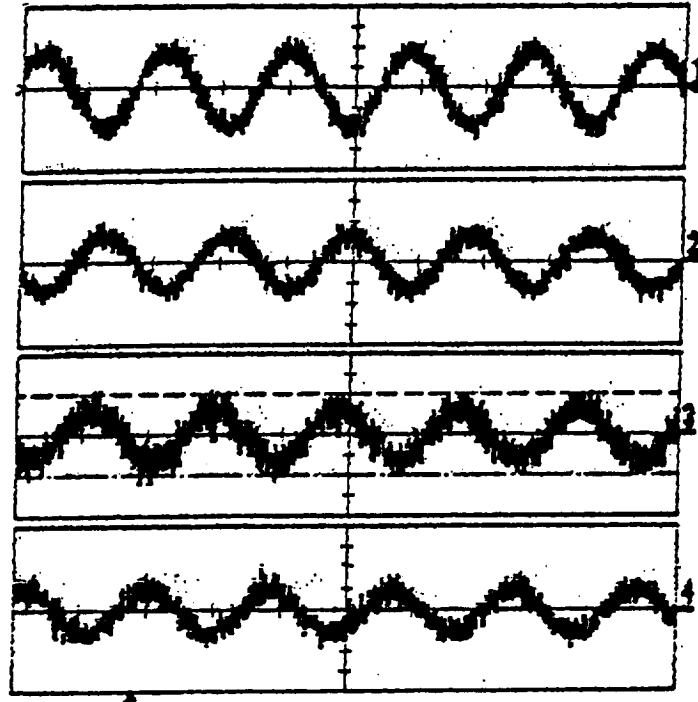


Fig.2 27 MHz Heterodyne Signals from 4 -channel Detectors

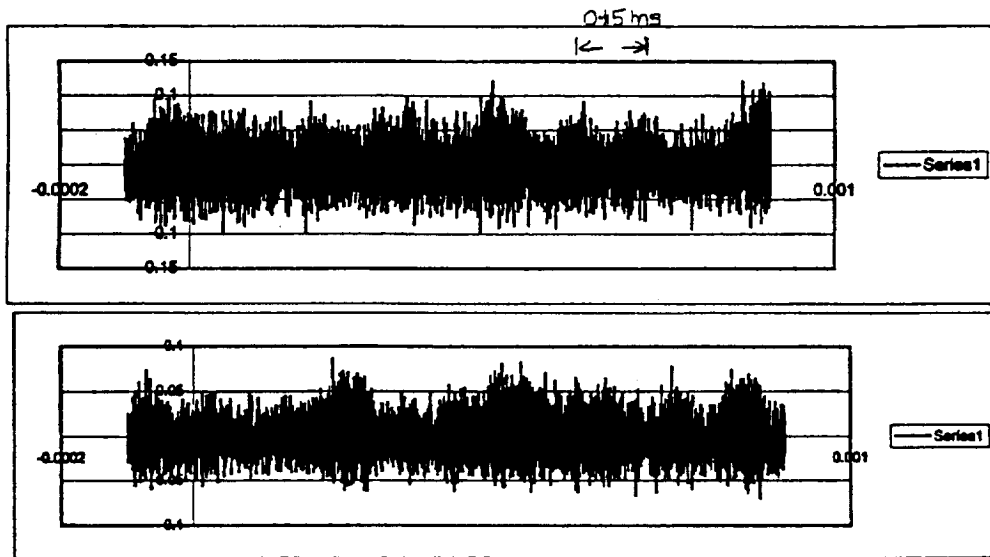


Fig.3 In-phase and Quadrature Heterodyne Signals from a target rotating at 35 Hz, with a decorrelation time of 0.15 ms.

MULTIPLE WAVELENGTH HETERODYNE ARRAY SENSING FOR SPACE OPTICS METROLOGY

Lenore McMackin and David G. Voelz

Air Force Research Laboratory
3550 Aberdeen Ave SE
Kirtland AFB, NM 87117-5776

Harold McIntire, Matthew Fetrow and Kenneth Bishop

Applied Technology Assoc.'s, Inc.
1900 Randolph Rd SE
Albuquerque, NM 87106

Abstract

Large space optical systems that are designed to deploy to optical tolerances after reaching their position in orbit require non-contact surface measurement as part of an autonomous deployment control system. We demonstrate the use of variable sensitivity, multi-wavelength heterodyne array interferometry for the automated measurement and control of adaptive optical systems with applications to remote space operation.

Large, lightweight optical mirrors for space applications will require systems for controlling the gross aspects of the mirror surface figure. We have developed an autonomously operating wavefront measurement system based on dual-wavelength heterodyne distance measurement techniques combined with heterodyne array imaging. A key feature of the technique is variable optical pathlength measurement sensitivity that allows the system to measure surface figure errors ranging from thousands of wavelengths down to fractions of a wavelength. Automatic sensitivity tuning combined with completely digital phase measurement over the entire surface allows the integration of this device in automated sensing and optical correction schemes. It is particularly suited for the measurement and control of spatially and temporally variable optical surfaces of the kind that would be found in a space-based adaptive optics system. We demonstrate aspects of the automated super-heterodyne system on an optical surface with surface profile structure height that varies from micron to mm sized features. We describe the hardware and software design of the heterodyne based measurement system that enable it to choose the appropriate synthetic wavelength to measure given areas of the variable surface profile. Software systems automatically select from available laser wavelengths. Spatial processing methods are discussed that allow the system to merge segments of images that have been measured at different synthetic wavelengths.

We have developed an autonomously operating adaptive optical control system based on dual-wavelength heterodyne distance measurement techniques combined with heterodyne array imaging^{1, 2}. In this approach the phase measurement is obtained by interfering an object and reference beam of slightly different frequencies. The resulting temporal beat frequency is sampled at each point in the interference pattern and from this the optical phase is calculated.

Measuring the optical phase in this way is often referred to as phase shifting interferometry.³ In the heterodyne interferometry system the phase shift is provided by the beat frequency creating a very convenient means of making a digital phase measurement as the interferometric fringes scan across the detector. This heterodyne measurement is made at each pixel of a sensor array so that a complex image, containing amplitude and phase values, is obtained. When the heterodyne array measurement is repeated at a different wavelength and the phases are differenced point-by-point in the computer, a result is produced that is equivalent to a measurement taken at a much longer wavelength, the synthetic wavelength. When used with a frequency tunable laser source, this digital "super-heterodyne" technique allows interferometric surface measurement over a range of sensitivities tunable in a completely digital format. The system can operate in an imaging mode profiling the surface features of complicated objects that have rough surfaces or in a non-imaging mode for interferometric optical metrology. Optical wavelengths can be scanned quickly and continuously from a single tunable laser creating a continuously variable-sensitivity wavefront sensor from which large and small surface deviations on the same surface can be measured.



Fig. 1 Machined aluminum part

Fig. 2 Phase map of the upper and middle portions of the aluminum part

The utility of having a range of synthetic wavelengths available to map out surface structure is illustrated by the measurement of a diffusely reflective aluminum part machined to have flat, tilted and curved surface areas. The part is shown in Fig. 1 and the phase map created from a heterodyne phase measurement of the curved and flat portions of the part is shown in Fig. 2. Each fringe in Fig. 2 is equivalent to one synthetic wavelength of phase, about 3 mm in this case. Just like a converting a contour map surface plot a surface profile is created by unwrapping the fringes to make a continuous sheet. However, if the surface is too steep and the surface height changes by more than a wavelength over the width of one fringe true height information is lost and the measurement becomes ambiguous. Figure 3 illustrates the effect of ambiguity in the phase measurement. The 3-mm step between the flat and curved sections of the part is evident in Fig. 3a where the synthetic wavelength is about 6 mm. In Fig. 3b this step

disappears when the wavelength is at 2mm because the height of the step is greater than the wavelength.

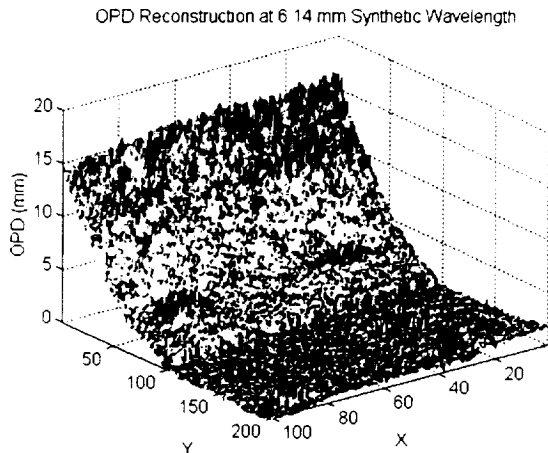


Fig. 3a. Surface reconstruction at 6mm synthetic wavelength showing step between the curved and flat surfaces

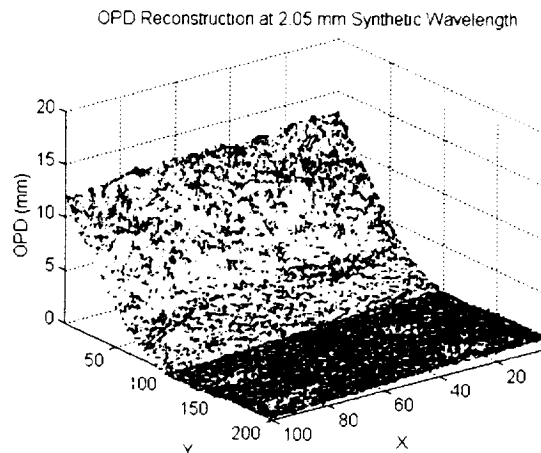


Fig. 3b. Surface reconstruction at 2mm synthetic wavelength where the step height has been lost at the step and over the curved surface

Although gross features like the step are measurable at longer wavelengths it is also evident from Fig. 3 that as the synthetic wavelength gets larger so does the noise amplitude. In order to create a surface profile that has accuracy at large and small feature size, it is necessary to combine the information from a range of synthetic wavelengths. Automating the process of selecting the proper laser wavelengths to create the most appropriate synthetic wavelengths to optimally map out large and small surface features has been the subject of research toward developing autonomous metrology systems for space optics⁴ and a simple mirror control system based on intelligent synthetic wavelength selection has been demonstrated.⁵

An intelligent phase unwrapper must choose the correct synthetic wavelength with which to measure each part of the target surface. This choice must balance the larger noise inherent in the use of larger synthetic wavelengths with the increase in unambiguous phase measurement range necessary to measure large surface feature depth without aliasing. The goal of the intelligent processing is to choose the proper synthetic wavelength with which to measure the surface at each pixel based on the quality of the surface reconstruction measured using a number of criteria: (1) performance at steep surface features, (2) signal to noise ratio of the detected slopes, (3) adequate spatial sampling of 2π phase range (i.e., how many pixels per fringe), and (4) trend in surface gradient measurements (detecting the onset of aliasing). Most of these criterion are measured using trend analysis starting from long synthetic wavelengths to shorter ones. The information regarding these criteria is embodied in a weighting function-- what we call a credibility factor-- from corresponding pixels at different synthetic wavelengths. The credibility factor results in a weighting applied to the value of the phase calculated at each synthetic wavelength. When the information at each wavelength is combined to form the optimal surface in a weighted averaging scheme, the weighting factor determines the influence a particular synthetic wavelength measurement has on the final surface reconstruction. At some point at each pixel the synthetic wavelength will be too small to adequately measure the surface

features. Weighting will tend toward zero at this point. Thus, the credibility vector comprises the four termination criteria above and contains the cumulative information that flows from larger synthetic wavelengths to smaller ones.

We have begun implementation of the intelligent selection of synthetic wavelengths for the autonomous measurement of surfaces with unknown feature depth. We have created a look-up table of available laser wavelengths that in combination create a scale of synthetic wavelengths from 10 meters to 50 microns. We are also developing an algorithm for the automated optimal surface estimation integrated from gradient estimates created at a number of synthetic wavelengths. In this algorithm, a baseline (long) synthetic wavelength is determined by examining the total phase variations over the image and determining the wavelength at which these variations begin to show 2π phase jumps. A graph of phase variation versus synthetic wavelength clearly delineates phase noise associated with larger wavelengths and phase jumps of smaller wavelengths. The synthetic wavelength is decreased across the image terminating at each pixel when the phase calculation fails the sampling criterion. In this way the surface becomes a composite estimate containing gross feature information from large synthetic wavelengths refined by accurate surface feature information from smaller wavelengths. We discuss these results and how we are using them to automate the multiple wavelength heterodyne technique.

¹ D. G. Voelz, L. McMackin, J. K. Boger, M. P. Fetrow, "Double exposure heterodyne imaging for observing line of sight deformation," *Opt. Lett.* 22 (13), 1027-1029 (1997).

² L. McMackin, D. G. Voelz and M. P. Fetrow, "Multiple Wavelength Heterodyne Array Interferometry," *Opt. Express* 1(11), 332-337 (1997). <http://epubs.osa.org/opticsexpress>.

³ K. Creath, "Step height measurement using two-wavelength phase-shifting interferometry," *Appl. Opt.* 26 2810-2816 (1987).

⁴ L. McMackin, D. G. Voelz, M. P. Fetrow, H. McIntire, K. P. Bishop, M. J. Kellum, "Multi-wavelength Heterodyne array system for large space optics control," *SPIE v. 3498*, 434-445 (1998).

⁵ Matt Fetrow, Lenore McMackin, Dave Voelz, Kishan Kumbla, "Multiple Wavelength Heterodyne Array-based Mirror control for adaptive optics," *Second International Symposium on Intelligent Automation and Control*, Anchorage AK, May 10-14, 1998.

Imaging Coherent Receiver Development for 3-D Lidar

Dr. Donald P. Hutchinson
Oak Ridge National Laboratory
P.O. Box 2008, MS-6004
Oak Ridge, TN 37831

Dr. Roger K. Richards
Oak Ridge National Laboratory
P.O. Box 2008, MS-6004
Oak Ridge, TN 37831

Dr. Marc L. Simpson
Oak Ridge National Laboratory
P.O. Box 2008, MS-6004
Oak Ridge, TN 37831

Abstract

Oak Ridge National Laboratory has been developing advanced coherent IR heterodyne receivers for plasma diagnostics in fusion reactors for over 20 years. Recent progress in wide-band IR detectors and high-speed electronics has significantly enhanced the measurement capabilities of imaging coherent receivers. Currently, we are developing a 3-D lidar system based on quantum-well IR photodetector (QWIP) focal plane arrays and a MEMS-based CO₂ laser local oscillator.¹ In this paper we discuss the implications of these new enabling technologies to implement long wavelength IR imaging lidar systems.

¹ M.L. SIMPSON, C.A. Bennett, M.S. Emery, D.P. Hutchinson, G.H. Miller, R.K. Richards, and D.N. Sitter, "Coherent Imaging Using Two-dimensional Focal-Plane Arrays: Design and Applications," *Applied Optics*, Vol. 36, No. 27, pp. 6913-6920, 20 September 1997.

What can really be gained using telescope arrays in coherent lidar receivers

Peter J. Winzer

Institut für Nachrichtentechnik und Hochfrequenztechnik, Technische Universität Wien,
Gußhausstraße 25/389, A-1040 Wien, Austria

1. INTRODUCTION

Telescope arrays¹⁻³ have gained increasing attention over the last years, as their use in optical receivers (both for lidar and optical communications) has the potential to mitigate the performance deteriorating speckle effect. From the above cited references, however, it is impossible to tell what can actually be gained by employing a perfectly phased telescope array receiver with N subapertures of size A_R each instead of a conventional, single-telescope receiver of aperture size NA_R : Ref. 1 compares the performance of such an array with that of a single-telescope receiver of aperture size A_R ; assuming different total receive areas, however, makes it impossible to tell which fraction of the performance gain owes to the ability of arrays to compensate for the speckle effect and which is due to the larger receive area. Refs. 2 and 3, on the other hand, compare the performance of a perfectly phased array with that of a non-phased array of the same size (i.e. an array whose phase control has been turned off), and claim that the latter behaves identical to a single-telescope receiver with the same total receive area. – That this claim does *not* hold true in general will be demonstrated below. It will further be shown

- how the performance of a single-telescope receiver relates to that of both a phased and a non-phased telescope array receiver of *the same effective receive area*, and
- what can really be gained by replacing a single-telescope receiver by a phased telescope array.

Unlike Refs. 2 and 3, we arrive at the conclusion that the improvement in terms of average carrier-to-noise ratio (CNR) of an array with respect to the single-telescope receiver does *not* equal N in general.

2. RELATIONS BETWEEN AVERAGE CARRIER-TO-NOISE RATIOS

A common figure of merit for heterodyne receivers is the (shot-noise limited) carrier-to-noise ratio (CNR). Following Ref. 1, we define this parameter as the ratio of the intermediate frequency (IF) power (the squared IF current averaged over a time scale long compared to the IF period but short compared to IF envelope fluctuations) to the (local oscillator (LO) shot-noise dominated) noise power. As the speckle effect causes the spatial (as well as temporal) distribution of the incident optical field to be random, the IF signal amplitude (and thus also the IF power and the CNR) become random quantities, too. In the frame of this work we are interested only in the ensemble average (CNR) of CNR. (Bold print indicates random quantities throughout this work.)

Single-telescope receiver

The IF current of a conventional heterodyne receiver with receive aperture size $A_{R,0}$ is given by the overlap integral between the incident (random) optical field, represented by its complex phasor $\mathbf{E}_R(\vec{r}, t)$ [$\sqrt{W/m^2}$], and the (complex conjugated) LO field's phasor $E_{LO,0}^*(\vec{r})$, backpropagated to the receive aperture plane \mathcal{A} with transverse coordinate \vec{r} , as⁴

$$\mathbf{i}_{IF,0}(t) = 2\text{Re}\left\{S \int_{\mathcal{A}} \mathbf{E}_R(\vec{r}, t) E_{LO,0}^*(\vec{r}) d\vec{r}\right\}, \quad (1)$$

where S stands for the detector sensitivity [A/W]. The (random) IF power then reads

$$P_{IF,0}(t) = \overline{\mathbf{i}_{IF,0}^2(t)} = 2S^2 \int_{\mathcal{A}} \int_{\mathcal{A}} \mathbf{E}_R(\vec{r}_1, t) \mathbf{E}_R^*(\vec{r}_2, t) E_{LO,0}^*(\vec{r}_1) E_{LO,0}(\vec{r}_2) d\vec{r}_1 d\vec{r}_2, \quad (2)$$

where the overline symbol denotes the above mentioned short-term time average. The shot noise variance is given by $\sigma^2 = 2eSP_{LO,0}B$, where e denotes the elementary charge, B stands for the electrical

For further author information:

Tel.: +43-1-58801/38965 (or /38901)

Fax: +43-1-5870583

e-mail: pwinzer@nt.tuwien.ac.at

bandwidth, and $P_{LO,0}$ denotes the detected LO power. We thus arrive at the well-known¹ expression for the average CNR of a single-telescope receiver,

$$\langle \text{CNR}_0(t) \rangle = \frac{\langle \mathbf{P}_{\text{IF},0}(t) \rangle}{\sigma^2} = \frac{\eta_q \eta_{\text{het},0}(t) P_{R,0}(t)}{h f B}, \quad (3)$$

where η_q denotes the detector quantum efficiency, and $h f$ stands for the photon energy at the considered (optical) frequency; the available power at the telescope input is defined as $P_{R,0}(t) = \int_{\mathcal{A}} \langle |\mathbf{E}_R(\vec{r}, t)|^2 \rangle d\vec{r}$, and $\eta_{\text{het},0}(t)$ is the single-telescope receiver's heterodyne efficiency, defined as⁴

$$\eta_{\text{het},0}(t) = \frac{\int \int_{\mathcal{A}\mathcal{A}} \langle \mathbf{E}_R(\vec{r}_1, t) \mathbf{E}_R^*(\vec{r}_2, t) \rangle E_{LO,0}^*(\vec{r}_1) E_{LO,0}(\vec{r}_2) d\vec{r}_1 d\vec{r}_2}{P_{R,0}(t) P_{LO,0}}. \quad (4)$$

The function $\langle \mathbf{E}_R(\vec{r}_1, t) \mathbf{E}_R^*(\vec{r}_2, t) \rangle$ is the first-order correlation function of the incident optical field. Albeit this function is not as illustrative as the frequently used (but not uniquely defined!) parameter 'speckle size' (the range of values for which the correlation function takes significant values), it is this function and *not* the speckle size that determines the performance of a heterodyne receiver.⁵ – Calculations based on the intuitive notion of 'speckle size' or 'number of speckles per receive aperture' (e.g. Refs. 2 and 3) can therefore only lead to very rough first estimates of a system's actual behaviour.

Non-phased array receiver

Consider next an array receiver consisting of N subapertures, each of size A_R , as depicted in Figure 1. Suppose that the N branches are *not* phased, i.e. the co-phasing and gain adjusting electronics are switched off. With the help of (1) and (2) we then find for the average IF power after summation

$$\langle \mathbf{P}_{\text{IF},\Sigma}(t) \rangle = \left\langle \left(\sum_{i=1}^N \mathbf{i}_{\text{IF},i}(t) \right)^2 \right\rangle = 2S^2 \left(\sum_{i=1}^N \int \int_{\mathcal{A}_i \mathcal{A}_i} \langle \mathbf{E}_R(\vec{r}_i, t) \mathbf{E}_R^*(\vec{r}'_i, t) \rangle E_{LO,i}^*(\vec{r}_i) E_{LO,i}(\vec{r}'_i) d\vec{r}_i d\vec{r}'_i + \sum_{\substack{i,j=1 \\ i \neq j}}^N \int \int_{\mathcal{A}_i \mathcal{A}_j} \langle \mathbf{E}_R(\vec{r}_i, t) \mathbf{E}_R^*(\vec{r}_j, t) \rangle E_{LO,i}^*(\vec{r}_i) E_{LO,j}(\vec{r}_j) d\vec{r}_i d\vec{r}_j \right), \quad (5)$$

where $E_{LO,i}(\vec{r}_i)$ denotes the LO field of the i -th array branch, backpropagated to the i -th subaperture \mathcal{A}_i . While the first sum of (5) takes account of correlations *within* one subaperture, the second term includes subaperture *cross-correlations*. Under the realistic assumptions that the LO field distributions are the same for all N branches, that all N detectors are equal, that the available power $P_{R,i}(t)$ is the same for all subapertures, and that the incident field's correlation function does not change over the array, we can, by comparison with (2) and (4), rewrite equation (5) as

$$\langle \mathbf{P}_{\text{IF},\Sigma}(t) \rangle_{\text{non-phased}} = 2S^2 N P_{R,i}(t) P_{LO,i} \eta_{\text{het},i}(t) + \text{cross-correlations}, \quad (6)$$

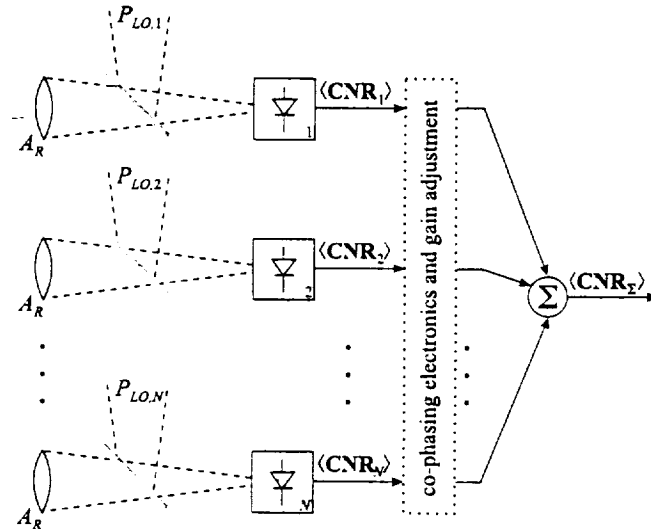


Figure 1. General setup of a phased-array heterodyne receiver with N subtelescopes of area A_R each.

where $P_{LO,i}$ denotes the detected LO power for one branch, as indicated in Figure 1. and $\eta_{het,i}(t)$ stands for the heterodyne efficiency of each of the N branches. Noting further that the shot noise variances of all N branches simply add (owing to their statistical independence), and assuming that the spacing between any two subapertures is much larger than the incident field's correlation distance (this assumption is always made in literature to facilitate analytical simplifications; to our knowledge, only Ref. 6 considers some effects of subaperture cross-correlations.), the average CNR of the non-phased array reads

$$\langle \text{CNR}_{\Sigma}(t) \rangle_{\text{non-phased}} = \frac{\eta_q \eta_{het,i}(t) P_{R,i}(t)}{hfB} \left(= \langle \text{CNR}_i(t) \rangle \right), \quad (7)$$

equaling (in accordance with the heuristic arguments presented in Ref. 1) the average CNR of a single branch, $\langle \text{CNR}_i(t) \rangle$.

However, comparing $\langle \text{CNR}_{\Sigma}(t) \rangle_{\text{non-phased}}$ with $\langle \text{CNR}_0(t) \rangle$ for $NP_{R,i} = P_{R,0}$, i.e. for equal total receive areas ($NA_R = A_{R,0}$), we find

$$\frac{\langle \text{CNR}_{\Sigma}(t) \rangle_{\text{non-phased}}}{\langle \text{CNR}_0(t) \rangle} = \frac{\eta_{het,i}(t)}{\eta_{het,0}(t)} \cdot \frac{1}{N} \neq 1. \quad (8)$$

We thus conclude that a single-telescope heterodyne receiver *cannot* be simulated by turning off the co-phasing electronics of an array receiver with equal total aperture area and uncorrelated subapertures in general, as claimed in Refs. 2 and 3! – The closest value to unity (8) can approach is given by the heterodyne efficiency for a deterministic input field, whose value depends on the receiver geometry and is usually smaller than unity: it is only approached for *very low coherence* of the incident optical field across $A_{R,0}$ (i.e. for a very large number of speckle cells per $A_{R,0}$) *and* for a very large number of subtelescopes.

Maximal ratio phased array receiver

If the signals of the array receiver's N branches are perfectly co-phased and if each signal is individually multiplied by a factor proportional to its IF amplitude, one arrives at the optimum phased array receiver, also known as maximal ratio (MR) heterodyne receiver.¹ (If the gain-adjustment is omitted, the resulting 'equal gain' receiver performs only slightly worse than the MR receiver.¹)

Under the assumptions preceding (6), the average CNR of the MR receiver is given by¹

$$\langle \text{CNR}_{\Sigma}(t) \rangle_{\text{MR}} = \frac{\eta_q \eta_{het,i}(t) NP_{R,i}(t)}{hfB} \left(= N \langle \text{CNR}_i(t) \rangle \right), \quad (9)$$

which is N times the average CNR of one of the N branches, as expected. By comparison with (3) and (7) we ultimately find

$$\frac{\langle \text{CNR}_{\Sigma}(t) \rangle_{\text{MR}}}{\langle \text{CNR}_0(t) \rangle} = \frac{\eta_{het,i}(t)}{\eta_{het,0}(t)}, \quad \text{and} \quad \frac{\langle \text{CNR}_{\Sigma}(t) \rangle_{\text{MR}}}{\langle \text{CNR}_{\Sigma}(t) \rangle_{\text{non-phased}}} = N. \quad (10)$$

Note that these relations between the three receiver structures investigated are entirely independent of the particular *statistics of the incident field* as long as the assumptions preceding (6) are met. Equations (10) are also independent of the *receiver geometry*, as long as the subapertures are uncorrelated.

3. EVALUATION FOR A SPECIFIC RECEIVER GEOMETRY AND CONCLUSIONS

To obtain expressions for the heterodyne efficiencies $\eta_{het,i}(t)$ and $\eta_{het,0}(t)$ for an evaluation of (10), we follow Ref. 7, assuming a fiber-coupled heterodyne receiver. We further assume that the (stationary) incident field's correlation function $\langle \mathbf{E}_R(\vec{r}_1) \mathbf{E}_R^*(\vec{r}_2) \rangle$ has a Gaussian shape with 1/e coherence radius ρ_c , which defines the correlation area (or 'speckle size') as $A_c = \rho_c^2 \pi$. (This definition of speckle size relates to the $1/\sqrt{e}$ -definition S_c used by e.g. Ref. 8 via $S_c = A_c/4$.)

Figure 2 shows the average CNR gain (achievable by replacing a single-telescope receiver by a MR phased array of the same total receive area) according to (10) as a function of N with the number of speckle cells (1/e-definition) per single-telescope aperture area $A_{R,0}$ as a parameter. While the solid curves give the actually expected CNR gain values, the dashed lines reveal their asymptotic behaviour: It is evident that the achievable CNR gain increases nearly linearly with N only as long as there are still a large number of speckles within A_R . As this number gets lower (i.e. as the incident field's coherence gets better over A_R), $\eta_{het,i}$ improves to its limit given by the deterministic heterodyne efficiency⁷: once the

incident field is reasonably coherent over A_R , splitting the total receive area into still more subapertures does not improve the average CNR. The limiting CNR gain is thus given by the ratio of the deterministic heterodyne efficiency for the specific receiver geometry to the single-telescope heterodyne efficiency $\eta_{het,0}$. For a typical space-based backscatter lidar system it can be shown^{5,7} that the heterodyne efficiency is a monotonically decreasing function of the ratio of transmit aperture size to receive (sub)aperture size. Thus (10) reveals that replacing a conventional single-telescope receiver using the same telescope for transmission and reception by a MR phased array of equal total receive area that reuses one of its subapertures for transmission, there is *no gain* in average CNR at all. Only if the transmit aperture is chosen larger than the receive-subapertures, a CNR gain can be expected⁶; as the heterodyne efficiency of the receiver geometry described here⁷ is 81% for the deterministic case and 42% for the conventional monostatic backscatter lidar case, the limiting CNR gain only amounts to about $3dB$.

Eventhough the achievable gain in average CNR can be quite low for some applications, it is worth considering the array option: The IF signal's fading strength improves with the number of subapertures,^{1,6} the effective receive area can fairly easily be increased, and the overall pointing requirements become less severe due to the smaller subtelescope sizes.

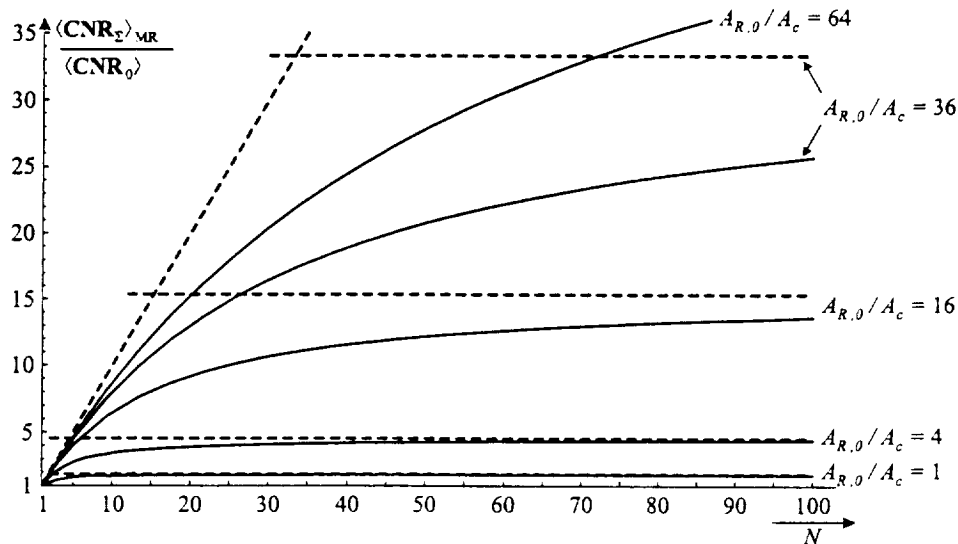


Figure 2. Average CNR gain (achievable by replacing a single-telescope receiver by a MR phased array) as a function of N with the number of speckle cells per single-telescope aperture area $A_{R,0}$ as a parameter.

ACKNOWLEDGEMENT

The author acknowledges valuable discussions of the manuscript with Walter R. Leeb.

REFERENCES

1. P.Gatt et al., *Coherent optical array receivers for the mitigation of atmospheric turbulence and speckle effects*, Appl. Opt. **35**, 5999-6009 (1996).
2. J.Xu, L.Andrews, R.Phillips, *Carrier-to-noise ratio gain factor of coherent array detection system for laser radar and communications under different conditions of atmospheric turbulence*, Proc. SPIE vol. 3615, paper no. 3615-33 (1999).
3. J.Xu et al., *Experimental comparison of coherent array detection and conventional coherent detection for laser radar and communications*, Proc. SPIE vol. 3615, paper no. 3615-06 (1999).
4. R.G.Frehlich, M.J.Kavaya, *Coherent laser radar performance for general atmospheric refractive turbulence*, Appl. Opt. **30**, 5325-5350 (1991).
5. W.R.Leeb, P.J.Winzer, K.H.Kudielka, *Aperture dependence of the mixing efficiency, the signal-to-noise ratio, and the speckle number in coherent lidar receivers*, Appl. Opt. **37**, 3143-3148 (1998).
6. P.J.Winzer, *Mitigation of the speckle effect in incoherent lidar systems using telescope arrays*, Proc. SPIE vol. 3494, 277-285 (1998).
7. P.J.Winzer, W.R.Leeb, *Fiber coupling efficiency for random light and its applications to lidar*, Opt. Lett. **23**, 986-988 (1998).
8. J.W.Goodman, *Statistical properties of laser speckle patterns* in 'Laser speckle and related phenomena', J.C.Dainty ed., Springer-Verlag (1975).

Receiver arrays in coherent Lidar wind measurement from space

A. Ouisse, I. Leike

DLR - Lidar group, PO Box 1116, 82230 Wessling, Germany, e-mail: Adelina.Ouisse@dlr.de

1. Introduction

An important limitation of wind Lidar measurement is the speckle effect due to the atmospheric fluctuations. Receiver arrays (telescope and detector arrays) are considered as a possible solution of this problem. Our intend is to find if such configurations are useful to improve the wind estimation precision. Results obtained by simulations of a telescope array in a space system are described in detail in a paper in preparation. Conclusions are briefly remembered. The present paper is more dedicated to the use of a detector array in wind Lidar systems from space.

2. Telescope array

The simulation theory of a telescope array, as well as wind measurement simulations from space is described in an article in preparation¹. It concludes that an array of N telescopes yields better performances than a single telescope of the same size, but not than N subsequent shots into the same atmosphere.

3. Detector array

Wind measurement with a (2x2) detector array is discussed in this section. A detector array allows independent signal processing of data coming from several regions of one telescope. For wind measurements from space the signals of the different channels are correlated. Simulation based on the back-propagated local oscillator theory² is thus not applicable. Instead, we simulate the back-scattered optical signal field in the receiver plane. The theory behind this simulation is described in references 1 and 3. Our Lidar simulation tool⁴ is written in LabVIEW[®]. The atmospheric return signal is received by a balanced heterodyne front-end, which is capable of detecting signals even at very low SNR conditions⁵, and a processing unit, which involves AD-conversion and frequency estimation.

Figure 1 shows statistics concerning a single detector but using the program, which computes the optical fields for a grid of spatial points on the detector surface (mapping algorithm). This figure shows that no difference exists between the back-propagated local oscillator and the mapping algorithms. Mean values as well as probability density functions are comparable for the two algorithms.

The non-homogeneity of the atmosphere is responsible of the scintillation phenomena, which results in temporal and spatial fluctuations of the back-scattered signal phase and amplitude. Using the new algorithm, spatial speckles are simulated for different ranges (Figure 2). This figure shows that the larger the distance atmosphere/receiver, the larger the correlation over the detector surface. In fact, the speckles are smaller for small ranges. Consequently, the wind estimation improvement capability will be different for a space or a ground system.

In the following simulations, we consider a space based system.

The complex heterodyne signal $S_c(t)$ is given by

$$S_c(t) = \int_A dA |V(\rho, t)| |V_{LO}(\rho)| \exp\{2\pi i t v_{OFF} + \phi(\rho, t)\}, \quad (1)$$

where $V(\rho, t)$ is the optical signal field, V_{LO} is the local oscillator field, A is the receiver surface, v_{OFF} is the offset frequency and $\phi(\rho, t)$ the phase difference of optical signal field and local oscillator field.

The physical meaningful quantity, the heterodyne signal $S(t) = 2\text{Re}[S_c(t)]$ is depicted in Figure 3. This figure shows that the speckle effect leads to destructive interference. This can be better understood, if the envelopes of the heterodyne signal and of the real integrated signal

$$S_c(t) = 2 \int_A dA |V(\rho, t)| |V_{LO}(\rho)|, \quad (2)$$

are compared. The real integrated signal represents the envelope of the heterodyne signal, if optical signal field and local oscillator field would be exactly matched in phase. The result is demonstrated in Figure 3. For three different times, the intensity and phases distributions of the optical signal field are displayed.

At t_2 , the heterodyne signal is lower as at t_1 but the intensity is higher. This is due to an interference of speckles present on the receiver surface. At t_2 , the three speckles interfere very strong whereas at t_1 the interference is lower. If each detector will receive a single speckle, the interference signal would be largest (see time t_3). In the case, where more than one speckle is present on the detector and interferes, a detector array, where each of the array elements receives a single speckle, may be useful.

From the simulations, it appears clearly that the fluctuations of the heterodyne signal represent not only the temporal speckle effect but also the spatial speckle effect (see time t_2).

An image of the array detector is built in the receiver plane and the four resulting fields are combined with the (back-propagated) local oscillator field to obtain four optical heterodyne signals. These four signals are then processed to obtain 4 electrical heterodyne currents.

Figure 4 shows statistical results for a detector array with a coherent summation process⁶. This figure shows that the results for an array detector are comparable with those of the single detector but no improvement has been reached. That means the effect of destructive interference in the presence of several speckles on the receiver discussed above does not influence the wind measurement significantly.

Previous articles on array detectors⁶⁻⁹ deal with good SNR, which is not the case here. Thus some work has to be done on signal processing which deal with low SNR.

4. Conclusion

We introduced a simulation of the back-scattered optical field in the receiver plane, which includes the temporal and spatial speckle effect. We showed that the new algorithm (mapping) and the classical back-propagated local oscillator algorithm are equivalent.

The improvement expected by using a detector array in coherent wind Lidar is dependent of the base of the system (ground, airborne or space). This is due to the property of speckles. We showed that a detector array will not improve the wind estimation in coherent Lidar measurement from space. This is due to the fact, that there are only few speckles on the telescope and the correlation of the signals of the detectors are therefore too strong to lead to a significant improvement.

Part of this work is supported by ESA in the frame of the contract No. 12852/NL/SB.

5. References

1. A. Ouisse and I. Leike, "Receivers arrays in coherent Lidar wind measurement from space", submitted to *Optical Engineering* (1999)
2. Ph. Salamitou et al., "Simulation in the time domain for heterodyne coherent laser radar", *App. Opt.* **34**, 499-506 (1995)
3. I. Leike, "Speckle patterns in Lidar wind measurements from space", *Proc. SPIE* **3583**, 373-379 (1998)
4. J. Streicher et al., "ALIENS: Atmospheric Lidar End-to-end Simulator", *Proc. SPIE* **3583**, 380-386 (1998)
5. "Coherent Detection at Low Photon Number per Measurement Interval – DELPHI", Final Report of ESA contract No. 11733/95/NL/CN, TU-Wien
6. K.P. Chan and D.K. Killinger, "Coherent summation of spatially distorted laser Doppler signals by using a two-dimensional heterodyne detector array", *Opt. Letters* **17**, 1237-1239 (1992)
7. P. Gatt et al., "Coherent optical array receivers for the mitigation of atmospheric turbulence and speckle effects", *App. Optics* **35** (30), 5999-6009 (1996)
8. A.R. Weeks, "Experimental verification and theory for an eight-element multiple-aperture equal-gain coherent laser receiver for laser communications", *App. Optics* **37** (21), 4782-4788 (1998)
9. X. Favreau et al., "Use of a detector array in the LMD CO₂ coherent laser radar", *9th Conference on Coherent Laser Radar*, 152-155 (1997)

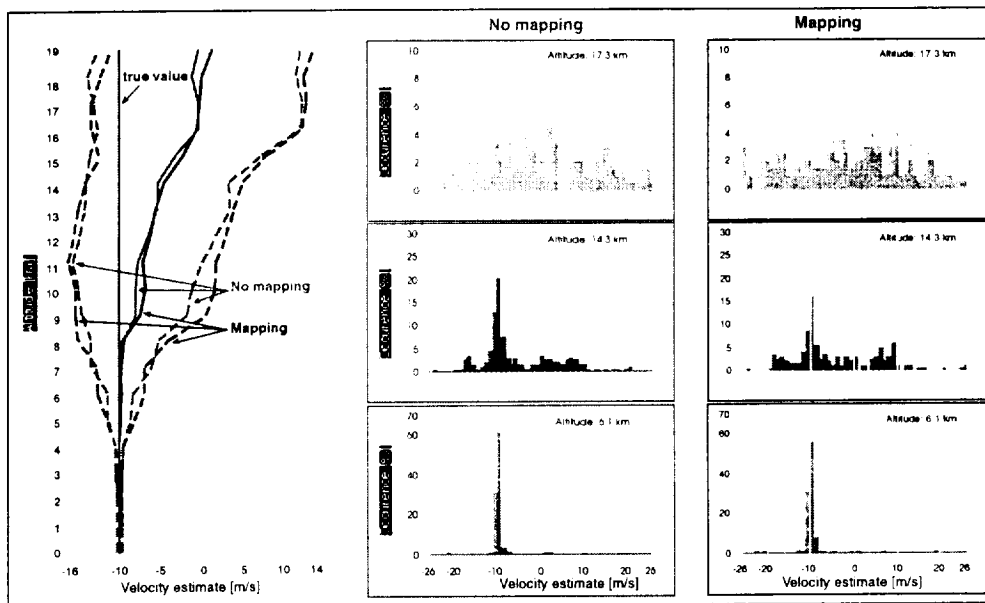


Figure 1: Comparison of mean results over 200 realisations for the back-propagated local oscillator algorithm (no mapping) and the receiver surface (mapping) algorithm. The left display shows true values (green curve), mean curves (solid lines) and standard deviations (dashed lines) as functions of altitude. The right curves show the corresponding probability density functions (PDF) at 6.1 (lower curves), 14.3 (middle curves) and 17.3 km (upper curves).

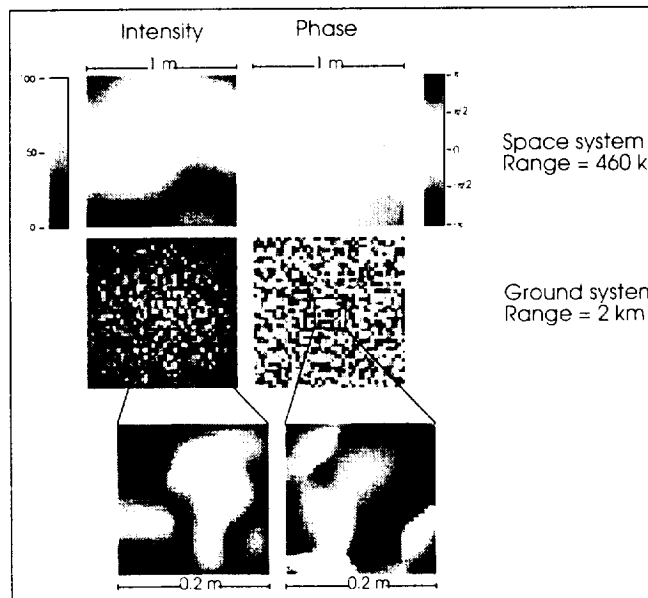


Figure 2: Speckle size comparison between a space system (range 460 km) and a ground system (range 2 km).

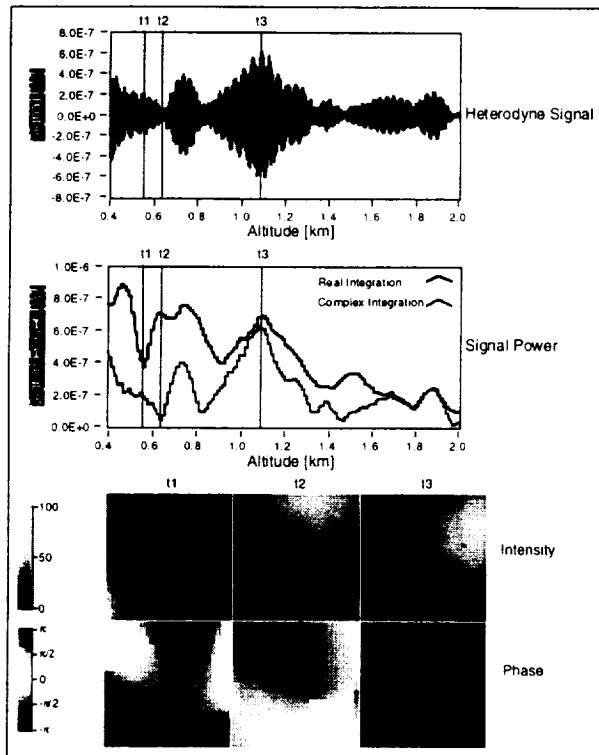


Figure 3: Speckle effect on the back-propagated signal. The heterodyne signal is issued from the optical field integration over the whole detector surface. Real integration means that only the amplitude of each optical field is integrated: this represents the illumination of the detector. Complex integration means that the complete optical field is considered (inclusive phases) and after the integration only the amplitude of the signal is considered: this is the envelope of the heterodyne signal. The lower picture represents the illumination and the phase on the detector surface at three times.

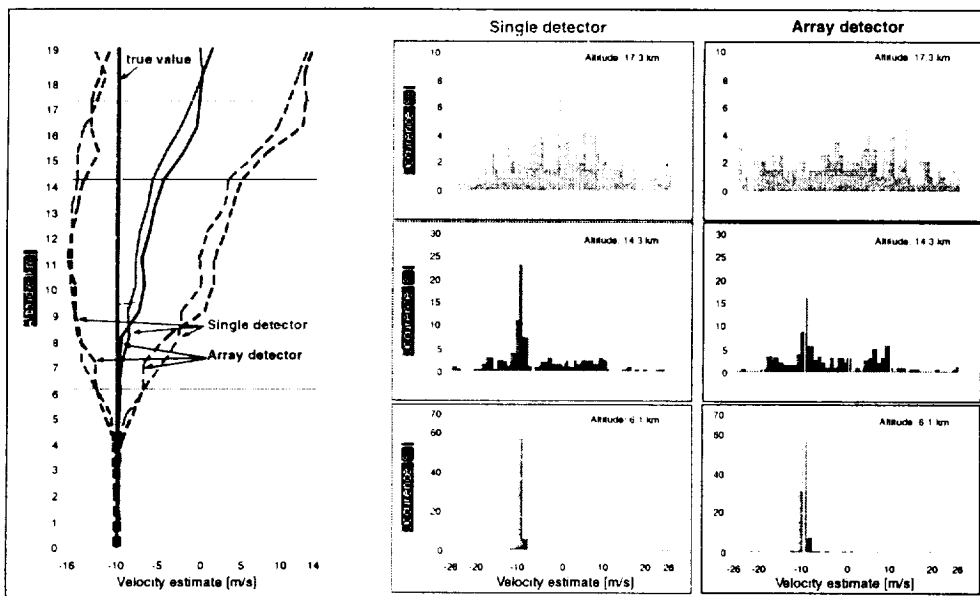


Figure 4: Comparison of mean results over 200 realisations for a single detector (mapping algorithm) and a 2x2 detector array (mapping algorithm). The four channels are coherently added. The left curve shows true values (green curve), mean values (solid lines) and standard deviations (dashed lines) as a function of altitude. The right curves show the corresponding probability density functions (PDF) at 6.1 (lower curves), 14.3 (middle curves) and 17.3 km (upper curves).

LASER ADVANCES

Presider: Christian Werner

Coherent Laser Radar using an injection seeded Q-switched Erbium:glass laser

Andrew McGrath, Jesper Munch and Peter Veitch
Department of Physics, The University of Adelaide
Australia 5005.
jmunch@physics.adelaide.edu.au

Introduction.

We have developed a promising new concept for a coherent laser radar, based on injection seeding of a Q-switched, Er:glass laser. This laser is attractive because it lases at the optimum wavelength for eye safe operation, and because it can make use of the technology developed for optical communications at $1.54\mu\text{m}$. The wavelength advantage permits the laser to emit 10 times more energy in a single pulse than is allowed at $2\mu\text{m}$ ¹. The Er:glass laser should therefore enjoy an increase in maximum useful range of a factor of 3 as compared with the $2\mu\text{m}$ system, with other factors kept constant for ease of comparison. However, the Q-switched Er:glass laser has suffered from a poor reputation for coherent sensing due to low pulse repetition frequency, limited by thermal conductivity of the glass, low efficiency due to being a 3 level laser, and due to the popular notion that a three level laser cannot be injection seeded. We shall attempt to demonstrate that these notions are unjustified, and that the Er:glass system may be an ideal approach for many coherent laser sensing applications.

Preliminary Experiments.

In recently published work², we demonstrated that the three level Er:glass laser could operate as a long pulse, Q-switched laser, and could be injection seeded to operate on a single, transform limited frequency. The laser used was a flash-lamp pumped, Q-switched laser capable of producing 30 mJ in a 400ns pulse at 1535nm. However, the master oscillator (MO) available, was a commercial, diode pumped, single frequency laser emitting 50mW at 1552nm, and the wavelength was not tunable. The capability to injection seed was therefore demonstrated at the latter wavelength by tuning the power oscillator away from line center using a grating as an end mirror in the laser. At this wavelength only 1-2mJ per pulse was produced. A diagram of the laser transmitter is shown in Figure-1. When injection seeded, the output pulse was transform limited as shown in Figure 2. More recently we used the laser to measure the Doppler shift of a moving, hard target to a resolution of 1m/s as shown in Figure 3. This work established that it was feasible to use an Er:glass host as a coherent laser radar. The first generation laser did suffer from several shortcomings, however, including the wavelength detuning, low pulse repetition rate, and a difficulty in maintaining reliable injection seeding from pulse to pulse. Below we shall discuss the improvements currently in progress.

Laser Radar design.

The new power oscillator will be an InGaAs-diode laser pumped Er:glass side pumped slab laser, based on the coplanar folded zig-zag slab laser (CPFS) architecture³, an architecture which we have previously successfully used for cw injection locking⁴. This architecture is advantageous because of the high slope efficiency achieved, approaching

that of end pumped architectures, its lack of need of optical coatings, and its ability to be scaled to high powers. Furthermore, the architecture is naturally suited for compact ring laser geometries, ideal for injection seeding. Although a three level laser will have a high pump threshold (approximately 300mJ), the total energy deposited in the glass using diode laser pumping will be at least a factor of 30 lower than that of flash lamp pumping, thus permitting a corresponding increase in the PRF, while keeping the glass at a comparable average temperature. We estimate that a 30mJ laser with 500ns pulses will be able to operate close to 100Hz, and will in practice be limited by the maximum average power from available pulsed diode pump lasers rather than the Er:glass host. This laser will be locked to a single frequency Er doped fiber laser.

We have already addressed and solved a major technical obstacle of reliable injection seeding of long pulse, comparatively low gain, Q-switched oscillators. Although injection seeding is a well-known technique, which is even available on commercial lasers, it is usually applied to short pulse, high gain lasers, initiating well above threshold. In this case injection seeding is very easy, because the seed is strongly amplified, and the frequency matching criteria for the MO into the power oscillator is relaxed. For long pulse, coherent laser radar applications, a large number of round trips of the seed is required to produce an injection seeded output pulse, and the frequency matching requirements are much more stringent. We have developed and demonstrated a new and improved servo system specifically developed for this application⁵. Our system uses the build-up time technique as the discriminant for frequency matching, but in contrast to existing servos, our system utilises a discrete stepping type feedback that is much more robust for Q-switched lasers with a narrow injection seeding range. The system has been demonstrated on a 20mJ per pulse, 50Hz PRF, Nd:YAG ring laser, and works with high efficiency, seeding every pulse, and resulting in guaranteed transform limited outputs as shown in Figure 4.

Conclusion.

We have shown that Er:glass lasers can be used as coherent laser radar transmitters, and we are currently building a reliable, second generation device, designed to operate efficiently near line center. The resulting laser is expected to deliver 30mJ per pulse at close to 50Hz PRF with 500ns long, transform limited pulses.

This work was supported in part by a research grant from the Australian Defence Science and Technology Organisation.

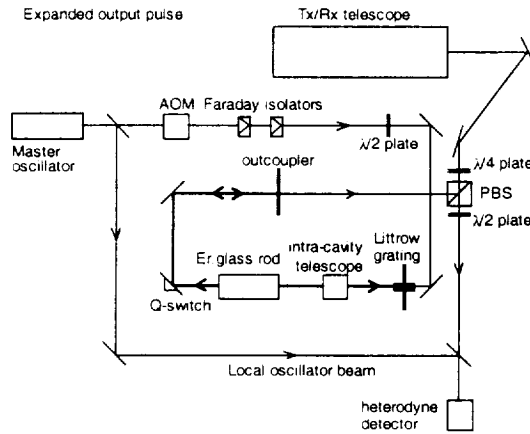


Figure 1: Laser system layout with injection via the diffraction grating. The injection path incident on the diffraction grating leaves the plane of the optical system. We also investigated injection through the Q-switch.

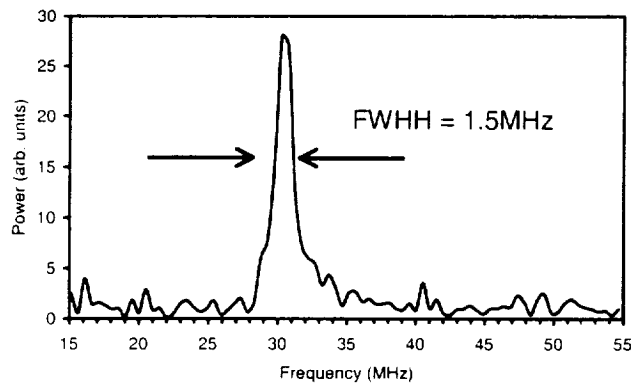


Figure 2: Spectrum of seeded pulse. Shown is the Fourier transform of the pulse, indicating a transform limited output pulse.

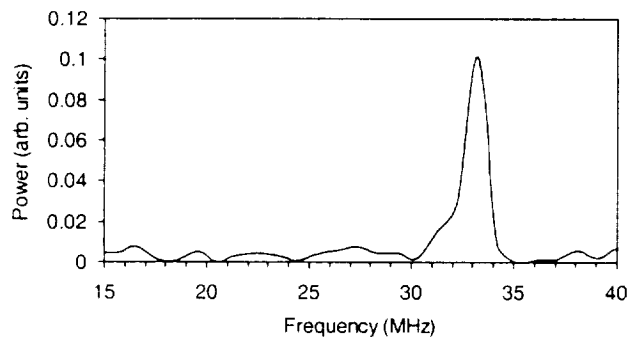


Figure 3: Spectrum of Doppler return from moving hard target (belt sander) for approaching motion (positive Doppler velocity). Shift of +3MHz from 30MHz corresponds to approaching radial velocity component of 2.5ms^{-1} .

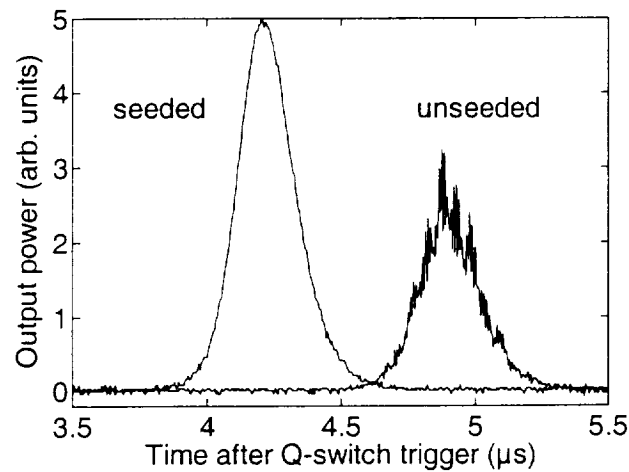


Figure 4: A plot of the temporal development of the injection-seeded (left-hand) and unseeded (right-hand) laser pulses as a function of time since Q-switching.

¹ Australian/New Zealand Standard for Laser safety, AS/NZ 2211.1-1997, based on IEC 825-1:1993

² A. McGrath, J. Munch, G. Smith, P. Veitch: *Injection-seeded, single frequency, Q-switched Er:glass laser for remote sensing*, Appl. Opt **37**, 5706-5709, 1998.

³ J. Richards, A. McInnes, *Versatile, efficient, diode pumped miniature slab laser*. Opt. Lett. **20**, 371-373, 1995.

⁴ D.J Ottaway, P.J. Veitch, M.W .Hamilton, C. Hollitt, D. Mudge, J. Munch *A compact injection locked Nd:YAG laser for gravitational wave detection*. IEEE JQE, **34**, 2006, 1998

⁵ Y. Matyagin, P.J. Veitch, J. Munch *Active stabilisation of injection seeded, Q-switched lasers* Submitted to Appl. Opt. April 1999.

High Efficiency End-Pumped Ho:Tm:YLF Disk Amplifier

Jirong Yu¹, Upendra N. Singh², Mulugeta Petros¹, Theresa J. Axenson¹ and Norman P. Barnes²

¹Science and Technology Corporation, 101 Research Drive, Hampton, VA 23666-1340

Email: jirong.yu@larc.nasa.gov

²NASA Langley Research Center, MS 474, Hampton, VA 23681-0001

Email: u.n.singh@larc.nasa.gov

1. Introduction

Space based coherent lidar for global wind measurement requires an all solid state laser system with high energy, high efficiency and narrow linewidth that operates in the eye safe region. A Q-switched, diode pumped Ho:Tm:YLF 2- μ m laser with output energy of as much as 125 mJ at 6 Hz with an optical-to-optical efficiency of 3% has been reported¹. Single frequency operation of the laser was achieved by injection seeding. The design of this laser is being incorporated into NASA's SPARCLE (SPACE Readiness Coherent Lidar Experiment) wind lidar mission. Laser output energy ranging from 500 mJ to 2 J is required for an operational space coherent lidar. We previously developed a high energy Ho:Tm:YLF master oscillator and side pumped power amplifier system² and demonstrated a 600-mJ single frequency pulse at a repetition rate of 10 Hz. Although the output energy is high, the optical-to-optical efficiency is only about 2%. Designing a high energy, highly efficient, conductively cooled 2- μ m laser remains a challenge. In this paper, the preliminary result of an end-pumped amplifier that has a potential to provide a factor 3 of improvement in the system efficiency is reported.

2. Experiment

A high energy Ho:Tm:YLF 2- μ m laser usually consists of an oscillator and multiple amplifier stages. Efficient amplification of the 2- μ m laser is important since the amplifier will consume most of the available electrical power. To date, most of the 2- μ m amplifiers have used a transverse or side-pumped laser rod configuration to pump the laser gain medium. In laser rod geometry, it is difficult to extract the energy stored near the lateral surfaces of the laser rod, which limits the efficiency of the system. A longitudinal or end-pumped configuration, on the other hand, only the center of the disk can be pumped which allows the beam to be amplified to access all of the pumped volume without suffering diffraction losses. Figure 1 shows the optical layout used in the end-pumped disk amplifier. The diode laser assembly consists of two laser diode arrays (LDA). Each LDA has 13 laser-diode bars with peak output power of 100 W per bar. A microcylindrical lens is attached near each surface of the laser bar. The effect of the cylindrical lens is to collimate the fast-axis radiation of a LDA from a FWHM spread of about 40° to 2°, increasing the brightness of the radiation³. The divergence of the slow-axis radiation of a diode array remains at ~10°.

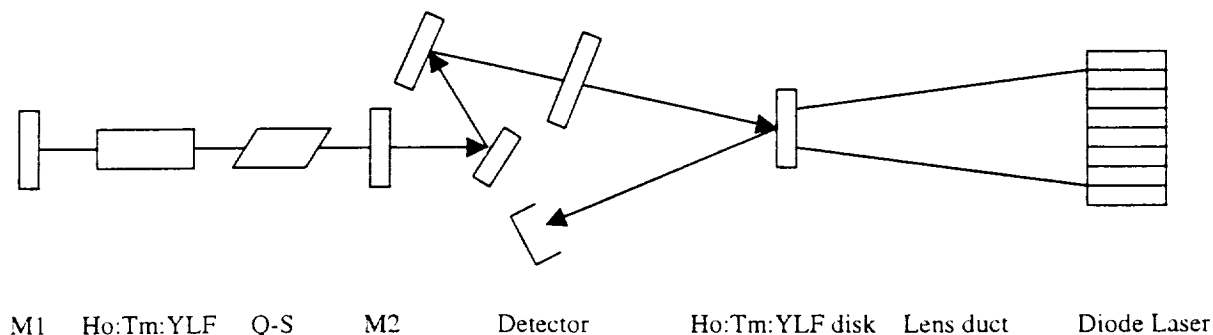


Figure 1. Optical layout of the end pumped disk amplifier

A nonimaging lens duct is used to couple the radiation from the laser diode arrays to the laser disk. The use of a lens duct can significantly increase the irradiance of LDA's on a laser disk⁴. The lens duct has the advantages of high coupling efficiency and simple structure, which are essential for the design of high power amplifiers with large laser diode arrays as the pump source. The lens duct consists of one spherical input surface and five planar surfaces. The spherical surface is designed to efficiently couple the output radiation from laser diode arrays into the lens duct. As the light rays travel through the lens duct, they may be incident on one of the four canted side surfaces. If so, they are totally reflected from the side surfaces. The output surface is octagonal with a diagonal distance of 0.35 cm, which mimics the circle shape of the laser gain medium. The input surface of the lens duct is 3.5 cm x 1.5 cm with a radius of curvature of 3.5 cm. The axial length of the lens duct from input surface to output surface is 10.3 cm. The measured coupling efficiency of the lens duct is greater than 83%. It is quite low compared to the ray trace model, which indicates a 98% coupling efficiency. The reason is that the microcylindrical lens may not be perfectly aligned with the emitting junctions of the laser diodes bar, resulting in poor transmission of the diode rays through the lens duct. The lens duct alignment is not sensitive to linear translation, but it is very sensitive to angular adjustment. The diode pump radiation enters the input surface of a Ho:Tm:YLF disk after leaving the lens duct. The input surface of the laser disk is located 0.5 mm from the output surface of the lens duct. The laser disk is currently water-cooled to a temperature of 15° C, but can easily be changed to a conductively cooled system. The input surface of the laser disk is dichroic, with high reflection at 2- μ m and high transmission at 792 nm. The exit surface of the laser disk is antireflection coated at 2- μ m. The c-axis of the laser disk is parallel to the polarization of the diode laser.

The probe beam from the oscillator is directed to the laser disk by two turning mirrors so it can be easily scanned through the laser disk to find a maximum gain position. A half wave plate is inserted into the beam path to align the probe beam polarization with the c-axis of the Ho:Tm:YLF disk. The probe beam enters into the disk with a small angle. It is reflected by the other side of the laser disk and double passes the gain medium. A detector is used to record the amplified laser energy.

3. Result and Discussion

A set of Ho:Tm:YLF disks with different doping concentrations and disk thickness is used in the amplifier experiment. The probe beam energy in normal mode is varied from 29 mJ to 198 mJ to cover wide input range. The probe energy in Q-Switch mode is varied from 27 mJ to 37 mJ. Figures 2a and 2b show the amplifier performance for the set of laser disks for a probe beam of 37 mJ in Q-switch mode and 198 mJ in normal mode, respectively.

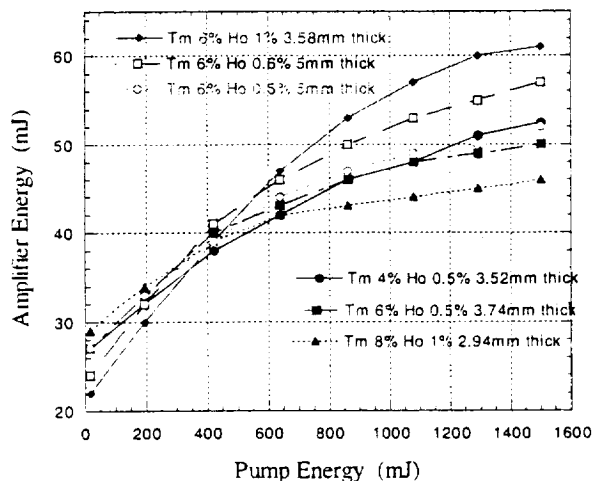


Figure 2a. End pumped disk Amplifier performance, with a probe beam energy of 37 mJ in Q-S mode

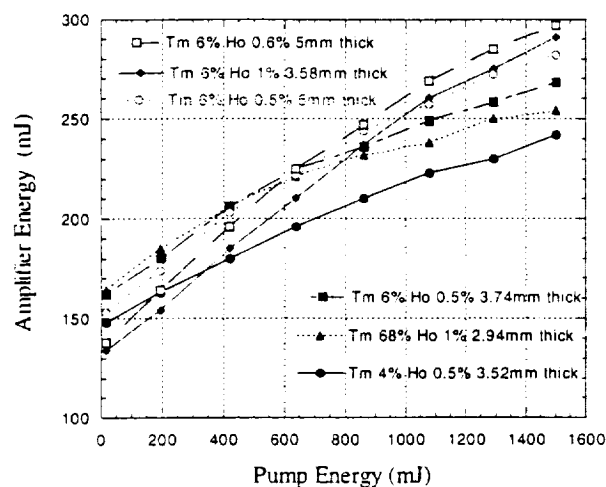


Figure 2b. End pumped disk Amplifier performance, with a probe beam energy of 198 mJ in normal mode

The amplifier reaches transparency at a pump energy of ~ 400 mJ in all cases. As the pump energy increases, the probe beam energy is amplified. The amplifier gain is a function of both doping concentration and disk thickness. For the laser materials examined in this study, a 6% Tm and 1% Ho doping concentration shows the most gain. These measurements concur with a model simulation, which indicated that the amplifier gain would increase with increasing Ho concentration for a certain pump energy level. With a small probe energy of 27 mJ in normal mode, a gain of 2 is obtained for a doping concentration of 6% Tm and 1% Ho. For a larger probe energy, the laser gain medium becomes saturated, thus reducing the gain to 1.5. More than 100 mJ of energy is extracted from the gain medium when a probe beam of 198 mJ is used. In Q-switch operation mode, the amplified energy is a little smaller than that in the normal mode. For a doping concentration of 6% Tm and 1% Ho laser disk, the gain is reduced to 1.72 for an input probe energy of 27 mJ in Q-switch mode.

A significant improvement in optical-to-optical efficiency has been obtained with the end-pumped disk amplifier. Previously, the side pumped rod amplifier yielded an optical efficiency of only 2%. With the same input energy an optical-to-optical efficiency of 5.6% has been obtained using the end-pumped configuration. The efficiency of this system can be further augmented by adjusting the alignment of the lens duct with the pump diodes and by optimizing the doping concentration and thickness of the laser disk.

4. Conclusion

An end-pumped Ho:Tm:YLF disk amplifier operating at room temperature has been demonstrated. Compared with a side pumped Ho:Tm:YLF amplifier, the end-pumped disk amplifier provides similar gain with much higher efficiency. An optical-to-optical efficiency of 6% is achievable with this system. The configuration of the end-pumped disk amplifier is quite simple and it can easily be conductively cooled. It is also relatively easy to scale up the energy by putting several amplifiers in series. This highly efficient disk amplifier is a promising candidate for use in an efficient, space lidar system.

5. References

1. Jirong Yu, Upendra N. Singh, Norman P. Barnes and Mulugeta Petros, "125-mJ diode-pumped injection-seeded Ho:Tm:YLF laser", *Opt. Lett.* 23, 780-782, (1998)
2. Upendra N Singh, Jirong Yu, Mulugeta Petros, Norman P. Barnes and et. al, "Injection-seeded, room-temperature, diode-pumped Ho:Tm:YLF laser with output energy of 600 mJ at 10 Hz", *OSA TOPS*, 19, 194-196, (1998)
3. J. J. Snyder, P. Reichert and T. Baer, "Fast diffraction-limited cylindrical microlenses", *Appl. Opt.*, 30, 2743-2747(1991)
4. Rulian Fu, Guangjun Wang et al, "Design of efficient lens ducts", *Appl. Opt.*, 37, 4000-4003 (1998)

A Proposed 1.55 μm Solid State Laser System for Remote Wind Sensing

Arun Kumar Sridharan, Todd Rutherford, William Tulloch, and Robert L. Byer
Ginzton Laboratory, Stanford University, Stanford, CA 94305-4085

A. Introduction

Coherent lidar is an important tool in weather prediction and the understanding of global climate. Specifically, this tool can be used to measure tropospheric winds from space. Measuring global winds would provide much needed data that can be incorporated into climate modeling¹. For many years, CO_2 lasers have been used as the transmitter source in these coherent lidar systems². In recent years there has been a move towards using diode-pumped solid-state lasers at $2 \mu\text{m}$ ³. We propose a new high-power diode-pumped solid-state laser based on Yb:YAG and an optical parametric amplifier system to serve as the source in lidar systems. This system is eye-safe³ with output at $1.55 \mu\text{m}$ and is scalable to the pulse energies appropriate for space based global wind sensing.

The operational specifications of the proposed laser transmitter are determined by the overall performance specifications of the lidar system. For example, a pulse energy of 2 J, at a wavelength of $1.55 \mu\text{m}$, is required to achieve adequate SNR to detect 1 m/s wind speeds for a 200 km altitude receiver⁴. To meet these system specifications we propose a new design approach that incorporates a novel laser-diode edge-pumped Yb:YAG slab amplifier, operating with 3.8 J, $1 \mu\text{s}$ pulses at a 10 Hz repetition rate, and an optical parametric amplifier to convert the $1.03 \mu\text{m}$ radiation to $1.55 \mu\text{m}$. Operating at $1 \mu\text{s}$ pulse lengths allows the 3.8 J amplifier to operate below the optical materials damage fluence level while maintaining efficient energy extraction. Operating at $1.55 \mu\text{m}$ decreases beam divergence compared to $2 \mu\text{m}$ and $10 \mu\text{m}$ sources with an equivalent aperture size³. Additionally, for wind velocity measurements, operation at shorter wavelengths enables better range resolution for equivalent velocity resolution. An important benefit of $1.55 \mu\text{m}$ wavelength operation is the opportunity to utilize telecommunications technology such as oscillators, erbium-doped fiber amplifiers (EDFA), pre-amplifiers, couplers, and detectors. Based on improvements in laser diode brightness, the edge-pumped slab geometry, and improved nonlinear optical materials, we will describe a laser system design that is efficient, robust and meets the power and heat requirements of a space based laser system. This paper focuses on the power-amplifier and the nonlinear frequency conversion subsystems.

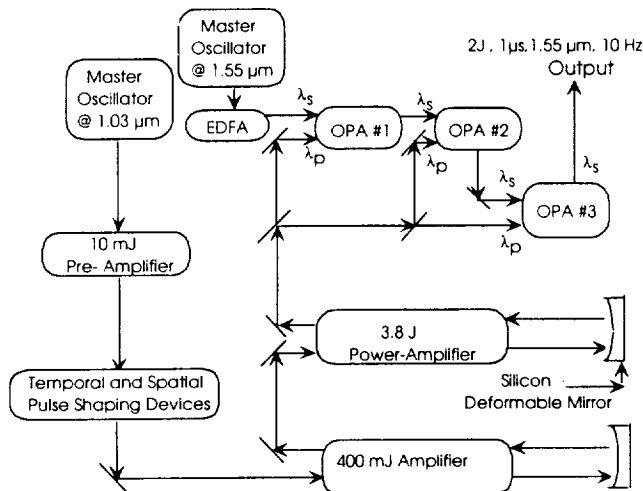


Figure 1: Schematic of the laser system for coherent lidar applications.

with arbitrary pulse lengths, good coherence control, and better power and timing stability than conventional Q-switched lasers.

The first step in the design of the laser is a master-oscillator that can be shaped and amplified to meet the final source specifications. Due to the master oscillator frequency and power stability requirements, we have selected the laser-diode-pumped non-planar ring oscillator (NPRO)⁵ as the basis for the master-oscillator design. The NPRO oscillates in single axial mode, with a few kHz linewidth. Research

B. Laser Transmitter

To meet the source requirements, we propose a laser system based on a MOPA configuration, a traditional technique for scaling laser systems to high powers while maintaining good beam quality and coherence. The proposed laser system consists of a master-oscillator, pre-amplifier, pulse shaper, 400 mJ amplifier, and a 3.8 J multi-pass power-amplifier. The MOPA configuration provides the ability to tailor the pulse width, beam divergence, and spectral width of the output pulses with low power components prior to the power amplifier. The scaling to high output pulse energy is determined by the power amplifier design. The MOPA design enables the system to operate

is under way to develop an Yb:YAG NPRO master oscillator. External modulation can be used to obtain the 1 μ s pulse at 10 Hz required at the input to the pre-amplifier.

To reach output energies of 3.8 J/pulse, several stages of amplification are required. The first amplification stage, the pre-amplifier, increases the 1 μ J pulses to an output energy of 10 mJ. A 62 dB gain multiple-pass slab geometry amplifier has been demonstrated in Nd:YAG systems^{6,7}. This system was capable of generating 10 mJ pulses, with μ s pulse lengths, at 10 Hz. The limitation to this flashlamp-pumped system's repetition rate were thermal effects, which can be reduced in laser-diode-pumped multiple-pass amplifier designs.

The proposed laser system should generate pulses that are square pulses in time, and have super-gaussian flat-top beam spatial profiles. The amplification process distorts the amplified beam, both temporally and spatially, due to gain saturation within the amplifier.^{8,9} Therefore, the input to the 400 mJ amplifier must be temporally and spatially tailored to ensure that the amplifier, while distorting the input, produces the required output pulse shape. Additionally, spatial profile shaping is critical to ensure efficient energy extraction from the power amplifier. For the purpose of this design, we estimate that the pulse shaping stage has a 10% efficiency so that 1 mJ is produced as input to the 400 mJ amplifier.

Due to thermal loading the pulse will undergo wavefront distortions as it passes through the power amplifier⁸. Recent advances in the development of micromachined silicon deformable mirrors indicate that these devices can be used to correct for thermally induced beam distortions without inducing significant loss or scatter on the beam.¹⁰

C. Power Amplifier

The key technical challenge in the design of a 3.8 MW peak power, 38 W of average power (3.8 J/pulse @ 1.03 μ m, 1 μ s, 10 Hz rep rate) laser system is the design of the power amplifier. The optimization of a power amplifier design that meets these requirements and operates below the materials optical damage fluence, while effectively saturating the amplifiers for efficient energy extraction, is the key to building an effective laser transmitter. At the 10 Hz repetition rate, the slab is well below the stress fracture limit. The maximum fluence that can be extracted in a 10 nsec pulse is limited by optical damage to about 10 J/cm² in Yb:YAG. Empirical studies indicate that the surface damage fluence increases as the square root of the pulse length⁹. Thus, we can expect to extract a maximum of 100 J/cm² in a 1 μ s pulse. Using this information we proceed with a brief description of the edge-pumping geometry and a preliminary point design for a 3.8 J/pulse power amplifier.

i. Edge-Pumped, Conduction-Cooled Slab Amplifier

Zig-zag slabs have been demonstrated as effective oscillator and amplifier geometries for power scaling laser systems while retaining good beam quality.¹¹ We propose a design based on Stanford's new edge-pumped, conductively cooled solid-state zig-zag slab lasers.

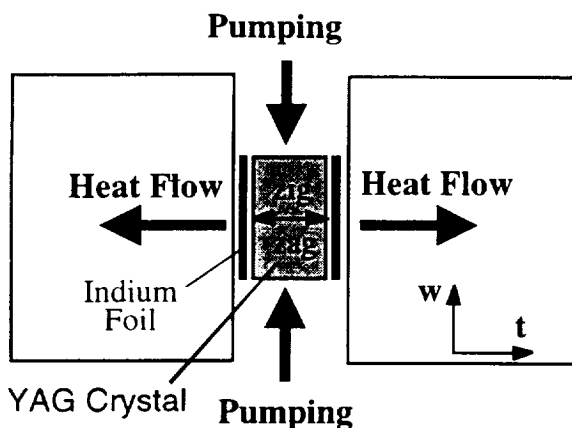


Figure 2 : Cross-sectional view of the edge-pumped slab amplifier geometry. The conductively-cooled slab is clamped in a copper housing. Pump light is incident from both the top and bottom of the slab. The optical path is out of the page. Indium foil is used to ensure a uniform thermal contact with the heat sink.

Figure 2 shows the basic geometry of a zig-zag slab amplifier illustrating edge-pumping and conductive cooling. The key idea is to decouple the cooling interface and the optical pumping interface. The result is a simpler, more robust, and more efficient amplifier. Pumping along the slab width also allows lower doping and thus reduces the threshold in comparison with face-pumped Yb:YAG. This new edge-pumped design is discussed by Tulloch et. al.¹²

This design can be power scaled by increasing the slab aperture, to avoid optical damage, while maintaining the pump power density. By using conduction cooling, the cumbersome use of water in space is avoided.

The edge-pumped laser concept has been demonstrated by our group using laser-diode-pumped Nd:YAG¹³. A 4.5 mm

wide slab with a 3:1 aspect ratio was recently operated as a multi-mode oscillator with a yield of 127 W of cw output power for 300 W of input pump power. The slope efficiency was 55%, and laser diode absorption efficiency was 95%. Two-sided pumping provides symmetric heating in the pumping direction and efficient pump absorption can be attained with limited thermal lensing.

An important feature of our design is the use of fiber-coupled laser diode arrays as the optical pumping source. Fiber-coupled laser diode arrays provide higher brightness pumping than 2-D diode arrays, which is critical for the Yb:YAG design. Additionally, there are several engineering advantages to the use of fiber-coupled laser diodes. Fiber coupling of the pump diodes allows the laser diodes and power supplies to be remotely located, separating the task of laser diode heat removal from the task of heat removal from the amplifier head. Further, large numbers of laser diodes offer slow degradation in performance since loss of a few laser diodes is relatively insignificant.

ii. Preliminary Point Design

The amplifier output vs. input curves can be calculated by using the Franz-Nodvik relations.^{9,13} The critical parameters in this calculation are the amplifier unsaturated gain, g_0l , and the saturation fluence of the gain medium, E_s . Amplified spontaneous emission and parasitic oscillations set the practical limitation on the gain in high power amplifiers. For these initial calculations the unsaturated single pass gain was set to $g_0l = 3$, a conservative estimate compared to data available in the current literature.⁹

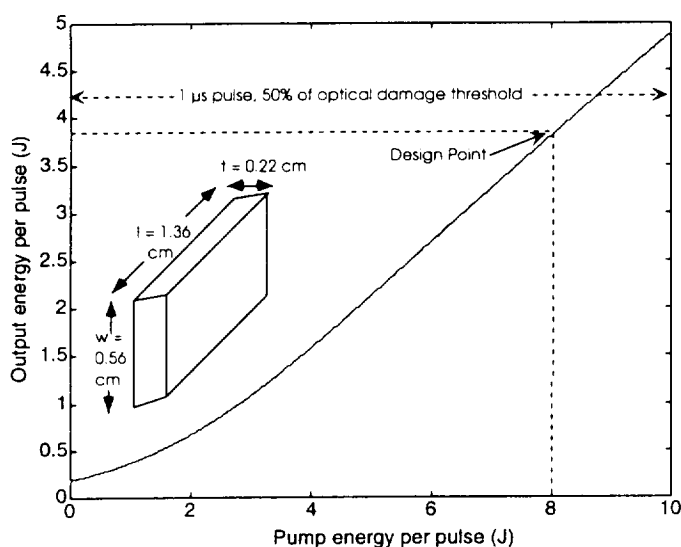


Figure 3: Yb:YAG power-amplifier output energy as a function of pump energy. The calculation includes a 400 mJ of input energy, 300 K crystal temperature, 2.6 % Yb doping concentration, $10\text{J}/\text{cm}^2$ saturation fluence, and 4 J energy stored in the gain medium. The optical damage threshold was conservatively chosen to be $70\text{J}/\text{cm}^2$.

operational duty cycle. The use of laser diodes at a 1% duty cycle should offer long operational lifetimes since each laser diode is rated $>20,000$ hours for cw operation.

Our design optimizes the length, width, and thickness of the slab by considering the following constraints: stress fracture, pumping absorption efficiency and uniformity of pumping, requisite slab area for close-packed pumping fibers, a small signal gain (g_0l) \cdot 3 to avoid parasitic oscillations, and a 55 % safety margin to prevent optical damage of crystal faces.

Figure 3 shows the Yb:YAG amplifier output energy vs. pump energy for a double pass amplifier operation with slab dimensions optimized for the 3.8 J operating point. The slab aperture of 0.12cm^2 and the operation fluence level of $23\text{J}/\text{cm}^2$, places the laser well below the expected $100\text{J}/\text{cm}^2$ damage level for 1 μs pulses. Thus, we can see from Figure 3 that an input of 400 mJ into the double-pass power-amplifier yields an output of 3.8 J in a 1 μs pulse.

Efficient energy extraction from an amplifier requires that the amplified pulse fluence is comparable to the saturation fluence of the amplifier. This design parameter makes reducing the cross sectional area of the amplifier desirable. However, the engineering optical damage limitation of $100\text{J}/\text{cm}^2$ makes increasing the cross sectional area of the amplifier desirable. This is the fundamental design tradeoff treated in this initial calculation.

At present laser diodes to pump Yb:YAG at 940 nm are able to deliver 50 W of cw power with a $600\text{ }\mu\text{m}$ core fiber. Since the upper state lifetime of Yb:YAG is 1 ms, we propose to modulate the cw laser diode source such that we obtain a 1 ms pump pulse at 10 Hz, corresponding to a 1 %

D. Nonlinear Frequency Conversion

Using nonlinear parametric conversion, the 1.03 μm laser can be frequency shifted to 1.55 μm for eye-safe operation. To accomplish this task, we propose periodically poled lithium niobate (PPLN) as the nonlinear frequency conversion material in a quasi-phasematched (QPM)¹⁴ optical parametric amplifier (OPA).¹⁵

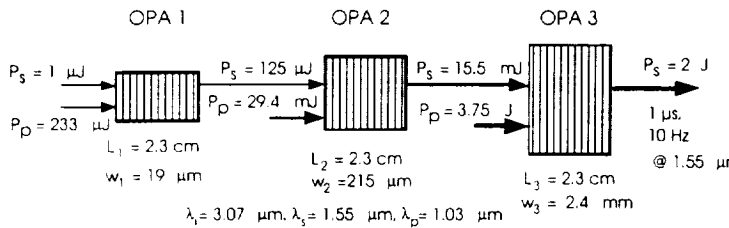


Figure 4: Three stage optical parametric amplifier. OPA crystal length, L, and pump beam waist, w, are provided for reference.

The local oscillator for the 1.55 μm light can be generated by a telecommunications laser diode followed by an erbium-doped fiber amplifier. Three OPA's are used in series to ensure that crystal lengths are long enough to achieve high conversion efficiency, but short enough to maintain reasonable temperature bandwidths. The crystal was

designed to have a grating period of 26 μm , and an operating point of 180 degrees C, to avoid photorefractive damage. The spot sizes are scaled up in each crystal to prevent optical damage while maintaining enough intensity for efficient conversion. The OPA's have been optimized to operate at 60% of the 33 J/cm² optical damage level¹⁴ for a 1 μs pulse. These calculations were based on the use of super-gaussian pump beams operating at 80% of the OPA theoretical conversion limit.

E. Summary

We have proposed a design for the laser transmitter that can be used for a space-based lidar system. The edge-pumped slab geometry and the availability of high brightness fiber-coupled laser diodes have enabled the design of the 3.8 J power amplifier. Extracting the energy in 1 μs pulses provides the ability to saturate the power amplifier for efficient energy extraction while operating below the optical damage limit. The low quantum defect of Yb:YAG results in high energy storage and low thermal loading in the power amplifier. This means that the potential overall electrical-to-optical efficiency of the transmitter is quite high. Parametric frequency conversion of the amplified 1.03 μm radiation to 1.55 μm provides an eye-safe source operating at a 10 Hz repetition rate with 2 J, 1 μs pulses. By selecting the 1.55 μm wavelength for the transmitter we can utilize the highly developed fiber telecommunications technology for the development of an OPA seed source and the coherent lidar receiver subsystem.

References

- ¹ Huffaker, R.M. et. al. Appl. Opt., Vol. **22**, 1655-1665, 1984.
- ² Menzies, R.T. Appl. Opt., Vol. **33**, 5698-5711, 1994.
- ³ Henderson, S. et. al. IEEE Trans. On Geoscience and Rem. Sensing, Vol. **31**, No. 1, Jan. 1993.
- ⁴ Menzies, R.T. Private Communication.
- ⁵ Kane, T. Byer, R.L. Opt Lett., Vol. **10**, 65-67, 1985.
- ⁶ Kane, T.J. et. al. Opt. Lett., Vol. **11**, 216, April, 1986.
- ⁷ Kane, T.J. et.al. Opt. Lett, Vol. **12**, 239, 1987.
- ⁸ Siegman, A. E. *Lasers*, University Science Books, Mill Valley, 311-328. 1986.
- ⁹ Koehner, W. *Solid State Laser Engineering*. Springer-Verlag. 180, 1996.
- ¹⁰ Mansell, J. Byer, R.L. "Micromachined Silicon Deformable Mirror." *Proceedings of SPIE. Adaptive Optical System Technologies*. Vol. **3353**. 896-901. 1998.
- ¹¹ Comaskey, B. et al. "A one kilowatt average power diode pumped Nd:YAG folded zigzag slab laser" *Proceedings of the SPIE - Diode Pumping of Average-Power Solid State Lasers*. Vol. **1865**, 9-16, Jan. 1993.
- ¹² Tulloch, W.M. et.al. "A 100 W transverse-pumped Nd:YAG conduction-cooled slab laser." MA4. To appear in OSA TOPS. Advanced Solid State Lasers Conference. 1999.
- ¹³ Eggleston, J.M. et al. IEEE. JQE, Vol **25**, No. 8, 1855-1862, Aug. 1989.
- ¹⁴ Myers, L. et. al. J. Opt. Soc. Am. B, Vol. **12**, No. 11, 2102-2116, Nov. 1995.
- ¹⁵ Baumgartner, et. al. IEEE JQE, Vol. **QE-15**, No. 6, 432-444, June. 1979.

SYSTEM ADVANCES

Presider: Alain Dabas

Abstract Submission for the
Tenth Biennial Coherent Laser Radar Technology and Applications Conference
28 June to 2 July, 1999

Optical Phased Arrays for Electronic Beam Control

By

Terry A Dorschner

Raytheon Systems Company
Sensors and Electronics Systems Segment
Advanced Optics and Reconnaissance Systems Center

131 Spring Street
Lexington, MA 02421

Terry_A_Dorschner@RES.Raytheon.com

The state of the art of optical phased arrays (OPA's) will be reviewed and prospective applications discussed, highlighting laser radar and other active sensors. Current OPA performance levels will be summarized and the near-term performance potential forecasted. Comparisons with conventional and emerging new technologies for beam control will be made.

High-Efficiency Autonomous Coherent Lidar

Philip Gatt, Sammy W. Henderson and Stephen M. Hannon
 Coherent Technologies, Inc.
 655 Aspen Ridge Dr.
 Lafayette, CO 80026

INTRODUCTION

A useful measure of sensor performance is the transceiver system efficiency η_{sys} . Which consists of the antenna efficiency η_a , and optical and electronic losses. Typically, the lidar equation and the antenna efficiency are defined in terms of the telescope aperture area. However, during the assembly of a coherent transceiver, it is important to measure the system efficiency before the installation of the beam-expanding telescope (i.e., the untruncated-beam system efficiency). Therefore, to accommodate both truncated and untruncated beam efficiency measurements, we define the lidar equation and the antenna efficiency in terms of the beam area rather than the commonly used aperture area referenced definition. With a well-designed Gaussian-beam lidar, aperture area referenced system efficiencies of 15 to 20 % (23-31% relative to the beam area) are readily achievable.

In this paper we compare the differences between these efficiency definitions. We then describe techniques by which high efficiency can be achieved, followed by a discussion several novel auto-alignment techniques developed to maintain high efficiency.

APERTURE REFERENCED EFFICIENCY

The lidar system efficiency η_{sys} represents the reduction in signal-to-noise ratio (SNR) from that predicted by the throughput (lidar) equation for an ideal lidar. For a coherent lidar illuminating a diffuse target, the SNR is given by

$$SNR = \eta_{sys} \frac{P_T \rho_\pi T^2 \gamma A_r}{h \nu B z^2} \quad (1)$$

Where, P_T is the transmitted laser power, ρ_π is the target backscatter reflectance (sr^{-1}), T is the one-way transmittance of the atmosphere, γ represents the loss due to refractive turbulence¹, A_r is the collection area of the receiver aperture (πa^2), h is Plank's constant, ν is the laser frequency, B is the receiver bandwidth and z is the target range.

The theoretical far-field system efficiency limit, for a Gaussian-beam lidar with a circular aperture has been

reported by many authors^{2,3,4,5}. The exact value is dependent upon the particular architecture chosen. For the case where both the transmit and the back-propagated local oscillator (BPLO) fields are matched truncated Gaussian beams the limit is 40.1%. Other losses prevent operation at this level. For example, using a near-optimal design and careful assembly procedures, CTI routinely obtains system efficiencies on the order of 15-20%. The system efficiency is a composite of many factors. Namely,

$$\eta_{sys} = \eta_h \eta_T \eta_o \eta_q \eta_{sn} \quad (2)$$

Where η_h is the heterodyne efficiency which accounts for beam misalignment and wavefront distortion, η_T represents the aperture truncation loss, η_o accounts for optical losses (Fresnel reflections, beam splitter losses, etc.), η_q is the detector quantum efficiency (assumed to be constant over the detector area) and η_{sn} is the reduction in SNR due to an imperfect shot-noise ratio.

The truncation efficiency, for a TEM₀₀ Gaussian beam truncated by a clear circular aperture, is given by $\eta_T = 1 - \exp[-2/\rho_T^2]$. Where $\rho_T = \omega_0/a$ is the beam truncation ratio, ω_0 is the $1/e^2$ intensity Gaussian beam radius at the telescope aperture and a is the aperture radius.

The shot-noise efficiency is given by $\eta_{sn} = (N_T - N_d)/N_T$. Where N_T is the total system noise including LO induced shot-noise and N_d is the dark noise (i.e., when the LO is deactivated).

The heterodyne efficiency, as defined by Fink⁶, is the ratio of the detected signal power to the available signal power, assuming perfect quantum efficiency. Using this definition, the SNR can be written as

$$SNR = \eta_h \frac{\eta_q P_s}{h \nu B} \quad (3)$$

Where, P_s is the average signal power available for detection. Fink showed that the heterodyne efficiency is given by the detector plane overlap integral of the signal field and the LO field.

$$\eta_h = \frac{\left(\int_{A_d} |U_s| |U_{LO}| dA \right)^2}{\int_{\infty} |U_s|^2 dA \int_{A_d} |U_{LO}|^2 dA} = \eta_{mix} \eta_p \quad (4)$$

Where, U_s and U_{LO} are the detector plane signal and LO fields respectively, and A_d is the area of the detector. The heterodyne efficiency is the product of the mixing efficiency η_{mix} and the fraction of the signal power collected by the aperture incident on the finite detector η_p . The mixing efficiency is defined as the overlap efficiency of the two fields on the detector and is unity if the two fields are proportional⁷. Throughout the rest of this paper we assume the detector is infinite and therefore make no further distinction between the mixing and heterodyne efficiencies.

When considering the optimal beam truncation ratio ρ_T , the efficiency parameter to optimize is the antenna efficiency $\eta_a = \eta_h \eta_T$, since it accounts for both beam truncation and heterodyne efficiency. In the far-field, with matched truncated Gaussian transmit and BPLO fields, the optimum truncation ratio is 80.2% corresponding to a peak antenna efficiency of 40.1% or a heterodyne efficiency of 41.9%³.

BEAM REFERENCED EFFICIENCY

In practice, it is desirable to measure the system efficiency of a coherent transceiver and compare this number to the theoretical optimum. These measurements provide a figure of merit of the coherent lidar. Furthermore it is often desirable to measure the sensors efficiency before the installation of the beam-expanding telescope.

Untruncated “small” beam efficiency measurements have several advantages over large-beam measurements. First, for small beam measurements, it is much easier to conduct the measurement in the far-field, where the efficiency is most sensitive to beam misalignments and wavefront distortion. Second, the efficiency loss due to refractive turbulence is minimized for the small beam measurements, since the far-field path-lengths are shorter yielding a turbulence-induced transverse coherence length ρ_0 which is much larger than the beam radius. Third, small beam measurements prior to installation of the telescope facilitate estimation of the losses from the telescope separate from the rest of the transceiver.

The standard form of the SNR equation does not lend itself to the calculation of the untruncated beam efficiency, since the aperture area of an untruncated beam is infinite and the corresponding antenna efficiency is zero. To mitigate this problem, we define the SNR in terms of the “effective” receiver area defined as the two dimensional spatial integral of

the receiver window function. For the case of an untruncated Gaussian transmit beam, the receiver window function is the transmit beam amplitude profile normalized to unit on-axis amplitude. For this receiver window, the effective area is just $\pi\omega_0^2$. Therefore, for an untruncated Gaussian beam lidar, we define the SNR as

$$SNR = \eta_{sys\omega_0} \frac{P_T \rho_\pi T^2 \gamma \pi \omega_0^2}{h\nu B z^2} \quad (5)$$

Where, $\eta_{sys\omega_0}$ is the system efficiency referenced to the beam area, which is given by

$$\eta_{sys\omega_0} = \eta_{a\omega_0} \eta_o \eta_q \eta_{sn} \quad (6)$$

and $\eta_{a\omega_0}$ is the beam area referenced antenna efficiency, which is equal to the aperture referenced antenna efficiency divided by the square of the truncation ratio. That is

$$\eta_{a\omega_0} = \eta_a / \rho_T^2 \quad (7)$$

In Figure 1, we plot these two antenna efficiencies versus the truncation ratio. This figure shows that the optimum truncation ratio is $\sim 80\%$ and the corresponding antenna efficiency is 40.1 % (62.6 % for the efficiency referenced to beam area).

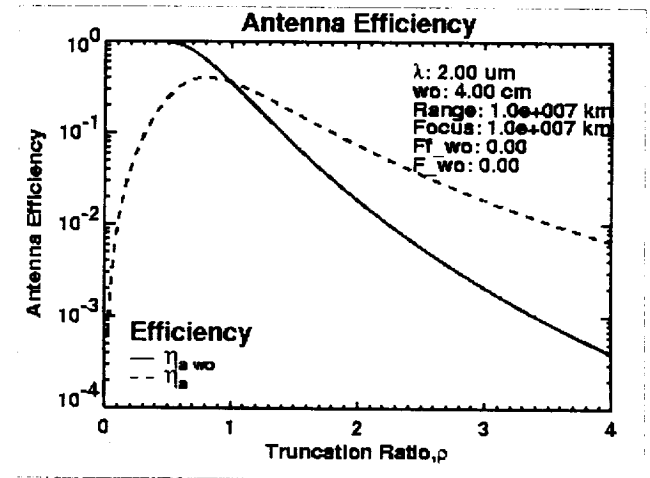


Figure 1. Collimated TEM₀₀ Gaussian beam antenna efficiency relative to the beam area η_{a_w0} (solid) and the aperture area η_a (dash), for a far-field target.

TECHNIQUES TO IMPROVE EFFICIENCY

For a well designed coherent lidar with a high quality TEM₀₀ Gaussian beam laser, a total system efficiency of 15-20% can be achieved. For example, the efficiency estimate from Figure 2 is 18.6% (29.1 % relative to the beam area). Note, in the Figure, a 90 % depolarization loss due to imperfect optics and a 90 % misalignment (or wavefront distortion) loss was included. Lower misalignment (or wavefront

distortion) losses can be achieved and maintained via the use of auto-alignment techniques. Lasers that produce non-diffraction limited beams can reduce this efficiency substantially. The detector quantum efficiency plays an important role in system efficiency budget. Recent advancements in 2 μm detector technology have produced detectors with quantum efficiencies greater than 90%.

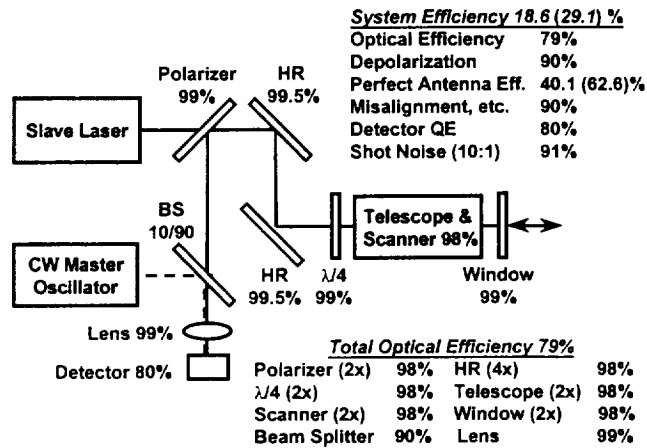


Figure 2. Coherent lidar block diagram and efficiency estimate. The system efficiency in parenthesis is the beam referenced system efficiency, $\eta_{\text{sys,wo}}$

TRANSCIEVER AUTOALIGNMENT

One of the largest potential efficiency loss mechanisms is the loss due to lateral and angular misalignment between the received photons and the local oscillator (LO). To maintain high efficiency throughout the sensor lifetime, transceiver autoalignment technologies are needed. CTI has investigated several novel autoalignment techniques. In the first technique, called “*Signal Tracking*,” the return signal photons are aligned to the local oscillator beam. In this approach, the heterodyne signals from a multi-element detector are used to estimate the axis of the received photons. This technique is attractive because it operates on the received signal photons. However, it requires multiple pulse averaging and needs a separate method to sense the lateral misalignments. The performance of this technique is in the process of being published elsewhere and will not be given further attention here.

CTI has developed another transceiver autoalignment technology called the “*Offset Frequency Differential Phase*” (OFDP) technique, which is depicted in Figures 3 and 4. In this technique, the LO beam is mixed with a back-propagated frequency-offset transmit beam (an alternate approach mixes a back-propagated LO with the transmit beam). The

resultant mixed field is detected on a quadrant photodetector (D1). The relative phase difference, $\Delta\theta$, between the RF photocurrents, i_a and i_b , from two vertically adjacent elements of the quadrant detector can be shown to be a measure of the relative tip (or tilt using horizontally adjacent detector elements) between the two beams.

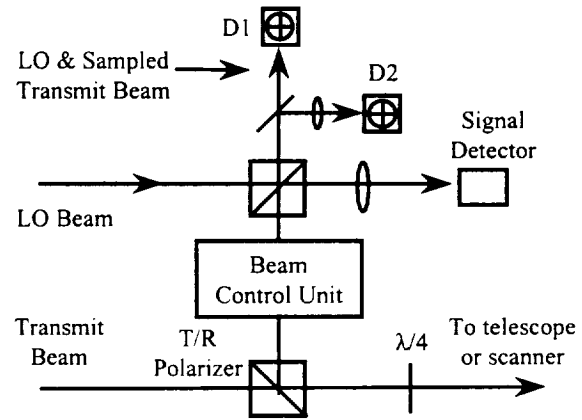


Figure 3. OFDP optical block diagram

The error signal, $\epsilon(t)$, depicted in Figure 4 is, under locked conditions, proportional to the RF phase difference when the phase delay, ϕ , is set to $\pi/2$. This error signal is used to drive a beam controller, which adjusts the tip (or tilt) of the sampled transmit beam in such a fashion as to drive the error signal to zero. Lateral beam offsets can also be sensed and compensated using a second set of servo electronics and an additional quadrant detector (D2) at the focus of a lens, which transforms lateral beam offsets into angular misalignments.

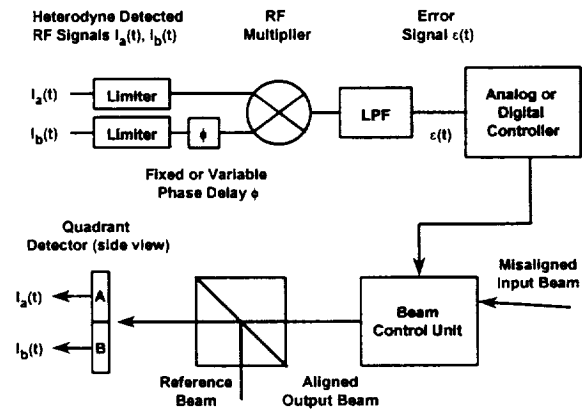


Figure 4. OFDP servo electronics functional diagram.

A beam and receiver simulation model was developed to predict the characteristic shape of the open loop error signal as a function of beam misalignment for a given set of beam parameters. In Figure 5, we present the dependence of the open loop error signal on relative beam tilts, ψ , for various values of the phase

delay ϕ . As can be seen in the figure, the open loop error signal is, for small tilts, directly proportional to the relative tilt between the two beams when ϕ is adjusted to $\pi/2$. The locking range of the closed loop servo can be shown to be slightly greater than $\pm \lambda/D_{\text{eff}}$, where D_{eff} is the smaller of the detector diameter or the beam diameter.

The figure also shows that by adjusting the phase delay ϕ , the system can lock the beams to arbitrary tilts (i.e., for fixed-lag-angle compensation). For example, given the base-case parameters indicated in Figure 5, a 1 mrad lag-angle offset can be maintained using an RF phase delay of $\sim \pi/4$.

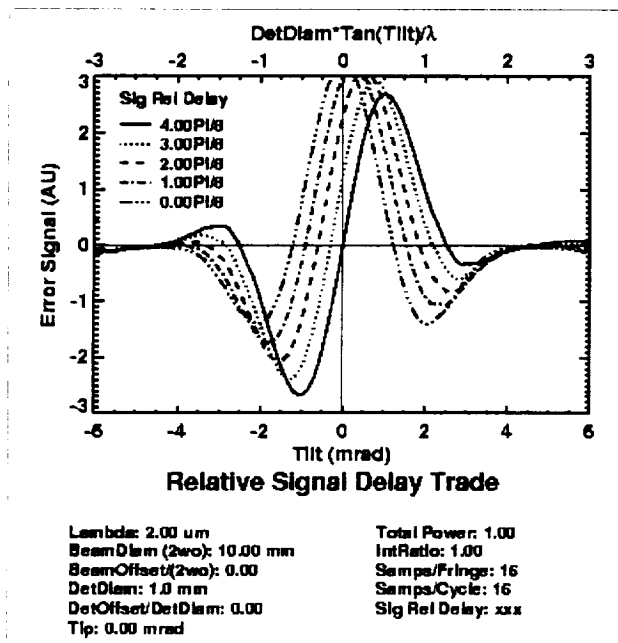


Figure 5. Open loop error signal as a function of beam tilt parametric in the RF phase delay, ϕ , for two Gaussian beams.

The simulation model was further exercised to estimate the performance of the servo as a function of various other parameters like beam tip, beam offset, beam intensity, detector misalignment, etc. Sample results corresponding to an analysis of the effect of relative beam tip on the OFDP tilt sensor are presented in Figure 6. From this figure one can see that the servo tilt sensing performance is maintained even when there is strong relative tip between the two beams.

SUMMARY

In this paper we have presented a survey of the different definitions of lidar efficiency. We then presented a definition which is applicable to both truncated and untruncated beams. We showed that a

system efficiency on the order of 15-20% (23-31% relative to the beam area) is achievable using efficient designs. We concluded with a discussion of novel techniques to maintain beam alignment and demonstrated the OFDP technique's open loop tilt sensing performance.

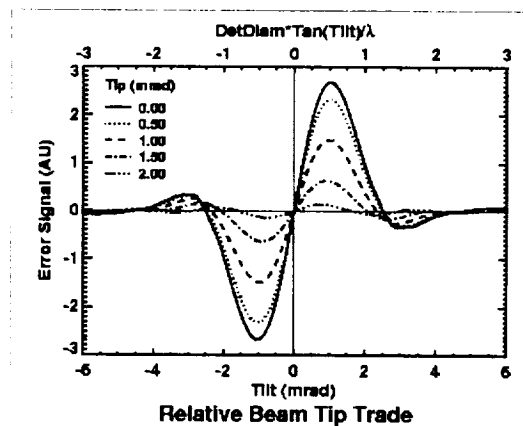


Figure 6. Open loop error signal as a function of beam tilt parametric in the relative tip between the two beams.

ACKNOWLEDGEMENTS

This work was funded by NASA MSFC under the SBIR program. The COTRs for these efforts were Michael Kavaya and Steve Johnson.

REFERENCES

- Henderson, S. W. et. al, "Coherent Laser Radar at 2 μm Using Solid-State Lasers," IEEE Trans on Geoscience and Remote Sensing, 31 (1993)
- Rye, B. J. "Primary aberration contribution to incoherent backscatter heterodyne lidar returns," Appl. Opt. 21, 839-844 (1982)
- Rye, B. J. and R. G. Frehlich, "Optimal truncation and optical efficiency of an apertured coherent lidar focused on an incoherent backscatter target," Appl. Opt. 31, 2891-2899 (1992)
- Wang, J. W, "Optimal truncation of a lidar transmitted beam," Appl. Opt. 27, 4470-4474 (1988)
- Zhao, Y., M. J. Post, and R. M. Hardesty, "Receiving efficiency of a pulsed coherent lidars: Theory," Appl. Opt 29, 4111-4119 (1990).
- Fink, D, "Coherent Detection Signal-to-Noise," App. Opt. 14, 689-690 (1975)
- Frehlich, R. G. and M. J. Kavaya, "Coherent laser radar performance for general atmospheric turbulence." Appl. Opt. 30, 5325-5334 (1991).

1.5 and 2 μm Coherent Lidar study for wind velocity and backscattering measurement.

Gaspard Guérit⁽¹⁾⁽²⁾, Béatrice Augère⁽²⁾, Jean-Pierre Cariou⁽²⁾, Philippe Drobinski⁽¹⁾, Pierre H. Flamant⁽¹⁾
 1) Laboratoire de Meteorologie Dynamique; 2) Office National d'Etudes et de Recherches Aérospatiales

Abstract

The potential of 1.5 μm and 2 μm solid-state technologies to multipurpose Coherent Doppler Lidar (HDL) application to measure wind velocity and species concentration in the planetary boundary layer, are discussed. Transverse coherence of a backscattered signal and its influence on power estimation accuracy are tested using hard target returns. The instrument design, signal processing technique and experimental results will be presented.

Introduction

Environmental and meteorological studies call for two types of atmospheric parameters measurement, the concentration of different species present in the atmosphere, and the wind velocity and turbulent parameters. Those two kinds need to be measured nearly at the same time to account for the atmospheric dynamics and chemical reactions, thus there is an increasing interest in combining those measurements with a single lidar.

Simultaneous range resolved measurements of atmospheric constituents and wind velocity have been investigated with a 10 μm heterodyne Doppler Lidar (Favreau 1997). Once more, the requirements of an accurate and reliable simultaneous power and Doppler shift estimations appear to be incompatible. Recently, a four-array receiver has been implemented on a 10 μm heterodyne lidar (Favreau 1997). A multi-array receiver's aim is to collect several decorrelated signals at the same time, thereby permitting their mutual rephasing, thereby allowing a greater receiving area, thus a better power measurement, without decreasing the spatial coherence of the detected signal, thereby keeping a good frequency estimation.

1.5 μm wavelength presents many advantages, the 1.5 optical material is already developed for the telecommunications, it is guidable in fiberoptic systems, it permits a not yet investigated frequency window for atmospheric constituent. Therefore the opportunity of a 1.5 μm multi-receiver coherent lidar for both wind and constituent measurement is conducted, and a comparison with 2 μm systems carried out. The present paper aims to show the first experiments concerning the transverse coherence of a hard-target backscattered signal without atmospheric turbulences, i.e. the spatial Speckle distribution. The influence of the receiver aperture size on the number of Speckle cells and the experimental determination of the coherent area of the backscattered signal on the receiver aperture are brought out.

Theory

The theoretical determination of the backscattered signal coherence length in the receiver plane has been approximated, (Frehlich & Kavaya 1991) with gaussian beam and lenses. It is the 1/e extinction of the mutual coherence function of the backscattered wave.

$$\frac{1}{r_0^2} = \frac{1}{4\sigma_t^2} + \frac{k^2 \sigma_t^2}{4z^2} \left(1 - \frac{z}{F_t} \right) \quad (1)$$

And the number of Speckle, (Goodman 1975), defined below has been evaluated numerically with the same assumption, (Dabas 1994).

$$M = \frac{\left(\int_D M_r(r, r) dR \right)^2}{\iint_{D^2} |M_r(r_1, r_2)|^2 dr_1 dr_2} = 1 + \frac{\sigma_{tel}^2}{4r_0^2} \quad (2)$$

Whith r_0 , the transverse coherence length in the receiver plane, σ_t , the 1/e extinction of the gaussian beam after the emission telescope, σ_{tel} , the 1/e extinction for the gaussian model of the emission telescope, D the receiver aperture size which is taken infinite for the gaussian assumption, and M_r , the mutual coherence function of the backscattered signal in the receiver plane.

The number of speckle cells in the receiver aperture can be evaluated involving the first and second statistical moments of the measured power of decorrelated signals, ie the mean and variance of a great number of power measurement, (Goodman 1975).

$$M = \left(\frac{\langle P_S \rangle}{\sigma_{P_S}} \right)^2 \quad (3)$$

Moreover, the probability density function for a set of power estimations of an integrated Speckle pattern can be approximated by a gamma density function.

$$p(P_S) = \frac{M^M}{\Gamma(M)} \left(\frac{P_S}{\langle P_S \rangle} \right)^{M-1} \exp\left(-M \frac{P_S}{\langle P_S \rangle} \right) \quad (4)$$

The determination of M allows a definition of a coherence area A_c of the backscattered signal in the receiver apperture, (Dabas 1996), which can be approximated as following

$$M \approx 1 + \frac{A_r}{A_c} \quad (5), \text{ with } A_r, \text{ the receiving apperture area.}$$

Experimental set up

The aims of the experiments carried out so far, are to observe the influence of the receiving aperture size on a hard target backscattered signal 1.5 μm signal transverse coherence and to provide experimentally its coherence area for a given emission apperture. Furthermore a similar series of experiments with a 2 μm cw lidar is to be conducted, for comparision.

Description

Statistical evluations call for a great number of decorrelated signal power measurements. That is to say that a great number of decorrelated backscattered signals need to be obtained in similar experimental condition. A hard diffusing target is used, but its stationnarity leads always to the same Speckle pattern in the receiver, no statistical evaluation are possible thru such set of power values, the need of decorrelation is satisfied moving the diffusers.

The condition that each measure is independant is obtained with the insurance that each measure is provided by a signal backscattered by different diffusers than others, so the illuminated part of the target must be different for every iteration. It is satisfied with a rotating hard target, considering its rotation velocity, and the dimension and place of the laser spot on the target. The time between each measure ensure that every target backscattering spot takes place on a different part of the target.

Material

The laser used is a 600 mW cw Er/Yt laser, made with two polarized Er/Yt doped fiberoptics, this laser provides two fiberoptic exit, one signal, and one local oscillator both polarised. The

aim of this source is to be used on a 1.5 cw multi-receiver lidar. Other materials are a 1.5 InAsGa photodiode, an emitting 1.5 lens, on which the beam 1/e waist is 1 cm, and a receiving 1.5 μm lens with a 19.2 cm focal distance and a 5 cm diameter in front of which a 0.4 to 5 cm diameter diaphragm has been placed, figure 1. Although diffusing, the rotating target is tilted to prevent the detector from any specular reflexion.

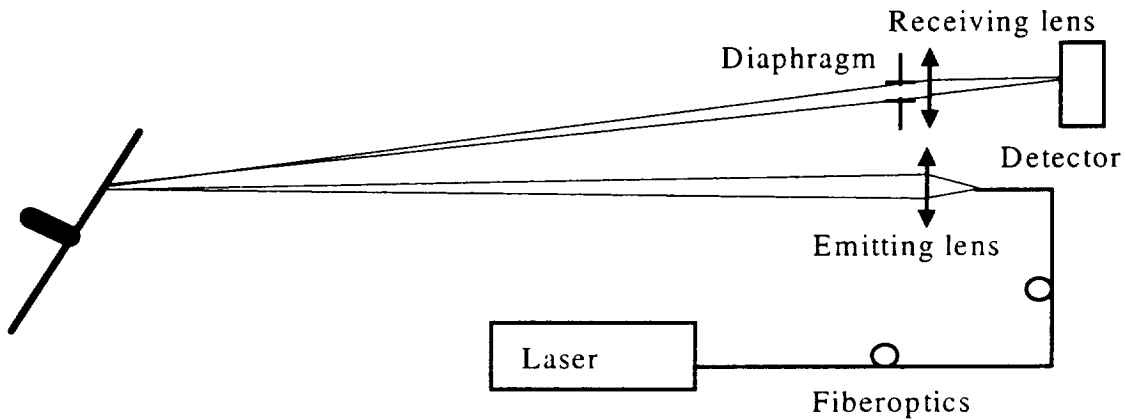


Figure 1 : Experiment description

The Receiving aperture size is varied from 0.4 cm up to 3 cm to prevent any side aberration of the lens, as the emitting waist is 1 cm., ie an area of 3.1416 cm². Considering the rotation velocity and the size and place of the spot on the target, the measures are taken every 20 μs, and a set contains 1024 iteration. For each receiving area, 4 statistical evaluation are made, ie four set of 1024 measures are constructed.

Results :

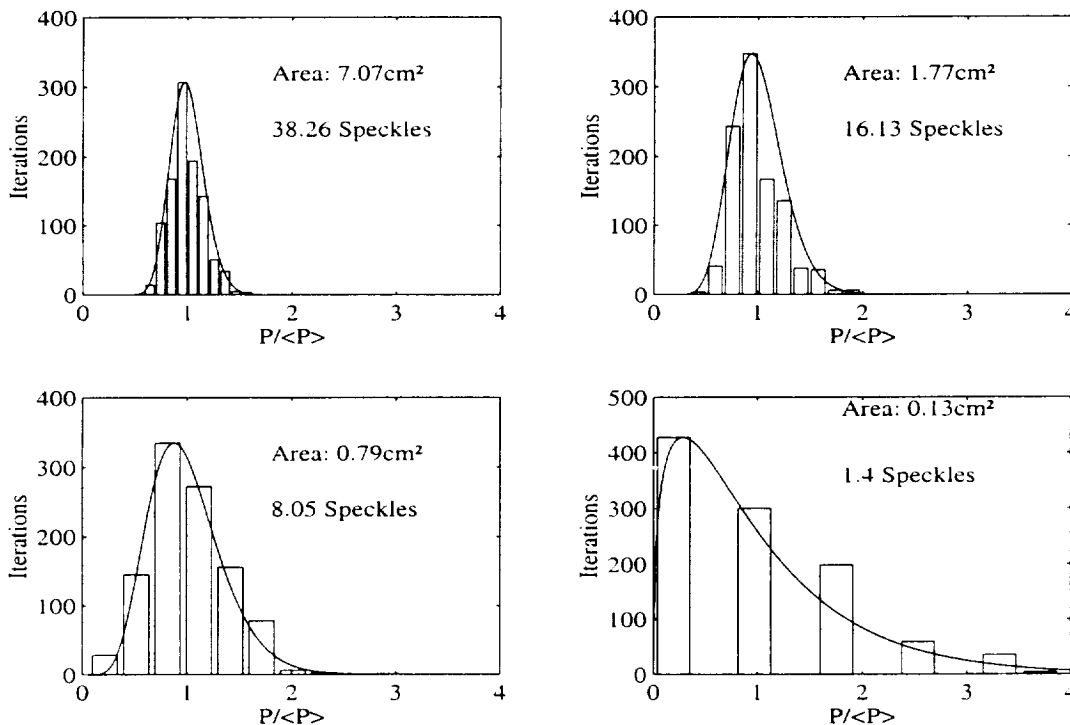


Figure 2 : Histogram and theoretical gamma pdf for several receiving area

The results show the evolution of the probability density function and an estimation of the number of speckle cells for different receiving area. Finally from the evolution of the number of speckle cells with the area, a linear regression is made to calculate the effective coherence area in the receiving aperture. Figure 2 shows that the greater is the number of cells, the more accurate is the power estimation, but the less coherent is the backscattered signal integrated in the receiving area. The, the impossibility of getting accurate power and wind velocity measurement directly with the same reception area appears clearly.

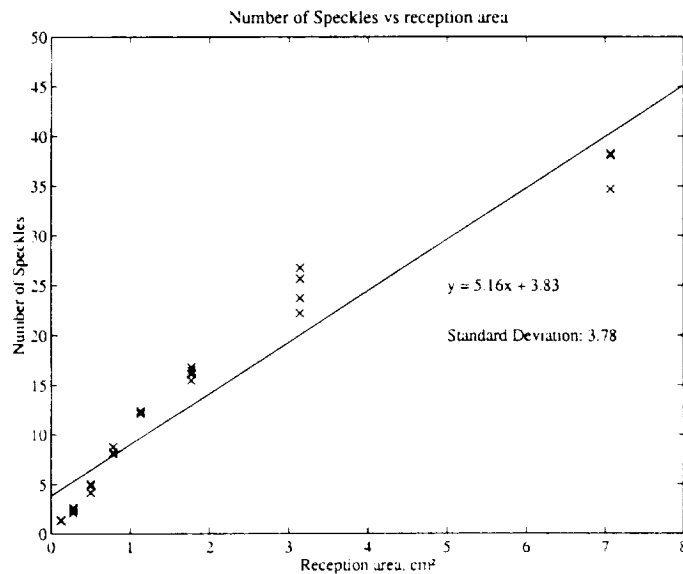


Figure 3 : Evolution of M with A_r , and linear regression to obtain A_c .

The figure 3 shows the linearity of the evolution of the number of cells with the reception area. A linear regression leads to the coherence area of the backscattered signal in the receiving aperture, (eq. 5). The calculation gives $A_c=0.19 \text{ cm}^2$.

Conclusion :

A method to measure the coherence area of a hard target backscattered signal has been presented, and a measure of this area has been carried out with a $1.5 \mu\text{m}$ cw system. The accuracy of power measurement of a backscattered signal has been measured for several receiving aperture, and a relation between this accuracy and the number of cells shown for a $1.5 \mu\text{m}$ cw system. Further investigation are to be made in the next weeks and could also be presented, especially, the same kind of experiments with a $2 \mu\text{m}$ cw system, and with aerosols targets. Finally this study aims to help in dimensionning a future multi-receptors $1.5 \mu\text{m}$ lidar.

References

- Favreau X. 1997 : Détection simultanée de puissance et de vitesse par Lidar hétérodyne. Thèse de doctorat de l'université Paris XI
- Frehlich R.G., Kavaya M.J. 1991 : Coherent laser radar performance for general atmospheric refractive turbulences. Appl. Opt.,30 p. 5325
- Goodman 1975 : Statistical properties of laser Speckle patterns, Laser Speckle and Related Phenomena J.C. Dainty, Springer-Verlag ed.
- Dabas A. & al., 1994 : Characterization of pulsed coherent Doppler Lidar with the Speckle effect, Appl. Opt., 33, p. 6524

CW LIDARS

Presider: Michael Vaughan

Bistatic Coherent Laser Radar Performance: CW SNR Calculations

Eric P. MAGEE*, Timothy J. KANE

Department of Electrical Engineering
121 Electrical Engineering East
The Pennsylvania State University
University Park, PA 16802
Phone: (814) 863-1470, FAX: (814) 863-8457
tjk7@psu.edu

*Author's Current Affiliation
Department of Electrical and Computer Engineering
Air Force Institute of Technology
2950 P Street, Wright-Patterson AFB OH 45433-7765
Phone: (937) 255-6565, FAX: (937) 656-4055
Eric.Magee@afit.af.mil

INTRODUCTION

Wind velocity can be obtained using a laser radar (LIDAR) system by measuring the Doppler shifted backscatter from aerosols and particulates in the atmosphere. Doppler lidar systems for wind velocity measurements can be classified into two categories: coherent detection and incoherent detection. Under each category there are novel approaches to measuring the return signal frequency. Regardless of the measurement process, the ultimate goal for both types is to measure a frequency shift between the transmitted laser pulse and the return laser pulse. This frequency shift is proportional to some component of the wind velocity, depending on the system configuration. How accurately these systems can measure the frequency shift, and thus the velocity, is dependent upon the system's characteristics. Existing Doppler lidar systems employ monostatic configurations which require scanning a volume to obtain wind speed and direction [1, 2]. Range resolution in these systems is normally obtained by using a pulsed laser system. This places a fundamental limit on the range-velocity resolution product [3, 4].

The purpose of this research is to investigate the feasibility of utilizing a multistatic configuration for measuring 3-dimensional vector winds. In the multistatic configuration, horizontal and vertical resolution are determined by the telescope field-of-view, laser divergence, and baseline separation distance between the laser and the telescope. This enables the use of a continuous-wave or long pulse laser transmitter (narrow spectral width) and eliminates the dependence between range and velocity resolution.

The results of this research have shown that a multistatic pulsed Doppler lidar system will provide accurate estimates of wind velocity within the tropospheric boundary layer (up to about 5 km) with high spatial resolution. Detailed signal-to-noise ratio (SNR) calculations indicate that small transmit and receive apertures actually improve system performance. Therefore, a compact transmitter and receiver design can be used. The spatial resolution achievable with this system will be better than previous anemometers (propeller as well as laser Doppler), yielding fine scale measurements of velocity fields.

ANALYSIS

The primary coordinate system used to locate the receiver, transmitter and target is a fixed reference system centered at the transmitter. The z -axis of this coordinate system is in the vertical direction and the x -axis is in the east-west direction. The fixed coordinate system is also used to define pointing directions of the transmit and receive optics. A north referenced coordinate system [5, 6] is used for all signal-to-noise ratio calculations. There will be a separate north referenced coordinate system associated with each transmitter/receiver pair. Figure 1 shows the typical geometry for a single transmitter/receiver pair.

For a multiple (N) receiver configuration, the Doppler shift can be written in matrix notation as

$$\Delta f_D = \frac{1}{\lambda} \mathbf{A} \mathbf{v}_w, \quad (1)$$

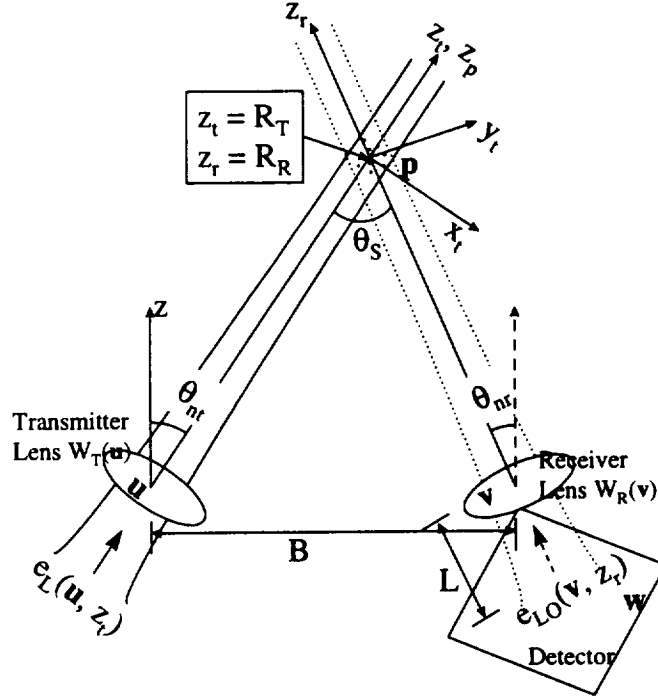


Figure 1. Geometry for a single transmit/receive pair. Dotted lines indicate the back-propagated local oscillator.

where $\Delta \mathbf{f}_D$ is a vector of the measured Doppler shifts at each of the N receivers, \mathbf{v}_w is the velocity vector, and \mathbf{A} is an $N \times 3$ matrix given by

$$\mathbf{A} = \begin{bmatrix} \frac{b_x^1}{R_R^1} & \frac{b_y^1}{R_R^1} & \frac{b_z^1}{R_R^1} \\ \mathbf{M} & \mathbf{M} & \mathbf{M} \\ \frac{b_x^N}{R_R^N} & \frac{b_y^N}{R_R^N} & \frac{b_z^N}{R_R^N} \end{bmatrix} - \begin{bmatrix} \frac{R_T + R_R^1}{R_T R_R^1} \\ \mathbf{M} \\ \frac{R_T + R_R^N}{R_T R_R^N} \end{bmatrix} [p_x \quad p_y \quad p_z], \quad (2)$$

where $b_{x,y,z}^i$ is the x , y , or z baseline separation for the i^{th} detector, R_T is the range from the transmitter to the scatterer (p_x, p_y, p_z) , and R_R^i is the range from the i^{th} receiver to the scatterer. This relationship can be inverted to yield

$$\mathbf{v}_w = \lambda (\mathbf{A}^T \mathbf{A})^{-1} \mathbf{A}^T \Delta \mathbf{f}_D. \quad (3)$$

For a distributed aerosol target where the particles are randomly positioned within the scattering volume, the phase of the scattered radiation for a single particle is random with respect to that from another particle. Therefore, the signal incident on the receiver is formed by the superposition of the radiation scattered from each individual particle [7]. The signal-to-noise ratio for a distributed aerosol is, then, the sum of the SNRs for each individual aerosol particle

$$\text{SNR}(t) = \frac{\eta_Q}{h\nu} \frac{1}{B_w} \int_0^{\infty} \langle P_L(t - R_T(z_p)/c) \rangle \beta(z_p, \theta_S) C(z_p, t) dz_p. \quad (4)$$

where P_L is the laser power, β is the total volume scattering coefficient,

$$C(z_p, t) = \lambda^2 \int_{-\infty}^{\infty} \langle j_T(\mathbf{p}, R_T(z_p), t - R_T(z_p)/c) j_{BPLO}(\mathbf{p}, R_R(z_p)) \rangle d^2 \mathbf{p} \quad (5)$$

is the target plane representation of the coherent responsivity, and

$$j_T(\mathbf{p}, R_T, t) = |e_T(\mathbf{p}, R_T, t)|^2 \quad \text{and} \quad j_{BPLO}(\mathbf{p}, R_R) = |e_T(\mathbf{p}, R_R)|^2 \quad (6)$$

are the random irradiance profiles of the normalized transmitter and BPLO fields at the target [8]. For a collimated Gaussian lidar system with independent propagation paths,

$$\langle j_T(\mathbf{p}, R_T) \rangle = \frac{1}{\pi \sigma_{BT}^2(R_T)} \exp\left(-\frac{x_p^2 + y_p^2}{\sigma_{BT}^2(R_T)}\right), \quad (7)$$

where

$$\sigma_{BT}^2(R_T) = \sigma_L^2 + \frac{R_T^2}{k^2 \sigma_L^2} + \frac{2R_T^2}{k^2 \rho_o^2(R_T)}, \quad (8)$$

σ_L is the $1/e$ intensity radius of the transmit beam, and ρ_o is the transverse field coherence length of a point source located at z_p . The irradiance profile for the BPLO beam is given by

$$\langle j_{BPLO}(\mathbf{p}, R_R) \rangle = \frac{1}{\pi \sigma_{BR}^2(R_R)} \exp\left(-\frac{(x_p \cos \theta_s + z_p \sin \theta_s)^2 + y_p^2}{\sigma_{BR}^2(R_R)}\right), \quad (9)$$

where

$$\sigma_{BR}^2(R_R) = \sigma_{LO}^2 + \frac{R_R^2}{k^2 \sigma_{LO}^2} + \frac{2R_R^2}{k^2 \rho_o^2(R_R)}, \quad (10)$$

and σ_{LO} is the $1/e$ intensity radius of the local oscillator beam. The resulting SNR is given by

$$\text{SNR}(R_T, t) = \frac{\langle P_L \rangle \eta_Q \beta(R_T, \theta_s) \lambda^2}{h\nu B_w \sin \theta_s \sqrt{\pi}} \left[\sigma_{BR}^2(R_R) + \sigma_{BT}^2(R_T) \right]^{-1/2}, \quad (11)$$

where $\langle P_L \rangle$ is the average power of the CW transmitter [9]. In deriving the above expressions, we have assumed the aperture sizes are large compared to the $1/e$ intensity radii of the transmit and LO beams. We have also assumed a square law structure function for the turbulence effects.

Figure 2 shows example plots of the SNR for various beam sizes. The scattering coefficient, $\beta(R_T, \theta_s)$, is determined using Mie scattering, a bimodal aerosol distribution, and an exponential aerosol concentration with a scale height of 1.4 km and 5000 particles per cm^3 at $z = 0$. This plot shows that there is an optimum beam size in terms of SNR performance. The optimum beam size is found by differentiating the expression for SNR with respect to σ_L , and is given by

$$\sigma_L^{\text{opt}} = \left[\frac{(2R_T^2 + B^2)}{2k^2} \right]^{1/4}. \quad (12)$$

In the near field limit ($R_T \rightarrow 0$), the optimum aperture approached 3.3 mm for $B = 100$ m and $\lambda = 1$ μm . Thus, if the aperture sizes are on the order of 20 mm, the effects of truncation can be ignored.

Figure 3 shows the reduction in SNR due to refractive turbulence effects. These effects are calculated using the definition of the transverse field coherence length, ρ_o , and an $h^{-4/3} C_n^2$ model. As can be seen from this plot, the effects of refractive turbulence are negligible under the conditions defined.

CONCLUSIONS

The results show that a multistatic configuration for coherent measurements of wind velocity is feasible. Figure 2 shows that for ranges less than approximately 1 km, the SNR is fairly constant and can be optimized with respect to transmit aperture size. For the system parameters outlined, the optimum size is approximately 3.3 mm in the near field. This aperture size is very appealing for design purposes, enabling a compact system. Another advantage of the small apertures and multistatic configuration is the very small scattering volume. For a 5 mm aperture the scattering volume is less than 100 cm^3 out to about 1 km [9]. Figure 3 shows that the refractive turbulence effects will be very small except at ranges greater than about 5 km, which is most likely beyond the feasible operating range of this system (due to geometric limitations).

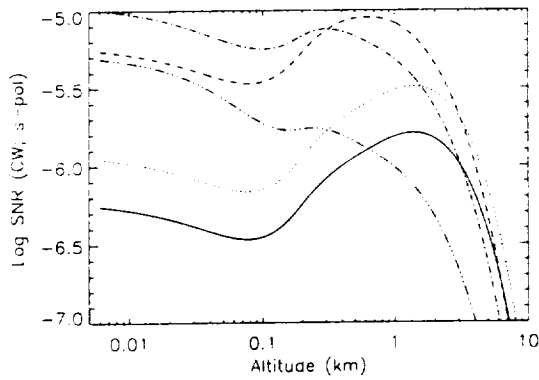


Figure 2. SNR for various beam sizes. $B=100$ m. $B_w=100$ MHz, $\lambda=1\mu\text{m}$, $\eta_0=0.5$, $P_L=5$ watts, $\sigma_{L0}=\sigma_L$, $\theta_{nr}=0$, $\phi_r=\phi_r=0$. $\sigma_L=100\text{mm}$ (solid); $\sigma_L=50\text{mm}$ (dotted); $\sigma_L=10\text{mm}$ (dashed); $\sigma_L=5\text{mm}$ (dash-dot); $\sigma_L=1\text{mm}$ (dash-triple dot).

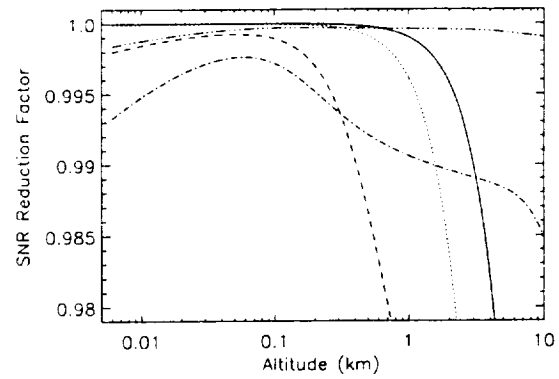


Figure 3. SNR reduction factor for various beam sizes and $C_n^2(h=1\text{m}) = 10^{-12} \text{m}^{-2/3}$. Parameters are the same as those defined in Figure 2.

REFERENCES

- [1] S. F. Clifford, J. C. Kaimal, R. J. Latatits, and R. G. Strauch, "Ground-based remote profiling in atmospheric studies: an overview," *Proc. IEEE*, vol. 82, pp. 313-355, 1994.
- [2] J. G. Hawley, et al., "Coherent launch-site atmospheric wind sounder: theory and experiment," *Appl. Opt.*, vol. 32, pp. 4557-4568, 1993.
- [3] S. F. Clifford, "The Classical Theory of Wave Propagation in a Turbulent Medium," in *Laser Beam Propagation in the Atmosphere*, vol. 25, *Topics in Applied Physics*, J. W. Strohbehn, Ed. New York: Springer-Verlag, 1978, pp. 9-43.
- [4] A. V. Jelalian, *Laser Radar Systems*. Norwood, MA: Artech House, 1992.
- [5] M. C. Jackson, "The geometry of bistatic radar systems," *IEE Proceedings*, vol. 133, Pt. F, pp. 604-612, 1986.
- [6] N. J. Willis, *Bistatic Radar*. Boston: Artech House, 1991.
- [7] R. T. Menzies and R. M. Hardesty, "Coherent Doppler lidar for measurements of wind fields," *Proc. IEEE*, vol. 77, pp. 449-462, 1989.
- [8] R. G. Frehlich and M. J. Kavaya, "Coherent laser radar performance for general atmospheric refractive turbulence," *Appl. Opt.*, vol. 30, pp. 5325-5352, 1991.
- [9] E. P. Magee, "Performance Analysis of a Multistatic Coherent Doppler Lidar," Ph.D. Thesis, Department of Electrical Engineering, The Pennsylvania State University, University Park, PA, 1998.

Ranging performance of an FMCW semiconductor laser with linearisation of the frequency sweep

Christer J. Karlsson and Fredrik Å. A. Olsson
Defence Research Establishment (FOA)
Department of Laser Systems
P. O. Box 1165, S-581 11 Linköping, Sweden
Tel: +46 13 378243, e-mail: chrkar@lin.foa.se

Semiconductor lasers are easy to modulate. By direct current modulation it is possible, for example, to frequency modulate the laser. There are various frequency modulation schemes that can be used. In radar applications, the most common is the linear chirp or triangular modulation function. When using a triangular modulation function, it is straightforward to deduce the range and radial speed of the target from frequency measurements. However, as the FM-response of a semiconductor laser generally is non-constant as a function of modulation frequency, the frequency of the laser will not be a linear chirp or triangular with time. The result is a signal spectrum that is broadened, resulting in a lower signal-to-noise ratio (SNR) and worse range and speed accuracies.

Various methods of accounting for the non-constant FM-response have been reported [1, 2]. In this paper, we report measurements of the FM-response, magnitude and phase as a function of modulation frequency, of an InGaAsP-InP distributed feedback (DFB) laser diode. The results of the measurements are used to programme an arbitrary function generator which generates a modulating function that results in a linear frequency sweep of the laser. Laser radar experiments indicate that it is possible to achieve a narrow spectral width of the signal. The width is found to be fundamentally limited by the measurement time rather than the non-constant FM-response. This allows for high range and speed accuracies. Furthermore, it is clear that the phase is as important as the magnitude. It is important to note that the work presented here only concerns a laser radar that uses the monochromatic peak in the signal spectrum. There are no obstacles for using the complete signal spectrum. In fact, in order to achieve longer ranges, a straightforward way can be to use the entire spectrum.

The experimental set-up used for the FM-measurements is shown in *Figure 1*. The arrangement is similar to selfhomodyne set-ups, which have been used for many years to estimate laser lineshapes.

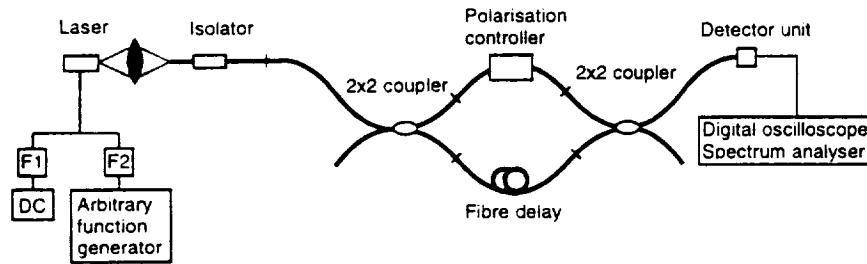


Figure 1. Experimental arrangement. The detected signal was analysed with a sweeping spectrum analyser or sampled with a digital oscilloscope and subsequently FFT-analysed.

The laser used in this study was a three-section InGaAsP-InP distributed feedback laser (DFB) laser diode emitting at 1.55 μm . The lowpass filtered (1 kHz, F1) DC drive currents, supplied by a battery, to the three sections were chosen in order to achieve the narrowest linewidth. The linewidth was estimated to be approximately 400 kHz by a curve-fit of a signal spectrum for a short delay (8 m optical fibre). The fibre arrangement allows the laser radiation to be split, by the first 2x2 coupler, into two different paths. One of the beams acts as the local oscillator (LO) and the other beam acts as the "target beam", i. e. it acts as the radiation reflected off a target. The second 2x2 coupler mixes the LO beam and the target beam and the interferometer signal is produced at the detector. The set-up is very useful for studies of FM since problems associated with pointing stability and the atmosphere are eliminated. A 12-bit digital arbitrary function generator was used. The quantized voltage was lowpass filtered and smoothed by a third order Bessel filter with a cut-off frequency of 200 kHz (F2). The detector signal was recorded with a digital oscilloscope or a sweeping spectrum analyser.

The FM-magnitude (Δf) for a particular modulation frequency was determined using sinusoidal modulation. When the modulation is sinusoidal (with modulation frequency f_{mod}), the frequency deviation of the homodyne signal ($f_{\text{h,max}}$) is approximately given by $f_{\text{h,max}} = \Delta f / 2 \sin(2\pi f_{\text{mod}} \tau)$, assuming a short delaytime (τ). The sweeping spectrum analyser or the digital oscilloscope with FFT analysis was used to measure $f_{\text{h,max}}$. The phase of the modulating signal relative to the phase of the laser frequency was determined by time measurements on the

digital oscilloscope. Defining $t_{m,0}$ as the time when the modulating signal is zero and $t_{h,0}$ as the time when the frequency of the homodyne signal is zero gives the phase ($\Delta\theta$) $\Delta\theta = 2\pi f_{mod,s}(t_{h,0} - t_{m,0}) - \pi/2$. The measured frequency excursion (Δf_s) and relative phase ($\Delta\theta_s$) for each modulation frequency were subsequently used to create a triangular modulating signal that is modified to compensate the FM-response.

Spectra shown in Figure 2 illustrate the compensation. It is clear from these spectra that the compensation works. The bandwidth of the signal peak is reduced significantly and the peak signal power is increased significantly. In addition, it is seen that the phase compensation is as important as the magnitude compensation.

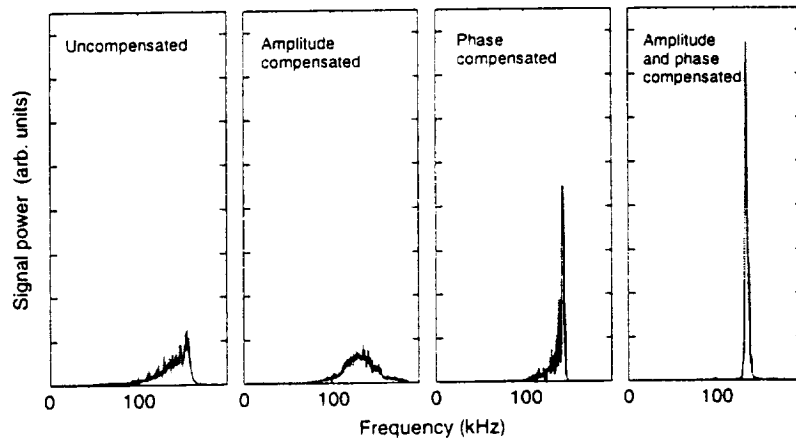


Figure 2. Signal spectra recorded using the sweeping spectrum analyser. For the "amplitude compensated" spectra, the phases of all harmonics were zero while for the "phase compensated" spectra the amplitudes of the different harmonics were those of a perfect triangular function. The modulation parameters were $f_{mod}=1$ kHz, $\Delta f=1.4$ GHz and the length difference in the interferometer was 10 m. 15 overtones were compensated.

The spectra in Figure 2 were recorded with compensation for harmonics up to $k=31$, i. e. the fundamental plus 15 overtones. Clear differences in the signal spectra were observed when adding compensation for each of the harmonics. The effect on the signal spectra is, of course, largest for the harmonics closest to the fundamental. Spectra recorded using harmonics up to $k=61$, corresponding to the 31 first nonzero harmonics, were almost entirely dominated by the signal peak, with a width limited by the measurement time, and phase noise. It is the narrow width that allows for a relatively good ranging capability, as described below.

The maximum range is here defined by the range which gives $SNR=16.5$ dB. The calculations of the SNR below are performed for a Gaussian monostatic CLR [3]. An assumption in the theory is that the coherence length of the laser is infinite. For semiconductor laser radar systems, this assumption is not valid and the calculations have to be modified. There are two factors which have to be accounted for [1, 4]. The first is the exponential decrease of the monochromatic peak with range. The second effect is that the broad band part of the signal spectrum, i. e. the phase noise, will contribute significantly to the noise. In fact, under many circumstances the phase noise of the laser will be the dominating noise source. The SNR is therefore calculated as

$$SNR = \frac{\eta_{tot} P_{rec}(R) \cdot e^{-\frac{2R}{c\tau_c}}}{h\nu B + \underbrace{\frac{\eta_{in}(R) P_{rec}(R) \cdot \tau_c}{1} \left(1 - e^{-\frac{2R}{c\tau_c}} \left(1 + \frac{2R}{c\tau_c} \right) \right)}_{\text{phase noise}}} \cdot B$$

which is approximately valid when the detection bandwidth (B) is much less than the linewidth of the laser. If not, the phase noise contribution must be integrated over B . η_{in} is an efficiency factor including e. g. quantum efficiency, P_{rec} is the received power, τ_c is the coherence time of the laser and η_{in} indicate the loss in efficiency when the detection bandwidth < the width of the signal peak. In Figure 3, calculations of SNR for ranging to a diffuse target for various laser powers, linewidths and detection bandwidths are shown. The bandwidths of 5 kHz and 200 Hz correspond to the modulation frequencies that were measured and compensated.

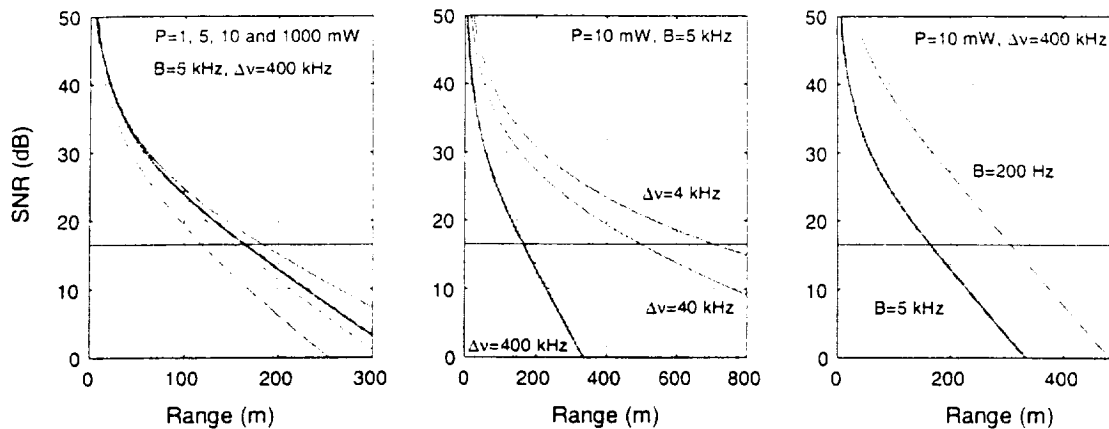


Figure 3. Calculated SRN as a function of range for various output powers, linewidths and bandwidths. The bold lines correspond to the laser radar measurements discussed below. Values for other parameters are stated in the appendix. The system is assumed to be focused for all ranges.

Several interesting observations can be made. The SNR up to a certain range is almost independent on the laser output power (above 10 mW) for a given $\Delta\nu$ (400 kHz) since the phase noise is dominating. At longer ranges, the noise eventually becomes dominated by shot noise, since the phase noise contribution decreases with range due to the decrease of the received power with range. The middle diagram in Figure 3 indicates the strong dependence of the SNR, and thus the maximum range, on the coherence length of the laser. Using a laser with a high output power and a narrow linewidth, quite impressive ranges can be achieved. The right-hand diagrams in Figure 3 indicate the dependence on bandwidth. As mentioned above, the values used in the calculations correspond to different modulation frequencies used in this study. For example, $f_{mod}=1$ kHz gives a resolution (and bandwidth) of 2 kHz. However, for practical reasons, the signal waveforms were only recorded for a time giving a frequency resolution of 5 kHz. Nevertheless, it is the very small bandwidth that allows surprisingly long ranges for low output powers. Note also that the maximum range can be extended by time or frequency domain integration.

Measurements, using a laser radar set-up according to Figure 4, on a diffuse target (ordinary white paper for copying machines and laser writers) gave SNR-values within 5-10 dB from the calculated values for ranges up to 90 m (corresponding to the longest range accessible indoors). Part of the discrepancy was found to be caused by unwanted reflections within the laser radar system which gives rise to excess phase noise when interfering with the LO. It is very important to reduce unwanted reflections or straylight and also to reduce the fibre lengths as much as possible in order to have optimal performance of a laser radar system [4]. The components used in the laser radar set-up were standard and not optimised for a coherent laser radar. Thus, even though a discrepancy of up to 10 dB exists between measurements and calculations, a proper laser radar design should give maximum ranges according to Figure 3 or close to.

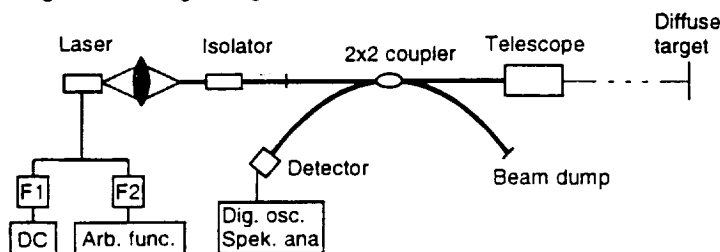


Figure 4. Laser radar measurement set-up. All fibres were terminated by FC/APC connectors except the end at the telescope, which was terminated by an FC/PC connector. This fibre-end reflect radiation which serves as the LO. One advantage with this set-up is the insensitivity to polarisation changes within the fibres. The set-up results

in a 6 dB loss of the SNR, compared to an ideal lossless system, if the measurements are shot noise limited, while the loss is 0 dB if the measurements are phase noise limited (by the interference between the LO and target reflection).

For OFDR measurements the theoretical range resolution (ΔR), assuming an FFT spectrum analyser, is often stated to be $\Delta R = c/2n\Delta f$ where n is the index of refraction. The resolution is given by the spacing between the FFT frequencies. However, there are several factors, of which each can be the dominating factor for the accuracy, which are not accounted for in the formula above. These are the non-constant FM-response, SNR and algorithms after the FFT, which can be applied to the data in order to improve the accuracy. The range accuracy,

defined as one standard deviation, from a more general point of view is given by $\sigma_R = c\sigma_{f_h} / 4\Delta f \cdot f_{mod}$, where σ_{f_h} is the standard deviation of the frequency measurement. It is assumed that no systematic errors prevail. Note that σ_{f_h} can depend linearly on f_{mod} and thus that σ_R can be independent on f_{mod} . The equations above indicate that increasing Δf should give higher range accuracy. This is indeed true as long as the FM-response (uncompensated or compensated) does not result in a signal peak which is significantly broadened. For sufficiently high Δf or long ranges we observed broadening due to imperfect compensation and thus the range accuracy is not only limited by the frequency excursion but also the FM-response. The exact values for range and Δf when the width of the signal peak will be dominated by the FM-response will depend on the details of the FM-response and the compensation. For the particular set-up used in this experiment we observed no broadening for ranges up to 90 m fibre and $\Delta f=2.4$ GHz ($f_{mod}=30$ Hz) and $\Delta f=1.4$ GHz ($f_{mod}=1000$ Hz). These particular combinations of values are not fundamentally limited. Rather, they are an indication of the measurement accuracy of the FM-response measurements. Thus, it should be straightforward to achieve the fundamental signal width for longer ranges and larger Δf by measuring the FM-response more accurately.

The range accuracies of some laser radar measurements on the diffuse target, using the set-up shown in *Figure 4*, are shown in *Figure 5*. The frequency was estimated by calculating the centre of gravity around the frequency for which the power was maximum. The experimental standard deviation for a single measurement was obtained from 30 measurements. Clearly, as mentioned above, the SNR has a direct influence on the range accuracy and thus the range accuracy will be range dependent. For the lowest SNR, corresponding to the SNR-level (16.5 dB) that defines the maximum range, the range accuracy was about 5 cm, while it was less than 2 mm for an SNR of 34 dB. The measured frequency accuracies correspond to quite high speed accuracies. For example, a frequency accuracy of 200 Hz corresponds to a speed accuracy of 0.1 mm/s. Note though that a requirement is a constant relative speed of the target. A spread in speeds within the measurement time may give a reduced SNR.

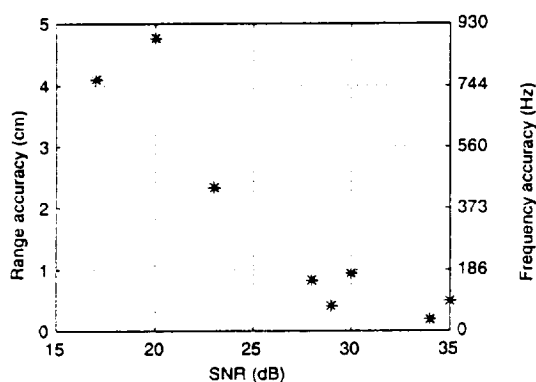


Figure 5. Measured frequency and range accuracy using $f_{mod}=1000$ Hz and $\Delta f=1.4$ GHz. Other parameters are stated in the section about SNR and in the appendix. The SNR was varied by changing the distance to the target or defocusing the beam.

To summarize, the performance of an FMCW semiconductor laser radar has been experimentally examined. The measurements indicate the possibility of achieving a spectral width of the signal peak that is transform limited, rather than limited by the FM-response of the laser, which permits the use of a narrow detection bandwidth. This, in turn, results in a relatively high signal-to-noise ratio for low output power and thus also relatively long range and high range accuracy.

Per-Otto Arntzen, Dietmar Letalick and Stan Zyra at FOA are acknowledged for critical discussions and for help with equipment. Mike Harris and Guy Pearson at DERA, UK are gratefully acknowledged for many discussions about short wavelength laser radar issues. Björn Broberg, Henrik Åhlfeldt and Adela Saavedra at IMC and Richard Schatz at KTH, Stockholm are gratefully acknowledged for providing the laser diode and for discussions about the FM-response. This work was supported by the Swedish Defence Materiel Administration (FMV).

1. R. Passy, N. Gisin, J. P. von der Weid and H. H. Gilgen, "Experimental and theoretical investigations of coherent OFDR with semiconductor laser sources", *J. Lightwave technol.*, **vol. 12**, p 1622-1630, 1994.
2. L.-T. Wang, K. Iiyama, F. Tsukada, N. Yoshida and K.-I. Hayashi, "Loss measurement in optical waveguide devices by coherent frequency-modulated continuous-wave reflectometry", *Opt. Lett.*, **vol. 18**, pp. 1095-1097, 1993.
3. R. G. Frehlich och M. J. Kavaya, "Coherent laser radar performance for general atmospheric refractive turbulence", *Appl. Optics*, **vol. 30**, pp. 5325-5352, 1991.
4. M. Harris, G. N. Pearson, J. M. Vaughnan, D. Letalick and C. Karlsson, "The role of laser coherence length in continuous-wave coherent laser radar", *J. Modern opt.*, **vol. 45**, pp. 1567-1581, 1998.

Interference of backscatter from two droplets in a focused continuous wave CO₂ Doppler lidar beam

Maurice A. Jarzembki

NASA/Marshall Space Flight Center

Global Hydrology and Climate Center, 977 Explorer Blvd., Huntsville, AL 35806

Vandana Srivastava

Universities Space Research Association

Global Hydrology and Climate Center, 977 Explorer Blvd., Huntsville, AL 35806

Interference due to the superposition of backscatter, β , from two micron-sized droplets using a NASA/MSFC cw CO₂ Doppler lidar at 9.1 μm wavelength was detected for the first time. The resultant single β signal from both droplets contained an interference structure with a well-defined periodicity which was accurately measured and compared with cw lidar theory.¹ The agreement between measurements and theory is excellent, indicating that the interference arises because the droplets are moving at different speeds and, therefore, the relative droplet separation is not constant. This gives the superimposed β signal from both droplets in the lidar beam moving in and out of constructive and destructive interference with a well-defined periodic structure.

Figure 1(a) shows a measurement of a time-resolved signal pulse with an oscilloscope of the combined β from two $\sim 14.12 \mu\text{m}$ in diameter silicone oil droplets responding to the Gaussian lidar beam intensity at the lidar beam focus. Full details of this laboratory experimental setup, particle generation method, measurement technique, and the cw lidar can be found elsewhere.^{2,3} The stream of silicone oil droplets resided at a Doppler-shift center-frequency of $f_D \sim (3.4 \pm 0.2)$ MHz, giving droplet speed $v \sim (21.9 \pm 1.3)$ ms^{-1} . Also shown on a separate channel is the corresponding signature using an amplitude demodulator circuit designed to detect the amplitude envelope of f_D within the pulse profile. β from simultaneous droplet events show a complete cyclic interference structure of maximum and minimum. The average period T of the complete cycle of interference is $13.02 \pm 0.39 \mu\text{s}$. Toward the right edge of the profile, the interference disappears because one of the droplets is leaving the lidar beam while the other one remains in the beam, thus, giving β for a single droplet.

Interference is due to the droplets having slightly different speeds in the lidar beam at the same time such that β from each droplet can interfere. As a result, the periodic process of constructive and destructive interference is established, depending whether β from each droplet is in phase or out of phase, respectively. Interference can be understood from the heterodyne β signal current i_s , produced by a single scatterer near focus, given as¹

$$i_s \propto \exp\left[-2\left(\frac{\pi R r}{\lambda L}\right)^2\right] \cos(\phi), \quad (1)$$

where ϕ is given by

$$\phi = 2kL + f_D t - \varphi_R + 2\varphi + 2 \tan^{-1}\left[\frac{\pi R^2}{\lambda L}\left(1 - \frac{L}{F}\right)\right], \quad (2)$$

where R is $(1/e)^2$ intensity radius at the telescope primary, L is range measured from the telescope primary mirror to the particle, F is range to center of the focal volume, λ is photon radiation ($k = 2\pi/\lambda$), f_D is Doppler-shift frequency caused by moving scatterers (heterodyne beat frequency between β and reference local oscillator), r is position of scatterer at distance L at a given time t , φ_R is phase of reference local oscillator signal relative to transmitted signal, and φ is a function³ which depends on lidar parameters L , F , R , λ , and r . In Eq. (1), the exponential term gives the outline of a particle's overall pulse profile in the lidar beam, as observed in Fig. 1(a). Since β was measured at focus, $L = F$, a range dependent term¹ in the argument of the exponential function as well as an additional term¹ multiplied by the exponential function, which gives range response of β , have both been neglected.

The cosine term gives the phase relationship which is responsible for f_D observed within each droplet pulse profile as well as the interference due to the superposition of more than one β pulse. The argument of the

cosine term, however, is slightly different for two droplets at different positions L , moving at different speeds in the lidar beam, having slightly differing values for f_D . Therefore, each droplet has a different value for ϕ , given by ϕ_1 and ϕ_2 . Rather than determining each term in ϕ_1 and ϕ_2 , the first droplet is given a value ϕ while the second droplet moving with respect to the first droplet having value $\phi + \delta$ where δ is expressed as a small fractional value of ϕ . Therefore, i_s can be expressed as the sum of individual β currents i_{s1} and i_{s2} for droplets 1 and 2, respectively, as

$$i_s \propto \cos(\phi) + \cos(\phi + \delta), \quad (3)$$

where it is assumed that the exponential term for each droplet is the same, as we are not too concerned here with the amplitude of the combined profile as it does not contain phase properties of β . Now i_s pulsates with a beat frequency which depends on the value of δ with respect to ϕ .

A relationship involving the phase relationship between δ and ϕ , and the two measurable experimental input parameters f_D and T can be determined. Each droplet has a specific f_{D1} and f_{D2} where the average is simply f_D , while the difference is the beat frequency f_{beat} , which is the inverse of T . The number of wavelengths corresponding to f_D occurring within T is given by $f_D T$. Also, the ratio δ/ϕ governs the number of wavelengths occurring within one period. Since the superposition of β from the two droplets is governed by Eq.(3) and since δ/ϕ controls the pulsation period T ; therefore, the interference structure is governed by the relation

$$\delta/\phi = 1/f_D T. \quad (4)$$

This simple relationship involves the phase relationship of δ with respect to ϕ in Eq. (3) and governs the complicated interference structure from the two droplets. Finally, since f_D from a single droplet along the lidar beam axis is given by $f_D = 2\nu \cos\theta/\lambda$, the interference condition is given by $1/T = f_{beat} = f_{D1} - f_{D2} = 2\Delta\nu \cos\theta/\lambda$, showing the relationship of the speed difference $\Delta\nu$ between droplet 1 and 2 in terms of λ , T , and θ .

Figure 1(b) shows calculation of Eq. (3) as a function of ϕ using $\delta = 0.0226\phi$. With the addition of δ , the cosine function pulsates with a period indicative of T or f_{beat} . Figure 1(c) shows the same function for only one period, showing a higher frequency contained within the envelope. For $f_D = (3.4 \pm 0.2)$ MHz and $T = (13.02 \pm 0.39)$ μ s, $f_D T = (44.27 \pm 2.92)$ which is the number of wavelengths within one T . Therefore, from Eq. (4), δ changed relative to ϕ by a factor of 0.0226. In Fig. 1(b or c), one period was completed for $\phi \sim 278$ radians, which leads to $\phi/T \sim 21.35$ radians per 1 μ s. For one complete period, $\delta \sim 0.0226 \times 278$ radians or $(2.000\pi \pm 6.6\%)$ radians, which shows that Eq. (4) gives excellent agreement with the expected value of 2π radians. This advancement of δ by 2π for each complete cycle of interference is indicative of a difference of one wavelength for the difference in the total optical path length (incident radiation plus β radiation) between the two droplets. Hence, within one complete cycle of interference contained in each T increment at an average f_D for both droplets, ϕ changed by 278 radians while, at the same time δ changed in an increment of 2π governed by Eq. (4). Furthermore, from the condition for interference, the relative speed difference $\Delta\nu$ between the two droplets is calculated to be $(0.49 \pm 3.0\%)$ ms^{-1} , which is well within the difference of ~ 2.6 ms^{-1} for expected.

In addition, a calculation of Eq. (3) modulated by the exponential term given in Eq. (1) can be performed which will give a representation of the pulse shape for two droplets as displayed on the oscilloscope. Assuming that the droplets move at constant ν and that they traverse the lidar beam through the axis of propagation at angle θ , Eq. (1) can be expressed in terms of ϕ as $\exp[-2\phi^2/K^2]$, where $K = \lambda F\phi/\pi R\nu t \sin\theta$, which defines the standard deviation of the exponential term in the phase domain. Substituting for the known parameters: $R = 0.0305$ m, $F = 9.53$ m, $\lambda = 9.1 \times 10^{-6}$ m, $\theta = 45^\circ$, $\nu \sim 21.9$ ms^{-1} , $\phi/t \sim 21.35$ radians/ μ s, gives $K \sim 1248$ radians. Figure 1(d) shows calculation of $\exp[-2(\phi/1248)^2] \times [\cos(\phi) + \cos(1.0226\phi)]$. The agreement of Fig. 1(d) with the measurement of two simultaneous droplets in a lidar beam [Fig. 1(a)] is excellent.

Figure 2 shows a summary of the results as a vector representation of the addition of two harmonic waves. This schematic depicts the stages of interference, including total constructive and total destructive interference, of the combined β from two droplets that can be observed by the resultant vector. Both ϕ and δ vary continuously with time such that i_{s1} , i_{s2} , and i_s rotate with different angular velocity. Figure 2(a) shows both droplets in phase with each other, giving the resultant current as the highest possible, thus, total constructive interference. As time advances, both ϕ and $\phi + \delta$ advance at different rates. After a certain time, such that ϕ has advanced by 10π radians for droplet 1, then $\phi + \delta$ has advanced by 10.226π radians for droplet 2 [Fig. 2(b)], giving nearly total constructive interference. For ϕ advancing by 40π radians for droplet 1, while $\phi + \delta$ has advanced by 40.904π radians for droplet 2 [Fig. 2(c)], gives nearly total destructive interference, depicted by the short length of i_s . Total destructive interference will occur for $\delta = \pi$ radians or when ϕ has advanced by $\sim 44.27\pi$ radians. This corresponds to one half period which is exactly half of $\phi = 278$ radians, as determined.

These measurements show that the interference of β from two micron-sized droplets on time scales of tens of microseconds can easily be measured with high resolution using a cw lidar. Since, interferometric investigations provide valuable as well as high-resolution information about physical processes, it is possible that this investigation may provide useful information on the dynamics of complex flow fields using particles as tracers and a cw Doppler lidar as a diagnostic tool. This technique, therefore, can not only make absolute velocity measurements of the tracers but can also determine the differential velocity between the tracers.

References

1. C. M. Sonnenschein and F. A. Horrigan, "Signal-to-noise relationships for coaxial systems that heterodyne backscatter from the atmosphere," *Appl. Opt.* **10**, 1600-1604 (1971).
2. M. A. Jarzembki, V. Srivastava, and D. M. Chambers, "Lidar calibration technique using laboratory-generated aerosols," *Appl. Opt.* **35**, 2096-2108 (1996) [Errata: λ needs to be in the numerator of Eq. (8)].
3. J. Rothermel, D. M. Chambers, M. A. Jarzembki, V. Srivastava, D. A. Bowdle, and W. D. Jones, "Signal processing and calibration of continuous-wave focused CO₂ Doppler lidars or atmospheric backscatter measurement," *Appl. Opt.* **35**, 2083-2095 (1996).

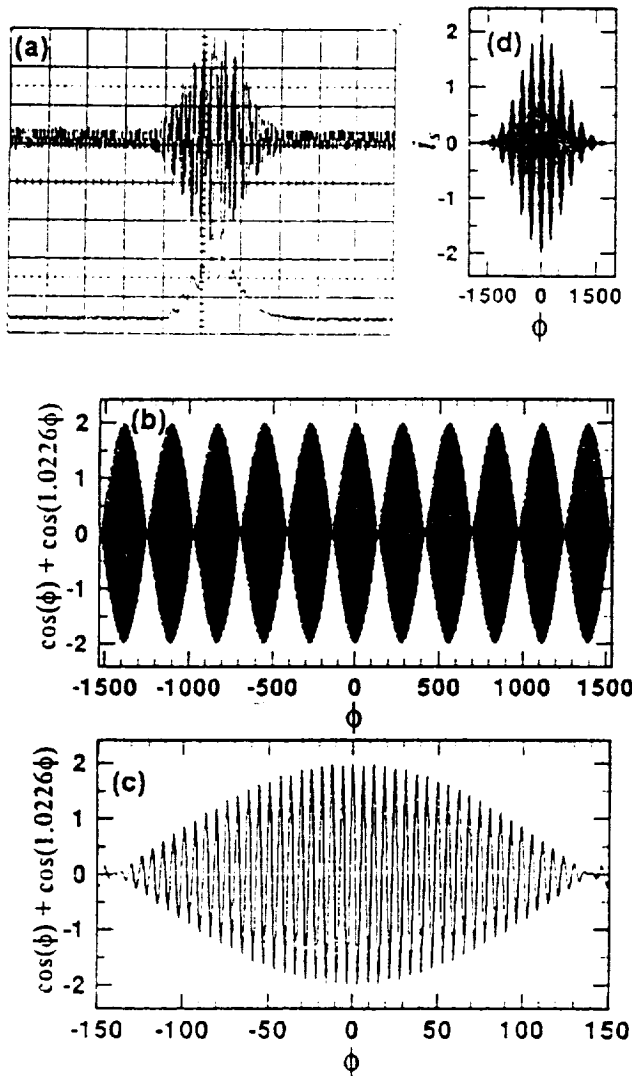


Fig. 1 (a) Time-resolved signal pulse measurement with high-speed transient LeCroy oscilloscope from two closely spaced silicone oil droplets giving a structure of constructive and destructive interference. Calculation of the function for $\delta = 0.0226\phi$ as a function of ϕ for: (b) 11 periods and (c) for 1 period with higher resolution, where the number of wavelengths contained within one period can be distinguished. Calculation of the (d) function $[\cos(\phi) + \cos(\phi + \delta)]$ modulated by $\exp[-2(\phi/K)^2]$ for $\delta = 0.0226\phi$ and $K = 1248$ to compare with Fig. 1(a) using $1 \mu s \approx 21.35$ radians. The time scale for Fig. 1(a) is $50 \mu s$ per division whereas the amplitude scale is $1 V$ per division.

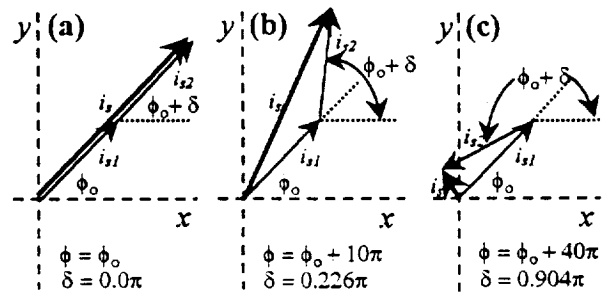


Fig. 2 Vector addition of the harmonic wave functions i_{s1} and i_{s2} for each droplet and the resultant harmonic wave function i_s (Eq. 3) for the case shown in Fig. 1(a) for an arbitrary initial condition of $\phi = \phi_0$ with: (a) $\delta = 0.0\pi$ (totally constructive interference), (b) $\delta = 0.226\pi$ (nearly constructive interference), and (c) $\delta = 0.904\pi$ (nearly destructive interference).

WIND MEASUREMENTS

Presider: David Tratt

Ground-based Remote Sensing of Wind Vector

Latest Results from Guideline Development

J. Bösenberg, H. Danzeisen, D. Engelbart, K. Fritzsche, V. Klein, Ch. Münkler, T. Trickl, L. Woppowa, and Christian Werner

1. Introduction

Methods which are in discussion to enter a VDI guideline will be presented. The VDI „Richtlinie VDI 3786 „Umweltmeteorologie“, is divided in many parts. VDI 3786 Part 14 shows the possibilities of remote sensing and describes the wind profile measurements. It is necessary for comparison with other instruments to have a guideline which describes also the calibration and performance tests.

Wind profiles in the atmospheric boundary layer are a very important parameter also to study atmospheric exchange processes. The wind field in the atmospheric boundary layer is highly variable in spatial and temporal scales. For a few possible applications a more frequent wind sensing is necessary, i.e.

- for airports located in low level jet areas,
- for chemical plants to get information of the transport of toxic gases from leakages,
- for meteorology in general to improve the weather forecast,
- for environment protection purposes like dispersion studies.

Only a few techniques can be applied to get the wind field in the boundary layer. Laser Doppler systems are candidates.

2. Doppler Lidar

A heterodyne lidar consists of a pulsed, frequency-controlled laser transmitter locked via a locking loop to the local oscillator, a transmit and receive telescope, a heterodyne detector, where the local oscillator radiation is mixed with the Doppler-shifted backscatter signal, and a signal processing system. The signal originates from the backscattering by small aerosol particles which move with the prevailing windspeed through the laser focus volume. The windshifted Doppler frequency directly determines the line-of-sight (LOS) component (V_{LOS}) of the wind vector.

One measures the backscattered, Doppler shifted radiation. Backscattering depends on the size and number density of the aerosol particles available in the volume of interest. The backscattered Doppler frequency directly determines the line-of-sight (LOS) component (V_{LOS}) of the wind vector. At CO_2 laser (wavelengths $\lambda = 10.6 \mu m$) a velocity component of 1 m/s corresponds to a frequency shift, Δf_D of 189 kHz. This is obtained from the equation

$$\Delta f_D = 2 \frac{V_{LOS}}{c} \cdot f_0$$

where c is the speed of light and V_{LOS} is the line-of-sight component.

By scanning the transceiver with a conical scan pattern (VAD) or by using the beam swinging technique (DBS) (see figure 1) one reaches different azimuth and elevation angles to combine the single LOS-components to a wind vector.

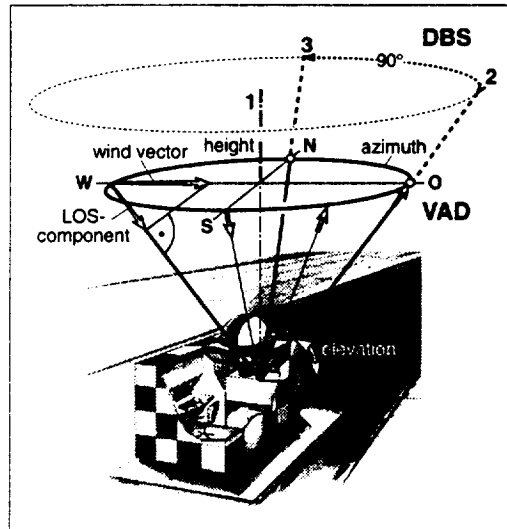


Fig. 1 Doppler lidar operations, VAD scan technique or DBS technique

By measuring at an azimuth angle θ and an elevation angle φ one gets a radial (line-of-sight) contribution V_{LOS} which depends on the wind vector components u , v , and w given by

$$V_{LOS} = u \sin\theta \cos\varphi + v \cos\theta \cos\varphi + w \sin\varphi$$

where

- u is the east-west wind component,
- v is the north-south wind component,
- w is the vertical wind component,
- θ is the scan angle clockwise from north, and
- φ is the elevation angle,

It is accepted worldwide that ground-based Doppler lidars can measure wind profiles in the atmosphere. Various field experiments have been carried out where balloon wind-sondes were launched simultaneously with wind profile measurements made by Doppler lidar (Hall et al., 1984; Köpp et al., 1984). Radiosonde winds have been averaged over height ranges comparable to the lidar range resolution. The route-mean-square (RMS) differences are below 1 m/s. Lidar velocities are determined from a Doppler shift whereas sonde velocities are determined from changes in the balloon range. The lidar sensing volume is centered over the scanner on the average, but the balloon drifts with the wind so that the two techniques measure different regions of the atmosphere that may have different wind values.

3. Height Determination

If the conical scan is performed with a pulsed system, each range element of the return signal corresponds to a given altitude. The wind estimation is made for the height elements, slices in the atmosphere covered with wind information. By scanning a large spatial average of the wind information is given. This spatial average can be converted in time averages required by the meteorologists to receive the so called „mean“ wind.

4. Representation of Measured Data

4.1 Comparison of a Doppler lidar with a point sensor

For the acceptance of the remote sensing method to determine the wind speed a first experiment was performed in comparison with a traditional Sonic anemometer. The Doppler lidar beam was focussed in to the measurement volume of the Sonic anemometer in 200 m distance. Figure 2 shows the comparison.

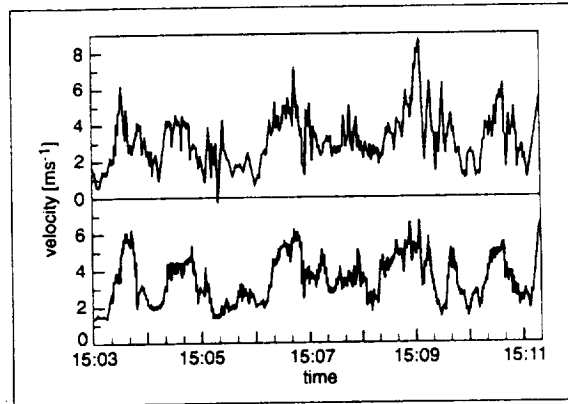


Fig 2: Radial wind component measurement using a Sonic anemometer (above) and a lidar (below)

The measurement was performed in 2 meters above ground. Turbulence is the main signature which was measured by both instruments. The comparison of both measurements gives a correlation factor of 0.97 for a lot of days with different wind velocities and turbulences.

4.2 Comparison with radiosonde data

Figure 3 shows a comparison with a radiosonde derived wind profile in the boundary layer. These kind of wind profiles were measured many times during a campaign in 1982. The standard deviation was 1.3 m/s in wind speed and about 12 degree in direction between both systems, the Doppler lidar and the radiosonde wind.

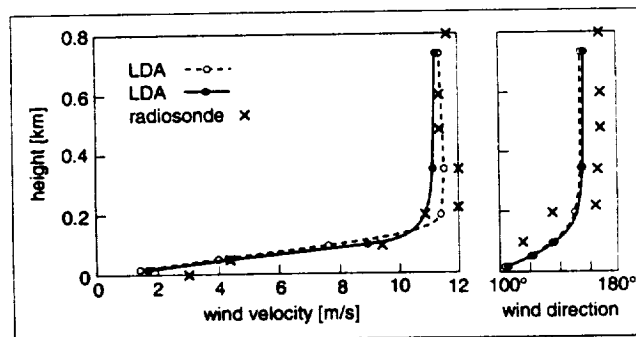


Fig 3 Comparison of two laser Doppler wind profile measurements with a radiosonde

4.3 Laser Remote Sensing of the Mean Wind (3D wind field)

The task of this work is the investigation of the representativity of LDA mean wind velocity measurements and variations of wind velocity profiles in the planetary boundary layer under different atmospheric stabilities and earth surface roughnesses in presence of mesoscale variations of the wind.

The random variation $V_D - V_{LOS}$ is connected mainly with the atmospheric turbulence. The question to be answered is: How long one has to measure to get the mean wind? The mean wind normally is measured with a point sensor averaged over 10 minutes. Doppler lidar averages over a large spatial volume compared to the point sensor. It is expected that the measurement time is much smaller than 10 minutes (Banakh et al. 1994, 1999). For the worst case, an unstable stratification and a roughness length of 1 m the time of measurement to get 1 m/s accuracy is about 12 seconds.

5. Comparison of different instruments

For comparison of different types of Doppler lidars a procedure was developed. Because the maximum range for the determination of the wind profile depends on the system parameters like laser power and shot accumulation, and also on the atmospheric aerosol concentration, the procedure has to be in accordance with these dependencies. The system parameters are known, the vertical aerosol profile varies. It was determined to perform the comparison near a horizontal path at visibility conditions of 10 km over a time period of 10 minutes with a range interval of 250 m. This gives the maximum range for the system to be examined. One has to know that the short wavelength systems (2 μm for example) are more affected by atmospheric turbulence than the 10 μm -systems. For the maximum range the turbulence is an additional parameter.

6. Summary

Remote sensing methods are well established. By publication of the guideline VDI 3786 page 14 a kind of standardisation is performed for the use of the new technique. It has been shown that time averaging and spatial averaging can be exchanged to meet the requirement for the estimation of the mean wind. Future systems should be small and simple for automatic operation in the area of environmental protection.

7. References

- V. A. Banakh, I. N. Smalikho, F. Köpp, Ch. Werner: "Representativity of the wind measurements by a CW Doppler Lidar in the Atmospheric Boundary Layer", Applied Optics, Vol. 34, 2055 - 2067, 1995
- V.A. Banakh, I. Smalikho, F. Köpp, Ch. Werner: „Measurements of turbulent energy dissipation rate with a cw Doppler lidar in the atmospheric boundary layer“, Journ. Atmospheric and Oceanic Technology, 1999
- Hall, F.F. Jr.; R.M. Huffaker, R.M. Hardesty, M.E. Jackson, T.R. Lawrence, M.J. Post, R.A. Richter, and B.F. Weber: Wind Measurement Accuracy of the NOAA Pulsed Infrared Doppler Lidar. Appl. Opt. 23, 2503, 1984
- Köpp, F.; R.L. Schwiesow, and Ch. Werner: Remote Measurements of Boundary-Layer Wind Profiles Using a CW Doppler Lidar. Journ. Climate and Appl. Meteor. 23, 148-154 (1984)

ABSTRACT

The Accuracy of the True Radial Velocity Measurements in the Turbulent Atmosphere
Alexander P. Shelekhov, Institute of Atmospheric Optics, SB Russian Acad. Science, Tomsk, Russian Federation

As a rule the accuracy of the Doppler measurements is studied using the assumption that the frequency estimation is equal to approximately the average Doppler shift or is proportional to the average true radial velocity. But the frequency estimation may be proportional to the true radial velocity. In this paper the accuracy of the true radial velocity measurement is investigated for the different state of the turbulent atmosphere, the different values of the signal-to-noise ratio, the number of the samples and other parameters. The cases of the stable, unstable, and indifferent stratification are considered.

DOPPLER LIDAR OBSERVATIONS OF WIND FEATURES NEAR COMPLEX TERRAIN

Lisa S. Darby, Alfred J. Bedard, and Robert M. Banta

National Oceanic and Atmospheric Administration/Environmental Technology Laboratory

325 Broadway, R/E/ET2

Boulder, CO 80303

ldarby@etl.noaa.gov; ph. 303-497-6593; fax 303-497-5318

1. Introduction

In the last decade the National Oceanic and Atmospheric Administration/Environmental Technology Laboratory's (NOAA/ETL) transverse excited atmospheric pressure (TEA) CO₂ Doppler lidar measurements have contributed significantly to the understanding of wind flow features associated with complex terrain. Positioning this Doppler lidar near mountainous terrain has proven to be an effective setting for measuring terrain-induced flows and the interaction of these flows with the ambient (larger-scale) meteorological conditions. In this paper we briefly review noteworthy results from air quality experiments at two such sites (near Denver, CO. and Vancouver, B.C.), and then present more detailed results from the Colorado Springs, CO. airport where we investigated wind features that could be hazardous to aviation.

2. An atmospheric transport study near Denver, CO. related to hazardous materials.

The Rocky Flats Plant (RFP), which is roughly 10 km east of the Rocky Mountains and is a nuclear facility, was an excellent site for measuring several types of wind events, including the horizontal and vertical structure of a well defined canyon exit jet that was narrow enough to escape detection by an enhanced network of surface instrumentation [1]. This narrow canyon exit jet transported a portion of SF₆ tracer along a trajectory that deviated from the path of the bulk of the tracer, which was transported by the mean surface winds. A transport model initialized with data from the enhanced network of surface instrumentation, but not lidar data, completely missed this secondary peak in the tracer concentration [2]. In this case, Doppler lidar data played a crucial role in assessing a diagnostic wind-flow model's results and

revealed the impact that a relatively small wind feature could have on the transport of hazardous substances.

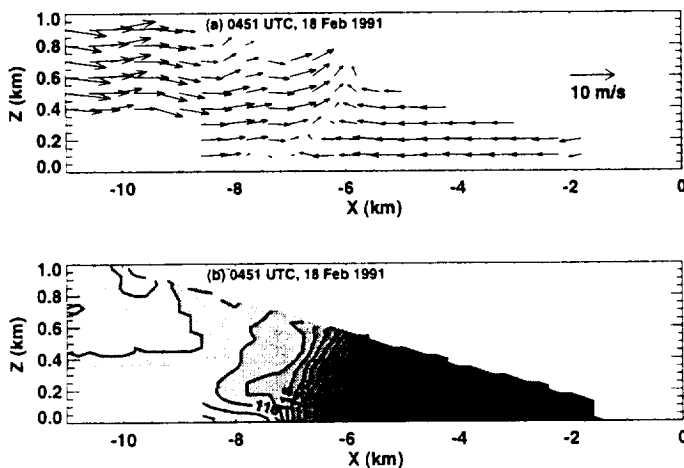


Figure 1 (a) Vector plot of lidar winds parallel to the plane of the scan and the vertical component of the wind derived from the continuity equation and (b) contour plot of lidar backscattered signal intensity (dB) derived from a vertical scan. The lidar is located at (0,0), left is to the west-northwest and z is up (vertical). The opening of the canyon is at $x = -10$ km. The gap in the data surrounding $x = -10$ km is due to terrain contamination.

With measurements from this same site, Doppler lidar data show the details of a boundary between warm, dry downslope winds and a cool, moist air mass that propagated westward through the RFP, reaching the foothills and penetrating into nearby canyons [3]. Figure 1 shows downslope westerly winds meeting the easterly winds associated with the cooler air mass. A strong gradient in backscatter existed along the boundary between the two air masses, showing that the canyon winds were much cleaner (i.e., lower aerosol backscatter values) than the winds behind the front. Lidar measurements revealed the density-current-like features of the moister air as it impinged upon the foothills, and the complete reversal of winds in nearby canyons and in the RFP region after the passage of this front. Again, this kind of wind feature could have a strong effect on the transport of hazardous

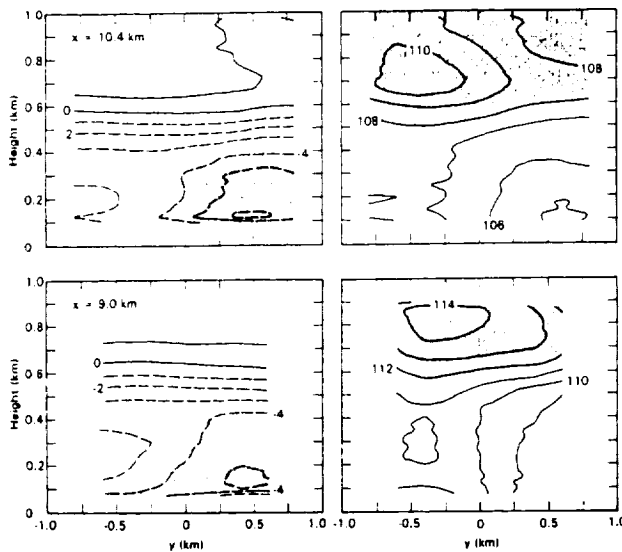


Figure 2 Lidar vertical cross sections (across the valley) of downvalley flow, derived from a high-resolution volume scan. The top two plots show contours of u_r (left, $m s^{-1}$) and backscattered signal intensity (right, dB) 10.4 km from the lidar. The bottom two plots show similar contours from the same volume, but at a distance of 9 km from the lidar. Radial velocities $> 4 m s^{-1}$ and areas of highest backscatter are shaded.

approaching or departing the airport [5]. In addition to documenting the regional scale winds, a variety of small-scale features (several hundred m to a few km in size) were seen in the lidar data, particularly while scanning in a vertical plane toward the mountains. Examples of these features included mountain waves of varying character, a series of propagating waves, directional and speed shear layers, breaking waves, rotors (at the surface and aloft) and cold front passages. In this paper we show lidar measurements from a case study involving high-amplitude mountain waves and rotors occurring on 1 April 1997. A comparison of lidar data and turbulence measurements from an instrumented King Air coincident in time and space with lidar measurements will show that the King Air flew through the edge of a rotor while encountering moderate turbulence. For more details on this case, including a comparison between lidar data and high-resolution mesoscale modeling results, see [6] and [7]. This study builds on an earlier study in which the same lidar was crucial in documenting the presence of a breaking mountain wave that helped rip an engine and part of a wing from a DC-8 jet over Colorado [8].

a. Experiment setting

The Doppler lidar was stationed on Peterson Air Force Base ~150 m east of the Colorado Spring airport's north-south runway. The complexity of the terrain surrounding the Colorado Springs airport includes Pike's Peak (~4300 m above sea level (ASL)) to the west and Cheyenne Mountain (~2700 m ASL) to the southwest. Throughout the experiment, lidar measurements indicated vertical wind shear was quite common near Cheyenne Mountain.

substances from the RFP.

3. An air quality study from near Vancouver, B.C.

Another prime site for lidar measurements was the Pitt Meadows Airport, near Vancouver, B.C., ~15 km from the mountains. Figure 2 shows the vertical structure of the wind flow and backscatter returns in an exit jet from the Pitt Lake valley, with dashed lines indicating downvalley flow. The strongest downvalley flow corresponds to the cleanest (i.e., lowest backscatter) air. Detailed vertical profiles of both the backscatter and velocity fields taken from scans like these, combined with surface and upper air chemistry measurements, led researchers to develop theories for possible removal mechanisms for pollutants in this region [4].

4. A study of clear-air turbulence aviation hazards near Colorado Springs, CO.

In the winter of 1997 the TEA CO₂ Doppler lidar was stationed 20 km east of the foothills of the Rocky Mountains at the Colorado Springs, CO. airport, almost directly east of Pike's Peak. While the previously referenced work focused on air quality issues, in Colorado Springs we had the task of searching for and documenting wind flow features that could be hazardous to aircraft

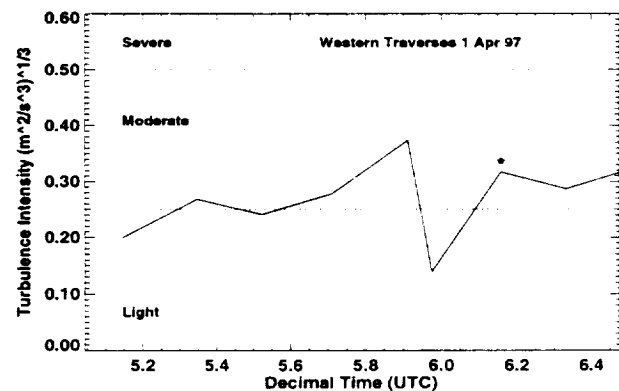


Figure 3 The cube root of the eddy dissipation rate derived from wind measurements taken onboard the Wyoming King Air, vs. time. The categories (light, moderate, and severe) represent approximate turbulence levels for a moderate-sized jet.

b. Lidar scanning strategy

During the Colorado Springs study, the lidar operated only when winds were expected to be strong. Lidar scans included vertical scans (maintaining a constant azimuth angle while sweeping in elevation) and horizontal scans (maintaining a constant elevation angle while sweeping in azimuth). The scanning strategy consisted of a sequence of survey scans every half-hour, with time left for scans designed specifically for the wind conditions at hand. For example, if a rotor was detected near the foothills, time would be devoted to performing high-resolution vertical scans through the rotor.

c. King Air research aircraft and Doppler lidar measurements

The Wyoming King Air measurements occurred during intense lee-wave activity and flow reversals. Turbulence measurements from flight transects along the foothills, about 10 km west of the airport and at 550 to 765 m above ground level (AGL), show an increase from the upper range of light turbulence to the mid-range of moderate turbulence (Fig. 3). The point in Fig. 3 marked with an asterisk is an average of measurements taken between 0609:30 and 0612:18 UTC, 1 April 1997. Bracketing this period of

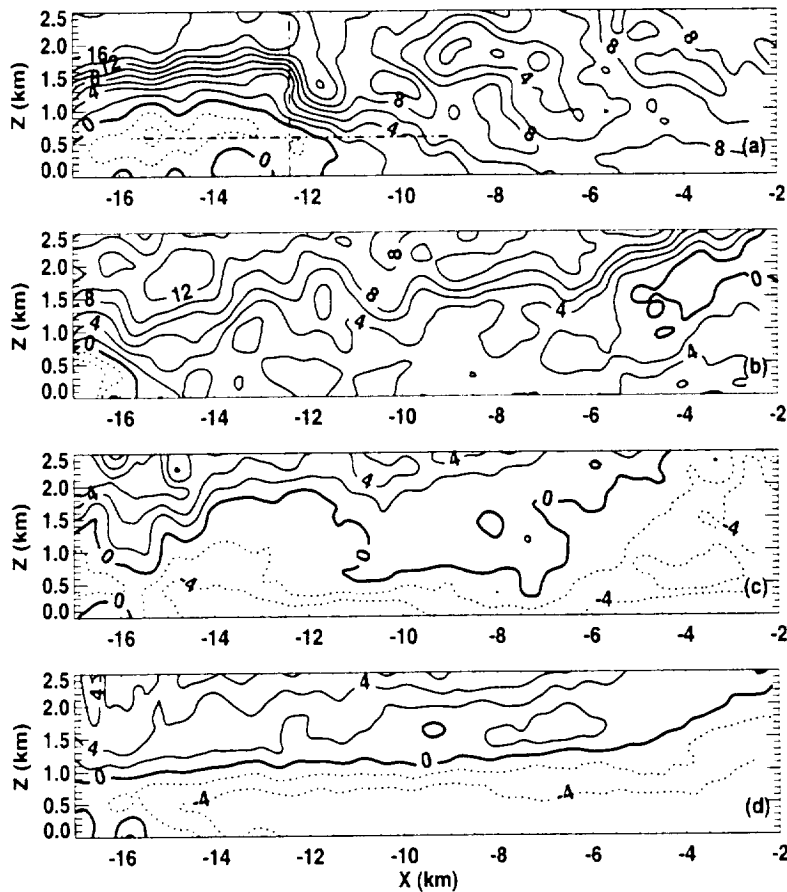


Figure 4 Contour plots of the component of the wind parallel to the plane of the lidar scan (scanner azimuth is 240° , nearly into the mean wind). Contours are in 2 m s^{-1} intervals. Solid lines indicate flow with a westerly component and dashed lines indicate flow with an easterly component. The lidar is located at $(0,0)$; west is to the left. The intersection of the dashed lines in (a) indicate the approximate location of the King Air as it was taking turbulence measurements. (a) 0610:04 UTC; (b) 0937:14 UTC; (c) 1031:36 UTC; (d) 1241:50 UTC.

turbulence measurements, the lidar performed vertical scans pointing toward the foothills, sampling the same region that the King Air was flying through. The component of the wind parallel to the 240° lidar scan coinciding with the King Air measurements is shown in Fig. 4a. The intersection of dash-dot lines in Fig. 4a indicates the approximate region the King Air flew through during its traverse to the west of the runway and encounter with moderate turbulence. The strong wind shear that was the cause of the turbulence is clearly evident in the lidar measurements. The mountain wave had winds up to 16 m s^{-1} and generated a region of flow reversal from 12 to 18 km away from the lidar, and about 1 km deep.

The remaining plots in Fig. 4 show the evolution of the wind with time. At 0937 UTC (Fig. 4b) the mountain wave had diminished considerably in size and intensity, as had the rotor (the flow reversal underneath the wave crest). Figure 4c shows easterly flow (dashed lines) associated with a recent cold front passage undercutting the southwesterly flow that had been dominating the region for hours. By 1241 UTC (Fig. 4d) the easterly flow had become a well established upslope flow, with snow showers occurring shortly after this time.

d. Summary

The vertical structure and evolution in time of strong flow over the mountains and its associated flow reversal near the foothills was documented by the NOAA/ETL Doppler lidar. The edge of the rotor was within 12 km of the Colorado Springs Airport. An instrumented aircraft penetrated the edge of the rotor, and wind measurements onboard the aircraft indicated moderate turbulence for a moderate-sized jet. The lidar measurements obtained during this field experiment provide some of the most detailed documentation of rotors, flow reversals, and mountain waves that are available.

ACKNOWLEDGMENTS

The authors wish to thank Jim Howell, Hutch Johnson and Dave Levinson (ETL/Lidar Division) for their hard work in obtaining the lidar data used in this paper. Dr. Peter Neilley (NCAR/RAP) graciously supplied the Wyoming King Air turbulence data. We are most grateful for the support of the Federal Aviation Administration and particularly thank Dr. Aston McLaughlin. The authors thank Janet Machol and Marty Ralph for helpful reviews.

REFERENCES

1. Banta, R.M., L.D. Olivier, and P.H. Gudiksen, 1993: Sampling requirements for drainage flows that transport atmospheric contaminants in complex terrain. *Radiat. Prot. Dosim.*, **50**(2-4), 233-248.
2. Banta, R.M., L.D. Olivier, P.H. Gudiksen, and R. Lange, 1996: Implications of small-scale flow features to modeling dispersion over complex terrain. *J. Appl. Meteor.*, **35**, 330-342.
3. Darby, L.S., W.D. Neff, and R.M. Banta, 1999: Multiscale analysis of a Meso- β frontal passage in the complex terrain of the Colorado Front Range. Accepted for publication in *Mon. Weather Rev.*
4. Banta, R.M., P.B. Shepson, J.W. Bottenheim, K.G. Anlauf, H.A. Wiebe, A. Gallant, T. Biesenthal, L.D. Olivier, C.J. Zhu, I.G. McKendry, and D.G. Steyn, 1997: Nocturnal cleansing flows in a tributary valley. *Atmos. Environ.*, **31**, 2147-2162.
5. Banta, R.M., A.J. Bedard, Jr., J. Brown, C. King, D. Levinson, P. Neilley, A. Praskovsky, and E. Szoke, 1998: A pilot experiment to define mountain-induced aeronautical hazards in the Colorado Springs area: Project MCAT97. Mountain-Induced Aeronautical Hazards Program Project Report (Interim Report), Ed. A.J. Bedard, Jr., and P. Neilley.
6. Poulos, G.S., and L.D. Olivier, 1998: Mountain wave/frontal interaction dynamics in the lee of Pike's Peak. *Preprints, 8th Conference on Mountain Meteorology*, August 2-7, 1998, Flagstaff, AZ. American Meteorological Society, Boston MA., 172-175.
7. Olivier, L.D., and G.S. Poulos, 1998: Frontal passage, mountain waves and flow reversals in the vicinity of the Colorado Springs, CO Airport, *Preprints, 8th Conference on Mountain Meteorology*, August 2-7, 1998, Flagstaff, AZ. American Meteorological Society, Boston MA., 176-181.
8. Ralph, F.M., P.J. Neiman, and D.H. Levinson, 1997: Lidar observations of a breaking mountain wave associated with extreme turbulence. *Geo. Res. Let.*, **24**, 663-666.

BISTATIC LASER DOPPLER WIND SENSOR AT 1.5 μ m

M Harris

Electronics Sector

Defence Evaluation and Research Agency

Malvern, Worcestershire WR14 3PS, U.K.

A coherent laser radar has been built using a MOPA arrangement where the master oscillator is an external cavity semiconductor laser, and the power amplifier is an erbium-doped fibre amplifier with ~ 1 Watt output. The beams are routed within single-mode optical fibre allowing modular construction of the optical layout with standard components. The system employs separate transmit and receive optics (a "bistatic" configuration), and has sufficient sensitivity for reliable Doppler wind speed detection under moderate scattering conditions at ranges of order 100m.

The bistatic arrangement leads to a well-defined probe volume formed by the intersection of the transmitted laser beam with the virtual back-propagated local oscillator "beam" (BPLO). This could be advantageous in applications where precise localisation of wind speed is required (e.g. wind tunnel studies) or where the presence of smoke, low cloud or solid objects can lead to spurious signals.

Proper alignment requires that the BPLO and transmit beam foci coincide in space, and this requirement is significantly more troublesome to achieve than in a conventional monostatic lidar. However, the difficulties are greatly mitigated by the use of optical fibre to define the BPLO receiver mode.

The confinement of the probe volume also leads to a reduction in the signal power. A theoretical study has been carried out on the reduction in wind signal strength in comparison to the monostatic arrangement, and the results compared with experimental observation.

MEASURING TURBULENCE PARAMETERS WITH COHERENT LIDARS

A. Dabas
Météo-France CNRM/GMEI
42 avenue Coriolis, 31057 Toulouse cedex 1,
FRANCE

Ph. Drobinski
CNRS Laboratoire de Météorologie Dynamique
Ecole Polytechnique
91128 Palaiseau cedex
FRANCE.

R. M. Hardesty
NOAA Environmental Technology Laboratory
325 Broadway
Boulder, Colorado, 80303
USA

A. Brewer
NOAA Environmental Technology Laboratory
325 Broadway
Boulder, Colorado, 80303
USA

V. Wulfmeyer
NCAR Atmospheric Technology Division
P.O. Box 3000
1850 Table Mesa Drive
Boulder, Colorado 80307
USA

A mini-campaign was held in December 1998 near Boulder, Colorado (USA) to validate two high resolution coherent Doppler lidars, the 10- μm mini-MOPA lidar developed by NOAA/ETL (Brewer et al., 1997), and the 2- μm AHRDL@ jointly developed by NOAA/ETL and NCAR/ATD (Grund et al., 1997). An automatic weather station from NCAR/ATD was deployed on the site. With a sonic-anemometer at 5 meters above the ground, the station allowed us to make direct comparison between lidar and sonic anemometer winds. The results show the various systems reached a good agreement as far as large-scale wind fluctuations are concerned (e.g., 5 minute-averages of recorded winds). Regarding short-scale turbulent fluctuations, we show that a proper treatment of lidar data aimed at partially compensating for the pulse-averaging effect produces wind spectra comparable to the spectra derived from sonic anemometer data. The possibility of measuring dissipative rates of turbulent kinetic energy (Mayor et al., 1997; Frehlich et al., 1998) is thus confirmed.

The results presented below were acquired on December 7, 1998, from 20:27 GMT to 21:25 GMT (13:27 to 14:25 local time). They concern MOPA lidar exclusively (HRDL data are currently under analysis). On that day, the weather was sunny with no clouds, the thermal stratification was unstable ($z/L < -1$), and the turbulent activity was rather strong ($u^* \approx 20 \text{ cm s}^{-1}$). The mean wind (5 minute-average) was from the east (80E) at -2.5 ms^{-1} . The lidars were staring horizontally towards the sonic anemometer at a range of 600m. The line-of-sight azimuth was approximately 350E perpendicular to the mean wind.

Lidars were operated at a repetition rate of 200 pulses per seconds. The processing of radial velocity profiles was done by pulse-pair with an accumulation factor of 200, so one profile was produced every second. For the mini-MOPA, the range increment between retrieved velocities was 15 m. The sonic anemometer was operated at a rate of 20 Hz; it delivered measurements for the three wind components.

Figure 1 compares 5 minute-average radial velocities from sonic anemometer (dotted line) and mini-MOPA lidar. For the sonic anemometer, the radial velocity is obtained by projecting the 3D wind vector recorded by the instrument onto the lidar line-of-sight. For the mini-MOPA, we considered the radial velocity measured by the instrument at the range of the sonic anemometer. The figure shows differences between the sensors of less than 20 cm s^{-1} . The sonic anemometer produces a point measurement, whereas the mini-MOPA lidar measures the average of the radial wind inside the volume illuminated by the pulse (about 90 m long). This at least partially explains the differences.

Figure 2 compares wind spectra derived from the two instruments (light line: MOPA, dark line: sonic anemometer) obtained by the Fourier transformation of time series. For the mini-MOPA, the time series is formed by

the velocities recorded at full time resolution at range 600m. We can see that the lidar spectrum is strongly affected by pulse averaging, with a slope significantly different from the expected $-5/3$. The constant level of spectral power above -0.1 Hz is due to measurement errors (since errors are decorrelated from one lidar profile to the other, the errors form a white noise in velocity time-series, and therefore, they contribute a constant level of power to the spectrum). The figure shows it is not possible to measure the dissipative rate of turbulence from fixed-range time-series of lidar radial velocities unless the pulse averaging effect can be compensated for.

Compensating for pulse-averaging is rather complicated when time-series are considered, because pulse averaging then operates on a direction (the line-of-sight direction) different from the \hat{A} direction of the time series (the direction of the mean advecting wind). It becomes, however, much easier (Frehlich 1997) when range-series of radial velocities are considered, for both directions are the same. Pulse-averaging then amounts to a simple linear filter.

Figure 3 presents spectra obtained by Fourier transforming and averaging the velocity profiles produced by the lidar over consecutive time periods of 468s (symbols +). Denoting $v_r^p(n)$ the radial velocity recorded on profile p at range $r = n \delta r$ (δr is the range increment), lidar spectra are obtained by:

$$\overline{\Phi}(\kappa) = \frac{\delta r}{200 \pi P} \sum_{p=0}^{P-1} \left| \sum_{n=33}^{133} v_r^p(n) \exp(-i \kappa n \delta r) \right|^2$$

Here, P is the number of velocity profiles ($P=468$) and κ is the wavenumber. The spectrum is computed over the range interval [500m;2000m] ($n=33$ to 133). Lidar spectra are compared to sonic anemometer spectra displayed with light lines. To obtain those spectra, frequencies have been transformed into wavenumbers by considering the mean wind (parameter $\langle u_h \rangle$ in the panels). In addition, a multiplicative factor (3/4) has been applied to account for the different direction of acquisition (lidar spectra are computed from longitudinal fluctuations of the longitudinal wind, whereas the sonic spectrum is computed from lateral fluctuations of the longitudinal wind).

Figure 3 shows good agreement between the lidar and the sonic anemometer spectra. The dotted lines obtained by fitting a $-5/3$ power law to lidar spectra produces a useful estimate for the dissipative rate of turbulence (parameter ϵ in the panels) since it is also a good fit to sonic anemometer spectra.

REFERENCES

- Brewer, W.A., B.J. Rye, R.M. Hardesty, and W.L. Eberhard. Performance characteristics of a mini-MOPA CO₂ Doppler lidar. Proceedings, 9th Conference on Coherent Laser Radar, Linköping, Sweden, 23-27 June 1997, FOA Defense Research Establishment.
- Grund, C.J., S.A. Cohn, and S.D. Mayor. The high resolution Doppler lidar: Boundary-layer measurements, applications and performance. Proceedings, 9th Conference on Coherent Laser Radar, Linköping, Sweden, June 23-27 June 1997, FOA Defense Research Establishment.
- Mayor S.D., D. L. Lenschow, R. L. Schwiesow, J. Mann, C. L. Frush, M. K. Simon, 1997, Validation of NCAR 10.6- μ m Doppler lidar radial velocity measurements and comparison with a 915-MHz profiler. *J. Atmos. Oceanic Technol.*, **14**, 1110-1126.
- Frehlich, R., 1997, Effects of wind turbulence on coherent Doppler lidar performance. *J. Atmos. Oceanic Technol.*, **14**, 54-75.
- Frehlich R., S.M. Hannon, S.W. Henderson, 1998, Coherent Doppler lidar measurements of wind field statistics. *Boundary-Layer Meteorol.*, **86**, 233-256.

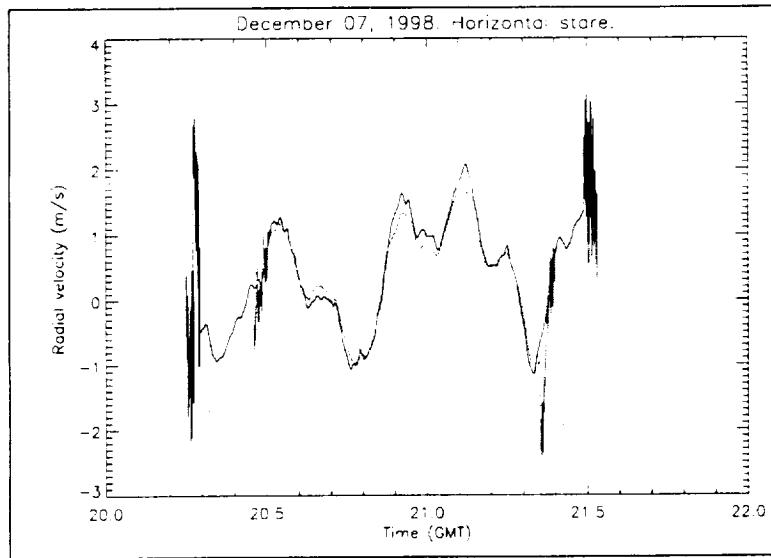


Figure 1 : Five-minute running average of sonic anemometer (solid line) and mini-MOPA radial velocities.

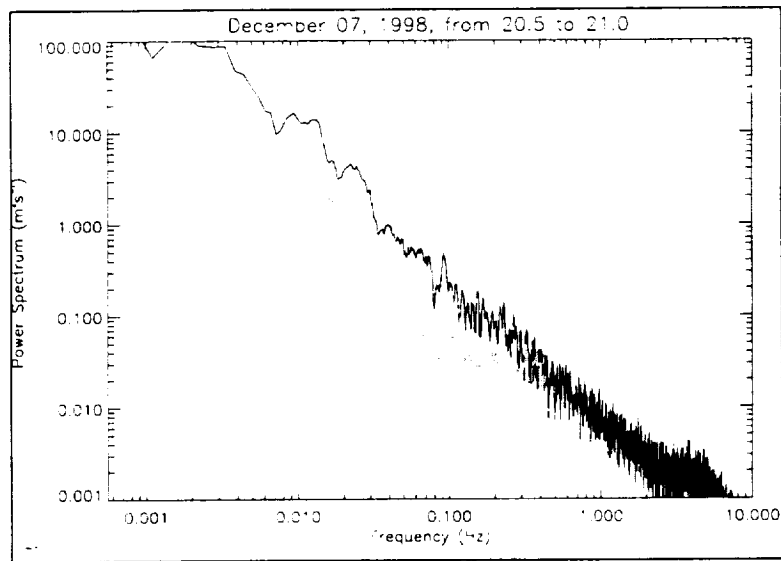


Figure 2 : Power spectra of sonic anemometer radial velocity (solid line) and lidar velocities (light line) at range 750m (the range of the sonic anemometer). The attenuation of lidar power densities is due to pulse-averaging. The light horizontal solid line is the error level.

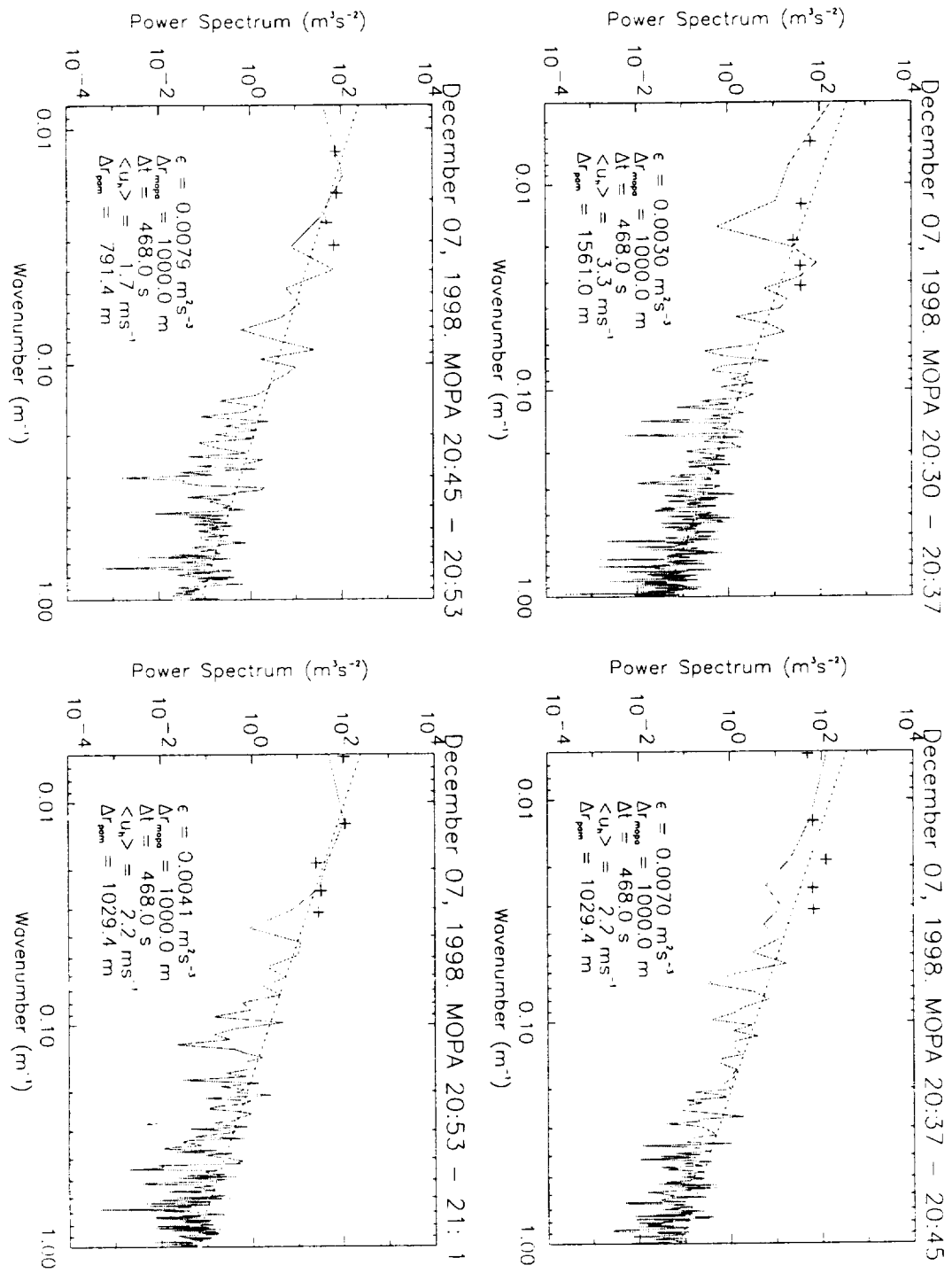


Figure 3 : Spectra of the range-variations of lidar velocities (symbols +) over the range interval [500m;1500m] obtained over 4 consecutive 7-minute time intervals. The light solid lines are the spectra of sonic anemometer data over the same time intervals. The dotted line is the best $-5/3$ power-law fit of lidar densities. It turns out to be a good fit to sonic anemometer spectra, and so produces a useful estimate for the dissipative rate of turbulence (parameter ϵ).

ABSTRACT

The Prediction of the Doppler Measurement Accuracy Using a Priori Information About the Turbulent Atmosphere

Alexander P. Shelekhov, Alexei L. Afanas'ev, Institute of Atmospheric Optics, SB Russian Academy Science, Russian Federation

The accuracy of the Doppler frequency measurement of the parameters of the turbulent atmosphere is studied for the cases of the stable, unstable, and indifferent stratification. The theoretical prediction of the Doppler measurement accuracy is based on the turbulent atmosphere models of Kaimal and Palmer.

SPACEBORNE LIDARS - 2

Presiders: Kasuhiro Asai and David Willetts

SPARCLE Optical System Design and Operational Characteristics

Farzin Amzajerdian, Bruce R. Peters, Ye Li, Timothy S. Blackwell, and Patrick Reardon
Center for Applied Optics
The University of Alabama in Huntsville
Huntsville, AL 35899

Phone: (205) 890-6030, Fax: (205) 890-6618, E-mail: farzin.a@msfc.nasa.gov

INTRODUCTION

The SPACe Readiness Coherent Lidar Experiment (SPARCLE) is the first demonstration of a coherent Doppler wind lidar in space. SPARCLE will be flown aboard a space shuttle in the middle part of 2001 as a stepping stone towards the development and deployment of a long-life-time operational instrument in the later part of next decade. SPARCLE is an ambitious project that is intended to evaluate the suitability of coherent lidar for wind measurements, demonstrate the maturity of the technology for space application, and provide a useable data set for model development and validation. This paper describes the SPARCLE's optical system design, fabrication methods, assembly and alignment techniques, and its anticipated operational characteristics.

Coherent detection is highly sensitive to aberrations in the signal phase front, and to relative alignment between the signal and the local oscillator beams. Consequently, the performance of coherent lidars is usually limited by the optical quality of the transmitter/receiver optical system. For SPARCLE having a relatively large aperture (25 cm) and a very long operating range (400 km), compared to the previously developed 2-micron coherent lidars, the optical performance requirements are even more stringent. In addition with stringent performance requirements, the physical and environment constraints associated with this instrument further challenge the limit of optical fabrication technologies.

DESCRIPTION OF OPTICAL SYSTEM

The functions of the optical system include expanding the laser beam, directing it to the atmosphere in a conical scan pattern, receiving the backscattered radiation, while maintaining a highly accurate pointing to ensure adequate extraction of the Doppler frequency shift due to the spacecraft and earth rotation velocities. The optical system consists of a beam expanding telescope, an optical wedge scanner, and an optical window used for environmentally isolating the lidar instrument. Figure 1 provides an optical schematic showing various optical components. As shown in this figure, two mirror assemblies are used for providing the proper alignment between the lidar transceiver and the telescope. The telescope expands the transmitter beam by 25X and directs it to an optical wedge that deflects the beam by 30 degrees. The wedge is rotated by a precision motor/encoder assembly in a step-stare fashion, to provide a conical pattern in the atmosphere. Compared with continuous scanning, step-stare scanning provides a greater operational flexibility, by allowing different scan patterns and laser shot accumulation. Step-stare scanning also eliminates the need for a dynamic lag angle compensator for correcting the signal misalignment due to the continuous motion of the scanner, thus reducing the complexity and cost of the instrument's optical system. The scanner wedge is then followed by a high optical quality window that provides the lidar optical interface with space. The optical window is made of fused silica with a rugged anti-reflection coating for efficiently transmitting 2-micron wavelength radiation. Both the transmitted beam and the backscattered laser radiation from the atmosphere follow the same path to the lidar transceiver.

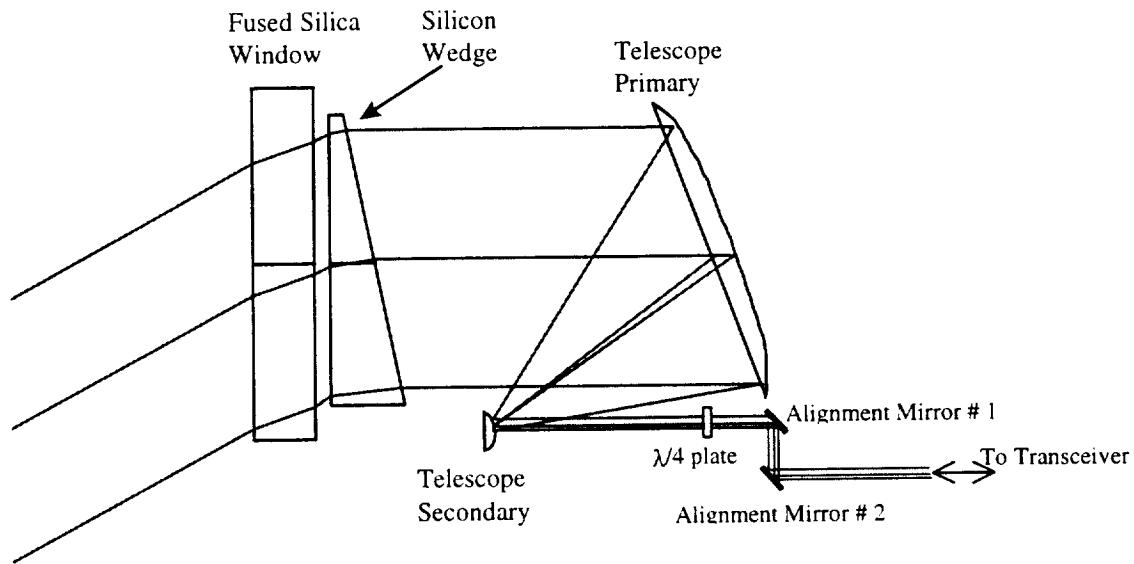


Figure 1. Optical System Schematic

The optical system along with the transceiver system will be housed in a pressurized Hitchhiker canister. The performance, physical and environmental specifications of the optical system are summarized in the table below.

Table 1. SPARCLE System Parameters

Clear Aperture Diameter	22.6 cm
Beam Expansion Ratio	25:1
Scan Angle (half angle)	30 degrees
Field Of View	80 μ rad
Maximum Conical Scan Rate	45 degrees/sec
Wavefront Quality	1/10 wave RMS
Optical Transmission	64%
Polarization	Less than 10% ellipticity
Beam Pointing Stability	4 μ rad/3 msec
Beam Pointing Error	28 μ rad in nadir and azimuth
Maximum Permitted Envelope	38 (dia.) x 43 (height) cm
Survivability Temperature	-40°C to 60°C
Operating Temperature	0°C to 25°C
Internal Pressure	0.5 atm

BEAM EXPANDING TELESCOPE

The telescope design is based on an earlier system that was designed and built to address the major design issues associated with a space-based coherent lidar such as size, mass, wavefront quality, polarization purity, and very low optical backscatter¹⁻³. By utilizing the lessons learned from the alignment and characterization of the first telescope, the optical and opto-mechanical designs were modified to further improve its robustness and to better comply with the specific environmental constraints associated with

SPARCLE mission.. The design changes also address the issues concerning the telescope assembly procedures and its integration with the lidar transceiver. For the most part, the design improvements take advantage of relaxed telescope constraints resulting from the selection of step-stare scanning over continuous scanning. The step-stare scanning reduced the telescope required field-of-view from 3 mrad to 40 μ rad and eliminated the need for a back-relief space that would have been necessary for accommodating the signal beam derotator and misalignment angle compensator. These changes in the requirements allowed for the elimination of the telescope refractive lens which in turn allowed for the use a smaller secondary mirror and lighter support structure.

The telescope consists of two off-axis parabolic mirrors in a Mersenne configuration as shown in figure 2. The off-axis configuration eliminates any central obscuration which will degrade beam quality due to diffraction effects. This configuration also reduces direct backscattering into the lidar system receiver optical path. The size and mass constraints for any space-based coherent lidar dictate that the system be considerably more compact than conventional configurations. The telescope fits within an envelope with dimensions 38X32X33 cm and weighs about 20 kg. To achieve such a compact package, a fast optical design was employed which led to more stringent fabrication and alignment tolerances⁴. To maintain the critical relative alignment between the primary and secondary mirrors over a relatively large operational temperature range and eliminate any misalignment due to differential thermal expansion, the telescope mirrors and its support structure are all made of the same aluminum material. This telescope system is considered athermal since the changes in the optical properties of the mirrors (radius of curvature, thickness, etc.) with temperature are perfectly balanced by the expansion or contraction of the structural supports such that the system maintains its alignment.

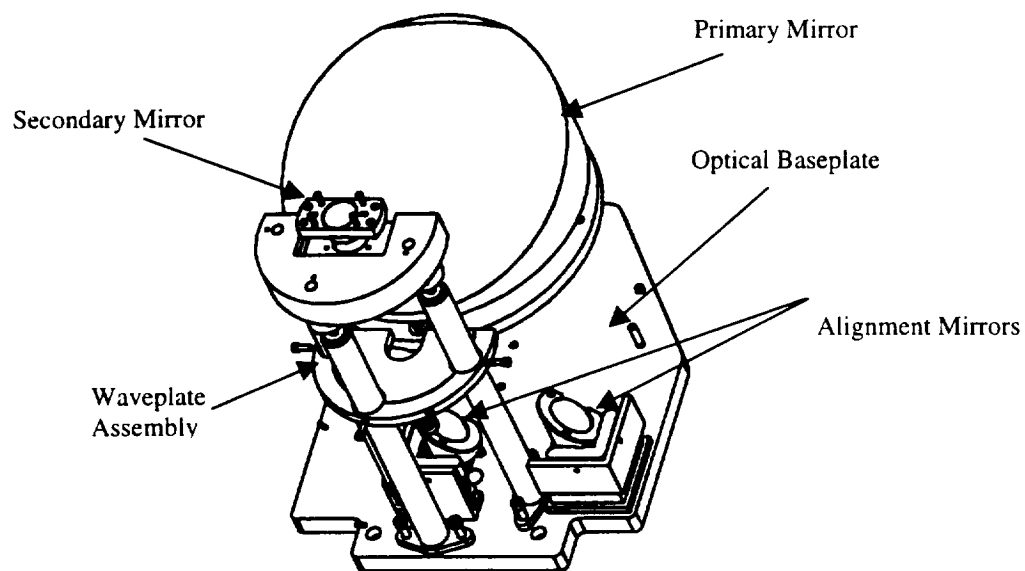


Figure 2. Beam Expanding Telescope

To achieve a minimum acceptable performance from the telescope, a high level of surface figure accuracy on the mirrors must be achieved. Selection of aluminum for the mirror base material coupled with the aspheric surface geometry required of the mirrors has necessitated using high precision single point diamond turning fabrication techniques. However, the level of surface roughness that can be obtained from a diamond turned surface is too high for coherent lidar application that requires a very low scattering and back-reflection by the optics. Therefore, the mirrors are plated by a thin layer of nickel, using an

electroless plating technique, before finish diamond machining. The nickel-plated mirrors are then post-polished to reduce their surface roughness to an acceptable level. Finally, the mirrors are coated with gold to achieve a high surface reflectivity approaching 99%.

OPTICAL WEDGE SCANNER

The lidar scanning is achieved by a 24.7 cm rotating silicon wedge that provides a 30 degree deflection angle. Selection of silicon as the wedge material was mainly driven by its many desirable optical and physical properties and the fact that sufficiently large silicon crystals with a single phase domain could be grown and polished. Because of the high index of refraction of silicon ($n=3.45$), the required deflection angle can be achieved by a relatively small wedge angle of 11.7 degrees which limits the mass of the wedge to about 4 kg. The optical wedge mass was one of the critical considerations, since it directly affects the power drawn by the scanner motor which results in more heat. One of the critical issues associated with the optical wedge that needed to be addressed was its sensitivity to the radial temperature profile that will be generated by the hot scanner motor and the wedge cold surroundings. Radial temperature variations in the wedge can produce a wavefront error due its non-symmetrical shape and its high dn/dT (change in index of refraction with temperature) value. To improve the thermal properties of the optical wedge, a multilayer coating is designed that can effectively reject any radiation in the solar and far-infrared regions of spectrum while efficiently transmitting the lidar beam at 2-micron wavelength. In this way, the wedge can be thermally decoupled from the surrounding environment, allowed to reach thermal equilibrium quicker, and thereby minimize the impact of dn/dT by reducing thermal gradients within the wedge.

OPTICAL WINDOW

The lidar instrument is environmentally isolated by a 5 cm thick, 32 cm diameter optical window made of fused silica. The main design considerations associated with the optical window are: (1) wavefront distortion due to the window substrate deformation under differential pressure condition in space; (2) depolarization due to stress-induced birefringence; (3) wavefront distortion due to any spatial temperature variation that may be present within the window material; and (4) Rejection of solar radiation for better thermal environment inside the canister. The optical window has a multilayer coating for high transmission at 2-micron wavelength and high reflection over the visible region of the spectrum.

This work was supported by NASA Marshall Space Flight Center through a cooperative agreement with The University of Alabama in Huntsville at the Center for Applied Optics.

REFERENCES

1. Feng, A. Ahmad and F. Amzajerjian, "Design and analysis of a spaceborne lidar telescope," Proc. SPIE Vol. 2540, pp. 68-77, 1995.
2. A. Ahmad, F. Amzajerjian, C. Feng and Y. Li, "Design and fabrication of a compact lidar telescope," Proc. SPIE Vol. 2832, pp. 34-42, 1996.
3. Li, Ye; Blackwell, Timothy S.; Geary, Joseph M.; Amzajerjian, Farzin; Spiers, Gary D.; Peters, Bruce R.; Chambers, Diana, "Characterization of an optical subsystem for 2-um coherent lidars," Proc. SPIE Vol. 3479, p. 122-123.
4. Peters, Bruce R.; Blackwell, Timothy S.; Li, Ye; Geary, Joseph M.; Amzajerjian, Farzin; Bailey, Deborah, "Optomechanical design of a multi-axis stage for the SPARCLE telescope," Proc. SPIE Vol. 3429, p. 48-55.

Optical Design and Analyses of SPARCLE Telescope

Ye Li, Farzin Amzajerjian, Bruce Peters, Tim Blackwell, Pat Reardon
Center for Applied Optics
University of Alabama in Huntsville
Huntsville, AL 35899
Phone: (205) 890-6030, Fax: (205) 890-6618, E-mail: liy@email.uah.edu

1. Introduction

NASA SPace Readiness Coherent Lidar Experiment (SPARCLE) is a technology demonstration on the space shuttle for space-based Doppler coherent lidar atmospheric wind velocity measurement [1]. The optical telescope system includes a 25cm off-axis beam expanding telescope, a 25-cm silicon wedge scanner, and a 32-cm Fused Silica optical window. The 2.0 microns wavelength laser source is expanded with this optical system at a power of 25x and transmitted to the atmosphere at a conical scanning angle of 30 degrees. The optical system also serves as receiver for the back scattered radiation signal from the atmosphere.

Coherent laser radar records information about the phase of the back-scattered radiation with respect to a local reference or local oscillator. The phase of the light contains information about the Doppler shifted mean frequency, frequency spectrum, and polarization of the photons. The wind velocity information, which is the main interest of SPARCLE, is encoded in the mean frequency. The signal-to-noise ratio of coherent lidar system is very sensitive to the optical performance of the transmitting and receiving beams. The major design issues for coherent detection lidar are the wavefront quality, polarization purity, and a minimum backscattering from the optical surfaces. Eliminating optical degradations from thermal effects on the mechanical structure and the optical components is also critical for the space-based coherent lidar system. In order to obtain a diffraction limited optical system, the optical fabrication technologies and tolerances, optical testing capabilities, and alignment sensitivities have to all be considered in the design phase to make sure that the optical system can be physically produced.

The SPARCLE telescope system was designed based on lessons learned from the prototype telescope[2], and employing state-of-the art optical fabrication technologies. These technologies include: utilizing the Large Optics Diamond Turning Machine (LODTM) at Lawrence Livermore National Lab for the primary mirror fabrication, primary mirror post polishing at Space Optics Research Labs (SORL), Laser gold plating of the mirrors at Epner Technology, optical window and silicon wedge multi-layer coatings for high transmission at 2-micron and high reflection of solar and IR radiation at Diversified Optical Products Inc..

2. Optical Design

2.1 Beam Expanding Telescope

The volume of the optical canister on the space shuttle and the step-stare scanning technique used by SPARCLE constrained us to choose a two paraboloid afocal Mersenne configuration as the beam expanding telescope. The off-axis beam expander was selected to eliminate the central obscuration and back scattering of an on-axis system which would degrade the heterodyne mixing efficiency and signal to noise ratio. The all reflective optical components can be built with the same aluminum alloy as the mechanical structures eliminate differential thermal expansion due to different materials.

The diffraction limited beam expander was designed and modeled by using ZEMAX optical software and verified by using SYNOPSIS optical software with a full field of view of 80 micro-radians, angular magnification of 25x, and a primary mirror aperture of 25 cm. The optical spacing between the primary and secondary mirror is 22.5 cm with a primary mirror operating at F#/0.9 and a de-center of 15 cm. The optical 3D layout is shown in Figure 1. In addition, a small optical flat with a width of 7 mm was designed on the outer radial edge of the primary mirror as a reference for optical fabrication, testing and system integration. The secondary mirror has a physical aperture of 3 cm with a symmetric shape to ease the optical fabrication and optical alignment stage. A portion of the mirror at 6 mm off-axis is used for delivering the laser beam. The backside of the secondary mirror was designed to have an optical flat

surface of 2.5cm diameter on the central area for telescope alignment and integration using a ZYGO interferometer.

2.2 Optical Wedge and Optical Window

The wedge scanner in SPARCLE telescope system is required for deflecting the expanded and collimated laser beam to a conical angle of 30 degrees. Several materials have been investigated based on their indexes of refraction, optical properties, and thermal properties. Single crystal silicon at optical window grade was the best choice of material for the wedge scanner. The wedge angle of 11.7 degrees for silicon with an index of refraction of 3.45 at a wavelength of 2.0 microns was calculated for the scanning angle of 30 degrees. The physical diameter of 24.8cm of the wedge was decided based on the bolt circle for mounting of the wedge holder to the scanner. The optical clear aperture is 22.6cm in diameter, which is the entrance pupil for the receiving optical system. The surface figure for both wedge surfaces need to be better than 1/6 waves peak to valley at 0.633 micron wavelength, which will provide a 1/30 wave RMS transmitted wavefront accuracy. The wedge will produce a transmission of better than 93% for the operating wavelength with a circular polarization maintained at better than a 95% ratio of minor and major axes of the polarization states.

Fused silica material has been selected as the optical window material for the Hitchhiker canister because of its high index homogeneity, high transmission in IR, low thermal expansion and thermal optical coefficient, and excellent mechanical properties. The optical window for SPARCLE serves as the interface between the pressurized optical canister and the outside vacuum. The half atmosphere pressure of dry nitrogen inside the canister could deform the flat window consequently degrade the optical wavefront quality. The window thickness of 5 cm was decided by simulating the window deformation curve with high order even aspheric surfaces in the ZEMAX model and analyzing the optical performance with the criterion of diffraction limited performance. The surface figure for both surfaces of the window will be fabricated in 1/6 wave peak to valley at 0.633 microns. Then the transmissive wavefront will be about 1/30 wave RMS at 2.0 microns. The total transmission will be approximately 90% with application of an anti-reflection coating at 2.0 microns.

3. Optical Analyses

3.1 Optical performance

A Zemax optical design model was set up to send a bundle of geometrical rays from infinity through the pressurized fused silicon window, silicon wedge, and the confocal parabola telescope from infinity at a deflection angle of 30 degrees with a full field of view of 80 micro-radians. The spot size was obtained by using an ideal lens to focus the collimated output rays down to a point. The focussed spot was contained within the diffraction limited Airy disc with the Strehl ratio of 93% and the RMS wavefront error of 1/25 wave at the operating wavelength. The optical performance is also shown in the Figure 1.

3.2 Tolerance and Sensitivity

Tolerance and sensitivity analysis is very important to build a working optical system. Parametric sensitivity and tolerance of the telescope have been analyzed to determine its optical performance for the fabrication and assembly.

3.2.1 Fabrication and Assembly Tolerances

The analyses assume a fixed focal point in space. However, the accepted focal point is surround by a volumetric tolerance.

Conic constant of primary mirror:	+/- 0.0003
Conic constant of secondary mirror:	+/- 0.001
Radius curvature of primary mirror:	+/- 10.0 μm
Radius curvature of secondary mirror:	+/- 5.0 μm
Total irregularity of each mirror:	0.5 fringes
y - tilt of primary mirror:	0.01 $^\circ$ (170 μrad)
x - tilt of primary mirror:	0.01 $^\circ$
x and y de-center of primary mirror:	10 μm

3.2.2 Secondary mirror alignment ranges and sensitivities

Secondary mirror is used as a compensator with 5 DOF. The criteria of optical performance was set to be 1/20 wave RMS wavefront error.

z - translation:	10 μm with resolution of 1.0 μm
x - de-center:	40 μm with resolution of 1.0 μm
y - de-center:	65 μm with resolution of 1.0 μm
x - tilt:	0.05 $^\circ$ with resolution of 0.001 $^\circ$
y - tilt:	0.05 $^\circ$ with resolution of 0.001 $^\circ$
z - tilt:	not needed due to the symmetry of the secondary mirror

3.2.3 Instability tolerances

To meet 0.05 waves RMS wavefront quality (Final required wavefront quality is 0.07 waves), the aligned telescope need to be stable within the following tolerances.

Mirrors spacing:	4.2 μm
x - de-center:	8.2 μm
y - de-center:	5.5 μm
x - tilt:	0.0013 $^\circ$ (22 μrad)
y - tilt:	0.002 $^\circ$ (35 μrad)
Radius curvature of pri. mir.:	8.5 μm
Conic constant of pri. mir.:	1.2 μm
Radius curvature of sec. mir.:	8.5 μm
Conic constant of pri. mir.:	3.0 μm

3.3 Thermal Analyses

The thermal effect has to be considered for any optical system used in space or any severe environment. Two thermal issues could affect the optical performance to the system. One is the thermal soak since the working temperature range for the telescope is from 0 to 25 $^\circ\text{C}$. Another one is the thermal gradient between or within the optical components. Both thermal issues were analyzed and considered in the optical and opto-mechanical designs [3].

3.3.1 Telescope operation over 0 to 25 $^\circ\text{C}$ soak temperatures

Since mirrors and structure made of the same material of aluminum alloy 6061-T6 with TCE (Thermal Coefficient of Expansion) of $23.5 \times 10^{-6} / ^\circ\text{C}$, the radius of curvature and spacing of the mirrors change simultaneously with the temperature. The analyses showed that as the temperature varies from 0 to 25 $^\circ\text{C}$, the change in the primary mirror radius of curvature is compensated by the changes in the mirror spacing and the secondary mirror radius of curvature. As a result, the telescope maintains its optical quality over its specified operational temperature range.

The effects of soak temperature variations on the optical wedge and window performance are also shown to be negligible, except for beam pointing angle. Due to the variation of the index of refraction with temperature, the optical wedge will introduce as much as 45 micro-radians/ $^\circ\text{C}$ changes in the beam pointing direction [3].

3.3.2 Telescope thermal gradient analyses

Physical mirror spacing changes due to temperature gradients existing within the beam expander support structure and mirrors were analyzed at different operating temperatures. It was shown that the telescope could tolerate up to 2 $^\circ\text{C}$ of steady state temperature gradients. During operation in space, the temperature gradients within the telescope assembly are not expected to exceed 1.5 $^\circ\text{C}$.

4. Optical Fabrication

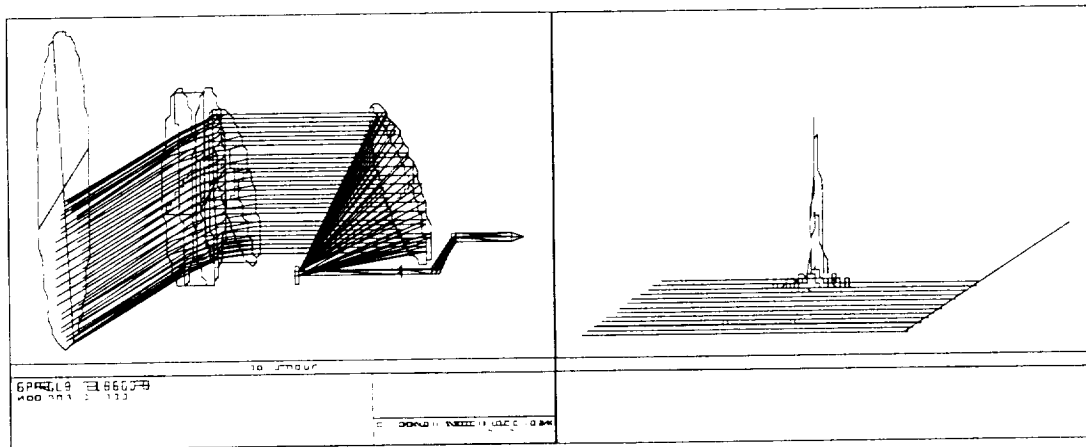
The beam expanding telescope mirrors and support structure are made of the same aluminum material providing for an athermal design. The telescope mirrors were fabricated using precision diamond turning technology. The mirrors were first diamond turned to within one wave of the desirable figure and then nickel plated before final diamond turning. The diamond turning of the primary mirror was performed at DTM3 and LODTM facilities at Lawrence Livermore National Laboratory and the secondary mirror was diamond turned at the Center for Applied Optics/UAH. A surface figure accuracy of 1/4 wave peak to

valley at HeNe wavelength and a surface finish of about 150 angstroms RMS were achieved for each mirror. Post-polishing the mirrors is expected to achieve a surface finish of better than 25 angstroms and a final surface figure of about 1/6 wave P-V at HeNe. The polished mirrors will be plated with high purity of gold to increase the reflectivity to 98.5% at 2.0 microns wavelength.

High purity Fused Silica and single crystal silicon will be used to fabricate the optical window and optical wedge scanner at DIOP. The optical surfaces will be polished to a figure accuracy of 1/6 wave peak to valley at HeNe. Due to thermal gradient effects on the window and wedge, a special coating will be applied to increase solar reflection and reduce mid-IR radiation transfer between the optical components. The coatings are also required to have better than 90% transmission at 2.0 wavelength and maintain circular polarization to within 10%.

References:

1. M. J. Kavaya, G.D. Emmitt, "The Space Readiness Coherent Lidar Experiment (SPARCLE) Space Shuttle Mission." Proc. SPIE Vol. 3380, Conference on Laser Radar Technology and application III, 12th Annual International Symposium on Aerospace/Defense Sensing, Simulation, and Controls, AeroSense, Orlando, FL, 1998.
2. A. Ahmad, C. Feng, F. Amzajerdian, Y. Li "Design and Fabrication of a Compact LIDAR Telescope", Proc. SPIE Vol. 2832, Denver, CO August 4-9, 1996.
3. P.J. Reardon, B.R. Peters, F. Amzajerdian, "Thermal Considerations for the SPARCLE Optical System," SPIE Proc. 3707, Orlando, FL., April 6-9, 1999.



A program of an ISS/JEM (Japanese Experiment Module)- borne Coherent Doppler Lidar

Toshikazu Itabe, Kohei Mizutani, Mitsuo Ishizu# and Kazuhiro Asai*

Communications Research Laboratory
Ministry of Posts and Telecommunications
Nukui-kita, 4-2-1, Koganei, Tokyo 184-8795, JAPAN
Tel:+81-42-327-7546, Fac:+81-42-3276692
E-mail : itabe@crl.go.jp,mizutani@crl.go.jp

Electronic and Information Technology Lab.
Office of Research and Development
NASDA
2-1-1,Sengen,Tsukuba, Ibaragi, 305-0047, JAPAN
E-mail : Ishizu.Mitsuo@nasda.go.jp

*Tohoku Institutes of Technology
Yagiyama Kasumi 35-1 , Taihaku-Ku, Sendai 982-. JAPAN
E-mail : asai@titan.tohtech.ac.jp

1. Introduction

Global wind measurement, more precisely speaking global horizontal wind, is crucially important for both Numerical Weather Prediction and studies on the global climate. Temperature and humidity profiles and surface pressure in addition to the wind profile are needed for the initial state condition for the Numerical Weather Prediction and the global climate model. The wind profiles are now available only from a global network of radio sonde observations at the ground. Very little information about the vertical profiles of the horizontal wind field is available from the ocean, in the tropics and in the Southern Hemisphere. If the present data deficiency of the global wind could be solved, the Numerical Weather Prediction and the global climate model will be improved dramatically. Now, global measurement of the wind profile in the troposphere can be realized only with the Doppler lidar in space.

A program of Japan for development of the coherent Doppler lidar in space was started by Communications Research Laboratories (CRL) from 1997 FY under the support of the Phase II study of Ground Research Announcement of NASDA and Japan Space Forum. Objective of the program is to make a feasibility study of the coherent Doppler lidar for Japanese Exposure Module (JEM) of the International Space Station. The coherent Doppler lidar will be design to install in a standard EF(Exposed Facility) payload of ISS/JEM and the mission of the lidar is made a demonstration of the wind measurements form space. The ISS/JEM-borne coherent Doppler lidar (JEM/CDL) can measure line-of-sight (LOS) winds in the troposphere from space in the accuracy of 1-2 m/s in the vertical resolution of about 1 km and the horizontal resolution 100km x100km

There are two methods to measure the atmospheric wind with the Doppler lidar from space. One of them is a coherent Doppler and another an incoherent one. Size of the incoherent Doppler lidar is not suitable for the ISS/JEM. We consider the coherent Doppler one as only one candidate for ISS/JEM.

2. A Coherent Doppler Lidar for ISS/JEM

ISS/JEM-CDL will be packed in one of standard payloads of the JEM-EF (Exposed Facility), which is 1850 x 1000 x 800. JEM/CDL is now under the feasibility study. Present parameters of the coherent Doppler lidar are shown in table 1.

Table 1 Parameters of ISS/JEM-borne CDL

Transmitting Laser	Tm.Ho:YLF (λ :2.06 μ m), Osc.-Amp. Laser
Output	2 Joule
Repetition	10pps

Wall-plug efficiency over 2% (Electrical-optical efficiency)

Transmitting Telescope off-axis Diameter 40cm

Scanning Step Scanning
under study of two methods

1)	Si-wedge scanner
with one telescope	
2)	side-scanning with
two telescopes	

Scanning method will be selected one of them. The Si-wedge scanner is the same one of the SPARCLE of NASA. The side-scanning is used two telescopes. One of the telescopes of the side-scanning will be installed to look forward at the angle of 60 degrees from the direction of ISS movement and another to look backward at the same angle. The both telescopes will be step-swunged from 6 degrees to 30 degrees around the direction of ISS movement. Now, trade-off study is under way.

LOS wind error is estimated by using an equation of the poly-pulse pair algorithm (Zrnic,1979, Kane, 1984). The lidar parameters shown in table 1 and total optical efficiency including the heterodyne efficiency is assumed as 0.04. The following aerosol height profiles is used in the studies of the LOS wind error of JEM/CDL.

Table 2 aerosol height profile $\beta(z)$ for the studies the LOS wind error

Height	aerosol height profile $\beta(z)$
0_2 km	$2 \times 10^{-8} (1/m/str)$
2_5 km	$1 \times 10^{-8} (1/m/str)$
5_12 km	$8 \times 10^{-9} (1/m/str)$

Results of the LOS wind error estimation will be described at the conference.

The following key technologies in addition to a conceptual design of the lidar of JEM will be described also at the conference in some detail.

- (1) 2 μ m Tm:Ho:YLF laser with 2 joule 10Hz slaved by a frequency stabilized CW laser.
- (2) scanning mechanism with 40cm diameter telescope.
- (3) a coherent detection system, which can compensate Doppler shift due to spacecraft velocity.

3. Concluding remarks

A program of Japan for development of the coherent Doppler lidar in space was started by CRL from 1997 FY under the support of the Phase II studies of the Ground Research Announcement of NASDA. Objective of the program is to make a feasibility study on the coherent Doppler lidar for the Japanese Exposure Module (JEM) of the International Space Station (ISS). The ISS/JEM-borne coherent Doppler lidar can measure tropospheric LOS winds from space in an accuracy to 1-2 m/s of the vertical resolution of about 1 km and the horizontal resolution 100kmx100km. Results of the feasibility study will be used for a proposal of 2ed JEM mission.

References

- Kane T. J., B. Zhou and R. L. Byer, 1984, Potential for coherent Doppler wind velocity lidar using neodymium laser, Appl. Opt., 31, 4202-4213.
- Zrnic D. S., 1979, Estimation of spectral moments for weather echoes, IEEE Trans. Geosci. Electron., GE-17, 113-128.

ALADIN Impact Study

Christian Werner, Werner Wergen, Alexander Cress, Victor Banakh , Igor Smalikho, Ines Leike and Juergen Streicher

1. Introduction

The weather services use all kind of wind data for their forecast models: Single level data from ground observations and from aircrafts in the flight level, wind profiles from radiosondes and wind profilers. The quality test of these data is necessary and this requires an accuracy of the wind information in the order of 2 m/s. Therefore the lidar has to produce nearly defendable data.

The block diagram of the impact study is shown in figure 1.

Three partners work on the study, the German Weather Service DWD, DLR with the Lidar Group and the Institute of Atmospheric Optics (IAO) with the turbulence group. DWD creates a global data set for a wind forecast. This data set is transferred to DLR and can be read by the Macintosh Power PC into the LabView software package. DLR transfers this data set also to IAO for turbulence calculation.

Beside this DWD starts an analysis of sensitive areas for the forecast, the so called targeted observation.

DLR is doing the virtual instrument signal simulation starting with the dynamics of the observation, an instrument which is close to the real Doppler lidar and the atmospheric conditions provided by the DWD. This data set is modified with turbulence and should be given back to DWD for an assimilation.

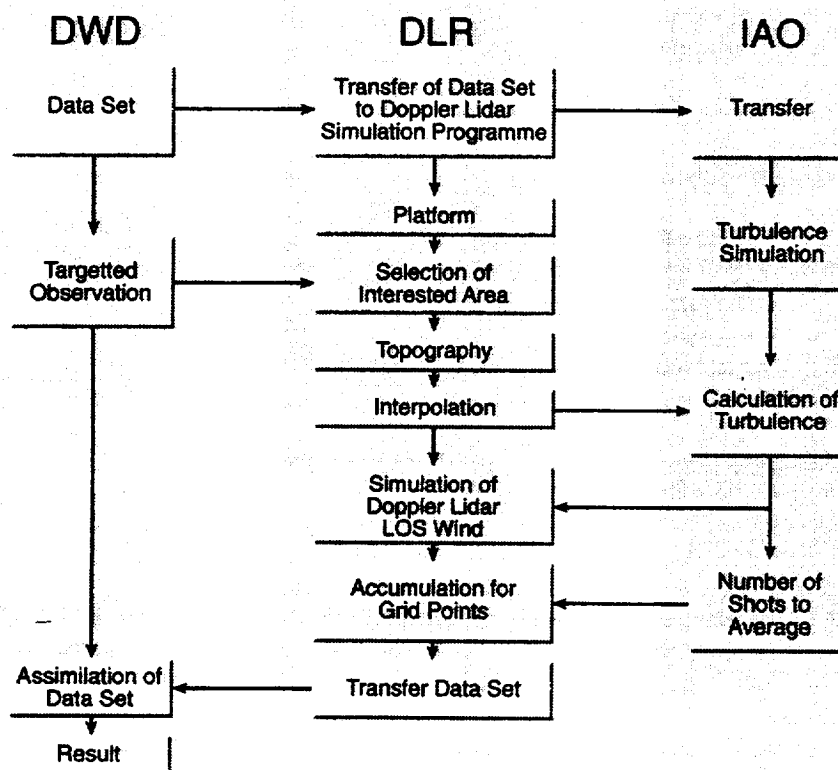


Figure 1 Block diagram of the work packages of the impact study

2 Virtual Sensor

A virtual sensor and its environment can be tested directly and can therefore be optimised without hardware development. For this study the sensor was placed on a space station orbit and was flying over the wind field (vertical profile of horizontal wind for every 200 km grid point) with the sensor parameters chosen. By accumulating many shots per grid point depending on the pulse repetition rate of the sensor, the data for one grid point to be delivered to the weather service are shown in figure 2. For this simulation a 15 J CO₂-laser was used (6 Hz, Telescope diameter 1 m, 57 shots accumulated).

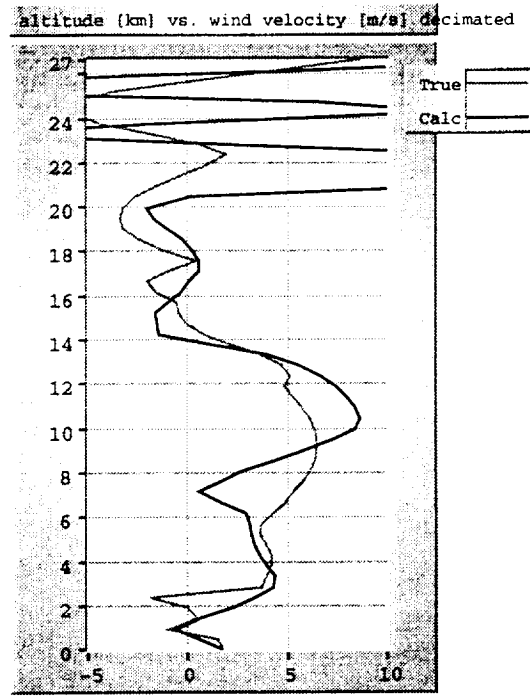


Figure 2 LOS components as a result of the simulation

The true value is the input profile (LOS component) and this is compared with the calculated one based on the ESA ALADIN sensor concept. The accuracy of the wind LOS is within 2 m/s in the atmosphere below 20 km. DWD selected the following time period (Jan 19, 1998 12Z - Jan 30, 1998, 12Z) and presented all wind profiles with additional data (clouds, temp., humidity, diffusion coefficients) to DLR. DLR selected a Space-Station as platform and could select different tracks of the platform. DLR and IAO calculated the LOS wind with turbulence influence for the North-American region. The sensor is pointed 30 degree Nadir and 45 degree in forward flight direction. This is a non scanning system concept.

If one uses all these LOS-informations available for the track and put these information in a color code so that wind from the laser gives red color and wind against the laser gives blue color, figure 3 shows the result.

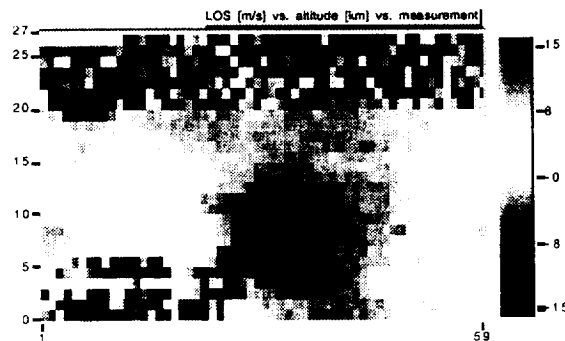


Figure 3 LOS wind information for track 5 using the CO₂ Doppler lidar (19.01.98 track 5: 14 Z)

3. Estimating the impact of lidar-winds on Numerical Weather Prediction

In order to estimate the potential benefit of the additional LOS lidar windprofiles on the numerical weather forecasts, an impact study was initiated. It consists of two parts. In the first study, the importance of wind profile data in general was assessed. In the second part, the impact of the additional lidar-winds will be estimated.

Role of wind observations

The basic prognostic variables of current Numerical Weather Prediction (NWP) models are geopotential, humidity and wind. In the extra-tropics, there exists a strong coupling between the geopotential and the wind field, the so-called geostrophic relation. It allows to derive approximate wind components from geopotential

gradients. It is therefore important to find out whether these geostrophic winds are sufficient or whether observed wind profiles result in a more realistic definition of the initial state for NWP. To answer this question, a parallel data assimilation with the Global-Model (GM) of DWD was performed in which the wind profile observations from radiosondes and aircraft over the United States and Canada were excluded. By comparing the forecast quality between the runs using or not using the wind data, an estimate of their importance can be given. By tracing back the differences in the forecasts to the initial difference, sensitive areas can be identified.

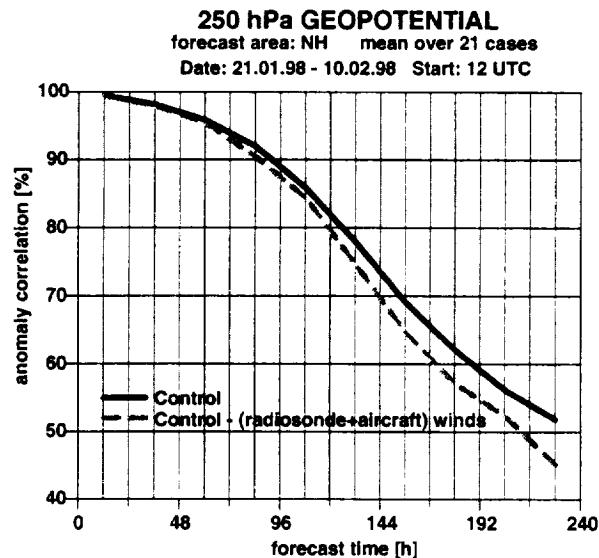


Figure 4 Anomaly correlation of the 250 hPa geopotential height field, averaged over 21 cases and for the area between 20° and 90°N as a function of forecast length. The full curve is for the control using all observations, dotted for experiments not using radiosonde and aircraft wind data over the US and Canada.

Fig. 4 shows the mean anomaly correlation for the 250 hPa geopotential, averaged between 20° and 90°N as a function of forecast length. Naturally, forecast quality deteriorates with forecast time and forecasts are usually considered of little value if the correlation falls below 60%. The control forecast (full) using all observations crosses the 60% line close to 192 hours into the prediction. By contrast, the forecasts not using wind profiles over the North American continent (dashed) crosses the 60% limit at 168 hours, thus resulting in a degradation of almost 24 hours in useable forecast length. This clearly highlights the importance of having wind observations for defining the initial state also in the extra-tropics.

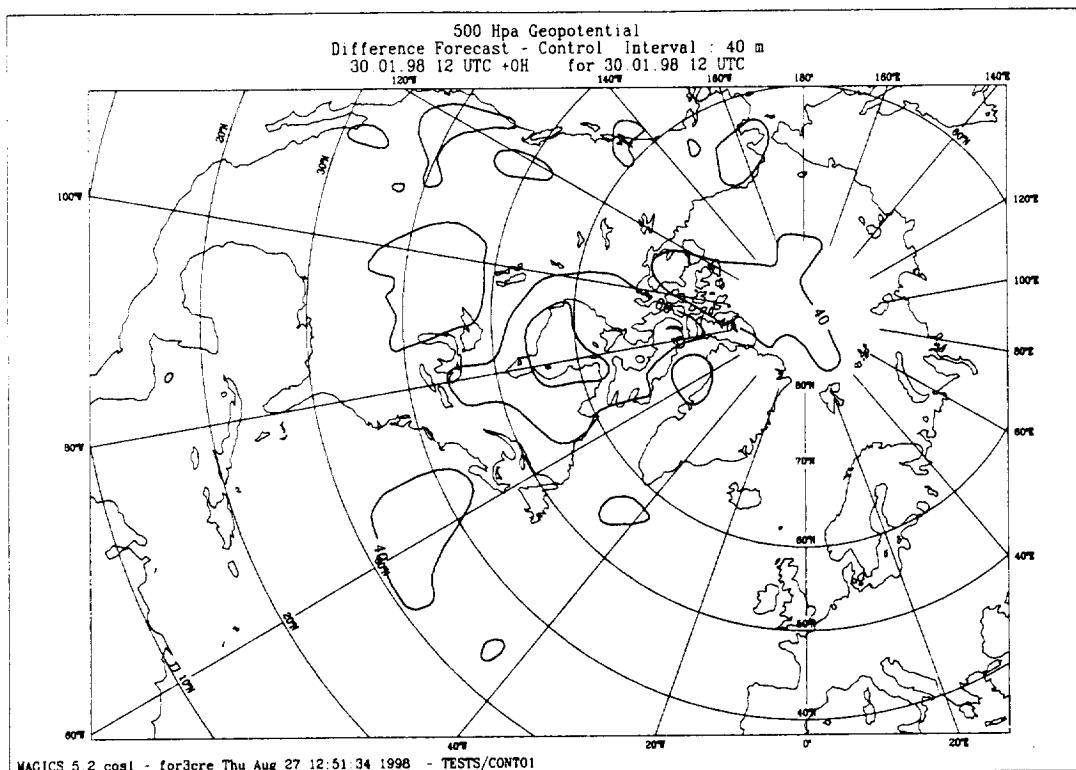


Figure 5 Initial difference for 12 UTC, 30 January 1998 in the 500 hPa geopotential height field between the assimilation using all data und the experiment not using radiosonde and aircraftwind data over the US and Canada.

Fig. 5 shows the differences in the initial states of a pair of forecasts started at 12 UTC on 30 January 1998, one was using all available observations and one was not using the wind profiles. The differences in the 500 hPa geopotential height field can mainly be found in higher latitudes with a maximum over the Hudson bay. This difference amplifies during the forecast and leads to a considerably less useful prediction over Europe for the case where the wind information from the US and Canada was missing. This result agrees well with classical theory which points to the higher latitudes as the most sensitive areas.

DLR - Lidar Group
P.O.Box 1116
D 82230 Wessling, Germany
Phone: 49 8153 282573
Fax: 49 8153 281608
e-mail: Christian.Werner@dlr.de

Deutscher Wetterdienst
FrankfurterStr. 135
63067 Offenbach
Phone: 49 69 80622713
Fax: 49 69 82361493
e-mail: wwergen@dwd.d400.de

Institute of Atmospheric Optics
Russian Academy of Sciences
1, Akademicheskii Avenue
Tomsk 634055, Russia
Phone 007 3822 258483
Fax: 007 3822 259086
e-mail: banakh@ldw.tomsk.su

Coherent Doppler Lidar Data Products from Space-Based Platforms

Rod Frehlich

Cooperative Institute for Research in the Environmental Sciences (CIRES)
University of Colorado, Campus Box 216, Boulder, CO 80309
Phone:303-492-6776 FAX:303-492-1149 Email:rgf@cires.colorado.edu

Introduction

Coherent Doppler lidar is a promising technique for the global measurements of winds using a space-based platform. Doppler lidar produces estimates of the radial component of the velocity vector averaged over the resolution volume of the measurement. Profiles of the horizontal vector winds are produced by scanning the lidar beam or stepping the lidar beam through a sequence of different angles (step-stare). The first design for space-based measurements proposed a conical scan which requires a high power laser to produce acceptable signal levels for every laser pulse. Performance is improved by fixing the laser beam and accumulating the signal from many lidar pulses for each range-gate [1, 2]. This also improves the spatial averaging of the wind estimates and reduces the threshold signal energy required for a good estimate. Coherent Doppler lidar performance for space-based operation is determined using computer simulations and including the wind variability over the measurement volume as well as the variations of the atmospheric aerosol backscatter.

Lidar Performance

The performance of Doppler lidar depends on the lidar parameters, the atmospheric conditions, and the velocity estimation algorithm. The transmitted pulse for a solid state lidar is well approximated as a Gaussian temporal power profile with a full width at half maximum (FWHM) pulse width Δt [1, 4]. The spectral width $w = 0.1874/\Delta t$ and the spectral width in velocity space $w_v = \lambda w/2$ where λ is the wavelength. The illuminated aerosol target region is a narrow pencil shaped volume that has a Gaussian intensity profile along the beam axis with a spatial width (FWHM) $\Delta r = \Delta t c/2$ where c is the speed of light in air. The line-of-sight range gate length $\Delta p = Tc/2$ is defined as the distance the illuminated

aerosol region travels during the data processing interval $T = MT_S$ where M is the number of complex lidar data points for each range-gate. For pulse accumulation, the along-track extent of the measurement volume $L = \Delta y N$ where N is the number of accumulated pulses and Δy is the horizontal separation between adjacent lidar pulses. The major instrumental error in the radial velocity is the frequency drift in the reference laser frequency (LO) which determines zero velocity. The effects of uncorrelated velocity error from pulse-to-pulse is included by adding a zero-mean Gaussian random velocity error with standard deviation σ_{vLO} to the zero velocity reference of each pulse. To simplify the analysis, we assume the lidar beam axis is perpendicular to the satellite track with a nadir angle θ where $\theta = 0$ is pointed to the center of the earth.

For a short range-gate located at range R and for constant aerosol backscatter coefficient $\beta(R)$, the magnitude of the Doppler lidar signal for one lidar pulse is defined by the parameter [1]

$$\Phi_1 = \frac{\eta_Q \beta(R) K(R)^2 c U_T A_R \eta_H T}{2h\nu R^2} \quad (1)$$

where η_Q is the detector quantum efficiency, $K(R)$ is the one way irradiance extinction, U_T is the transmitted laser pulse energy, A_R is the receiver area, η_H is the heterodyne efficiency, h is Planck's constant, and ν is the laser frequency. Φ_1 is the effective number of coherent photons detected per range-gate per pulse.

The Space Readiness Coherent Lidar Experiment (SPARCLE) is the first space mission to attempt coherent Doppler lidar wind measurements [5] For most experiments, the lidar beam will be fixed with a nadir angle of 30° and various azimuth angles.

The turbulent wind field over the resolution cell is described by the radial velocity fluctuations $v(y, z)$ where z is the distance along the lidar beam axis and

y is the horizontal distance defined by the satellite track. The mean radial velocity $V(y, z)$ includes a constant vector V_0 and a shear component v_{shr} . For stationary conditions, the radial velocity fluctuations $v(y, z)$ are described by the covariance function

$$C_v(y, z) = \langle v(y_0, z_0)v(y_0 + y, z_0 + z) \rangle \quad (2)$$

where z is the lag along the lidar beam axis and y is the lag along the horizontal direction. A simple model for the covariance function is

$$C_v(y, z) = \sigma_v^2 G(r/L_0) \quad (3)$$

where σ_v^2 is the variance of the radial velocity, r is the magnitude of the vector (y, z) , L_0 is the outer scale, and

$$G(x) = 0.5925485 x^{1/3} K_{1/3}(x) \quad (4)$$

is the Von Karman turbulence model where $K_{1/3}(x)$ is the modified Bessel function and the energy dissipation rate ϵ is

$$\epsilon = 0.933668 \sigma_v^3 / L_0. \quad (5)$$

An important aspect of measurements over a random wind field is the definition of the desired or true wind measurement v_{ave} which is required for the definition of error. For single pulse velocity estimates [6], v_{ave} is well approximated by the linear average of the radial velocity over the range-gate length Δp if the pulse volume Δr is less than the range-gate dimensions Δp . We extend this result to the two-dimensional space-based multi-pulse measurement, i.e.,

$$v_{ave} = \frac{1}{L_z L_y} \int_{y_0}^{y_0+L_y} \int_{z_0}^{z_0+L_z} v(y, z) dz dy \quad (6)$$

where $L_z = \Delta p$ and the average variability of the radial velocity over the measurement volume is

$$s_r^2 = \frac{1}{L_z L_y} \int_{y_0}^{y_0+L_y} \int_{z_0}^{z_0+L_z} \langle [v(y, z) - v_{ave}]^2 \rangle dz dy \quad (7)$$

which is the average squared difference between the velocity fluctuations $v(y, z)$ and the mean velocity v_{ave} .

For a lidar beam with nadir angle θ , the radial velocity $v(y, z)$ along the lidar beam axis consists of the projection of the horizontal velocity $h(y, z)$ and the vertical velocity $w(y, z)$, i.e.,

$$v(y, z) = h(y, z) \sin(\theta) + w(y, z) \cos(\theta). \quad (8)$$

Then Eq. (6) is

$$v_{ave} = h_{ave} \sin(\theta) + w_{ave} \cos(\theta) \quad (9)$$

where h_{ave} and w_{ave} are the linear average over the resolution cell of the horizontal and vertical velocity fluctuations, respectively. Assuming $h(y, z)$ and $w(y, z)$ are uncorrelated, the total wind variability is

$$s_t^2 = s_v^2 + s_{shr}^2 \quad (10)$$

where

$$s_v^2 = s_h^2 \sin^2(\theta) + s_w^2 \cos^2(\theta) \quad (11)$$

is the radial velocity component Eq.(7) and

$$s_{shr}^2 = v_{shr}^2 (\Delta p)^2 / 12 \quad (12)$$

is the shear component. For the wind field model of Eq. (3)

$$s_h^2 = 4\sigma_h^2 \int_0^1 \int_0^1 (1-t)(1-u) H(\sqrt{t^2 L_z^2 / L_{0h}^2 + u^2 L_y^2 / L_{0h}^2}) dt du \quad (13)$$

where σ_h^2 is the variance of the $h(y, z)$ and $H(x) = 1 - G(x)$. Similar results follow for s_w^2 .

A common approximation for the effects of wind turbulence is the effective Gaussian pulse with effective spectral width in velocity space w_{eff} given by

$$w_{eff}^2 = s_v^2 + s_{shr}^2 + w_v^2 + \sigma_{vLO}^2. \quad (14)$$

A real atmosphere also has random variations in the aerosol backscatter β which is assumed to have a log-normal distribution with mean $\langle \beta \rangle$ and standard deviation σ_β . The spatial distribution of β is approximately a Von Karman model [7] with an outer scale $L_{0\beta}$.

Doppler lidar data is generated using a Monte Carlo technique [6] with the random radial velocity $v(y, z)$. The variations in backscatter over the range-gate has a small effect on velocity estimator performance [8]. Shot to shot backscatter variability is added using simulations of aerosol backscatter $\beta(y)$. The N pulses of simulated data are processed with the Capon estimator using the accumulated signal covariance [1].

Results

The lidar parameters are chosen to match the SPARCLE lidar for boundary-layer measurements, i.e., $\lambda = 2.051 \mu\text{m}$, $\Delta t = 0.2 \mu\text{s}$, $\Delta r = 30.0 \text{ m}$,

$M = 32$, $\Delta p = 246.1$ m, $w_v = 0.961$ m/s, $T_s = 0.051275$ μ s, $v_{search} = 20.0$ m/s, $\sigma_{vLO} = 1.0$ m/s, and $\Delta y = 1.0$ km. The atmospheric parameters are chosen for a turbulent boundary layer to investigate a worst-case scenario, i.e., $\epsilon = 0.01$ m²/s³, $L_{0w} = 1.0$ km, $L_{0h} = 2.0$ km, $\sigma_w = 2.2043$ m/s, $\sigma_h = 2.7772$ m/s, $\sigma_v = 2.3606$ m/s, $L_{0\beta} = 0.5$ km, $v_{shr} = 10$ m/s/km. For $N = 10$ pulses per estimate, $L = 10$ km, $s_w = 2.0526$ m/s, $s_h = 2.4157$ m/s, $s_v = 2.4746$ m/s, $w_{veff} = 2.6546$ m/s. For $N = 100$ pulses per estimate, $L = 100$ km, $s_w = 2.1883$ m/s, $s_h = 2.7365$ m/s, $s_v = 2.6398$ m/s, and $w_{veff} = 2.8092$ m/s.

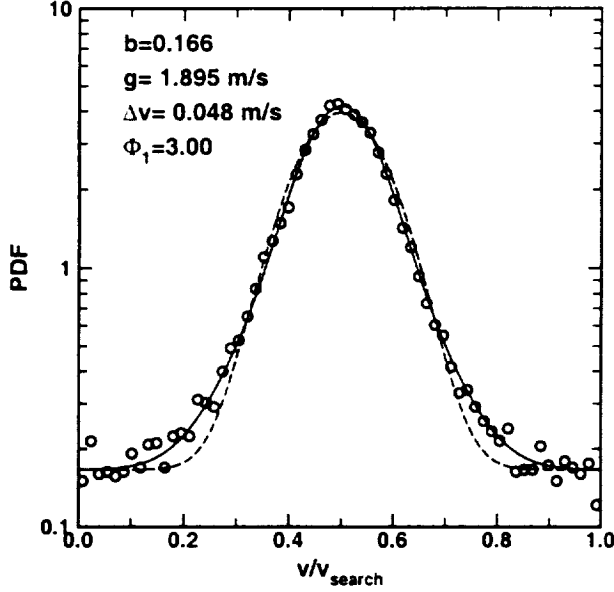


Fig. 1. Example Probability Density Function (PDF) (\circ) from 20,000 velocity estimates, $N = 10$ lidar pulses and $\Phi_1 = 3.0$. The best fit Gaussian model (---) and the best fit two component Gaussian model (—) are shown.

The performance of Doppler lidar estimates of the radial velocity v is described by the Probability Density Function (PDF). An important issue for space-based measurements is the performance of the velocity estimates in weak signal regimes where the PDF has a uniform distribution of random outliers and a localized distribution of good estimates with mean value v_g and standard deviation g . An example PDF for a weak signal regime is shown in Fig. 1. The bias Δv is

$$\Delta v = \langle v_{ave} - v_g \rangle. \quad (15)$$

The PDF's are well approximated by a Gaussian PDF (dashed line) but the 2-component Gaussian PDF (solid line) is the best fit. In addition, the bias Δv was small for all cases.

The performance of the lidar velocity estimates is defined by the parameters b and g as a function of Φ_1 . An example is shown in Fig. 2 for $N = 10$ accumulated lidar pulses per velocity estimate and $\sigma_{\beta} = \langle \beta \rangle$. The optimal Capon filter order p is chosen by the minimum standard deviation g and has a weak dependence on Φ_1 and therefore can be reliably determined from the data. The best-fit models are in good agreement with the simulated results.

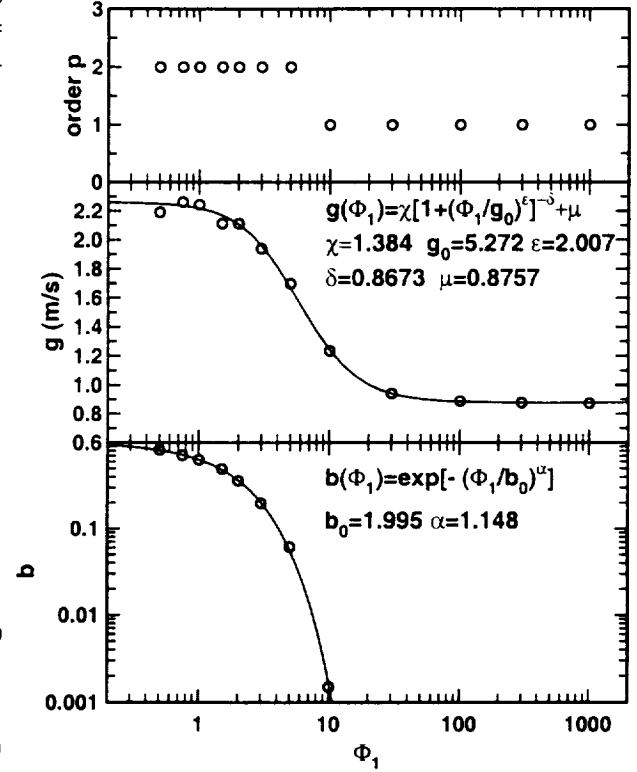


Fig. 2. Performance of the Capon velocity estimator for $N=10$ pulses per estimate with optimal order p , standard deviation g of the good estimates, and fraction b of bad estimates versus signal strength Φ_1 [Eq. (1)] for a single lidar pulse.

The performance for $N = 10$ accumulated lidar pulses per velocity estimate is shown in Fig. 3 for constant aerosol backscatter and for $\sigma_{\beta} = \langle \beta \rangle$. The same results are shown in Fig. 4 for $N = 100$ accumulated lidar pulses per velocity estimate. The backscatter variability ($\sigma_{\beta} = \langle \beta \rangle$) increases the standard deviation of the good estimates and produces a small increase in the fraction of outliers which is essentially negligible for the $N = 100$ cases. The predictions for the effective Gaussian lidar pulse are in agreement with the turbulent wind field when $b > 0$ and the agreement improves with larger N . However, the agreement with the standard deviation at large signal levels Φ_1 is poor because the effective

Gaussian lidar pulse assumes uncorrelated statistics from pulse to pulse.

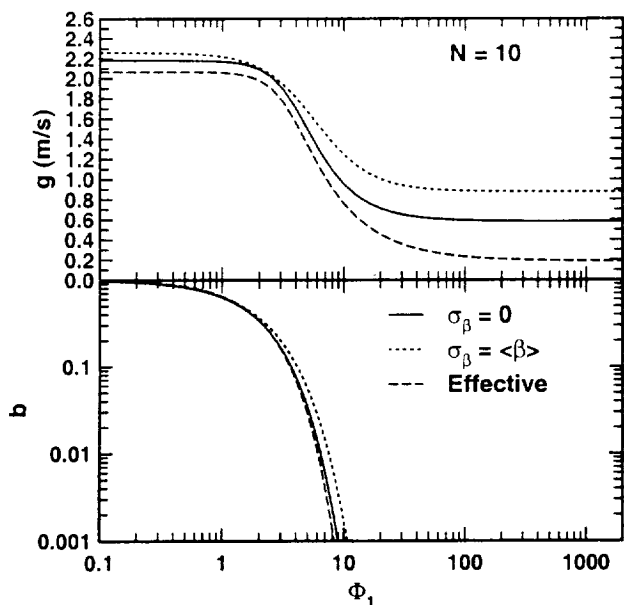


Fig. 3. Performance of the Capon velocity estimator for $N=10$ pulses per estimate with standard deviation g of the good estimates, and fraction b of bad estimates versus signal strength Φ_1 [Eq. (1)] for a single lidar pulse. The results of simulations using the Gaussian pulse approximation with w_{eff} Eq. (14) are also shown.

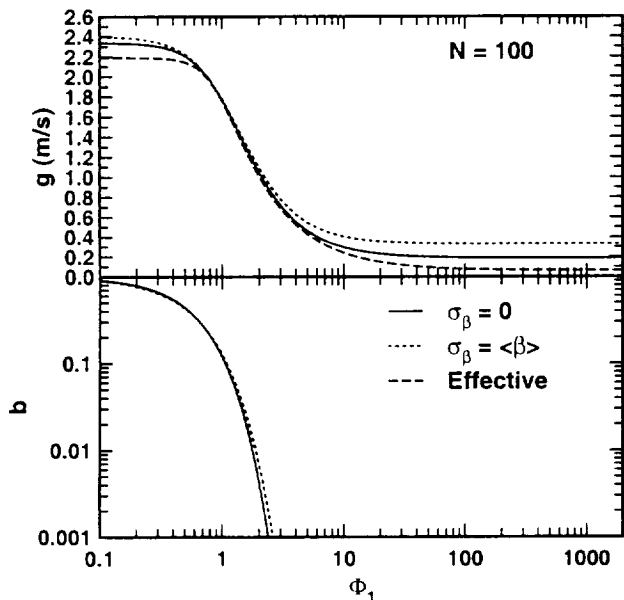


Fig. 4. Performance of the Capon velocity estimator for $N=100$ pulses per estimate and the same cases as Fig. 3.

The fraction b of random outliers defines the threshold signal level for useful velocity estimates,

i.e., $\Phi_{1threshold}$ is defined by $b(\Phi_{1threshold}) = Q$. For example, the choice of $Q = 0.1$ (10% random outliers) produces a threshold signal level $\Phi_{1threshold} \approx 3.3$ for $N = 10$ in Fig. 3 and $\Phi_{1threshold} \approx 1.0$ for $N = 100$ in Fig. 4. The threshold signal level scales as $N^{-1/2}$ as predicted by previous work using the effective turbulence model [3].

Acknowledgments

This work was supported by the National Aeronautics and Space Administration, Marshall Space Flight Center, Michael J. Kavaya and Steve Johnson, Technical Officers.

References

- [1] R. G. Frehlich and M. J. Yadlowsky, "Performance of mean frequency estimators for Doppler radar and lidar," *J. Atm. Ocean. Tech.* **11**, 1217-1230 (1994).
- [2] B. J. Rye, and R. M. Hardesty, "Discrete spectral peak estimation in incoherent backscatter heterodyne lidar. I. Spectral accumulation and the Cramer-Rao lower bound." *IEEE Trans. Geo. Sci. Remote Sensing* **31**, 16-27 (1993); II. Correlogram accumulation," **31**, 28-35 (1993).
- [3] R. G. Frehlich, "Simulation of coherent Doppler lidar performance in the weak signal regime." *J. Atm. Ocean. Tech.* **13**, 646-658 (1996).
- [4] R. Frehlich, S. Hannon, and S. Henderson, "Coherent Doppler lidar measurements of winds in the weak signal regime," *Appl. Opt.*, **36**, 3491-3499, (1997).
- [5] M. J. Kavaya and G. D. Emmitt, "The Space Readiness Coherent Lidar Experiment (SPARCLE) Space Shuttle Mission." *Proc. SPIE*, **3380**, 2-11, (1998).
- [6] R. G. Frehlich, "Effects of wind turbulence on coherent Doppler lidar performance." *J. Atmos. Ocean. Tech.* **14**, 54-75 (1997).
- [7] D. A. Bowdle, "Aerosol backscatter spatial structure: Preliminary results." NASA Contract Number NCC8-22, Dryden Flight Research Center, (1997).
- [8] B. J. Rye, "Spectral correlation of atmospheric lidar returns with range-dependent backscatter," *J. Opt. Soc. Am. A.*, **7**, 2199-2207, (1990).

Considerations for Designing a Space Based Coherent Doppler Lidar

Gary D. Spiers
 Center for Applied Optics
 University of Alabama in Huntsville
 Huntsville
 AL 35899
 Gary.Spiers@msfc.nasa.gov
 (256) 544 5787

Michael J. Kavaya
 Mail Code SD60
 Global Hydrology and Climate Center
 NASA Marshall Space Flight Center
 Huntsville
 AL 35812
 Michael.Kavaya@msfc.nasa.gov
 (256) 922 5803

Introduction

An orbiting coherent Doppler lidar for measuring winds is required to provide two basic pieces of data to the user community. The first is the line of sight wind velocity and the second is knowledge of the position at which the measurement was made. In order to provide this information in regions of interest the instrument is also required to have a certain backscatter sensitivity level. This paper outlines some of the considerations necessary in designing a coherent Doppler lidar for this purpose.

Line of sight velocity accuracy

A lidar instrument measures wind velocity by measuring a frequency difference between the transmitted laser beam and the return signal. This frequency difference is due to the transmitted frequency being Doppler shifted by the line of sight velocity seen by the instrument. The line of sight velocity is comprised of velocity components due to the satellite velocity, the earth's rotational velocity and the velocity of the target.

The magnitude of the combined line of sight velocity is given by:

$$\begin{aligned}
 los_vel := & htrgtv \cos(-trgta + az + orblat(lat, inc)) \sin(nadalt(orbh, n, alt, lat)) \\
 & + vtrgtv \cos(nadalt(orbh, n, alt, lat)) + hsatv \cos(az) \sin(n) + vsatv \cos(n) \\
 & + Vlat(lat) \sin(orblat(lat, inc) + az) \sin(nadalt(orbh, n, alt, lat))
 \end{aligned} \tag{1}$$

where the first and second terms are the line of sight components of the target velocity with respect to the local WGS84 [1,2] earth ellipsoid surface. The third and fourth terms are the line of sight components of the spacecraft horizontal and vertical velocities. The final term is the component of the earth's rotational velocity along the line of sight. Table 1 lists the parameters and functions called out in equation (1) and table 2 lists the sensitivity of the

Symbol	Parameter
htrgtv	target horizontal velocity
vtrgtv	target vertical velocity
trgta	angle of the target velocity with respect to the local meridian
az	azimuth angle with respect to the spacecraft velocity vector
lat	latitude of the spacecraft
inc	orbit inclination angle
orbh	orbit height

n	instrument nadir angle
alt	altitude of the target with respect to the local WGS84 ellipsoid surface
hsatv	local horizontal component of the spacecraft velocity
vsatv	local vertical component of the spacecraft velocity
orblat(lat,inc)	the angle of the satellite velocity vector to the local meridian
nadalt(orbh,n,alt,lat)	The nadir angle the line of sight makes with the target with respect to the local WGS84 ellipsoid surface.
vlat(lat)	The earth's rotational velocity at a latitude, lat

Table 1) 'Base' parameters.

'base' parameters to error for an instrument at a nominal orbit height of 300 km and an orbit inclination of 52 deg with a nadir angle at the spacecraft of 30 deg.

Parameter	Maximum Error Rate	Error required to give 1 m/s los error
Azimuth angle	68 (m/s)/deg	256 μ radians
Nadir angle	118 (m/s)/deg	125 μ radians
Orbit height	0.31 (m/s)/km	3.22 km
Latitude	24 (m/s)/deg	725 μ radians
Orbit inclination	3.7 (m/s)/deg	4.7 mradians
Target altitude	0.02 (m/s)/km	50 km
Satellite local horiz. velocity	0.5 (m/s)/(m/s)	2 (m/s)
Satellite local vert. velocity	0.87 (m/s)/(m/s)	1.15 (m/s)

Table 2) LOS velocity sensitivities for a 300 km, 52 deg inclination orbit

Note that the error due to each of the parameters is generally a complex function of other parameters (typically azimuth and/or latitude) and the values in table (2) represent a worst case analysis for each parameter. It should be noted that the sensitivities above are valid for any instrument, regardless of measurement technique, that is intended to measure wind velocities on a single shot basis.

In addition to the line of sight velocity sensitivities listed above there will be sensitivities associated with the measurement technique itself and with atmospheric refraction. Both of these effects are dependent on the actual design and wavelength of the lidar under consideration. At the 2 μ m wavelength frequently considered for a space-based coherent lidar the large Doppler shifts due to the line of sight component of the spacecraft velocity result in a large frequency offset of the return signal from the outgoing frequency. This offset is greater than the bandwidths typically required for obtaining a high quantum efficiency from currently available detectors. This is overcome by tuning either the local oscillator or the transmitted outgoing pulse to offset for the spacecraft induced Doppler shift and hence the bandwidth requirement on the detector [3]. A consequence of this scheme is an increase in the number of frequencies that must be measured compared to a typical ground or aircraft based coherent lidar. The velocity measurement accuracy due to the receiver portion of the instrument including the effect of the velocity algorithm used is $\sim 0.5 - 1$ m/s for a 2 μ m system for good (>10 coherent photoelectrons) signal conditions.

Atmospheric refraction produces 'bending' of the lidar beam as it travels down through the atmosphere and this creates a change in the nadir angle at the target. For a 2 μ m lidar at a 300 km orbit with a 30 deg nadir angle this effect causes a 150 – 200 μ radian reduction in the nadir angle at the target with the actual value dependent on local atmospheric conditions. This will contribute a 1.3 – 1.7 m/s line of sight velocity error if not correctly accounted for.

Target position

This can be broken down into two issues, the first is knowledge of the instrument position with respect to some known global coordinate system, typically WGS84 [1,2]. The second is knowledge of the measurement location with respect to the instrument.

Knowledge of the measurement location with respect to the instrument is dictated by knowledge of the azimuth and nadir angles of the instrument. Errors in the azimuth or nadir angle cause the line of sight to describe a cone about the 'true' or 'ideal' value. The position of the measurement relative to the instrument is simply:

$$Z_{lvlh} := \frac{1}{2} c t_{rtrp} \cos(n) \quad (2)$$

in the vertical and

$$R_{lvlh} := \frac{1}{2} c t_{rtrp} \sin(n) \quad (3)$$

is the radial distance, neglecting the effect of refraction, from the sub-instrument point to the target location, c and t_{rtrp} are the velocity of light and the round trip time of flight respectively. We must constrain the azimuthal direction such that the circumferential distance from the 'true position' can be determined. This distance is simply $(R_{lvlh} \times daz)$ where daz is the error in azimuth angle. This provides the target position in a local coordinate frame that can then be transformed to obtain the target position with respect to WGS84 if the position of the instrument with respect to WGS84 is known.

Parameter	Error Rate	Error required to give 1m error
Instrument vertical position	1 m/m	1 m
Nadir angle	44 m / 200 μ rad	4.55 μ rad
Round trip time	40 m / 300 ns	7.5 ns

Table 3) Vertical position assignment sensitivity

Parameter	Error Rate	Error required to give 1m error
Instrument horizontal position	1 m/m	1 m
Nadir angle	40 m / 100 μ rad	2.5 μ rad
Round trip time	24 m / 300 ns	12.5 ns
Azimuth angle	24 m / 100 μ rad	4.17 μ rad

Table 4) Horizontal position assignment sensitivity

Instrument position and attitude

The method by which the instrument obtains its attitude and position relative to WGS84 will be dependent on the platform and instrument configuration. One technique is to use an INS/GPS to provide both attitude and position. The performance of an INS/GPS on orbit is typically degraded over that achievable on the ground. In order to meet the error budgets required by a Doppler lidar they must be operated in 'military' or PPS mode. One problem with an instrument dedicated INS/GPS is that unlike a launch vehicle the unit is not powered on through launch and so it must be initialised once on orbit. The lidar can be used to both perform this function as well as track and correct for drift in the INS attitude solution [4].

Instrument sensitivity

The calculation of coherent Doppler lidar sensitivity has been extensively discussed in the literature [5] and this paper will only mention issues pertaining to deployment from a space platform. In order to optimise the sensitivity of a coherent lidar it is desired to have good wavefront matching of the local oscillator signal and the return signal. A 300 km altitude, 30 deg nadir angle instrument has a round trip time of flight of the optical pulse from the lidar to the ground and back of ~2.3 milliseconds. During this time the transmit/receive optical axes must remain aligned with respect to each other and any jitter of the lidar during the round trip time will therefore contribute to a loss in sensitivity. Contributors to this misalignment that are not typically of concern for a ground or airborne system are platform attitude drift and nadir tipping due to rotation about the earth's center. A platform attitude drift of ~0.04 deg/sec will contribute ~1.6 μ radians of misalignment between the transmit/receive beams while nadir tipping will

contribute ~ 2.7 μ radians of misalignment. For a 25 cm aperture instrument a total angular offset of ~ 7 μ radians will result in a 3 dB reduction in SNR.

Finally it should be noted that the Doppler shift due to the component of the spacecraft platform velocity seen by the lidar is a function of the scanner azimuth angle (equation (1)). The bandwidth of the return signal that results from this can result in an azimuthally dependent atmospheric extinction and hence an azimuthally dependent sensitivity.

Summary

An overview of some of the issues specific to designing a space based coherent Doppler lidar have been presented and examples for an instrument with a 25 cm aperture in a 300 km, 52 degree inclination orbit altitude presented.

Acknowledgements

Funding for this work has been provided by Dr. Ramesh K. Kakar, NASA Code Y and by the NASA NMP EO-2 SPARCLE program.

References

- [1] MIL-STD-240, "Department of Defence World Geodetic System (WGS)", 11 January 1994.
- [2] DMATR 8350.2, "Department of Defence World Geodetic System 1984, Its Definition and Relationships with Local Geodetic Systems", Second Edition 1 September 1991.
- [3] G. D. Spiers, "Analyses of Coherent Lidar Wind Measurement Missions", Final Report on Contract No. NAS8-38609, Delivery Order No. 128, Report Date 8/28/96.
- [4] G.D. Emmitt, T. Miller and G.D. Spiers, "Pointing Knowledge for SPARCLE and Space-based Doppler Wind Lidars in General", Tenth Biennial Coherent Laser Radar Technology and Applications Conference, Mount Hood, 28th June – 2nd July 1999.
- [5] See for example R.G. Frehlich and M.J. Kavaya, "Coherent laser radar performance for general atmospheric refractive turbulence", Appl. Opt. 30, 5325, December 1991.

2 μm Space lidar breadboards for wind measurements

J.B Ghibaudo, J.Y. Labandibar ; ALCATEL Space Industries, Optical Instrument Department, 100 bd Midi, BP99, 06156 Cannes la Bocca, France ;

E. Armandillo ; European Space Agency, ESTEC, P.O. Box 299, 2200 AG Noordwijk, The Netherlands ;

M. Faucheux ; Quantel, Av. de l'Atlantique, BP 93, 91941 Les Ulis, France ;

M. A. Cosentino ; ALENIA, 2 Via dei Romani, 00040 Pomezia - Roma, Italy ;

P. Flamant ; Laboratoire de Météorologie Dynamique, Ecole Polytechnique, 91128 Palaiseau Cedex, France ;

1. INTRODUCTION

This paper presents the design of the most relevant lidar subsystems such as the 2 μm laser and the detection chain, the associated breadboard results, and eventually the architecture of a 2 μm lidar instrument accommodated on the International Space Station (ISS).

The mission of this lidar instrument is to measure with good accuracy and reliability the wind velocity in the Planetary Boundary Layer (PBL) from the ISS. The precise mission and instrument requirements are provided in Table 1-1. From these requirements, the subsystems requirements have been established modelling the lidar instrument and including signal processing aspects. Indeed, the lidar instrument performance mainly depend on laser energy, pulse repetition frequency, laser pulse duration, capabilities of the coherent detection chain to work at very low atmospheric useful signals.

DWL mission requirements
<ul style="list-style-type: none">• International Space Station orbit,• Measurement of the Line Of Sight (LOS) component of the wind velocity vector (For each cell, a single LOS measurement is accepted),• Minimum nadir angle = 30°,• Wind velocity range : $\pm 100\text{m/s}$,• Measurement accuracy : 2 m/s in the PBL (0 to 2 km altitude),• Reliability : > 80 % in the PBL,• Horizontal cell size: 200km x 200km,• Vertical cell size : 500 m,• Maximum cluster area : 35km x 35km

Table 1-1 : Mission and instrument requirements

2. LASER BREADBOARD DESIGN AND PERFORMANCES

After trade-off analyses, the selected 2 μm laser architecture for the complete laser providing a 1 J energy per pulse is the MOPA configuration. The breadboards have been focused on the seeder and the injected Q-switch oscillator.

2.1. Seeder definition and performances

The seeder has been designed considering an airtight cavity filled up with nitrogen, a piezo-electric actuator on the mirror cavity to compensate for parasitic Doppler shifts (Figure 2-1).

The main performance of this seeder are recalled hereafter :

- Output power 54 mw in multi-mode operation at 0° C of crystal temperature
- Output power > 30 mW
- Divergence < 1.1 diffraction limited
- Linewidth < 0.5 MHz.

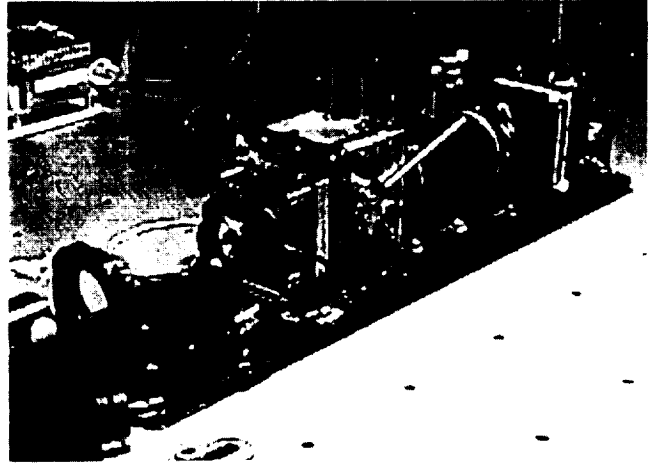
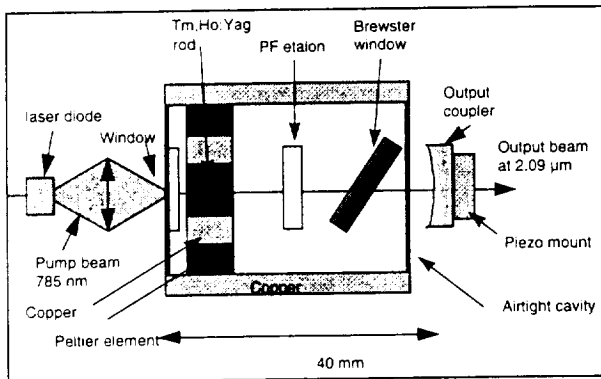


Figure 2-1 : Seeder design (by Quantel courtesy)

2.2. Injected Q-switch oscillator design and performance

The oscillator cavity is composed of 2 laser heads arranged up and down to reduce thermal beam distortion (Figure 2-2). The 2 laser heads have been assembled, tested and implemented in the laser resonator (Figure 2-3). Each set of 4 diode stacks emits 1.1 J on each rod during 800 μ s at 10 Hz. The extracted energy in free running modes is 165mJ in the operational conditions.

For Q-switching, the electro-optics device (Lithium Niobate) has been selected for the breadboard due to high injection stability. The simulations and optimisations have led to a 0.8 m linear cavity length.

The injection seeding mode has been optimised to match the seeder and the oscillator wavelengths.

The final injection performance obtained is 10 mJ at 10 Hz with a 200 ns pulse duration once the mechanical instability troubles of the oscillator and the optical bench have been solved.

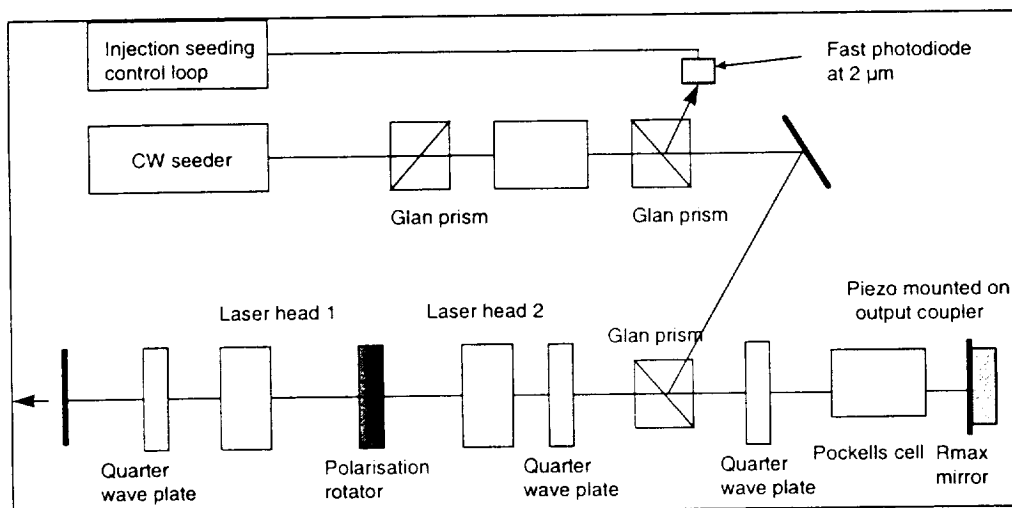


Figure 2-2 : Injection seeded Q-switch oscillator

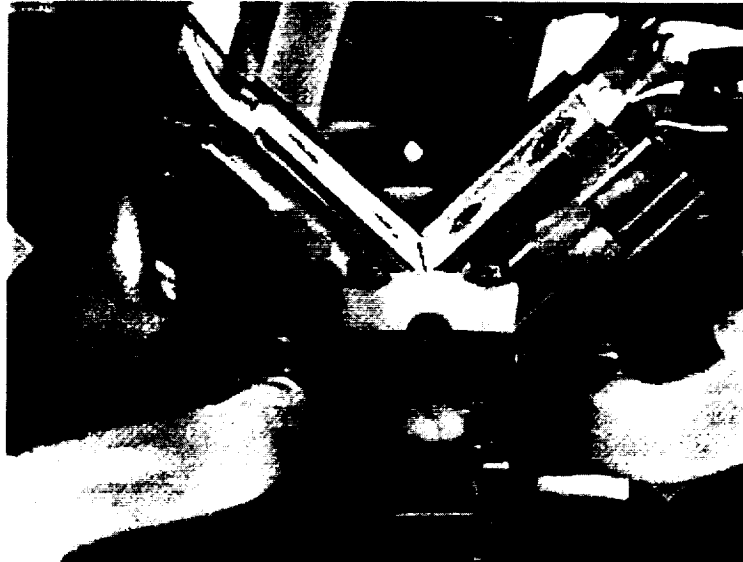


Figure 2-3 : Laser head with cooling system (by QUANTEL courtesy)

3. RECEIVER BREADBOARD DESIGN AND PERFORMANCE

The goal of the breadboard is to characterise and optimise the $2\ \mu\text{m}$ coherent receiver functioning in spaceborne DWL real conditions. The core element is composed of a $2\ \mu\text{m}$ photodiode, a preamplifier and a matched filter, and is decisive for coherent receiver performance determination (Figure 3-1).

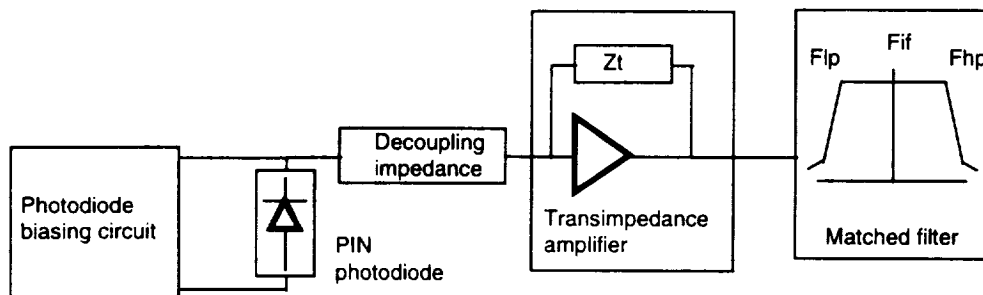


Figure 3-1 : Receiver breadboard architecture

An optical test equipment has been realised in order to determine the performance of the receiver breadboard. The role of this optical test equipment is to generate an optical signal simulating the real lidar atmospheric return signal (Figure 3-2).

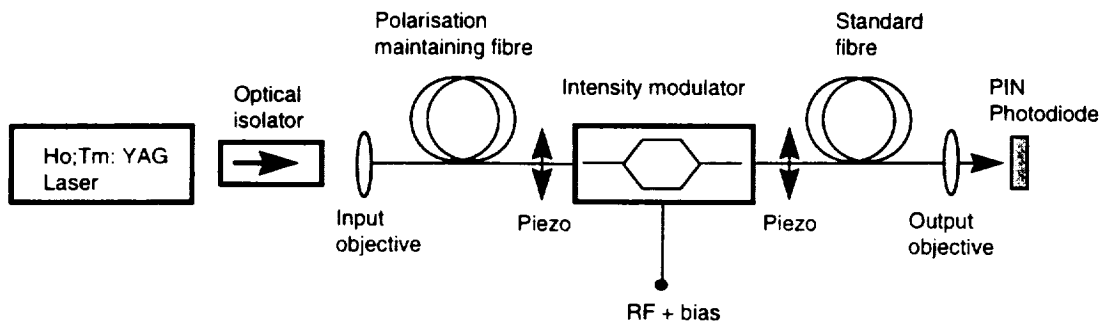


Figure 3-2 : Optical test equipment design

With the level of accuracy required, all the optical test equipment and receiver breadboard components have been characterised with respect to frequency response, gain, amplitude linearity, distortion, maximum input signal power, noise density, noise factor, and SNR.

The achieved performance can be summarised by a noise factor introduced by the electronics lower than 0.5 dB with a local oscillator power of 1 mW with the state of the art 2 μm technology (Figure 3-3). Thus, it has been demonstrated that the receiver chain is nearly shot noise limited.

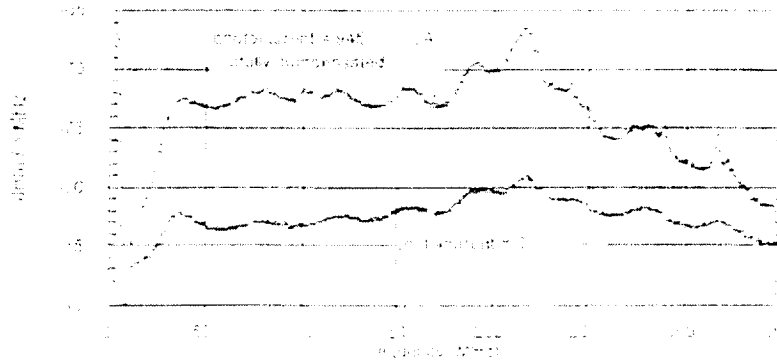


Figure 3-3 : Shot noise spectral density of the amplifier and photodiode (by Alenia courtesy)

4. LIDAR INSTRUMENT DESIGN AND PERFORMANCE

After trade-off analyses on the lidar instrument accommodation on the ISS, the Japanese Exposed Module location has been selected because it offers the possibility to implement a large mass instrument and large radiative surfaces. The Doppler Wind Lidar instrument presents the following interfaces with ISS :

Interfaces	Assessment
Mass	325 Kg
Power	620 W
Volume	1200 x 860 x 1250
Radiative surface area	1.5 m ²
Data rate	8.8 Mbit/s

The results of the laser and detection breadboards have been introduced in the simulations in order to consolidate the lidar performance. The wind performance due to SNR is better than 1.5 m/s with a reliability higher than 80% up to 12 Km height. In addition to these wind velocity performance, instrumental bias and Doppler shift compensation errors are estimated at 0.7 m/s.

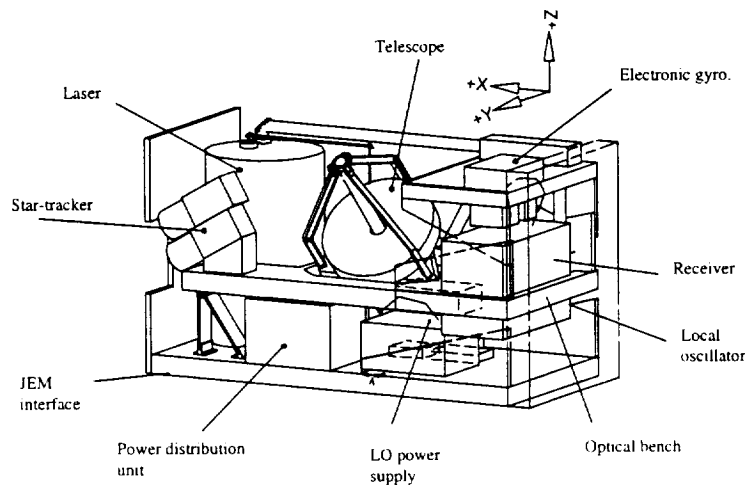


Figure 4-1 : 2 μm DWL instrument architecture on ISS

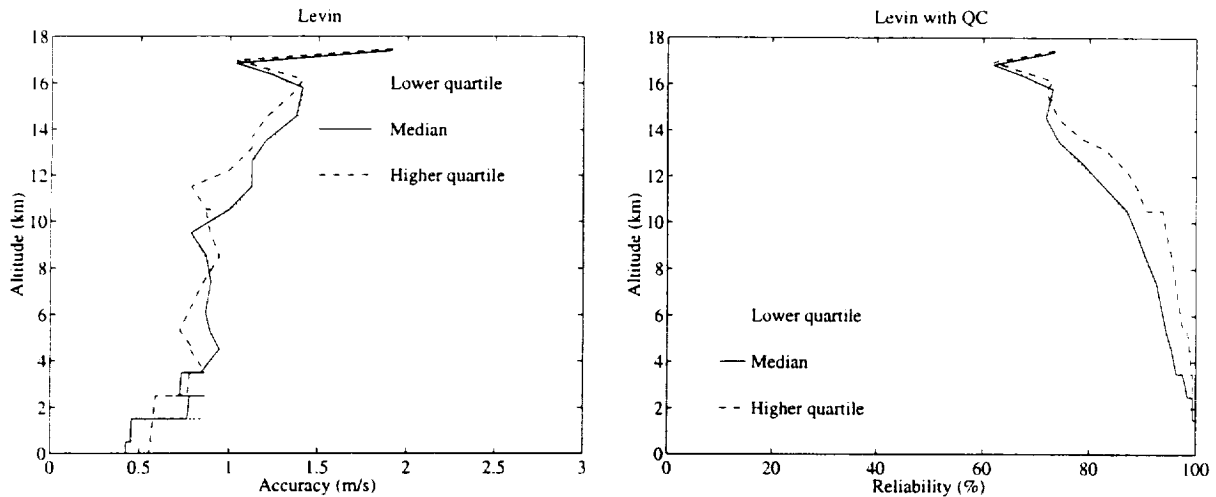


Figure 4-2 : Wind velocity accuracy and reliability versus height for 3 scattering coefficients

(Levin with quality control (QC) algorithm)

5. CONCLUSION

This work gives the demonstration that the relevant performances on the laser and the heterodyne receiver chain at $2 \mu\text{m}$ are achievable through the presented breadboard results. It also summarises the lidar instrument capability to measure a wind velocity along the telescope line of sight with an accuracy and reliability respectively higher than 2 m/s and 80 % up to 12 Km height.

For the next step, the main challenge is first to improve the optical power of the laser, and secondly to combine the laser, detection and frequency control breadboards in order to realise a $2 \mu\text{m}$ lidar based on ground.

6. ACKNOWLEDGEMENT

This work was performed by Alcatel Space Industries, Quantel, Alenia, Laboratoire de Météorologie Dynamique, under ESA contract.

DEVELOPMENT OF PROTOTYPE MICRO-LIDAR USING NARROW LINEWIDTH SEMICONDUCTOR LASERS FOR MARS BOUNDARY LAYER WIND AND DUST OPACITY PROFILES

*Robert T. Menzies, Greg Cardell, Meng Chiao, Carlos Esproles,
Siamak Forouhar, Hamid Hemmati and David Tratt*

Jet Propulsion Laboratory, California Institute of Technology

4800 Oak Grove Drive, Pasadena, CA 91109, USA

Phone: 818-354-3787; FAX: 818-393-6984; Email: Robert.T.Menzies@jpl.nasa.gov

1. Introduction

We have developed a compact Doppler lidar concept which utilizes recent developments in semiconductor diode laser technology in order to be considered suitable for wind and dust opacity profiling in the Mars lower atmosphere from a surface location. The current understanding of the Mars global climate and meteorology is very limited, with only sparse, near-surface data available from the Viking and Mars Pathfinder landers, supplemented by long-range remote sensing of the Martian atmosphere. The *in situ* measurements from a lander-based Doppler lidar would provide a unique dataset particularly for the boundary layer. The coupling of the radiative properties of the lower atmosphere with the dynamics involves the radiative absorption and scattering effects of the wind-driven dust (Haberle, et al., 1982). Variability in solar irradiance, on diurnal and seasonal time scales, drives vertical mixing and PBL (planetary boundary layer) thickness. The lidar data will also contribute to an understanding of the impact of wind-driven dust on lander and rover operations and lifetime through an improvement in our understanding of Mars climatology.

In this paper we discuss the Mars lidar concept, and the development of a laboratory prototype for performance studies, using local boundary layer and topographic target measurements.

2. Instrument Description

We have developed a laboratory prototype Doppler lidar utilizing a novel technique for measuring wind speed profiles. It uses technologies which provide a path towards development of a robust, low-power instrument for deployment on the surface of Mars. The lidar currently utilizes commercially available semiconductor diode laser master oscillator and fiber laser amplifier devices in order to attain transmitter power output between 100-200 mW, depending on the transmitter modulation technique. The specific lidar wavelength selected is not constrained to a particular spectral region by the measurement objectives, consequently the 1.5 micron wavelength region has been selected to be compatible with the large market of optical fiber-compatible components. This wavelength also makes the lidar much more convenient for various Earth boundary layer measurement studies because it is in the Aeye safe@ region.

The lidar uses a modulated cw transmitter and heterodyne detection. Pulsed operation, desirable for many reasons when profiling is the goal, is not compatible with the very narrow-linewidth

semiconductor laser transmitter required for the Doppler measurements. Diode lasers do not store population inversion energy efficiently, particularly if narrow linewidth is required. For a lidar measurement application such as this, for which the transmitter output power is of the order of hundreds of mW, the transmitter power requirement is a significant contributor to the overall power budget. Thus it is attractive to use a diode laser transmitter rather than suffer the loss of efficiency in converting diode pump optical power to pulsed power from a crystal laser medium. Since heterodyne detection is used, the LO is derived by splitting a portion of the cw master oscillator output. The LO component frequency is shifted 20 MHz using an acousto-optic shifter. The output from the transmitter leg of the splitter passes through a modulator. This then passes through the fiber amplifier and is coupled through a transmit/receive duplexer to an off-axis afocal telescope. The receiver comprises a high-speed, low noise InGaAs photodiode suitable for ambient temperature operation, with a matched preamplifier, RF filtering, programmable amplifier, high-speed low power 12-bit analog-to-digital converter (ADC), followed by Fast Fourier Transform (FFT) electronics and power spectrum analysis and processing. The processing and control computer provides the transmitter modulation waveform and the detected signal demodulation and correlation functions. An important consideration for this lidar is the selection of a modulation and spectrum analysis strategy which accounts for the decorrelation time of the signals backscattered from the atmospheric aerosol. The decorrelation time in the boundary layer depends on the turbulence intensity. The range of correlation times in the Earth's boundary layer over land surfaces places a more stringent demand on the lidar than is expected based on inferred correlation times for the Mars boundary layer.

3. Summary

Laser technology is advanced to the level required for planetary missions, examples being the laser transmitter for the Mars Observer Laser Altimeter (MOLA) currently orbiting Mars and the laser *in situ* water vapor sensor in the Mars Volatiles and Climate Sensor (MVACS) currently on its way to Mars. The compact lidar concept described here for atmospheric wind and dust profiling measurements uses robust laser technology and relies on high performance signal processing as a fundamental component of its operation. A prototype Doppler lidar has been constructed for use in local boundary layer measurements to assess the capability to derive wind profiles using PN code modulation of the transmitter. Incorporation of monolithic semiconductor diode lasers with 100-200 mW output power will take place as these devices become available in the near future.

Acknowledgement

This work was carried out by the Jet Propulsion Laboratory, California Institute of Technology, under contract to the National Aeronautics and Space Administration.

REFERENCES

Haberle, R.M., C.B. Leovy, and J.B. Pollack (1982). Some effects of global dust storms on the atmospheric circulation of Mars. *Icarus*, **50**, 322-367.

Follow-on Missions to SPARCLE

G. D. Emmitt
Simpson Weather Associates
Charlottesville, Va. 22902
804-979-3571

T. L. Miller
Global Hydrology and Climate Center
NASA/MSFC
Huntsville, AL 35812
256-922-5882

Abstract

Global tropospheric wind observations are considered the number one unaccommodated atmospheric observation for the new series of NPOESS platforms. The operational meteorology communities have long recognized the potential for improved forecasting skill if accurate wind observations were available around the globe. Recent analyses suggest that wind observations such as those that could be made by a space-based Doppler wind lidars would even result in greater improvements than better temperature soundings. In this paper we present a roadmap that begins with the NASA approved SPACe Readiness Coherent Lidar Experiment (SPARCLE) and ends with an operational DWL on an NPOESS platform.

The Importance of Global Wind Observations

There is evidence that today's weather forecast models are limited more by the lack of good input data for initialization than they are by imperfect modeling of the atmospheric system. Forecasts begin with 3D statements of the current state of the atmosphere. These analyses are the consequence of integrating real observations such as those from rawinsondes, satellite sounders, and various other remote and in situ observing systems with the forecast model's "guess" of the global atmospheric state. Where there are no real observations, the model uses its own guesses as the initial state for the next forecast interval. Always assimilating and interpolating in time and space, the global models move forward. Reanalyses (or hindcasting) of the model outputs and reprocessing of the real data results in a set of analyses that are available for use by various research communities, in particular the climate research community. Thus it can be asserted that to improve our understanding of the timeline of climate variability we need to improve our forecasting skills. To improve our forecasting skills we need better observations.

The question is what do we need to observe better than we are already doing. Today we have a global network of rawinsondes released twice per day to get soundings of winds, temperature and moisture. Most of these releases take place over the populated landmasses of the Northern Hemisphere. We also get a global set of less accurate profiles of temperature and moisture from polar orbiting satellites. Over the oceans we are now obtaining estimates of the winds near the surface from space-based scatterometers. What are missing from the globally observed set of basic atmospheric state variables are the winds throughout the troposphere. More precisely, we need to do a much better job of observing the divergent component of the wind, which dominates in the tropics and in the vicinity of higher latitudinal jets.

Quantifying the importance of this observational “gap” or “weakness” has been the subject of a series of OSEs and OSSEs. Without going into the details of these experiments (REFERENCES), they have clearly validated the intuition-based claims that a global set of accurate wind observations will have a bigger impact on weather forecasting (and thus analyses) than improving any of the current operational observing systems. Thus, the leading justifications for a global wind observing capability are expressed in terms of forecast improvements. Consequently, the roadmaps for DWL technology development and mission concepts tend to lead to a presence on the new generation of operational weather satellites known as NPOESS.

The first in a series of NPOESS platforms is scheduled for launch in the 2008-2009 time frame. From our perspective, SPARCLE is the first major milestone on that road map. The challenge is to lay out a plan that will result in a DWL being flown on C1 or C2 of the NPOESS series. There is an obvious need for a mission between SPARCLE and the NPOESS deployment. The remainder of this paper offers a view of what the intermediate instrument and mission might be if coherent detection is determined to be the best technology for the initial NPOESS operational mission. We refer to this next step after SPARCLE as a “prototype operational” mission.

A Roadmap to an Operational System

The SPARCLE is being designed to address several key risks (real and perceived) associated with operating a DWL in space. A few of those issues are:

- Maintaining far-field alignment
- Validating modeled sensitivity (throughput)
- Validating modeled observation accuracy
- Demonstrating the relative merits of several candidate scanning/sampling strategies for use by an operational DWL

There are other issues important to an operational mission that are not being addressed by SPARCLE. Listed among those capabilities yet to be demonstrated are:

- Autonomous lidar operations for multiple years

- Autonomous/active optical alignment
- Lightweight scanning optics of the > 50cm diameter class
- Conductively cooled, end pumped .5 – 1 joule class lasers

Figure 1 describes a proposed roadmap for developing and flying the key technologies needed for a 3-5 year operational mission. Table 1 combined with Figure 2 illustrate the progression towards full tropospheric soundings with a coherent system. Along the road from SPARCLE to the “full profile” (clouds permitting) system, there are several non-technical questions that need to be answered. These questions have to do primarily with the cost benefit curve for global coverage and observational accuracy. A few of those questions are related to:

- Incomplete vertical coverage for individual profiles (cloud or aerosol effects)
- Spatial resolution of observations vs. model grid size
- Adaptive targeting to optimize impact on forecasts and analyses
- Accuracy of observations relative to alternative sources of tropospheric winds

A prototype operational mission will go far in helping us answer these questions. Given the way 4DDA is used by today’s models, it is very unlikely that the cost of “full” global coverage will be justified in the near future. The key issues may be more related to accuracy and where new and observed wind profiles are needed.

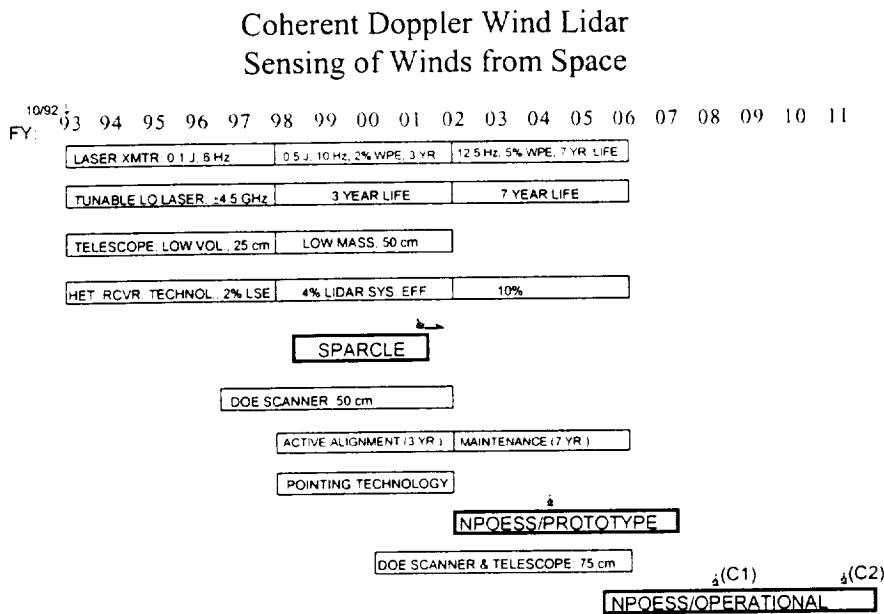


Figure 1: Technology development roadmap from SPARCLE, through prototype, to NPOESS operational flight.

Table 1: DWL concepts from SPARCLE to Operational

	SPARCLE (2001)	Operational Prototype (2005)	NPOESS/ Operational (2011)
Laser Energy (J)	0.1	.5	1
Laser PRF (Hz)	6	10	12.5
Telescope Diameter (m)	0.25	0.5	1
Orbit altitude assumed	300 km	400 km	833 km
Nadir angle assumed	30	30	45
Number of shots averaged for sensitivity calc.	50	290	603
Backscatter Sensitivity (8-point scan)	3×10^{-7} $m^{-1} sr^{-1}$	1×10^{-8} $m^{-1} sr^{-1}$	1×10^{-9} $m^{-1} sr^{-1}$
Spatial Resolution (km)	62	100	317

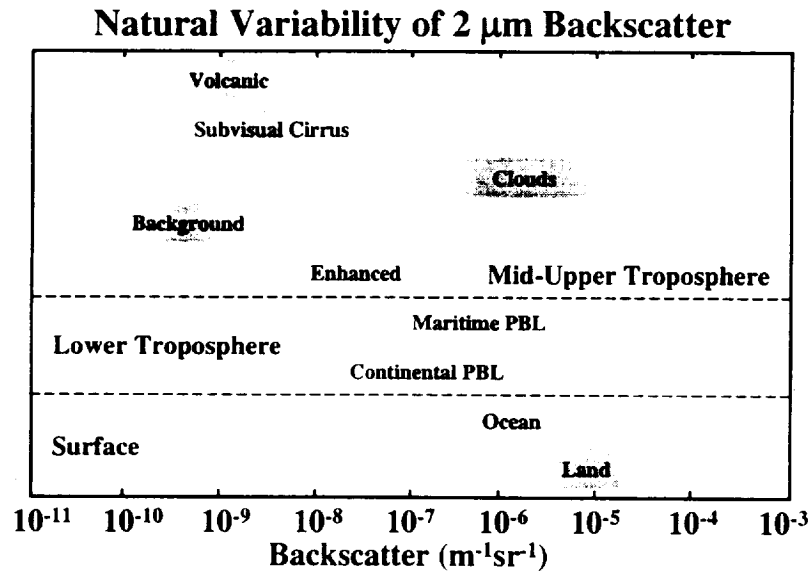


Figure 2: Backscatter opportunities at 2 microns

Acknowledgments

The authors recognize the support from NASA Headquarters and the contributions of the following organizations to the SPARCLE mission: University of Alabama at Huntsville, Marshall Space Flight Center, Jet Propulsion Laboratory, Langley Research Center, National Oceanographic and Atmospheric Administration, Goddard Space Flight Center, Coherent Technologies Inc. and Simpson Weather Associates, Inc.

Index

A

Abstracts, 1-10
Aircraft Missions, 1, 28
Aircraft Operations, 1, 11
Allgood, Glenn O., 40-41
Amzajerjian, Farzin, 284-287, 288-291
Armandillo, E., 306-310
Arntzen, Per-Otto, 202
Asai, Kazuhiro, 178-181, 292-293
Asaka, Kimio, 198-201
Atkinson, Robert J., 160-162
Augère, Béatrice, 251-254
Axenson, Theresa J., 238-240

B

Bagley, Hal R., 20-23
Bailey, Howard, 62-65
Banakh, Victor A., 82-85, 132-135, 294-297
Banta, Robert M., 273-276
Barker, Ben C., Jr., 12-15
Barnes, Norman P., 238-240
Bedard, Alfred J., 273-276
Belmonte, Aniceto, 78-81
Bishop, Kenneth, 220-223
Blackwell, Timothy S., 284-287, 288-291
Blockley, A. F., 123-126
Boger, James K., 212-215
Bogue, Rodney K., 20-23, 151
Bogenberger, Richard, 16-19
Boitel, Ch., 33-36
Bösenberg, Jens, 72-75, 268-271
Bowdle, David A., 20-23, 147-150, 151
Brewer, W. Alan, 76, 78-81, 278-281
Britt, Charles L., Jr., 12-15
Britten, J. A., 111-114
Brockman, Philip, 12-15,
Bruneau, D., 33-36
Byer, Robert L., 241-244

C

Cardell, Greg, 311-312
Cariou, Jean-Pierre, 251-254
Chambers, Diana M., 111-114, 119-122
Chen, Shen-en, 43-47
Chiao, Meng, 311-312
Clarke, A. D., 147-150
Cole, Helen J., 111-114
Colson, Carl, 98-101
Cornman, Larry, 24-27
Cosentino, M. A., 306-310
Cress, Alexander, 294-297
Crisp, David, 38-39
Culoma, A., 141-143
Cutten, Dean R., 29-32, 147-150, 160-162
CW Lidars, 8, 255

D

Dabas, Alain, 174-177, 278-281
Daly, J., 43-47
Danzeisen, H., 268-271
Darby, Lisa S., 29-32, 273-276
Davis, Richard E., 68-71
Delville, P., 33-36
D'Epagnier, David M., 98-101, 115-118
Detection Advances, 7, 211
Devereux, R. W. J., 123-126
Dharamsi, Amin, 68-71
DIAL, 2-3, 67
Dierking, Matt, 62-65
Dixit, S. N., 111-114
Dorschner, Terry A., 246
Drobinski, Philippe, 33-36, 174-177, 251-254, 278-281

E

Ehernberger, L. Jack, 20-23
Emmitt, G. D., 88-93, 182-186, 313-316
Engelbart, D., 268-271
Esproles, Carlos, 311-312

F

Faucheux, M., 306-310
Fetrow, Matthew, 220-223
Flamant, Pierre H., 33-36, 136, 141-143, 251-254, 306-310
Flesia, C., 141-143
Foord, R., 123-126
Forouhar, Siamak, 311-312
Frehlich, Rod, 24-27, 298-301
Frouin, Robert, 137-140
Fritzsche, K., 268-271

G

Gas, Bruno, 174-177
Gatt, Philip, 58-61, 62-65, 247-250
Geddes, N., 141-143
Ghibaudo, J. B., 306-310
Gibbens, Matt, 98-101
Goodrich, Robert, 24-27
Graham, D., 123-126
Grann, Eric
Guérit, Gaspard, 251-254

H

Häfner, Frank, 187-190
Hale, Charley P., 98-101, 115-118
Haner, D. A., 144-146
Hannon, Stephen M., 20-23, 24-27, 58-61, 62-65, 151, 247-250
Hansson, Göran, 202
Hardesty, R. Michael, 29-32, 76, 78-81, 278-281
Häring, R., 33-36
Harris, M., 203-206, 207-210, 277
Hasselmann, Dieter, 72-75
Heinrichs, Richard, 48-51
Hemmati, Hamid, 311-312
Henderson, Sammy W., 58-61, 98-101, 115-118, 247-250
Hirano, Yoshihito, 198-201
Howell, James N., 29-32
Hutchinson, Donald P., 40-41, 224

I

Ingram, C., 123-126
Ishizu, Mitsuo, 292-293
Itabe, Toshikazu, 292-293

J

Jarzembski, Maurice A., 128-131, 147-150, 160-162, 163-166, 264-266
Jedlovec, Gary J., 160-162
Jenkins, R. M., 123-126

K

Kane, Timothy J., 256-259
Karlsson, Christer, 202, 260-263
Kaushik, S., 48-51
Kavaya, Michael J., 88-93, 111-114, 119-122, 153-155, 156-159, 302-305
Killinger, Dennis, 43-47, 216-219
Klein, V., 268-271
Klier, M., 33-36
Koch, Grady J., 12-15, 68-71
Kocher, D. G., 48-51
Köpp, F., 33-36

L

Labandibar, J. Y., 306-310
Lampe, Thomas, 202
Laporta, P.
Laser Advances, 7-8, 223
Leeb, Walter R., 191-194
Leike, Ines, 16-19, 229-232, 294-297
Li, Ye, 284-287, 288-291
Linné, Holger, 72-75
Loth, Claude, 33-36
Lovett, Alexander R., 66
Luther, Michael R., 87

M

Magee, Eric P., 256-259
Mamidipudi, Priyaradan, 43-47, 216-219
Marcus, S., 48-51
Marseille, G. J., 102-105
Matsui, Ichiro, 178-181
Meissonnier, M., 33-36
Menzies, Robert T., 29-32, 147-150, 311-312
Miller, T. L., 88-93, 182-186, 313-316
Mizutani, Kohei, 292-293
Munch, Jesper, 234-237
Münkel, Ch., 268-271

Mc

MacDonald, Kenneth R., 212-215
McCarthy, John C., 68-71
McCaul, Eugene W., Jr., 160-162
McGrath, Andrew, 234-237
McIntire, Harold, 220-223
McKay, Jack A., 106-109
McMackin, Lenore, 212-215, 220-223

N

Nagel, E., 33-36
New Technology, 4, 110
Nguyen, Dung Phu Chi, 12-15
Nordin, Gregory P., 119-122
Norris, Douglas, 24-27

O

Ouisse, Adelina, 187-190, 229-232
Olsson, Fredrik A. A., 260-263

P

Papetti, T., 123-126
Paules, Granville E. III, 87
Peters, Bruce R., 284-287, 288-291
Petros, Mulugeta, 12-15, 68-71, 238-240
Phillips, Mark, 98-101
Popescu, Alexandru F., 191-194
Poster Session, 5-7, 152
Potter, J., 43-47
Primmerman, C. A., 48-51
Pueschel, Rudy F., 160-162

Q

Quarrell, J., 123-126

R

Rahm, Stephan, 16-19, 187-190
Raymond, Carol, 38-39
Reardon, Patrick, 284-287, 288-291
Reinhardt, G. A., 48-51
Reitebuch, O., 33-36
Richards, Roger K., 40-41, 224
Richmond, Richard D., 52-57
Romand, B., 33-36
Rothermel, Jeffry, 29-32, 147-150, 163-166
Rutherford, Todd, 241-244
Rye, Barry J., 76, 78-81, 195-197

S

Sauvage, L., 33-36
Schnal, Dane, 98-101
Schrecker, M., 33-36
Schulte, Hans Reiner, 94-97
Shelekhov, Alexander, 272, 282
Shen, Chyau N., 66
Shore, B. W., 111-114
Simpson, Marc L., 224
Singh, Upendra N., 238-240
Smalikho, Igor, 82-85, 132-135, 294-297
Soreide, Dave C., 20-23
Spaceborne Lidars - 1, 3-4, 86
Spaceborne Lidars - 2, 9-10
Special, 1-2, 37, 283
Spiers, Gary D., 167-169, 170-173, 182-186, 302-305
Spinhirne, J. D., 147-150
Sridharan, Arun K., 241-244
Srivastava, Vandana, 128-131, 147-150, 160-162, 163-166, 264-266
Stephens, T., 48-51
Stetter, Roger, 62-65
Stoffelen, A., 102-105
Streicher, Juergen, 16-19, 33-36, 294-297
Sugata, Tetuya, 178-181
Sugimoto, Nobuo, 178-181
System Advances, 8, 245

T

Tamamushi, Kouro, 178-181
Target Characterization, 4-5, 127
Theory and Simulation, 3, 77
Thomas, E., 43-47
Thomson, J. Alex L., 58-61
Tratt, David M., 29-32, 137-140, 144-146, 311-312
Trickl, T., 268-271
Tulloch, William M., 241-244

V

Vaughan, J. M., 141-143, 203-206
Veitch, Peter, 234-237
Vibration Measurements, 2, 42
Voelz, David G., 212-215, 220-223

W

Wergen, Werner, 294-297
Werner, Christian, 16-19, 33-36, 82-85, 132-135, 268-271, 294-297
Westphal, Douglas L., 137-140
Wildgruber, G., 33-36
Williams, John, 24-27
Wind Measurements, 8-9, 267
Winzer, Peter J., 191-194, 225-228
Woppowa, L., 268-271
Wulfmeyer, Volker, 76, 278-281

Y

Yanagisawa, Takayuki, 198-201
Young, R. I., 203-206
Yu, Jirong, 238-240

Z

Zarader, J. L., 174-177
Zyra, Stan, 202

REPORT DOCUMENTATION PAGEForm Approved
OMB No. 0704-0188

Public reporting burden for this collection of information is estimated to average 1 hour per response, including the time for reviewing instructions, searching existing data sources, gathering and maintaining the data needed, and completing and reviewing the collection of information. Send comments regarding this burden estimate or any other aspect of this collection of information, including suggestions for reducing this burden, to Washington Headquarters Services, Directorate for Information Operation and Reports, 1215 Jefferson Davis Highway, Suite 1204, Arlington, VA 22202-4302, and to the Office of Management and Budget, Paperwork Reduction Project (0704-0188), Washington, DC 20503

1. AGENCY USE ONLY (Leave Blank)**2. REPORT DATE**

November 1999

3. REPORT TYPE AND DATES COVERED

Conference Publication

4. TITLE AND SUBTITLETenth Biennial Coherent Laser Radar Technology
and Applications Conference**5. FUNDING NUMBERS****6. AUTHORS**

M.J. Kavaya, Compiler

7. PERFORMING ORGANIZATION NAME(S) AND ADDRESS(ES)George C. Marshall Space Flight Center
Marshall Space Flight Center, Alabama 35812**8. PERFORMING ORGANIZATION
REPORT NUMBER**

M-948

9. SPONSORING/MONITORING AGENCY NAME(S) AND ADDRESS(ES)National Aeronautics and Space Administration
Washington, DC 20546-0001**10. SPONSORING/MONITORING
AGENCY REPORT NUMBER**

NASA/CP-1999-209758

11. SUPPLEMENTARY NOTESProceedings of a conference held in Mount Hood, Oregon, June 28-July 2, 1999
Prepared for Earth Science Department, Science Directorate**12a. DISTRIBUTION/AVAILABILITY STATEMENT**Unclassified-Unlimited
Subject Category 35
Standard Distribution**12b. DISTRIBUTION CODE****13. ABSTRACT (Maximum 200 words)**

The tenth conference on coherent laser radar technology and applications is the latest in a series beginning in 1980 which provides a forum for exchange of information on recent events current status, and future directions of coherent laser radar (or lidar or lader) technology and applications. This conference emphasizes the latest advancement in the coherent laser radar field, including theory, modeling, components, systems, instrumentation, measurements, calibration, data processing techniques, operational uses, and comparisons with other remote sensing technologies.

14. SUBJECT TERMS

coherent, lidar, heterodyne

15. NUMBER OF PAGES

330

16. PRICE CODE

A15

**17. SECURITY CLASSIFICATION
OF REPORT**

Unclassified

**18. SECURITY CLASSIFICATION
OF THIS PAGE**

Unclassified

**19. SECURITY CLASSIFICATION
OF ABSTRACT**

Unclassified

20. LIMITATION OF ABSTRACT

Unlimited